

Confocal Microscopy Studies of Fluorescence Blinking of Semiconductor Quantum Dots, Metal  
Nanoparticle Photogeneration, and Multiphoton Photoemission from Thin Metal Films and  
Metal Nanoparticles

by

Thomas Athanasius Baker

B.S., Massachusetts Institute of Technology, 2000

M.A., Texas Tech University, 2002

A thesis submitted to the  
Faculty of the Graduate School of the  
University of Colorado in partial fulfillment  
of the requirement for the degree of Doctor of Philosophy  
Department of Chemistry

2012

This thesis entitled:  
Confocal Microscopy Studies of Fluorescence Blinking of Semiconductor Quantum Dots, Metal  
Nanoparticle Photogeneration, and Multiphoton Photoemission from Thin Metal Films and  
Metal Nanoparticles  
written by Thomas Athanasius Baker  
has been approved for the Department of Chemistry

---

David J. Nesbitt

---

Steven T. Cundiff

Date \_\_\_\_\_

The final copy of this thesis has been examined by the signatories, and we find that both the content and form meet acceptable presentation standards of scholarly work in the above mentioned discipline.



Baker, Thomas Athanasius (Ph.D., Chemical Physics)

Confocal Microscopy Studies of Fluorescence Blinking of Semiconductor Quantum Dots, Metal Nanoparticle Photogeneration, and Multiphoton Photoemission from Thin Metal Films and Metal Nanoparticles

Thesis directed by David J. Nesbitt

### Abstract

Since the advent of single molecule spectroscopy in 1989, advances in the field have revealed a wealth of information on dynamics and sample heterogeneity unobtainable by traditional ensemble studies. Microscopy experiments are a common technique to characterize and probe single molecule dynamics, due to the combination of the diffraction limited spatial resolution and the availability of sensitive single photon/electron detectors. Additionally, high excitation power densities can be achieved by the use of large numerical aperture objectives with moderately intense light sources. Fluorescence intermittency, or blinking, is a unique property found in the emission of single molecules. A series of experiments are undertaken to elucidate contributions to the blinking dynamics in nanocrystal semiconductors, or quantum dots (QDs). Investigations of the transitions from “on” to “off” (and vice versa) in the absence of laser illumination allow for the determination of the roles of *light* versus *non-light* induced processes for single blinking QDs. Small molecules are found to influence QD blinking by altering the surface trap state distribution due to changes in the electrochemical potential of the solution. However, fluorescence detection is only one implementation to investigate single molecule systems by microscopy. Nanoscale metal materials possess many interesting electronic and optical properties that enable single molecule or particle detection. Silver and gold metal nanoparticles are of particular interest due to their surface plasmon resonances (SPRs), a

collective electron oscillation excited in the near ultraviolet and visible range. As a result of the coherent electron oscillations on the surface of the particle, large electric fields are generated in the vicinity of the nanostructure. This local enhancement of the electric field enables molecular detection in the vicinity of particles by surface-enhanced Raman scattering (SERS). One difficulty with conventional systems used to study SERS is the large enhancement variability observed between nanoparticles on the same substrate, where typically only 1 in 100-1000 are found to have the necessary enhancement factors. Photogeneration of Ag nanoparticles within a thin silver perchlorate/polystyrene polymer film form reproducible SERS active nanoparticles that can be monitored and characterized by Raman microscopy. Insight into the growth mechanism of the nanoparticles is provided by analysis of the time dependent data with an Avrami kinetic phase transformation model. The environment in which the nanoparticles are generated is found to influence both the photogeneration kinetics and the nanoparticles SERS activity. Information on the size and morphology of the nanoparticles provided by AFM and dark field scattering measurements allowing for correlation of photophysical properties with nanoparticle shape. Lastly, the electric field enhancements, exploited by SERS in the Ag nanoparticle system, are investigated for Au single nanoparticles by multi-photon photoemission (MPPE). The construction of a Scanning Photoionization Microscope (SPIM) combines the spatial resolution of an optical microscope with the sensitivity for electron detection arising from photoionization of metal nanostructures by femtosecond laser pulses. Investigations into thin metal films determine the viability of the technique to probe multi-photon photoemission. Examinations of various nanostructures provide insight into the role of the plasmon in the photoemission process. The magnitude of the enhancement field is intimately related to the

photoelectron yield, such that simulations of near-field effects are able to explain wavelength and polarization dependence for photoemission from metal nanostructures.

This thesis is dedicated to my parents,  
for taking me to a science museum in every city we visited.

## Acknowledgements

This thesis is enriched by the influence and aid of many people throughout, and even before, graduate school. This section is a small attempt to acknowledge and thank them for their invaluable contribution to my scientific growth.

Firstly, I thank my parents - Tom and Jane - for always being there for me as well as their encouragement through the years. Whenever we visited a new city as I was growing up, education was always a top priority, from historical sites to museums to local culture. As I got older, the museums we chose to visit became more tailored to my interests in science. Graciously, my parents always let me explore the exhibits to completion without a sense of being rushed. For their support, I am eternally grateful.

My interest in chemistry began at Lubbock High School in Mr. Chuang's chemistry class. While I was in his class, he began an outreach program for the school district entitled "Chemistry Circus." The idea was to do chemistry demonstrations in elementary schools in order to teach simple chemical concepts and encourage interest in science. A secondary, and more personal, result was my total infatuation with chemistry. He allowed me to go through demonstration books to select new and interesting experiments to try in the lab; even the ones he knew would never be allowed to travel to the schools. This thesis might not have been written if it wasn't for the thermite reactions, alcohol rockets, dancing gummy bears (in molten potassium chlorate), and paraffin fireballs that we practiced on Friday mornings during class.

In addition to teaching me two years of chemistry, Mr. Chuang also got my research career started by finding a summer research program for me to attend. At the Welch Summer Scholars program at the University of Texas - Arlington, H.K. McDowell was my first research

advisor. The next summer I worked with Greg Gellene at Texas Tech University on electronic structure calculations of conjugated dye molecules. These experiences continued to fuel my interest in chemistry as well as my attraction to research. I went to college, majored in chemistry (Course V) and did undergraduate research with Kit Cummins at MIT. After college, I returned to Greg Gellene's group at TTU to pursue a Masters in physical chemistry. I had found my true niche in PChem – the artful blend of math, computer science, physics, and chemistry.

I thank the entire chemistry faculty at CU, especially the professors who taught the first year courses: Casey Hynes, David Jonas, David Nesbitt, and Robert Parson. Their lectures and problem sets provided an excellent base for my graduate career. I also want to thank my thesis committee members: Veronica Bierbaum, Eric Cornell, Steve Cundiff, David Nesbitt, and Mathias Weber. Their questions and comments helped make this thesis what it is.

This thesis cannot be approximated as a spherical object in a vacuum, and I must thank my coworkers in the Nesbitt group. Of special note are the postdocs I worked with most closely in the lab: Oliver Monti-Masel, Jose Hodak, Vasiliy Fomenko, Jeff Peterson, Volker Schwiekard, Andrej Grubisic, Kevin Early, Lora Nugent-Glandorf, and Larry Fiegland. Other postdocs in the group provided many useful discussions or advice: Richard Walters, Erin Sharp-Williams, and Rob Roscioli. My fellow graduate students in the group also played a large role. A special thank you to Bradford Perkins for being my Tuesday morning meeting partner for many years. A general thanks to the other graduate students I worked with while I was here: Erin Whitney, Mike Deskevich, Alex Zolot, Mike Ziemkiewicz, Julie Fiore, Melanie Roberts, Andy Gisler and Erik Holmstrom. A nod to fellow graduate students from my entering class, Jack Barbara and Troy Walton, for many conversations, lunches, and bike rides.

Thank you to David Nesbitt for being my advisor and mentor. His breaking a problem down to the simplest physical picture is a trait I have incorporated into my scientific toolkit. I also learned from him that while signal is important, understanding noise is crucial. I will always understand the noise in any experiment I perform, and will help others by understanding their noise as well. Additionally, his helpful advice in developing a story for presentations and papers has helped make this thesis what it is and will greatly aid in my future work

I must thank all the JILA staff as well. Their help and assistance is immeasurable, which is saying something since they are associated with NIST. The electronics group was always there to help troubleshoot a circuit, fix broken equipment, or loan a useful device. Computing also kept things running smoothly in the lab, especially J R Raith who was always willing to switch out my computer power supply when it failed. The JILA machine shop crew always went above and beyond to help. A special thanks to Hans Green and Todd Asnicar for making (or fixing) something that worked better than my initial plans. I give a wealth of gratitude to Dave Alchenburger for his help and assistance. Dave was responsible for important steps in sample preparation, and taught me several characterization techniques that helped each project. He was always willing to do a last minute deposition so that I could make a sample with minimal surface contamination.

I also want to thank the funding agencies that provided the financial support necessary to complete these studies. The Department of Education's Graduate Assistance in Areas of National Need (GAANN) program supported me for several years in the beginning of my career. The Air Force Office of Scientific Research and National Science Foundation both contributed throughout the years as well.

A thank you to Boulder in general, especially the roads in the area where I solved many problems while on a long bike ride. A note of appreciation to the Sundown Saloon for their dart boards and pool tables that were sure to help after a long week.

Lastly, I must give a tremendous thank you to my amazing wife, Sarah, for her support and continual cheering. It was quite the process, but her words of encouragement helped greatly in the final push to the end.



## Contents

1 Introduction.....	1
1.1 Quantum Dot Fluorescence Intermittency .....	2
1.2 SERS Active Photogenerated Silver Nanoparticles .....	4
1.3 Multiphoton Photoemission of Metal Nanostructures .....	7
References .....	8
2 Experiment.....	11
2.1 Confocal Microscope .....	11
2.2 Wide Field Detection .....	15
2.3 Scanning Photoionization Microscopy.....	21
References .....	26
3 Single Molecule Studies of Quantum Dot Fluorescence Intermittency: Evidence for Both Dark and Light-Assisted Blinking Dynamics.....	27
3.1 Introduction .....	27
3.2 Experiment .....	33
3.3 Results .....	36
3.4 Discussion .....	43
3.5 Summary .....	51
References .....	52
4 Blinking Suppression for Quantum Dots in Aqueous Solution by Phenol.....	56
4.1 Introduction .....	56
4.2 Experiment .....	61
4.3 Results .....	63
4.4 Discussion .....	69

4.5 Summary .....	75
References .....	76
<b>5 Fluorescence Trajectory Simulations of QD Blinking .....</b>	<b>79</b>
5.1 Introduction .....	79
5.2 Simulation Details .....	82
5.3 Traditional Threshold Analysis .....	85
5.4 Additional Analysis Approaches .....	91
5.5 Conclusions .....	103
References .....	105
<b>6 Kinetic Studies of the Photogeneration of Silver Nanoparticles .....</b>	<b>107</b>
6.1 Introduction .....	107
6.2 Experiment .....	112
6.3 Results .....	116
6.4 Avrami Kinetic Analysis .....	125
6.5 Summary .....	136
References .....	137
<b>7 Vapor Phase Chemical Influences on Silver Nanoparticle Surface Enhanced Raman and Photogeneration Kinetics .....</b>	<b>141</b>
7.1 Introduction .....	141
7.2 Experiment .....	144
7.3 Effect of Environment .....	148
7.4 Wide-field Experiments .....	158
7.5 Summary .....	163
References .....	164

8 Imaging Nanostructures with Scanning Photoionization Microscopy .....	167
8.1 Introduction .....	167
8.2 Experiment .....	169
8.3 Results .....	172
8.4 Discussion .....	178
8.5 Summary .....	182
References .....	183
9 Multi-photon Scanning Photoionization Microscopy for Single-Particle Studies of Plasmonic Metal Nanostructures .....	186
9.1 Introduction .....	189
9.2 Setup and Materials .....	194
9.3 Imaging Lithographic Metal Nanostructures .....	196
9.4 Photoemission from Single Gold Nanorods .....	200
9.5 Summary and Conclusions .....	211
References .....	212
10 Plasmonic Electron Photoemission Microscopy of Au Nanoholes and Nanohole Dimers .....	219
10.1 Introduction .....	219
10.2 Experiment .....	222
10.3 Nanohole Monomers .....	226
10.4 Nanohole dimers .....	236
10.5 Discussion .....	241
10.6 Summary .....	247
References .....	250

11 Bibliography .....	253
A Analysis Code .....	287
A.1 Main Panel and Functions .....	287
A.2 Blinking Analysis .....	297
A.3 Multichannel Analysis.....	306
A.4 F-Number Analysis .....	310
A.5 Maximum Likelihood Estimation .....	320
A.6 Correlation and Power Spectral Density .....	328
A.7 Intensity Change Point Analysis .....	346
A.8 Shutter Analysis .....	358
A.9 Avrami Fit .....	369
B Simulation Code.....	373
B.1 User Interface .....	373
B.2 Main Program .....	375
B.3 Simulation Details .....	378
B.4 Extra Functions.....	382

## List of Figures

2.1	Photon antibunching measurements .....	15
2.2	Wide field extension .....	16
2.3	CCD calibration .....	19
2.4	Home built <i>in vacuo</i> microscope .....	22
2.5	Calibration of piezo elements .....	24
2.6	SPIM Schematic.....	25
3.1	Kinetic scheme for QD blinking.....	32
3.2	Experimental setup for shutter studies.....	36
3.3	Sample data for observed dark transitions.....	37
3.4	Variability of the survival probability between different QDs.....	39
3.5	Time dependent survival probabilities.....	41
3.6	$S_{\text{on-on}}$ and $S_{\text{off-off}}$ under different experimental conditions.....	43
3.7	Comparison between light and dark rates.....	47
4.1	Two possible models for blinking suppression. ....	59
4.2	Sample trajectories in the absence and presence of phenol.....	64
4.3	Sample “on” time distributions and effect of phenol on $m_{\text{on}}$ .....	65
4.4	Phenol effects on other metrics.....	68
4.5	Constant PhOH or PhO <sup>-</sup> slices .....	69
4.6	Complete data set for different phenol concentrations and pH.....	70
4.7	Effects of different species on $F_{\text{on}}$ .....	74
5.1	Sample simulation of blinking data .....	86
5.2	Threshold “on”/”off” analysis for the previous trajectories .....	87
5.3	Extracted power law slope versus input value.....	88
5.4	Analysis of a power dependent simulation series.....	89

5.5	Binning effects in observed probability distributions .....	90
5.6	Fraction "on" time as a function of $m_{on}/m_{off}$ .....	92
5.7	Correlation and power spectra density plots for an exponential distribution .....	95
5.8	Sample power spectral density plots for a power law distribution .....	96
5.9	Extracted power law slope from PSD versus input value .....	98
5.10	PSD sample data for different fastest rates .....	99
5.11	PSD plots for a truncated power law distribution .....	100
5.12	PSD plots showing the effect of truncation time on the shape .....	102
5.13	Effect of signal to background ratio on PSD plots .....	103
6.1	Experimental setup .....	114
6.2	Raman intensity images .....	117
6.3	Raman spectra from photogenerated nanoparticles .....	118
6.4	AFM of photogenerated nanoparticles .....	120
6.5	Raman spectra after doping with thiophenol .....	123
6.6	Sample trajectories of silver nanoparticle photogeneration .....	126
6.7	Least squares fits of the data to the Avrami model .....	131
6.8	Excitation power dependence of fit parameters .....	132
7.1	Experimental setup .....	145
7.2	Comparison of Ar and O <sub>2</sub> purge .....	149
7.3	O <sub>2</sub> effects in silver nanoparticle generation .....	151
7.4	Trajectories before and after water vapor exposure .....	152
7.5	Trajectories during water vapor exposure .....	154
7.6	Trajectories showing water vapor pressure dependence .....	155
7.7	Avrami parameters for different partial pressures of water .....	157
7.8	Dark field spectra of photogenerated particles .....	159

7.9	Series of frames from a wide-field Raman movie .....	160
7.10	Comparison of wide-field Raman, darkfield and AFM images.....	161
7.11	Time trajectories from wide-field Raman movie.....	163
8.1	Experimental setup.....	170
8.2	Example fluorescence image .....	173
8.3	Power dependence of photoemission current .....	174
8.4	Comparison between AFM and SPIM images.....	176
8.5	Retarding field measurement .....	177
8.6	Spatial resolution of electron source.....	179
8.7	Two photon photoemission as a function of film thickness .....	180
9.1	SPIM setup.....	189
9.2	SPIM images.....	195
9.3	Gold nanorod data.....	197
9.4	Polarization dependence of gold nanorods .....	199
9.5	Silver sphere data.....	201
9.6	Polarization dependence of silver spheres .....	206
9.7	Photoemission yield from various nanostructures .....	207
9.8	Time dependence of photoemission signal .....	210
10.1	Sample preparation .....	223
10.2	AFM and SPIM images of small nanohole monomers.....	227
10.3	Polarization data for small nanohole monomer .....	228
10.4	Polarization data for a large nanohole monomer .....	229
10.5	COMSOL predictions for nanohole monomers.....	232
10.6	Polarization data for small nanohole dimer .....	236
10.7	Polarization data for large nanohole dimer .....	237

10.8	COMSOL predictions for nanohole dimers .....	238
10.9	Theoretical and experimental polarization dependences for nanohole dimers .....	242



## Chapter 1

### Introduction

Experiments in chemistry and physics are often restricted to ensemble studies of molecules due to detection sensitivity or other experimental concerns. The consequence of this limitation is that many experiments are able to determine average properties well, but are unable to detect dynamics or heterogeneity within the sample. In 1989, the first experiments were reported for absorption spectroscopy of single pentacene molecules by Moerner and Kador at liquid helium temperatures.<sup>1</sup> The following year, Orrit and Bernard reported the detection of fluorescence from individual pentacene molecules,<sup>2</sup> which lead to new insights into previously unobservable dynamics.<sup>3</sup> Single molecule experiments have expanded since these early studies to include a variety of novel fluorescence methods<sup>4-9</sup> and force spectroscopies.<sup>10</sup> The ability to monitor only one molecule at a time has exposed the presence of sub-populations in biomolecular systems previously masked in the ensemble.<sup>11,12</sup> Tracking the motion of individual molecules has also allowed the determination of precise step sizes for molecular motors.<sup>13</sup> These are just a few examples showing the unique information obtained from single molecule studies.

Confocal microscopy is a subset of fluorescence microscopy and a common technique to characterize and probe single molecule dynamics by laser excitation in the visible. The diffraction limited spatial resolution ( $d = \frac{1.22\lambda}{2NA}$ ) restricts the excitation volume, while the confocal pinhole further confines the detection volume in the z-direction to a few microns.<sup>14</sup> If the molecules are in sufficiently low concentration to be well separated from each other, it is possible to excite only an individual molecule. When combined with sensitive detectors, such as

avalanche photodiodes (APDs) in the visible, the routine detection of individual molecules is achieved. Another benefit of confocal microscopy is the ability to use relatively inexpensive low power lasers, yet still achieve high power densities, due to focusing with large numerical aperture objectives. Confocal microscopy can be adapted to investigate a broad range of systems by varying the excitation or detection method. Three different experimental approaches are presented here: i) fluorescence blinking of quantum dots, ii) surface enhanced Raman scattering from silver nanoparticles, and iii) multiphoton photoemission microscopy of nanostructured materials.

### **1.1 Quantum Dot Fluorescence Intermittency**

The first section of this thesis investigates the phenomenon of intermittency, or blinking, found in the fluorescence emission of single molecules. The intensity from a single emitter is subject to abrupt fluctuations between states of high (“on”) and low (“off”) quantum yield for emission, despite the molecular system being subjected to continuous illumination.<sup>3</sup> Initial predictions of such blinking behavior were confirmed in single molecule laser induced fluorescence studies, which were interpreted based on photoinduced conversion between singlet and triplet manifolds.<sup>3,15</sup> In particular, these systems yield cleanly single exponential behavior in the distributions of times in the “off” manifold, corresponding to combined kinetic relaxation of the metastable triplet through either radiative (phosphorescence) or nonradiative (quenching) channels.

However, other systems revealed intermittency over time scales longer than could be accounted for by phosphorescent pathways. These systems required a more profound change in the molecular system to accompany both the blinking and recovery.<sup>16</sup> Since these early studies, “blinking” has proven to be a remarkably ubiquitous phenomenon observed in a wide array of

single molecule microscopy studies, though the fundamental origins of this process still remain incompletely understood. Unfortunately, detailed kinetic investigations of such blinking dynamics over sufficiently wide ranges of time scales are seriously limited by the finite number of photon absorption events that are obtained prior to irreversible photobleaching of the molecular system.

A major experimental advance in achieving this understanding was therefore afforded through pioneering studies of semiconductor colloidal quantum dots (QD) by Bawendi and coworkers,<sup>17</sup> which revealed one of the earliest examples of pronounced blinking dynamics at the single nanoparticle level. QDs allow for a particularly interesting experimental platform, by virtue of their large absorption cross section and greater long term photostability.<sup>18</sup> These experimental improvements in both signal and photolongevity enabled Kuno et al.<sup>19,20</sup> to probe single QD blinking dynamics over an unprecedented range of time scales, from 100s of sec down to 100s of  $\mu$ s. Of special interest, these studies revealed highly non-exponential blinking time distributions, but which proved to be remarkably well characterized by a power law, i.e.,  $P(t) \propto (1/t)^m$ , over 8-9 orders of magnitude in probability and 5-6 orders of magnitude in time. Such strikingly non-exponential behavior invalidated the simple picture of individual rate constants for blinking and recovery, and instead required more complex models based on “distributed kinetics” which access a wide dynamic range of rate processes.<sup>21</sup>

One widely held interpretation of this phenomenon has been that the switching from “on” to “off” is a result of a photoassisted charge ejection process (either hole or electron) that leaves the core of the QD charged, thereby allowing fast and efficient non-radiative recombination rates to dominate.<sup>22</sup> RENEUTRALIZATION of the core then returns the QD to its normal fluorescent state. With this model in mind, many experiments were designed to elucidate the origin of these

broadly distributed power law time scales. For example, the composition,<sup>23-25</sup> size<sup>20</sup> and shape<sup>26</sup> of the QD have all been varied in an attempt to alter the charge ejection process and better understand the mechanism of the blinking.

In this thesis, a series of experiments are undertaken to further elucidate the dynamics of QD blinking. Previous studies of QD blinking have been performed in the presence of constant illumination of the sample, either with cw lasers or high repetition rate pulsed lasers. While this allows for the constant interrogation of the QD state, it does not permit the observation of pure *non-photoactivated* kinetics for blinking or blinking recovery. Investigations here of the transitions from “on” to “off” (and vice versa) in the absence of laser illumination allow for the determination of the role of light versus non-light induced processes for single blinking QDs. Several small molecules have been found to suppress QD blinking in aqueous solution<sup>27,28</sup> or in thin films.<sup>29</sup> Two distinct models are set forth to elucidate the mechanism by which small molecules influence QD blinking. In the first, the molecule acts as a Lewis base and fills surface trap states by forming an adduct with the QD. Alternatively, the molecule influences the trap state population by changing the electrochemical potential of the solution. In order to reveal which model is correct, phenol is selected due to its ability to act as both a Lewis base and a redox agent in aqueous solution. Lastly, theoretical simulations are developed to enable the examination of simple models to account for the blinking and afford connections to experimental analysis techniques.

## **1.2 SERS Active Photogenerated Silver Nanoparticles**

A secondary theme in this thesis focuses on metal nanoparticles that enable single molecule or particle characterization without fluorescence detection. Nanoscale metal materials possess many interesting electronic and optical properties not present for the bulk metal sample.

Synthetic and sample preparation techniques have improved to allow for the study of the size and shape dependence of ensemble properties such as absorption and emission characteristics of noble metal nanoparticles.<sup>30-32</sup> Silver and gold are of particular interest due to their surface plasmon resonance (SPR), a collective electron oscillation that is excited in the near ultraviolet and visible range. The convenience of visible laser excitation in this region coupled with the strong size, shape and proximity dependence on the spectral properties make these metals a natural choice for a multitude of research and commercial applications.

The SPR properties of gold particles have long been recognized and empirically exploited in the development of stained glass since medieval times.<sup>33</sup> Mie provided the first modern physical understanding of the phenomenon by solving Maxwell's equations for the interaction of light with small spherical particles, which has been applied frequently to predict the optical properties of metallic nanostructures. Improved synthesis techniques<sup>30,34</sup> have allowed for the experimental confirmation of the plasmon resonance in a variety of shapes and sizes, as well as control by varying the nanoparticle chemical composition.<sup>35-37</sup>

Study of the SPR is not merely limited to the sensitivity of its optical absorption to the morphology of the nanoparticle. As a result of the coherent electron oscillations on the surface of the particle, for example, large electric fields are generated in the vicinity of the nanostructure. Theoretical and experimental efforts have been made to understand the nature of these local induced electric fields in the vicinity of the nanoparticle as a result of optical excitations of the SPR.<sup>38,39</sup> These local fields can be further enhanced by bringing multiple particles into proximity with one another. Experiments on nanoparticles fabricated by electron and ion beam lithography techniques have provided a greater level of control and thus a better understanding of the effects. Specifically, dimers of nanoparticles have demonstrated nonlinear enhancement of

electric fields localized in the interstitial regions between particles.<sup>40-43</sup> Theoretical investigations<sup>40</sup> have suggested that enhancements as large as  $10^5$  in the local electric field are possible in the region between closely spaced nanoparticles.

The middle chapters of this thesis center on the photogeneration of silver nanoparticles that enable surface-enhanced Raman scattering (SERS), which arises from the local enhancement of the electric field in the vicinity of particles due to the SPR. Studies indicate that SERS has resulted in Raman cross section enhancements by as much as 8 orders of magnitude, allowing for detection of single molecules<sup>44,45</sup> with signal levels comparable to fluorescent dyes. The original SERS effect was discovered on roughened silver electrodes and subsequently much effort has been expended into producing more efficient substrates. Colloidal silver nanoparticles offer another option due to the ability to tailor particle shape and size. Results from several groups,<sup>39,44</sup> however, indicate that only 1 in 100-1000 particles/clusters show measureable SERS activity. This low activity is thought to arise because only a few particles, or collections of particles, have the geometries necessary to produce large local electric field enhancements. Indeed, Camden et al.<sup>45</sup> combined single molecule SERS and high-resolution transmission electron microscopy to correlate nanostructure shape with single molecule sensitivity. They observed a wide range of structures which resulted in SERS, from dimers to more complicated overlapping structures. Interestingly, they found no *single* nanocrystals that showed single-molecule activity, providing further evidence that SERS arises from excitation of molecules that reside in high local field regions (i.e. “hot spots”), of dimers and clusters. These hot spots are typically located in the interface and junctions between nearby (<1 nm) silver particles, as further confirmed by theoretical calculations.<sup>46,47</sup>

The unique combination of excitation and detection provided by confocal microscopes provides an ideal way to study the photogeneration of Ag nanoparticles with high spatial and temporal resolution. Examinations of the formation kinetics of silver particles formed by the photoreduction of silver ions in a thin silver perchlorate/polystyrene polymer film are presented herein. The particle growth is monitored via intense surface-enhanced Raman scattering of molecules on the silver nanoparticle surface. Insight into the growth mechanism of the nanoparticles is provided by analysis of the time dependent data with an Avrami kinetic phase transformation model. The environment in which the nanoparticles are generated is found to influence both the photogeneration kinetics and the nanoparticle SERS activity. Wide field super resolution techniques are employed to elucidate the cause of the highly dynamic signals observed for fully generated features. Additional information on the size and morphology of the nanoparticles is provided by AFM and dark field scattering measurements.

### **1.3 Multiphoton Photoemission (MPPE)**

As a final focus of this thesis, the electric field enhancements of metal nanoparticles are probed by multi-photon photoemission (MPPE), in which electrons are photoionized from metal nanostructures by intense laser pulses. The construction of a scanning photoionization microscope (SPIM) combines the spatial resolution of an optical microscope with the sensitivity of electron detection. For this experiment, an ultrafast laser is focused to the diffraction limit by a reflective objective in vacuum which results in electron emission from metal structures. Detection of the electrons is achieved in transmission by either a pico-ammeter (1<sup>st</sup> generation) or electron channeltron (2<sup>nd</sup> generation). Investigations into thin metal films determine the viability of the technique to probe multi-photon photoemission. Examinations of nanostructures provide insight into the role of the plasmon in the photoemission process. The magnitude of the

enhancement field is intimately related to the electron yield, such that simulations of near-field effects are able to explain wavelength and polarization dependence for photoemission from a variety of metal nanostructures.

## References

- (1) Moerner, W. E.; Kador, L. *Phys. Rev. Lett.* **1989**, *62*, 2535.
- (2) Orrit, M.; Bernard, J. *Phys. Rev. Lett.* **1990**, *65*, 2716.
- (3) Basche, T.; Kummer, S.; Brauchle, C. *Nature* **1995**, *373*, 132.
- (4) Moerner, W. E.; Fromm, D. P. *Rev. Sci. Instr.* **2003**, *74*, 3597.
- (5) Patterson, G.; Davidson, M.; Manley, S.; Lippincott-Schwartz, J. *Ann. Rev. Phys. Chem.* **2010**, *61*, 345.
- (6) Roy, R.; Hohng, S.; Ha, T. *Nature Methods* **2008**, *5*, 507.
- (7) Eggeling, C.; Fries, J. R.; Brand, L.; Günther, R.; Seidel, C. A. M. *Proc. Nat. Acad. Sci.* **1998**, *95*, 1556.
- (8) Ha, T.; Enderle, T.; Chemla, D. S.; Selvin, P. R.; Weiss, S. *Phys. Rev. Lett.* **1996**, *77*, 3979.
- (9) Weiss, S. *Science* **1999**, *283*, 1676.
- (10) Neuman, K. C.; Nagy, A. *Nature Methods* **2008**, *5*, 491.
- (11) Rueda, D.; Bokinsky, G.; Rhodes, M. M.; Rust, M. J.; Zhuang, X.; Walter, N. G. *Proc. Nat. Acad. Sci.* **2004**, *101*, 10066.
- (12) Tomov, Toma E.; Tsukanov, R.; Masoud, R.; Liber, M.; Plavner, N.; Nir, E. *Biophys. J.* **2012**, *102*, 1163.
- (13) Yildiz, A.; Forkey, J. N.; McKinney, S. A.; Ha, T.; Goldman, Y. E.; Selvin, P. R. *Science* **2003**, *300*, 2061.
- (14) Conchello, J.-A.; Lichtman, J. W. *Nature Methods* **2005**, *2*, 920.
- (15) Vogel, M.; Gruber, A.; Wrachtrup, J.; Vonborczyskowski, C. *J. Phys. Chem.* **1995**, *99*, 14915.
- (16) Cichos, F.; von Borczyskowski, C.; Orrit, M. *Curr. Opin. Colloid Interface Sci.* **2007**, *12*, 272.



- (17) Nirmal, M.; Dabbousi, B. O.; Bawendi, M. G.; Macklin, J. J.; Trautman, J. K.; Harris, T. D.; Brus, L. E. *Nature* **1996**, *383*, 802.
- (18) Klimov, V. I. *Semiconductor and Metal Nanocrystals: Synthesis and Electronic and Optical Properties*; CRC Press, 2003.
- (19) Kuno, M.; Fromm, D. P.; Hamann, H. F.; Gallagher, A.; Nesbitt, D. J. *J. Chem. Phys.* **2001**, *115*, 1028.
- (20) Kuno, M.; Fromm, D. P.; Hamann, H. F.; Gallagher, A.; Nesbitt, D. J. *J. Chem. Phys.* **2000**, *112*, 3117.
- (21) Frantsuzov, P. A.; Marcus, R. A. *Phys. Rev. B* **2005**, *72*, 155321.
- (22) Efros, A. L.; Rosen, M. *Phys. Rev. Lett.* **1997**, *78*, 1110.
- (23) Kuno, M.; Fromm, D. P.; Gallagher, A.; Nesbitt, D. J.; Micic, O. I.; Nozik, A. J. *Nano Lett.* **2001**, *1*, 557.
- (24) Shimizu, K. T.; Neuhauser, R. G.; Leatherdale, C. A.; Empedocles, S. A.; Woo, W. K.; Bawendi, M. G. *Phys. Rev. B* **2001**, *63*, 205316.
- (25) Verberk, R.; van Oijen, A. M.; Orrit, M. *Phys. Rev. B* **2002**, *66*, 233202
- (26) Wang, S.; Querner, C.; Emmons, T.; Drndic, M.; Crouch, C. H. *J. Phys. Chem. B* **2006**, *110*, 23221.
- (27) Fomenko, V.; Nesbitt, D. J. *Nano Lett.* **2007**, *8*, 287.
- (28) Hohng, S.; Ha, T. *J. Am. Chem. Soc.* **2004**, *126*, 1324.
- (29) Antelman, J.; Ebenstein, Y.; Dertinger, T.; Michalet, X.; Weiss, S. *J. Phys. Chem. C* **2009**, *113*, 11541.
- (30) Mock, J. J.; Barbic, M.; Smith, D. R.; Schultz, D. A.; Schultz, S. *J. Chem. Phys.* **2002**, *116*, 6755.
- (31) Lee, K.-S.; El-Sayed, M. A. *J. Phys. Chem. B* **2006**, *110*, 19220.
- (32) Kelly, K. L.; Coronado, E.; Zhao, L. L.; Schatz, G. C. *J. Phys. Chem. B* **2002**, *107*, 668.
- (33) Kerker, M. *J. Colloid Interface Sci.* **1985**, *105*, 297.
- (34) Wiley, B. J.; Im, S. H.; Li, Z. Y.; McLellan, J.; Siekkinen, A.; Xia, Y. A. *J. Phys. Chem. B* **2006**, *110*, 15666.
- (35) Oldenburg, S. J.; Averitt, R. D.; Westcott, S. L.; Halas, N. J. *Chem. Phys. Lett.* **1998**, *288*, 243.

- (36) Link, S.; Wang, Z. L.; El-Sayed, M. A. *J. Phys. Chem. B* **1999**, *103*, 3529.
- (37) Lee, K. S.; El-Sayed, M. A. *J. Phys. Chem. B* **2006**, *110*, 19220.
- (38) Kelly, K. L.; Coronado, E.; Zhao, L. L.; Schatz, G. C. *J. Phys. Chem. B* **2003**, *107*, 668.
- (39) Emory, S. R.; Nie, S. *J. Phys. Chem. B* **1998**, *102*, 493.
- (40) Hao, E.; Schatz, G. C. *J. Chem. Phys.* **2004**, *120*, 357.
- (41) Atay, T.; Song, J. H.; Nurmikko, A. V. *Nano Lett.* **2004**, *4*, 1627.
- (42) Fromm, D. P.; Sundaramurthy, A.; Schuck, P. J.; Kino, G.; Moerner, W. E. *Nano Lett.* **2004**, *4*, 957.
- (43) Talley, C. E.; Jackson, J. B.; Oubre, C.; Grady, N. K.; Hollars, C. W.; Lane, S. M.; Huser, T. R.; Nordlander, P.; Halas, N. J. *Nano Lett.* **2005**, *5*, 1569.
- (44) Michaels, A. M.; Nirmal, M.; Brus, L. E. *J. Am. Chem. Soc.* **1999**, *121*, 9932.
- (45) Camden, J. P.; Dieringer, J. A.; Wang, Y. M.; Masiello, D. J.; Marks, L. D.; Schatz, G. C.; Van Duyne, R. P. *J. Am. Chem. Soc.* **2008**, *130*, 12616.
- (46) Jin, R. C.; Cao, Y. W.; Mirkin, C. A.; Kelly, K. L.; Schatz, G. C.; Zheng, J. G. *Science* **2001**, *294*, 1901.
- (47) McMahon, J. M.; Henry, A. I.; Wustholz, K. L.; Natan, M. J.; Freeman, R. G.; Van Duyne, R. P.; Schatz, G. C. *Anal. Bioanal. Chem.* **2009**, *394*, 1819.

## Chapter 2

### Experiment

This chapter is split into three sections to address the main experimental apparatus used and constructed to accomplish the research outlined in the Introduction. In the first section, details of our confocal microscope are presented. The specifics for the wide field extension of an inverted microscope to study both Raman and dark field scattering are described secondly. In the last section, the aspects of a scanning photoionization microscope are presented.

#### 2.1 Confocal Microscope

The laser excitation for these experiments is provided by either a pulsed 434 nm diode (PicoQuant, 40 ps) or a continuous wave 532 nm (QED, doubled 1064 nm Nd:YVO<sub>4</sub>). The former is passed through a cylindrical lens telescope (4:1) in order to transform the output elliptical Gaussian focus to a circular beam shape. No astigmatism needs to be corrected for the 532 nm laser. The beam is then sent to combination of a half-wave plate, mounted in a rotation holder, and a polarization cube. This allows the adjustment of the illumination power to arbitrary levels by rotating the laser polarization before selecting the vertical polarization component with the cube. When desired, a quarter-wave plate then optionally converts the beam from vertically to circularly polarized light.

To obtain diffraction limited images, the beam must be expanded to overfill the back aperture of the microscope objective. A common rule is to make sure the 1/e electric field beam radius ( $w$ ) is equal to or larger than the radius of the back aperture.<sup>1</sup> An easy way to determine

the beam size is by measuring the power transmitted through an iris of a given diameter. The power transmitted through a circular aperture is given by  $P(r) = P_o [1 - e^{-2r^2/w^2}]$  where  $r$  is the radius of the aperture and  $w$  is the 1/e electric field radius of the beam. When the diameter of the aperture is equal to  $w$  the equation becomes:  $P_o [1 - e^{-1/2}] = 0.39 * P_o$ . The use of an adjustable iris allows the 1/e electric field beam radius to be easily found, *i.e.*, when the iris is set such that 39% of the total power is detected with a power meter. Therefore, the resultant *diameter* of the iris needs to be at least as large as the *radius* of the back aperture of the microscope objective to achieve diffraction limited resolution. A more accurate way to determine the beam diameter is using drill blanks. By closing the iris around the drill blank, a well-defined opening is achieved and the diameter can easily be measured from the drill blank itself rather than the adjustable iris. This also makes it easy to extract a variety of diameters so the power readings at different radii can then be fit with the equation above instead of using a single point measurement. In the first confocal setup, the 434 nm light is further expanded by an 8:1 telescope. This large expansion is necessary because the objective typically used, 1.4 NA 60X Oil immersion, has a back aperture of 13 mm. Additionally, the use of a Keplerian telescope ( $f_1 = 50$  mm,  $f_2 = 400$  mm) is chosen so that a small aperture fast shutter ( $t_{\text{response}} < 1$  ms) can be placed at the interior focus of the telescope to control the illumination. For the second apparatus, where a fast shutter is not necessary, the 532 nm beam is expanded by a 5:1 Galilean telescope ( $f_1 = -50$  mm,  $f_2 = 250$  mm) to save space on the laser table. This lower magnification is sufficient due to the smaller back apertures for the objectives used in these studies (typically 4-7 mm).

The laser path then enters a periscope to reach the rear input port of the inverted microscope frame where a dichroic reflects the excitation beam upwards through the objective. The two mirrors of the periscope are used to align the beam through the objective. This is achieved by removing the objective and placing a long (>16 inch) lens tube assembly with irises at each end onto the objective mount. By confirming that the beam is centered in both irises over such a distance, the beam is certain to be centered within the back aperture and passing straight through the objective.

The red-shifted luminescence is collected by the same objective, but this time passes through the dichroic, where it is focused by a tube lens out the side port of the microscope frame. The optical detection path is enclosed in lens tubes with baffles to prevent any stray light from being detected. A 75  $\mu\text{m}$  pinhole is placed at this confocal plane to eliminate background fluorescence occurring from regions outside the desired excitation volume – typically 200-400 nm in the lateral dimension and 2-3  $\mu\text{m}$  in the vertical. A single lens placed at  $2f$  collects the light and reimages the pinhole onto an avalanche photodiode (APD, SPCM-AQR-14), which resides in a light tight box.

In order to obtain additional information, a dichroic is often inserted after the lens to separate the emission onto two APDs. This detection scheme allows the determination of the average wavelength of the emission based on the ratio of the signals on each detector. To enable relatively easy changes of this filter, a dichroic wheel from a microscope mounted at  $90^\circ$  is placed in the beam path. The wheel holds up to 7 different filters and kinematically rotates filters in place resulting in minimal mis-alignment. Alternatively, a 50/50 beam splitter is rotated in place to enable analysis of cross correlations or cross power spectral densities.

The signals from the APDs are sent to a time correlated single photon counting (TCSPC) card, where every photon detected is tagged with its macrotime (wall time since start of acquisition), microtime (time between laser pulse and detected photon), and channel (which APD was triggered). These data are temporarily stored in a first in first out (FIFO) buffer which allows data to be continuously acquired while previously attained data are saved to a file. The time tagged format allows for arbitrary binning of the data post-acquisition and does not limit subsequent analysis to a particular observation window. This storage method also allows for the lifetime, obtained from a microtime histogram, to be extracted for any arbitrary window in time or number of photons.

Photon anti-bunching experiments provide confirmation that the observed signal is arising from a single emitter. Unfortunately, the usual setup involves reconnecting the inputs of the TCSPC card in a Hanbury Brown-Twiss (HBT) arrangement, as well as reconfiguring the software settings. In the HBT setup, one detector initiates the timing while the other detector stops the measurement. One common outcome of this alteration is a low duty cycle experiment with loss of signal. Also, in this arrangement, trajectories are unusable for measuring kinetics due to the loss of photons. However, insertion of a delay line (1-4  $\mu\text{s}$ ) in one of the APD channels provides a simple work around when using pulsed laser excitation<sup>2</sup>. The small time delay is not enough to shift the trajectory (fastest binning is usually 1 ms), but does enable the cross correlation of the data to show an anti-bunching dip centered at the delay time. In this manner, confirmation that the trajectories are arising from single emitters is possible while maintaining a high duty cycle and good signal levels. Moreover, the microtime information is preserved which allows the simultaneous extraction of lifetime information.

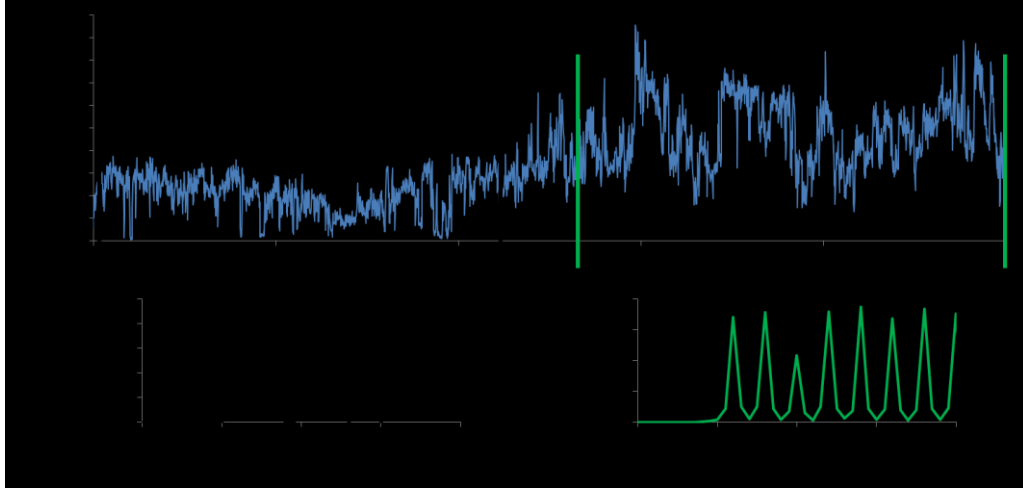


Figure 2.1: Photon antibunching measurements. Sample quantum dot trajectory (upper panel) for two quantum dots in the focus. In the early time (black) of the trajectory there is only one emitter as evidenced by the lack of a signal at  $1 \mu\text{s}$  lag. At later times (green), the correlation at  $1 \mu\text{s}$  is about  $\frac{1}{2}$  the neighboring peaks, indicating the fluorescence is arising from two independent emitters.

Figure 2.1 is data from a QD blinking experiment with a  $1 \mu\text{s}$  delay in one of the channels. The intensity levels in the trajectory suggest either 2 QDs or a single QD with an intermediate state. Inspection of the cross correlation of the data between 30 and 40 seconds (lower left, black trace) reveals a pronounced lack of correlation signal at a lag of  $1 \mu\text{s}$ . Conversely, the cross correlation obtained for data between 42 and 55 seconds (lower right, green trace) shows the  $1 \mu\text{s}$  lag has only a factor of  $\sim 2$  diminishment when compared to neighboring peaks. This corresponds to 2 independent emitters present in the probe volume at one time.

## 2.2 Wide Field Detection

The inclusion of wide field capabilities to the experiment requires additional design and optical elements in the detection side. In order to enable the inclusion of both modes, confocal

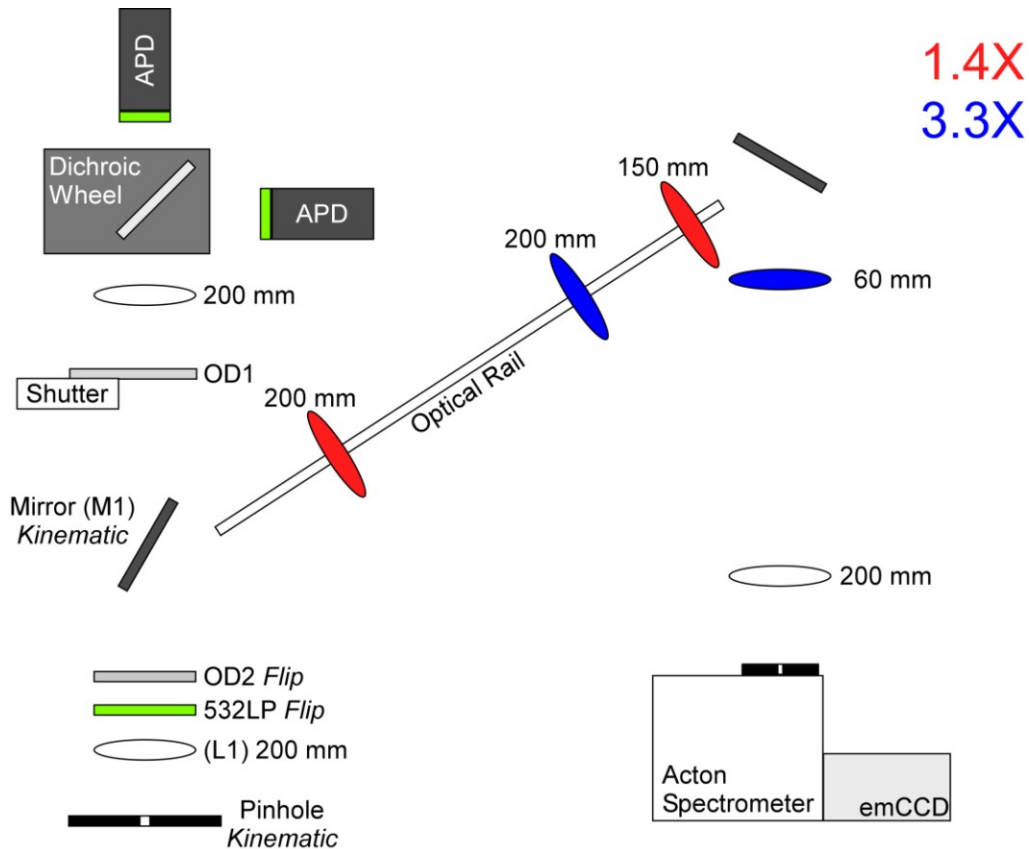


Figure 2.2: Optical layout used for inclusion of both confocal and wide field detection. The *Kinematic* label indicates optics that are mounted on magnetic base plates and can be easily switched in or out. This allows for quick alternations between confocal and wide field imaging modes.

and wide field, the detection arm located in an expanded light tight box is constructed to facilitate easy conversion. The layout of the optical table within this “dark” box is shown in Figure 2.2 and will be now be discussed.

The confocal path, with the mirror (M1) removed, on the left of the figure is similar to that previously described, with a few modifications. The first alteration is that the lens (L1) is no longer at  $2f$ , but now at  $f$  to collimate the beam after passing through the pinhole. This enables the confocal detection path to be arbitrarily extended without the use of long focal length lens, and for the inclusion of various optical elements in the infinity space. A computer controlled (on-off) neutral density filter ( $OD = 1$ ) is included in this region to attenuate the luminescence to



count rates  $< 1$  MHz in order to protect the APDs, for samples which may show exceptionally high signal levels. A dichroic wheel from a microscope is again used, in order to benefit from the ability to rapidly switch between luminescence separation schemes. The signals are monitored by APDs with matched filters (540 nm long pass) mounted in removable lens tubes on the front of the detectors. Moreover, in order to protect the APDs when the dark box is open for adjustments or alignment, a manual beam shutter mounted in a lens tube assembly allows the detector to be completely blocked from light.

To switch into wide field mode, the pinhole is removed and the mirror (M1) is inserted. These two optical elements are mounted on kinematic magnetic base plates that allow quick and easy toggling between modes. To maximize the usability of the experiment with a variety of objectives, two possible telescopes are included in the imaging path which is shown on the right side of the figure. The 2" achromatic doublet lenses are mounted in flip mounts on an optical rail to be swapped in as necessary as well as to maintain the lateral alignment. Telescope 1 (red lenses,  $f_1 = 200$  mm,  $f_2 = 150$  mm) provides a magnification of 1.4X, while telescope 2 (blue lenses,  $f_1 = 200$  mm,  $f_2 = 60$  mm) has a magnification of 3.3X. A final lens ( $f = 200$  mm) focuses the image onto the entrance plane of a spectrometer (Acton SpectroPro 150) described further below.

The spectrometer is a Czerny-Turner design that has a turret able to hold two different gratings. This allows the acquisition of both relatively low resolution spectra (150 grooves/mm,  $\sim 500$  nm bandwidth) and high resolution spectra (600 grooves/mm,  $\sim 125$  nm bandwidth) without loading a new grating. The wavelength axis is calibrated by measuring known lines from either an Hg/Ar or He lamp. The settings for each grating are stored such that the spectrometer can reproducibly switch between the gratings and still maintain its wavelength accuracy. In addition,

the spectrometer operates as a 1:1 imaging system which allows for imaging of the entrance plane/slits while simultaneously acquiring spectra of the luminescence.

For wide field imaging, the slits are lowered so as not to obstruct the incident image while the grating is set to zero order where it operates as a mirror. This allows a two dimensional intensity image to be acquired for the entire field of view. For a 100X objective plus the additional 3.3X telescope, the field of view on the camera corresponds to 30  $\mu\text{m}$  in the sample plane. The largest field of view typically investigated is 180  $\mu\text{m}$  which is a combination of a 40X objective and the 1.4X telescope.

To acquire spectra, the object of interest is centered within the image field of view. The slits are reinserted and set to approximately 10  $\mu\text{m}$  width, which results in a good signal to background ratio. Alternatively, the slits may need to be adjusted such that only one object is contained between the slits. The grating angle is then set such that a given wavelength range is dispersed on the CCD. If the full spectrum extends beyond the range of a single image, multiple spectra can be concatenated from different wavelength scans. Due to the imaging capabilities, the spectra from objects along the vertical axis are separately resolved enabling parallel acquisition.

The camera used in these studies is a 512 x 512 emCCD (Cascade II) with 16  $\mu\text{m}$  x 16  $\mu\text{m}$  pixels. It is thermoelectrically cooled to -60  $^{\circ}\text{C}$  to reduce dark counts which allows for longer acquisition times per frame. As a rule of thumb, dark counts double for every 5-9  $^{\circ}\text{C}$  increase in temperature. By operating at -60  $^{\circ}\text{C}$ , the dark counts are typically around 0.005 per pixel per second. The camera is designed to be sensitive in the visible region with quantum efficiency near 90% between 500 nm and 700 nm, and falling to only 40% by 900 nm. It can be run in two modes with different sensitivities and timing characteristics. In the traditional serial mode the

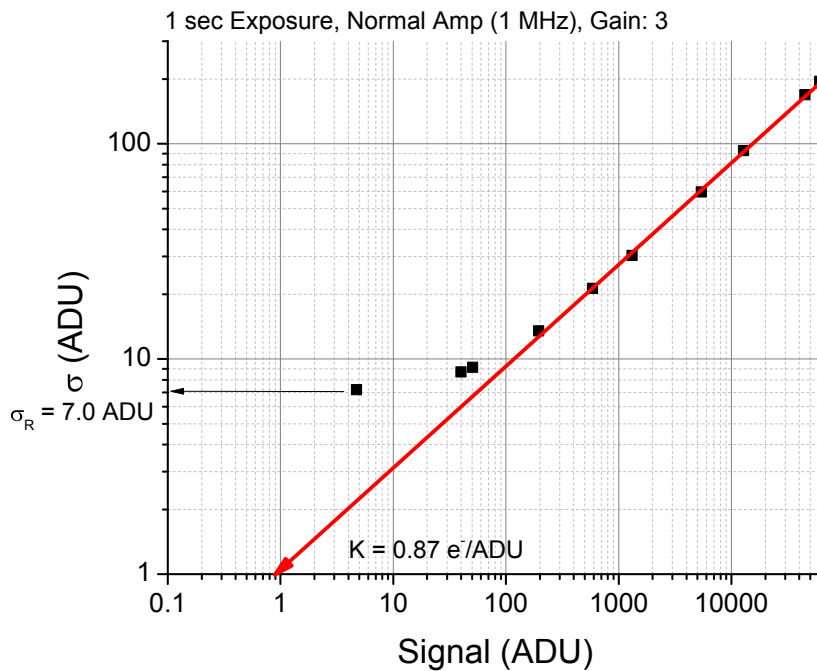


Figure 2.3: Calibration of CCD. The gain (e<sup>-</sup>/ADU) can be calculated from a series of images with increasing illumination. The intercept of the red line with  $\sigma = 1$  is the measured gain, while the read noise is the asymptote at small signal levels.

read noise is small, and the gain is 0.9 analog digital unit (ADU) /e<sup>-</sup> which compares well to most commercial CCD cameras. In the “Electron Multiplier” (EM) mode, additional amplification is provided upon readout, thus the read noise is larger but the gain is now 0.006 ADU/e<sup>-</sup>. Also EM mode, the data can be recorded at 10 MHz, as opposed to only 1 or 5 MHz for the traditional mode. This extends the use of the camera to single photon conditions at faster frame rates for the EM mode.

The conversion between ADUs and electrons is determined from measurements of the noise as a function of signal levels.<sup>3</sup> The noise present in image readout has two components: i) the noise inherent in the CCD readout electronics and ii) the shot noise from electron counting. In order to quantify both components, pairs of images are taken while the light incident on the CCD is increased gradually. Care should be taken to use weak and diffuse light (optics tissue

works as a diffuser in a pinch). To eliminate any remaining illumination inhomogeneity, image pairs are subtracted from each other. The standard deviation of the ADUs is calculated for the processed image and divided by two to provide the noise contribution from one image. These values are then plotted versus the average signal level from one of the images on a log-log plot, an example is shown in Figure 2.3. The plot reveals an initially horizontal (zero slope) region that corresponds to the read noise inherent in the CCD electronics. At larger signal levels,  $\sigma$  increases proportionally to the signal (slope of  $\frac{1}{2}$  on a log-log plot corresponding to shot noise). The intercept of this line (shown in red) with  $\sigma = 1$  represents the gain in e-/ADU.

The widefield experiments can be performed in three different excitation schemes. In the first, wide field Raman is achieved by placing a 500 mm lens in the 532 nm laser excitation path such that it focuses at the back aperture of the microscope. A 540LP filter is placed in the detection path to eliminate laser scatter. The image can be studied by super-resolution techniques, or spectra of individual objects can be obtained as described above.

Bright field images of the substrate can be obtained by using illumination from above the sample. A white light source is focused by a second microscope objective to overlap the collection of the primary inverted objective. The contrast in bright field is low for the majority of the samples studied here. However, it does provide an easy way to make sure the illumination column is aligned with the collection objective.

The last wide field mode used here is dark field scattering, which provides much better contrast for our samples than bright field. A special condenser provides illumination only at angles greater than the collection objective can admit. For example, a 0.65 NA collection objective is used in conjunction with a dark field condenser that only provides light at 0.7-0.9 NA. This results in low to no background, while objects that scatter light become bright spots.

Images of the objects can be obtained to get an idea of coverage as well as the specific locations on the surface. Secondly, dark field scattering spectra can be obtained for the objects as well. This provides the ability to compare single object dark field spectra with a variety of other techniques.

### **2.3 Scanning Photoionization Microscope (SPIM)**

This experiment has two major differences from the previously discussed experiments. Firstly, the aim is to detect multi-photon photoelectrons as opposed to luminescence, and therefore the heart of the microscope is in vacuum. Secondly, the excitation is provided by a femtosecond laser to deliver the high peak powers necessary for a multiphoton process, while maintaining moderate average powers to prevent sample photodamage.

The vacuum chamber is maintained below  $5 \times 10^{-7}$  Torr by a pair of turbo pumps. This pressure ensures that low kinetic energy ( $E < 1$  eV) electrons have a mean free path of nearly 5 m, which is larger than the distance from the sample to the detector (1 cm). The pressure is measured with a photoionization gauge before and after experiments. During experiments the gauge must be off, otherwise the detectors are swamped by the electron emission from the filament.

To use a microscope in vacuum, a few alterations from standard procedures are required. For example, a standard refractive objective should not be used because the forces on the interior lenses during pump down and venting the chamber cause the lenses to shift. This results in an objective which no longer properly focuses to the diffraction limit. A reflective Cassegrain type objective is used instead, in order to eliminate the pressure stresses due to its open and thus naturally vented design. Another benefit of the reflective objective is there is no chromatic

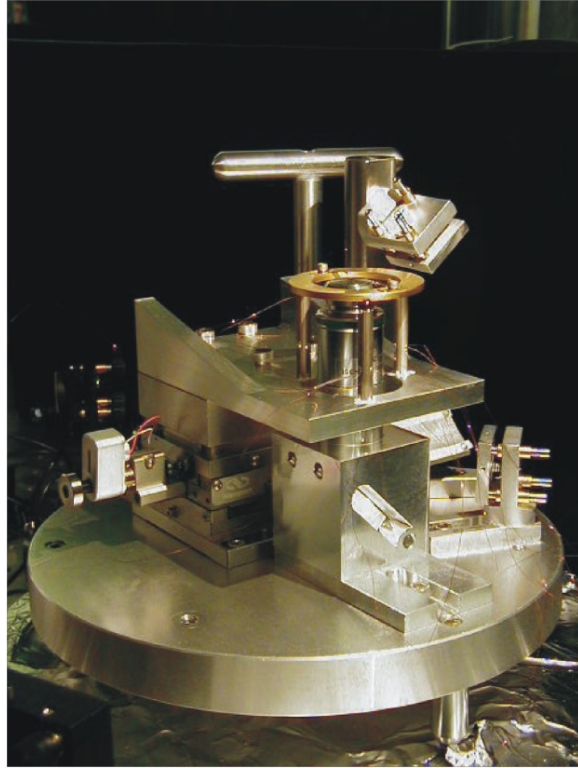


Figure 2.4: Home built *in vacuo* inverted microscope frame

aberration as well as substantially lower group velocity dispersion (GVD), something important to consider when using ultrafast lasers.

A home built inverted microscope frame, shown in Figure 2.4, consists of a series of steering mirrors and a two part scanning stage. The four mirrors permit the excitation to enter from a side port and be directed upwards through the objective. Two of the mirrors are adjustable and are aligned in the same manner as the periscope previously described in the confocal setup through the use of two irises and a long lens tube.

The scanning stage has two sets of elements that provide both coarse and fine sample scanning. The coarse scanning is achieved by a vacuum modified, three dimensional translation stage (1.2 cm travel) controlled by vacuum compatible picomotors. The picomotors enable the stage to move without breaking vacuum in order to observe different regions of the substrate.

Fine scanning of the sample by as much as 40  $\mu\text{m}$  is achieved by a tip/tilt stage consisting of three quadranted piezotubes 120° apart. The hollow piezotubes are affixed to the coarse stage with epoxy. A sample holder ring rests on sapphire balls placed in the tops of the hollow tubes. This ring provides a kinematic support and electrical isolation for the samples to be studied.

Calibration of the fine scanning stage can be accomplished in two ways. In the first, the microscope assembly is removed from vacuum and placed on the laser table. A Michelson interferometer is constructed where the moving arm is a mirror placed on the scanning stage. Using a 633 nm HeNe as the light source, the interference fringes are counted as a function of applied voltage to the piezotubes. The distance versus applied voltage calibration is fit with a second order polynomial and the coefficients are recorded to be used in the acquisition code (SPIM A3). Alternatively, the calibration can be accomplished in vacuum using a resolution standard Cflat TEM grid (Protochip Inc,) where the pitch (4  $\mu\text{m}$ ) and size (2  $\mu\text{m}$ ) of the features is well known. Images are taken of the standard, and a second order polynomial is again fit to the data to reproduce the known spacings and obtain a non-distorted image of the sample, before and after images are shown in Figure 2.5. Care should be taken to not apply voltages to the piezos outside  $\pm 200$  V, which would result in moderate depoling of the material and the need to properly repole the piezos. If the piezos do need to be repoled for any reason, 1200 V is applied for 12 hrs. This is typically done under vacuum inside the chamber. However, if a vacuum chamber is unavailable, the repoling can be performed in an oil bath which prevents dielectric breakdown due to the high fields present. The stage needs to be recalibrated after the repoling.

Electron emission is measured either by a Faraday detector or a channeltron electron multiplier. In the former, a Keithley picoammeter is connected in series between the sample and a copper strip (acting as a Faraday cup) is suspended approximately 5 mm above the sample. A

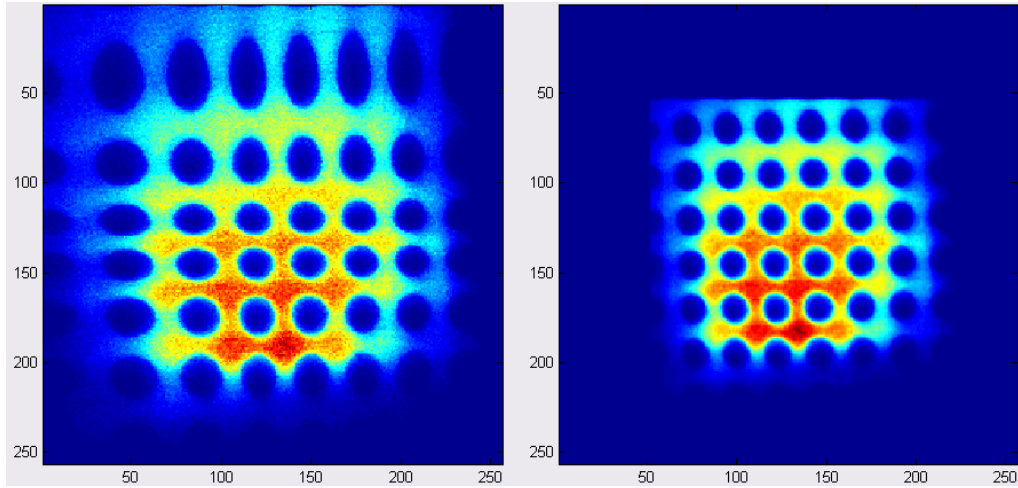


Figure 2.5: Calibration of the piezo stage. Raw (left) and corrected (right) images of a C-Flat TEM grid showing the result of a properly calibrated stage.

+10 V bias is applied to the copper strip in order to collect all the photoemitted electrons. The output of the picoammeter is digitized and recorded on the acquisition computer at a bin size of  $\sim 100$  ms per pixel. This bin size is necessary to overcome the settling time of the picoammeter and represents the fastest scan rate possible in this mode. An upgrade to the detection system permits the detection of single photoelectrons through the use of a channeltron electron multiplier. For this setup, the copper strip and picoammeter are replaced with a channeltron and amplifier/discriminator. This provides the ability to count single electrons while also lowering the acquisition time per pixel to 1-10 ms, where sufficient signal to noise is attained.

An ultrafast Ti:Sapphire laser is used to produce the photoelectrons and the layout is shown in Figure 2.6. A 532 nm Verdi pumps a KM Labs tunable Ti:Sapphire which outputs 30-50 fs pulses at 85 MHz. For these experiments either the fundamental (700-900 nm) or the doubled (350-450 nm) can be used to excite the photoelectrons. Wavelength tuning of the Ti:Sapphire is achieved through KMCtrl software where a set of slits inside the cavity adjust the wavelength components of the pulse. For the fundamental, the pulse is first GVD pre-compensated by a prism pair such that transform limited pulses can be achieved at the



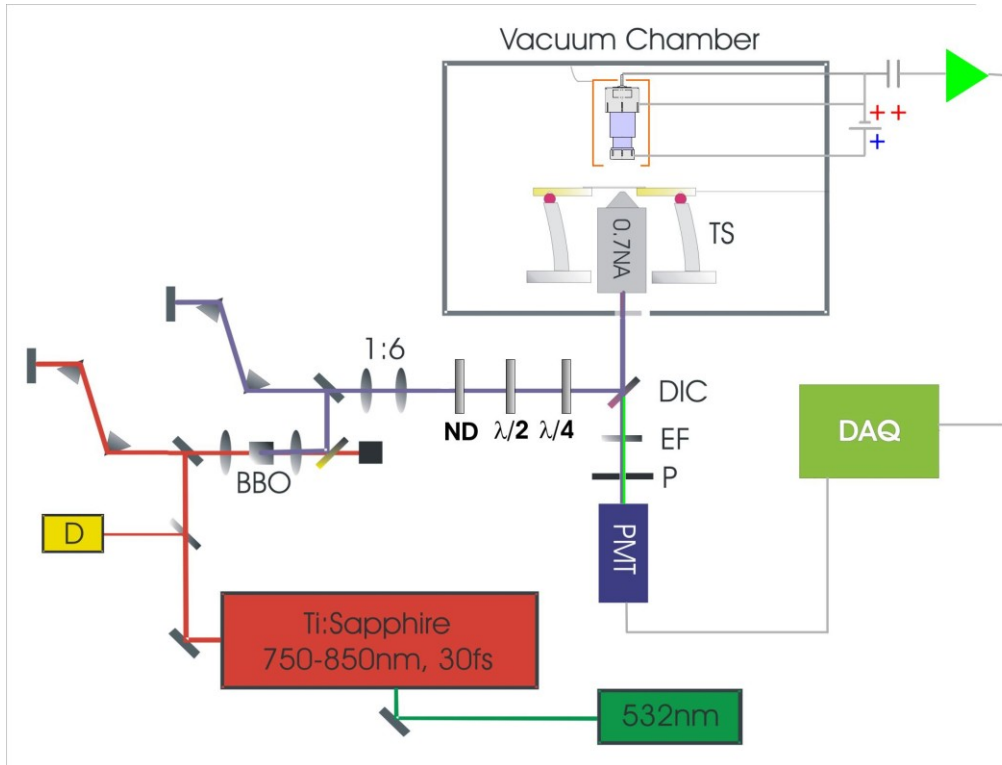


Figure 2.6: SPIM schematic. The basic layout of the SPIM experiment showing the optical path when using the doubled light.

microscope focus. This is generally optimized by maximizing the multi-photon electron emission yield from ITO or C-Flat which scales with the peak power.

The fundamental beam is expanded by a 1:6 telescope in order to overfill the back aperture of the microscope objective. After passing a set of reflective neutral density (ND) filters for excitation power attenuation and polarization optics ( $\lambda/2$  and/or  $\lambda/4$  waveplates for 800 nm) to attain either linear or circular polarized light, it enters the vacuum chamber through a quartz windowed side port. Alternatively, the fundamental can be doubled in a BBO crystal to obtain near UV (350-450 nm) ultrafast pulses. A  $\lambda/2$  waveplate rotates the blue beam to vertical polarization before it is GVD pre-compensated in a second folded prism pair. The beam is

expanded by a separate 1:6 telescope and the same ND filters provide the attenuation as in the case of the fundamental. For polarization rotation a  $\lambda/2$ -plate (400 nm) in front of the telescope is used. In order to provide circularly polarized light, a separate  $\lambda/4$ -plate for 400 nm is inserted into the beam path before entering the chamber.

## References

- (1) Hess, S. T.; Webb, W. W. *Biophys. J.* **2002**, *83*, 2300.
- (2) Weston, K. D.; Dyck, M.; Tinnefeld, P.; Müller, C.; Herten, D. P.; Sauer, M. *Anal. Chem.* **2002**, *74*, 5342.
- (3) Janesick, J. R.; Klaasen, K. P.; Elliott, T. *Opt. Eng.* **1987**, *26*, 972.

## Chapter 3

### Single Molecule Studies of Quantum Dot Fluorescence Intermittency: Evidence for Both Dark and Light-Assisted Blinking Dynamics\*

#### 3.1 Introduction

Fluorescence intermittency corresponds to abrupt fluctuations between states of high (“on”) and low (“off”) quantum yield for emission, despite the molecular system being subjected to continuous illumination. Initial predictions of such blinking behavior were confirmed in single molecule laser induced fluorescence studies, which could be interpreted based on photoinduced conversion between singlet and triplet manifolds.<sup>1,2</sup> In particular, such systems yield cleanly single exponential behavior in the distributions of times in the “off” manifold, corresponding to combined kinetic relaxation of the metastable triplet through either radiative (phosphorescence) or nonradiative (quenching) channels. However, other systems were soon found that revealed intermittency over time scales too long to be accounted for simply by phosphorescent pathways, requiring a more profound change in the molecular system to accompany both the blinking and recovery event<sup>3</sup>. Indeed, since these early studies, such fluorescence intermittency, or “blinking” has proven to be a remarkably ubiquitous phenomenon, observed in a wide array of single molecule microscopy studies, though the fundamental origins of this process still remain incompletely understood. Unfortunately, detailed kinetic investigations of such blinking dynamics over sufficiently wide ranges of time scales can be seriously limited by the finite number of photon absorption events prior to irreversible photobleaching of the molecular system.

---

\* Adapted from: Baker, Thomas A.; Rouge, Jessica L.; Nesbitt, David J. *Mol. Phys.* **2009**, *107*, 1867.

A major experimental advance in achieving this understanding was therefore provided by pioneering studies of semiconductor colloidal quantum dots (QD) by Bawendi and coworkers,<sup>4</sup> which revealed one of the earliest examples of pronounced blinking dynamics at the single nanoparticle level. One widely held interpretation of this phenomenon has been that the switching from “on” to “off” is a result of a photoassisted charge ejection process (either hole or electron) that leaves the core of the QD charged, thereby allowing fast and efficient non-radiative recombination rates to predominate.<sup>5</sup> Neutralization by either tunneling or further charge removal then returns the QD to its normal fluorescence emission state. QD systems make for a particularly interesting experimental platform, by virtue of their i) large absorption cross section and ii) greater long term photostability.<sup>6</sup> These two features allow for detailed observation of emission properties of single QDs over thousands of seconds with high detection band width and signal to noise. Such experimental improvements in both signal and photolongevity enabled Kuno et al.<sup>7,8</sup> to probe single QD blinking dynamics over an unprecedented range of time scales, from 100 s of sec down to 100 s of  $\mu$ s. Of special interest, these studies revealed a highly non-exponential blinking time distributions, but which proved to be well characterized by a power law, i.e.,  $P(t) \propto (1/t)^m$ , over 8-9 orders of magnitude in probability and 5-6 orders of magnitude in time. Such strikingly non-exponential behavior invalidated the simple picture of individual rate constants for blinking and recovery, instead requiring more complex models based on “distributed kinetics” accessing a wide dynamic range of rate processes.<sup>9</sup>

Many experiments have been subsequently performed to elucidate the origin of these broadly distributed power law time scales. For example, the influence of composition,<sup>10-12</sup> size,<sup>8</sup> and shape<sup>13</sup> of the QD have all been varied in an attempt to better understand the mechanism of the blinking. “On” time distributions are observed that obey a power law at short times, but show

approximately exponential deviations in the long time tail.<sup>11,13</sup> The time scale on which the power law falls off for the “on” times is also found to vary depending on the temperature and illumination intensity.<sup>4,8,11,14,15</sup> Specifically, the fall-off time was observed to decrease with increasing temperature of the sample, suggesting that there is a thermally activated contribution to the “on”-“off” blinking rate.<sup>11</sup> Illumination intensity was found to have a similar effect, with higher photon fluences resulting in earlier fall off times for the “on” power law distributions<sup>14</sup> as well as a possible threshold dependence on photon frequency.<sup>16</sup> This fall off behavior has been recently studied in more detail<sup>17</sup> at much lower cw confocal intensities (down to 10 nW), improved statistics ( $10^7$  photon events) and correspondingly longer experimental observation windows, which clearly reveal a *quadratic* power dependence consistent with biexciton formation and a sequential two-photon photoionization process. By way of contrast, the “off” time distributions have proven considerably more robust, with nearly perfect power law behavior ( $m \approx 1.60$ ) persisting out to the longest experimentally observed off-time event durations of  $\approx 20$  sec. Composition, shape, temperature and illumination intensity have been shown to have negligible effect on the “off” time slopes and linearity of the power law plots. This relative insensitivity of the “off” time distributions to experimental conditions might at first suggest a more universal kinetic pathway for blinking recovery in QDs, at least in the presence of laser light illumination.

Various models for the blinking have been proposed to account for the observed behavior. The “on”-“off” blinking transition is commonly assumed to be light induced, consistent with the observation of a dependence on illumination intensity. However, such a requirement is not entirely obvious, as the state of the QD and blinking transitions thereof are necessarily monitored under light interrogation. Based on an Auger ionization model, an entirely

plausible reason for the blinking rate to be light dependent is that the “off” state due to an ionized QD might only be energetically accessible via the photoexcited state. However, another explanation of blinking is offered by Stefani et al.<sup>14</sup> in which the power law distribution of “on” times is light independent, but with a photon-assisted pathway proceeding in parallel to explain the observed power law truncation at  $1/k$ . In their model, the “off” state can be reached both thermally and by direct photo-excitation from the ground state, which yields simulations capable of reproducing their experimental data. By way of contrast, the “off”-“on” transition corresponding to blinking recovery is generally assumed to be independent of photon absorption, and often ascribed to electron/hole tunneling by virtue of its insensitivity to a range of external control variables such as temperature and illumination intensity.

It is important to note, however, that these previous studies have been performed in the presence of either pulsed or cw laser illumination of the sample, with the repetition rate for pulsed interrogation typically at MHz level or higher. Although convenient for rapidly probing the fluorescent state of the QD, it does not allow one to cleanly assess the potential relevance of purely *non-photoactivated* pathways for both blinking and blinking recovery. Figure 3.1 provides a highly simplified but more general schematic model for QD blinking between an “on” ( $|0\rangle$  and  $|1\rangle$ ) and “off” ( $|2\rangle$  and  $|3\rangle$ ) manifold of states. In the “on” manifold, states  $|0\rangle$  and  $|1\rangle$  are coupled by initial laser excitation, with the quantum yield (QY) and time scale ( $1/k_{\text{fluor}}$ ) for  $1 \rightarrow 0$  fluorescence determined by competition between radiative ( $k_{\text{rad}}^{1 \rightarrow 0}$ ) and nonradiative ( $k_{\text{nrad}}^{1 \rightarrow 0}$ ) pathways by  $\text{QY} = k_{\text{rad}}^{1 \rightarrow 0} / (k_{\text{rad}}^{1 \rightarrow 0} + k_{\text{nrad}}^{1 \rightarrow 0})$  and  $k_{\text{fluor}} = k_{\text{rad}}^{1 \rightarrow 0} + k_{\text{nrad}}^{1 \rightarrow 0}$ . The “off” manifold consists of states  $|2\rangle$  and  $|3\rangle$ , which in principle can also be coupled by laser excitation, but differs from the “on” manifold by having a low quantum yield for emission due to fast nonradiative relaxation ( $k_{\text{nrad}}^{3 \rightarrow 2} \gg k_{\text{rad}}^{3 \rightarrow 2}$ ). The relative energy separations between the two

manifolds are intentionally unspecified; in the context of an Auger ionization model, for example,  $E_2$  might be lower though comparable to  $E_1$  but considerably higher than  $E_0$ .

In such a kinetic model, there are six possible pathways between the “on” and “off” manifold, with three paths being light assisted (solid arrows) and three proceeding in the dark (dashed arrows). The light assisted paths take place out of the excited states of each manifold, states  $|1\rangle$  and  $|3\rangle$ , and therefore require absorption of a photon to proceed. The lower states  $|0\rangle$  and  $|2\rangle$  can interconvert with each other directly as well as by transitions from  $|2\rangle$  to  $|1\rangle$  in a thermally activated (i.e., photon independent) process. In order to describe the model proposed by Stefani et al.,<sup>14</sup> an additional light mediated process would also connect states  $|0\rangle$  and  $|2\rangle$  directly. The key point in this kinetic framework is that experiments under both pulsed and cw excitation conditions have so far been investigating the combined effect of both *light induced and dark* processes, rather than isolating the photon mediated from non-photon mediated dynamics. It should be noted for later discussion however, that a few dark ensemble experiments have been carried out. Chung and Bawendi<sup>18</sup> monitored bulk QDs in solution, which showed that light induced loss of fluorescence intensity would recover to near its initial value with sufficient time in the dark. The recovery occurred on time scales of a few hours, indicating the presence of an exceptionally slow and light independent transition from the “off” to “on” manifolds. Wide field single molecule experiments by Brokmann et al.<sup>19</sup> investigated QDs on a surface, and showed that total fluorescence signals recovered if the sample was left in the dark for 10-15 minutes. Dark recovery was also observed by Cichos et al.<sup>20</sup> in ensemble silicon nanocrystals. These experiments provide useful comparisons for our results and will be

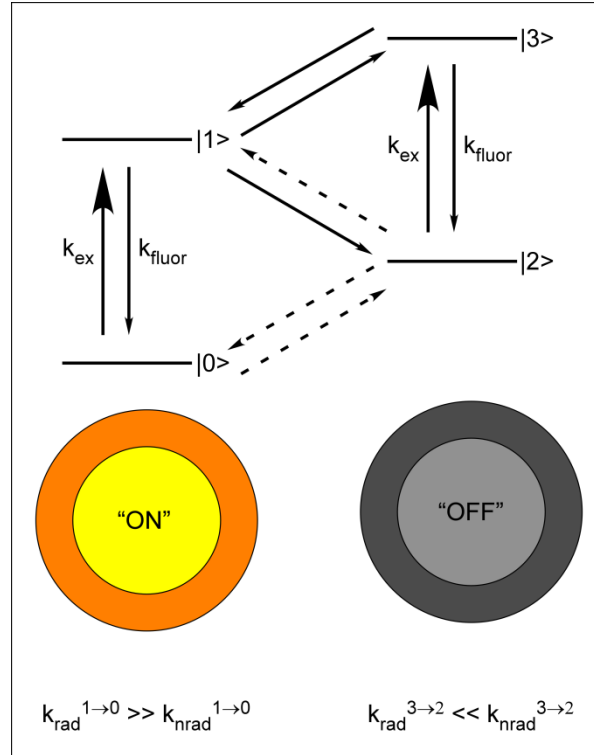


Figure 3.1: Kinetic scheme for QD blinking. The possible pathways between QD manifolds of high (“on”) and low (“off”) quantum yields. Transitions out of excited states  $|1\rangle$  and  $|2\rangle$  are denoted by solid lines representing a light induced pathway, while the dashed line transitions between lower states  $|0\rangle$  and  $|2\rangle$  (as well as from  $|2\rangle$  to  $|1\rangle$ ) indicate process that can occur in the dark.

discussed in more detail later.

The main thrust of this experimental study is to elucidate the role of light versus non-light induced processes in blinking at the single QD level, which requires investigation out to long time scales. In order to accomplish this, we periodically probe the “on” versus “off” state of a single QD over an extended time series, where between such short lived probe events the QD is kept in the dark for variable time duration. This permits us to probe the conditional probabilities for i) “on-on” and ii) “on-off”, as well as iii) “off-off” and iv) “off-on” events as a function of time in the dark. By varying this dwell time, we can therefore develop a statistical picture for “on”-“off” manifold interconversion rates for non-photon activated processes under single QD,



room temperature conditions. We find that the rate for “on” to “off” blinking ( $k_{\text{on-off}}$ ) is negligibly slow in the dark, which would be thermodynamically consistent with Figure 3.1, as well as in agreement with many previous experiments.<sup>4,7,8,11</sup> However, the present studies also clearly reveal a *finite* rate (or distribution of rates) for “off” to “on” recovery in the dark. Of special importance, this dark recovery process is orders of magnitude slower than predictions based on power law behavior observed in multiple previous experiments.<sup>4,8,11,14</sup> As one immediate consequence, this implies that there must be a dominant light induced component to the “off” to “on” blinking recovery process for QDs under essentially all laser illuminated single molecule experimental conditions.

The organization of the rest of this chapter is as follows. In section 3.2, the experimental setup and sample preparation is described. Section 3.3 presents sample data and results from the study. Section 3.4 focuses on interpretations of the results and discusses insights into the underlying dynamics. A summary of the results is provided in section 3.5.

## 3.2 Experiment

Measurements are made on an inverted epi-fluorescence confocal microscope (Olympus IX-70) with single photon detection capabilities.<sup>21</sup> Laser excitation is provided by a 434nm GaN diode laser (Picoquant, LDH 400) with a pulse width of  $\sim 70$  ps and a repetition rate of 5 MHz or a doubled 1064 nm Nd:YVO<sub>4</sub> continuous laser (532 nm). The excitation is right hand circularly polarized, expanded by an 8:1 collimating telescope, reflected from a dichroic (Chroma Z434DC) and then focused on the surface with a 100x 1.4 NA oil immersion objective (Olympus PlanApo). Fluorescence is collected through the same objective, transmitted through the dichroic, spatially filtered by focusing through a 50  $\mu\text{m}$  pinhole, and reimaged onto a pair of

avalanche photodiodes (APD, Perkin Elmer, SPCM-AQR14), with additional bandpass filters (Chroma 580-70M) mounted in front of each APD to suppress light outside of the peak QD emission range. The dual detectors provide additional flexibility for separating the emission photons by polarization or color, a capability which is not exploited in the present studies. The laser power is attenuated to 55 nW at the sample by a series of neutral density filters. The choice of these low powers is dictated by a compromise between minimizing biexcitonic induced blinking events<sup>17</sup> and yet achieving adequate signal-to-noise levels in a 5 ms time bin (20:1) to distinguish “off” from “on” states with high statistical certainty. It is important to note, however, that if there is a light induced pathway for blinking and recovery, there will always be a small but finite probability of changing the state of the QD prior to completion of the first integration time bin. Indeed, such measurement effects are readily apparent and must be taken into consideration in the kinetic analysis.

A computer controlled mechanical shutter (Newport, 846HP) is placed at the focus of the telescope to block the laser excitation with an effective response time  $< 1$  ms. An experimental schematic is shown in Figure 3.2. The amount of time the shutter is open ( $T_{\text{open}}$ ) is kept fixed at 150 ms, while the shutter closed time ( $T_{\text{close}}$ ) is varied between 150 ms and 30000 ms. The reported results show no sensitivity to the choice of  $T_{\text{open}}$ ; the only quantity of relevance is the state of the QD in i) the last bin prior to closing the shutter and ii) the first bin after the shutter reopens. One issue that does arise is asynchronicity between the clock that controls the shutter opening/closing and the much more precise clock that measures time correlated single photon arrivals. To ensure exact synchronization over many hours of data collection, a small amount of the excitation light is picked off between the shutter and the microscope and sent to an additional timing APD to monitor the state of the shutter. The outputs from all three APDs are sent to a

router (HRT-81) and then to a time-correlated single photon counting card (Becker-Hickl TCSPC-130). This provides time-tagged fluorescence measurements with  $\sim 50$  ns macrotime resolution, which enables the data to be binned post acquisition for any desired time interval. For the current experiment, trajectories are analyzed with a 5 ms bin time, with typical “on” count rates of 80 kHz. This translates into  $\approx 400$  photons per integration window, which yields a shot noise limited  $S/N \approx 20:1$ . The amount of light on the timing APD is attenuated to 15 kHz while the shutter is open, which is sufficient to determine the opening and closing events to much faster than the minimum bin time.

Two sample preparations are considered in which QDs are embedded in a polymer film or tethered to the surface in solution. In the first, CdSe/ZnS QDs are purchased from NN-Labs and have an absorption peak at 561 nm and an emission peak at 576 nm. Samples are prepared by spin coating a dilute concentrations of QDs in 0.5% g/mL poly(methylmethacrylate) / toluene solutions on ozone cleaned glass cover slips. The resulting films are  $\sim 10$  nm thick as measured by AFM, with  $0.3$  QDs/ $\mu\text{m}^2$ . The latter sample preparation uses streptavidin-conjugated CdSe/ZnS QDs obtained from Invitrogen with an absorption peak at 550 nm and an emission peak at 565 nm. The samples are made by tethering the streptavidin-conjugated QDs to biotin-BSA/BSA (1:10) coated glass slides in a microfluidic channel sample holder. Surface coverage density for the solution studies is typically  $0.4$  QDs/ $\mu\text{m}^2$ .

In order to obtain data, images are first created by raster scanning the sample on a piezoelectric closed loop stage (PI P-517.3CL), which reveals single QDs with a near diffraction limited spot size of 240 nm full width half maximum. After obtaining an image, the stage is moved sequentially under close loop control to center a single QD in the laser focus. Shuttered fluorescence trajectories are monitored for 30-3000 s depending on the shutter duty cycle to

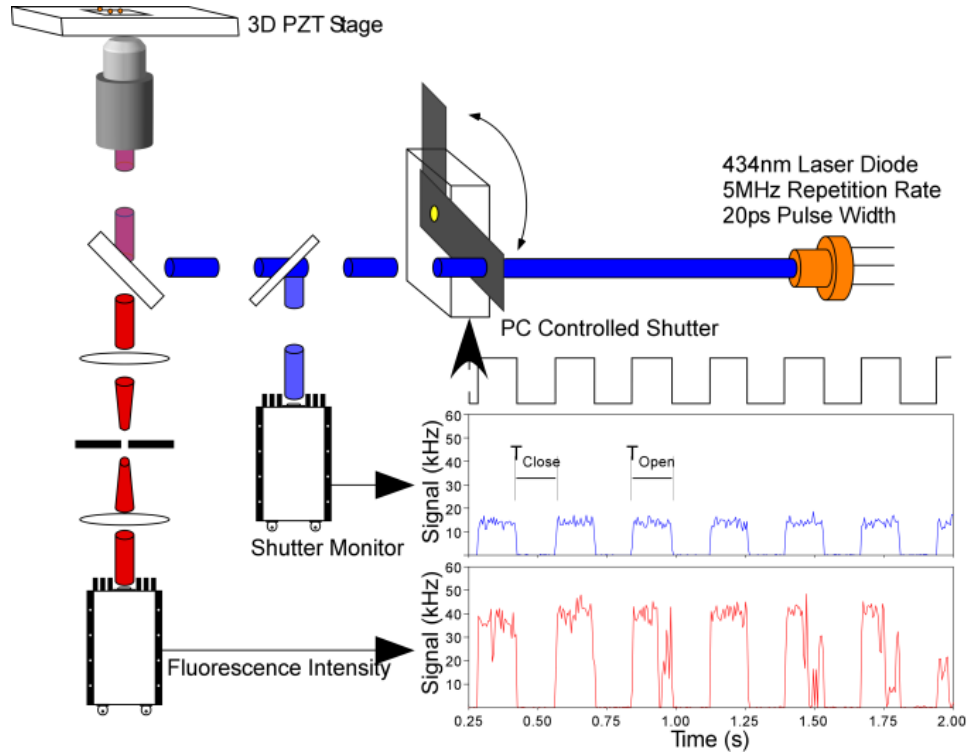


Figure 3.2 Experimental setup for shutter studies.

obtain data on approximately 100 shutter transitions. A sample trajectory showing the two different APD signals is included in Figure 3.2. Acquisition and analysis software is written in-house and based on LabWindows modules and drivers.

### 3.3 Results

Shuttered fluorescence trajectories from single QDs contain four types of transitions. The initial and final states are determined by looking at the intensity in the integration bin immediately before and after, respectively, the shutter closes and reopens, comparing it to an intensity threshold. Due to shot noise fluctuations in “on” state intensities within the integration time bin, the threshold is selected at  $f \approx 30\%$  of the maximum value, corresponding roughly to the mid point between the lowest “on” and highest “off” intensities observed. The kinetic results

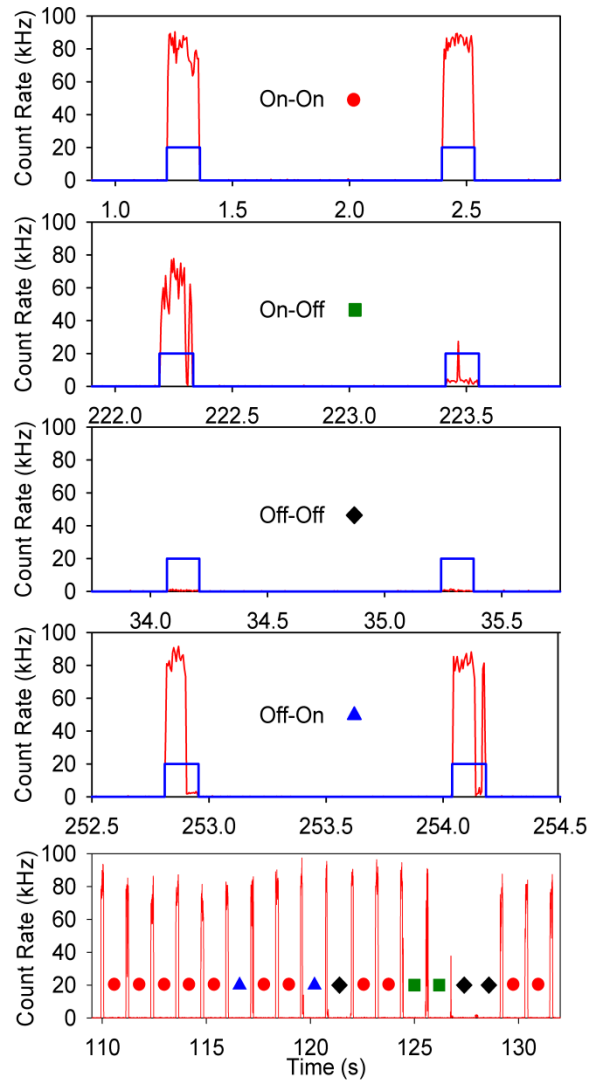


Figure 3.3: Sample data for observed dark transitions. The first four graphs depicting the possible transitions observed for a shutter close time of  $T_{\text{close}} = 1$  s. The last panel shows a sample 20 s trajectory with  $T_{\text{close}} = 1$  s, revealing several different transitions within a single trace.

reported have been tested to be insensitive to the choice of this value, though this does influence the number of false positive “on”-“off” and “off”-“on” events counted in the first time bin after shutter opening (vide infra). Examples of the four different possible classes of transitions are shown in Figure 3.3 for  $T_{\text{close}} = 1$  s. The first two traces show a QD that is “on” before the

shutter is closed. In the first trace, the QD remains “on” when it is next interrogated; while, in the second trace the QD has turned off in the 1 s that the shutter was closed. Similarly, two types of behavior can be distinguished for QDs that are declared “off” before the shutter closes, as denoted “off”-“off” and “off”-“on” in the third and fourth trace.

In order to obtain sufficient statistics, the same QD is interrogated many times in one trajectory at a fixed  $T_{\text{close}}$ . A 20 s portion of such a trajectory is shown in Figure 3.3e, where the different symbols correspond to the 4 different types of transitions. To obtain sufficiently good statistics, typically 100 transitions are investigated at each value of  $T_{\text{close}}$  for a single QD and the experiment is repeated for approximately 20-50 QDs, i.e., 2000-5000 shuttering events. For each QD, the survival probabilities of  $S_{\text{on-on}}$  and  $S_{\text{off-off}}$  are calculated as  $S_{x-x} = N_{x-x}/(N_{x-x}+N_{x-y})$ , where  $N_{x-x}$  and  $N_{x-y}$  refer to the number of non-state changing and state changing events, respectively. Sample results for 50 QDs with a 1 s  $T_{\text{close}}$  are shown in Figure 3.4, where the error bars for each QD are calculated from propagation of the counting statistics,  $\sigma^2 = S_{x-x}N_{x-y}/(N_{x-y}+N_{x-x})^2$ . For a 1 s shutter closed time,  $S_{\text{on-on}}$  clusters around 0.91 for essentially all of the QDs, while  $S_{\text{off-off}}$  has a lower average value with much larger scatter. In anticipation of potential power law kinetic behavior, this analysis is repeated for all  $T_{\text{close}}$  values investigated, with the average value and standard deviation of the mean for both  $S_{\text{on-on}}$  and  $S_{\text{off-off}}$  summarized in a log-log plot shown in Figure 3.5.

The data from these experiments provides several observations worth noting. First, the average  $S_{\text{on-on}}$  for the series of QDs in Figure 3.4 is clearly less than unity. These deviations arise from false positive events as a result of finite time binning of the data. Specifically, while the shutter opens in  $< 1$  ms, the QD is exposed to light for an average of 5 ms prior to evaluation, during which there is a finite probability of switching from “on” to “off”. Consistent with this

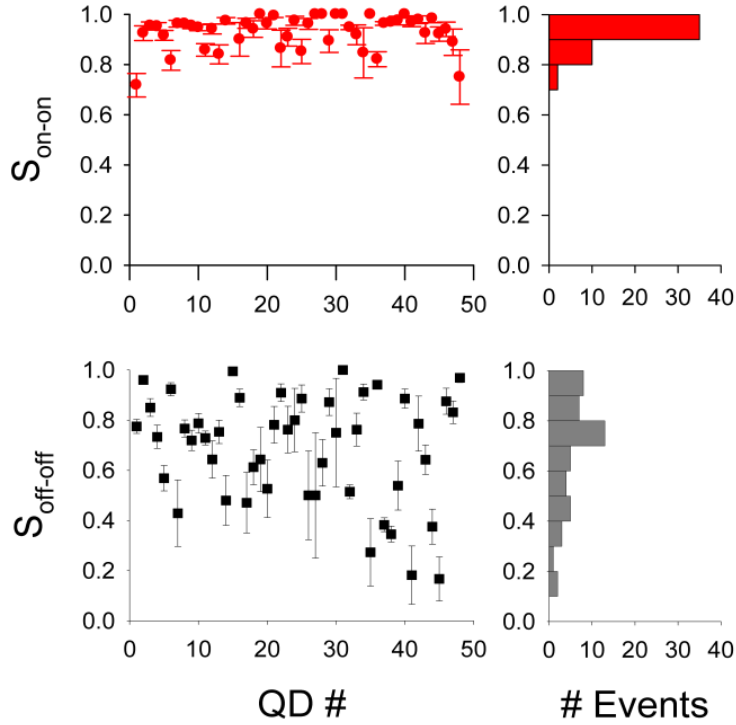


Figure 3.4: Variability of the survival probability between different QDs. The values of  $S_{\text{on-on}}$  and  $S_{\text{off-off}}$  for individual QDs at a value of  $T_{\text{close}}$  of 1 s, where the error bars represent the error from counting statistics. The particularly large QD variation in  $S_{\text{off-off}}$  values is indicative of a broad distribution in blinking recovery rates, which would be consistent with underlying power law kinetics. Histograms of the data binned at 0.1 probability unit are shown on the right.

interpretation, we find that i) increasing the bin size or ii) averaging over more bins adjacent to the shutter event results in additional deviation in the average of  $S_{\text{on-on}}$  below unity. We can statistically discretize this effect by treating the “on”-“off” transitions as being power law distributed, i.e.

$$P(\tau) = \frac{A}{\tau^m} = A' \left( \frac{\tau_{\min}}{\tau} \right)^m \quad (3.1)$$

where  $P$  represents a probability density (units 1/s) and  $\tau_{\min}$  reflects the minimum bin size. For discrete bin time conditions, the summation over  $P(\tau)$  can be normalized, provided that the power law exponent  $m > 1$ . For typical power law slopes of  $m \approx 1.6$  and a threshold at  $f \approx 30\%$ ,

one can therefore roughly estimate the fraction of true “on”-“off” or “off”-“on” events to be  $S_{\text{true}} \approx 1-(m-1)/m \approx 0.89$ . In addition, there may be effects due to imperfect synchronicity between shutter and data acquisition clocks. However, the above estimate is already in reasonable agreement with the  $S_{\text{on-on}} = 0.91(2)$  values observed at the shortest shutter times, which suggests that deviations below unity are indeed probe light-induced and sufficiently well described in our data analysis.

Qualitatively consistent with this picture,  $S_{\text{on-on}}$  exhibits values close to  $\approx 0.9$  for all shutter times, with a slight decreasing trend from 100 ms to 30 s (see Figure 3.5). The *insensitivity* of  $S_{\text{on-on}}$  to  $T_{\text{close}}$  supports the assumption that  $k_{\text{on-off}}$  is at least dominated by a *light assisted* pathway. We do see evidence for small but finite decrease in the data as a function of  $T_{\text{close}}$ , which could reflect a possible dark pathway. If we treat this as an exponential process, the slow trends with increasing shutter time would be consistent with an “on”-“off” exponential rate constant of  $k_{|0\rangle\rightarrow|2\rangle} \approx 0.0014(7) \text{ s}^{-1}$ . However, an equivalently good power law analysis of the data yields  $m \approx 1.0041(33)$  for the  $P(\tau_{\text{on}})$  distribution. Here it should be noted that the survival probabilities,  $S(t)$ , in Figure 3.5 represent the integral of the actual probability density,  $P(\tau)$ , from time  $t$  to infinity, i.e. the probability of having a transition take place at any time  $\tau$  greater than  $t$ .

By way of contrast, the dark probability for remaining in the “off” state ( $S_{\text{off-off}}$ ) after  $T_{\text{close}} = 1 \text{ s}$  clearly is much lower than the false positive upper limit of 91(2)%, with considerable scatter illustrated in the histogram in Figure 3.4b. This high degree of scatter between dots is indicative of a broad dispersion in rate constants for dark “off”-“on” blinking recovery (i.e.  $k_{|2\rangle\rightarrow|0\rangle}$ ). Averaged over many QDs, there is now an unambiguous time dependence to  $\langle S_{\text{off-off}} \rangle$  (see



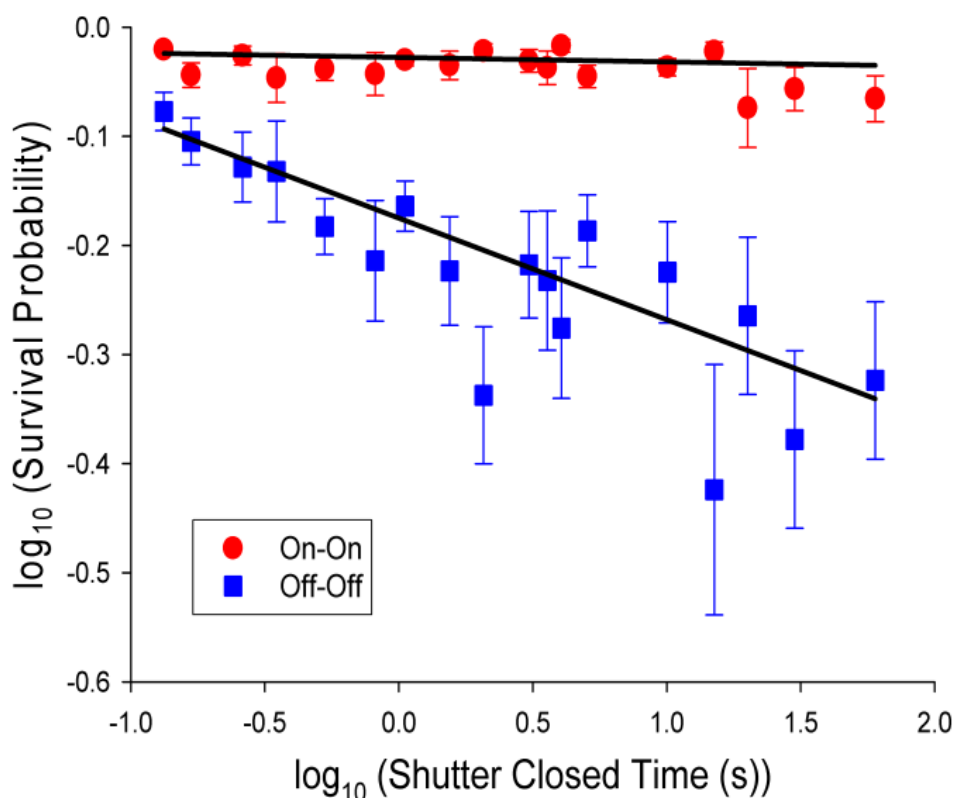


Figure 3.5: Time dependent survival probabilities. Base 10 log-log plots of the time dependent survival probabilities,  $S_{\text{on-on}}$  (red) and  $S_{\text{off-off}}$  (blue), as a function of the shutter close time ( $T_{\text{close}}$ ) for 434 nm excitation of QDs in PMMA. The slopes of the two curves correspond to blinking and blinking recovery power law kinetic behavior in the probability densities (see Eq. 3.2) with  $m_{\text{on}-1} \approx 0.0041(33)$  and  $m_{\text{off}-1} \approx 0.093(12)$ . The much more rapid decrease in  $S_{\text{off-off}}$  with shutter time is indicative of a slow but finite pathway for blinking recovery in the absence of laser illumination.

Figure 3.5), with the value decreasing with increasing  $T_{\text{close}}$ . This unequivocally indicates the presence of a finite *light unassisted* pathway for QD blinking recovery.

The dynamic range of these changes is sufficiently large to provide insight into the underlying kinetic processes for dark recovery. Specifically, conventional semilogarithmic plots of the data prove to be highly nonlinear, which would rule out a single rate constant recovery model at the single QD level. Plots of  $\log \langle S_{\text{off-off}} \rangle$  vs  $\log T_{\text{close}}$ , on the other hand, are scattered but approximately linear over 2.5 orders of magnitude, which indicates a more distributed power

law kinetic model governed by many rate constant processes. Indeed, this is also consistent with the high degree of scatter observed in Figure 3.4b for QD values at  $T_{\text{close}} = 1$  s, which in a distributed kinetic picture would arise from a wide distribution in recovery rate constants. If we assume a power law form of Eq. 1, the blinking recovery data can be fit to a probability density of recovery times with  $m \approx 1.093(12)$ . Though qualitatively consistent with early ensemble experiments by Chung and Bawendi,<sup>18</sup> we shall see that the present results are orders of magnitude slower than would be predicted from power law kinetics based on previous single QD studies obtained under continuous illumination.<sup>8,11,14</sup> Implications of these results with the proposed kinetic scheme will be discussed in the following section.

In order to investigate possible environmental influences on these dark blinking or recovery processes, additional experiments have also been conducted for: i) different excitation wavelengths (532 nm versus 434 nm) with spun cast QDs in PMMA and ii) the same 434 nm wavelength but for streptavidin-conjugated QDs tethered in aqueous buffer solution. Figure 3.6 shows a summary of the data compiled for all three experiments, with the original data taken at 434 nm in a PMMA film shown in blue circles. Within experimental scatter, there appears to be consistency between data sets for each choice of excitation wavelength, QD size and structure, and polymer versus aqueous environment. Specifically, there are very slight decreases in the average  $S_{\text{on-on}}$  survival probability distributions with shutter time, suggesting only a very slow pathway for *light unassisted* blinking. On the other hand, there is unambiguous decrease in average  $S_{\text{off-off}}$  survival probabilities under each set of experimental conditions, consistent with a slow and highly distributed rate process for QD blinking recovery in the absence of laser illumination.

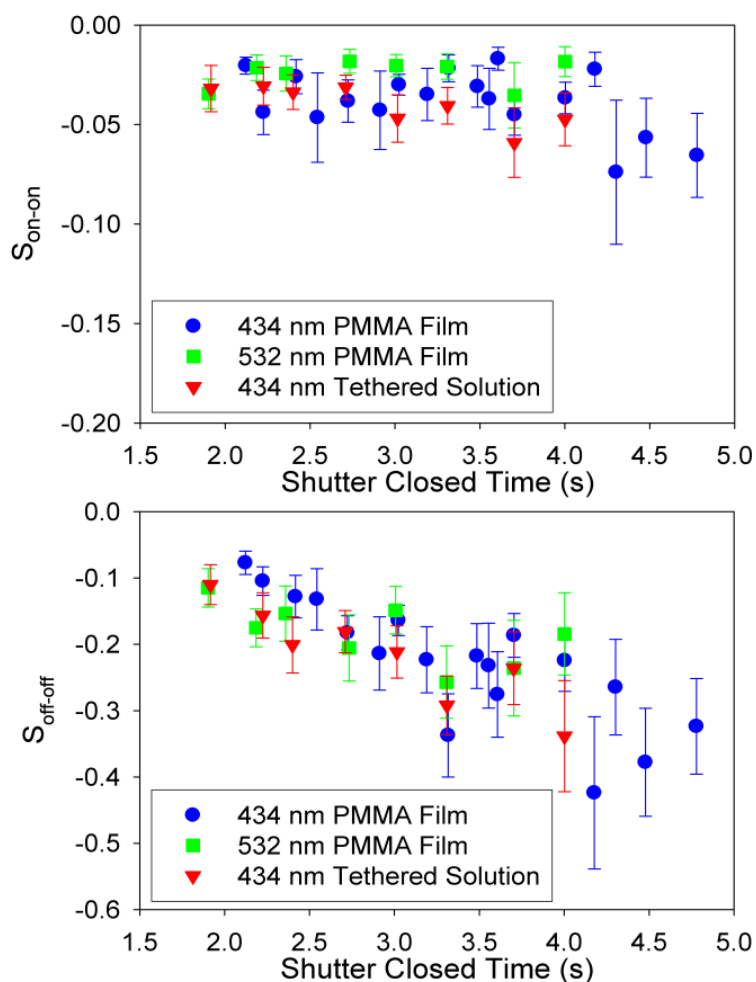


Figure 3.6:  $S_{\text{on-on}}$  and  $S_{\text{off-off}}$  under different experimental conditions. Circles (blue) are data previously shown for 434 nm excitation of QDs spin coated in PMMA. The squares (green) represent data for 432 nm excitation of QDs in PMMA, while the triangles (red) reflect 434 nm excitation of streptavidin conjugated QDs tethered on a cover slip in aqueous buffer solution.

### 3.4 Discussion

The above insensitivity to excitation wavelength for both blinking and blinking recovery provides a good starting point for discussion. Since we are probing recovery dynamics in the dark, changes in the excitation wavelength could in principle affect  $S_{\text{off-off}}$  in an Auger model, for example, by energetically accessing different trap states in the “off” manifold for the ejected

electron or hole. Specifically, a 2.96 nm radius CdSe QD translates into a 2.16 eV energy separation between ground electron/hole states based on an effective mass approximation, spherical square well potential and a bulk band gap of 1.74 eV.<sup>22,23</sup> In addition, there is a ZnS shell which has a 2.70 eV separation between the top of the bulk CdSe valence band and bottom of the ZnS conduction band. The initial experiments are at 434 nm (2.86 eV), which is sufficient energy to excite the electron into the conduction band of ZnS. Conversely, a 532 nm provides a 2.34 eV photon which limits the energy of the electron and potentially removes accessibility to traps of higher energy that might be available with bluer excitation. The lack of measurable difference in blinking recovery behavior suggest in our simple kinetic model (Figure 3.1) that the lower state ( $|2\rangle$ ) in the “off” manifold accessed by either photon energy is the same. This is not surprising, based on experiments by Podhorodecki et al.<sup>24</sup> exciting core shell CdSe/ZnS QDs progressively further in the UV. In particular, they observed photoluminescence spectra with features corresponding to exciton recombination in the ZnS shell when exciting  $> 4$  eV, i.e., substantially higher than the ZnS band gap. On the other hand, for excitation with lower energy photons below the band gap of ZnS but still energetic enough to excite either an electron or hole in the ZnS, only the lowest energy exciton emission was observed, suggesting that electron or hole excited states in the ZnS shell rapidly relax to the lowest energy level in the CdSe core. Furthermore, tunable excitation experiments on blinking in single QDs,<sup>16,17</sup> have demonstrated “off” time distributions to be insensitive over similar changes in wavelength, although of course under continuous laser illumination conditions.

Changing the environment could potentially influence the recovery rate in the dark, for example, by occupation of surface trap sites or reneutralization by species near the QD. On this topic, there has been a wide range of experimental blinking recovery data reported under

continuous illumination, with observations ranging from negligible sensitivity<sup>14,25</sup> to a weak but systematic dependence<sup>26,27</sup> of power law exponents to the environment. At a qualitative level, the recovery behavior appears to be similarly insensitive to the immediate polymer vs aqueous environment in the dark, with the results showing nearly identical power law trends and slopes within scatter for all values of  $T_{\text{close}}$  investigated. One reason for this may be that the tethered solution QDs are coated with a polymer as well as streptavidin bioconjugation, which could limit access to the QD by the aqueous solution environment.

After accounting for the finite survival probability in the “on”-“on” transitions, what remains is a very weak dependence on  $T_{\text{close}}$  for the “on”-“on” survival probability. A survival power law fit indicates a probability density slope corresponding to  $m - 1 \approx 0.0041(33)$ . Based on the kinetic model presented in Figure 3.1, this would be consistent with the presence of a very slow pathway from  $|0\rangle$  to  $|2\rangle$  via a dark (i.e., thermal) process at room temperature. However, the data are equally well described by an average value for all  $T_{\text{close}}$ , indicating that there are statistically few changes from state  $|0\rangle$  to  $|2\rangle$  through a thermal process at room temperature even on time scales as long as 60 seconds. In any event, the lack of any predominant channel for “on”-“off” blinking in the dark is certainly consistent with the majority of models proposed,<sup>5,11,12,28,29</sup> for which the transition from the “on” to “off” manifold occurs through the excited state  $|1\rangle$  and therefore requires absorption of one or more photons. It should be noted that these observations do not require the transitions to the “off” manifold to be exclusively through the excited state  $|1\rangle$ . For example, the direct pathway proposed by Stefani et al.<sup>14</sup> from state  $|0\rangle$  to  $|2\rangle$  upon absorption of a photon is also possible, though not probed in the current experiment.

By way of contrast, the probability of observing an “off”-“on” transition presents strikingly different behavior. A majority of QD blinking investigations have indicated that such “off”-“on” rate processes are i) independent of light intensity and ii) governed by a power law with slope  $m \approx 1.60$ .<sup>4,8,11,14</sup> Indeed, the power law slope for the off time distribution under continuous illumination is found to be 1.59(2) in the current experiment, *vide infra*. If such kinetics also characterize blinking recovery in the dark, the probability of observing an “off”-“on” transition in a shutter time  $T_{close}$  would be given by

$$S_{off-on} = 1 - S_{off-off}(T_{close}) = 1 - \int_{T_{close}}^{\infty} P(\tau) d\tau \quad (3.2)$$

where the normalized probability density  $P(\tau)$  is given in Eq. 1. This leads to a survival probability of observing an “off”-“off” event that decreases also in a power law fashion, but with a slope exponent diminished by 1, i.e., to  $m-1$ . Indeed, the survival probability data presented in Figure 3.5 is consistent with a power law distribution. However, the observed power law slope of  $m - 1 \approx 0.093$ , which is > 6-fold smaller than the predicted value of  $m - 1 \approx 0.60$ .

We make this comparison more explicit in Figure 3.7, which shows the rapid decrease in survival probably predicted from previous kinetic studies in the light (dash line), as well as the much slower drop off in “off”-“off” survival probabilities observed in the dark (filled squares). Included as an inset is the distribution of the “off” times power law slope under continuous illumination for the same QDs included in the shuttering experiment which shows a value of  $m_{off} = 1.59(2)$ . The data is clearly not well represented by this description, with the two sets of data differing by two orders of magnitude on time scales out to 30 s. This provides unambiguous evidence for a *light unassisted* process able to recover the QD from the “off” to the “on” state. Of equal importance, such a large difference between light and dark QD recovery rates

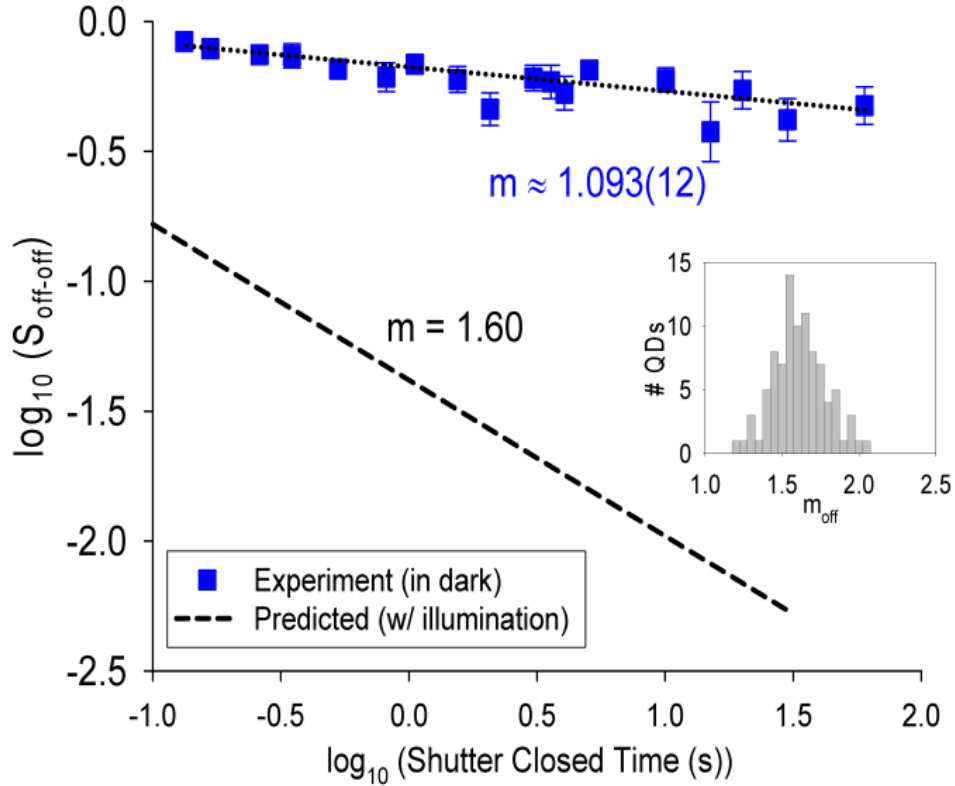


Figure 3.7: Comparison between light and dark rates. The experimentally observed  $S_{\text{off-off}}$  values in the dark are compared to survival time distributions predicted from previous studies, based on blinking recovery probability densities that are power law distributed with slow of  $m_{\text{off}} = 1.60$ . Note the several orders of magnitude discrepancy between predicted (dashed line) and observed (blue squares) distributions. This indicates the dominance of a strongly *light assisted* mechanism for QD blinking recovery under typical experimental conditions. Inset: Experimentally observed distribution of power law exponents under continuous laser illumination conditions, revealing an average value of  $m_{\text{off}} = 1.59(2)$ .

necessarily implies that the blinking dynamics observed previously under continuous illumination conditions must be dominated by *light assisted* processes.

These results can be interpreted with respect to the kinetic model presented in Figure 3.1. The key process responsible for QD blinking at room temperature is a result of photon absorption, suggesting that it proceeds from the excited state, i.e. that  $k_{|1\rangle\rightarrow|2\rangle} + k_{|1\rangle\rightarrow|3\rangle} \gg k_{|0\rangle\rightarrow|2\rangle}$ . The thermal contribution to blinking,  $k_{|0\rangle\rightarrow|2\rangle}$  is shown to have a minimal contribution for the time scales investigated, with a rate constant of  $0.0014(7) \text{ s}^{-1}$  or a power law slope of  $1.0041(33)$ .

Alternatively, the process of QD blinking recovery has distinct light and dark pathways. The light unassisted transition,  $k_{|2\rangle\rightarrow|0\rangle}+k_{|2\rangle\rightarrow|1\rangle}$ , is found to be non-exponential and governed by a power law with  $m \approx 1.093(12)$ . Such slow dark rates are insufficient to explain previous results of single QD blinking recovery under continuous illumination. Based on our model, this would imply that relaxation from the excited state in the “off” manifold,  $k_{|3\rangle\rightarrow|1\rangle}$  is the dominant process observed under continuous illumination and is described by a power law with  $m \approx 1.60$ . Such a model does not include direct photon mediated transitions,  $k'_{|0\rangle\rightarrow|2\rangle}$  or  $k'_{|2\rangle\rightarrow|0\rangle}$ , in which a photon is absorbed but blinking/blinking recovery does not necessarily proceed through  $|1\rangle$  and  $|3\rangle$  excited states of the on and off manifolds, respectively. Under normal experimental conditions of laser illumination, however, all such low energy photoassisted transitions would be indistinguishable from processes occurring through the excited states.

A potential explanation of our results can be found from Verberk et al.,<sup>12</sup> who developed a simple model for power law blinking that relates the power law slope to tunneling barriers. In their model, a larger barrier for reneutralization would result in a smaller power law exponent. This suggests that the barrier between  $|2\rangle\rightarrow|1\rangle$  is larger than  $|3\rangle\rightarrow|1\rangle$  or that the energy from the absorbed photon is available to accelerate the reneutralization through an Auger process. The lack of previous observation of these dark rates can be understood if the number of transitions between  $|2\rangle$  and  $|3\rangle$  in an experimental window is taken into account. Even under the lowest excitation conditions of 20 nW investigated by our group,<sup>17</sup> the photon absorption rate from state  $|2\rangle$  to state  $|3\rangle$  is  $\approx 500$  KHz, corresponding to  $\approx 500$  events even for 1 ms time bins. Such a large number of opportunities for light induced conversion from state  $|3\rangle$  to the “on” manifold (i.e., either  $|1\rangle$  or  $|0\rangle$ ) is apparently sufficient to dominate the much slower dark process.



However, these results suggest that at even lower powers,  $< 2$  nW, the two pathways may begin to compete and could both be observed.

As a final comment, the present results should be compared to previous ensemble dark experiments. Chung and Bawendi<sup>18</sup> investigated the ensemble behavior of colloidal QDs under illumination and in the dark. Under constant illumination, the sample showed a significant decrease in total intensity, which, for example, would be consistent with power law behavior in both the on and off times with  $m_{\text{on}} > m_{\text{off}}$ . However, upon blocking illumination and periodically checking the photoluminescence intensity, they noted nearly complete recovery of the ensemble QD fluorescence, though the behavior could not be well described by exponential kinetics. Specifically, the fluorescence signals exhibited a  $\approx 1000$  s induction period at depressed quantum yield after blocking excitation, which recovered to approximately half the initial value on a further time scale of 3000 s. Though clearly in qualitative agreement, this range of dark time scales would appear to be much *slower* than with what we observe at the single QD level, i.e., for which we see QD recovery on time scales of 10 s. However, one must be cautious in making time scale comparisons when power law kinetics may be present, which predicts an infinite average event duration for  $m < 2$ . A more conservative conclusion would be that this indicates multiple processes in the dark proceeding at significantly different rates, which could be consistent with highly distributed kinetics. In a different semiconductor material, Cichos et al.<sup>20</sup> studied the bleaching and recovery of silicon nanocrystals ensembles. After illuminating the sample for 10 s and then leaving the sample in the dark for a variable time, the emission intensity recovered consistent with the value of the power law “off” slope observed under continuous illumination. Taking these results together suggest that the reneutralization of silicon

nanocrystals is different from CdSe nanocrystals and that the former proceeds through state  $|2\rangle$  even under continuous illumination.

The present investigation of blinking and blinking recovery kinetics in the dark confirm some aspects of previous models, while revealing interesting dynamics not previously observed. First of all, the dark survival probability for the QD in an “on” state is nearly independent of shutter duration out to times scales of minutes. This indicates that in order for a QD to blink to an “off” state, a photon is required to activate the process. Based on the kinetic scheme in Figure 3.1, this would mean access to the “off” manifold involves at least a single transition through the upper state  $|1\rangle$ , though parallel contributions involving direct photoexcitation from  $|0\rangle$  to  $|2\rangle$  can not be ruled out. In contrast, the “off” survival probability for a QD reveals a clear dependence on the dark dwell time, demonstrating that QDs are able to recover to the “on” state without absorption of a photon. With regard to the kinetic model in Figure 3.1, this would imply a finite distribution of blinking recovery rates, either directly from  $|2\rangle$  to  $|0\rangle$ , or, depending on the relative energetics of the two manifolds, by indirect, non-photoactivated excitation to  $|1\rangle$  followed by fluorescence to the  $|0\rangle$  ground state.

Of particular importance, however, the power law kinetic behavior for blinking recovery in the dark is qualitatively different than observed under previous conditions of laser illumination, with more than 2 orders of magnitude differences in survival probabilities predicted for time scales out to 30 s. This implies that nearly all previous confocal studies of blinking recovery dynamics at the single QD level are either influenced by or likely dominated by light induced transitions from the “off” to “on” manifolds. The suggested mechanism for such transitions is schematically indicated in Figure 3.1, whereby QDs in the “off” manifold continue to absorb photons, though with a dramatically reduced quantum yield for fluorescence. Despite

short fluorescence lifetimes due to rapid non-radiative relaxation from  $|3\rangle$  to  $|2\rangle$ , photon absorption in the “off” manifold can still provide a finite excited state relaxation pathway from  $|3\rangle$  to  $|1\rangle$ . At the very least, these studies point to the critical relevance of such photon assisted paths in QD blinking recovery, evidenced simply by observation of blinking kinetics in the dark.

### 3.5 Summary

The present work reflects a systematic study of single QD blinking behavior in the *absence* of illumination, with a specific focus on elucidating the role of photoexcitation on the long time dynamics. First of all, we find the probability of a QD transitioning in the dark from a high quantum yield (“on”) state to a low quantum yield (“off”) state to be extremely low and essentially independent of dwell time from 100 ms to 100 s time scales. The absence of a dark pathway is consistent with many models for QD blinking, for example, such as photoassisted electron/hole ejection to surface trap states and thereby charging of the QD. On the other hand, blinking *recovery* statistics (from “off” to “on” state) do reveal a power law dependence on dwell time, consistent with *non-photoactivated* and highly distributed kinetics in the dark. However, such QD blinking recovery to the “on” state is orders of magnitude slower than predicted by previous power law kinetic studies and therefore signals the presence of both light-activated and dark pathways. Most importantly, the present kinetic analysis underscores that most if not all previous single QD studies have necessarily been performed under conditions where blinking recovery is dominated by the light-activated channel.

Future extensions of QD blinking and recovery in the dark hope to further elucidate the non-light mediated processes observed here. The “off” time distribution has been observed to be independent of temperature,<sup>8,11</sup> but so far only under continuous illumination conditions. By

eliminating light-induced pathways, the current experiment permits one to focus directly on thermal transitions to/from the ground state of the “off” manifold. QD blinking recovery, i.e.,  $\langle S_{\text{off-off}}(T_{\text{close}}) \rangle$ , could therefore be explored as a function of temperature to probe activated rate processes for transitions from state  $|2\rangle$  to  $|0\rangle$ . The rates for QD blinking in the dark could also be studied by sample temperature, probing thermally activated promotion from the “on” to “off” manifolds. In order to explore alternative light mediated blinking processes suggested by Stefani et al.,<sup>14</sup> a second laser at energies below the QD band gap could be implemented. This would provide continuous illumination of the sample and allow light activated blinking to occur without access to the excited state. The effect of wavelength and illumination intensity on  $S_{\text{on-on}}$  and  $S_{\text{off-off}}$  would nicely compliment these temperature dependence investigations, providing important information about photon mediated transitions between lower states in the “off” and “on” manifolds.

Further studies can also target environmental effects on light- and non-light mediated blinking processes. Blinking kinetics have been shown to be weakly influenced by immediate environment for QDs<sup>26</sup> as well as for single dye molecules in a conductive polymer.<sup>30</sup> Indeed, functionalized QDs have shown blinking suppression in phenylene vinylene oligomers,<sup>31,32</sup> suggesting that QDs in conductive polymers may in general have altered blinking kinetics. The addition of small molecules to solutions of tethered QDs has resulted in changes to the blinking behavior of single QDs.<sup>33,34</sup> In the next chapter, the mechanism by which these molecules influence the blinking in solution will be investigated under continuous illumination conditions.

## References

- (1) Basche, T.; Kummer, S.; Brauchle, C. *Nature* **1995**, 373, 132.

- (2) Vogel, M.; Gruber, A.; Wrachtrup, J.; Vonborchyskowski, C. *J. Phys. Chem.* **1995**, *99*, 14915.
- (3) Cichos, F.; von Borczyskowski, C.; Orrit, M. *Curr. Opin. Colloid Interface Sci.* **2007**, *12*, 272.
- (4) Nirmal, M.; Dabbousi, B. O.; Bawendi, M. G.; Macklin, J. J.; Trautman, J. K.; Harris, T. D.; Brus, L. E. *Nature* **1996**, *383*, 802.
- (5) Efros, A. L.; Rosen, M. *Phys. Rev. Lett.* **1997**, *78*, 1110.
- (6) Klimov, V. I. *Semiconductor and Metal Nanocrystals: Synthesis and Electronic and Optical Properties*; CRC Press, 2003.
- (7) Kuno, M.; Fromm, D. P.; Hamann, H. F.; Gallagher, A.; Nesbitt, D. J. *J. Chem. Phys.* **2001**, *115*, 1028.
- (8) Kuno, M.; Fromm, D. P.; Hamann, H. F.; Gallagher, A.; Nesbitt, D. J. *J. Chem. Phys.* **2000**, *112*, 3117.
- (9) Frantsuzov, P. A.; Marcus, R. A. *Phys. Rev. B* **2005**, *72*, 155321.
- (10) Kuno, M.; Fromm, D. P.; Gallagher, A.; Nesbitt, D. J.; Micic, O. I.; Nozik, A. J. *Nano Lett.* **2001**, *1*, 557.
- (11) Shimizu, K. T.; Neuhauser, R. G.; Leatherdale, C. A.; Empedocles, S. A.; Woo, W. K.; Bawendi, M. G. *Phys. Rev. B* **2001**, *63*, 205316.
- (12) Verberk, R.; van Oijen, A. M.; Orrit, M. *Phys. Rev. B* **2002**, *66*, 233202
- (13) Wang, S.; Querner, C.; Emmons, T.; Drndic, M.; Crouch, C. H. *J. Phys. Chem. B* **2006**, *110*, 23221.
- (14) Stefani, F. D.; Knoll, W.; Kreiter, M.; Zhong, X.; Han, M. Y. *Phys. Rev. B* **2005**, *72*, 125304.
- (15) Banin, U.; Bruchez, M.; Alivisatos, A. P.; Ha, T.; Weiss, S.; Chemla, D. S. *J. Chem. Phys.* **1999**, *110*, 1195.
- (16) Knappenberger, K. L.; Wong, D. B.; Romanyuk, Y. E.; Leone, S. R. *Nano Lett.* **2007**, *7*, 3869.
- (17) Petterson, J. J.; Nesbitt, D. J. *Nano Lett.* **2008**, in press.
- (18) Chung, I. H.; Bawendi, M. G. *Phys. Rev. B* **2004**, *70*, 165304.
- (19) Brokmann, X.; Hermier, J. P.; Messin, G.; Desbiolles, P.; Bouchaud, J. P.; Dahan, M. *Phys. Rev. Lett.* **2003**, *90*, 120601.

- (20) Cichos, F.; Martin, J.; von Borczyskowski, C. *Phys. Rev. B* **2004**, *70*, 115314.
- (21) Mention of commercial products is for information only; it does not imply National Institute of Standards and Technology recommendation or endorsement, nor does it imply that products mentioned are necessarily the best available for the purpose.; Mention of commercial products is for information only; it does not imply National Institute of Standards and Technology recommendation or endorsement, nor does it imply that products mentioned are necessarily the best available for the purpose.
- (22) Gomez, D. E.; Califano, M.; Mulvaney, P. *Phys. Chem. Chem. Phys.* **2006**, *8*, 4989.
- (23) Mao, H. B.; Chen, J.; Wang, J. Q.; Li, Z. F.; Dai, N.; Zhu, Z. Q. *Physica E* **2005**, *27*, 124.
- (24) Podhorodecki, A.; Misiewicz, J.; Nauka, K. *Phys Status Solidi (C)* **2006**, *3*, 3836.
- (25) Pelton, M.; Grier, D. G.; Guyot-Sionnest, P. *Appl. Phys. Lett.* **2004**, *85*, 819.
- (26) Issac, A.; von Borczyskowski, C.; Cichos, F. *Phys. Rev. B* **2005**, *71*, 161302.
- (27) Verberk, R.; Chon, J. W. M.; Gu, M.; Orrit, M. *Physica E* **2005**, *26*, 19.
- (28) Kuno, M.; Fromm, D. P.; Johnson, S. T.; Gallagher, A.; Nesbitt, D. J. *Phys. Rev. B* **2003**, *67*, 125304
- (29) Tang, J.; Marcus, R. A. *Phys. Rev. Lett.* **2005**, *95*, 107401
- (30) Clifford, J. N.; Bell, T. D. M.; Tinnefeld, P.; Heilemann, M.; Melnikov, S. M.; Hotta, J.; Sliwa, M.; Dedecker, P.; Sauer, M.; Hofkens, J.; Yeow, E. K. L. *J. Phys. Chem. B* **2007**, *111*, 6987.
- (31) Early, K. T.; McCarthy, K. D.; Hammer, N. I.; Odoi, M. Y.; Tangirala, R.; Emrick, T.; Barnes, M. D. *Nanotechnology* **2007**, *18*, 424027.
- (32) Odoi, M. Y.; Hammer, N. I.; Early, K. T.; McCarthy, K. D.; Tangirala, R.; Emrick, T.; Barnes, M. D. *Nano Lett.* **2007**, *7*, 2769.
- (33) Fomenko, V.; Nesbitt, D. J. *Nano Lett* **2008**, *8*, 287.
- (34) Hohng, S.; Ha, T. *J. Am. Chem. Soc.* **2004**, *126*, 1324.

## Chapter 4

### Blinking Suppression for Quantum Dots in Aqueous Solution by Phenol

#### 4.1 Introduction

Colloidal semiconductor quantum dots (QDs) are widely used in many experimental fields because they have continuous absorption spectra with large absorption cross sections and good photostability.<sup>1</sup> Ensemble studies use them as fluorescent probes in many assays – detection of glucose,<sup>2,3</sup> antimony cation,<sup>4</sup> and sulfide anion<sup>5</sup> as a few examples. Labeling the QD surface with specific markers allows for the determination of uptake and expression of a wide range of proteins, antibodies and antigens.<sup>6-8</sup> However, ensemble techniques are not the only area of interest and use for QDs. When coupled with sensitive detection techniques, the unique optical properties also allow the detection of single QDs over extended experimental time windows and with high spatial localization. Researchers have demonstrated the use of single QDs in real time tracking of biological processes such as intracellular diffusion and cellular transport<sup>9,10</sup> as well as in super resolution techniques<sup>11,12</sup> for localizing cellular machinery.<sup>13</sup>

In the one of the first investigations into single QD fluorescence, Bawendi and coworkers observed fluorescence intermittency (blinking), distinct transitions between a high quantum yield (“on”) state and a low quantum yield (“off”) state.<sup>14</sup> Blinking of single molecule fluorescence had previously been observed in several dye molecule systems and had been interpreted in those cases as a photoinduced transition between singlet and triplet manifolds<sup>15,16</sup> One common interpretation of this blinking is that the switching from “on” to “off” is a result of a photoassisted charge ejection process (either hole or electron) that results in the core of the QD

being charged, whereby fast and efficient non-radiative recombination rates dominate.<sup>17</sup>

Neutralization is a result of the charge returning to the core and consequently the QD resumes its normal fluorescence state. However, the intermittency observed by Bawendi and coworkers revealed time scales too long to be attributed to simple phosphorescent channels. Subsequent investigations by Kuno et al.<sup>18,19</sup> extended the experimental observational window to hundreds of seconds and revealed that the distribution of times for both the “on” and “off” state was highly non-exponential. In fact, the distribution was well characterized by a power law ( $P(t) \propto t^{-m}$ ) over 8-9 orders of magnitude in probability and 5-6 orders of magnitude in time. This remarkable non-exponential behavior requires a more complex model based “on” ‘distributed kinetics’ for the charge ejection and neutralization accessing a wide range of rate processes.<sup>20</sup>

Many experiments have been subsequently implemented to clarify the origin of these largely distributed power law time scales. The influence of the composition,<sup>21-23</sup> size,<sup>18</sup> and shape<sup>24</sup> have all been probed to better understand the mechanism of the blinking and the nature of the proposed charge ejection state. In each case, the “on” time distributions follow a power law that varied between 1.3-1.7 with differences in the long time tail described by an exponential truncation found to vary based “on” temperature<sup>22</sup> and illumination intensity.<sup>25</sup> The “off” time distributions are more insensitive to changes showing a typical slope of 1.60 for a variety of QD compositions, sizes and shapes.

If the blinking is a result of trap state dynamics, the environment around a QD can significantly change the blinking dynamics observed. For example, epitaxially grown InGaAs QDs embedded in solid GaAs blink infrequently at room temperature.<sup>26</sup> In order to better approximate the epitaxial grown QDs, synthetic protocols began including 1-5 monolayer shells of a larger band gap material, typically ZnS, to the QDs in order to better passivate the surface of



the QD where the traps are most likely to occur. Ensemble QY are found to increase with increasing shell thickness which does suggest that the QDs spend more time in the “on” state. More recently, Klimov and coworkers synthesized “super shell QDs”, colloiddally grown CdSe cores with 10-12 monolayers of ZnS shell.<sup>27,28</sup> They report single molecule QD trajectory studies showing blinking suppression, i.e. the QDs spend the majority of the time in the “on” state.

Suppression of blinking has also been achieved through control of the environment around the QD by changing the ligands or adding molecules to the solution. Most typically thiols are found to have a large effect, for example. The addition of mercaptoethylamine was found to suppress the blinking of surface absorbed QDs in a buffer solution.<sup>29</sup> Ha and coworkers<sup>30</sup> demonstrated reversible suppression of blinking by addition of millimolar quantities of  $\beta$ -mercaptoethanol (BME) to CdSe/ZnS QDs tethered to a surface. Follow up work by Jeong et al.<sup>31</sup> showed that the effect was controlled by pH and due to the presence of the thiolate anion in solution. Lastly, dithiolthreitol doped polymer films demonstrate near complete blinking suppression characterized by low (<5%) “off” state populations in count rate histograms.<sup>32</sup>

An alternative to thiol containing compounds was provided by Fomenko et al.<sup>33</sup> who investigated the effect of propyl gallate (3,4,5 – trihydroxybenzoic propyl ester) “on” QD fluorescence by monitoring the count rate (QY) and the fluorescence lifetime ( $\tau_{FL}$ ) of individual QDs. Complete blinking suppression was observed for the system upon addition to the sample. In addition, the peak count rates observed remained constant, while the fluorescence lifetime showed a 5 fold decrease. This was interpreted as a decrease of the radiative lifetime with little change in the non-radiative lifetime.

A common theme in these ligand exchange and small molecule addition studies is the idea that the molecule is a Lewis base and reacts with a positively charged surface trap site. As

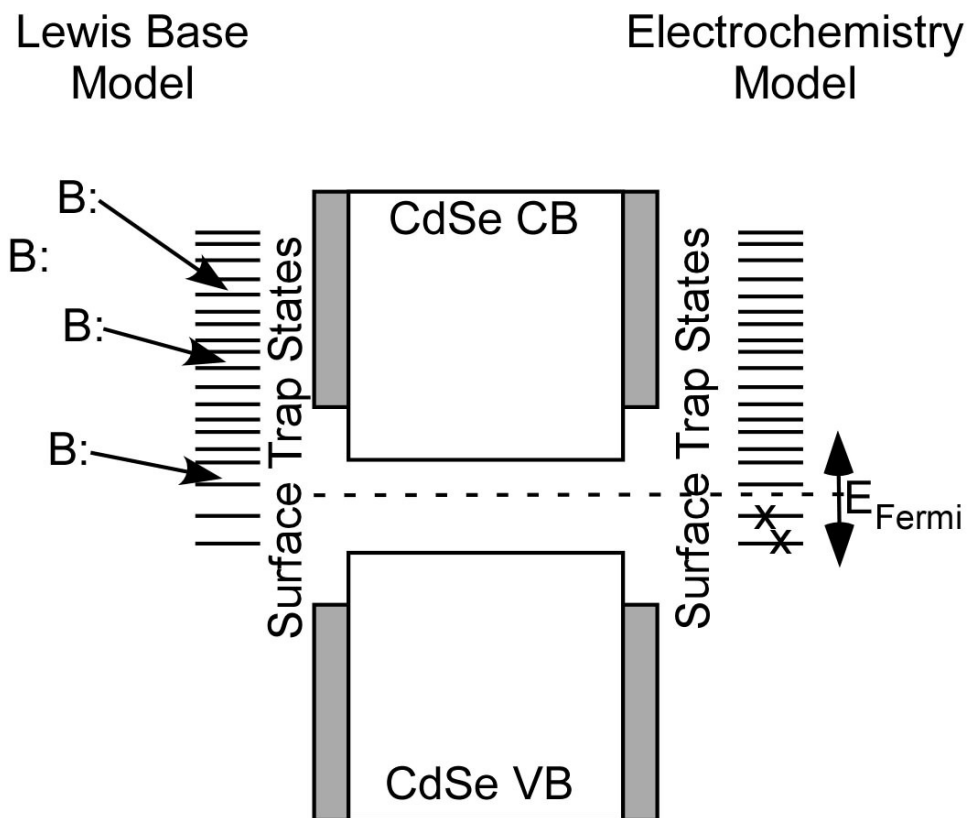


Figure 4.1: Two possible models for blinking suppression. On the left, the molecule is a Lewis base and donates electron density to fill surface trap sites on the QD. In the second, depicted on the right, the molecule changes the electrochemical potential of the solution which shifts the Fermi energy to fill (or empty) trap sites in the QD.

more surface sites become occupied in this manner, the QD remains in the “on” state longer as there are fewer traps sites for the ejected electron. This is schematically represented “on” the left side of Figure 4.1. It is important to note, that in this model only surface states that are solvent accessible will be occupied, while those located in the interior of the QD will remain as possible “off” state sites.

An alternative picture for how a given molecule affects the surface trap state distribution arises from considering an electrochemical view of the solution. Several experiments from the Lian group have investigated electron<sup>34-36</sup> or hole<sup>37</sup> transfer to suitable accepting species in solution. They found that the transfer rate depended “on” the relative energy difference between the molecular LUMO (or HOMO) energy and that of the photoexcited electron (or hole)

suggesting that a redox couple is formed by the molecule and QD. Other experiments have investigated individual QDs in electrochemically controlled cells, and found that fluorescence QY and lifetime were effected by applying a negative potential.<sup>38,39</sup> A simple schematic for this is shown “on” the right side of Figure 4.1, where the Fermi level is shifted up or down based “on” the applied bias. The electrochemical cell thus fills (or empties) trap states in the QD below (or above) to maintain a fixed potential. When the Fermi level rises above the valance band, electrons are transferred to the core of the QD and this greatly affects the fluorescence QY and lifetime.

The experiments presented here will elucidate which of these models, Lewis base or electrochemical potential, correctly describes the mechanism for blinking suppression by small molecules. In order to properly test both scenarios, a requirement of the study is that both the potential modes of suppression must be present to determine which is the dominant process in solution. We chose to investigate phenol, based on our previous work in aqueous solution with propyl gallate (PG). Phenol represents the simplest hydroxybenzyl compound and has no secondary chemistry (basic de-esterfication is a problem with PG). It has a single well known  $pK_a$  of 9.8, and is stable in water for extended periods of time. The one electron redox potential ( $E_0$ ) of phenol is 5.5 V (vacuum) which is near the Fermi energy for CdSe (5.75 V). Therefore, phenol provides the ability to change the concentration of the neutral (phenol), the concentration of the anion (phenoxy) and tune the redox potential by varying the pH between 8 and 10. Two related benzenediol species (hydroquinone and resorcinol) are explored that have similar  $pK_a$  values, but different  $E_0$ , in order to probe the role of reduction potential over a wider range of values.

Initially, in order to quantify the degree of blinking suppression we look at three metrics - the fraction of time a QD spends in the “on” state ( $F_{\text{on}}$ ) and the power law slope of the “on” and “off” time distributions – as a function of phenol concentration. We observe a marked increase in the  $F_{\text{on}}$  as we increase the concentration of the phenol, as well as a change in  $m_{\text{on}}$ , but no variation for  $m_{\text{off}}$ . To test whether the Lewis base model is accurate, we vary the pH in order to determine if the active species is the phenol molecule or the phenoxy anion. We show that the effect does depend on the phenoxy anion concentration rather than neutral phenol concentration. However, when comparing the two different molecules that have comparable Lewis base activity, dramatically different results are obtained, which suggest the role that redox potential has in blinking suppression.

The paper is organized as follows. In section 4.2, the experimental setup and sample preparation are described. Section 4.3 presents sample data and results from the concentration and pH dependence of blinking suppression for phenol. Section 4.4 focuses on interpretations of the results and addresses the two possible models of blinking suppression. A summary of results and suggestions of future work are provided in section 4.5.

## **4.2 Experiment**

Experiments are performed on an inverted epi-fluorescence confocal microscope (Olympus IX-70) with single photon detection capabilities. Laser excitation is provided by a 434 nm GaN diode laser (Picoquant, LDH 400) with a pulse width of  $\sim 70$  ps and a repetition rate of 5 MHz. The excitation is right hand circularly polarized, expanded by an 8:1 collimating telescope, and attenuated by a series of neutral density filters before entering the back of the microscope. A dichroic (Chroma Z434DC) reflects the light into a 100x 1.4 NA oil immersion

objective (Olympus PlanApo) which focuses in the sample at the diffraction limit. The fluorescence is collected by the same objective, transmitted by the dichroic, and then spatial filtered by a 50  $\mu\text{m}$  pinhole. The emission is separated by a second dichroic centered at 561 nm before being focused onto a pair of avalanche photodiodes (APD, Perkin Elmer, SPCM-AQR-14) with additional band-pass filters (Chroma 580-70M) mounted in front of the APDs to suppress light outside of the QD emission range.

The signals from the APD are sent to a router (HRT-81) and then to a time correlated single photon counting card (Becker-Hickl TCSPC-130) which provides time-tagged fluorescence measurements with both “macrotime” (i.e., time since start of the experiment,  $\sim 50$  ns resolution) and “microtime” information (i.e., time between excitation pulse and photon emission, 200 ns maximum with  $\sim 49$  ps resolution) as well as which APD detected the photon (which allows separation by emission wavelength or polarization). The advantage of this technique is that it allows the data to be binned post acquisition into any desired time interval, or alternatively, segments containing a fixed number of photons.

Streptavidin-conjugated CdSe/ZnS quantum dots in standard borate buffer (25 mM, pH 8.3) with an absorption peak at 550 nm and emission peak at 565 nm are obtained from Invitrogen. The samples are made by tethering the QDs to biotin-BSA/BSA (1:10) coated glass slides in a homemade microfluidic channel sample holder, which leads to a surface coverage density of  $\sim 0.6$  QD/ $\mu\text{m}^2$ . Previous QD blinking experiments have shown that biexcitonic Auger ionization provides a maximal limit to the “on” time distribution. In order to balance this process with the detected signal levels, the laser power is attenuated to  $\sim 55$  nW at the sample. At these power levels, the characteristic fall-off time is  $\sim 0.25$  s and an adequate signal-to-noise level (5:1) is achieved so that a threshold “on”-“off” analysis with 1 ms bin time is possible.

To obtain a typical data set, images are first created by raster scanning the sample on a piezoelectronic closed loop stage (PI P-517.3CL), which reveals single QDs with a near diffraction limited spot size of 240 nm full width half maximum. The stage is then moved under closed loop control to center a single QD in the laser focus. Fluorescence trajectories are obtained for 30 s, after which the stage is moved to the next QD in the image. Acquisition and analysis software is written in-house and based on LabWindows modules and drivers.

### 4.3 Results

The first experiment is to determine if phenol has a measurable effect on the QD blinking. The sample is prepared as usual and studied to determine initial surface coverage and blinking behavior of individual QDs (Figure 4.2, upper left panels). Subsequently, 200  $\mu\text{L}$  of 15 mM phenol in borate buffer at pH 8.3 is flushed through the microfluidic chamber (20  $\mu\text{L}$  volume) and the sample reimaged. The number of QDs observed is comparable to the initial surface coverage in the absence of phenol; however the amount of time an individual QD remains in the “on” state is noticeably higher (Figure 4.2, lower left panels). A second flush with buffer returns the QDs to the initial blinking behavior, suggesting that phenol has a reversible effect on the QDs, much as was observed in the BME studies of Hohng and Ha.<sup>30</sup>

In order to quantify the blinking suppression observed, trajectories are binned at 1 ms and analyzed by determining if the signal is above (“on”) or below (“off”) an intensity threshold level to establish the QD emission state. The choice of threshold for this study is half way between the “on” and “off” intensity levels. However, deviations from this specific choice do not influence the results presented here. In order to estimate the degree of blinking suppression, the fraction “on” time ( $F_{\text{on}}$ ) is calculated by the amount of time the QD was in the “on” state divided

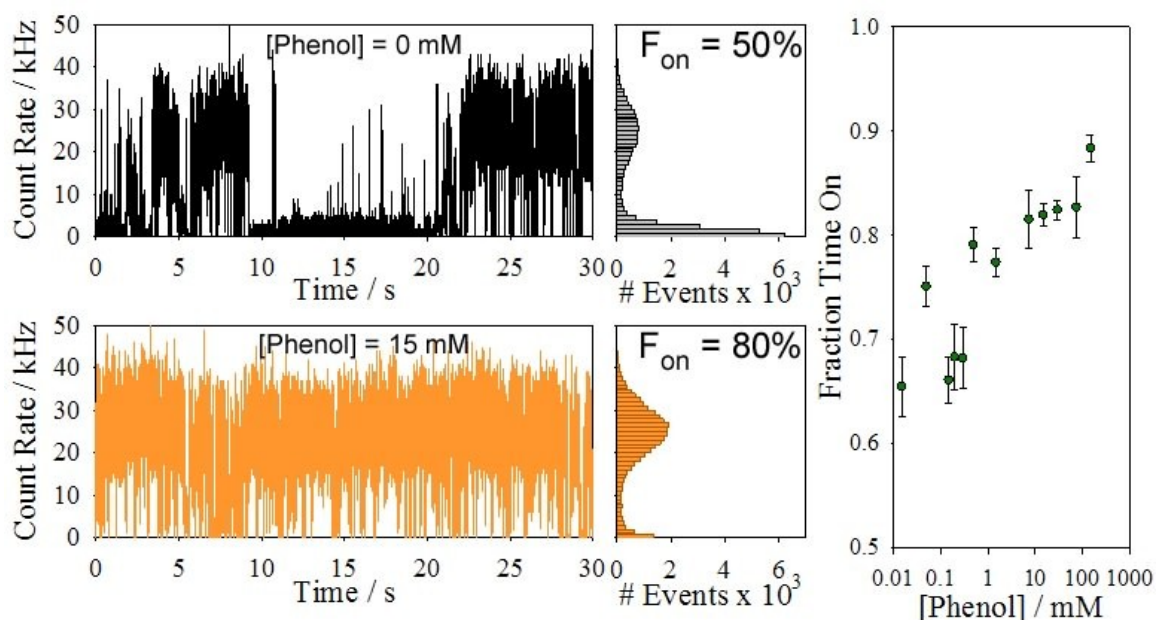


Figure 4.2: Sample trajectories in the absence and presence of phenol. On the left, the top panel displays a typical blinking QD trajectory observed in buffer only conditions, while the bottom panel exhibits blinking suppression in the presence of 15 mM phenol. Histograms for each are included that show the change from 50% to 90%  $F_{on}$  after addition of phenol. The rightmost panel presents the data from a large number of QDs for  $F_{on}$  versus phenol concentrations which shows an increasing “on” time fraction with increasing phenol concentration.

by the total time of the trajectory. Although power laws do not have strictly defined averages, this is a useful metric because the trajectories are acquired for the same total time between different conditions. This results in defined averages of “on” and “off” times over the finite range of the experimental time window. A more rigorous metric for the blinking behavior is obtained by fitting the probability densities of the “on” and “off” times and fitting the resulting distribution to a power law. The data is well described by a simple power law,  $P(\tau_{on/off}) = A\tau_{on/off}^{-m}$ , over 3 orders of magnitude in time and 4 orders of magnitude in probability presented for the “on” times in the upper panels of Figure 4.3.

To investigate the dependence of phenol in blinking suppression, the concentration of phenol is varied over 4 orders of magnitude (0.015 mM to 150 mM) and the results are analyzed

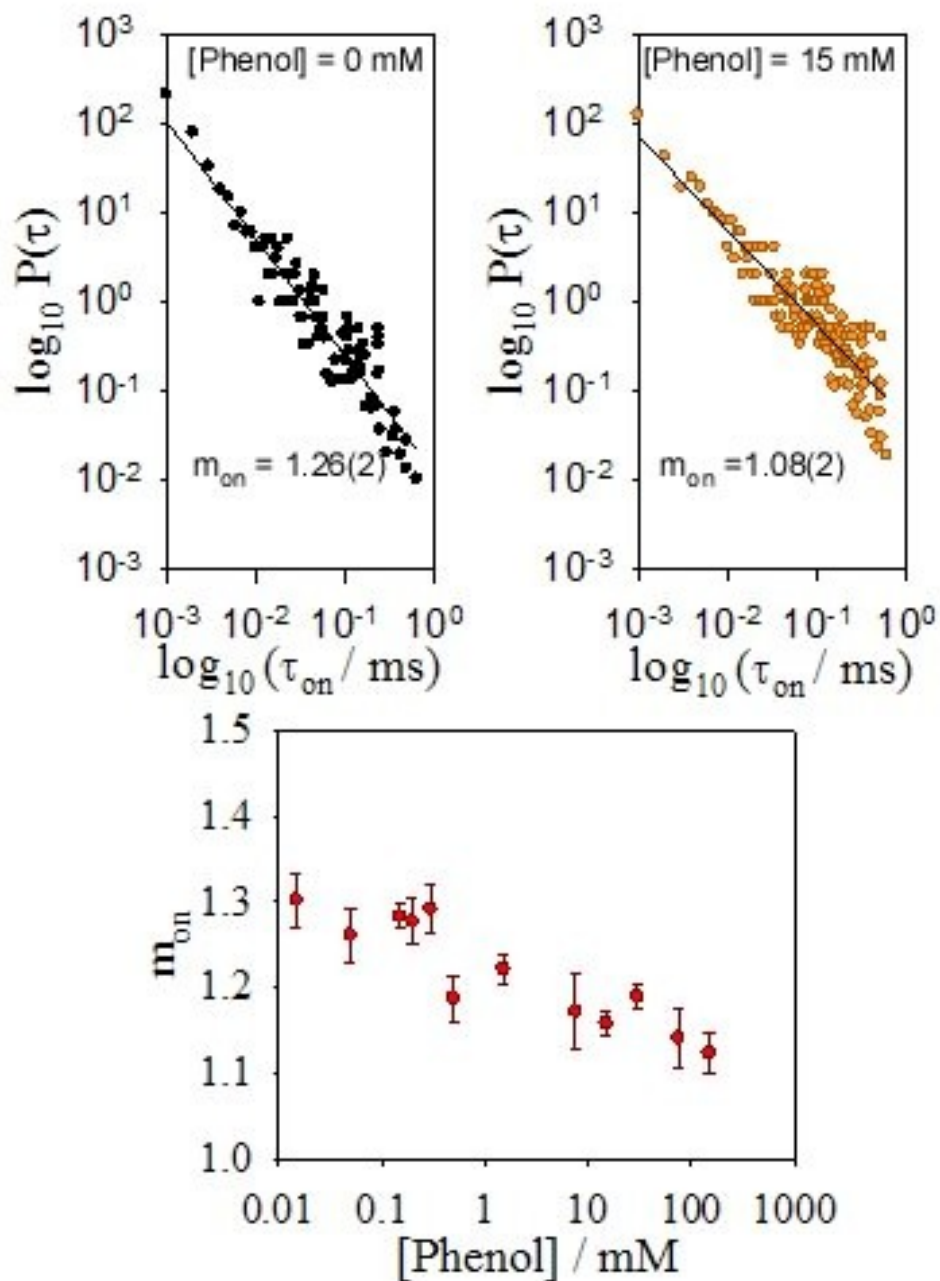


Figure 4.3: Sample “on” time distributions and effect of phenol on  $m_{\text{on}}$ . The upper panels show the “on” time distributions for the traces in Figure 2 are well described by a power law fit over more than 3 orders of magnitude in time. A summary of observed power law slopes for the “on” time distribution ( $m_{\text{on}}$ ) versus phenol concentration is shown in the lower panel. The increase of  $\sim 50\%$  for  $F_{\text{on}}$  shown previously is caused by a  $\sim 10\%$  decrease in  $m_{\text{on}}$ .



in the same way as before. The right most panel of Figure 4.2 shows that the value of  $F_{\text{on}}$  clearly increases from a value near 0.65(3) to 0.88(1) with increasing phenol concentration (presented on a log scale), thus phenol qualitatively acts as a blinking suppression agent. More interestingly, the lower panel of Figure 4.3 shows that the slope of the power law for the “on” time distribution ( $m_{\text{on}}$ ) also decreases from 1.30(3) to 1.12(2), while the “off” time distribution is relatively unchanged with a power law slope of  $m_{\text{off}} = 1.70(5)$  over the same concentration range. Interestingly, in buffer containing no phenol, the value of  $m_{\text{on}}$  is 1.22(1) which is statistically different from the value obtained at the lowest phenol concentration, suggesting that the concentration is not the only parameter influencing the blinking.

In conjunction with the results obtained from the macrotime data, there is additional information in the microtime distribution and channel tag. A histogram of the microtimes contains information about the fluorescence lifetime ( $\tau_{Fl}$ ) for the excited state and is well described by a single exponential decay. Specifically, the microtimes are separated into 200 photon segments which are fit to a single exponential decay by a maximum likelihood estimator (MLE) method. The average value of  $\tau_{Fl}$  is representative of the lifetime for individual trajectories and is found to be insensitive to the choice of the number of photons included in a segment. Lastly, the dichroic separates the emission into two channels based on wavelength. A ratio of the signals on both detectors,  $F_{\#} = \frac{I_{APD1}}{I_{APD1} + I_{APD2}}$ , can therefore be related to the emission color of the QD. This value can be calculated for the total counts, as a trajectory for each time bin, or in segments of photons. In each of these cases, the obtained quantity is similar and only the average trajectory result is presented here.

This provides three additional monitors for the effect of phenol on QD dynamics – the average “on” count rate ( $I_{\text{on}}$ ), the average lifetime ( $\tau_{Fl}$ ) and the color of the emission ( $F_{\#}$ ) – each

of which is shown in Figure 4.4 as a function of phenol concentration. Unlike the observations for  $F_{\text{on}}$  and the “on” power law slopes, there is no change in either the  $I_{\text{on}}$  or  $\tau_{FL}$  over the investigated concentration range. With both  $I_{\text{on}}$  and  $\tau_{FL}$  remaining constant, this implies that the radiative and non-radiative rates from the excited state to the ground state are not being influenced by phenol in the same way as they were for PG. It also suggests that the phenol is influencing the rate of the QD transitioning from “on” to “off” in a manner that doesn’t contribute to a non-radiative component of the decay from the excited state. Lastly, the insensitivity of  $F_{\#}$  to varying phenol concentrations suggests that there is no dramatic change in the charge distribution around the QD. Changes in this distribution have been shown to alter the local electric field which induces a Stark shift of the fluorescence.<sup>40</sup>

In order to determine the mechanism by which phenol is affecting the QD blinking dynamics, studies into the specific species that influence the blinking have been implemented. Initial experiments are performed at a pH of 8.3, *i.e.*, below the  $pK_a$  of phenol (9.8), with additional investigations carried out up to pH 10. The same qualitative trends (increasing  $F_{\text{on}}$ , decreasing  $m_{\text{on}}$ , constant  $m_{\text{off}}$ ) are observed with increasing phenol concentration at a given value of pH, though the effects of low concentrations at high pH appear to have a similar magnitude to those at high concentrations but at the lower pH. In order to determine which species, phenol (PhOH) or phenoxy anion (PhO<sup>-</sup>), is responsible for the effect, conditions of fixed PhOH or PhO<sup>-</sup> are obtained by varying the total concentration of phenol species and pH. If PhOH is the active species, plots of  $F_{\text{on}}$  or  $m_{\text{on}}$  versus [PhO<sup>-</sup>] for a fixed [PhOH] should be characterized by horizontal lines. The leftmost panel of Figure 4.5 demonstrates the changes of  $m_{\text{on}}$  under this constraint for three different concentrations of [PhOH] = 0.13 mM, 0.27 mM, and 1.40 mM. The

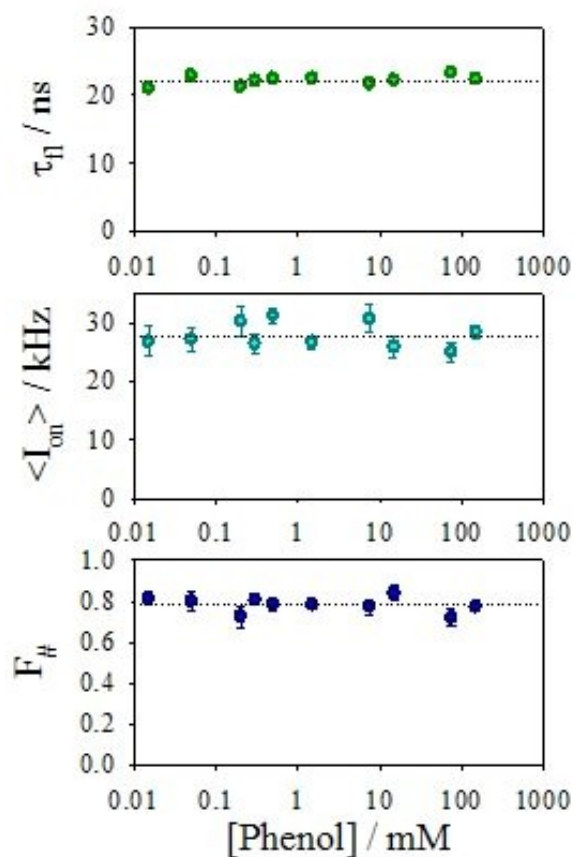


Figure 4.4: Phenol effects on other metrics. Phenol concentration dependence for the TCSPC extracted values: Fluorescence lifetime (uppermost), intensity of the “on” state (middle) and  $F_{\#}$  (lowest) which is related to the emission wavelength. None of these show a dependence “on” the phenol concentration suggesting that the phenol is not influencing the radiative or non-radiative rates of the excited state in the “on” manifold.

three data set slices display a clear trend with increasing  $[\text{PhO}^-]$  and are not characterized by a line with zero slope, suggesting that  $\text{PhOH}$  is not responsible for the suppression by itself.

Conversely, if phenoxy anion is the relevant species, as thiolate anion was relevant in the BME experiment, graphs of  $m_{\text{on}}$  plotted at a fixed value of  $[\text{PhO}^-]$  would be independent of  $[\text{PhOH}]$ . Three such slices are shown in the right panel of Figure 4.5 for  $m_{\text{on}}$  for conditions where  $[\text{PhO}^-] = 0.03 \text{ mM}$ ,  $0.18 \text{ mM}$ , and  $1.70 \text{ mM}$ . Plotted in this way, the obtained values do lie on a horizontal line which suggests that the phenoxy anion is the species in solution that is

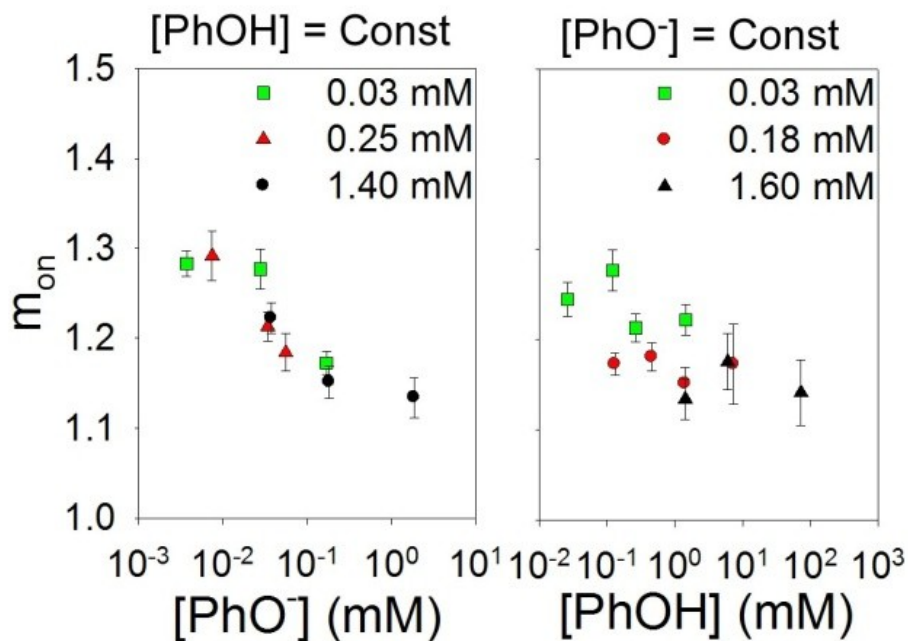


Figure 4.5: Constant PhOH or PhO<sup>-</sup> slices. The dependence of  $m_{on}$  separated by species in solution. The left panel is the case where the concentration of PhOH is held constant ([PhOH] = 0.13 mM, 0.25 mM, and 1.4 mM) but PhO<sup>-</sup> and pH are varied. This should be contrasted with the results “on” the right where PhO<sup>-</sup> is held constant ([PhO<sup>-</sup>] = 0.03 mM, 0.18 mM and 1.6 mM), but PhOH and pH are varied. In the latter case, the data lies “on” a horizontal line for a given [PhO<sup>-</sup>] suggesting that the active species is phenoxy anion.

influencing the blinking. The full dataset of all phenol concentrations and pH values investigated are shown for both  $F_{on}$  and  $m_{on}$  in Figure 4.6 plotted versus [PhO<sup>-</sup>], where the black circles represent the original pH 8.3 data, the red squares the values at other pH, and the black dash line the zero phenol concentration data. The data plotted in this manner overlap suggesting that there is indeed a relationship between the total concentration and pH and that the phenoxy anion may be the pertinent species in solution.

#### 4.4 Discussion

These results provide potentially valuable insight into the dynamics that underlie the blinking transitions. The phenol has a clear effect on transitions between the “on” and “off”

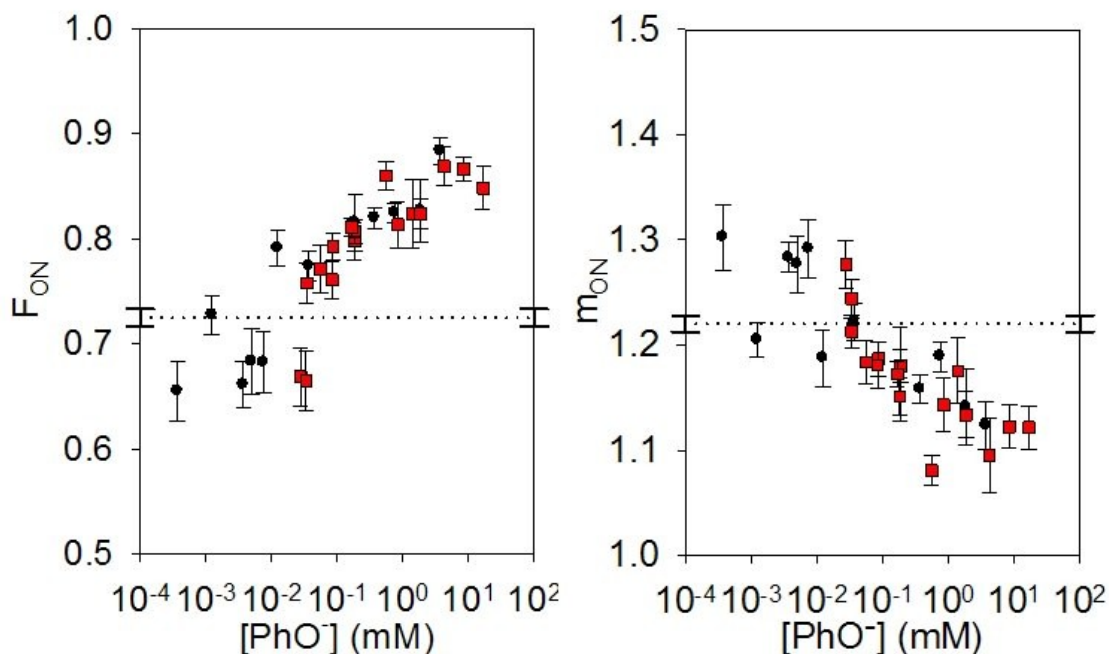


Figure 4.6: Complete data set for different phenol concentrations and pH. Complete data set for different concentrations of phenol and pH plotted against  $[PhO]$ . The data for pH > 8.5 (red squares) overlap that of the pH 8.3 data (black circles). The results in the presence of zero phenol concentration (buffer only) are included as a dashed line with error bars. The low concentration data is statistically distinct from the zero concentration values, signifying that the phenoxy anion is not solely responsible for the effect.

manifold as demonstrated by decreases in  $m_{on}$ . In the presence of phenol, the QD has a higher probability of remaining in the “on” state for longer times characterized by a lower power law slope. When this effect is combined with no change in  $m_{off}$ , blinking suppression, a larger value of  $F_{on}$ , is observed as the phenol concentration is increased. Interestingly, no change is reflected in either the quantum yield of the “on” state or the fluorescence lifetime which remain constant over the range of concentrations investigated. This implies that the radiative and non-radiative rates for the transitions from the excited state to the ground state are unaltered by the phenol, in clear contrast to the results for propyl gallate.<sup>33</sup>

In addition to the single molecule results, the effect of phenol is also observed in ensemble fluorometry experiments. Ensemble QY measurements can be thought of as a product of the “on” state QY, measured by single molecule techniques, multiplied by the fraction of QDs that are in the “on” state. While the QY of a single QD does not change upon addition of phenol,  $F_{\text{on}}$  is dependent on the phenol concentration. Changes in  $F_{\text{on}}$  therefore should correspond to changes in the fraction of QDs that are in the “on” state during the fluorometry experiment; thus the ensemble QY should increase upon addition of phenol. The relative emission intensity measured as phenol is added stepwise to a sample of 1 nM QDs. The emission is found to increase by ~12% when increasing the phenol concentration from 0.015 mM and 25 mM at pH 8.3. This closely matches the increase observed for  $F_{\text{on}}$  (~15%) over the same concentration range, which suggests that the effect of blinking suppression is also observable and confirmed in ensemble measurements.

The pH dependence of the effect suggests that the phenoxy anion is the relevant species to consider in a model for blinking suppression. In the case of BME, Jeong et al.<sup>31</sup> suggested that the thiolate anion is able to donate electrons into undercoordinated surface sites on the QD and therefore reduce the number of trap sites for photo-ejected electrons leading to less frequent transitions to the “off” state. This could be analogous to the present experiments, where the oxyanion donates electron density and thus the degree of blinking suppression is related to the phenoxy concentration. However, if this is the complete answer, the values of  $F_{\text{on}}$  and  $m_{\text{on}}$  should approach the zero concentration values in the asymptotic limit of low concentration. Instead, the values obtained at low concentration ( $[\text{PhO}^-] < 0.1 \text{ mM}$ ) are different by nearly 10% and outside of the approximate uncertainty (Figure 4.6).

In order to address these results, the electrochemical cell model initially proposed is considered. The redox potential of a solution includes contributions from both concentration of the molecule and the overall pH of the solution. The Nernst equation for a pH dependent redox couple is:

$$E_{red} = E_o - 0.0592 \log \frac{[red]}{[ox]} + 0.0592 pH \quad (4.1)$$

where [red] and [ox] are the concentrations of the reductant and oxidant, respectively. In the specific case of phenol, the oxidant form (phenoxy radical) is unstable and rapidly undergoes dimerization or other chemistry. A true poised electrochemical cell is not attained for phenol, because the concentration of the oxidant is near zero. Nevertheless, the one electron reduction potential of phenol is measured to be 5.5 V (relative to the vacuum level) by cyclic voltammetry. This places the redox potential of the solution between the valence band (6.62 V) and conduction band (4.88 V). This value is also quite close to the QD Fermi level at 5.75 V. Closer inspection of the  $F_{on}$  and  $m_{on}$  curves reveals that the concentration of  $PhO^{\cdot}$  is approximately 0.05 mM when the curves intercept the values obtained in the absence of phenol. The electrochemical potential of the solution could be influencing the Fermi level which changes the trap state distribution. Above ~0.05 mM phenoxy concentrations, the trap states become occupied resulting in blinking suppression, while at lower concentrations more trap states are available so that blinking increases.

To further test this hypothesis, two additional benzenediol compounds have been investigated – resorcinol (1,3- benzenediol,  $pK_a = 9.3$ ,  $E_o = 5.0$  V) and hydroquinone (1,4- benzenediol,  $pK_a = 9.8$ ,  $E_o = 4.6$  V). Both compounds have similar  $pK_a$  values to phenol (9.8) but lower values of  $E_o$ . If the important role of the compound is merely the oxyanion concentration, then at a given pH and total concentration, each compound should give similar

results to those obtained for phenol. Conversely, if the reduction potential is the important property, the results may be drastically different as the hydroquinone reduction potential is near the conduction band at 4.88 V. Previous electrochemistry studies showed a decrease in the intensity, and an increase in the blinking when the potential of the cell was near the conduction band level.<sup>38,39</sup> Alternatively, resorcinol has a reduction potential that is similar to phenol and lies within the CdSe band gap. The inset of Figure 4.7 indicates the relevant potentials for a CdSe/ZnS QD and the compounds investigated in this paper. Normalized count rate histograms for sample traces are presented in Figure 4.7. Both phenol and resorcinol display a 90% “on” state population that is greater than buffer only conditions (72%), while hydroquinone is found to spend only 10% of the time in the “on” state.

Additionally, these results may be compared with experiments involving QD/dopamine conjugates that have been used as sensors for in vitro and intracellular pH.<sup>6</sup> They report that the photoluminescence yield and fluorescence lifetime changes linearly with pH and attribute their results to a pH dependent dopamine reduction potential. Dopamine has an  $E_0$  of 5.25 V which places it in the band gap and would be entirely consistent with our interpretation of the data. More recently, studies of the pH dependence for photoluminescence quenching by dopamine concluded that electron transfer to and from redox active dopamine was responsible for the increase in ensemble QY and decrease in fluorescence lifetime with increasing pH.<sup>41</sup>

The apparent blinking dependence on the reduction potential can also be compared to recent results by Galland and coworkers where they constructed an electrochemical cell to directly control the Fermi level of the system.<sup>38</sup> In particular, they observed a pronounced degree of blinking suppression (characterized by an increased  $F_{on}$ ) for an electrochemical potential between the conduction and the valance band attributed to the circuit filling traps



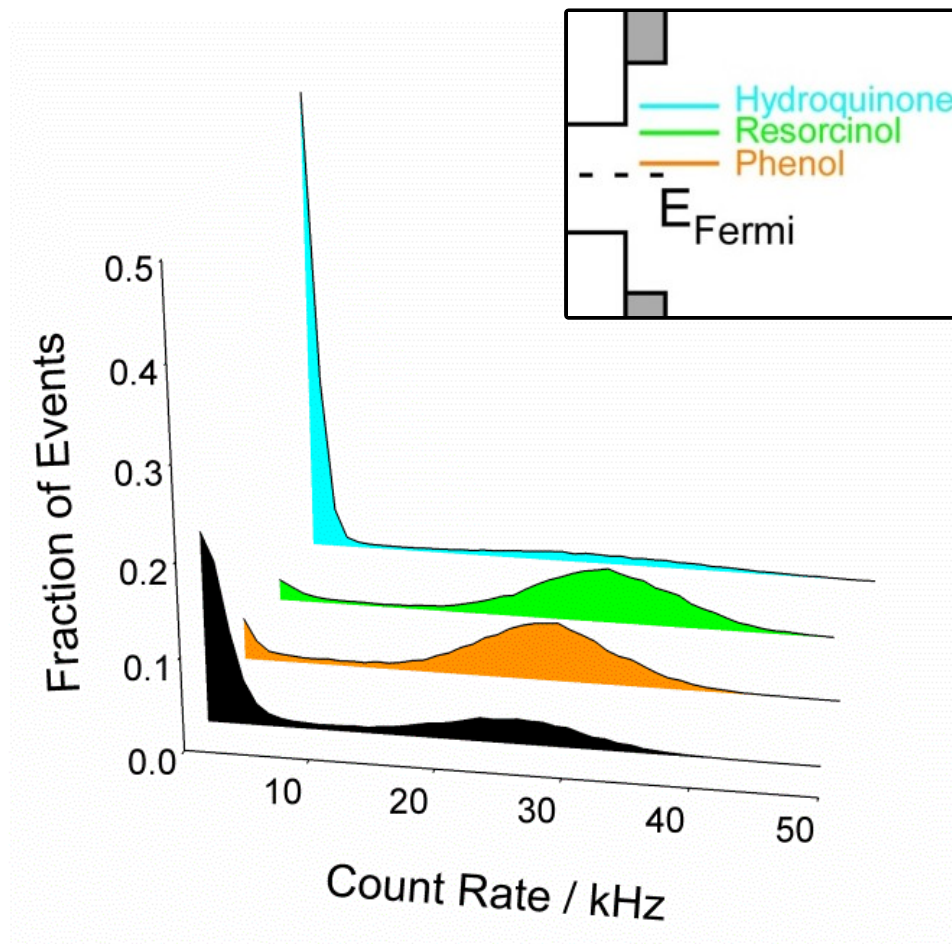


Figure 4.7: Effects of different species on  $F_{on}$ . Count rate histograms of trajectories showing the effect “on”  $F_{on}$  for the different conditions. In buffer only (black) the QD is “on” 50% of the time, while in the presence of phenol (orange) and resorcinol (green) the QD is “on” closer to 90% of the time. This is contrasted by the results with hydroquinone (blue) where the QD spends only 10% of the time “on”. Phenol, resorcinol and hydroquinone have similar  $pK_a$  values, thus the concentration of the hydroxyanions are comparable in each case. However, the one electron reduction potential of the molecules (shown schematically in the inset) shifts the Fermi level up in solution with phenol and resorcinol, but still within the band gap; conversely, the Fermi level in the presence of hydroquinone is shifted nearer the conduction band.

located in that energy region. Upon raising the Fermi level above the conduction band, they observed a decrease in the photoluminescence intensity and a decrease in the lifetime corresponding to charge injection into the  $1S_e$  state of the QD. These studies support the conclusion that it is the overall solution chemical reduction potential that influences the blinking, not the phenoxy anion acting as a Lewis base in solution.

#### 4.4 Summary

The present work reflects a systematic and quantitative investigation to probe the role molecules in solution have on QD blinking. First, we find that phenol influences the “on” to “off” rates in a concentration and pH dependent manner. The lack of an effect in the average “on” intensity and the fluorescence lifetime suggests that phenol is not altering the radiative or non-radiative lifetime of the excited state, but only the transitions from the “on” to “off” manifold. Phenol influences the “on” time distributions, for which a decrease in the power law slope from 1.30(3) to 1.12(2) is observed over 5 orders of magnitude of phenol concentration. This small change leads to dramatic visual differences in fluorescence trajectories where the fraction of time a QD spends “on” increases nearly 50% by adding ~10 mM of phenol. The experimental results are consistent with an electrochemical model where the reduction potential of the solution is controlled by varying the concentration of phenol and pH. Subsequent investigations of species with similar oxyanion concentrations, but different reduction potentials, further support the conclusion that the blinking is influenced by the energy of the Fermi level. The results here are also consistent with three other similar experimental observations in the literature under different experimental conditions.

Suggestions for future experiments include aqueous solution control with a poised electrochemical half-reaction where the relative concentration of the oxidant and reductant can be independently tuned through the conduction band, such as methyl viologen ( $E_0 = 4.7$  V), or related compounds in the same range. One interesting extension is to analyze power spectral densities or correlation functions of the trajectories to obtain information about dynamics occurring on time scales faster than 1 ms. These two approaches to data analysis eliminate the need to bin the data or establish a threshold for the “on”-“off” states and allow dynamics to be

probed down to microsecond rather than millisecond time scales. This type of analysis will be included in the next chapter when discussing blinking simulations.

## References

- (1) Klimov, V. *Semiconductor and Metal Nanocrystals Synthesis and Electronic and Optical Properties*; CRC Press, 2003.
- (2) Priyam, A.; Chatterjee, A.; Bhattacharya, S. C.; Saha, A. *Photochem. Photobiol. Sci.* **2009**, *8*, 362.
- (3) Duong, H. D.; Il Rhee, J. *Talanta* **2007**, *73*, 899.
- (4) Ge, S. G.; Zhang, C. C.; Zhu, Y. N.; Yu, J. H.; Zhang, S. S. *Analyst* **2010**, *135*, 111.
- (5) Zhang, B. H.; Wu, F. Y.; Wu, Y. M.; Zhan, X. S. *J. Fluoresc.* **2010**, *20*, 243.
- (6) Medintz, I. L.; Uyeda, H. T.; Goldman, E. R.; Mattoussi, H. *Nature Mat.* **2005**, *4*, 435.
- (7) Goldman, E. R.; Anderson, G. P.; Tran, P. T.; Mattoussi, H.; Charles, P. T.; Mauro, J. M. *Anal. Chem.* **2002**, *74*, 841.
- (8) Chan, W. C. W.; Nie, S. M. *Science* **1998**, *281*, 2016.
- (9) Chang, Y. P.; Pinaud, F.; Antelman, J.; Weiss, S. *J Biophotonics* **2008**, *1*, 287.
- (10) Ruan, G.; Agrawal, A.; Marcus, A. I.; Nie, S. *J. Am. Chem. Soc.* **2007**, *129*, 14759.
- (11) Lidke, K. A.; Rieger, B.; Jovin, T. M.; Heintzmann, R. *Opt. Express* **2005**, *13*, 7052.
- (12) Shi, X. B.; Xie, Z. Q.; Song, Y. H.; Tan, Y. J.; Yeung, E. S.; Gai, H. W. *Anal. Chem.* **2012**, *84*, 1504.
- (13) Derfus, A. M.; Chan, W. C. W.; Bhatia, S. N. *Adv. Mater.* **2004**, *16*, 961.
- (14) Nirmal, M.; Dabbousi, B. O.; Bawendi, M. G.; Macklin, J. J.; Trautman, J. K.; Harris, T. D.; Brus, L. E. *Nature* **1996**, *383*, 802.
- (15) Basche, T.; Kummer, S.; Brauchle, C. *Nature* **1995**, *373*, 132.

- (16) Vogel, M.; Gruber, A.; Wrachtrup, J.; Vonborczyskowski, C. *J. Phys. Chem.* **1995**, *99*, 14915.
- (17) Efros, A. L.; Rosen, M. *Phys. Rev. Lett.* **1997**, *78*, 1110.
- (18) Kuno, M.; Fromm, D. P.; Hamann, H. F.; Gallagher, A.; Nesbitt, D. J. *J. Chem. Phys.* **2000**, *112*, 3117.
- (19) Kuno, M.; Fromm, D. P.; Hamann, H. F.; Gallagher, A.; Nesbitt, D. J. *J. Chem. Phys.* **2001**, *115*, 1028.
- (20) Frantsuzov, P. A.; Marcus, R. A. *Phys. Rev. B* **2005**, *72*, 155321.
- (21) Kuno, M.; Fromm, D. P.; Gallagher, A.; Nesbitt, D. J.; Micic, O. I.; Nozik, A. J. *Nano Lett.* **2001**, *1*, 557.
- (22) Shimizu, K. T.; Neuhauser, R. G.; Leatherdale, C. A.; Empedocles, S. A.; Woo, W. K.; Bawendi, M. G. *Phys. Rev. B* **2001**, *63*, 205316.
- (23) Verberk, R.; van Oijen, A. M.; Orrit, M. *Phys. Rev. B* **2002**, *66*, 233202
- (24) Wang, S.; Querner, C.; Emmons, T.; Drndic, M.; Crouch, C. H. *J. Phys. Chem. B* **2006**, *110*, 23221.
- (25) Peterson, J. J.; Nesbitt, D. J. *Nano Lett.* **2009**, *9*, 338.
- (26) Pistol, M. E.; Castrillo, P.; Hessman, D.; Prieto, J. A.; Samuelson, L. *Phys. Rev. B* **1999**, *59*, 10725.
- (27) Chen, Y.; Vela, J.; Htoon, H.; Casson, J. L.; Werder, D. J.; Bussian, D. A.; Klimov, V. I.; Hollingsworth, J. A. *J. Am. Chem. Soc.* **2008**, *130*, 5026.
- (28) Vela, J.; Htoon, H.; Chen, Y. F.; Park, Y. S.; Ghosh, Y.; Goodwin, P. M.; Werner, J. H.; Wells, N. P.; Casson, J. L.; Hollingsworth, J. A. *J. Biophotonics* **2010**, *3*, 706.
- (29) Biebricher, A.; Sauer, M.; Tinnefeld, P. *J. Phys. Chem. B* **2006**, *110*, 5174.
- (30) Hohng, S.; Ha, T. *J. Am. Chem. Soc.* **2004**, *126*, 1324.
- (31) Jeong, S.; Achermann, M.; Nanda, J.; Lvanov, S.; Klimov, V. I.; Hollingsworth, J. A. *J. Am. Chem. Soc.* **2005**, *127*, 10126.
- (32) Antelman, J.; Ebenstein, Y.; Dertinger, T.; Michalet, X.; Weiss, S. *J. Phys. Chem. C* **2009**, *113*, 11541.
- (33) Fomenko, V.; Nesbitt, D. J. *Nano Lett* **2008**, *8*, 287.
- (34) Boulesbaa, A.; Huang, Z. Q.; Wu, D.; Lian, T. Q. *J. Phys. Chem. C* **2010**, *114*, 962.

- (35) Huang, J.; Huang, Z. Q.; Yang, Y.; Zhu, H. M.; Lian, T. Q. *J. Am. Chem. Soc.* **2010**, *132*, 4858.
- (36) Jin, S. Y.; Hsiang, J. C.; Zhu, H. M.; Song, N. H.; Dickson, R. M.; Lian, T. Q. *Chem. Sci.* **2010**, *1*, 519.
- (37) Song, N. H.; Zhu, H. M.; Jin, S. Y.; Lian, T. Q. *ACS Nano* **2011**, *5*, 8750.
- (38) Galland, C.; Ghosh, Y.; Steinbruck, A.; Sykora, M.; Hollingsworth, J. A.; Klimov, V. I.; Htoon, H. *Nature* **2011**, *479*, 203.
- (39) Jha, P. P.; Guyot-Sionnest, P. *J. Phys. Chem. C* **2010**, *114*, 21138.
- (40) Empedocles, S. A.; Bawendi, M. G. **1997**, *278*, 2114.
- (41) Ji, X.; Palui, G.; Avellini, T.; Na, H. B.; Yi, C. Y.; Knappenberger, K. L.; Mattoussi, H. *J. Am. Chem. Soc.* **2012**, *134*, 6006.

## Chapter 5:

### Fluorescence Trajectory Simulations of QD Blinking

#### 5.1 Introduction

Single molecule fluorescence trajectories provide unique insight into the dynamics of the physical processes controlling the emission. One unique property often found in single molecules is fluorescence intermittency, or blinking.<sup>1</sup> This is characterized by transitions from high quantum yield states (“on”) to low quantum yield states (“off”) which is sometimes referred to as telegraph noise. The time scale for the transitions is related to the physical process that is responsible for the state switching. The initial studies of blinking dye molecules were found to have exponential distributions of “off” times that were due to the molecule being in the triplet state.<sup>2</sup> Since those early studies more complex blinking behavior has been observed and characterized. One of the most challenging results to explain is the observation of power law distributed blinking in colloidal semiconductor quantum dots (QDs).<sup>3,4</sup>

Power law distributions, given by  $P(t) = At^{-m}$ , have several unique properties that make analysis complicated. The first is the lack of a characteristic time scale. For example, in a fluorescence trajectory governed by a power law, event durations are often observed to be fractal-like and display a self-similarity of scale which is independent of the time window investigated.<sup>3</sup> One additional implication of the distribution is that while long duration events are rare, they are relatively likely when compared to an exponential distribution. Another difficulty is the lack of a defined average for the distribution. The average of a power law distribution is related to limits of the integration and thus the experimental parameters. This complicated early

analysis of QD blinking which focused on average “on” or “off” times, but was quickly overcome by fitting the actual distribution of times.<sup>4</sup> In this analysis, the probability of a given “on”/“off” time is plotted versus the “on”/“off” time and fit on a log-log scale to a line where the slope is the power law exponent. For colloidal semiconductor QDs, the power law exponent is found to lie typically between 1 and 2 for a variety of samples.

An interesting outcome of fitting the distribution of times was the observation of a truncated power law, given by  $P(t) = At^{-m}e^{-t/\tau}$ , for the “on” time distribution in several different materials upon observation over an extended experimental window (>200 s).<sup>5,6</sup> One explanation of this upper limit involves the small, but finite, probability of creating a biexciton which then can undergo an Auger process. One possible result of the Auger recombination leads to a photoionization event that leaves the QD in the “off” state. The dependence of the truncation time has been found to depend quadratically on the excitation intensity which is consistent with this picture.<sup>5</sup>

While the truncation time has a fairly well agreed upon model, the origin of the power law is much more debated. One way to obtain a power law distribution is from an “exponential of exponentials”. In this model, the process is governed by an exponential distribution of exponential rates, where the probability of a faster rate is greater than a slower rate. There are a few model systems that would be described this way: a fluctuating barrier, distribution of trap states, etc.<sup>7</sup> Another proposed model is based on diffusion of energy levels which leads to “on”/“off” transitions due to a tunneling process.<sup>8,9</sup> There are still many questions about which model is correct and many studies aim to elucidate the physical process responsible for the blinking in QDs.

The ability to extract quantitative parameters from a fluorescence trajectory is thus important in order to reveal the underlying physical process. Typically the data is binned and then a threshold between the “on” and “off” state to be set. These two choices are often limited by the signal to noise of the given experiment. The distribution of times is then fit to an appropriate functional form (exponential, power law, truncated power law) to extract the relevant parameters. Alternatively, the fraction of time the system is in the “on” state ( $F_{\text{on}}$ ) can be calculated which has been used as a coarse metric to characterize blinking suppression<sup>10</sup> Some complications do exist for these approaches. For a simple exponential processes, the bin time has been found to effect some of the extracted parameters.<sup>11,12</sup> This leads to many studies being limited in the time scale that can be investigated and experimental details which may influence the end results artificially. When the kinetics are described by a power law distribution of waiting times, the results are more prone to artifacts due to binning and threshold choices.<sup>6</sup> One alternative solution is to calculate the correlation function<sup>11,13</sup> or power spectral density<sup>9,14,15</sup> which removes the binning and arbitrary thresholding from the analysis. These different approaches provide a variety of analytical methods that extract information about the underlying kinetics from a fluorescence trajectory.

In this chapter, the focus will be the analysis of fluorescence intermittency that is a result of underlying power law distributions. Most theoretical studies have focused on reproducing a power law distribution<sup>7-9,16-18</sup> with a given power law slope, typically  $m = 1.5$ . However, there have been few systematic studies on how well typical analysis routines extract results from the simulations.<sup>6</sup> The goal is thus to vary key parameters in the model such as the power law slope and determine how well a given analysis approach is able to extract the input values.



The simulation routine, which is able to simulate both exponential and power law distributions, is presented in section II. Section III presents the results of traditional “on”/”off” threshold analysis for a variety of different combinations of  $m_{\text{on}}$  and  $m_{\text{off}}$ . This section will also include the results of including a biexciton photoionization pathway that leads to a truncated power law. In section IV two other analysis approaches,  $F_{\text{on}}$  and power spectral densities, will be presented. The first is found to provide a quick qualitative way to characterize the blinking, while the latter is able to extract more quantitative results.

## 5.2 Simulation Details

The simulation is based on an “absorption” clock where each photon absorbed determines the fluorescence trajectory as opposed to relying only on detected photons. This enables a more robust simulation where fast “on”/”off” events (compared to a typical bintime of 1 ms) are included explicitly even if they would not lead to a detected photon. Another benefit of structuring the simulation this way is that multi-exciton dynamics can be included easily as well as expansion for other kinetic models. Each laser pulse is explicitly queried to determine if excitation of the QD occurs and the simulation determines the observables (for a detected photon) and if any changes in the QD state occur.

Random deviates ( $\varepsilon \in [0,1]$ ) are determined from a pseudorandom number generator (ran3) in Numerical Recipes. These random deviates are then compared to the probability of different events occurring during the experiment to determine the fluorescence trajectory of a single QD. The simulations are structured to provide comparable information to experimental data from time correlated single photon counting (TCSPC), which includes information on macrotime, microtime and the channel of detected photons. The macrotime represents “wall

time” or the photon arrival time since the start of the experiment with 50 ns timing resolution. Microtime data is determined by the fluorescence lifetime and denotes the time between excitation and detection, divided into 4096 bins between each laser pulse. The channel is defined by which detector the photon impinges. Because the simulations are designed to follow the same basic physics as experiments, data is stored in a TCSPC format. This enables us to take advantage of the programs already written in house used to analyze experimental trajectories, as well as easily apply our analytical approaches to experimental data. The particulars of the simulations, which are chosen to closely match the experimental conditions usually investigated, are expanded upon in the next several paragraphs.

Simulations for this study are limited to QDs excited by a pulsed laser excitation; however, the scheme can be extended to include continuous wave illumination. The fundamental “clock” for these simulations is set at the repetition rate of the laser, which is chosen to be 5 MHz in order to match the laser system. Each laser pulse has a probability of generating an absorption that results in exciton formation determined from the absorption rate which depends on the QD cross section ( $\sigma$ ), laser power ( $Power$ ) and laser spot size ( $d$ ) ( $k_{ex} = \frac{Power \cdot \lambda}{hc}$ ;  $P_{abs} = \frac{4\sigma}{\pi d^2}$ ;  $k_{abs} = k_{ex} \cdot P_{abs}$ ). The number of excitons formed from the pulse is determined from a Poissonian distribution based on the average number of excitons formed:

$$N_{pulse} = \frac{k_{abs}}{k_{Rep}} \text{ with } P_{N=0} = e^{-N}, P_{N=1} = N \cdot e^{-N}, \text{ and } P_{N>1} = 1 - P_{N=0} - P_{N=1}. \text{ This}$$

allows the inclusion of pathways such as state transitions due to multiexciton photoionization. If the laser pulse does not lead to formation of an exciton, subsequent laser pulses are queried until the QD becomes excited.

Once an exciton (or multi-exciton) is created the second phase of the simulation begins. In the case of a QD in the “on” state, the probability of it turning “off” since the last absorption

( $\delta t$ ) is calculated ( $P_{off} = k_{off} \cdot \delta t$ ). This value is compared to another  $\epsilon$  determine whether the QD transitioned to the “off” state in this time period. Additionally, the inclusion of biexciton photoionization in the model allows multi-exciton states to shift to the “off” state at a given fixed probability ( $P_{ion}$ ) if more than 1 exciton was formed. If the QD is in the “off” state, a similar calculation of the probability ( $P_{on} = k_{on} \cdot \delta t$ ) determines if the QD switches to the “on” state. Once the QD is found to switch states, a new rate is selected from a distribution given by  $k = k_o e^\gamma$  where  $\gamma = \frac{1}{\alpha} \log(1 - \epsilon)$ . This results in a power law distribution for “on” and “off” times which arises from an exponential distribution of exponential rates.<sup>7</sup> In the event that exponentially distributed kinetics are of interest, the rate constant can be held constant throughout the simulation.

The determination of photon detection occurs in the third phase of the simulation. QDs in the “on” state are able to emit with a probability given by the quantum yield (chosen to be 1.00 here), while the “off” state is defined to have a quantum yield of zero for this study. An additional factor which determines if a photon is detected is given by the collection efficiency ( $\eta$ ) of the microscope system. By allowing this to vary, various collection efficiencies can be compared with the more typical 4% collection efficiency attained in experiments in order to identify artifacts arising from limited signal levels.

Once it is determined that a photon is detected, the last phase of the simulation defines the photon observables mentioned previously. The macrotime is calculated by determining which pulse created the exciton and converting that value to time since the start of the experiment ( $iMacro = N_{pulse} \cdot k_{rep} \cdot 50ns$ ). The microtime is distributed exponentially based on an average lifetime ( $t_{micro} = -\tau_{FL} \cdot \log \epsilon$ ,  $iMicro = t_{micro} \cdot k_{rep}$  4096). Finally, the channel is selected from a 50/50 distribution to mimic a 50/50 beamsplitter separating the

emission onto two matched avalanche photodiodes. Both the microtime and channel information are expandable to allow for more complex behavior, i.e. incorporating an instrument response function to the microtime, and channel determined by spectral diffusion. However, at this time only the simplest model for these two observables is investigated at this time.

This entire process is repeated, pulse by pulse, until the desired simulation duration has been achieved. The final trajectory is saved in SPC format to be analyzed by traditional analysis programs. In addition, summaries of the trajectory parameters and results are saved in a series of data files. One such file provides “on” and “off” time distributions for the “perfect” data ( $QY = 1$ ,  $\eta = 100\%$ ) with a 50 ns time resolution. This permits the easy comparison between “perfect” data and the result of binned/thresholded data.

An additional feature of the simulations is the ability to include background signal. Photons are added based on an average count rate, which permits the inclusion of both dark counts and background fluorescence. The microtimes of these photons are set to occur uniformly as opposed to exponentially distributed, while the channel is still selected from a 50/50 distribution. The inclusion of background enables more direct comparison to experiments and the study of signal to background artifacts.

### **5.3 Traditional Threshold Analysis**

Two sample simulations are shown in Figure 5.1, where in the left panel the event times are exponentially distributed ( $k_{\text{on}} = k_{\text{off}} = 1 \text{ s}^{-1}$ ) while in the right panel the times are distributed

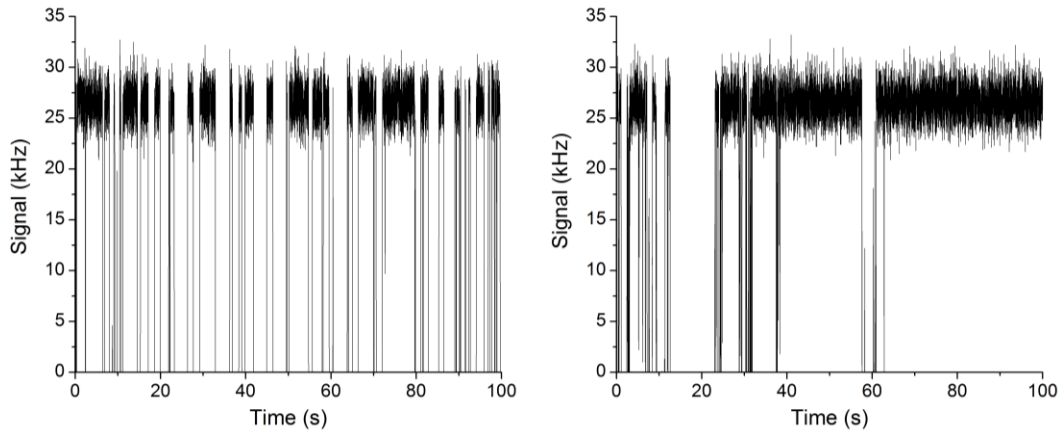


Figure 5.1 Sample simulations of blinking data. Upper panel is simulated using a single exponential distribution with  $k_{\text{on}} = k_{\text{off}} = 1 \text{ s}^{-1}$ . The lower panel uses a power law distribution with  $m_{\text{on}} = m_{\text{off}} = 1.5$ .

according to a power law ( $m_{\text{on}} = m_{\text{off}} = 1.5$ ). The noticeable variation between the two conveys the qualitative differences between an exponential and power law distribution. In the exponential case the distribution of “on”/”off” times is narrow and an average “on”/”off” time is visible. This is in contrast to the lower panel which shows a much broader distribution of “on”/”off” times, from the very shortest observable, a single bin, to as long as 38 s.

The difference between the two traces becomes clearer when analyzed by the typical “on”/”off” threshold method shown in Figure 5.2. In the case of the exponential simulation, the results are plotted on a log-linear scale. The upper two panels show the expected linear dependence with a slope near the input value of  $1 \text{ s}^{-1}$  for both the “on” and “off” times. This is in contrast to the lower panels which are linear on a log-log scale indicating a power law distribution of “on”/”off” times. The determined slopes are near the input value of 1.5. These results demonstrate that our simulation is able to reproduce either an exponential or power law distribution of “on”/”off” times.

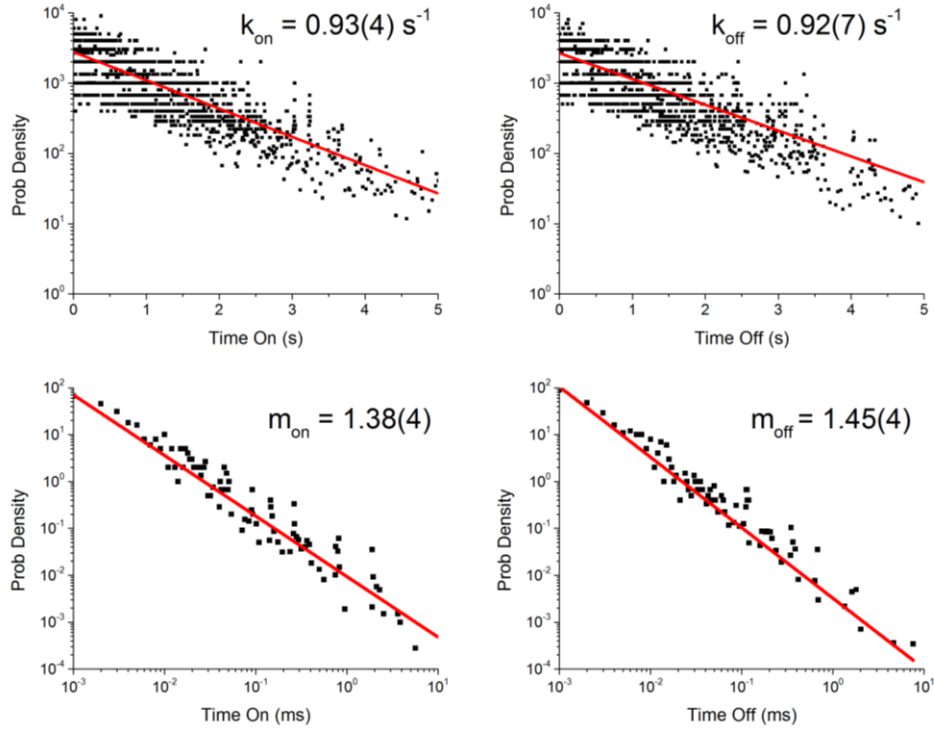


Figure 5.2: Threshold “on”/”off” analysis for the traces shown in Figure 1. Upper panels are the “on” and “off” time distributions fit with a single exponential decay and plotted on a log-linear plot. Lower panels are displayed on a log-log plot and fit to a straight line. Red lines represent the least squares fit with the results indicated.

The study is extended by investigating the analyzed power law slope as a function of the input power law for a variety of input combinations of  $m_{\text{on}}$  and  $m_{\text{off}}$  between 1.4 and 1.8. For each data point, five 300 s trajectories are simulated then analyzed via the threshold analysis with 1 ms bin time. The results of this extended data set are summarized in Figure 5.3, with the red line corresponding to where the fit result equals the input value. While the trend is apparent, the extracted results are most often lower than the actual input values. This is possibly due to the finite nature of the data sets which leads to under sampling the tail of the distribution. An additional effect may be related to the data binning of the trajectory. Events with duration shorter than the bin time merge the events before and after, which results in a net event that is longer than the two original events. This increase in the length of the events, coupled with the

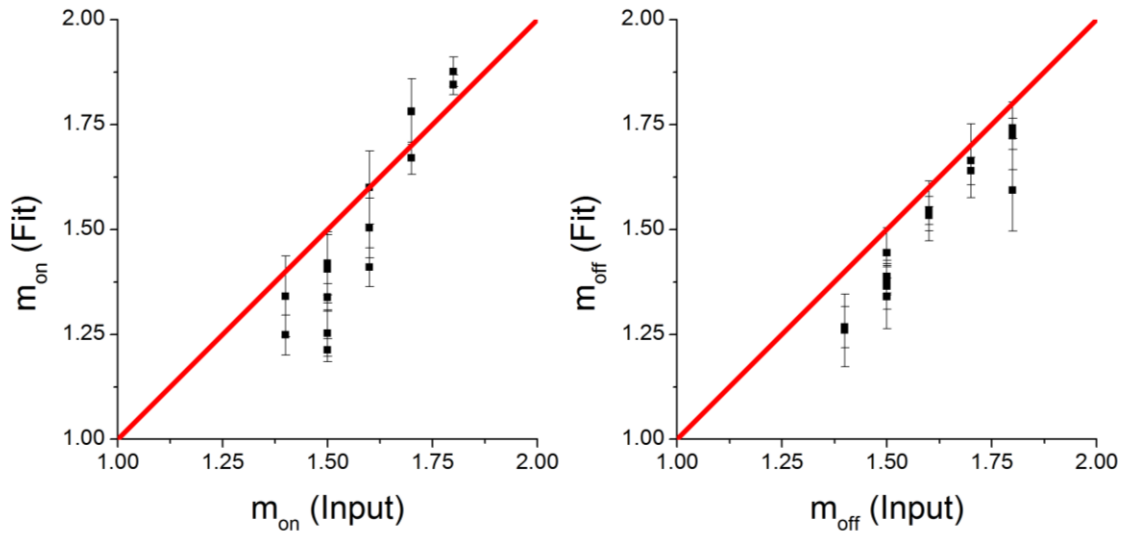


Figure 5.3 Plots of the extracted “on” and “off” power law slopes as a function of the input value. The red line corresponds to if the input equaled the fit value.

loss of short events tends to decrease the observed power law slope. Indeed, a sample bin size dependence on the extracted power law slope has been observed in prior studies.<sup>6</sup> They also saw that the “on”/“off” histogram analysis of power law distributed processes could lead to a systematic under-prediction of the true power law slope

The studies are extended to test whether the simulations are able to reproduce a truncated power laws distribution. One proposed model in the literature is that the multi-exciton state Auger relaxes to eject the electron resulting in an “off” QD.<sup>5</sup> Though the probability of forming a biexciton is relatively low on a per pulse basis ( $N = 0.046 \text{ excitons/pulse}$ ,  $P_{N>1} < 0.001$ ), there are many chances during a given trajectory for this to occur. For our initial study the ionization probability from a multi-exciton state is set to be  $10^{-4}$ , which is comparable to what was observed experimentally. A series of trajectories is simulated in which the excitation power is varied over a range of excitation powers. The resultant “on” time distributions are shown in Figure 5.4 for four different powers. The most noticeable trend is the decrease in the truncation

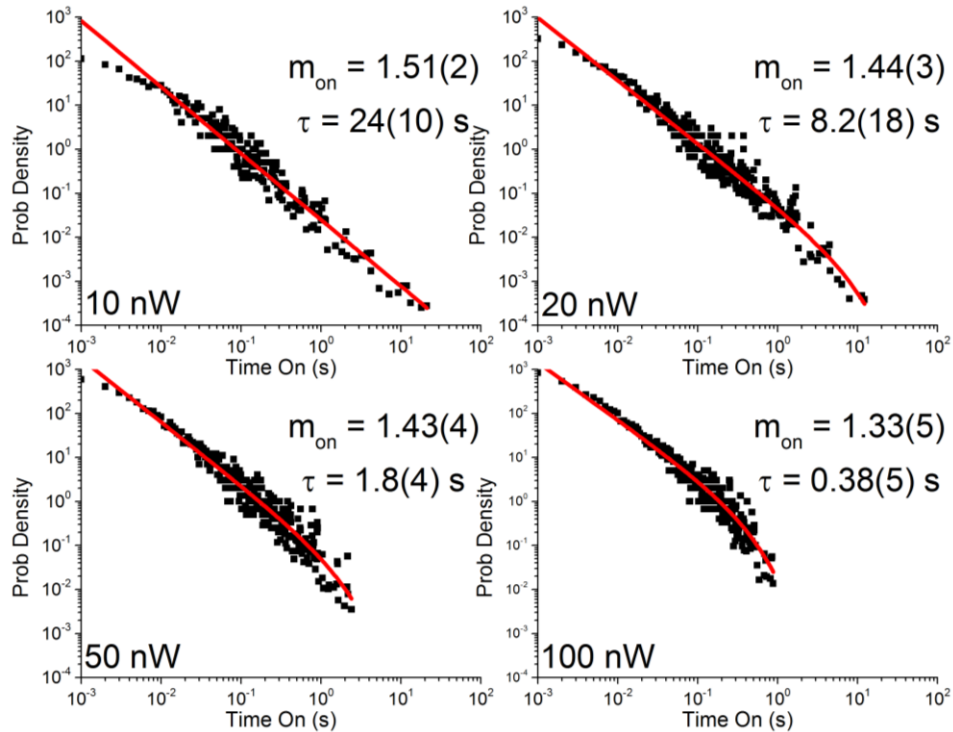


Figure 5.4 Analysis of a power dependent simulation series showing the presence of a truncation time. As the power is increased, the truncation time decreases as expected for a biexcitonic process. Interestingly, the observed power law slope decreases as well.

time as the power is increased. Another interesting trend is the apparent decrease of the power law exponent as the power is increased. This is surprising because the input value of  $m_{on}$  is fixed at 1.6 for each simulation and the power law at early times shouldn't be altered by the multi-exciton process. This again is similar to what was observed in prior truncated power law studies on experimental trajectories<sup>5,6</sup>, and further suggests that the extracted power law exponent is *not* necessarily representative of the true power law for the underlying process. This potential artifact of the analysis should be kept in mind when interpreting experimental data.

A common feature of “on”/“off” time distributions found in the literature, as well as Figure 5.4, is the “fattening” of the distribution in the middle. Closer inspection of the data reveals that this occurs when the number of events in a given bin is near 1 and the events are



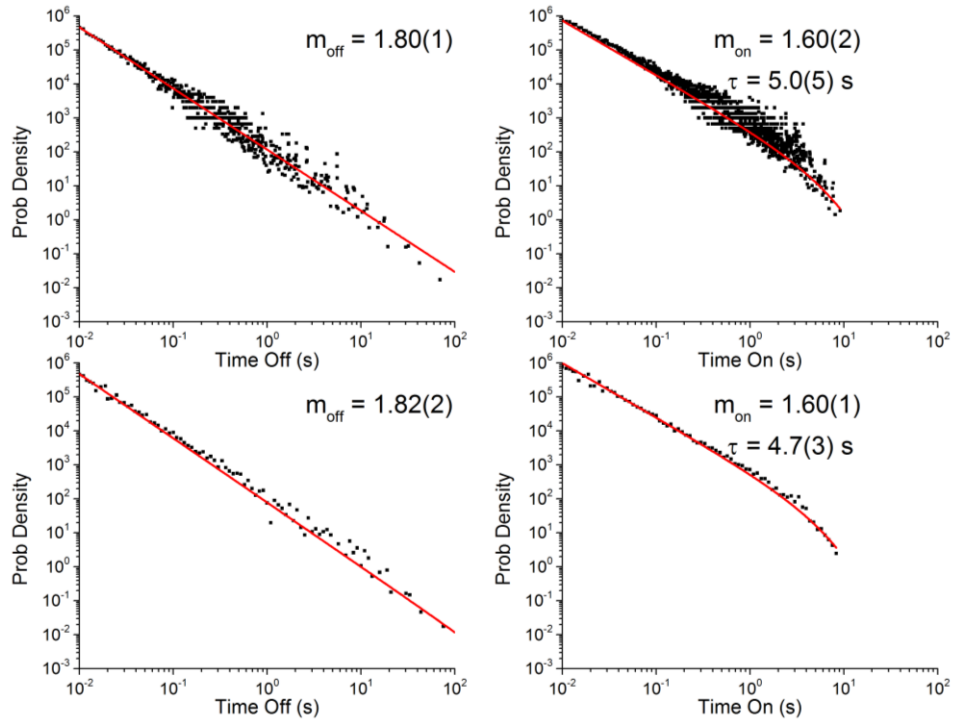


Figure 5.4 Top : The broadening of the observed probability distributions arises from counting statistic noise. Bottom: Log spaced binning smooth the data and better reveals the underlying shape.

closely spaced, suggesting that this is from something like shot noise. At early times, there are 100s to 1000s of events in a given bin and so the contribution of counting statistic noise is relatively small. Likewise, at later times, the events are spaced by several 10s to 100s of bins which also lessens the impact of counting statistics when calculating the probability density. In order to more properly present the data on a log-log scale, the probability is calculated with the bins spaced logarithmically. This technique is shown in Figure 5.5 for both strict power law (“off” times, left) and truncated power law (“on” times, right) which effectively smooth the data while not altering the extracted parameters. The logarithmic binning is easily incorporated into the analysis and removes the noise artifact seen in most studies.

Lastly, Figures 5.4 and 5.5 both show that the distribution of times obtained from a threshold style analysis can be well described by a truncated power law. In the literature, the

functional form is usually assumed and no specific kinetic model has been posited that leads to a truncated power law. In the model used in this study, there are two paths for the QD to transition from “on” to “off”, an exponentially distributed rate constant process (A) and transitions arising from the multi-exciton state (B). The probabilities for these two paths are independent of each other, thus the probability of A and B occurring can be described as the probability of A and B occurring:  $P(A \cap B) = P(A) \cdot P(B)$ . The truncated power law functional form is consequently due to two independent probabilities where one is described by a power law, and the other by an exponential.

#### **5.4 Additional Analysis Approaches**

As mentioned in the introduction, there are two other approaches to analyzing power law distributed data – the fraction “on” ( $F_{on}$ ) and the power spectra density (PSD). The first is closely related to a traditional threshold technique while the second is a fundamentally different type of analysis. Each method has its strengths and weaknesses and compliments the traditional analysis method.

##### *Fraction On Time*

The fraction “on” ( $F_{on}$ ) is defined as the total time spent in the “on” state divided by the total time of the trajectory. This is complicated for power law distributions due to the lack of a well-defined average as mentioned previously. One way around this difficulty is to acquire data

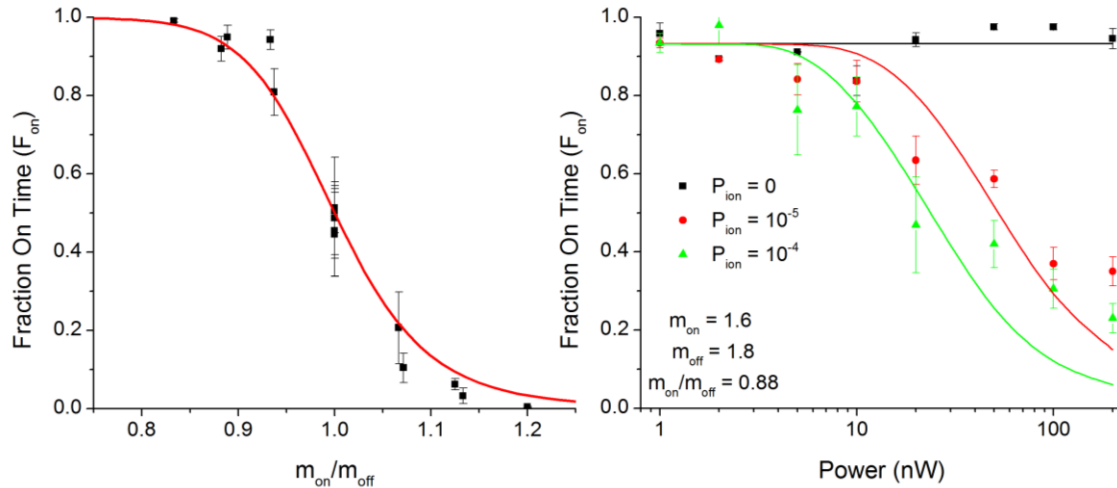


Figure 5.5 Fraction “on” time as a function of the ratio of  $m_{\text{on}}$  to  $m_{\text{off}}$ . The red line is a calculated value based on average “on” and “off” times for different “on” and “off” slopes given fixed upper and lower limits of the power law distributions.

always at the same total time, so that the average is defined on that interval. A previous study of quantum dot blinking has shown that after  $\sim 300$  s the value of  $F_{\text{on}}$  is nearly converged to an asymptotic limit.<sup>10</sup> With these two ideas, the  $F_{\text{on}}$  is extracted for the previously studied  $m_{\text{on}}$  and  $m_{\text{off}}$  used to generate Figure 5.3 and plotted versus the ratio  $m_{\text{on}}/m_{\text{off}}$ . The result is shown in the left of Figure 5.6. The trend is steeply sigmoidal and crosses  $F_{\text{on}} = 0.5$  when  $m_{\text{on}} = m_{\text{off}}$  which is to be expected since the power laws are equal in slope and no one distribution as more (or less) long (or short) events. As the ratio increases, the “on” power law becomes steeper which means there are more short events and fewer longer events. This leads to a decrease in the average “on” time and thus decreases  $F_{\text{on}}$ .

This result can be directly compared with calculations for  $F_{\text{on}}$  given certain constraints. It is true that the average for a power law is ill-defined, however assumptions can be made about the upper and lower limits of the integral, typically the experimental duration ( $t_f$ ) and bin time ( $t_o$ ) for a trajectory respectively. Under these conditions the average “on” or “off” time can be described as

$$t_{on\ off} = \frac{1-m_{on\ off}}{2-m_{on\ off}} \frac{t_o^{2-m_{on\ off}} - t_f^{2-m_{on\ off}}}{t_o^{1-m_{on\ off}} - t_f^{1-m_{on\ off}}} \quad (5.1)$$

The value for the “on” time fraction is then determined by  $F_{on} = \frac{t_{on}}{t_{on} + t_{off}}$ , which can be calculated for different values of  $m_{on}$  and  $m_{off}$ . The result of the expression with  $t_o = 0.001$  s and  $t_f = 500$  s is shown as a red line in Figure 6a which is in good agreement with the results from the simulation.

It is also interesting to study the effect of  $P_{ion}$  has on  $F_{on}$ . These results are presented on the left of Figure 5.6 as a function of incident power and value of  $P_{ion}$ . When  $P_{ion}$  is 0, the value of  $F_{on}$  is independent of power, which is to be expected since there is no intensity dependent process occurring. However, when  $P_{ion}$  is non-zero the value of  $F_{on}$  is now dependent on the excitation intensity as would be expected. A finite value of  $P_{ion}$  leads to a truncation of the “on” time distribution which results in a shorter average “on” time and thus a decrease in  $F_{on}$ . The effect of the truncation time on  $F_{on}$  can be calculated by numerically calculating the average “on” time from  $t_{on} = \frac{\int_0^{t_f} t \cdot P_{on}(t) dt}{\int_0^{t_f} P_{on}(t) dt}$ , where  $P_{on}(t)$  is given by a truncated power law with  $\tau$  determined from the settings of the simulation ( $\tau = k_{ion} = k_{abs} \cdot P_{N>1} \cdot P_{ion}$ ). The solid lines in Figure 5.6b are the corresponding predictions for  $F_{on}$ , and qualitatively describe the data well considering the limited statistics arising from only 5 trajectories for the data points.

These two effects – changing  $m_{on}/m_{off}$  ratio and changing  $P_{ion}$  – are impossible to disentangle when calculating  $F_{on}$  from typical blinking trajectories. Thus blinking suppression, an increase in  $F_{on}$ , can be due to three causes: a decrease in  $P_{ion}$ , an increase of  $m_{on}$ , a decrease of  $m_{off}$ , or some combination thereof. This limits the usefulness of  $F_{on}$  as a robust characterization of intermittency, though it does provide a quick means to establish qualitative changes in blinking behavior in experiments such as the previous chapter. However, the changes in  $F_{on}$

should be accompanied by other techniques to determine the precise cause of observed changes in  $F_{on}$ .

### *Power Spectral Density*

A very different type of analysis is to examine the raw photon data streams at 50 ns resolution. This has the unique ability to quantify the blinking behavior without binning the trajectory or setting an arbitrary threshold. Two common methods are to look at the correlation or power spectral density, which are related by a Fourier transform. In the correlation, the signal at time  $t$  is compared to the signal at time  $t + \tau$ , which relates how much the signal at different time lags ( $\tau$ ) is self-similar. In order to perform this calculation quickly, typically a numerical approach based on a multi-tau algorithm is used instead of direct integration.<sup>19</sup> Alternatively, the power spectral density (PSD) is a measure of how much power is present at each frequency for a given signal. It is calculated as the square magnitude of the Fourier transform of the time series. Thus with the multitude of fast Fourier transform methods the PSD can be easily calculated and analyzed.

Before analyzing the more complicated power law model, the results of the well understood two state system described by exponential kinetics is studied. The correlation of a two state system is well known<sup>11</sup>:

$$C(\tau) = \frac{k_{on}k_{off} (I_{on} - I_{off})^2}{k_{on}I_{on} + k_{off}I_{off}} e^{-k_{on} + k_{off} \tau} + 1 \quad (5.2)$$

For our studies this can be altered to  $C(\tau) = \frac{k_{off}}{k_{on}} e^{-k_{on} + k_{off} \tau} + e^{-2\tau/T}$  since  $I_{off} = 0$ , and the last term arises from the finite nature of the experiment. As previously mentioned, the PSD is

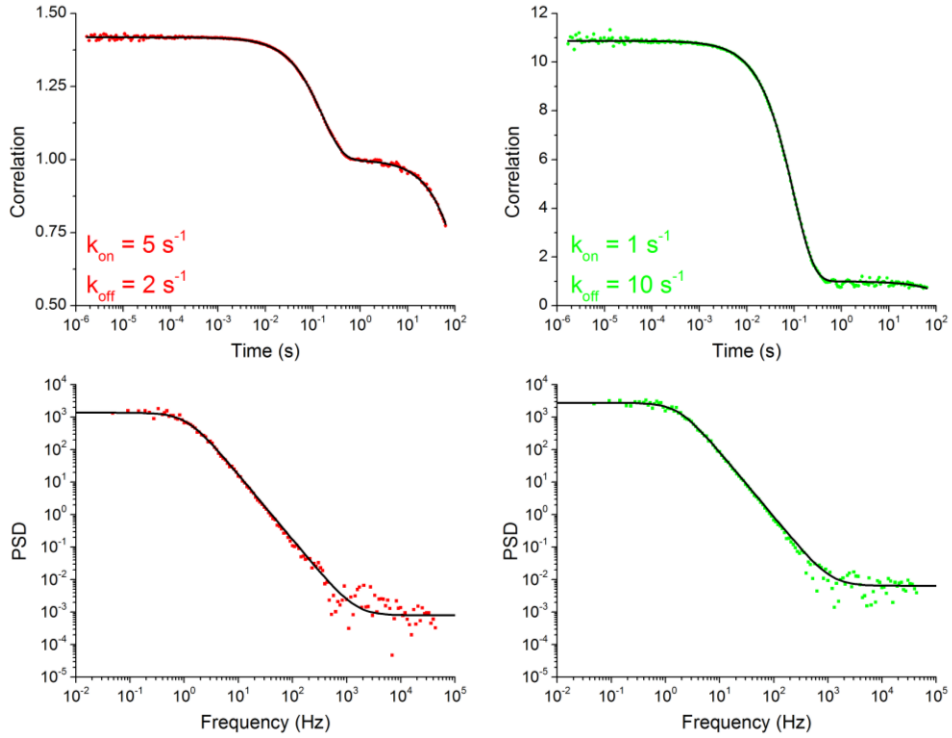


Figure 5.6 Correlation and power spectra density plots for exponential kinetics. Left:  $k_{on} = 5 \text{ s}^{-1}$ ,  $k_{off} = 2 \text{ s}^{-1}$ . Right:  $k_{on} = 1 \text{ s}^{-1}$ ,  $k_{off} = 10 \text{ s}^{-1}$ . The solid black lines are not fits, but plots of the known functional form.

related to the correlation by a Fourier transform and a few normalizations. This results in a functional form for the PSD described by a Lorentzian:

$$PSD \omega = A \frac{a}{\omega^2 + a^2} + P_o \quad (5.3)$$

with  $A = Intensity = \frac{k_{on}}{k_{on} + k_{off}} I_{on}$ ,  $a = k_{on} + k_{off} \pi$ , and  $P_o$  the magnitude of shot

noise. Both the correlation and PSD are calculated for sample trajectories with two different input parameters, shown in Figure 5.7. The solid lines in the graph are not fits, but predictions from the known functional form described in the previous paragraph. The solid lines in each case describe the data quite well. Based on this success we extend the PSD analysis to the more complex kinetics involving power law distributions. The PSD that arises from power law distributions of waiting times has been considered in the theory of sandpiles and avalanches.<sup>20,21</sup>

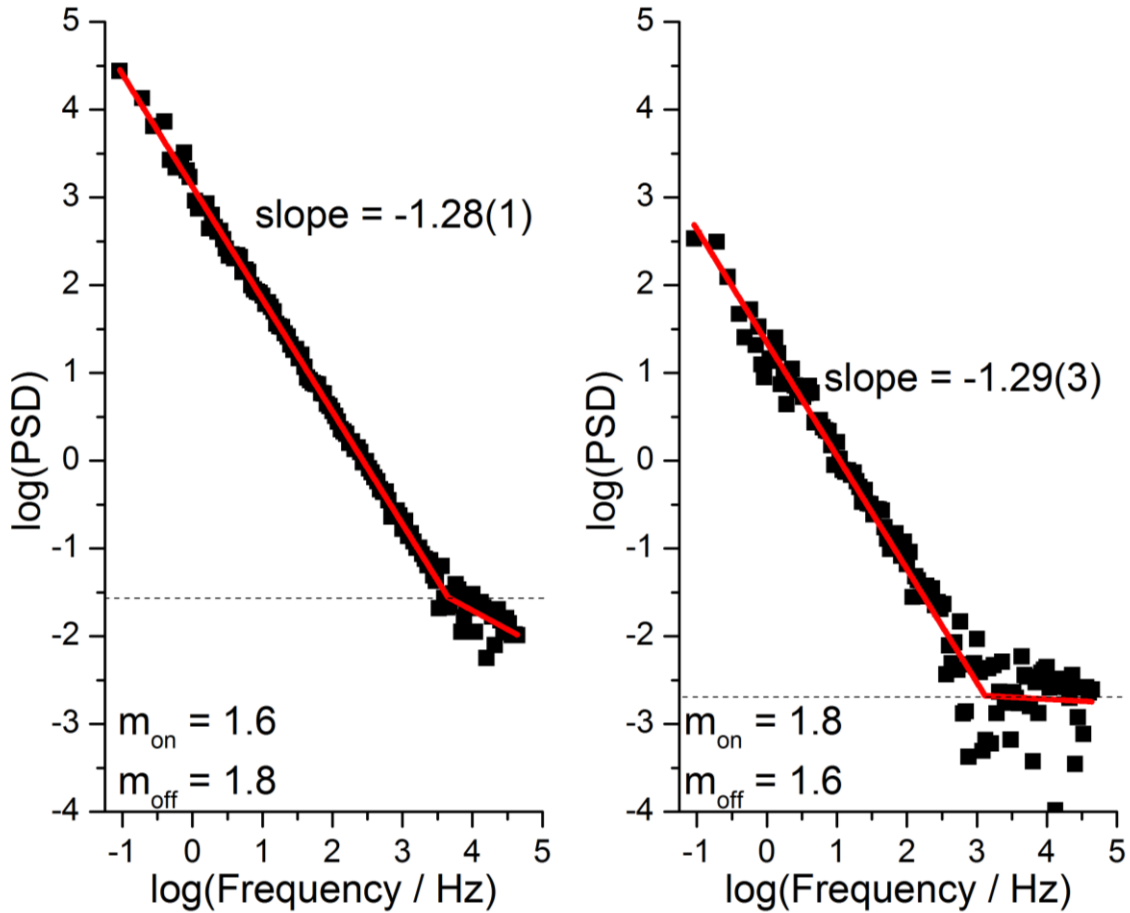


Figure 5.7 Power spectral density plots (log-log) for two different cases of power law distributions which show the same slope arising from the larger of the power law slopes.

For a distribution of times described by a truncated power law ( $P(T) \propto T^{-m} e^{-T/T_0}$ ;  $T \in [t_0, \infty)$ ), the PSD is found to be described piecewise as:

$$PSD(\omega) \propto \begin{cases} const & \omega < 1/T_0 \\ \omega^{m-3} & 1/T_0 < \omega < 1/t_0 \\ \omega^{-2} & \omega > 1/t_0 \end{cases} \quad (5.4)$$

This functional form provides a way to start interpreting the PSD for a variety of trajectories with different parameters.

Two sample PSD plots are shown in Figure 5.8 where in the left plot  $m_{on} = 1.6$   $m_{off} = 1.8$  and in the right plot  $m_{on} = 1.6$  and  $m_{off} = 1.8$ . In both plots the slope of the PSD is near -1.2

which corresponds to a power law slope of 1.8, the larger of the two power law exponents. Previous experiments utilizing correlation or PSD analysis have also shown that the larger of the two slopes is responsible for the apparent slope in the data and dominates the PSD.<sup>9,15,22</sup> Close inspection reveals that the slope of each of the PSD is actually -1.28(2), which should lead to a power law slope of 1.72(2) less than the input value of 1.8. This is similar to the degree of under-prediction from the threshold analysis as well. Interestingly, analysis of the raw 50 ns histogram for the two trajectories shows a slope of 1.73(2) which is in excellent agreement with the PSD analysis. The only real difference between the two traces is the overall amplitude of the PSD. In the left plot  $m_{\text{on}}$  is less than  $m_{\text{off}}$  which, as discussed in the previous subsection, leads to a larger value of  $F_{\text{on}}$ . This corresponds to a larger total power in the trajectory when compared to the case on the right. The kink in the PSD near a y value of  $10^{-2}$  corresponds to where the shot-noise limit begins to dominate the PSD.

To further investigate the observation that the largest slope dominates the PSD, a series of trajectories were conducted with either  $m_{\text{on}}$  or  $m_{\text{off}}$  fixed at 1.5 and varying the other power law slope from  $m_x = 1.3$  to 1.8. Figure 5.9 shows the summary of this study. Indeed, the PSD slope is found to be dominated by the larger of the two power laws, regardless of whether it is the “on” or “off” slope. The black line is described by a constant when  $m_x < m_{\text{on/off}}$  and has a slope of 1 when  $m_x > m_{\text{on/off}}$ . This is consistent with the PSD being described by only the larger of the two underlying power law slopes. In the analysis so far, the PSD appears to contain less information than the traditional “on”/“off” threshold method by extracting only one power law slope component and not knowing whether it is from the “on” or “off” distribution. In order to further establish the usefulness of this approach the PSD under various other scenarios are studied.



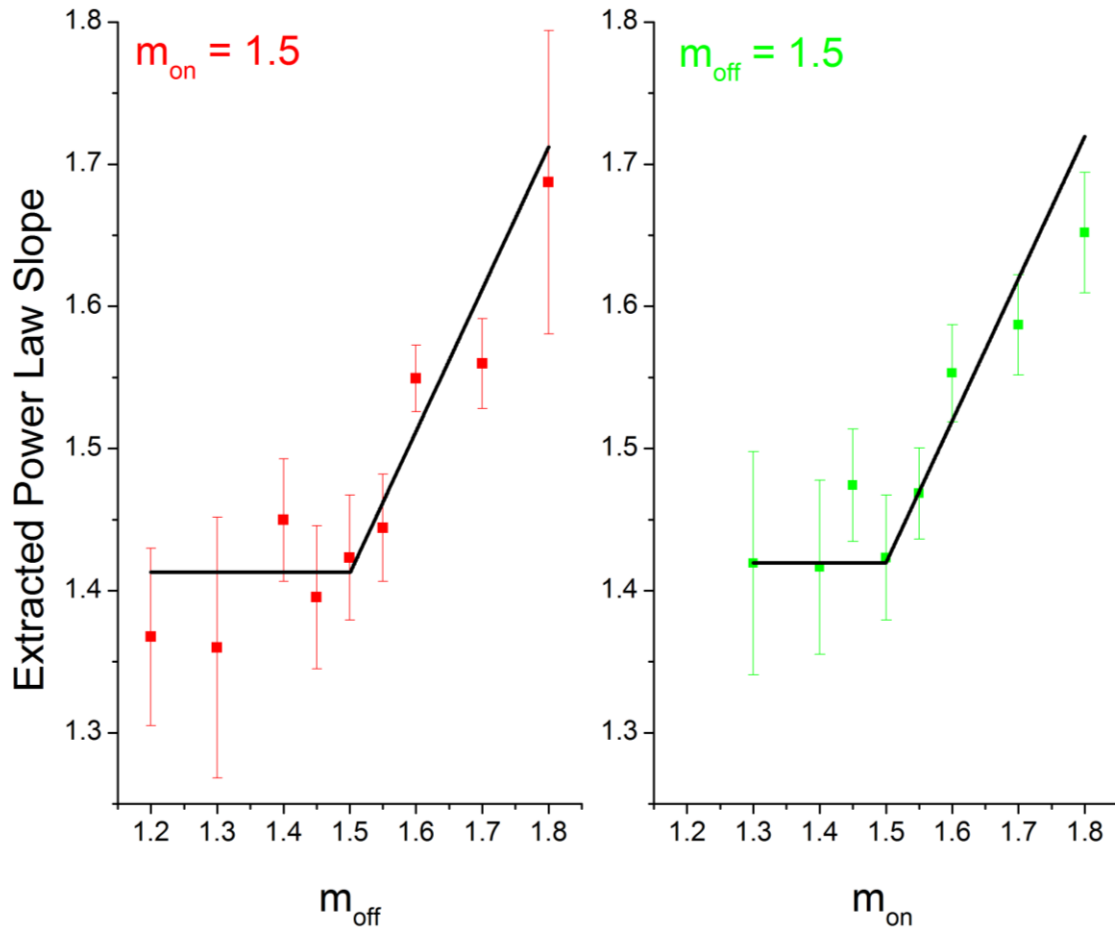


Figure 5.8 Extracted power law slope from the PSD for a series of trajectories where one power law is fixed at 1.5 and the other varied. The power law slope responsible for the PSD is found to be the larger of the two, irrespective of whether it is from the “on” or “off” distribution.

First, the fastest rate ( $k_0$ ) is varied from  $10^5 \text{ s}^{-1}$  to  $10^2 \text{ s}^{-1}$  to see what effect this has on the PSD. Based on the theory presented above, the PSD should transition from slope  $m-3$  to  $-2$  above the fastest frequency included in the simulation. In the case of a traditional “on”/“off” binned analysis, the fastest rate typically observed corresponds to the bin time (1 ms) and any changes from  $10^3 \text{ s}^{-1}$  to  $10^5 \text{ s}^{-1}$  lead to no noticeable changes in the probability distribution. The PSD is shown for 4 different values of  $k_0$  in Figure 5.10. The low frequency region corresponds

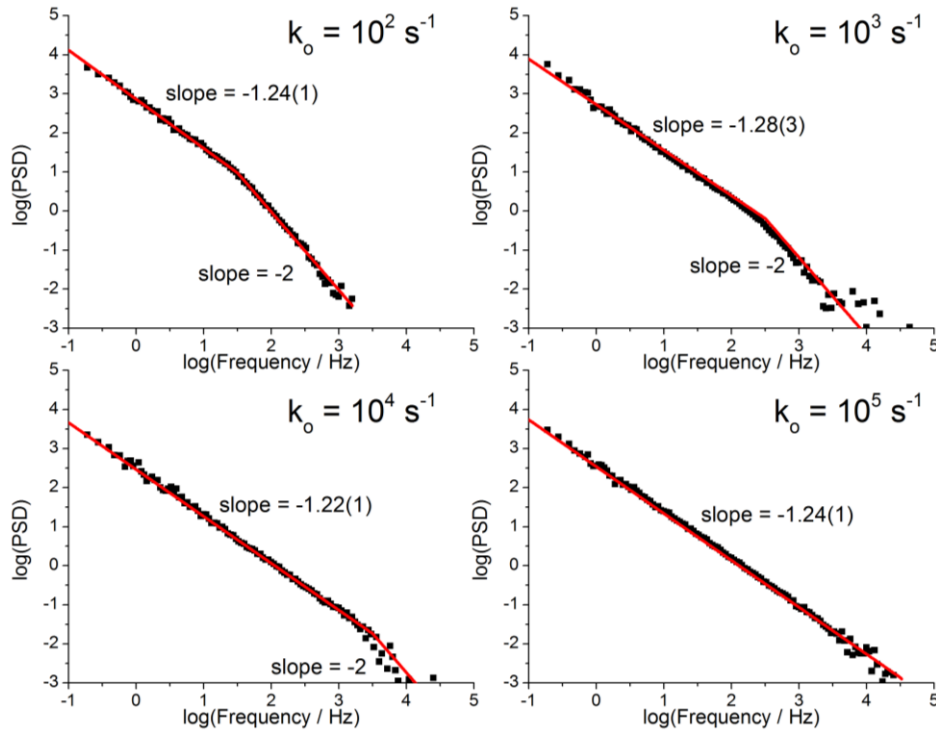


Figure 5.9 PSD for a series of trajectories where the fastest rate included is varied. Red lines are fits where the PL slope and the location of the transition to slope -2 is floated.

to the previously shown case related to the underlying power law slope (slope =  $3 - m_{\text{PL}}$ ) which in this simulation corresponds to -1.2. However, at a given frequency the slope changes to -2 which is due to the domination of other sources of noise.<sup>20</sup> In addition, the frequency at which this occurs is directly related to the fastest rate defined in the simulation to within 5%. This result indicates that the PSD can provide further insight into the previously hidden details of the blinking kinetics on faster time scales.

Next the low frequency region of the PSD is explored. The model predicts that the PSD should transition to constant (slope = 0) below a frequency that corresponds to the truncation time. In order to test this, the “on” time distribution was based on a truncated power law ( $m_{\text{on}} = 1.6$ , Power = 10 nW,  $P_{\text{ion}} = 10^{-4}$  or  $10^{-3}$ ) and the “off” time distribution was set as a single

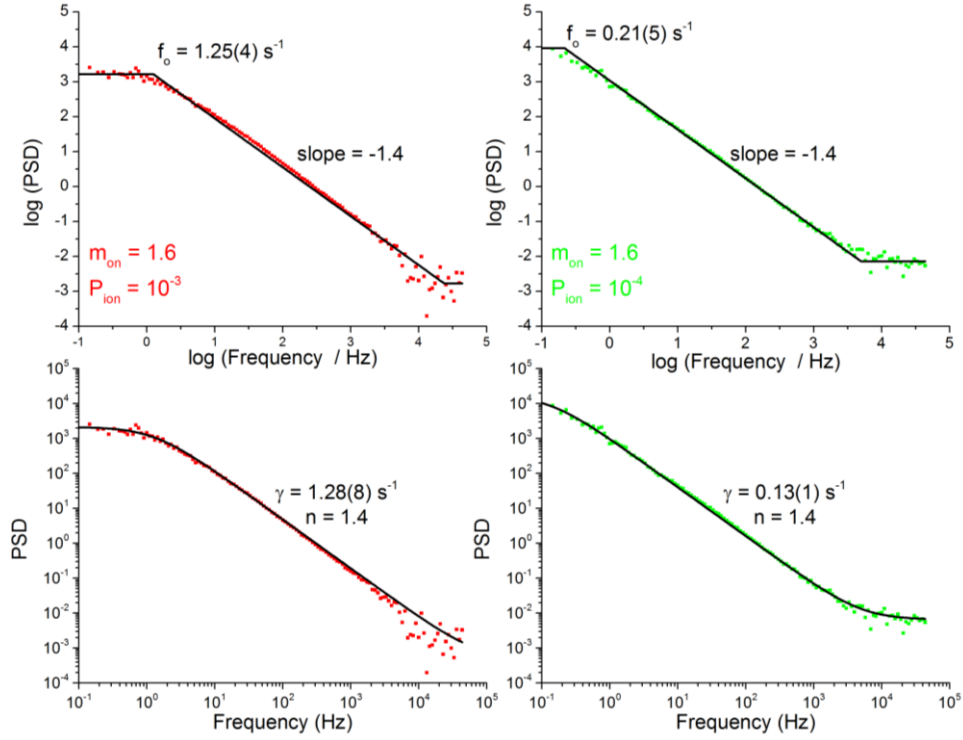


Figure 5.10 PSD plots for simulations where the “on” time are described by a truncated power law, and the “off” times by a single exponential. Top: Piecewise fits based on the equation from sandpiles. Bottom : Fits to a modified Lorentzian.

exponential rate of  $100 \text{ s}^{-1}$ . Figure 5.11 shows the PSD plots for two data sets on a log-log scale.

The upper panels show the fit with the piecewise function described above that was developed for sandpile avalanches. The model with the slope fixed at -1.5 does a decent job of describing the data and extracts reasonable values for the cut off time. In order to better model the data, a functional form based on a modified Lorentzian is proposed:

$$PSD \omega = A' \frac{\gamma^{n-1}}{\omega^{n+\gamma^n}} + P_o \quad (5.5)$$

The frequency response is much better described at low frequencies and is able to obtain the truncation time to match the input settings within 3%. This suggests that the truncation time for trajectories can be determined from the PSD.

The more complex, and realistic, scenario is investigated next : a truncated power law for the “on” times and a power law for the “off” times. To isolate the effect of the truncation time, a series of simulations were calculated for different excitation intensities with  $P_{\text{ion}} = 10^{-4}$ ,  $m_{\text{on}} = 1.6$ ,  $m_{\text{off}} = 1.8$  and the collection efficiency varied such that the intensity of the “on” state was kept constant. This last choice allowed the power density amplitude to remain nearly constant throughout the series. The results for four different powers are shown in Figure 5.12. The first visible trend is a weak kink in the PSD plots at low frequencies that shifts to the left as the incident intensity decreases. The high frequency region corresponds to the power law dominated region discussed previously for strict power laws and has a slope of  $\sim -1.2$  in agreement with the prediction based on a largest power law slope of 1.8. The low frequency component appears to have a shallower slope which is near -1, not 0 as predicted. One possible reason for this is due to the presence of the power law component for the “off” times which still have sufficient power to prevent the PSD from flattening out completely. This complicates the extraction of the truncation time, due to the relatively small difference in slopes. However, the extracted values for the kink are within 10% of the predicted truncation times. It is worth noting that in this specific simulation the “off” time distribution dominates the PSD at higher frequencies because it has the larger power law slope. Yet the truncation of the “on” probability distribution influences the PSD at low frequency, even though the “off” distribution persists to infinite time, and thus zero frequency. Further investigations into this turn over region are necessary to better understand these results

In the last investigation of the PSD, the signal to background ratio (S:B) is varied to determine the limits of the technique in the low signal regime. This ratio is of concern in the traditional “on”/“off” threshold because it is necessary that the “on” and “off” state are well

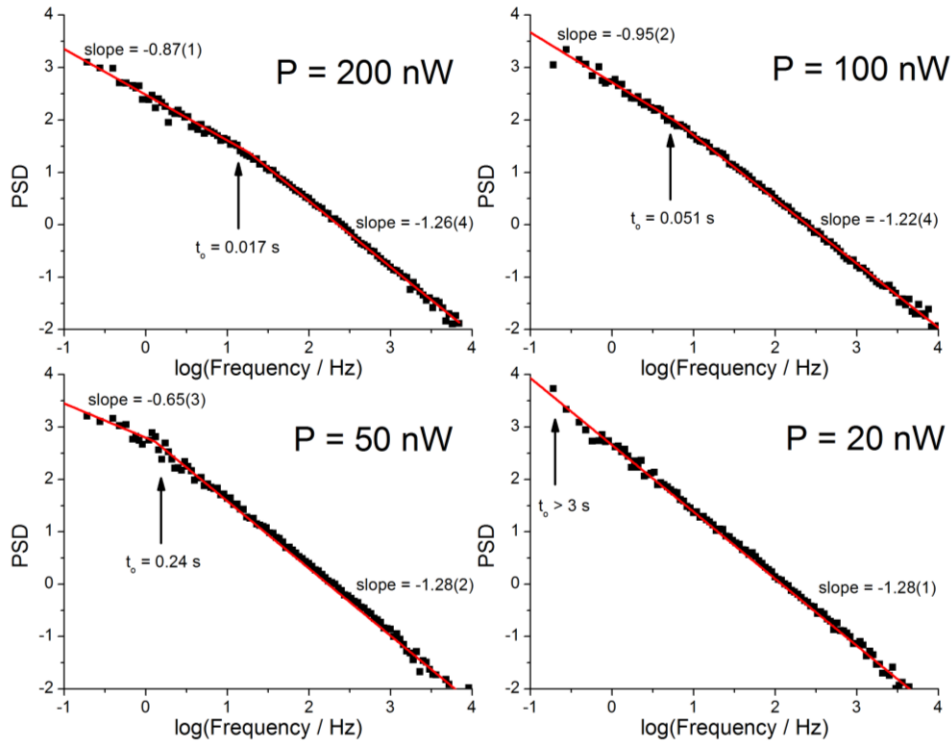


Figure 5.12 PSD plots for a series of trajectories in which the power was varied to determine the effect of the truncation time on the shape.

separated. To explore the effects of S:B, a series of simulations are run with the same parameters, including the random number seed, except with different collection efficiencies. The data set chosen is for  $m_{\text{on}} = 1.6$ ,  $m_{\text{off}} = 1.8$ ,  $P_{\text{ion}} = 10^{-4}$  and 50 nW excitation in order to investigate truncated power law type PSD functions. The results of four different collection efficiencies corresponding to S:B values of 72:1, 3:1, 1:1, and 1:2 are shown in Figure 5.13. Each subplot shows the PSD plot along with the binned trajectory as the inset. The first noticeable trend is that once again, as the S:B decreases so does the overall amplitude of the PSD due to the decrease in the average intensity for the trajectory. The data is analyzed with a piecewise fit in the same manner as before for the power dependent studies in Figure 5.12. Down to a S:B of 3:1 the data is well described by the PSD model and the truncation time can be

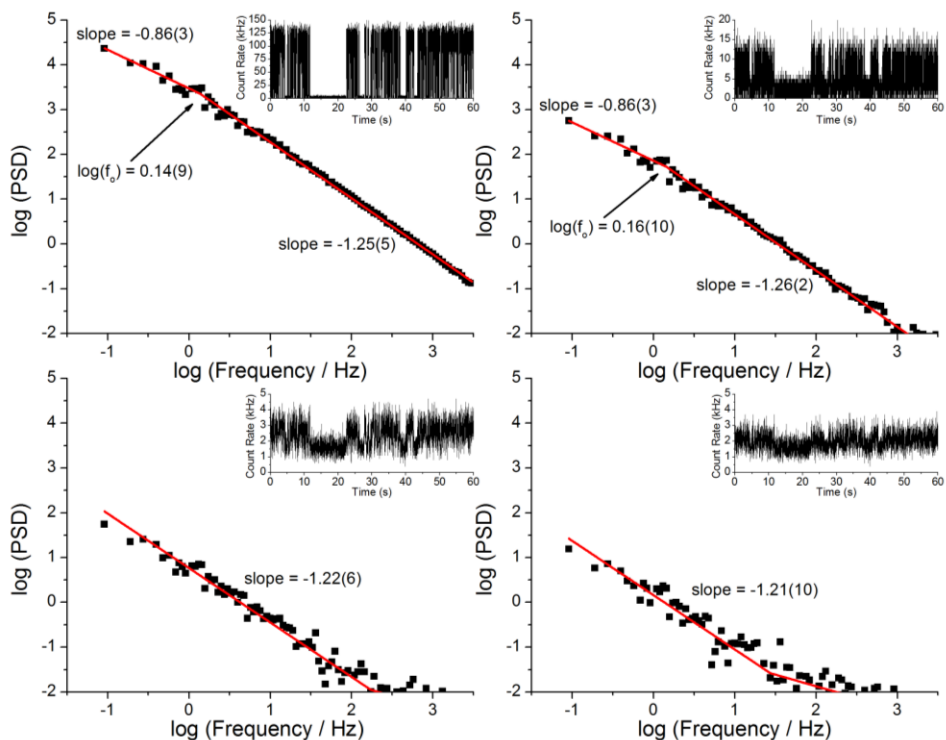


Figure 5.14 PSD plots for the same simulation with different ratios of S:B (72:1, 3:1, 1:1, 1:2). Insets are the intensity trajectory. Even at a ratio of 3:1 the knee due to truncation time is visible. At a ratio of 1:2 the power law exponent can be determined even though a traditional threshold analysis would be impossible.

easily extracted. Pushing the S:B limit even further, the truncation time becomes difficult to distinguish while the PSD slope still well describes the underlying power law. In fact, even when the background contributes more to the total intensity than the signal, the PSD recapitulates the underlying power law behavior in a situation where the threshold analysis would be impossible even at 100 ms bin time. This suggests that the PSD analysis method is quite effective for low intensity measurements.

## 5.5 Conclusions

The ability to simulate fluorescence blinking trajectories with well-defined assumptions enables a thorough investigation of various analysis techniques where the result can be directly

compared to the input values. In the initial study, the typical threshold analysis reveals that in the case of strict power laws, the results tend to be consistently lower than the input values. This is due to the presence of events shorter than the bin time that tend to merge adjacent “on”/“off” times thereby increasing the observation of longer events. The presence of an exponential contribution due to inclusion of an additional pathway introduces a characteristic time scale for the process and influences the “on” time distribution. The probability density for the “on” times in this case is well described by a truncated power law which is found to arise from two independent probability distributions.

These simulations also allow newer analysis approaches to be studied in a clear and precise manner. The fraction “on” time is found to work as a metric for blinking suppression, though it only identifies the ratio of the power law slopes and not the individual values for strict power law distributions. In the case of the truncated power laws, care should be taken when ascribing the effects to changes in the ratio or differences in the truncation time. Statistical methods such as power spectral densities present a new powerful tool in the analysis of fluorescence intermittency. Two important advantages are using the raw unbinned data and the removal of an arbitrary threshold choice. This allows the analysis to proceed in a consistent manner for a broad range of situations. One drawback is that only the larger of the two power laws can be extracted leaving the other unknown. If one of the distributions is described by a truncated power law, the truncation time can be extracted from the PSD with fidelity as good as the traditionally threshold analysis. Due to the increased time resolution of the PSD, the fastest rate of the distribution can be identified from the location of the kink in the PSD where it switches to being described by a slope of -2. One last benefit of the PSD technique is the ability to extract meaningful data even when the signal to background ratio is extremely low ( $\sim 1:2$ ).

These studies demonstrate the power of being able to simulate real world quality data with a precise underlying model where the parameters can be changed in a deterministic manner. The simulations allow the vetting of various analysis techniques under known conditions and are a useful tool to include when studying fluorescence intermittency.

## References

- (1) Cichos, F.; von Borczyskowski, C.; Orrit, M. *Curr Opin Colloid Interface Sci* **2007**, *12*, 272.
- (2) Stefani, F. D.; Hoogenboom, J. P.; Barkai, E. *Phys Today* **2009**, *62*, 34.
- (3) Kuno, M.; Fromm, D. P.; Hamann, H. F.; Gallagher, A.; Nesbitt, D. J. *J Chem Phys* **2000**, *112*, 3117.
- (4) Kuno, M.; Fromm, D. P.; Hamann, H. F.; Gallagher, A.; Nesbitt, D. J. *J Chem Phys* **2001**, *115*, 1028.
- (5) Peterson, J. J.; Nesbitt, D. J. *Nano Lett* **2009**, *9*, 338.
- (6) Crouch, C. H.; Sauter, O.; Wu, X.; Purcell, R.; Querner, C.; Drndic, M.; Pelton, M. *Nano Lett* **2010**, *10*, 1692.
- (7) Kuno, M.; Fromm, D. P.; Johnson, S. T.; Gallagher, A.; Nesbitt, D. J. *Phys Rev B* **2003**, *67*.
- (8) Frantsuzov, P. A.; Marcus, R. A. *Phys Rev B* **2005**, *72*.
- (9) Pelton, M.; Smith, G.; Scherer, N. F.; Marcus, R. A. *PNAS* **2007**, *104*, 14249.
- (10) Zhao, J.; Chen, O.; Strasfeld, D. B.; Bawendi, M. G. *Nano Lett* **2012**, *12*, 4477.
- (11) Lippitz, M.; Kulzer, F.; Orrit, M. *Chemphyschem* **2005**, *6*, 770.
- (12) Perroud, T. D.; Huang, B.; Zare, R. N. *Chemphyschem* **2005**, *6*, 905.
- (13) Stefani, F. D.; Vasilev, K.; Bocchio, N.; Gaul, F.; Pomozzi, A.; Kreiter, M. *New J. Phys.* **2007**, *9*.
- (14) Frantsuzov, P. A.; Volkan-Kacso, S.; Janko, B. *Nano Lett* **2013**, *13*, 402.
- (15) Pelton, M.; Grier, D. G.; Guyot-Sionnest, P. *Appl Phys Lett* **2004**, *85*, 819.



- (16) Efros, A. L.; Rosen, M. *Phys Rev Lett* **1997**, *78*, 1110.
- (17) Uchaikin, V. V.; Sibatov, R. T. *J Exp Theo Phys* **2009**, *109*, 537.
- (18) Frantsuzov, P. A.; Volkan-Kacso, S.; Janko, B. *Phys Rev Lett* **2009**, *103*.
- (19) Laurence, T. A.; Fore, S.; Huser, T. *Opt. Lett.* **2006**, *31*, 829.
- (20) Jensen, H. J.; Christensen, K.; Fogedby, H. C. *Phys Rev B* **1989**, *40*, 7425.
- (21) Hwa, T.; Kardar, M. *Phys Rev A* **1992**, *45*, 7002.
- (22) Verberk, R.; Orrit, M. *J Chem Phys* **2003**, *119*, 2214.

## Chapter 6

### Kinetic Studies of the Photogeneration of Silver Nanoparticles\*

#### 6.1 Introduction

Nanoscale metal materials possess many interesting optical and electronic properties. Progress in synthetic and sample preparation techniques have allowed for the study of the size and shape dependence of properties such as absorption and emission characteristics of noble metal nanoparticles.<sup>1</sup> Silver and gold are of particular interest due to their surface plasmon resonance (SPR), a collective electron oscillation that is excited in the near ultraviolet and visible range. The convenience of visible laser sources coupled with the strong size, shape and proximity dependence on the spectral properties make these metals a powerful choice for research ranging from biophysics to nanooptics.

The SPR properties of gold particles have long been recognized and indeed empirically exploited in the development of stained glass since medieval times.<sup>2</sup> Mie provided the first modern physical understanding of the phenomenon by solving Maxwell's equations for the interaction of light with small spherical particles, which has been applied frequently to predict the optical properties of metallic nanostructures. Improved synthesis techniques<sup>1,3</sup> have allowed for the experimental investigation of the plasmon resonance in a variety of shapes and sizes, as well as control by varying the nanoparticle chemical composition.<sup>4-6</sup> The strong absorption of gold nanoparticles has been used in the medical imaging field and even as a treatment of some

---

\* Adapted from: Baker, Thomas A.; Monti, Oliver L.A.; Nesbitt, David J. *Journal of Physic Chemistry C* **2011**, *115*, 9861.

cancers based on highly localized heating of tumor cells.<sup>7,8</sup> Sensors that detect changes in the surface plasmon due to variations in the local dielectric environment upon molecular absorption have been reported.<sup>9-11</sup> Other technologies that take advantage of the SPR properties include plasmonic waveguides<sup>12</sup> and sub-diffraction limit lithography using nanoapertures in a metal film.<sup>13</sup>

Study of the SPR is not merely limited to the unique optical absorption properties. As a result of the coherent electron oscillations on the surface of the particle, for example, large electric fields are generated in the vicinity of the nanostructure. Theoretical and experimental efforts have been made to understand the nature of these local induced electric fields arising due to optical excitations of the SPR in nanoparticles.<sup>14,15</sup> These local fields can be further enhanced by bringing multiple particles into proximity with one another. Experiments on nanoparticles fabricated by electron and ion beam lithography techniques have provided a greater level of control and thus a better understanding of the effects. Specifically, dimers of nanoparticles have demonstrated nonlinear enhancement of electric fields localized in the interstitial regions between particles.<sup>16-19</sup> An alternative technique, using periodic nano-arrays produced by nanosphere lithography, also allowed for study of how nanostructures interact with each other in close proximity.<sup>10,20</sup> Theoretical investigations<sup>16</sup> have suggested that effects as large as  $10^5$  in electric field enhancements are possible in the region between closely spaced nanoparticles.

This local enhancement of the electric field can enable molecular detection in the vicinity of particles by surface-enhanced Raman scattering (SERS). Indeed, studies indicate that SERS has resulted in Raman cross section enhancements by as much as 8 orders of magnitude, allowing for detection of single molecules.<sup>21,22</sup> The original SERS effect was discovered on roughened silver electrodes and subsequently much effort has been expended into producing

more efficient substrates. Colloidal silver nanoparticles offer another powerful route due to the ability to tailor particle shape and size. Results from,<sup>15,21</sup> however, indicate that only 1 in 100-1000 particles/clusters show SERS activity. This low activity is thought to arise because only a few particles, or collections of particles, have the geometries necessary to produce large local electric field enhancements. Indeed, Camden et al.<sup>22</sup> combined single molecule SERS and high-resolution transmission electron microscopy to correlate nanostructure shape with single molecule sensitivity. They observed a wide range of structures resulting in SERS, from dimers to more complicated overlapping structures. Interestingly, they found no *single* nanocrystals that showed single-molecule activity, providing further evidence that SERS arises from excitation of molecules that reside in high local field regions (i.e. “hot spots”), of dimers and clusters. These hot spots are typically located in the interface and junctions between nearby (< 1 nm) silver particles, as further confirmed by theoretical calculations.<sup>23,24</sup>

Silver nanoparticles are traditionally synthesized via the chemical reduction<sup>25,26</sup> of silver salts in solution. This process results in a variety of sizes, shapes and activities, but the addition of ligand capping agents and other chemicals has led to more reproducible and narrower size distributions. The use of hydrogen reduction<sup>27</sup> has resulted in the ability to produce relatively monodisperse naked (i.e. no ligands present) silver particles in aqueous solution. An alternative to the chemical reduction technique is to generate silver nanoparticles by *in situ* photoreduction of silver ions. For example, Gaddy et al.<sup>28</sup> achieved this by impregnating PVA/PAA polymer films with silver ions and then exposing them to a UV lamp, whereby the formation kinetics was found to depend on the square of the intensity of the light.<sup>29</sup> A variety of films have been investigated in a similar manner including SPEEK/PVA<sup>30</sup>, PVA/ethylene glycol,<sup>31</sup> cellulose,<sup>32</sup> and microgels.<sup>33</sup> The use of an underlying solid support that also acts as the electron source

upon light excitation is another method to generate silver nanoparticles. Yamashita et al.,<sup>34</sup> for example, used UV light to excite an electron into the conduction band of TiO<sub>2</sub> as a reducing agent for the silver ions. A related technique used by Eustis et al.<sup>35</sup> involves combining silica gel (SiO<sub>2</sub>) and benzophenone as a UV activated reducing agent. While the majority of these studies have been directed towards producing conductive films or catalytic surfaces, they nevertheless provide further examples for photoreduction of ionic silver precursors to make silver particles.

The use of photogenerated silver nanoparticles as SERS active species is of particular interest for development of sensors. Peyser et al.<sup>36</sup> reported the UV photoactivation of silver oxide, resulting in the formation of small silver clusters Ag<sub>n</sub> (n = 2-8) that show SERS activity. Silver nanoparticles were also generated with nanosecond UV laser pulses by Henley and Silva via photoreduction of AgNO<sub>3</sub> solution.<sup>37</sup> Visible light has also been used to produce silver nanoparticles, though to a lesser degree. Initial SERS colloid investigations by Ahern<sup>38</sup> produced silver nanoparticles via 514 nm irradiation of aqueous silver nitrate solutions with various organic compounds. More recently, Muniz-Miranda found that it was possible to generate SERS active silver nanoparticles by 514 nm irradiation of silver solutions containing silica particles.<sup>39,40</sup> Previous work by Monti et al. demonstrated that silver nanoparticles can be formed in thin polymer films with a variety of laser excitation sources.<sup>41</sup> UV/vis absorption measurements indicated that a distribution of silver nanoparticle sizes between 1 nm and 20 nm were generated. The nanoparticles also showed strong Raman scattering which arose due to molecules on the nanoparticles surface. Most recently, Sanchez-Cortes' group used 514 nm in a confocal setup to photoreduce silver nanoparticles on the glass surface from a silver nitrate solution in a well slide.<sup>42</sup> These particles revealed a variety of sizes and shapes, and were capable of yielding SERS signals from alizarin in the solution. This same technique was then

used to make a SERS sensor by photogenerating silver nanoparticles on the end of an optical fiber.<sup>43</sup>

The search for the optimal SERS sensor has focused on creating substrates that are reliable, easy to use, and robust.<sup>44</sup> The first important goal is to make a substrate that can consistently generate SERS active clusters. Since the SERS activity is related to the presence of hot spots, the technique should be able to reproducibly generate clusters of the appropriate size and proximity, which would achieve an increase in effective SERS activity by > 100 fold over traditional colloidal techniques. Secondly, the technique should allow for robust generation of hot spot clusters in known positions on the surface that can be located with a minimum of effort. Thirdly, the SERS substrate should be designed such that an analyte can be easily introduced into the hot spots. In order to create an optimal surface meeting these requirements, Anderson and Moskovits used silver particles tethered to an underlying silver film.<sup>44</sup> They produced a nanostructured surface that showed reproducible SERS activity over nearly the entire surface and was able to detect species at the few molecule level via confocal microscopy. The focus of the present work describes an alternative method to generate (and subsequently study) SERS active substrates by combining confocal microscopy with the photogeneration of silver nanoparticles by visible light.

Confocal microscopy has often been used as a technique to characterize efficient SERS substrates and observe single molecule spectra. The diffraction limited spatial resolution combined with sensitive detectors allows for the investigation of individual nanoparticles and small clusters. Another benefit of confocal microscopy is the ability to use relatively low power lasers, yet still achieve high power densities due to focusing with large numerical aperture objectives. This unique combination of tools also provide an ideal way to study the

photogeneration of Ag nanoparticles with high spatial and temporal resolution. As a particular focus of the work, we present studies on the formation growth kinetics of silver particles formed by the photoreduction of silver ions in a thin silver perchlorate/PS polymer film, where the particle growth is monitored via intense surface-enhanced Raman scattering of molecules on the silver nanoparticle surface. Insight into the growth mechanism of the nanoparticles is provided by analysis of the time dependent data with an Avrami kinetic phase transformation model.

The organization of this thesis chapter is as follows: Section 6.2 describes the experimental protocol and apparatus. Section 6.3 provides evidence for the photogeneration of silver particles, establishes the origin of the signal, and reveals details of the morphology of the nanoparticles. Section 6.4 focuses on the time dependence of the generation including the use of a kinetic model to describe the data. A summary of the results and conclusions is presented in Section 6.5.

## **6.2 Experiment**

The experimental procedure consists of two steps: i) generation of the silver nanoparticle features ("writing" phase) and ii) subsequent characterization of the features ("reading" phase). For the generation, light is focused through a microscope objective onto a thin polymer film containing silver perchlorate. Silver nanoparticles are formed by photoreduction of the silver ions in the diffraction limited spot, as shown in the inset of Figure 6.1 and monitored in real time by Raman scattering, *vide infra*. Optical characterization of the nanoparticles is obtained with the same setup, based on i) raster scanning the sample to construct intensity images as well as ii) positioning on a particular location to obtain spectral properties. The samples are also

characterized by atomic force microscopy (AFM) to determine the morphology of the nanoparticles.

Silver perchlorate (99.9%) and polystyrene (Polystyrene Standard, molar mass 18,700 g/mol) are used as received from Aldrich. Toluene (Spectral grade, >99.9%) is dried over Type 3A molecular sieves to remove trace water and then bubbled with He for 30 min to remove oxygen. Solutions of 10 mM  $\text{AgClO}_4$  in toluene (0.074 % by volume) with 1 mg polystyrene per 1 mL toluene (0.094% by volume) are made fresh for each sample and used within an hour of being prepared. A 25  $\mu\text{L}$  aliquot is spun cast onto an ozone-cleaned glass microscope coverslip, with registration marks to facilitate rapid and accurate relocation of particles on the surface multiple times. The resultant film is  $\sim 7$  nm thick, as measured by tapping mode AFM at a step edge formed from scoring the film. The sample is placed on a three-axis closed-loop piezoelectric flexure stage (Physik Instrumente) and an argon purge volume is immediately established around the sample. The choice of argon atmosphere is designed to restrict the chemistry involved in the nanoparticle generation, specifically by exclusion of water and oxygen. Interestingly, this diminishes the ultimate nanoparticle induced SERS intensity by as much as an order of magnitude, but results in a more reproducible time dependence particularly relevant for the kinetic studies presented here. The effect that water and oxygen have on both the nanoparticle morphology and SERS activity is of particular practical relevance for sensor development and will be considered in future studies.

A commercial upright microscope equipped with an air objective (100x, 0.90 NA) is operated in an epi-fluorescence mode as shown in Figure 6.1. The excitation source is a doubled 1064 nm Nd:YVO<sub>4</sub> continuous laser (532 nm) that is expanded to overfill the back aperture of the objective. Prior to entering the microscope, the beam is filtered with a narrow band-pass to



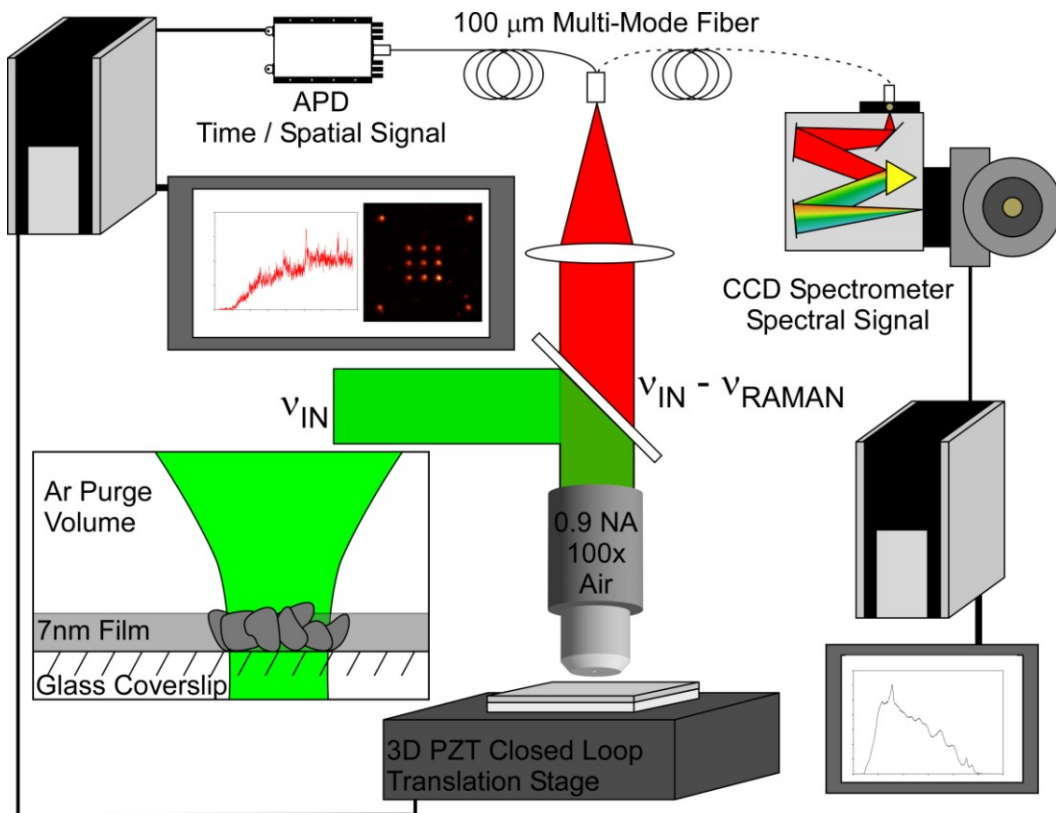


Figure 6.1: Experimental setup. A confocal microscope is used to generate and investigate silver nanoparticles. Detection options include an APD for time correlated single photon counting (TCSPC) and a CCD spectrometer for measuring Raman spectra. Inset: Close-up cartoon of laser-sample interaction. Silver perchlorate in a thin polymer film is photoreduced to silver nanoparticles under an argon atmosphere.

remove fluorescence from optical components. A dichroic beam splitter reflects the excitation beam to the objective, while transmitting the collected red-shifted emission. Residual excitation light is further suppressed by an interference filter (Chroma HQ545LP, OD > 6 @ 532 nm) and then focused onto the aperture of a multimode fiber (100 μm core diameter) that acts as the limiting confocal pinhole.

Use of an optical fiber as pinhole aperture provides the additional flexibility of directing the light into two different detection systems and allows for two modes of data collection, shown schematically on the top of Figure 6.1. In the first mode, the fiber is connected to a fiber coupled single photon counting avalanche photodiode (Perkin Elmer, SPCM-AQR-15-FC). The output

of the APD is directed to a Becker & Hickl SPC-134 PCI card operating in a time correlated single photon counting (TCSPC) mode that stores each photon arrival with respect to the laser pulse (microtime) and start of the data acquisition (macrotime). In the second mode, the fiber is coupled to a Czerny-Turner-type spectrometer (grating 600 lines/mm,  $f = 4$ ) and spectrally dispersed onto a liquid nitrogen cooled CCD detector. The scan range is chosen so that the Raman spectra between  $500\text{ cm}^{-1}$  and  $3000\text{ cm}^{-1}$  can be collected at a single exposure at  $\sim 20\text{ cm}^{-1}$  resolution. This provides the ability to monitor fluctuations in the complete Raman spectra over periods as short as 0.1 s and out to 1000 s.

The photogeneration of the particles is observed in real-time by moving the stage to a specific location, and opening a shutter to expose the sample to light for a well defined time interval of laser excitation (typically 60 s at  $60\text{ }\mu\text{W}$ ). After a finite induction period of several seconds, the signal begins to increase dramatically above background photon noise levels and eventually reaches an asymptotic value by  $t \approx 50 - 100\text{ s}$ . After the feature is generated, the spatial and spectral properties can be studied. The spatial extent of the feature is determined by raster scanning the sample and creating a two-dimensional image (256 pixels by 256 pixels) that contains the intensity of the Raman scattering as a function of position on the surface. This image provides the ability to identify specific features and allows them to be compared before and after various treatments of the surface. Spectral information is obtained by moving the stage to a specific location determined from the image and sending the Raman scattering into the spectrometer, thereby allowing the spectral characteristics of an individual feature to be investigated. Acquisition and analysis software is written in house and developed in C++/Labwindows. AFM images are obtained in tapping mode using a tip with a 5-10 nm radius of curvature which provides the ability to determine the morphology of the nanoparticles. The

registration mark on the sample provides the ability to correlate the SERS signal intensity observed in the confocal microscope with the morphology of the particles revealed by AFM.

### 6.3 Results

As discussed in the introduction, a robust ability to create reliable substrates is critical in the development of a SERS sensor platform. By way of demonstration, a sample  $20\ \mu\text{m} \times 20\ \mu\text{m}$  image of a regular pattern of photogenerated features is shown in Figure 6.2a. The SERS spots are formed by moving the sample to a specific location and then exposing at an intensity of  $280\ \mu\text{W}$  for 30 seconds, which is enough time for the silver nanoparticle generation kinetics to reach the asymptotic limit. After the pattern is "written", an image is "read" at a  $\sim 20$ - $100$  fold lower intensity of  $8\ \mu\text{W}$  and a dwell time of  $2\ \text{ms/pixel}$ , conditions that do not result in further generation of nanoparticles. The image in Figure 6.2a shows that the bright regions, with signal to background (S/B) of  $> 70:1$ , appear only in locations exposed to the higher intensity "write" beam. The spatial extent of these bright spots is approximately Gaussian with a FWHM of  $720(20)\ \text{nm}$ , two-fold larger than the diffraction limit of  $360\ \text{nm}$  and will be discussed later with the AFM results. Nevertheless, the data clearly demonstrate reliable laser based generation of SERS active features in any grid pattern and at any desired location on the substrate.

The confirmation that the signal we observe is indeed Raman scattered light is obtained from the spectral distribution and the emission lifetime of the signals as shown in Figure 6.3. The emission displays a broad feature that is red-shifted from the excitation, as well as a peak at approximately  $1550\ \text{cm}^{-1}$ . The peak is commonly observed in many SERS experiments<sup>45,46</sup> and attributed to the presence of a carbonaceous impurity. Previously, experiments under similar conditions at other excitation wavelengths showed similar features red-shifted by a constant

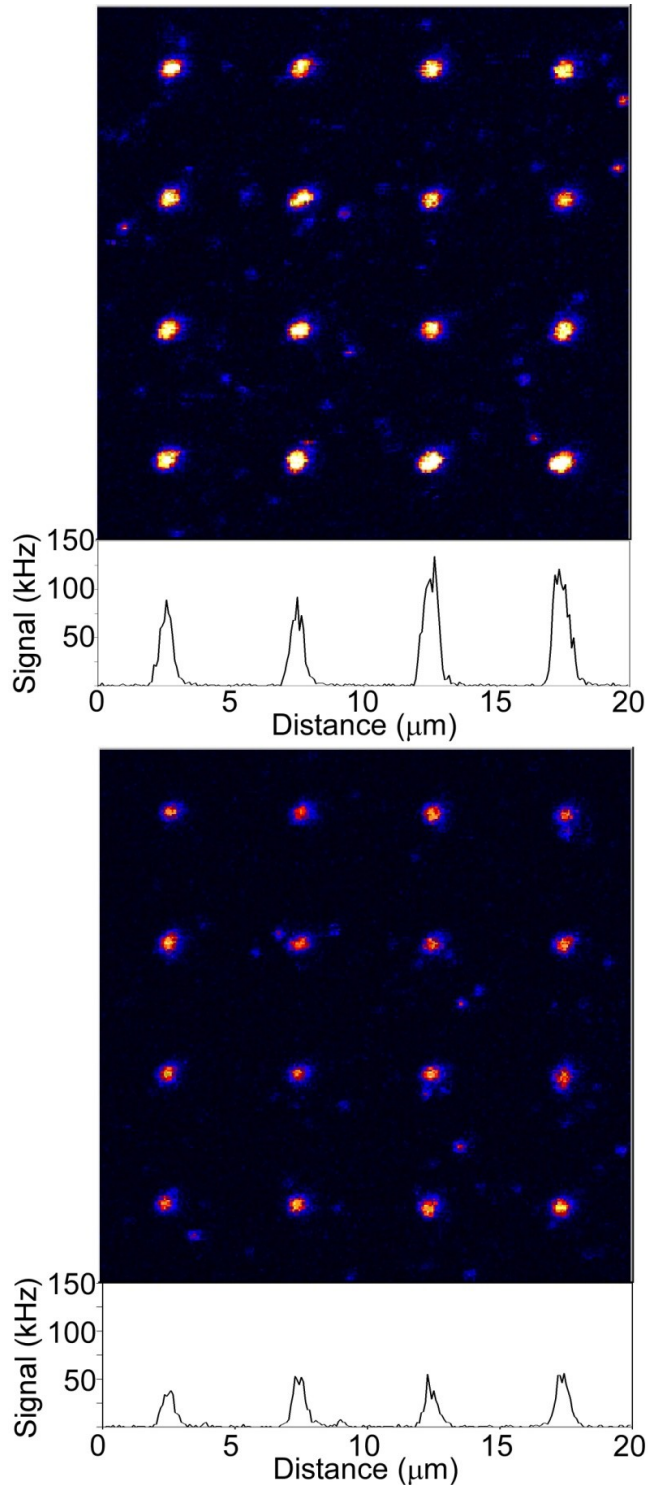


Figure 6.2: Raman intensity images.  $20\ \mu\text{m} \times 20\ \mu\text{m}$  images of photogenerated silver nanoparticles in a thin film (8 nm) of  $\text{AgClO}_4/\text{PS}$  generated by  $280\ \mu\text{W}$  illumination ( $17\ \text{kW}/\text{cm}^2$ ) for 30 s before (a) and after (b) removal of initial starting material. Laser power for the read out process is  $8\ \mu\text{W}$  ( $500\ \text{W}/\text{cm}^2$ ). Lineouts are included below the images showing the features have a FWHM of  $720(20)\ \text{nm}$ .

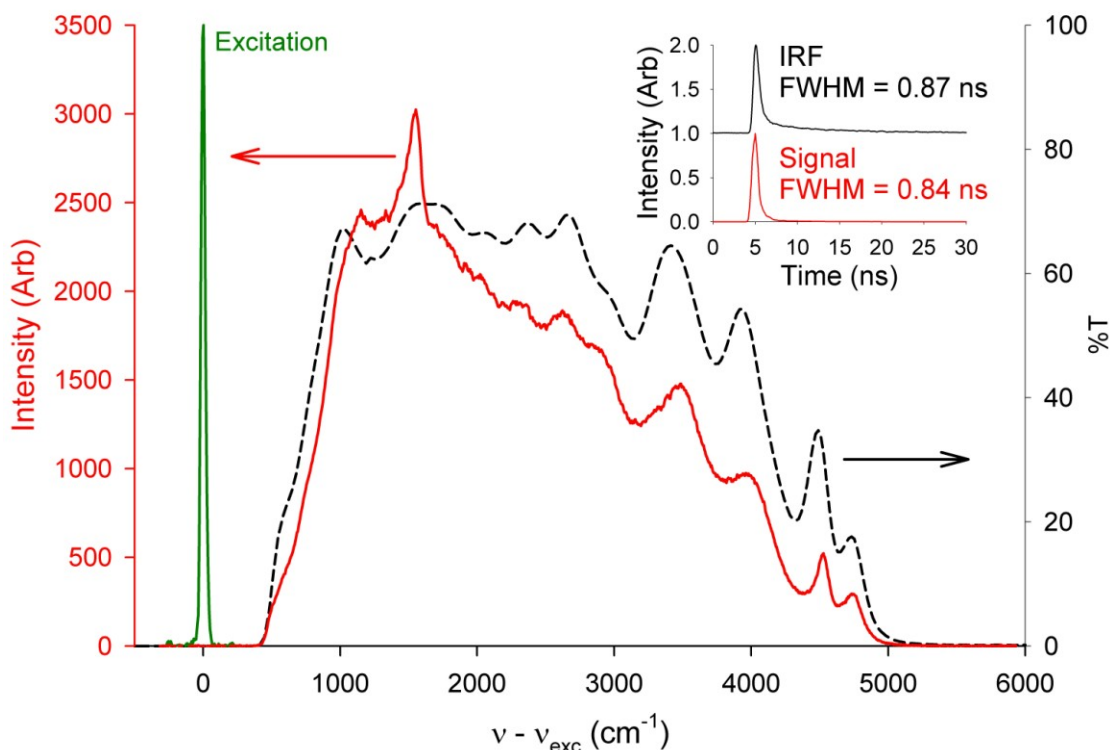


Figure 6.3: Raman spectrum of photogenerated nanoparticles. The spectrum (red) shows a broad feature with a peak corresponding to carbonaceous impurities at  $1550\text{ cm}^{-1}$ . The spectral resolution is demonstrated by the excitation source (green) and the transmission spectra of the dichroic and emission filter (black) are shown as well. Inset: Time response of the signal compared to the instrument response function (IRF) measured from Raman scattering of  $\text{H}_2\text{O}$ .

frequency offset from the excitation regardless of excitation wavelength<sup>41</sup>. Furthermore, experiments using a 30 ps pulsed laser source in our lab have been conducted (see inset Figure 6.3), which verifies the photon arrival relative to the excitation pulse to be instrument limited. This indicates that the emission process is either prompt or fast ( $< 30\text{ ps}$ ). Both the spectral characteristics and the prompt photon arrival signify that the light arises from a Raman rather than fluorescence process.

The stability of the features is an important property if the samples are for single molecule sensing. We have observed that after formation, the SERS active features remain unchanged over periods up to one year. Over this same time period, there is a slight 2-fold

increase of the background (from 100 Hz to 200 Hz), though the signals remain completely dominated ( $> 30:1$ ) by SERS emission from the nanoparticles. To prevent any such increase in background levels, potentially due to parallel light or dark reduction processes also resulting in nanoparticle generation on time scales longer (i.e.  $>$  days) than our experiment, attempts were made to remove the starting material film from the sample without disturbing the photogenerated nanoparticles. Specifically, after creating a pattern, the coverslip is spun at 1500 RPM and rinsed first with 2 mL of toluene and subsequently by 2 mL of water. The former is chosen because it is a good solvent for both components of the thin film, while the latter was chosen due to the 5-fold greater solubility for silver perchlorate to remove all remaining unreduced silver salt from the substrate. As seen in Figure 6.2b, all features initially "written" are indeed distinctly recovered by "reading", however with a  $\approx 2$ -fold decrease in Raman signal due to the loss of a small fraction of silver nanoparticles insufficiently strongly bound to the surface. Indeed, multiple rinses have no further effect on the SERS signal strengths. This demonstrates reliable laser based generation of stable SERS active nanoparticles on registered substrates, which begins to meet Anderson and Moskovits requirements for an optimal SERS sensor.<sup>44</sup>

In order to further characterize the generated particles, AFM studies were conducted. This was facilitated due to the easy removal of initial starting material as well as the ability to find the particles based on registration marks present on the coverslip. Figure 6.4 shows a tapping mode AFM of the same sample shown in Figure 6.2b. The features exhibit a diameter of approximately 600 nm with an average height of 7 nm. The height of the structures is comparable to the initial film thickness, consistent with a simple picture of the film-constrained growth of the nanoparticles. The lateral size is similar to the observations from the Raman scattering intensity image where the xy-spatial full width half max was 720(20) nm. This is

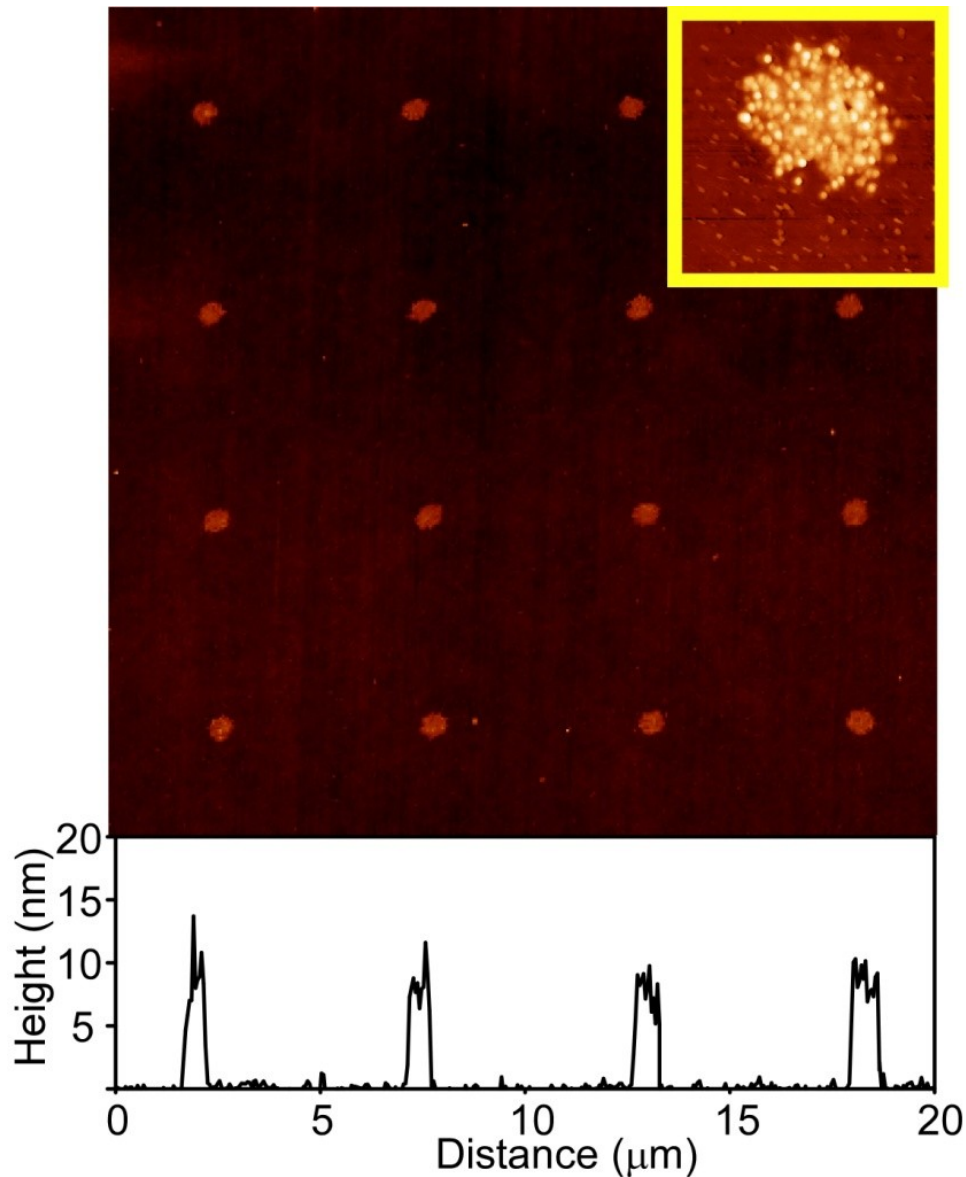


Figure 6.4: AFM image of photogenerated silver nanoparticles. 20 μm x 20 μm AFM of photogenerated silver nanoparticles generated at 280 μW for 30 s after removal of the initial starting material. Same sample as shown in Figure 2b. Lineouts are included below the images showing features have a diameter of ~600 nm. Inset: 1 μm x 1 μm AFM of a single feature which is observed to be comprised of 100s of individual disks that are 7 nm tall and ~40 nm diameter.

larger than the theoretical diffraction limit (360 nm) for 532 nm light with a 0.9 NA objective.

We can confirm that the imaging system is operating at the diffraction limit by looking at single dye molecules, which display a FWHM of 375(10) nm. However, since the objects being

observed have a spatial extent larger than a single molecule, the FWHM from the Raman image should be interpreted as a convolution of the physical size of the nanostructure and the diffraction limited resolution. This approach results in the determination of a physical size for the features of 623 nm, which is consistent with the lateral dimensions of the structures as measured by AFM.

Analysis of the AFM images also allow for the determination of the fraction of the initial  $\text{Ag}^+$  that is reduced based on the volume of material observed in an AFM image. The films contain 44% silver perchlorate by volume based on the relative proportions of polystyrene and silver perchlorate in the original solution. Therefore, in a 7 nm thick initial film that is 600 nm diameter, corresponding to the diffraction limited spot size, there are  $\sim 3.0 \times 10^7$   $\text{Ag}^+$  in the volume available to be reduced. Examination of the AFM shows that the total volume of the nanoparticles is  $\sim 3.4 \times 10^{-16}$   $\text{cm}^3$  for a typical feature. This is equivalent to  $2.0 \times 10^7$  Ag atoms and thus an efficiency for  $\text{Ag}^+$  reduction of  $\sim 2/3$ . If we include a consideration that a fraction of the nanoparticles may be washed away during cleaning, as evidenced by the loss in Raman signal, this suggests that the asymptote of the observed growth is a result of the exhaustion of all available  $\text{Ag}^+$ . The photogeneration of silver nanoparticles is thus limited by the availability of silver ions in the diffraction limited spot and the observed kinetics represent the complete transformation of silver ions to silver nanoparticles.

Closer inspection of a single feature by AFM, inset of Figure 6.4, shows that it is actually clusters or “constellations” of multiple smaller disk-like nanoparticles. In each diffraction limited area, there are approximately 100 individual disks that are 7 nm tall and  $\sim 40$  nm in diameter. The disks are in close proximity to each other and have contacts with multiple neighbors. This suggests the possible presence of “hot spots” formed at the junctions of disks



within the diffraction limited laser excitation. The Raman spectrum of the features also suggests that there are multiple emitters present within the diffraction limited spot. The peak at  $1550\text{ cm}^{-1}$  has a FWHM of  $150\text{ cm}^{-1}$ , which is substantially larger than both the  $20\text{ cm}^{-1}$  spectral resolution of the instrument as well as Raman spectral widths obtained for neat toluene,  $33\text{ cm}^{-1}$  FWHM for the  $990\text{ cm}^{-1}$  band, using the same apparatus. The width of the  $1550\text{ cm}^{-1}$  band is therefore likely due to multiple emitters contained within the diffraction limited area. This is consistent with results from Kudelski and Pettinger, who investigated the Raman bands of carbon chains on silver and gold films in a Raman microscope.<sup>47</sup> Specifically, on the fast time scales they observed rapidly fluctuating spectral structure between  $800\text{ cm}^{-1}$  and  $1700\text{ cm}^{-1}$ . When averaged temporally or spatially, however, the emission resulted in broad inhomogeneous bands centered at  $1350\text{ cm}^{-1}$  and  $1550\text{ cm}^{-1}$ , much as observed in the present studies. Indeed, on ms scales we also see more than one order of magnitude fluctuations in the signal intensities (see below), which we speculate come from molecules in the junctions between the nanoparticles, similar to the “hot spots” reported by Brus and coworkers.<sup>48,49</sup> If this is the case, the rapid fluctuations in signal intensities and spectral peaks most likely indicate the presence of a small but multiple number of such hot spots within the diffraction limited focus, which would be consistent with the many close overlaps and connections between the plate-like Ag structures observed in AFM.

In order to confirm the suitability of the technique for use in molecular sensing, spectral observation of a known molecule, thiophenol, was investigated. Figure 6.5a shows the spectrum of a generated feature. The starting material was then removed as described above for the AFM measurements and the sample incubated with  $150\text{ }\mu\text{L}$  of a  $10\text{ mM}$  thiophenol solution in ethanol for  $15\text{ min}$ . The sample was subsequently rinsed with  $2\text{ mL}$  of ethanol to remove any excess thiophenol from the surface and the spectrum in Figure 6.5b was obtained at  $74\text{ }\mu\text{W}$  for  $10\text{ s}$ . For

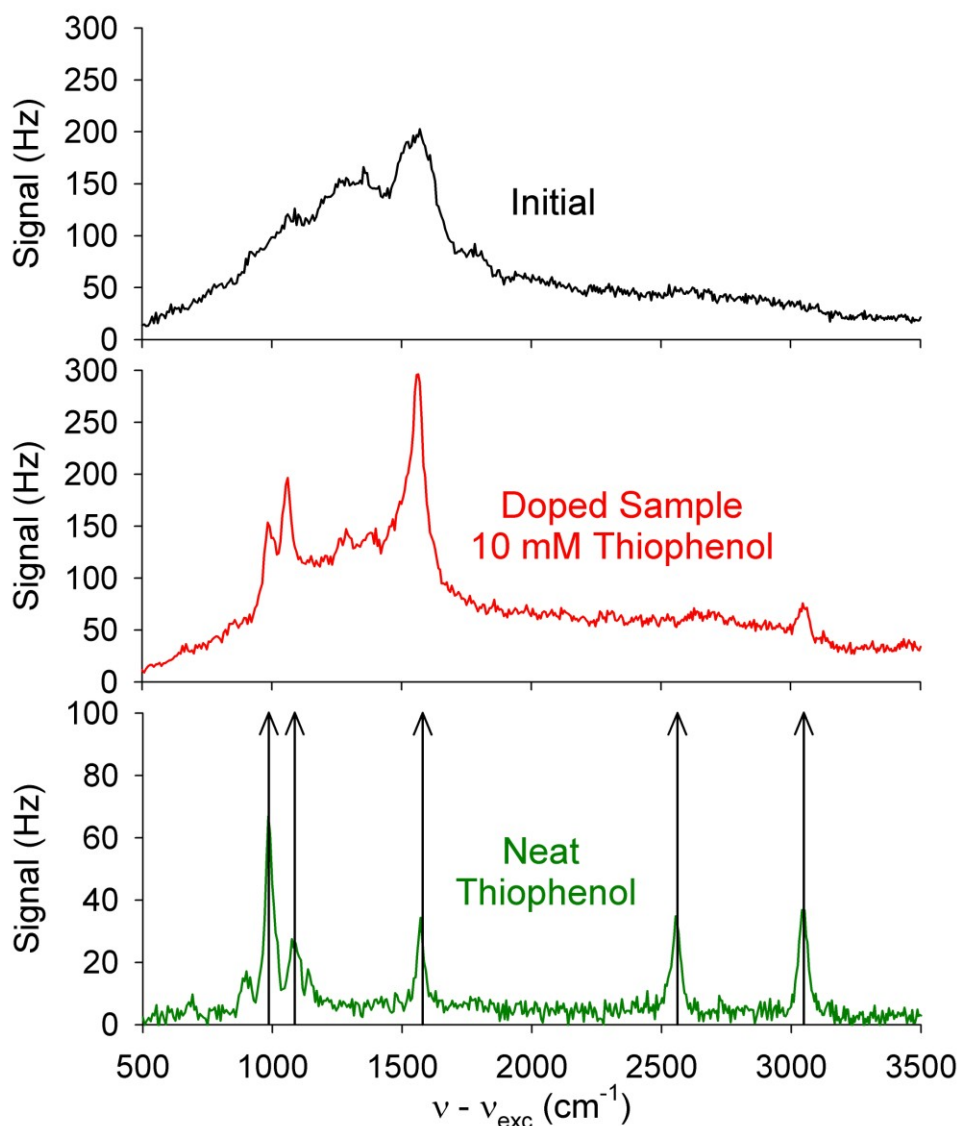


Figure 6.5: SERS spectra upon doping with thiophenol. Spectra obtained at  $74 \mu\text{W}$  for 10 s of a photogenerated feature (a) as initially generated and (b) after removal of starting material and doping with thiophenol. (c) Reference spectrum of thiophenol. Several spectral signatures of thiophenol are observable, with the loss of the  $\nu_{\text{SH}}$  ( $2570 \text{ cm}^{-1}$ ) indicating the chemisorption of the molecule to the surface

comparison, the reference spectrum of thiophenol is displayed in Figure 6.5c. Four peaks are observed in the thiophenol doped silver nanoparticle spectrum that agree with the known spectrum of thiophenol. A notable observation is the loss of the SH stretch at  $2570 \text{ cm}^{-1}$ .

Several experiments<sup>50-52</sup> reported the loss of this peak due to chemisorption of the thiophenol

onto the silver substrate in the limit of sub-monolayer coverage. Lastly, the broad background initially observed between 1000 and 1550  $\text{cm}^{-1}$  is greatly reduced after removal of starting material and exposure to thiophenol, but not eliminated. This effect was observed in a similar experiment by Norrod and Rowlen wherein they observed that thiol/ethanol removed impurities from the surface of a SERS active roughened Ag foil.<sup>45</sup> The spectral observation of thiophenol from the photogenerated silver nanoparticles indicates that we can introduce a specific analyte and detect its characteristic spectra.

The magnitude of this Raman enhancement is a particularly interesting property since this controls the overall sensitivity conditions for use when the analyte is at a low concentration. An exact enhancement factor can not be calculated rigorously for the system due the unknown number of active sites, but we can at least estimate a lower and upper limit. As a conservative lower limit, we can assume the signals arise equally from a near monolayer coverage of thiophenol molecules on the Ag nanocrystals. The Raman cross section of the 1594  $\text{cm}^{-1}$  band of thiophenol was measured by Aggarwal et al.<sup>53</sup> to be  $8.9 \times 10^{-30} \text{ cm}^2$  at 785 nm, which based on scaling with  $\lambda^{-4}$ , would predict a Raman cross section of  $4.2 \times 10^{-29} \text{ cm}^2$  at 532 nm. The expected Raman signal for a single thiophenol in a diffraction limited spot at 74  $\mu\text{W}$  would therefore be  $1.44 \times 10^{-8} \text{ Hz}$ , which takes into account the experimentally measured detection efficiencies of the collection system ( $\eta_{\text{microscope}} = 0.03$ ,  $\eta_{\text{spectrometer}} = 0.06$ ). If we assume monolayer coverage ( $0.5 \text{ nmol/cm}^2$ ) within the diffraction limited area, this implies  $2\text{-}3 \times 10^5$  molecules, Compared with the observed intensity of  $1.7 \times 10^3 \text{ Hz}$  for the 1594  $\text{cm}^{-1}$  band, this yields a *lower* limit of the enhancement factor already to be  $\sim 4 \times 10^5$ . However, based on the high amplitude fluctuations evident in the signal levels, the data suggest a much more likely scenario of signals arising from only a few to a few dozen emitters. This alternative scenario

leads to a much larger upper limit for the enhancement factor of  $\sim 1 \times 10^{11}$ , which starts to be quite respectable. Future experiments based on fluorescence correlation analysis are designed to more accurately determine the number of active sites and emitters within the diffraction limited area, and thereby obtain a better estimate of the enhancement factor due to the photogenerated silver nanoparticles.

#### **6.4 Avrami Kinetic Analysis**

The analysis so far has focused on features that were created by exposing the sample until the signals reached the asymptotic limit. However, additional valuable information about the photogeneration kinetics is obtained by the time dependence of the signals. By way of example, the time traces in Figure 6.6a show data obtained at four different excitation powers that display similar behavior, specifically a general increase in the signal as a function of time as well as rapid fluctuations in the signal on a shorter time scale. The fast fluctuations are observed as bursts, i.e. periods of increased photon count rates often doubling at times with a duration from 10 ms to 1 s. These bursts appear to occur randomly throughout the growth and asymptotic phase of the experiment, with the fractional changes observed independent of excitation power and time. Time correlation studies with a dual photon counting detector system are currently underway to extract further information about the kinetics of these rapid fluctuations as well as the number of highly SERS active emitters. The bursts are superimposed on a monotonically increasing signal that grows sigmoidally and approaches an asymptotic limit at later times. It is this slower time dependence that provides insight into the kinetics of nanoparticle formation which is the focus of the current work. To investigate the dependence on photon flux, the data are taken over several orders of magnitude of illumination intensity. Comparison of the traces at

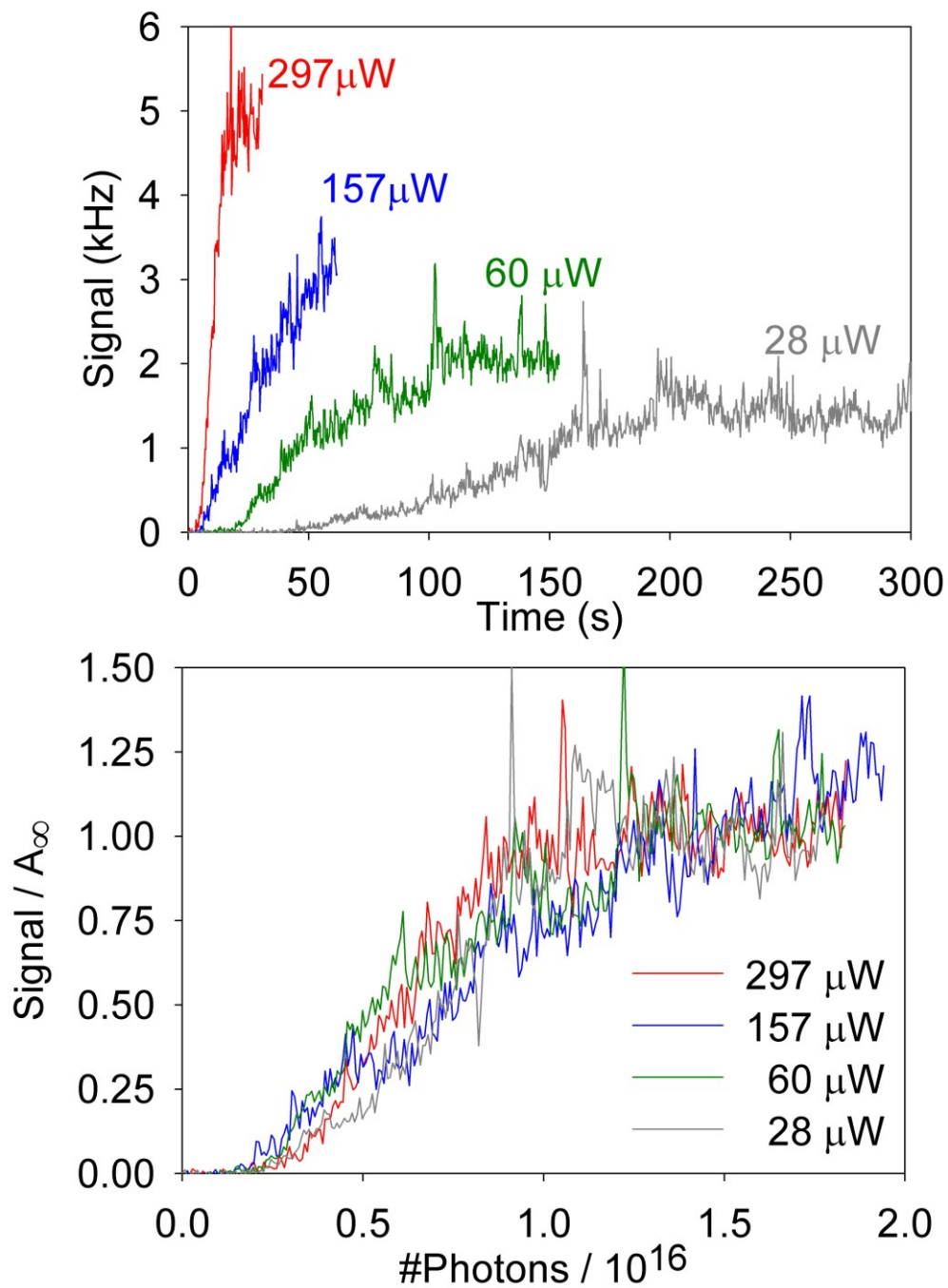


Figure 6.6: Sample trajectories of silver nanoparticle photogeneration. (a) Sample traces exhibiting time dependent generation of SERS active silver nanoparticles at different "write" 532 nm laser powers: 297  $\mu\text{W}$  (red), 157  $\mu\text{W}$  (blue), 60  $\mu\text{W}$  (green), and 28  $\mu\text{W}$  (grey). (b) The same traces in (a) normalized to asymptotic intensity and total number of photons to demonstrate the similarity of the traces

these different powers reveals sigmoidal behavior throughout this range, with the amount of time required for the signal to reach a fraction of its asymptotic limit decreasing systematically with increasing laser power.

In a simple first attempt at kinetic analysis and interpretation, the individual signals can be normalized to the average asymptotic intensity to account for the overall SERS brightness of the features. This is particularly relevant to SERS signals, which for a given static Ag nanoparticle, are predicted to be linear with respect to the laser excitation. Furthermore, if single photon photoreduction of silver ions represents the rate limiting step, the kinetics should depend simply on the number of photons delivered to the sample rather than the exposure duration. Figure 6.6b represents such replotting of the data in Figure 6.6a with the two axis rescalings described above. The traces now superimpose on each other well within the noise of the signal fluctuations, indicating that the kinetics depend on the total number of photons impinging on the sample as well as suggesting a more "universal" curve for describing the underlying nanoparticle formation kinetics.

This clearly motivates a more detailed analysis of the kinetic process. In particular, a very powerful and useful model for solid state material transformation is that of Avrami kinetics, which describes crystallization and precipitation reactions involving nucleation and growth stages.<sup>54-56</sup> The key idea is that nucleation sites are formed and expand to transform the volume into a new phase. As the sites expand, they fill the available volume and eventually come in contact with each other and can no longer grow. The model relates the actual transformed volume fraction ( $\eta_T$ ) and the ideal or "extended" volume fraction that would be transformed if the sites could have grown without any competition or overlapping regions ( $\eta_X$ ). The relationship between  $\eta_T$  and  $\eta_X$  are given by the simple differential expression:

$$dn_T = (1 - v_T) dn_x \quad dn_T = (1 - v_T) dn_x \quad (6.1)$$

which contains the simple stoichiometry that as the volume of the new phase grows and expands, less volume remains available to be transformed. Integration of Equation 6.1 yields the volume fraction transformed as a function of the extended volume fraction:

$$n_T = 1 - v_T^{-x} \quad (6.2)$$

Consequently, the time dependence of the actual transformed volume fraction can be simply obtained from the time dependence of the extended volume fraction.

A first reasonable approximation is that the transformation proceeds at a constant temperature. Even under maximum illumination power (3 mW), our sample should not have appreciable heating. Based on the bulk heat capacity of  $C_p^{Ag}(300K) = 0.236 \text{ kJ}/(\text{kg}\cdot\text{K})$  and density  $\rho^{Ag} = 10.5 \text{ g}/\text{cm}^3$ , the initial temperature rise from the absorption of a 500 nm photon is 35 K for a 1 nm radius spherical silver particle. The time between photon absorption events at the highest intensities investigated ( $\sim 1 \times 10^6 \text{ W}/\text{cm}^2$ ) is approximately 0.1 ns, based on Mie cross section of  $\sigma_{\text{abs}}(500 \text{ nm}) = 3 \times 10^{-15} \text{ cm}^2$  for a 1 nm radius silver particle. The time for this heat to dissipate is around 30 ps, calculated from heat transport through the polystyrene matrix and a value of  $k^{PS} = 0.187 \text{ W}/(\text{K} \cdot \text{m})$  for the bulk thermal conductivity. This is two orders of magnitude faster than the average time between photon absorptions, which implies that the sample is well maintained at thermal equilibrium with the cover slip.

One key assumption of the Avrami model is that the nucleation events are randomly dispersed throughout the element of interest. This does not eliminate the possibility that there are preferential sites in the volume, merely that there are at least many sites in the smallest volume investigated. This condition is well satisfied, since the minimal observation region is determined by the diffraction limited illumination area (360 nm for  $\lambda = 532 \text{ nm}$  and 0.9 NA

objective) and, from the AFM studies, clearly represent clusters of many (i.e., 10-100) silver particles. This condition is also empirically supported by our ability to generate similar intensity features at arbitrary points in the thin film.

This permits a simple empirical formulation for the time dependence of  $\eta_x$ . The extended volume is the product of the volume of a single particle, i.e.,  $V_{\text{particle}}$ , times the number of nucleation sites, i.e.,  $N(t)$ . The expansion of a particle is assumed to occur in  $b$  dimensions and thus  $V_{\text{particle}}(t) \approx (k_{\text{grow}}t)^{bp}$ , where  $k_{\text{grow}}$  is the rate constant for growth in 1D and  $p$  is determined by the nature of the growth mechanism. In the case of diffusion controlled growth, for example, the radius of a particle scales as  $(Dt)^{1/2}$  and therefore  $p = 1/2$ . However, in the current case such as precipitation and interface controlled reactions, growth corresponds to a linear increase in radius with time and therefore  $p = 1$ . Conversely, the number of nucleation sites can be empirically expressed as  $N(t) = k_{\text{nuc}}t^a$ . For  $a = 0$ , for example, no new nucleation sites are assumed to be formed, with many intermediate possibilities such as i) sub-linear ( $0 < a < 1$ ), ii) constant ( $a = 1$ ), iii) or accelerating ( $a > 1$ ) rates of nucleation site creation.

Within this Avrami model framework, the excluded volume fraction ( $n_x$ ) can therefore be expressed as a power law function in time:

$$n_x = V(t) \times \tau_{\text{particle}}(t) = (k_{\text{nucleation}} \times t)^a \times (k_{\text{grow}} \times t)^{bp} \approx (kt)^{a+bp} \quad (6.3)$$

The terms in Equation 6.3 effectively combine the details of the Avrami transformation into a single parameter  $n$

$$a + bp = n \quad (6.4)$$

where theoretical simulations<sup>57,58</sup> provide additional confirmation of the connection between  $n$  and the time dependent nucleation rate ( $a$ ), the rate of the growth ( $p$ ) and the dimensionality of the growing particles ( $b$ ). The general form of the Avrami model can therefore be written as:



$$n_T(t) = 1 - e^{-kt)^n} \quad (6.5)$$

where  $n$  is the so called Avrami exponent and  $k$  is an effective rate constant containing both nucleation and growth rate constants. The time dependent signal intensity,  $S(t)$ , is then simply given by a stretched exponential

$$S(t) = A_\infty \times n_T(t) = A_\infty (1 - e^{-kt)^n) \quad (6.6)$$

where  $A_\infty$  reflects normalization to the asymptotic SERS brightness of the nanoparticle feature. More quantitatively,  $k$  embodies how fast the transformation reaches the 1-1/e point (63% transformed), while the stretching exponent  $n$  affects how steeply the Avrami curve rises through that point.

Further physical insight about the growth of the silver nanoparticles can be obtained via study of these kinetic parameters as a function of excitation power. A total of 24 nanoparticle features, arranged in a grid with 5  $\mu\text{m}$  spacing have been generated on a single substrate as a function of laser power (30  $\mu\text{W}$  to 3 mW). This permits systematic variation of the illumination intensity over two orders of magnitude, with multiple trajectories at each power to allow a determination of statistical reproducibility. The resultant time traces are then independently fit with a nonlinear least squares algorithm to Equation 6.6. Sample fits are presented in Figure 6.7 corresponding to the four time traces shown in Figure 6.6. The respectably high fit quality indicates that the data are well represented by the Avrami model over a large dynamic range of illumination powers. Figure 6.8a shows a log-log plot for  $A_\infty$  versus laser power revealing a slope of 0.97(1). A similar log-log plot for  $k$  versus laser power, displayed in Figure 6.8b, also has a near linear slope of 1.05(4). However, the exponential stretching parameter averaged over all 24 trajectories was found to be  $n \approx 3.2(6)$ .

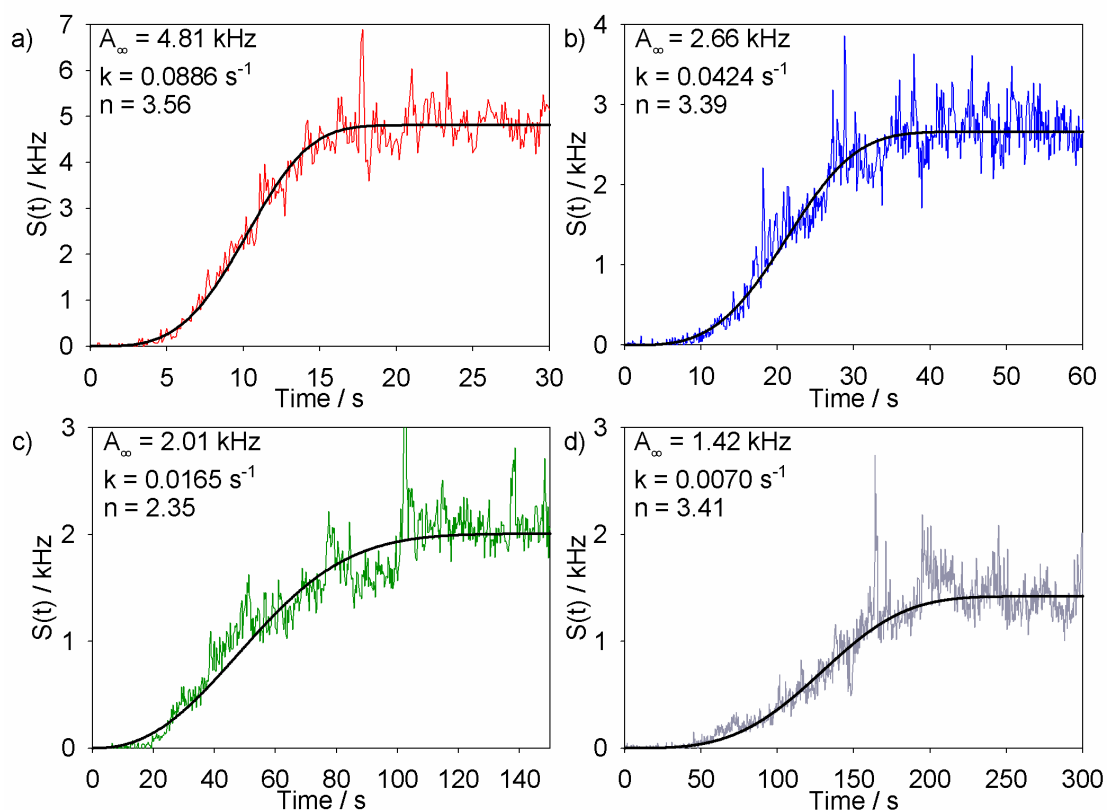


Figure 6.7: Least squares fits of the data to the Avrami model. Avrami functional (Equation 6.6) fits to the time traces shown previously: 297  $\mu\text{W}$  (a, red), 157  $\mu\text{W}$  (b, blue), 60  $\mu\text{W}$  (c, green), and 28  $\mu\text{W}$  (d, grey). Fit parameters are listed in the insets.

The linear scaling of  $A_\infty$  as a function of laser formation intensity (i.e., slope = 0.97(1)) implies that each diffraction limited collection of Ag nanoparticles exhibits the same SERS intensity per unit laser "read" power, irrespective of "write" power level at which they were generated. From quantitative analysis of a series of AFM images of features generated at different powers, we find the number of nanoparticles observed (e.g. Figure 6.4) to be independent of "write" laser intensity. Indeed, as discussed previously, analysis of the nanoparticle volumes from these AFM images also indicates that all the silver ion starting material in the diffraction limited focal region is being harvested into nanostructures. Combining these observations, this would be consistent with a simple picture that the number of SERS

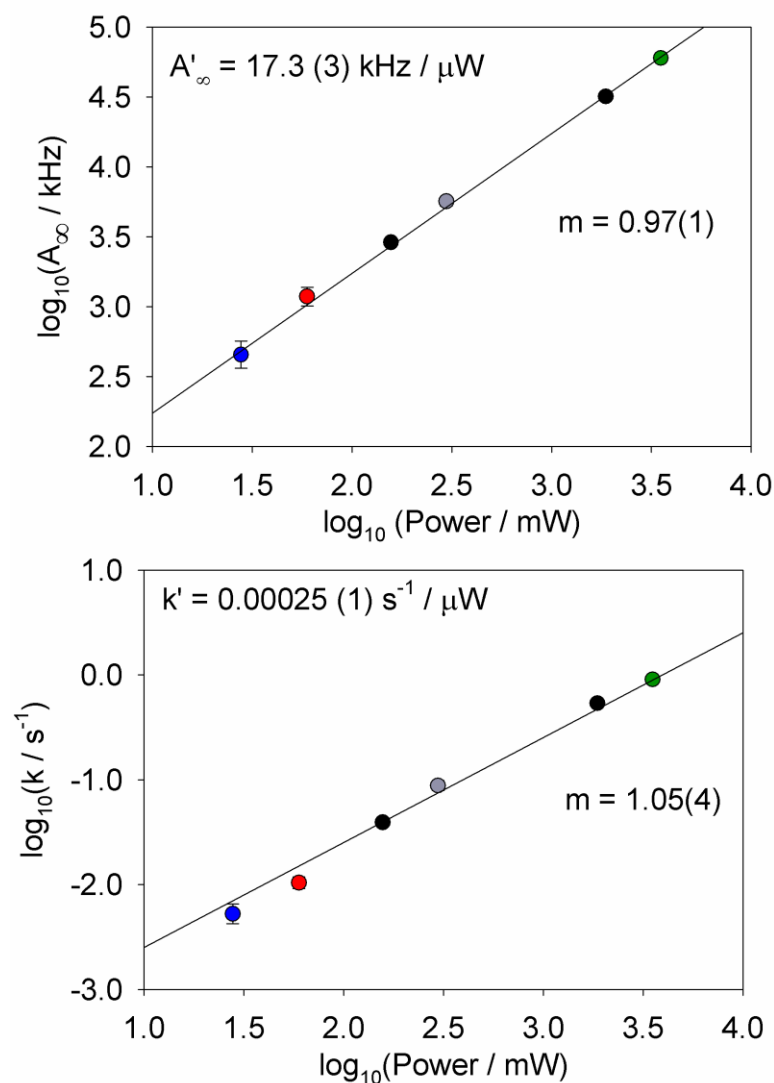


Figure 6.8: Excitation power dependence of fit parameters. Power dependence of  $A_\infty$  (a) and  $k$  (b) for the photogeneration of silver nanoparticles displayed as a log-log plot. Solid black line is a linear fit to the data.

emitters generated is independent of laser formation intensity. If the overall brightness of a feature is taken to be the sum of contributions from each hot spot generated therein, then a linear dependence of  $A_\infty$  on laser generation power would mean that the same number of hot spots, and potentially SERS active particles, is being formed independent of excitation power. Explicit

confirmation of this will require a higher spatial resolution analysis of such nanoparticle samples with transmission electron microscopy.

A clear linear scaling of the rate constant  $k$  (i.e., slope = 1.05(4)) with laser power is more surprising and speaks to the mechanism responsible for reducing the silver ions. The formation of the silver particles requires the neutralization of silver ions, and therefore the generation of an electron or a reducing species. Initial expectation, based on results from Gaddy et al.,<sup>28,29</sup> would be that the reduction would require two photons due to the relatively low energy of a single 532 nm photon (2.33 eV) compared to typical ionization energies ( $> 5$  eV), and thus the rate constant should depend quadratically, or a higher order, on laser power. However, results by Ahern<sup>38</sup> showed that the 514 nm line of an Argon ion laser was able to generate silver colloids from an aqueous solution of  $\text{AgNO}_3$  and various organic materials in a one photon process. More recent results by Muniz-Miranda showed that  $\text{AgNO}_3$  in the proximity of silica (both colloidal and mesoporous) was able to be photoreduced under single photon conditions as well.<sup>59,60</sup> The speculation offered in that work is that the photoactive species is Si-O-Ag formed after the silver ions are hydrolyzed to AgOH which then react with the silica; the O-Ag bond is then cleaved by a photon to make Si-O $\cdot$  and  $\text{Ag}^0$ .

In the present work, the thin film necessarily includes silver ion contact with a glass silica coverslip, suggesting that the substrate plays a role. Indeed, we have noted that formation of bright SERS nanoparticle emitters is hindered by an initial thin film of PVA lifting the silver perchlorate/PS away from the silica interface. Interestingly, we have also performed preliminary experiments on gold or platinum coated coverslips where the ability to photogenerate SERS active silver nanoparticles is still present. In this regard, it is also worth noting one other system where the one photon reduction of metal ions has been observed. Eustis and Al-Sayed<sup>61</sup> reported

on the kinetics of gold nanoparticle generation that also showed a linear dependence on the excitation power. They determined that an activated gold complex is formed initially from a single photon excitation, and the subsequent gold reduction is of this transient species without further excitation. It is possible that our single photon excitation could be generating a similar transient species that reacts quickly with something present in the film to form silver neutral. Clearly more work will be necessary to identify the photoreduction mechanism unambiguously.

This one-photon photoreduction laser dependence should be compared to the results of previous experiments,<sup>41</sup> in which signal intensities were measured after a fixed time interval as a function of laser power. The original log-log plot of these data vs laser pulse energy suggested a slope of  $\approx 3$ , which based on a known linear dependence of the SERS signal on laser power was interpreted to imply a *quadratic* intensity dependence for the  $\text{Ag}^+$  photoreduction rate constant. However, these early studies focused on the initial rise and did not adequately sample the asymptotic regime predicted from the more sophisticated Avrami kinetics presented in this work. Indeed, based on a linear laser intensity dependence noted in this work for  $A_\infty$  and  $k$ , the SERS signals should be expected to scale as  $(I_{\text{laser}})^{n+1}$ , or approximately 4.2(6) for an Avrami stretching exponent of  $n = 3.2(6)$ . This is *higher* than the previously reported 3.3(5) value, despite a *lower* (i.e., linear vs quadratic) dependence currently reported for the photoreduction rate constant on laser power. Given the high sensitivity of the SERS nanoparticle growth and signal levels to atmospheric water and oxygen levels, however, any residual discrepancies with the present studies could be due to improved signal stability with inert Ar purge gas protecting the samples. Further research into the environmental effects is presented in the next chapter to examine this possibility more conclusively.

As a final comment, it is possible to extract additional physical insight from the observed Avrami stretching exponent  $n = 3.2(6)$ , which we know from Equation 6.4 is given by  $n = a + bp$ . The diffusion constant for silver perchlorate diffusing in a PS matrix is extremely small ( $D \approx 10^{-14} - 10^{-15} \text{ cm}^2/\text{s}$ ), requiring time scales on the order of hours even to diffuse across a 360 nm diffraction limited spot. Furthermore, we are able to generate Ag nanoparticle features in close proximity to each other, indicating that  $\text{Ag}^+$  does not move diffusively into the diffraction limited spot from outside the illuminated area. The rate limiting step for growth is therefore clearly not diffusive, but rather expansion of the interface between the growing particle and the starting material, from which a variety of experiments<sup>58</sup> suggest that  $p \approx 1$ . Similarly, the morphology of the nanoparticles determines the value of  $b$ , the dimensionality of growth. The expectation is that the particles grow initially in three dimensions; however the vertical direction constrains them such that they are only able to expand in the lateral two dimensions of the film. Thus, for our experimental conditions  $b \approx 2$ , as further supported by the AFM results which show that the nanoparticles as thin disks with 7 nm height and 40 nm diameter.

Combining these values for  $p$  and  $b$  allows us to extract a value for  $a \approx 1.2(6)$  based on Equation 6.4 and value of  $n$  from the kinetic analysis. Despite the uncertainty, this value clearly suggests an *increase* in the number of nucleation sites with time throughout the transformation. It should be noted that  $a \approx 1$ , i.e., a scenario with a linear increase in the number of nucleation sites with time, might be physically consistent with constant illumination of the nanoparticle surface during the growth process. Thus, in the framework of the Avrami model, the particles are generated by a single photon excitation reaction, and grow in a non-diffusion limited manner into two dimensional shapes (disks) that eventually harvest all the initial silver ions present in the diffraction limited spot.

## 6.5 Summary

We are able to reproducibly and routinely photogenerate silver nanoparticles that exhibit intense SERS activity in an arbitrary spatial grid. The SERS signal most likely comes from “hot spots” formed in the junctions of silver nanoparticles constellations that are a result of the photoreduction of silver salt inside the diffraction limited spot. The silver salt can be converted at near 100% efficiency to silver metal via a one photon process in a matter of minutes even at very low laser intensities ( $< 50 \mu\text{W}$ ). The resulting particles are stable to removal of the initial polymer support as well as multiple washing steps thereby allowing for the exposure of the nanoparticles to various analytes and for use in multiple applications. Analysis of the kinetics is consistent with an Avrami based kinetic model for nucleation and growth, whereby the addition of material to the nanoparticle is not diffusion limited ( $p \approx 1$ ) and growth is constrained to two dimensions due to the thin film support ( $b \approx 2$ ).

The technique described in this work provides several powerful advantages over previous chemical reduction and/or laser photoreduction efforts. 1) First and foremost, the SERS active nanoparticles can be written in arbitrary locations on a 2D surface and reproducibly located at a later time. Secondly, our method also provides a means to experimentally control and subsequently measure the growth kinetics. Thirdly, the ability to rapidly relocate the features greatly facilitates ancillary investigations using other techniques, such as AFM or TEM, to probe the morphology of the photogenerated particles. The next chapter will expand on the work presented here to study the generation of features under various experimental conditions. Specifically, oxygen and water will be added to the environment around the film to determine inhibition or enhancement for the rate of formation or SERS signal.

## References

- (1) Mock, J. J.; Barbic, M.; Smith, D. R.; Schultz, D. A.; Schultz, S. *J. Chem. Phys.* **2002**, *116*, 6755.
- (2) Kerker, M. *J. Colloid Interface Sci.* **1985**, *105*, 297.
- (3) Wiley, B. J.; Im, S. H.; Li, Z. Y.; McLellan, J.; Siekkinen, A.; Xia, Y. A. *J. Phys. Chem. B* **2006**, *110*, 15666.
- (4) Oldenburg, S. J.; Averitt, R. D.; Westcott, S. L.; Halas, N. J. *Chem. Phys. Lett.* **1998**, *288*, 243.
- (5) Link, S.; Wang, Z. L.; El-Sayed, M. A. *J. Phys. Chem. B* **1999**, *103*, 3529.
- (6) Lee, K. S.; El-Sayed, M. A. *J. Phys. Chem. B* **2006**, *110*, 19220.
- (7) Loo, C.; Lowery, A.; Halas, N.; West, J.; Drezek, R. *Nano Lett.* **2005**, *5*, 709.
- (8) Gobin, A. M.; Lee, M. H.; Halas, N. J.; James, W. D.; Drezek, R. A.; West, J. L. *Nano Lett.* **2007**, *7*, 1929.
- (9) Haes, A. J.; Zou, S. L.; Schatz, G. C.; Van Duyne, R. P. *J. Phys. Chem. B* **2004**, *108*, 6961.
- (10) Haynes, C. L.; Van Duyne, R. P. *J. Phys. Chem. B* **2001**, *105*, 5599.
- (11) Brolo, A. G.; Gordon, R.; Leathem, B.; Kavanagh, K. L. *Langmuir* **2004**, *20*, 4813.
- (12) Charbonneau, R.; Lahoud, N. *Opt. Express* **2005**, *13*, 977.
- (13) Srituravanich, W.; Fang, N.; Sun, C.; Luo, Q.; Zhang, X. *Nano Lett.* **2004**, *4*, 1085.
- (14) Kelly, K. L.; Coronado, E.; Zhao, L. L.; Schatz, G. C. *J. Phys. Chem. B* **2003**, *107*, 668.
- (15) Emory, S. R.; Nie, S. *J. Phys. Chem. B* **1998**, *102*, 493.
- (16) Hao, E.; Schatz, G. C. *J. Chem. Phys.* **2004**, *120*, 357.
- (17) Atay, T.; Song, J. H.; Nurmikko, A. V. *Nano Lett.* **2004**, *4*, 1627.
- (18) Fromm, D. P.; Sundaramurthy, A.; Schuck, P. J.; Kino, G.; Moerner, W. E. *Nano Lett.* **2004**, *4*, 957.



- (19) Talley, C. E.; Jackson, J. B.; Oubre, C.; Grady, N. K.; Hollars, C. W.; Lane, S. M.; Huser, T. R.; Nordlander, P.; Halas, N. J. *Nano Lett.* **2005**, *5*, 1569.
- (20) Haynes, C. L.; McFarland, A. D.; Smith, M. T.; Hulteen, J. C.; Van Duyne, R. P. *J. Phys. Chem. B* **2002**, *106*, 1898.
- (21) Michaels, A. M.; Nirmal, M.; Brus, L. E. *J. Am. Chem. Soc.* **1999**, *121*, 9932.
- (22) Camden, J. P.; Dieringer, J. A.; Wang, Y. M.; Masiello, D. J.; Marks, L. D.; Schatz, G. C.; Van Duyne, R. P. *J. Am. Chem. Soc.* **2008**, *130*, 12616.
- (23) Jin, R. C.; Cao, Y. W.; Mirkin, C. A.; Kelly, K. L.; Schatz, G. C.; Zheng, J. G. *Science* **2001**, *294*, 1901.
- (24) McMahon, J. M.; Henry, A. I.; Wustholz, K. L.; Natan, M. J.; Freeman, R. G.; Van Duyne, R. P.; Schatz, G. C. *Anal. Bioanal. Chem.* **2009**, *394*, 1819.
- (25) Vlckova, B.; Matejka, P.; Simonova, J.; Cermakova, K.; Pancoska, P.; Baumruk, V. *J. Phys. Chem.* **1993**, *97*, 9719.
- (26) Turkevich, J.; Stevenson, P. C.; Hillier, J. *Discuss Faraday Soc* **1951**, 55.
- (27) Evanoff, D. D.; Chumanov, G. *J. Phys. Chem. B* **2004**, *108*, 13948.
- (28) Gaddy, G. A.; Korchev, A. S.; McLain, J. L.; Slaten, B. L.; Steigerwalt, E. S.; Mills, G. *J. Phys. Chem. B* **2004**, *108*, 14850.
- (29) Gaddy, G. A.; McLain, J. L.; Korchev, A. S.; Slaten, B. L.; Mills, G. *J. Phys. Chem. B* **2004**, *108*, 14858.
- (30) Korchev, A. S.; Konovalova, T.; Cammarata, V.; Kispert, L.; Slaten, L.; Mills, G. *Langmuir* **2006**, *22*, 375.
- (31) Bernabò, M.; Pucci, A.; Galembeck, F.; Leite, C. A. d. P.; Ruggeri, G. *Macromol. Mater. Eng.* **2009**, *294*, 256.
- (32) Miyama, T.; Yonezawa, Y. *J. Nanopart. Res.* **2004**, *6*, 457.
- (33) Zhang, J. G.; Xu, S. Q.; Kumacheva, E. *Adv. Mater.* **2005**, *17*, 2336.
- (34) Kelly, K. L.; Yamashita, K. *J. Phys. Chem. B* **2006**, *110*, 7743.
- (35) Eustis, S.; Krylova, G.; Smirnova, N.; Eremenko, A.; Tabor, C.; Huang, W. Y.; El-Sayed, M. A. *J. Photochem. Photobiol. A-Chem.* **2006**, *181*, 385.
- (36) Peyser, L. A.; Vinson, A. E.; Bartko, A. P.; Dickson, R. M. *Science* **2001**, *291*, 103.
- (37) Henley, S. J.; Silva, S. R. P. *Appl. Phys. Lett.* **2007**, *91*.

- (38) Ahern, A. M.; Garrell, R. L. *Anal. Chem.* **1987**, *59*, 2813.
- (39) Muniz-Miranda, M. *Appl. Spectrosc.* **2003**, *57*, 655.
- (40) Muniz-Miranda, M. *J. Raman Spectrosc.* **2002**, *33*, 295.
- (41) Monti, O. L. A.; Fourkas, J. T.; Nesbitt, D. J. *J. Phys. Chem. B* **2004**, *108*, 1604.
- (42) Canamares, M. V.; Garcia-Ramos, J. V.; Gomez-Varga, J. D.; Domingo, C.; Sanchez-Cortes, S. *Langmuir* **2007**, *23*, 5210.
- (43) Zheng, X. L.; Guo, D. W.; Shao, Y. L.; Jia, S. J.; Xu, S. P.; Zhao, B.; Xu, W. Q.; Corredor, C.; Lombardi, J. R. *Langmuir* **2008**, *24*, 4394.
- (44) Anderson, D. J.; Moskovits, M. *J. Phys. Chem. B* **2006**, *110*, 13722.
- (45) Norrod, K. L.; Rowlen, K. L. *Anal. Chem.* **1998**, *70*, 4218.
- (46) Taylor, C. E.; Garvey, S. D.; Pemberton, J. E. *Anal. Chem.* **1996**, *68*, 2401.
- (47) Kudelski, A.; Pettinger, B. *Chem. Phys. Lett.* **2000**, *321*, 356.
- (48) Michaels, A. M.; Jiang, J.; Brus, L. *J. Phys. Chem. B* **2000**, *104*, 11965.
- (49) Jiang, J.; Bosnick, K.; Maillard, M.; Brus, L. *J. Phys. Chem. B* **2003**, *107*, 9964.
- (50) Taylor, C. E.; Pemberton, J. E.; Goodman, G. G.; Schoenfish, M. H. *Appl. Spectrosc.* **1999**, *53*, 1212.
- (51) Gi, X.; Ma, M.; Zhang, J. F.; Lu, Y.; Carron, K. T. *J. Colloid Interface Sci.* **1992**, *150*, 1.
- (52) Joo, T. H.; Kim, M. S.; Kim, K. *J. Raman Spectrosc.* **1987**, *18*, 57.
- (53) Aggarwal, R. L.; Farrar, L. W.; Diebold, E. D.; Polla, D. L. *J. Raman Spectrosc.* **2009**, *40*, 1331.
- (54) Avrami, M. *J. Chem. Phys.* **1941**, *9*, 177.
- (55) Avrami, M. *J. Chem. Phys.* **1940**, *8*, 212.
- (56) Avrami, M. *J. Chem. Phys.* **1939**, *7*, 1103.
- (57) Ranganathan, S.; Vonheimendahl, M. *J. Mater. Sci.* **1981**, *16*, 2401.
- (58) Christian, J. W. *The Theory of Transformations in Metals and Alloys*, 2nd ed.; Pergamon Press, 1975.
- (59) Muniz-Miranda, M.; Ottaviani, M. F. *Laser Phys.* **2004**, *14*, 1533.

- (60) Muniz-Miranda, M. *J. Raman Spectrosc.* **2004**, *35*, 839.
- (61) Eustis, S.; Hsu, H. Y.; El-Sayed, M. A. *J. Phys. Chem. B* **2005**, *109*, 4811.

## Chapter 7

# Vapor Phase Chemical Influences on Silver Nanoparticle Surface Enhanced Raman and Photogeneration Kinetics

### 7.1 Introduction

Metal nanoparticles have many unique and interesting optical properties when compared to properties of the bulk material. Nanoparticles have been utilized since medieval times when they were incorporated into the development of stained glass.<sup>1</sup> In 1857, Faraday reported the production of a brilliant red colored solution produced from dissolution of a thin gold film postulated to be composed of gold nanoparticles.<sup>2</sup> Silver and gold nanoparticles are of particular interest due to the presence of a surface plasmon resonance (SPR), a collective oscillation of electrons, which can be excited from the near-ultraviolet to the near-infrared. The SPR of spherical nanoparticles was solved from Maxwell's equations in 1908 by Mie.<sup>3</sup> Since then, numerical solutions for arbitrary shaped particles have been developed,<sup>4</sup> allowing for direct comparison between theory and experiments on variations in size, shape and composition of the nanoparticle.<sup>5-7</sup> Indeed, plasmonics have provided many advances in the fields of medicine,<sup>8,9</sup> molecular detection,<sup>10-12</sup> and nano-fabrication techniques.<sup>13</sup>

The investigations of the SPR are not only limited to the explorations of unique optical absorption properties. In addition, the coherent oscillation of electrons is able to generate local electric field enhancements, on the order of  $10^2$ , in the near field vicinity around the nanostructure.<sup>14</sup> Experimental and theoretical efforts have been carried out to identify the nature of these local fields that arise due to the optical excitation of isolated nanoparticle SPR.<sup>15,16</sup> If

two nanoparticles are brought into close proximity, the resultant local field can be enhanced by a factor as large as  $10^5$  in the interstitial region.<sup>14</sup> Precise control of nanoparticle dimers produced by various lithography techniques have demonstrated the nonlinear enhancement of electric fields located in the interstitial spaces between particles.<sup>14,17-19</sup>

The local AC electric field can facilitate the detection of molecules in the vicinity of this enhanced region by surface-enhanced Raman scattering (SERS). Several studies have reported single molecule detection via SERS which implies an enhancement in the Raman cross section of nearly 8 orders of magnitude.<sup>20,21</sup> Unfortunately, the silver nanoparticles which are commonly used in SERS experiments show activity in only 1 in 100-1000 particles/clusters of this magnitude.<sup>15,21</sup> This has been explained by positing that only few configurations of nanoparticles/clusters have the correct geometry to produce a large local field enhancement.<sup>20</sup> In fact, recent super-resolution experiments by Stranahan and Willets<sup>22</sup> have shown that the enhancement is confined to limited locations on the surface of the nanoparticles. These areas are typically near the junctions between nanoparticles and are termed “hot spots” due to the high local fields in the region.<sup>23,24</sup> Thus, there is much interest in producing these “hot spots” reliably and reproducibly.

The traditional synthesis of silver nanoparticles is by chemical reduction of silver salts in solution.<sup>25,26</sup> Many improvements to this technique have allowed for better control of size<sup>12,16,27,28</sup> and shape,<sup>16,23,29,30</sup> however, the location of active “hot spots” for use in SERS studies once dispersed on a substrate becomes problematic due to the previously mentioned low active population. To overcome this obstacle, substrates where the entire surface has reproducible SERS enhancements have been developed<sup>29</sup> and used to detect species at the few molecule level by confocal microscopy. This technique is commonly used to study SERS

activity and spectra from a variety of substrates. The combination of the diffraction-limited spatial resolution and sensitive detectors allow for the study of individual particles and small clusters with high signal to noise. However, confocal microscopy is not limited to study only prepared substrates, but it can also be used to generate SERS active substrates. Work by Monti et al. initially demonstrated that SERS active silver nanoparticles were generated in thin polymer films with a variety of laser excitation sources.<sup>31</sup> More recently, we expanded on the technique and investigated the formation kinetics and SERS enhancements for silver nanoparticles in a thin polymer film.

In our previous work, we demonstrated the photogeneration of SERS active silver nanoparticles in a thin polystyrene film under an inert argon atmosphere.<sup>32</sup> The SERS signal was postulated to originate from molecules located in “hot spots” formed at the junctions between silver nanoparticle constellations within the diffraction limited spot. The kinetics of the formation are consistent with an Avrami-type model of the form:

$$S(t) = A_{\infty}(1 - e^{-kt^n})$$

where  $A_{\infty}$  is the asymptotic SERS brightness of the nanoparticle feature. The rate constant  $k$  is an amalgamation of the nucleation and growth rate constants and represents how fast the transformation reaches the 1/e point. The rate constant showed a linear dependence on excitation intensity, which implies that the rate limiting step for the photoreduction is a one photon process. The value of  $n$ , the Avrami exponent, affects how steeply the curve rises through the 1/e point and can be connected with details of the nucleation and growth mechanism. Specifically, in our experiments the growth was found not to be diffusion limited, and constrained to two dimensions due to the nature of the thin film support (~7 nm). Furthermore, the asymptotic behavior of the

kinetics and AFM studies indicated that the silver salt starting material was converted with near 100% efficiency to silver metal.

The SERS enhancements observed for clusters generated by *in situ* photoreduction of silver salts was between  $10^5$  and  $10^{10}$ . For the technique to be viable for single molecule detection, necessary enhancements in the Raman cross section for nonresonant molecules need to be consistently on the order of  $10^{10}$  or higher.<sup>33</sup> We expand on our previous studies by investigating how the composition of the atmosphere above the substrate influences the photogeneration kinetics and more importantly the SERS brightness of the features. In addition, we include wide field studies of the constellations by both dark field scattering and Raman. The dark field spectra indicate the presence of closely spaced dimers in constellations that show large SERS enhancement. Wide field Raman super resolution experiments reveal the nature of the intensity fluctuations observed previously for generated features.

The organization of the chapter is as follows: Section 2 describes the experimental apparatus and protocol. Section 3 presents the results for different gas environments under which the kinetics were investigated and provides insight into what effects the photogeneration rates. The wide field studies of photogenerated features are presented in Section 4. Section 5 includes a summary of the results and conclusions.

## 7.2 Experiment

The *in situ* generation of silver nanoparticles is achieved by photoreducing silver perchlorate embedded in a thin film using light focused through a microscope objective, as seen in the inset of Figure 1. The kinetics of the formation of silver nanoparticles inside the diffraction limited spot are followed in real time by monitoring the Raman scattering of the

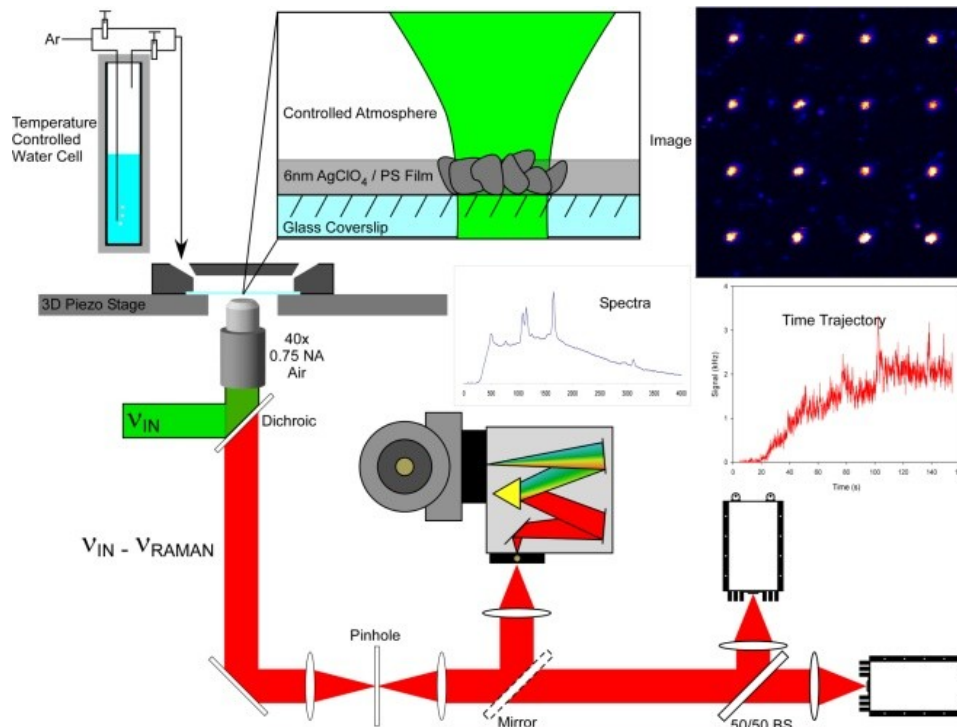


Figure 7.1: Experimental setup. A confocal microscope is used to generate and investigate silver nanoparticles. Detection options include an APD for time-correlated single photon counting (TCSPC) and a CCD spectrometer for measuring Raman spectra. A gas manifold with a water pick-up cell provides the control of the atmospheric composition around the sample. (Inset) Close-up cartoon of the sample. Silver perchlorate in a thin polymer film is photoreduced to silver nanoparticles under a controlled atmosphere.

resultant nanoparticles, seen as a time trajectory in the inset to Figure 7.1. Subsequently, the sample can be further characterized by (i) raster scanning the sample to generate an intensity image; or (ii) selecting a particular location to study time dynamics or spectral properties.

Samples are additionally characterized by atomic force microscopy (AFM) to determine their size, shape and spatial distribution within the diffraction limited spot.

Polystyrene (Polystyrene Standard, molar mass 18,700 g/mol) is used as received from Aldrich. Silver perchlorate (99.9%) is stored over drierite in a refrigerator to keep the hydrate formation to a minimum. Toluene (Spectranal grade, >99.9%) is also dried over Type 3A molecular sieves to remove any trace water and then bubbled with He for 30 min to remove oxygen. For typical samples, 1 mL of a 10 mM  $\text{AgClO}_4$  in toluene (0.074% by volume) and 1



mg polystyrene per 1 mL toluene (0.094%) are made fresh and used within an hour of being prepared. A 25  $\mu$ L aliquot of this solution is dynamically spun cast (1500 RPM) onto an ozone-cleaned glass microscope coverslip that contains a registration mark for rapid and accurate relocation of the particles on the surface on a variety of instruments. The film is  $\sim$ 7 nm thick, as measured by tapping mode AFM at a step edge formed from scoring the film. The sample is then placed on a three-axis closed-loop piezoelectric flexure stage (Physik Instrumente) with an argon purge volume initially established around the sample. For the present studies, the purge volume is connected to a manifold such that the composition of the gas environment around the sample can contain various fractions of argon, oxygen, and water. The water vapor is provided by a temperature controlled pick-up cell that is used to introduce a known partial pressure of water vapor. A digital hygrometer is placed in-line before the sample to monitor the relative humidity of the purge volume, with a mass flow meter to measure the flow rate of the gas mixture. Under typically operating conditions, the flow rate is 100 sccm chosen such that the time to purge the gas line and sample is approximately 30 seconds.

The excitation is provided by a doubled 1064 nm Nd:YVO<sub>4</sub> continuous wave laser (532 nm) that is expanded to overfill the back aperture of the coverslip corrected air objective (40x, 0.75 NA) mounted on a commercial inverted microscope (Olympus, IX71) operated in epi-fluorescence mode. A dichroic beam splitter (Semrock, LPD01-532RS-25) reflects the excitation beam to the objective, while transmitting the collected red-shifted emission. A 50  $\mu$ m pinhole is placed at the confocal imaging plane at the side port of the microscope; a lens recollimates the emission, which can then be directed into one of two different optical paths. In the first path, the emission is sent to a 50/50 beamsplitter before being focused onto a pair of single photon counting avalanche photodiodes (APD, Perkin-Elmer, SPCM-AQR-15) through

matching filters (Semrock, LP03-532RS, OD > 6 @ 532 nm) to remove any remaining scattered incident light. The transmission spectra of the dichroic and filters leads to a detection bandwidth for Raman scattering between  $500\text{ cm}^{-1}$  and  $5000\text{ cm}^{-1}$ . The APD outputs are directed to a router (HRT-81) and then to a time-correlated single photon counting card (TCSPC, Becker & Hickl, SPC-130 PCI card), which provides time-tagged fluorescence measurements with a  $\sim 50\text{ ns}$  macrotime resolution and allows the data to be binned post acquisition for any desired time interval. The second optical path option directs the emission into a Czerny-Turner-type imaging spectrometer (600 lines/mm grating,  $f = 4$ ), where the light is dispersed onto an emCCD (Photometrics CascadeII) detector. Orientation of the grating at zero-order enables the collection of two dimensional images by either dark field using white light with a special condenser or Raman using laser wide field excitation. Dark field scattering spectra of constellations are collected in two wavelength windows, 400-750 nm and 650-900 nm, to span the visible region of interest. The Raman spectra are collected with  $\sim 20\text{ cm}^{-1}$  spectral resolution from 500 to  $3000\text{ cm}^{-1}$  in a single exposure and time resolution from 0.1 s out to 1000 s.

The photogeneration is monitored in real-time by moving the stage to a specific location, opening the laser shutter, acquiring an intensity trace over a given time period, and then closing the shutter. Excitation intensities are  $17\text{ }\mu\text{W}$  at the sample ( $\sim 9\text{ kW/cm}^2$ ) which results in a fully generated feature in approximately 60 s under argon purge conditions. This process is repeated at least 5 times to obtain meaningful statistics for the kinetic parameters. Experiments are performed both on single samples under a variety of conditions, as well as the same conditions across multiple samples to identify robust results and diminish reproducibility errors. After generation of the features, an image is acquired by raster scanning the sample to create a two-dimensional image (256 pixels by 256 pixels) that represents the Raman scattering intensity as a

function of position on the surface. Acquisition and analysis software is written in house and developed in CVI/Labwindows. Samples can be washed with water and toluene to remove the starting material and thus expose the silver nanoparticles, thereby allowing AFM studies to be conducted in tapping mode with a 10-20 nm radius of curvature tip. The registration mark on the glass slide provides the ability to correlate AFM images and morphology with SERS intensity.

### **7.3 Effect of Environment on Photogeneration Kinetics**

Silver nanoparticles grown while exposed to air generally grow more quickly (factor of 5) and have a brighter asymptotic limit (roughly an order of magnitude) than those grown in an inert argon atmosphere, albeit with large variation from sample to sample.<sup>32</sup> In order to determine the species responsible for making “bright” particles, a systematic approach wherein the atmosphere is varied in a controlled manner was undertaken. We chose to investigate the role of the two most likely chemically important gasses in the atmosphere – oxygen which is present at 20% by volume, and water vapor which can vary from day to day. The results for oxygen are presented first, before moving to the slightly more complicated effects of water vapor.

The effect of oxygen is established by generating features in a 100% oxygen atmosphere and comparing the kinetics to argon purge conditions on the same substrate. Features are grown for 60 seconds, an amount of time that guarantees the kinetics have reached the asymptotic limit. A sample image showing features generated when alternating between argon and oxygen purge is shown on the right of Figure 7.2 with a lineout below. The first notable difference is in the apparent brightness of the features, the argon grown features are ~4 times brighter than the features generated under oxygen. Both conditions lead to roughly the same spatial extent of

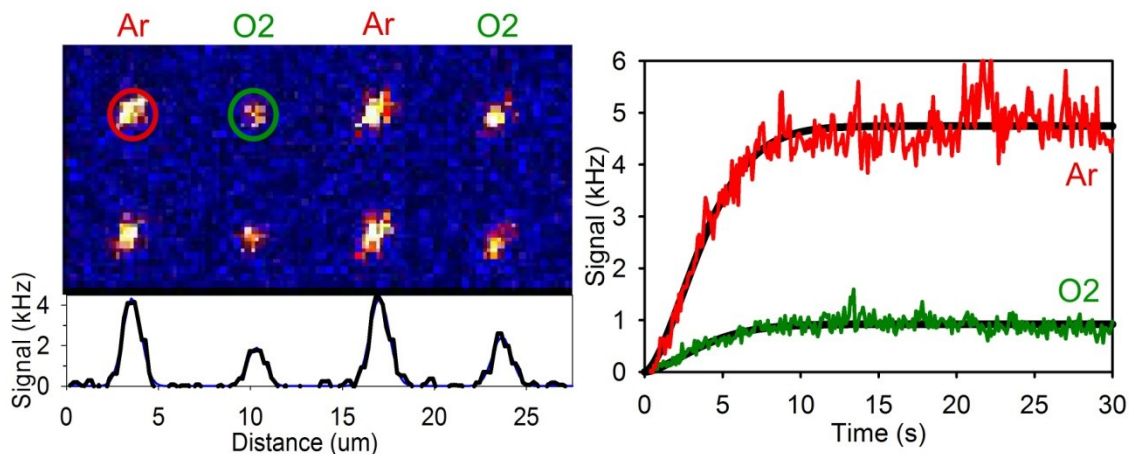


Figure 7.2: Comparison between Ar purge and O<sub>2</sub> purge. (Left) 20 μm x 10 μm Raman intensity image of photogenerated silver nanoparticles generated under argon (Red circle) and oxygen (Green circle) conditions. Lineouts are included below the image. (Right) Sample time trajectory for the features circled in A showing that the asymptotic value is decreased in the presence of oxygen, but the rate of the formation is unchanged.

715(25) nm which is standard for this technique. This indicates that in each case the asymptotic limit corresponds to the complete “harvesting” of all Ag<sup>+</sup> in the focal volume as was previously observed.

Further insight can be extracted by examining the time dependence of the signals under the different conditions. Sample temporal trajectories for the photogeneration of silver nanoparticles under an argon and oxygen atmosphere are shown in the left of Figure 7.2. Again, the first obvious difference is the asymptotic limit for oxygen is less than that under argon conditions which perfectly reproduces the result from the image. Another interesting result is that the kinetics occur on a similar time scale since the 63% point of the transformation appears to be about 5 seconds under both conditions. In order to assess any irreversible effects caused by the introduction of oxygen to the sample, the kinetics of multiple “writes” have been monitored for several switches between argon and oxygen. The time trajectories are then fit via a non-linear least squares to the Avrami model in order to extract values for  $A_{\infty}$ ,  $k$ , and  $n$ , with results of this more detailed analysis shown in Figure 7.3. Oxygen appears to only influence the SERS

brightness of the features in a reversible manner (Figure 7.3A), while the kinetics for the nanoparticle formation appear unchanged upon exposure to oxygen (Figure 7.3 B and C). Experiments by Verneker and Maycock on the photolysis of silver perchlorate by a low-pressure mercury lamp showed that oxygen exposure before the photolysis had no effect on the rate of decomposition measured by gas evolution,<sup>34</sup> which further supports the notion that oxygen does not poison or affect the sample permanently. The similarity of the rate constant under oxygen to that observed in argon purge conditions suggests that oxygen does not participate in the reduction of silver ions into silver metal. This is not a surprising result, as molecular oxygen is unable to act as a reductant or electron source.

The decrease in the asymptotic signal when the sample is exposed to oxygen can be due to several causes. It is possible, that in the presence of oxygen, the number of hot spots decreases, the enhancement by the hot spots is diminished, or the SERS reporter molecule is different. AFMs of the samples show no drastic difference between oxygen and argon grown features, in terms of either the sizes of the constituent nanoparticles or total number of nanoparticles. Most likely, oxygen is altering the photodegradation chemistry of the polymer and changing either the concentrations or the identities of what is most likely the carbonaceous-type impurities that we observe via SERS.<sup>35</sup> Experiments with only 20% oxygen in argon also show the same factor of four decrease in asymptotic signal as observed in 100% oxygen, again with no change in the Avrami kinetics. These results suggest that the unusually bright features created in air are not due to the presence of oxygen nor does oxygen appear to affect the kinetics of silver ion photoreduction.

The more dominant influence on the kinetics and brightness arises from water vapor. In order to determine the specific influence, if any, that water vapor has on the kinetics,

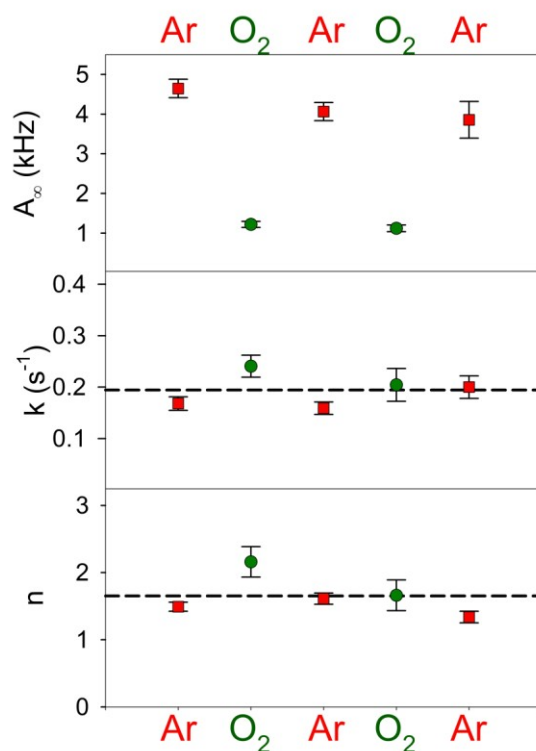


Figure 7.3: Oxygen effects in silver nanoparticle photogeneration. Extracted Avrami fit parameters showing the reproducible and reversible effects of oxygen exposure.  $A_{\infty}$ (top) shows a factor of 4 decrease upon exposure to oxygen, while  $k$  (middle) and  $n$  (lower) are relatively unaffected suggesting that the kinetics for the photogeneration are insensitive to oxygen. The dashed lines in the lower two panels represent the average value for the series of experiments.

experiments are performed while carefully controlling the partial pressure of water vapor over the sample using a temperature controlled pick-up cell. First, a sample is prepared in the same manner as under argon purge conditions (“dry”) and in a simple series of data is collected to establish a baseline – Figure 7.4A black line. The gas mixture is switched to contain 10 Torr of water vapor (“wet”) and the sample allowed to equilibrate for 15 min, then the formation kinetics are observed, Figure 4B blue line, which differs dramatically from the initial argon result. The brightness of the feature is  $\sim 7$  times more intense, and in addition dynamical fluctuations on the order of the average signal appear. Not only is the asymptotic limit affected, but the rate constant is nearly 8 times larger as well. Thus, water greatly influences both the brightness and

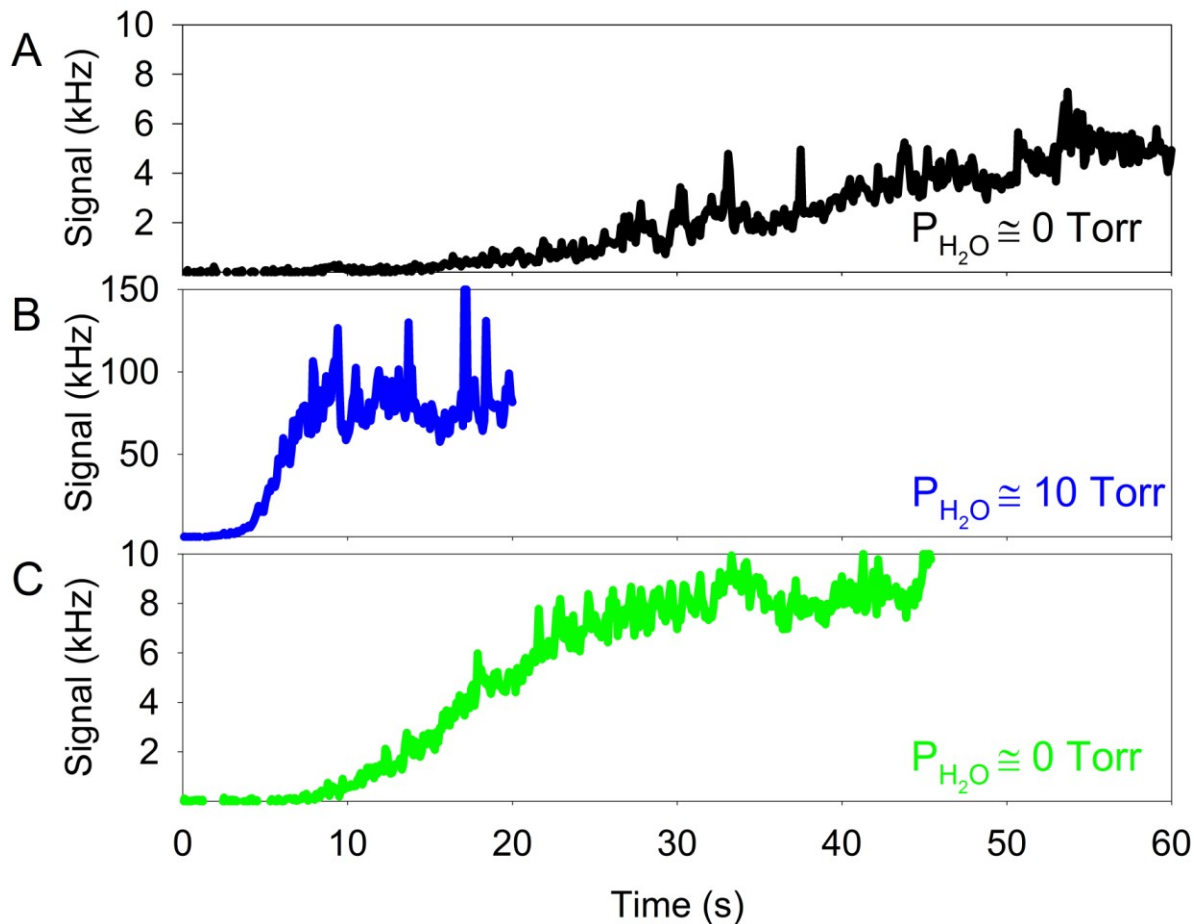


Figure 7.4: Sample trajectories before, during, and after exposure to water vapor. Sample traces contrasting the magnitude of and rate for nanoparticle generation under an argon atmosphere (black), in the presence of 10 Torr water vapor (blue) and back to argon atmosphere (green). The asymptotic signal levels increase by roughly an order of magnitude (note the vertical axis scale change) when exposed to water vapor.

the kinetics of SERS active nanoparticle growth, in contrast with oxygen which only affects the brightness.

Silver perchlorate is a well-known deliquescent material that requires careful storage to remain anhydrous<sup>36</sup>, thus a simple argon purge is probably not able to remove any water absorbed during the “wet” exposure. In order to test this prediction, the sample is exposed to “dry” conditions for 15 min and reexamined. The photogeneration kinetics (Figure 7.4C, green

line) appear different from either the initial “dry” or “wet” conditions. The rate constant seems to be intermediate to the two extremes, while the asymptotic brightness appears to be the same as is observed initially under an argon atmosphere. The difference in the rate constant suggests that the addition of water causes an irreversible change in the thin film; however, this change does not appear to effect the SERS brightness of the features.

In order to better understand the role that water vapor has in the formation kinetics and to better quantify the transient behavior that is observed, the kinetics are monitored at fixed time intervals starting from the initial introduction of the “wet” conditions. Figure 7.5 represents five “snapshots” of the kinetics at different exposure times. At 1 min into the purge (Figure 7.5A), the trace initially appears much like typical argon-like conditions with  $A_{\infty}$  around 5 kHz and  $k$  of  $0.02 \text{ s}^{-1}$ . However, after just 9 min (Figure 7.5B), the brightness of the feature has increased dramatically to 100 kHz and the reaction rate sped up to  $0.1 \text{ s}^{-1}$ . The brightness maintains its intensity while the reaction rate continues to increase out to 20 min (Figure 7.5C). Finally, at times greater than 30 min (Figure 7.5D and 7.5E) the brightness begins to decrease to an asymptotic level, though still higher than the initial “dry” value, while the rate begins to stabilize as well. These sample traces demonstrate the transient effect of water vapor that eventually settles to a constant level which is different than that obtained under argon purge conditions.

The effect of water on the photogeneration is also studied by observing the kinetics as a function of water vapor partial pressure. In order to prevent the transient type results observed previously when purging with water vapor, samples are equilibrated with 10 Torr of water vapor for approximately 60 min which is enough time for the kinetics to reach a steady state. Next features are generated while alternating between various partial pressures of water vapor and “dry” argon to confirm that there is no cumulative effect upon exposure to water vapor. Sample



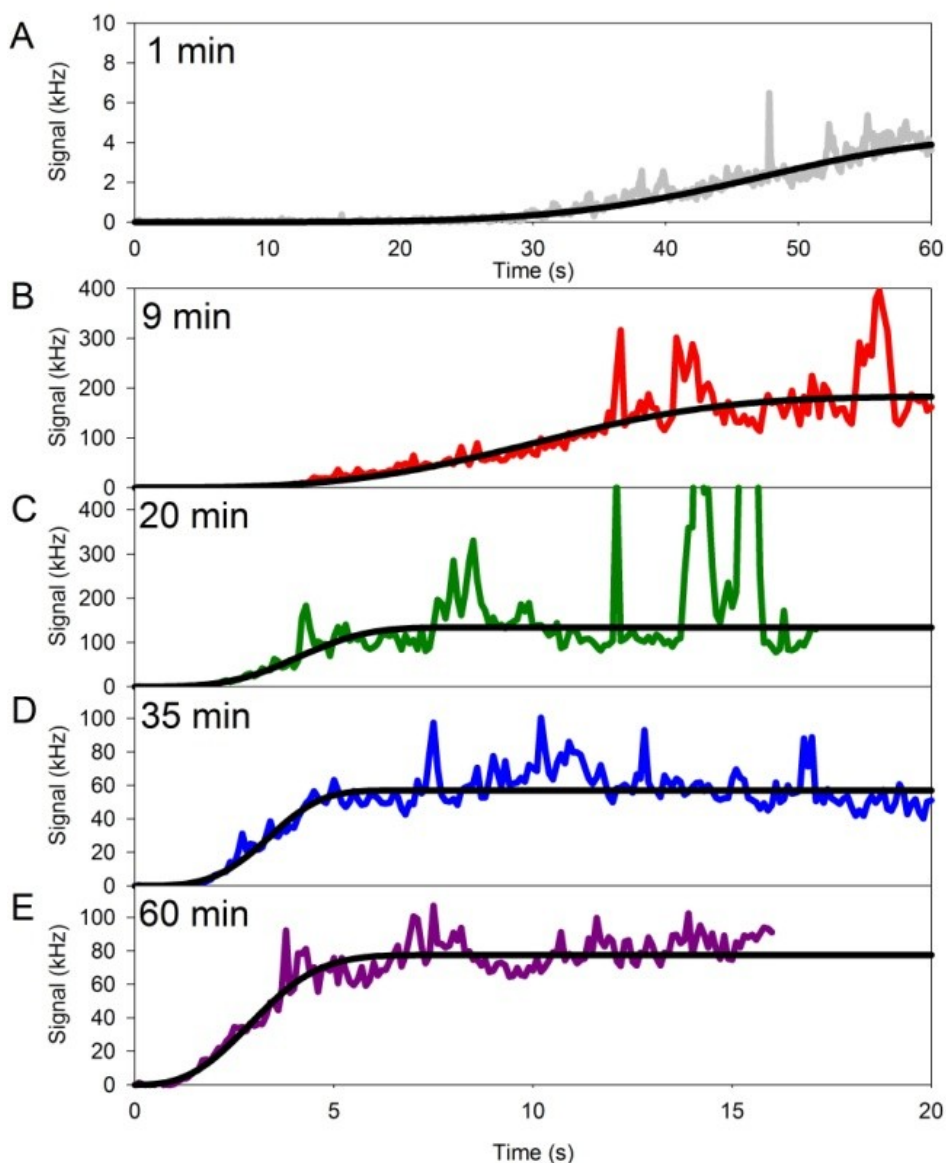


Figure 7.5: Trajectories obtained during exposure to water vapor. Trajectories at various times during exposure to 10 Torr of water vapor. (A) Initially the generation proceeds as under argon purge. (B) After 9 min, the brightness has increased 40 times and the rate has increased as well. Subsequent snapshots (C-E) show an ever increasing rate, but a gradual decrease of the brightness to 5-10 times the initial value.

traces for four different partial pressures of water vapor are shown in Figure 7.6. Most interestingly, the  $A_{\infty}$  values are similar for each partial pressure of water vapor. This further supports our previous assertion that the transient changes in the  $A_{\infty}$  observed during the exposing experiments are not due to changes in the identity of the reporter molecule but due to the

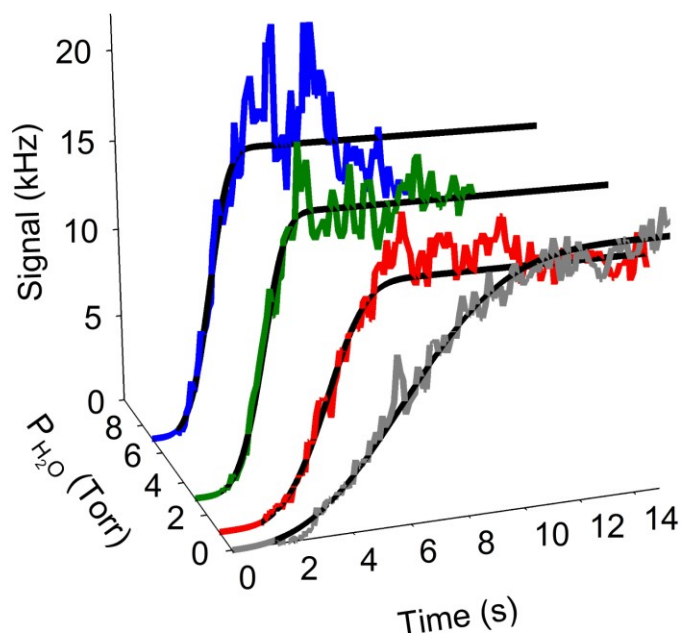


Figure 7.6: Sample traces showing water vapor pressure dependence. Sample traces showing water vapor dependent photogeneration after complete saturation of the film with water (10 Torr H<sub>2</sub>O, 60 min). Water increases the rate of the transformation by as much as a factor of 4.

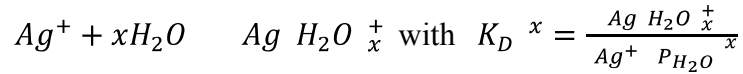
presence of water. A more surprising result is that the rate constant appears to be strongly affected by the presence of water vapor, even when the film is already fully hydrated. This suggests that even if the silver perchlorate is fully hydrated, there is an additional reversible addition of water that influences the kinetics.

The extracted Avrami fit parameters as a function of water vapor pressure is shown in Figure 7.7. Inspection of the rate constant data (Figure 7.7B) reveals a sigmoidal increase of the rate with increasing water vapor pressure over the sample. Furthermore, the experiments are performed in an alternating order to determine the reversibility of the additional water vapor. The rate constants lie on a smooth sigmoidal curve with no indication of reversible drift. This suggests that the rate constant is larger in the presence of additional water vapor. In addition, it appears that equilibrium between the silver ions and hydrated silver ions is reached during the 5

minute purge time. Guided by these results, we propose a simple model that incorporates these observations. In the model, there are two reaction rates for silver ions ( $\text{Ag}^+$ ) and hydrated silver ions ( $\text{Ag}[\text{H}_2\text{O}]_x^+$ ) to form silver nanoparticles (AgNP),  $k_0$  and  $k_1$  respectively:



Additionally, a rapid equilibrium is established between the two forms of silver ions based on:



This leads to a simple expression for the observed unimolecular rate constant ( $k_{\text{obs}}$ ) as a function of  $\text{H}_2\text{O}$  pressure above the sample:

$$k_{\text{obs}} = \frac{k_0 K_D^x + k_1 P_{\text{H}_2\text{O}}^x}{K_D^x + P_{\text{H}_2\text{O}}^x}$$

This model describes the data well and the resultant fit is shown as a dashed line in Figure 7.7B.

The rate constant in the presence of extra water is ~3 times that when there is no additional water. This is consistent with our previous assertion that the rate limited step is influenced by a number of water molecules around the silver ion. One of the parameters extracted is the number of water molecules involved ( $x = 3.5(9)$  obtained from multiple trials) which implies that the cage of water molecules is 4.5(9), due to the pre-existence of the monohydrate, that leads to the most efficient photoreduction of silver ions. Our result is in very good agreement with the number of water molecules observed ( $n \approx 4$ ) in the first hydration shell for silver ions measured spectroscopically<sup>37</sup> or with neutron diffraction.<sup>38</sup> The other value obtained is the equilibrium pressure of the absorbing waters,  $K_{\text{eq}} \approx 2.8(4)$  Torr, which corresponds to a relative humidity of ~15%.

These studies demonstrate that the photogeneration kinetics of silver nanoparticles are unaffected by the presence of oxygen, but proceed up to 4 times faster upon exposure to water

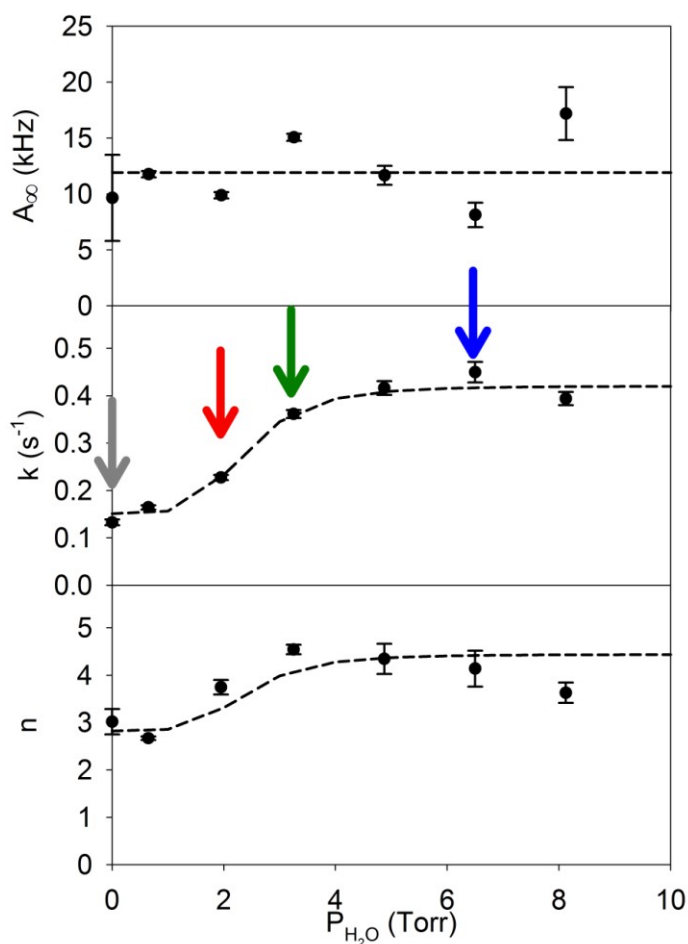


Figure 7.7: Avrami parameters as water vapor partial pressure above the sample is varied. Summary of the water vapor pressure dependence on the kinetics for silver nanoparticle photogeneration for water saturated films. Data points represent the average and standard deviation of the mean for 9 measurements at a given partial pressure. (Top) No change in  $A_{\infty}$  as a function of additional water vapor. However the rate constant (Middle) and Avrami coefficient (Bottom) can be described by a simple two state model (dashed line) where the photogeneration can occur from either  $Ag^+$  or  $Ag(H_2O)_x^+$  at different rates. Extracted values from the fit are  $K_{eq} \sim 2.8(8)$  Torr with  $x = 3.5(9)$  waters involved. Arrows represent trajectories shown in Figure 6.

vapor. The kinetics are irreversibly influenced by water vapor due to the hygroscopic nature of silver perchlorate. The SERS brightness from features in the presence of water is found to be comparable to the signals observed in room air, while the signals in the presence of oxygen are 5 times weaker. This suggests that water is the important species that results in the formation of

“bright” SERS sensors. We now extend our studies on SERS active silver nanoparticles to wide-field experiments. Dark field scattering spectra of the features provide information on the plasmon of the nanoparticles as well as the occurrence of closely spaced dimers in “bright” SERS constellations. In addition, wide field Raman super resolution experiments allow the study of the dynamic signal observed even after all the silver ions have been converted to silver nanoparticles.

#### **7.4 Wide-field Experiments**

Samples of photogenerated silver nanoparticles are prepared as described in the previous section using the confocal microscope. The apparatus is switched into wide field mode by removing the confocal pinhole and directing the light from the APDs to the imaging spectrometer. The light source is provided by either a white light dark field condenser for obtaining scattering spectra of the features, or an epi-luminescent wide field laser for detecting Raman signals.

The water exposed features have a SERS brightness that is nearly 100 times that of features grown under an argon purge, as discussed previously. This suggests that there is a qualitative difference in the particles grown between the two conditions. However, AFM experiments show that approximately the same size and quantity of nanoparticles are present in the constellations. In order to explore differences in optical properties between the features, dark field scattering spectra are obtained from both types of features.

A sample scattering spectrum of an argon grown feature, shown in Figure 7.8A, exhibits a primary peak around 470 nm that is broadened toward longer wavelengths. The spectrum is similar to the scattering spectrum from theoretical calculations<sup>39</sup> of a silver nanodisc (40 nm

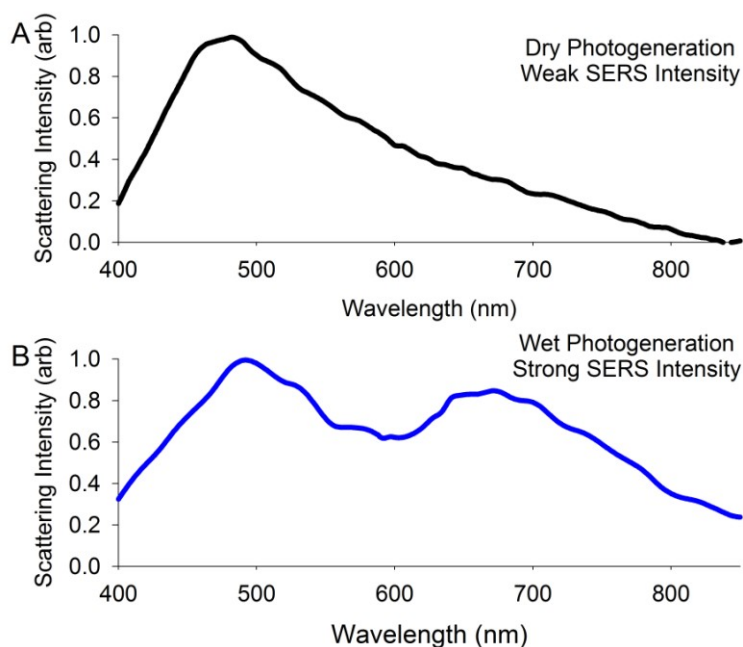


Figure 7.8: Dark field spectra of photogenerated nanoparticles. Dark field scattering spectra from features grown in (A) dry conditions, under argon purge, and (B) wet conditions, exposed to 10 Torr water vapor. Both show a peak around 475 nm corresponding to small silver nanodiscs with 40 nm diameter and 7 nm height. The feature grown with exposure to water vapor shows a secondary peak near 700 nm which likely corresponds to closely spaced dimers.

diameter ,7 nm height, *i.e.*, the average dimensions observed by AFM)<sup>32</sup> which has a peak at 480 nm. This is in contrast to the spectrum of features generated in the presence of water vapor, Figure 7.8B, which shows both the 470 nm peak and a second peak around 700 nm. This second peak could arise from nanodiscs with diameter 80 nm and height 7 nm, however objects that large are not observed in AFM images. An alternative explanation is that the peak near 700 nm is the result of closely spaced dimers within the constellation. Hao and Schatz, simulated the spectrum from dimers of nanoparticles separated by a small gap.<sup>14</sup> In their simulations, they observe the appearance of a second red shifted peak when considering dimers of various shapes. Furthermore, they predict an increase in the red shift of this second peak as the gap between dimers decreases. An increase in the local electric field, or “hot spot”, accompanies this spectral signature as well. This suggests that the “bright” SERS active features could be due to the

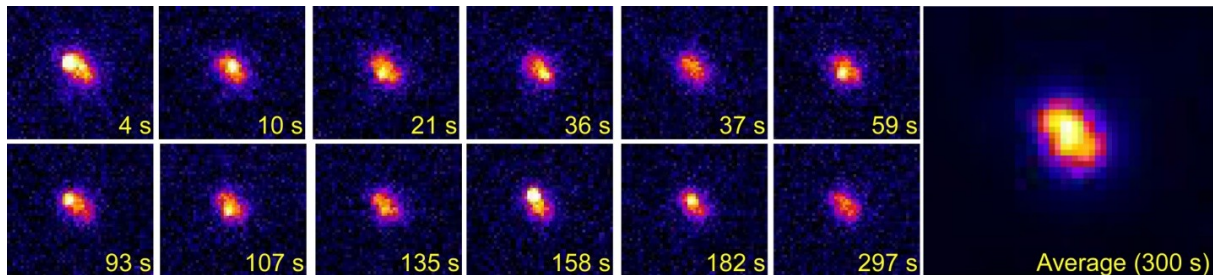


Figure 7.9: Series of frames from a wide-field Raman movie. Snapshots from a 300 s movie which show different regions become more intense for certain times. Some frames ( $t = 37$  s, 135 s, and 297 s) display a weak broad background, while others show intense signals from diffraction limited regions. The average of all 300 frames is shown on the right and appears as a single 800 nm FWHM feature.

formation of closely spaced dimers within the constellations. This would also suggest the presence of an inert argon atmosphere hinders the formation of these hot spots, while water vapor appears to promote the formation of closely spaced dimers.

The previous wide field scattering experiments indicate the presence of hot spots by the characteristic spectral signatures of dimers. In order to identify the number and location of the hot spots, experiments using wide field laser excitation with Raman detection are conducted. In particular, previous work by Stranahan and Willets has shown that the hot spot can be localized to better than the diffraction limit using a super-resolution approach.<sup>22</sup> Inspired by their experiments, we collect wide field Raman movies (integrating over all wavelengths), typically 300 frames with 1 second exposure. Figure 7.9 contains several frames of one such movie with an image of the average over all frames shown on right. The average of the frames reveals a single 800 nm broad feature, shown on the right of Figure 7.9, similar to that observed in confocal scanning images. Some frames, e.g.  $t = 37$  s, appear similar to the average image, while other snapshots show a different intensity distribution characterized by a single diffraction limited bright (greater than twice the average intensity) region on top of the broad feature. This suggests that the intense signal fluctuations arise from only small regions of the feature for short

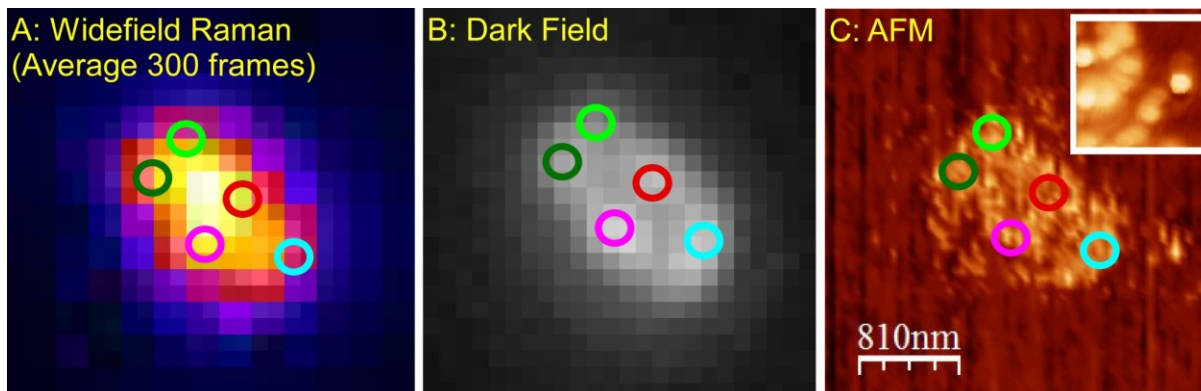


Figure 7.10: Comparison of wide-field Raman, dark field and AFM images. (A) The average wide-field Raman image with the hot spots identified from individual frames circled. (B) The dark field scattering and (C) AFM image from the same feature. Inset: 230 nm x 230 nm zoom of a similar feature showing the size of the individual nanoparticles (~40 nm diameter, 7 nm height).

amounts of time. More information can be obtained by careful analysis of the movies, as described below.

We are able to localize the individual hot spots to better than the diffraction limit because of the high signal to noise ratio. These locations can be compared directly with the dark field scattering image (Figure 7.10B) and the AFM (Figure 7.10C) for the same feature. The dark field scattering image shows a general correspondence between scattering intensity and average Raman intensity. There is also a moderate correlation between the location of the hot spots (circled in the image) and the regions of greatest dark field intensity; however, the signal to noise is too low to allow an exact comparison. Additionally, the dark field scattering image displays no time dependence upon illumination with either the white light or laser source. This supports the idea that the fluctuations observed in the wide field Raman are arising from diffusion of molecules through the hot spots. Lastly, the hot spot locations can be compared to the AFM of the same feature. Due to the low resolution (~20 nm) of the AFM image, the location of specific hot spots is not obtainable. However, the locations observed do correspond to regions of high local particle density where the likelihood of a closely spaced dimer occurring is highest. Future



studies with a high resolution AFM tip (radius < 2 nm) and closed loop stage will provide the necessary connection. An AFM image with a 5 nm tip, shown as an inset in Figure 7.10C, reveals that a typical feature is comprised of many small discs (~40 nm diameter, 7 nm height) as was previously reported.<sup>32</sup>

The time dependence of the signals can provide additional information about the nature of the observed fluctuations. Previous work,<sup>40</sup> has suggested that these fluctuations arise from molecules diffusing in and out of the hot spots. The intensity trajectory of the movie presented in Figure 9 is shown as the black trace at the top of Figure 7.11. The highly dynamic bursts are evident as short excursions from the baseline; however, the intensities of the bursts differ by factors as large as 3. This variation complicated attempts to use a correlation analysis to determine the number of emitters or relevant times scales previously. The identification of individual hot spots from a movie enables the isolation of trajectories for small regions of interest. The time traces from the 5 hot spots identified by color circles in Figure 10 are shown in the lower section of Figure 7.11. The separation of the total intensity into the individual traces reveals that each hot spot appears to have a characteristic burst intensity. The variation observed for the magnitude of the bursts is possibly due to small difference (factors of 2 or 3) in the enhancement factors. Furthermore, the duration of the bursts varies widely between the different regions. A few traces (Figure 7.11, light green and cyan) show bursts lasting only 1 to 2 seconds. This is contrasted in other traces (Figure 7.11, dark green and magenta) which exhibit bursts lasting more than 20 seconds. This broad distribution of time scales is consistent with a model for the bursts occurring due to molecule diffusion on a surface. This suggests that the fluctuations previously observed in trajectories are a result of single reporter molecules diffusing in and out of a few hot spots. Investigations of several different photogenerated features reveal

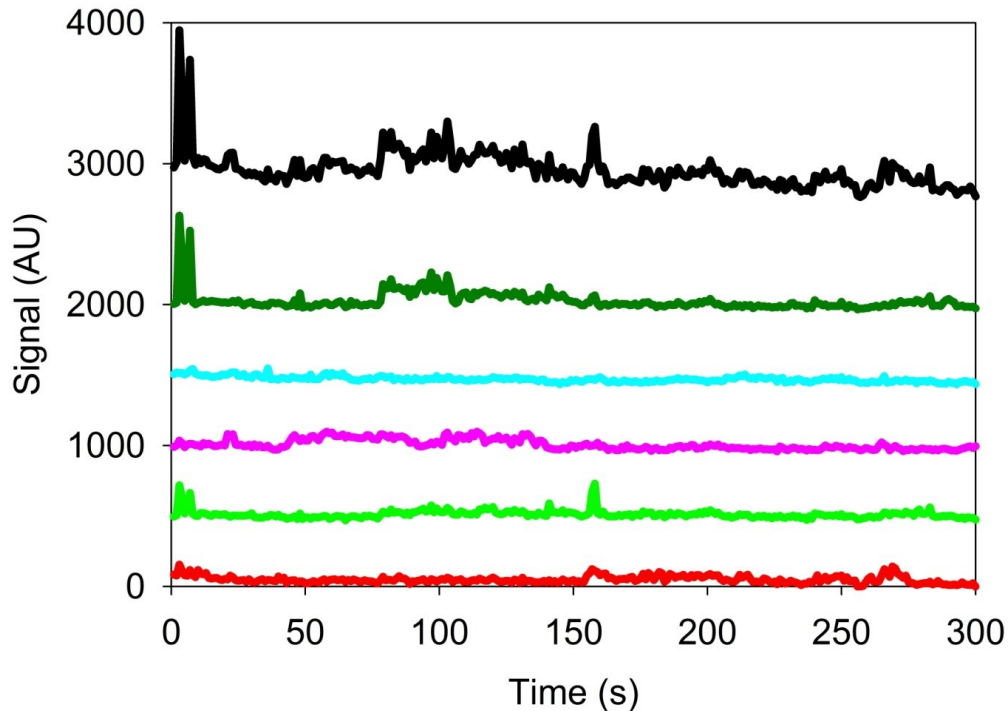


Figure 7.11: Time trajectories from the movie. The top trace (black) is the total intensity from the image which displays fluctuations of varying magnitude. Lower traces correspond to only intensity located in regions of interest near the hot spots identified in Figure 7.10. Each region shows a characteristic intensity for the bursts which suggests small variations in the hot spot enhancement.

the same behavior – a broad featureless average image with individual frames revealing diffraction limited bursts occurring from only a few specific regions. Typically, only 3 to 7 hot spots appear within a single feature. This indicates that our photogeneration technique is able to reliably generate a small number of bright SERS active sites within the diffraction limited spot.

## 7.5 Summary

The photogeneration of silver nanoparticles from silver salts imbedded in a polymer films is shown to be influenced by the environment as well as treatment of the sample. Specifically, oxygen has no effect on the kinetics of the photogeneration of silver nanoparticles, but does alter the brightness of the features by potentially changing the reporter molecule. On the other hand,

water vapor strongly influences both the kinetics and the SERS activity of the photogenerated particles. As the silver perchlorate is hydrated, the rate of the photogeneration increases by more than an order of magnitude. During this process, the SERS activity of nanoparticles generated at a low degree of hydration appears to increase to more than 60 times that of the argon purge conditions. Once the silver perchlorate is fully hydrated, the SERS activity is independent of the water vapor pressure above the sample. However, the rate of the photogeneration increases as additional water is reversibly absorbed by the film. The analysis suggests that the formation of the first hydration shell consisting of 4 waters increases the photogeneration rate constant by a factor of 3.

Analysis of dark field scattering spectra from features grown under different conditions reveals a correlation between SERS brightness and specific spectral features. The “bright” SERS features generated in the presence of water show the signature of a strong secondary peak most likely associated with closely spaced ( $< 3$  nm) dimers. Super resolution studies demonstrate that the dynamic fluctuations observed in time trajectories arise from multiple distinct locations within the diffraction limited spot. These regions are analyzed independently and found to be consistent with molecule diffusion through a single hot spot. Each photogenerated feature is found to have 3 to 7 hot spots demonstrating that the *in situ* photoreduction of a silver salt can reliably generate intensely SERS active nanoparticles.

## References

- (1) Kerker, M. *J. Colloid Interface Sci.* **1985**, *105*, 297.
- (2) Faraday, M. *Philos. T. Roy. Soc.* **1857**, *147*, 145.
- (3) Mie, G. *Ann. Phys.* **1908**, *330*, 377.

- (4) Bohren, C. F.; Huffman, D. R. *Absorption and Scattering of Light by Small Particles*; Wiley-VCH Verlag GmbH, 2007.
- (5) Lee, K. S.; El-Sayed, M. A. *J. Phys. Chem. B* **2006**, *110*, 19220.
- (6) Link, S.; Wang, Z. L.; El-Sayed, M. A. *J. Phys. Chem. B* **1999**, *103*, 3529.
- (7) Oldenburg, S. J.; Averitt, R. D.; Westcott, S. L.; Halas, N. J. *Chem. Phys. Lett.* **1998**, *288*, 243.
- (8) Gobin, A. M.; Lee, M. H.; Halas, N. J.; James, W. D.; Drezek, R. A.; West, J. L. *Nano Lett.* **2007**, *7*, 1929.
- (9) Loo, C.; Lowery, A.; Halas, N.; West, J.; Drezek, R. *Nano Lett.* **2005**, *5*, 709.
- (10) Brolo, A. G.; Gordon, R.; Leathem, B.; Kavanagh, K. L. *Langmuir* **2004**, *20*, 4813.
- (11) Haes, A. J.; Zou, S. L.; Schatz, G. C.; Van Duyne, R. P. *J. Phys. Chem. B* **2004**, *108*, 6961.
- (12) Haynes, C. L.; Van Duyne, R. P. *J. Phys. Chem. B* **2001**, *105*, 5599.
- (13) Srituravanich, W.; Fang, N.; Sun, C.; Luo, Q.; Zhang, X. *Nano Lett.* **2004**, *4*, 1085.
- (14) Hao, E.; Schatz, G. C. *J. Chem. Phys.* **2004**, *120*, 357.
- (15) Emory, S. R.; Nie, S. *J. Phys. Chem. B* **1998**, *102*, 493.
- (16) Kelly, K. L.; Coronado, E.; Zhao, L. L.; Schatz, G. C. *J. Phys. Chem. B* **2003**, *107*, 668.
- (17) Atay, T.; Song, J. H.; Nurmikko, A. V. *Nano Lett.* **2004**, *4*, 1627.
- (18) Fromm, D. P.; Sundaramurthy, A.; Schuck, P. J.; Kino, G.; Moerner, W. E. *Nano Lett.* **2004**, *4*, 957.
- (19) Talley, C. E.; Jackson, J. B.; Oubre, C.; Grady, N. K.; Hollars, C. W.; Lane, S. M.; Huser, T. R.; Nordlander, P.; Halas, N. J. *Nano Lett.* **2005**, *5*, 1569.
- (20) Camden, J. P.; Dieringer, J. A.; Wang, Y. M.; Masiello, D. J.; Marks, L. D.; Schatz, G. C.; Van Duyne, R. P. *J. Am. Chem. Soc.* **2008**, *130*, 12616.
- (21) Michaels, A. M.; Nirmal, M.; Brus, L. E. *J. Am. Chem. Soc.* **1999**, *121*, 9932.
- (22) Stranahan, S. M.; Willets, K. A. *Nano Lett.* **2010**, *10*, 3777.

- (23) Jin, R. C.; Cao, Y. W.; Mirkin, C. A.; Kelly, K. L.; Schatz, G. C.; Zheng, J. G. *Science* **2001**, *294*, 1901.
- (24) McMahon, J. M.; Henry, A. I.; Wustholz, K. L.; Natan, M. J.; Freeman, R. G.; Van Duyne, R. P.; Schatz, G. C. *Anal. Bioanal. Chem.* **2009**, *394*, 1819.
- (25) Turkevich, J.; Stevenson, P. C.; Hillier, J. *Discuss. Faraday Soc.* **1951**, 55.
- (26) Vlckova, B.; Matejka, P.; Simonova, J.; Cermakova, K.; Pancoska, P.; Baumruk, V. *J. Phys. Chem.* **1993**, *97*, 9719.
- (27) Evanoff, D. D.; Chumanov, G. *J. Phys. Chem. B* **2004**, *108*, 13957.
- (28) Jacob, J. A.; Kapoor, S.; Biswas, N.; Mukherjee, T. *Colloid Surf. A-Physicochem. Eng. Asp.* **2007**, *301*, 329.
- (29) Anderson, D. J.; Moskovits, M. *J. Phys. Chem. B* **2006**, *110*, 13722.
- (30) Mock, J. J.; Barbic, M.; Smith, D. R.; Schultz, D. A.; Schultz, S. *J. Chem. Phys.* **2002**, *116*, 6755.
- (31) Monti, O. L. A.; Fourkas, J. T.; Nesbitt, D. J. *J. Phys. Chem. B* **2004**, *108*, 1604.
- (32) Baker, T. A.; Monti, O. L. A.; Nesbitt, D. J. *J. Phys. Chem. C* **2011**, *115*, 9861.
- (33) Blackie, E. J.; Ru, E. C. L.; Etchegoin, P. G. *J. Am. Chem. Soc.* **2009**, *131*, 14466.
- (34) Verneker, V. R.; Maycock, J. N. *J. Phys. Chem.* **1968**, *72*, 2798.
- (35) Chang, H.; Feng, Z. R.; Wei, X. L. *Neurocomputing* **2008**, *72*, 278.
- (36) Hill, A. E. *J. Am. Chem. Soc.* **1921**, *43*, 254.
- (37) Texter, J.; Hastreiter, J. J.; Hall, J. L. *J. Phys. Chem.* **1983**, *87*, 4690.
- (38) Sandstrom, M.; Neilson, G. W.; Johansson, G.; Yamaguchi, T. *J. Phys. C* **1985**, *18*, L1115.
- (39) Myroshnychenko, V.; Rodriguez-Fernandez, J.; Pastoriza-Santos, I.; Funston, A. M.; Novo, C.; Mulvaney, P.; Liz-Marzan, L. M.; Garcia de Abajo, F. J. *Chem. Soc. Rev.* **2008**, *37*, 1792.
- (40) Emory, S. R.; Jensen, R. A.; Wenda, T.; Han, M.; Nie, S. *Faraday Discuss.* **2006**, *132*, 249.

## Chapter 8

### Imaging Nanostructures with Scanning Photoionization Microscopy<sup>\*</sup>

#### 8.1 Introduction

Recent advances in optical microscopy have shown convincingly the value of investigating physical and chemical processes at a local or perhaps single particle level [for an overview see Ref. (1)], primarily relying on strongly fluorescent<sup>2</sup> or Raman active<sup>3,4</sup> objects as reporter of the local environment. Experimental advances are required to broaden the scope of observable systems to structures that may lack the high fluorescence quantum yields or Raman cross-sections necessary for efficient detection from the small area of a diffraction-limited spot.

Photoelectron emission, used successfully in photoelectron spectroscopy (PES) to elucidate electronic structure of atoms, molecules and surfaces in the form of ultraviolet and X-ray photoelectron spectroscopies (UPS and XPS),<sup>5,6</sup> fulfills the prerequisite of high sensitivity necessary for any optical microscopy. Starting in the early 1990s, a number of groups investigated the possibility of scanning a light beam over a sample to initiate photoionization from a confined area.<sup>7-11</sup> Initial efforts, based on UV-lamp excitation, were restricted to mapping differences in workfunction only and achieved a spatial resolution in the few- $\mu\text{m}$  range.<sup>12</sup> More recently, Munakata *et al.* presented an improved set-up based on VUV laser excitation and time-of-flight photoelectron analysis,<sup>13-15</sup> achieving an energy resolution of approximately 40 meV and an estimated spatial resolution of about 300 nm.<sup>14</sup>

---

<sup>\*</sup> Adapted from: Monti, Oliver L.A.; Baker, Thomas A.; Nesbitt, David J. *Journal of Chemical Physics* **2006**, *125*, 154709

These intense and ongoing efforts illustrate the importance of developing chemically sensitive photoelectron spectroscopy with high spatial and temporal resolution. The combination of high detection sensitivity, structural information and strong surface specificity make such an approach particularly desirable for investigating heterogeneous nanostructured materials in complex environments, such as on electrodes or sensors. As a complementary approach to existing work, it would be especially valuable to combine the advantages of spatially resolved photoelectron spectroscopy with the opportunities offered by optical fluorescence or Raman detection. Of particular interest in this context is understanding the effects of plasmonic field enhancement for molecular surface-enhanced Raman scattering (SERS) on noble metal nanostructures and nanoparticles.<sup>16</sup>

Based on new developments extending PES to two-photon photoemission (TPPE) methods,<sup>17-19</sup> we present here initial efforts to address this challenge by combining the spatial resolution of optical microscopy with the sensitivity of multiphoton photoemission. As a first step, we demonstrate the feasibility of imaging local two-photon emissivity from thin metallic films on a submicron level. The presented scanning photoionization microscopy (SPIM) technique offers the potential to yield detailed chemically selective *local* spectroscopic and spatial information on nanostructured materials, and in principle, even down to the single molecule level.

The chapter is structured as follows: A detailed description of the apparatus is given in the experimental section (8.2). We then present first results on imaging and spectroscopy from thin metal structures in section 8.3. This is followed in section 8.4 by a detailed discussion of the contrast mechanism in SPIM, yielding insight into electronic properties in different metal films. A summary of the current limitations and opportunities for SPIM are presented in section 8.5.

## 8.2 Experiment

Figure 8.1 shows a schematic of the experimental apparatus used for scanning photoionization microscopy. A train of ultrashort laser pulses from a frequency-doubled mode-locked Ti:Sapphire laser is focused *in vacuo* to a nearly diffraction-limited spot, with the sample scanned over the stationary laser beam. Fluorescence or Raman photons are collected in an epifluorescence detection geometry by a single-photon counting detector; alternatively, the photoemission current is measured on a sensitive picoammeter.

The experiments are performed using a frequency-doubled diode-pumped solid state Nd:Vanadate laser at 532 nm as a pump source for an ultrafast laser. The Kerr-lens passively mode-locked Ti:Sapphire oscillator produces a pulse-train at 85.1 MHz. After dispersion compensation by an external LaFN28 prism pair, the pulses at 830 nm are 33 fs short as determined by second harmonic frequency-resolved optical gating (SHG FROG). The output from this laser is frequency-doubled in a beta-barium borate (BBO) crystal (0.5 mm thickness), with the second harmonic separated and dispersion-compensated in a fused silica prism pair to an estimated pulse width of 100 fs. The near-UV beam at 415 nm is expanded to overfill the back aperture of the microscope objective. After passing a set of reflective neutral density filters for pulse energy control, it enters the vacuum chamber through a quartz port, where it is focused to a nearly diffraction-limited spot by a Schwarzschild-type reflective microscope objective (52X, 0.65 NA), aberration compensated for the cover-glass thickness of 170  $\mu\text{m}$ . Typical operation is with 415 nm pulse energies of 0.18 nJ at the focus of the microscope objective.

For fluorescence measurements, the photons are collected by the same objective and spectrally separated by a short-pass dichroic mirror ( $> 0\%$  reflectivity at emission wavelengths



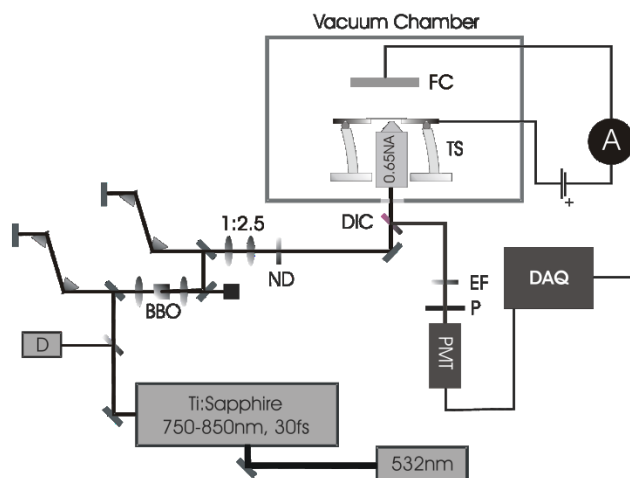


Figure 8.1: SPIM Experimental Setup. Schematic of experimental apparatus. D: Laser pulse diagnostics; BBO:  $\beta$ -barium borate frequency-doubling crystal; ND: Neutral density filters; DIC: Dichroic long-pass filter; EF: Emission filter; P: Confocal pinhole; TS: Piezoelectrical translation stage; FC: Faraday cup; DAQ: Data acquisition hardware and software; A: Picoammeter.

of  $\lambda_{\text{em}} > 450 \text{ nm}$ ) outside the vacuum chamber. A combination of two interference filters (optical density  $OD > 5$ ) suppresses any residual photons at the excitation wavelength. The remaining red-shifted photons are focused onto a  $100 \mu\text{m}$  confocal pinhole and detected by a single-photon counting photomultiplier module with a quantum yield of approximately 16% near 400 nm and a dark count rate of 10 cps. The fluorescence rate is measured using a multifunction board equipped with two 20 MHz counters and stored as a function of sample position to generate a confocal microscopy image.

In the photoionization imaging mode, emission is induced by multiphoton absorption. The high repetition rate of the ultrafast light source offers the advantage of high peak intensity with low average power on the sample, thus reducing the risk of sample damage. The photoelectrons are collected by a simple Faraday cup placed approximately 5 mm above the sample. For all experiments described herein, we choose to keep the sample grounded and apply a voltage to the Faraday cup, with the photocurrent measured by a picoammeter acting as a

transimpedance amplifier. The resulting analog signal (0–2 V) is digitized [12 bit analog to digital converter (ADC)] by a multifunction board and displayed as a function of sample position. To acquire electron kinetic energy distributions, the Faraday cup bias is slowly varied from -5 to +10 V, while the sample is raster scanned over several  $\mu\text{m}$  to avoid excessive laser exposure of a single spot.

The microscope head is kept under vacuum (typically  $8 \times 10^{-8}$  Torr) in a custom-made stainless steel vacuum chamber. To displace the sample with respect to the stationary laser beam, the sample rests on two independent scanning stages: (1) A three dimensional vacuum-modified stainless steel translation stage with remote-controlled actuators and a travel range of 12 mm for coarse translation and focusing, and (2) a homebuilt piezoelectrically actuated tripod stage for image acquisition. The design of the fine translation stage is based on the deflection of a quarter-segmented piezoelectric tube<sup>20,21</sup> (length  $l = .5''$ , diameter  $D = /4''$ , wall thickness  $d = .02''$ , material PZT-5H). Applying equal voltages  $U$  with opposite sign on opposing electrodes causes the tube to bend by

$$\Delta = \frac{2\sqrt{2}d_{31}Ul^2}{\pi Dd}, \quad (8.1)$$

where  $d_{31}$  is the relevant piezoelectric tensor component. The complete stage consists of three such tubes arranged in an isosceles triangle. As a result, the sample can be scanned in a plane over a range of approximately  $60 \mu\text{m}$  in both horizontal dimensions, with scanner calibration achieved via independent interferometric studies. In SPIM mode, typical scan sizes are  $15 \times 15 \mu\text{m}$  with a resolution of  $128 \times 128$  pixels and an integration time of 100 ms/pixel.

Samples are fabricated by photolithography using negative photoresist on glass cover slips as substrates. Prior to photolithography, glass cover slips are cleaned meticulously in boiling piranha solution for 30 min, rinsed with isopropanol, and finally dried on a hot plate.

After exposure and developing, thin metallic films are deposited either by thermal or electron gun evaporation at a pressure of approximately  $10^{-5}$  mbar. In the case of evaporating Au, the glass cover slips are coated with a 2.4 nm thin Pt film to produce uniform polycrystalline Au films, thus preventing Au island formation on the glass surface. It is assumed that the two materials form completely separate layers, although some partial interfacial alloying cannot be excluded. Following lift-off, the patterned films are soaked for 24 h and rinsed with spectroscopic grade acetone to wash off any remaining traces of photoresist. Pattern fidelity and film thicknesses are verified with a commercial atomic force microscope (AFM) stationed in a clean room environment and operated in the tapping mode configuration.

## 8.3 Results

### 8.3a *Confocal Microscopy*

We first establish the imaging capabilities of the microscope in the one-photon-excitation confocal microscopy mode. For this purpose, a 600 pM aqueous solution of microsphere beads (100 nm diameter) stained with a UV-absorbing dye (absorption maximum at 350 nm) are spin-cast onto a cover glass slip. Figure 8.2 shows a  $10 \times 10 \mu\text{m}$  section of the cover slip with several strongly fluorescent polystyrene beads, demonstrating the near-diffraction-limited performance of the imaging system. In contrast with conventional refractive imaging systems, the primary feature in the Airy-like point-spread function for the reflective objective is less intense (51% vs. 84% for a refractive optic).<sup>22</sup> Inherent to the Schwarzschild objective design, the front mirror obscures parts of the light path causing a slightly larger focal spot and a more pronounced secondary ring in the Airy-like feature. From this and similar images, the focal spot sizes

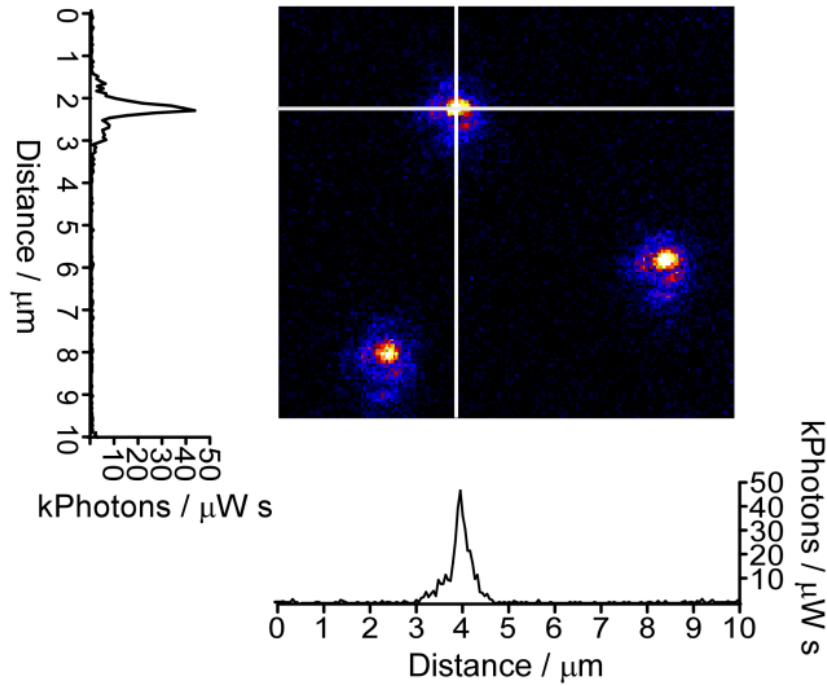


Figure 8.2: Example fluorescence image. One-photon-excited confocal fluorescence microscopy image of dye-impregnated 100 nm polystyrene beads using 0.6  $\mu\text{W}$  excitation power, excitation wavelength of 385 nm and fluorescence maximum at 440 nm. Intensity profiles are shown for the marked bead.

$\Gamma_x = 21(73)$  nm and  $\Gamma_y = 17(51)$  nm are determined, where  $\Gamma_x$  and  $\Gamma_y$  are the full-width-half-maximum (FWHM) of a Gaussian fit to the fluorescence intensity distribution along the scan axes  $x$  and  $y$ . The optical resolution is further increased in the case of two-photon excitation such as is used for SPIM, since the photoionization probability depends on the square of the illumination intensity. This results in estimated spot diameters of  $\Gamma_x^{SPIM} \approx 140$  nm and  $\Gamma_y^{SPIM} \approx 70$  nm and a negligible contribution from the secondary Airy feature to the point-spread function in SPIM.

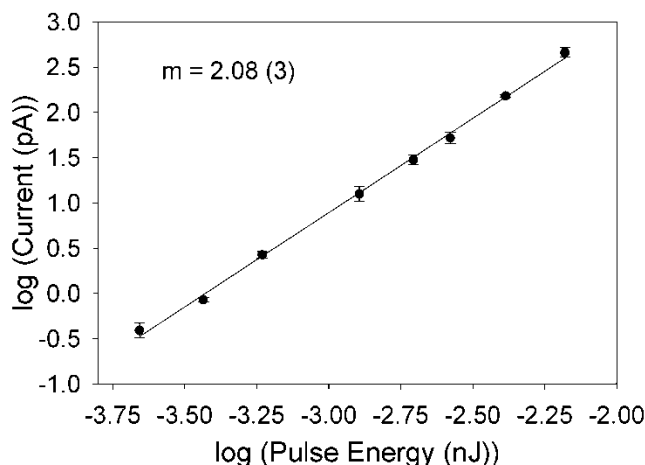


Figure 8.3: Power dependence of photoemission current. Log –log plot of photoemission current versus pulse energy for a thermally evaporated 17 nm thick Ag film on glass cover slip. Excitation wavelength  $\lambda_{ex} = 415$  nm.

### 8.3b Scanning Photoionization Microscopy

As a next step towards scanning photoionization microscopy, photoionization from a 17 nm thin Ag film is investigated. The film is deposited on a glass cover slip using thermal evaporation with the thickness monitored by a quartz-crystal microbalance and confirmed by atomic force microscopy. Figure 8.3 shows the dependence of the photoemission current on incident intensity. To avoid sample damage at the highest intensities, the sample is exposed for less than 1 s to the focused laser source, and a new sample position is chosen for the next data point. The photoemission current scales quadratically with the illumination intensity [slope  $m = 2.08(3)$ ]. The work function of polycrystalline Ag is 4.26 eV,<sup>23</sup> well above the energy of a 415 nm photon (3.0 eV). Photoionization can therefore only occur with a minimum absorption of two photons, in agreement with the measured approximate quadratic power dependence. Further confirmation in our apparatus is also derived from the current vs. power curve for polycrystalline

Pt thin film samples, with results [slope  $m = .94(6)$ ] consistent with a reported work function of 5.65 eV.<sup>23</sup>

The spatial imaging capabilities of SPIM are best demonstrated by imaging a patterned surface. Using photolithography, a regular pattern sandwiched between two 10 mm square contact pads, separated by 100  $\mu\text{m}$  and held at a constant potential is generated (Figure 8.4a). The pattern extends only along part of the length of the pads. It is deposited on a cover glass slip and consists of  $3 \times 3 \mu\text{m}$  holes in a 61.5 nm thin thermally evaporated Ag film. Bordering the contact pads on either side, one row of holes with dimensions  $6 \times 3 \mu\text{m}$  is used. Figure 8.4b shows an atomic force microscope (AFM) image of the highlighted area. Comparison of this image with SPIM of approximately the same region (Figure 8.4c) shows excellent agreement with the much higher resolution AFM measurement. The contours of the holes and the pattern edge are clearly resolved in correspondence with the overview photograph of part a of the figure. Most interestingly, the strongest photoemission currents are measured at the glass/silver discontinuities. All edges in the AFM image are represented with high accuracy even for defect details below 1  $\mu\text{m}$  size.

By way of comparison, Figure 8.4d shows a comparison of SPIM and AFM traces for a horizontal lineout marked at the arrow position in Figure 8.4c. The photoemission current does not reflect features measured by AFM smaller than approximately 400 nm, *i.e.* the diffraction-limited optical resolution in the present set-up. As noted above, the largest currents are only measured in a few locations in the SPIM image. From the AFM trace, it is seen that these correspond to steps from glass to silver and silver to glass, with the silver film being relatively smooth (RMS roughness 1.8 nm) and the photoionization current dropping down to 1.77(14) pA away from the steps, slightly above the picoammeter background level of 1.37(7) pA when

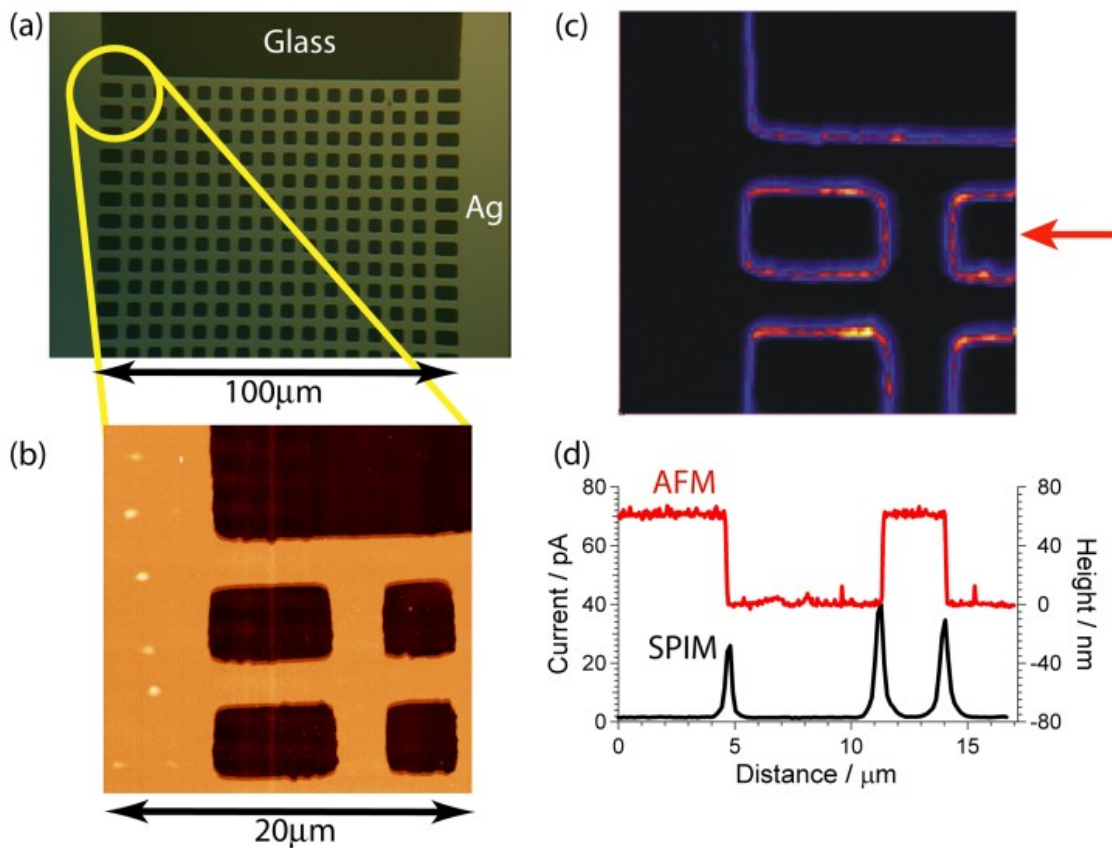


Figure 8.4: Comparisons between AFM and SPIM images. (Panel a) Photographic microscope image of photolithographic 61.5 nm thin Ag pattern thermally evaporated onto a cover slip. The holes (dark in the image) are on average  $3 \times 3 \mu\text{m}$  large except for the two final rows left and right, which are  $6 \times 3 \mu\text{m}$  in size. The solid silver (light in the image) serves as contact material to keep the sample at a well-defined potential. (Panel b) Tapping-mode AFM image of area highlighted in panel a;  $20 \times 20 \mu\text{m}$ . (Panel c) SPIM image of corner area highlighted in panel a; 13 pJ pulse energy,  $\lambda_{ex} = 415 \text{ nm}$ , +10 V bias potential. (Panel d) Comparison of AFM (red) and SPIM (black) traces. The traces are taken at the arrow in Panel b and c respectively.

scanning. This observation will be discussed in more detail below. In summary, Figure 8.4 clearly demonstrates that both high contrast and high spatial resolution can be achieved in two-photon scanning photoionization microscopy. In combination with the confocal scanning optical microscopy discussed in the previous section, SPIM offers the capability of correlated photoelectron and fluorescence or Raman imaging.

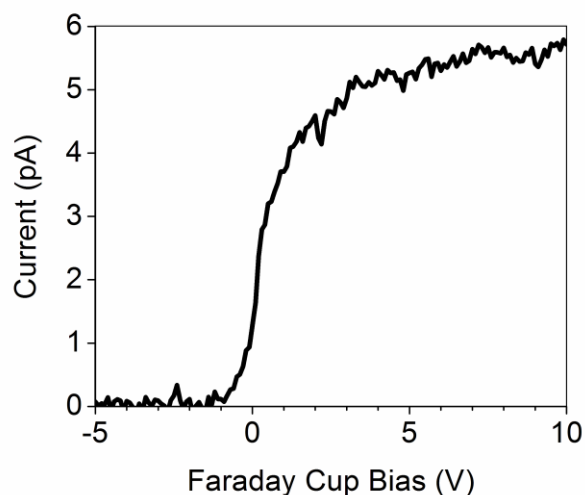


Figure 8.5: Retarding field measurement. Photoelectron yield as a function of Faraday cup bias voltage for a 2.4(8) nm electron gun evaporated Pt film. Fluence:  $0.8 \text{ mJ/cm}^2$ .

### 8.3c Photoelectron Spectroscopy.

Further information may be obtained by analyzing the photoelectron energy, *i.e.* extending these SPIM methods toward *spatially resolved* photoelectron spectroscopy. By way of a test demonstration, we implement a simple retarding field method<sup>24</sup> for energy analysis, where the potential on the Faraday cup is varied continuously while we monitor the photocurrent. Figure 8.5 shows the SPIM current as a function of the Faraday cup bias voltage for a 2.4(8) nm thick electron-gun-evaporated Pt film. Noticeable photocurrent, defined as twice the background-corrected noise floor of 0.3 pA, is detected at and above -0.4 V. Based on the room temperature work function of polycrystalline Pt (5.65 eV)<sup>23,25</sup> and a two-photon excitation energy of 6.0 eV, the photoelectrons are expected to have excess energies of 0.0 to 0.4 eV. This should therefore require a maximum retarding potential of -0.4 V to suppress the photoemission current, in good agreement with our measurements. Considerable improvements in both detection sensitivity and the spectroscopic energy resolution are achievable with a combination of a multichannel plate



detector and a magnetic bottle time-of-flight spectrometer. Such efforts are currently under way in our laboratory.

## 8.4 Discussion

We observe photoemission at several distinct intensity levels, as is apparent from Figure 8.4c : 1) Zero detectable photocurrent from the glass cover-slip, in agreement with glass being a wide band-gap insulator; 2) small but finite photocurrent from the solid parts in the polycrystalline thin metal film; and 3) strong photoemission at the metal film edges. This observation is confirmed for all metals investigated and raises the question of identifying a mechanism for such edge-enhancement. One possibility is enhancement of photoionization<sup>26,27</sup> near the sharp film discontinuity, which might be attributed to localized surface plasmons present in silver film roughnesses<sup>28</sup> or confined nanoparticles.<sup>29</sup> Excitation of a surface plasmon generates very strong, localized electric fields, believed to be responsible *e.g.*, for the ability to measure single molecule Raman spectra on colloidal Ag particles.<sup>30</sup> Other alternatives for significantly larger photocurrents near metal edges may lie in the enhancement of the electron escape probability from an edge or, given the short electron escape depths,<sup>6</sup> possibly from a section of film with reduced thickness. Indeed, close inspection of AFM and SPIM images indicate a correlation between film thickness and photoemission intensity: Figure 8.6a shows a  $15 \times 15 \mu\text{m}$  SPIM image of a 69 nm thick Au film deposited by thermal evaporation onto a glass cover slip, to be compared with the AFM close-up of the marked hole (Figure 8.6b). The topography image shows clearly the existence of a 5 nm thick and 250 nm wide “shelf” lining the metal-glass edge. This thin layer of Au is a result of the photolithographic process and its position corresponds to the location of strongest photoionization, as can be seen clearly in Figure

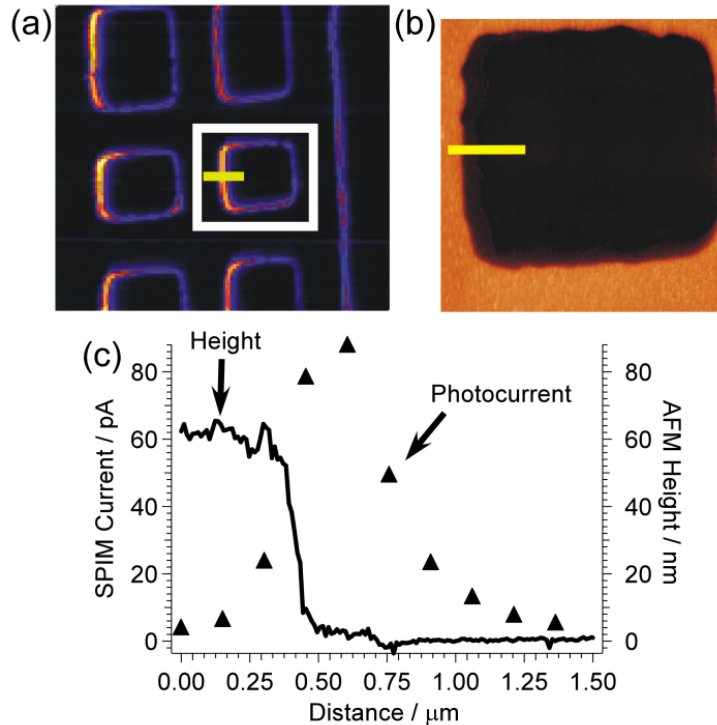


Figure 8.6: Spatial resolution of electron source. (Panel a)  $15 \times 15 \mu\text{m}$  SPIM image of a 69 nm thick Au film deposited by thermal evaporation onto a glass cover-slip with enhanced current at the film/glass edges. Center hole highlighted. (Panel b) AFM close-up of highlighted hole on a  $5 \times 5 \mu\text{m}$  scale. (Panel c)  $\blacktriangle$ : SPIM trace taken at  $1.5 \mu\text{m}$  scale bar in Panel a.  $\text{—}$ : Corresponding AFM trace from close-up in Panel b.

8.6c. Note also that peak currents of 90 pA are measured where the strip is widest, with much weaker photoionization occurring in places such as the top right corner in Figure 8.6b, where the additional photolithographic shelf is almost negligible.

This correlation is further confirmed by investigating SPIM currents from thin Au films as a function of thickness. Terraced Au films are deposited onto a glass cover slip by electron gun evaporation and a moving mask, with the film thickness verified by AFM for each position. Typically, an amorphous granular polycrystalline film structure is obtained by this preparation with an average grain diameter of approximately 25 nm, well below the spatial resolution presently obtained by SPIM. Figure 8.7 displays a semilogarithmic plot of photoionization current vs sample thickness, which is clearly

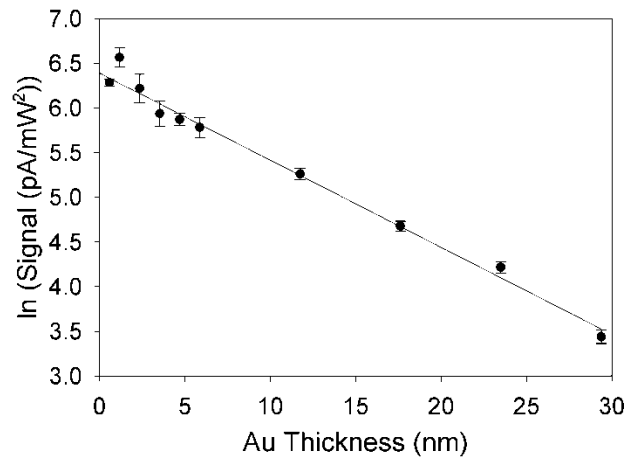


Figure 8.7: Two photon photoemission as a function of film thickness. Measured (circles) and model (solid line) two-photon photoemission yield as a function of film thickness for electron gun evaporated Au films on 2.4 nm Pt supported on a glass cover-slip.

dominated by exponential decay. The thickness-dependent photoelectron yield can be simply modeled by two-photon photoemission ( $\propto I^2$ ) moderated by optical attenuation in the Au film, where the effect of constant attenuation on the optical penetration depth due to the thin Pt support ( $\approx 2.4$  nm) may be neglected. The solid trace in Figure 8.7 represents a fit based on such a model to the experimentally observed photoelectron yield. From twice the slope in Figure 8.7, the measured optical penetration depth for these Au films is  $\alpha = 20.5(14)$  nm. This is larger than the bulk value in Au ( $\alpha = 16.9$  nm at 415 nm),<sup>31</sup> and in contrast to the stronger absorption and shorter penetration lengths expected in the presence of plasmonic interactions. However, such a 20% increase in optical penetration depth may arise simply from the nature of polycrystalline particulated Au film, whose optical and electronic properties are not well represented by a smooth film with average thickness. Indeed, several studies<sup>32,33</sup> have shown that the optical constants for thin metallic films of Au may differ by up to 50 % from the bulk values as reported by Palik<sup>31</sup> as a result of preparation method, effective porosity and density of defects. As a

sidelight, the present approach may therefore provide a useful alternative for obtaining effective optical constants for such polycrystalline films.

A look at the two-photon photoemission cross-section sheds further light onto the mechanism for observed enhanced photoionization near the edges. Analysis of the SPIM data in Figure 8.7 fits yield two-photon cross sections at 415 nm of  $\beta = .82(10) \cdot 10^{-5} \frac{\text{cm}^2 \text{s} \# \text{e}}{(\# \text{phot})^2}$ . This value is in good agreement with theoretical estimates by Smith<sup>34</sup> and Marinchuk,<sup>35,36</sup> as well as being of comparable magnitude to experimental values reported by Bloembergen and coworkers for 532 nm fs pulsed laser studies of several different transition metals.<sup>37</sup> These are appreciably smaller than values reported for 100 nm thick evaporated polycrystalline Au films excited by ns laser pulses at 347 nm,<sup>38,27</sup> though some increase in two-photon photoionization yield with energy above the ionization threshold is expected. However, experimental determination of two-photon cross-sections is known to be exceptionally sensitive to the excitation beam profile, pulse energy and duration and the nature of the surface itself, resulting in orders of magnitude differences between measured value.<sup>35</sup> The high quality beam profile used in the SPIM imaging, in combination with high vacuum conditions and fs time scale excitation (i.e. high rep rate, low pulse energy) reduces many of these concerns, yielding results that clearly support theoretical value by Smith and Marinchuk.

This suggests that the edge-enhancement seen in SPIM images is likely dominated by film thickness rather than direct plasmonic contributions, at least for the Au surface samples explored herein. If dominated by plasmonic excitation, it would be expected to yield large *enhancements* over bulk film results. For example, experiments by Moskovits and coworkers have shown that the two-photon photoemission process on rough Ag films can, in fact, be *enhanced* 1000-fold when compared to smooth Ag films.<sup>26,27</sup> This trend is also consistent with

the plasmon resonance for Au ( $\approx 500$  nm), *i.e.*, considerably red shifted from the 415 nm excitation wavelength. Additional studies with a variety of metals, excitation wavelengths, plasmonic resonances, and surface adlayers would clearly be of interest in further elucidating the two-photon electron ejection dynamics. Ongoing SPIM studies of nanostructured Ag materials near  $\approx 400$  nm are currently in progress, which permit probing of plasmonic coupling effects more nearly resonant with the laser excitation.

## 8.5 Summary

A new method is presented to enhance and complement existing microscopy techniques, which combines the advantages of diffraction-limited optical excitation with detection of both photons and low kinetic energy photoelectrons *in vacuo*. As a first test application, spatially resolved photoelectron emission and spectroscopy in thin nano- and meso-structured polycrystalline metal patterns has been demonstrated. Scanning photoionization microscopy allows simultaneous measurement of optical penetration depth and two-photon photoemission cross section from a diffraction-limited spot. In conjunction with atomic force microscopy scans, these measurements indicate that photoionization contrast in Au films at 415 nm is dominated by electron escape depths and thickness variations across the sample. Use of retarding fields allows the implementation of a simple form of spatially resolved photoemission spectroscopy, which can be greatly expanded by use of time of flight electron energy analysis. The capability of local simultaneous determination of electronic properties such as penetration depth and multiphoton cross-sections is likely to be of key importance for the principal target of SPIM, *i.e.* investigation of surface-enhanced Raman scattering (SERS) in conjunction with photoelectron emission, from nanolithographically grown structures as well as SERS active nanoparticles. Even more

interesting would be to tune over a series of excitation wavelengths and thereby map out plasmonic contributions to photoemission spectroscopy explicitly in the frequency domain. Experiments to investigate the extent of such plasmonic effects are discussed in the next chapters.

## References

- (1) Xie, X.; Trautman, J. *Ann. Rev. Phys. Chem.* **1998**, *49*, 441.
- (2) Moerner, W. E.; Fromm, D. P. *Rev. Sci. Instrum.* **2003**, *74*, 3597.
- (3) Kneipp, K.; Wang, Y.; Kneipp, H.; Perelman, L. T.; Itzkan, I.; Dasari, R.; Feld, M. S. *Phys. Rev. Lett.* **1997**, *78*, 1667.
- (4) Nie, S. M.; Emory, S. R. *Science* **1997**, *275*, 1102.
- (5) Eland, J. H. D. *Photoelectron Spectroscopy : An Introduction to Ultraviolet Photoelectron Spectroscopy in the Gas Phase*, 2 ed.; Butterworths: London, 1984.
- (6) Cardona, M.; Ley, L. Introduction. In *Photoemission in solids*; Cardona, M., Ley, L., Eds.; Springer-Verlag: Berlin ; New York, 1978; Vol. 1; pp 1.
- (7) Rotermund, H. H. *Surf. Sci. Rep.* **1997**, *29*, 267.
- (8) Meister, G.; Goldmann, A. *J. Electron Spectrosc.* **1997**, *84*, 1.
- (9) Kurpick, U.; Westhof, J.; Meister, G.; Goldmann, A. *J. Electron Spectrosc.* **1993**, *63*, 311.
- (10) Vonoertzen, A.; Rotermund, H. H.; Jakubith, S.; Ertl, G. *Ultramicroscopy* **1991**, *36*, 107.
- (11) Rotermund, H. H.; Jakubith, S.; Kubala, S.; Vonoertzen, A.; Ertl, G. *J. Electron Spectrosc.* **1990**, *52*, 811.
- (12) Rotermund, H. H.; Ertl, G.; Sesselmann, W. *Surf. Sci.* **1989**, *217*, L383.
- (13) Munakata, T.; Sugiyama, T.; Sonoda, Y. *Surf. Sci.* **2005**, *593*, 38.
- (14) Munakata, T.; Masuda, T.; Ueno, N.; Sakaya, S.; Sugiyama, T.; Takehiro, N.; Sonoda, Y. *Surf. Sci.* **2003**, *532*, 1140.

- (15) Munakata, T.; Masuda, T.; Ueno, N.; Abdureyim, A.; Sonoda, Y. *Surf. Sci.* **2002**, *507*, 434.
- (16) Monti, O. L. A.; Fourkas, J. T.; Nesbitt, D. J. *J. Phys. Chem. B* **2004**, *108*, 1604.
- (17) Petek, H.; Ogawa, S. *Prog. Surf. Sci.* **1997**, *56*, 239.
- (18) Zhu, X. Y. *Ann. Rev. Phys. Chem.* **2002**, *53*, 221.
- (19) Zhu, X. Y. *J. Phys. Chem. B* **2004**, *108*, 8778.
- (20) Besocke, K. *Surf. Sci.* **1987**, *181*, 145.
- (21) Chen, C. J. *Appl. Phys. Lett.* **1992**, *60*, 132.
- (22) Born, M.; Wolf, E. *Principles of Optics : Electromagnetic Theory of Propagation, Interference and Diffraction of Light*, 6th ed.; Pergamon Press: Oxford ; New York, 1980.
- (23) Michaelson, H. *J. Appl. Phys.* **1977**, *48*, 4729.
- (24) Lee, J. *Rev. Sci. Instrum.* **1972**, *43*, 1291.
- (25) Eastman, D. E. *Phys. Rev. B* **1970**, *2*, 1.
- (26) Shalaev, V. M.; Douketis, C.; Haslett, T.; Stuckless, T.; Moskovits, M. *Phys. Rev. B* **1996**, *53*, 11193.
- (27) Stuckless, J. T.; Moskovits, M. *Phys. Rev. B* **1989**, *40*, 9997.
- (28) Jeanmaire, D. L.; Van Duyne, R. P. *J. Electroanal. Chem.* **1977**, *84*, 1.
- (29) Bohren, C. F.; Huffman, D. R. *Absorption and Scattering of Light by Small Particles*, 1 ed.; John Wiley & Sons: New York, 1983.
- (30) Emory, S. R.; Nie, S. **1997**, *69*, 2631.
- (31) Palik, E. D.; Ghosh, G. *Handbook of Optical Constants of Solids*; Academic Press: San Diego, 1998.
- (32) Theye, M. L. **1970**, *2*, 3060.
- (33) Tompkins, H. G.; Tasic, S.; Baker, J.; Convey, D. *Surf. Interface Anal.* **2000**, *29*, 179.
- (34) Smith, R. L. *Phys. Rev.* **1962**, *128*, 2225.
- (35) Barashev, P. P. *Phys. Status Solidi A* **1972**, *9*, 9.
- (36) Marinchuk, M. E. *Phys. Lett. A* **1971**, *A 34*, 97.

- (37) Bechtel, J. H.; Smith, W. L.; Bloembergen, N. *Phys. Rev. B* **1977**, *15*, 4557.
- (38) Logothetis, E. M.; Hartman, P. L. *Phys. Rev.* **1969**, *187*, 460.



## Chapter 9

# Multi-photon Scanning Photoionization Imaging Microscopy for Single-particle Studies of Plasmonic Metal Nanostructures \*

### 9.1 Introduction

One of the most exciting recent developments in materials science is the increased control over size, shape, and composition of chemically synthesized nanoparticles. Such nanostructures already comprise several technologically and scientifically interesting classes of materials, from semiconductor nanocrystals<sup>1,2</sup> to metal nanoparticles,<sup>3-12</sup> and nanomagnets.<sup>13,14</sup> Metal nanoparticles, due to their large surface-to-volume ratios and their ability to act as electron reservoirs, have long been recognized also as promising catalytic materials.<sup>15,16</sup> Only recently, they have also begun to emerge as important materials for future optoelectronics technologies<sup>3,17-23</sup> due to their exceptional light scattering and absorption properties as well as their ability to concentrate optical fields to deep-sub-wavelength volumes.<sup>24-28</sup> In both applications, finer aspects of the particles' size, shape, and morphology, have been known to exert a crucial influence on their functionality,<sup>11,29-37</sup> making detailed single-particle studies essential to building up a fundamental understanding of the underlying physics.<sup>32,37-39</sup>

Single-particle studies present a unique opportunity for revealing heterogeneities in samples of nominally identical objects, for which bulk measurements can only reveal ensemble-averaged quantities.<sup>40</sup> For example, the surprising phenomenon of fluorescence blinking

---

\* Adapted from: Schweikhard, Volker; Grubisic, Andrej; Baker, Thomas A.; Nesbitt, David J. *Journal of Physical Chemistry C* **2011**, *115*, 83.

dynamics of colloidal semiconductor quantum dots was first identified in single-molecule experiments.<sup>41-43</sup> Single-molecule studies have also provided crucial information for understanding the biological functions of nominally covalently identical molecules,<sup>44</sup> in which kinetic heterogeneity can arise from different folding configurations or ligand binding events. To date, the vast majority of single-particle studies have relied on optical detection, such as fluorescence,<sup>45</sup> elastic<sup>46,47</sup> or inelastic (Raman) light scattering.<sup>48</sup> In a few favorable cases, even single-particle absorption measurements have been possible.<sup>49-51</sup>

Spatial resolution in each of these techniques is constrained by the diffraction limit. In recent years, a major advance in optical imaging came about, when several techniques achieved sub-diffraction limited resolution (i.e., "super-resolution"). These techniques rely on the fact that the electromagnetic radiation originates from a fluorophore that is much smaller than the diffraction-limited signal detected in the far-field. Consequently, the location of the fluorophore can be determined more precisely than the diffraction limit suggests by proper analysis of the obtained signal.<sup>52,53</sup> Of largest practical importance are techniques based on photoswitching or photoactivation of sparse subsets of molecules (PALM,<sup>54</sup> STORM,<sup>55</sup> and FPALM<sup>56</sup>) as well as on stimulated emission depletion in fluorophores (STED<sup>57</sup>). These techniques have been applied to a wide variety of particularly, biological applications.<sup>58</sup> Furthermore, several near-field optical techniques have been successfully employed for studying metal and semiconductor nanoparticles below the diffraction-limit.<sup>59-63</sup>

Photoionization techniques, on the other hand, yield information complementary to optical studies, and hold promise for expanding the scope of single particle studies to non-fluorescent objects. Multi-photon photoemission is a very sensitive technique that has been widely used to study bulk surfaces, surface-adsorbate systems<sup>64</sup> and nanoparticles.<sup>65</sup> Even in the

limit of surfaces sparsely covered with metal nanoparticles, plasmon-resonant enhancement of photoelectron emission can in certain cases allow ensemble-averaged photoelectron emission properties of the adsorbed particles to be studied.<sup>66</sup> In this way, the detailed photoemission mechanisms of femtosecond photoionization<sup>67</sup> and the role of plasmon excitations in photoionization have been investigated.<sup>25-28,65,68-71</sup> In addition, there has recently been a growing interest in developing photoionization techniques that provide spatial resolution,<sup>25,72-74</sup> as well as time-resolved information.<sup>25-28,75,76</sup> Photoelectron emission microscopy (PEEM) has been used successfully to image patterned metal films and metal clusters,<sup>73</sup> as well as to reveal spatial profiles of plasmon modes in metal nanowires<sup>77</sup> and fractal metal nanostructures.<sup>78</sup> Locally enhanced photoemission in PEEM images can be used to map the local near-field distributions,<sup>79</sup> as demonstrated on crescent-shaped silver nanostructures. Powerful interferometric pump-probe photoemission microscopy techniques have been developed and exploited, for example, to study the dynamics of localized surface plasmon modes on silver gratings.<sup>25</sup> However the level of sophisticated electron optics makes PEEM particularly challenging to implement, as well as vulnerable to signal distortion associated with charged-particle imaging. Such distortions may arise in particular due to sample charging or the presence of spatially inhomogeneous electric fields in the vicinity of metal nanoparticles and sharp metal tips.<sup>73</sup>

In this work, we present a comparatively simple, complementary single-particle technique based on (i) spatially resolved photoionization and (ii) single-electron detection sensitivity. It allows diffraction-limited images of a sample's local multi-photon photoelectron emissivity to be acquired. The technique capitalizes on two advantages of photoionization: (1) the naturally high sensitivity of charged-particle detection, combined with an optically nonlinear

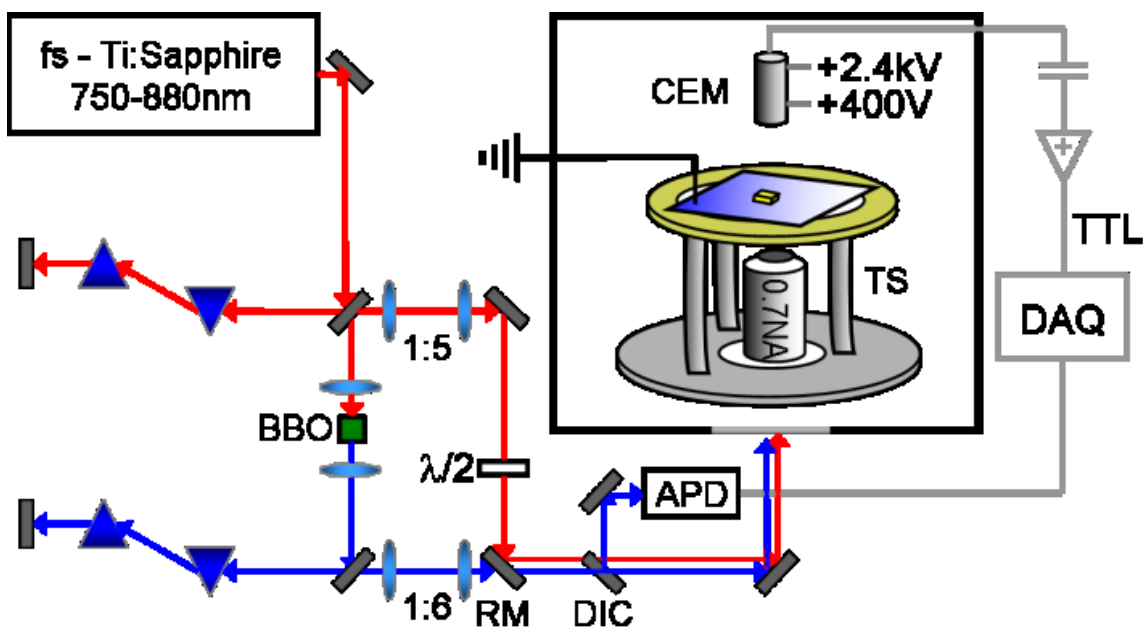


Figure 9.1: SPIM Setup. Multi-photon photoemission is initiated in a diffraction-limited laser excitation *in vacuo*, yielding an image of local photoelectron emissivity by scanning the sample using piezoelectric transducers. The fundamental, “red” light (tuning range 750 – 880 nm) or optionally doubled, “blue” (tuning range 380 - 440 nm) light from a femtosecond Ti:Sapphire laser is used for excitation with external prism pairs compressing pulses nearly to their Fourier transform limit ( $\sim 40$  fs) in the sample focal plane. Electrons are detected using either a Faraday cup and a picoammeter, or a channeltron electron multiplier (CEM), amplifier/discriminator and a 20 MHz counter.

excitation mechanism that yields high spatial resolution, and (2) the potential for chemical selectivity via various resonance-enhanced multiphoton excitation pathways.

## 9.2 Setup and Materials

The basic experimental technique of scanning photoionization microscopy has been described previously.<sup>74</sup> In this article, major improvements to the setup are described, specifically those pertaining to the implementation of *multi*-photon photoemission and single-electron detection. Both additions enhance the flexibility and sensitivity of the technique, thus allowing single metal nanoparticles to be studied. A schematic of the upgraded setup is shown in Figure 9.1.

### 9.2a *Scanning Photoionization Microscopy (SPIM)*

Multi-photon photoemission is initiated in a near-diffraction limited ultrafast laser spot, generated by overfilling the back aperture of a reflective microscope objective in vacuo (numerical aperture, NA=0.65). Images of local photoelectron emissivity are acquired by scanning the sample across a stationary focal spot of the excitation laser. In addition to photoelectron detection, the setup allows for observation of photons in a confocal microscope geometry, which can be employed to correlate the electronic and optical properties of nanomaterials in future studies. The output from an 85 MHz mode-locked Ti:Sapphire laser serves as the excitation light source. We either use spectrally relatively narrow “red” light (840 nm with full-width-at-half-maximum (FWHM) value of 24 nm) corresponding to a Fourier-transform-limited pulse duration of 43 femtoseconds (fs), or the second harmonic of the Ti:sapphire output, “blue” light (420 nm with FWHM = 6.5 nm corresponding to a Fourier-transform-limited pulse width of 40 fs). External prism compensators for both the blue and the red light provide nearly Fourier-transform-limited pulses at the focal spot on the sample ( $\tau_P \sim 50$  fs). For both blue and red light, the prism separation and insertion are optimized by maximizing the photoelectron yield from a uniform 3 nm thick platinum film. Neither a single “blue” nor “red” photon supplies enough energy to photoemit electrons from materials with a typical work function  $\Phi \sim 5$  eV. Instead, photoelectrons are emitted by a multi-photon process, where the required minimum number of photons  $n$ , with energy  $E_{\text{photon}}$ , is given by the threshold condition,  $n \times E_{\text{photon}} \geq \Phi$ .

Although the excitation conditions vary somewhat between the different samples examined and laser wavelengths employed, in typical conditions under 840 nm illumination the energy per laser pulse is  $E_P \sim 0.4$  pJ, corresponding to  $\sim 1.7 \times 10^6$  “red” photons per pulse. Pulses are

focused to a diffraction-limited spot area  $A_{\text{spot}} = 1.2025 \times \text{FWHM}^2 = 7.5 \times 10^{-9} \text{ cm}^2$ , where  $\text{FWHM} = 0.515 \lambda/\text{NA}$  ( $\lambda = 840 \text{ nm}$  and  $\text{NA} = 0.65$ ). If we assume a nearly Fourier-transform-limited pulse width ( $\tau_p \sim 50 \text{ fs}$ ), the peak pulse intensity is  $I_p \sim 1.1 \times 10^9 \text{ W/cm}^2$ , with a time-averaged intensity  $I_{\text{AV}} \sim 4.7 \text{ kW/cm}^2$ . Despite these relatively weak laser pulse conditions, about  $100 \text{ e}^-/\text{s}$  (electrons per second) can be optimally detected from gold nanorods (see below), which can be compared with a background of  $0.5 \text{ e}^-/\text{s}$  from 3 nm thick platinum films.

### 9.2b *Electron detection*

Electrons are detected using either a Faraday cup or a channeltron electron multiplier. In the initial experiments described herein, the Faraday cup is placed approximately 5 mm above the sample. The sample is grounded, while a +10 V bias is maintained on the Faraday cup. We have verified that at +10V the measured SPIM current is independent of any further increase in voltage (i.e., saturated) indicating that effectively all the emitted electrons are collected. The photocurrent is measured by a picoammeter and digitized using an analog-to-digital converter.

To achieve single-electron counting sensitivity, a channeltron electron multiplier (Photonis Magnum CEM 5901) has been installed, replacing the Faraday cup.<sup>80</sup> The quantum efficiency of channeltrons is typically 90 % for electrons with approximately 400 eV of kinetic energy and drops off dramatically for electrons with kinetic energy  $< 50\text{-}100 \text{ eV}$ . Thus, the electrons are accelerated by a 400 V bias applied between the sample and the detector entrance to maximize the detector signal. The CEM and high-voltage electrodes are enclosed in a copper shield that prevents the photoelectrons from being diverted from the detector entrance. The amplified signal pulse (gain  $\sim 10^7$  at the operating voltage of 2 kV) is fed to an

amplifier/discriminator (Advanced Research Instruments) and registered by a 20 MHz counter, with an essentially background free dark count rate of  $\sim 0.03 \text{ e}^-/\text{s}$ .

Comparison of the photocurrents from platinum films (see below), measured by the Faraday cup and the CEM under identical excitation conditions, yields an estimate for the CEM collection efficiency of  $\sim 35 \%$ , when the CEM is placed vertically, approximately 1 cm above the sample. In our range of excitation conditions no measurable electron signal is found to arise from either the blue or red light directly incident on the CEM in this configuration. We note that in the initial experiments, the CEM had been instead placed parallel to the sample,  $\sim 2$  cm above it and displaced sideways by  $\sim 2$  cm. In this configuration, a maximum collection efficiency of only 7 % is obtained, which in addition to the bias at the detector entrance requires a corresponding bias to the copper cage of +125 V in order to attract electrons sideways towards the detector entrance. However, this bias is not required in the much improved vertical configuration of the CEM, whereby the electrons can follow obstruction-free trajectories from the sample to the detector.

### 9.2c *Sample preparation*

To provide transparent, conductive substrates, 3 nm thick platinum (Pt) layers were thermally evaporated onto glass coverslips (Corning No. 1 1/2). Alternatively, 10 nm thick films of indium tin oxide (ITO) cold-deposited on glass coverslips were purchased from Advanced Thin Films. For studies of microstructured gold films, 2 nm thick gold pads were photolithographically patterned on top of the Pt substrates, following the procedures described in the literature.<sup>74</sup>

CTAB-capped gold (Au) nanorods (45 nm length x 10 nm diameter) in aqueous solution were purchased from Nanopartz and used as received. The solution absorption spectrum [Figure 9.3(a)] shows the rods' long-axis dipolar plasmon resonance centered at 830 nm with a FWHM  $\sim$  180 nm and an ensemble-averaged peak cross section of  $2 \times 10^{-12}$  cm<sup>2</sup> per rod. The weaker transverse plasmon is centered at 510 nm, on top of a broad interband-absorption feature appearing as a tail at shorter wavelengths. Typically, 30 microliters of stock solution containing  $5 \times 10^{11}$  Au rods per milliliter are spin-coated onto the Pt substrates at 1500 revolutions per minute, and are immediately transferred into the vacuum chamber.

Silver (Ag) nanospheres of 40 nm diameter were purchased from Nanocomposix ("biopure" nanospheres in citrate-stabilized aqueous solution, concentration  $3 \times 10^{10}$  particles/ml). In contrast to the single-crystalline Au rods, these spheres are polycrystalline and adopt structures that may deviate from perfect spherical geometry implied from their name. The solution absorption spectrum [Figure 9.5 (a)] exhibits a narrow dipolar plasmon resonance at 413 nm, with a FWHM of 66 nm, and no other discernable features in the visible / near-infrared region. From the solution absorption spectrum, an ensemble-averaged linear absorption cross section of  $4.7 \times 10^{-11}$  cm<sup>2</sup> per particle is obtained at the peak of the plasmon resonance. Note that for excitation wavelengths around 840 nm (i.e., far detuned from the plasmon resonance) the solution absorption cross section is lower by a factor of  $\sim 10^3$ , i.e.,  $\sim 5 \times 10^{-14}$  cm<sup>2</sup> per particle. Forty microliters of diluted stock solution (1:10 dilution in deionized H<sub>2</sub>O), are spin-coated onto Pt- or ITO-coated coverslips (the solution is drop-cast onto a static coverslip, and then spun up to 1500 RPM). All spin-coated samples are immediately transferred into the vacuum chamber.



### 9.3 Imaging Lithographic Metal Nanostructures

The spatial imaging capability of SPIM is demonstrated by imaging 2-photon photoemission under 420 nm illumination and 4-photon photoemission under 840 nm excitation from micro- and nanoscale structures. To this end, SPIM images of photolithographically patterned gold pads on a platinum substrate are acquired with blue [Figure 9.2(a)] and red excitation light [Figure 9.2(b)] with signals recorded using the Faraday cup detector. In both cases, a clear contrast between the Pt substrate and the Au pads is obtained. 4-photon photoemission provides a larger signal-to-background (S/B) ratio and captures features that are barely visible in 2-photon photoemission images, such as the small spot approximately 2  $\mu\text{m}$  above the gold pad visible in Figure 9.2(b). Lineouts through the Au pad in Figures 9.2(a) and 9.2(b) are plotted in Figures 9.2(c) and 9.2(d), respectively. The rise in signal (10 % - 90 %) at the edge of the gold pad occurs over a distance of 560(60) nm for 420 nm excitation, while for 840 nm excitation the rise occurs over 375(75) nm. This rise represents the convolution of the step function of the gold height profile with the multi-photon excitation profile from an Airy-like excitation spot. From comparison with simulated step profiles, we infer laser spot sizes (FWHM of the linear intensity profile) of 690(140) nm for 840 nm excitation (i.e., within error of the diffraction limit of 650 nm) and a 760(100) nm spot for 420 nm excitation (i.e., close to but somewhat larger than the diffraction limit of 330 nm). The reason for a non-diffraction-limited 420 nm excitation spot in this image arises from slight imperfections in the spatial profile of the frequency-doubled excitation laser beam. This problem has since been remedied by further expanding the beam prior to entering the microscope objective.

The lineouts in Figures 9.2(c) and 9.2(d) demonstrate the enhanced signal-to-background ratio (S/B  $\sim$  100:1) achieved with 4-photon photoemission over that with two-photon

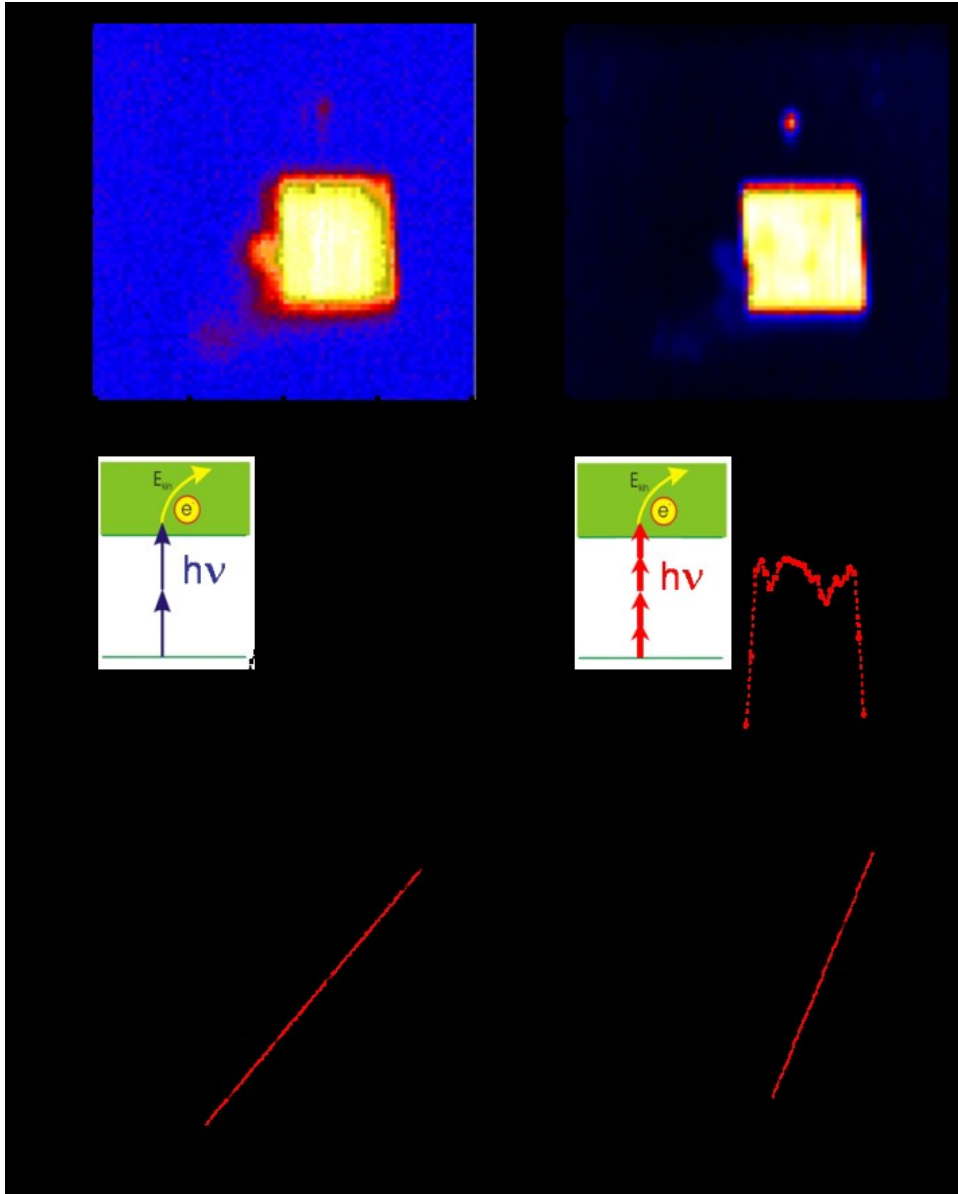


Figure 9.2: SPIM images. SPIM images of photolithographically patterned gold pads on a platinum substrate, excited with (a) blue and (b) red light. In both cases, clear contrast between the Pt substrate and the Au pads is obtained. Four-photon photoemission provides a larger signal-to-background ratio and captures features barely discernable in the 2-photon photoemission image. (c), (d) Lineouts through the Au pads in (a), (b), respectively demonstrating the improved signal-to-background ratio achieved with 4-photon photoemission. The dashed, red line in (d) is obtained from a repeated scan of the same sample area. Even the fine features are reproducible and represent real structure in the local photoemissivity. (e), (f) Log-log plots of photocurrent from Au pads on a Faraday cup as a function of excitation intensity at 400 and 800 nm, respectively, with the slope of the data confirming the expected two-photon and four-photon dependence at 400 and 800 nm, respectively.

photoemission (S/B ~ 6:1). The dashed red line in Figure 9.2(d) is a lineout obtained during a repeated scan of the same sample area. It is remarkable that even the fine features in the scan are reproduced, and thus represent real structure in the local photoelectron emissivity of these gold pads. Note the photo-induced reduction in photocurrent (~15 %) for the re-scan. At such high laser intensity, enough energy is absorbed during each pulse to heat the material within the laser focus close to the melting temperature of gold. We suspect that the strong laser intensity levels ( $8 \times 10^{10} \text{ W/cm}^2$ ) employed to demonstrate the high signal-to-background ratio between gold and platinum using the relatively insensitive Faraday cup detector may cause laser-induced local smoothing of the initially rough gold surface and thus a reduction in photoelectron yield. Such photo-induced surface modifications do not, however, represent any limitation on the technique. Due to the single-electron sensitive channeltron detector used in the subsequent experiments, excitation intensities typically two to three orders of magnitude lower can be employed, thus avoiding any significant laser-induced surface modifications. Photocurrent from Au pads measured as a function of excitation intensity at 400 and 800 nm is plotted in Figures 9.2(e) and 9.2(f), respectively. The slope in the plots corresponds to the order of the photoemission process and confirms that the photoemission from gold is a two-photon process at 400 nm and a four-photon process at 800 nm.

#### **9.4 Photoemission from Single Gold Nanorods**

To demonstrate the single-nanoparticle sensitivity of SPIM, the CEM detector was installed, and photoelectron images of a collection of gold nanorods on 3 nm thick Pt substrate were acquired by using linearly polarized, 820 nm excitation light. This wavelength is near the particles' long axis dipolar plasmon resonance in aqueous solution [see Figure 9.3 (a)]; hence a

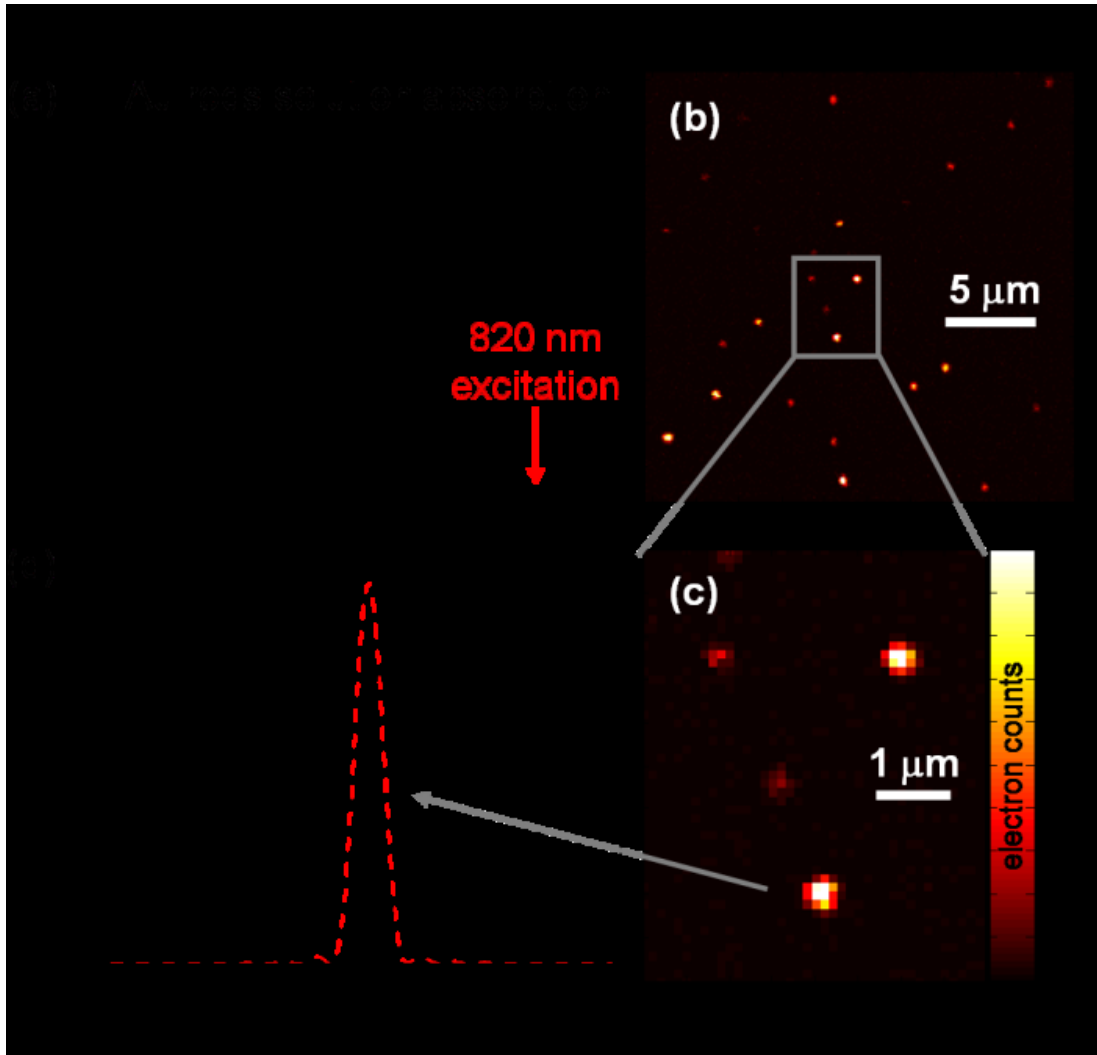


Figure 9.3: Gold nanorod data. (a) Solution absorption spectrum of 45 nm x 10 nm Au rods exhibits the long-axis dipolar plasmon resonance at 830 nm, and the weaker transverse resonance at 510 nm. (b) Multi-photon photoemission image ( $24 \times 24 \mu\text{m}^2$  scan area) of a collection of gold nanorods on 2 nm thick Pt substrate under 820 nm laser illumination, where each bright spot corresponds to a single Au nanorod. Intensity differences between the rods arise mainly due to a random, non-collinear orientation of rods with respect to the linear laser polarization. (c) Magnification of the highlighted area in (b). (d) Lineout of a scan through the indicated (gray arrow) gold nanorod (data points, 340 nm FWHM). The theoretical diffraction limited fourth-order emission profile expected for 820 nm excitation light is shown in red (FWHM = 325 nm). In this and the remaining set of figures, electrons are detected using a channeltron electron multiplier (CEM).

plasmon-enhanced, strongly orientation-dependent response may be expected. A photoelectron image of a  $24 \times 24 \mu\text{m}^2$  area of the Au rod sample on ITO is shown in Figure 9.3(b) with the

indicated area shown in magnified in Figure 9.3(c). A comparable density of spots in SPIM images and the coverage seen in AFM images of identically prepared samples suggests that the spots in SPIM arise due to emission from individual Au rods rather than their aggregates. A lineout of the scan through a sample gold nanorod [(Figure 9.3(d)] demonstrates the *diffraction-limited* four-photon photoemission signal. The average width of the photoelectron signals from all rods in Figure 9.3(b) is  $\text{FWHM}_4 = 345(45) \text{ nm}$ , where the subscript refers to the 4<sup>th</sup> order photoemission process (the order of the photoemission process was verified by observing a fourth-order dependence of photoemission signal from individual Au nanorods on the excitation laser's intensity)<sup>84</sup>. For a photoemission process of order  $m$  the spot width is given by  $\text{FWHM}_m = \text{FWHM}_1 / \sqrt{m}$ , where  $\text{FWHM}_1$  is the FWHM of the excitation laser's intensity profile (i.e., Airy pattern). In case of  $\lambda = 820 \text{ nm}$  and objective's  $\text{NA} = 0.65$  the diffraction-limited  $\text{FWHM}_1 = 0.515 \lambda / \text{NA} = 650 \text{ nm}$ . Thus, the diffraction-limited width for a four-photon photoemission signal is calculated to be  $\text{FWHM}_4 = 325 \text{ nm}$ , within experimental error of the measured value.

Large differences in photoemission intensity between different rods are observed in Figure 9.3 for a fixed linear polarization of the excitation light. With our measurement sensitivity limited by the signal-to-background ratio for Au rods on Pt, the intensities differ by as much as two orders of magnitude among particles. Such a large range may intuitively be expected to arise due to differences in excitation efficiency of the long-axis dipolar plasmon for rods with different random orientations with respect to the laser polarization. To investigate this possibility, a series of scans was recorded at different linear polarizations of the laser. Figure 9.4 shows a typical measured polarization dependence of photoemission from individual Au rods. Photoemission from Au rods on Pt is found to obey a  $\cos^8(\theta - \theta_0)$  dependence on the laser's polarization angle  $\theta$ , consistent with a fourth order photoemission process from a purely dipolar source, where the

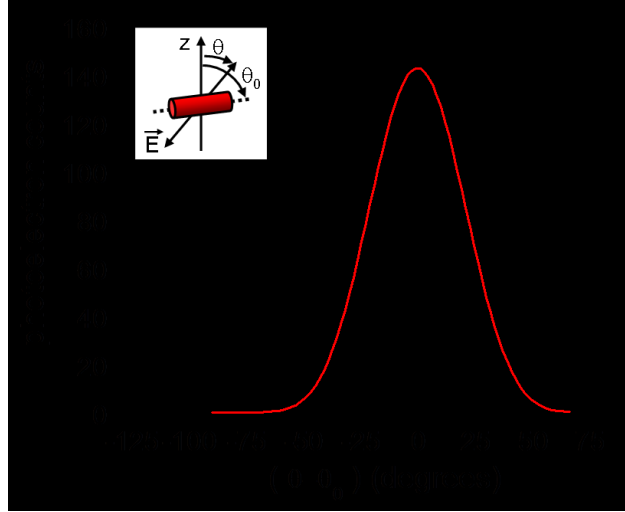


Figure 9.4: Polarization dependence of photoelectron emission from Au rods on Pt. The observed  $\cos^8(\theta-\theta_0)$  dependence of photoemission suggests that the underlying process is a fourth order photoemission from a dipolar source, consistent with emission being initiated by excitation of the Au rod long-axis dipolar plasmon.

dipole is oriented at some random angle  $\theta_0$  (e.g., orientation of the rods' long axis). For angles that are more than  $60^\circ$  off-axis, photoemission is dominated by the Pt substrate. This behavior was observed consistently for all studied gold nanorods, suggesting that photoemission is indeed initiated by excitation of the gold rods' long-axis dipolar plasmon, and/or enhanced by the concentrated electric fields at the rods' tips. In contrast to the large rod-to-rod variations in photoemission strength at a fixed linear polarization [Figure 9.7(a)], their peak photoemissivity (i.e., photoemission strength at a laser polarization angle that corresponds to that particular rod's  $\theta_0$ ) varies only by a factor of  $\sim 10$  [Figure 9.7(b)]. This is a remarkably small factor, given the likely, high sensitivity of a fourth order photoemission process on the strength of the local electric field surrounding the emitter, thus confirming the high degree of homogeneity among the Au rods.

Au nanorods occupy only a tiny fraction ( $A_{\text{rod}}/A_{\text{spot}} \sim 10^{-3}$ ) of the diffraction-limited excitation spot. The mere fact that they are distinguishable from the Pt substrate indicates that their photoemissivity on a “per-area” basis must be substantially larger than that from the Pt

substrate (note that the large differences in emissivity are not expected to arise from differences in the *vertical* dimension since the diameter of gold rods is only about three times larger than the Pt substrate thickness. In addition, escape depths for low-energy electrons are on the order of a few nanometers, thus presumably attenuating electron emission from regions deep inside the rods). In fact, the largest S/B ratio for an individual rod, presumably well aligned with the laser polarization, is  $\sim 300$  [see Figure 9.3(b)]. Such a large value implies that the ratio of per-area emissivity  $\epsilon$  between an aligned Au rod and the Pt substrate is  $(\epsilon_{\text{Au-rod}} / \epsilon_{\text{Pt}}) = (S/B) \times (A_{\text{spot}}/A_{\text{rod}}) \sim 3 \times 10^5$ . In contrast, that ratio for Au pads and the Pt substrate in Figure 9.2 is only  $(\epsilon_{\text{Au-pad}} / \epsilon_{\text{Pt}}) \sim 100$ . The corresponding factor of  $(\epsilon_{\text{Au-rod}} / \epsilon_{\text{Pt}}) / (\epsilon_{\text{Au-pad}} / \epsilon_{\text{Pt}}) \sim 3 \times 10^3$  fold difference between the Au nanorod and Au pad systems is striking. We attribute this large factor to either the field enhancement at the nanorod tips (i.e., the well-known lightning-rod effect),<sup>81</sup> and / or to a near-resonant plasmonic enhancement.<sup>82</sup> The possibility of photoemission enhancement due to a plasmon resonance will be investigated in greater detail using wavelength-tunable femtosecond light sources in a separate study.

## 9.5 Photoemission Imaging of Silver Nanoparticles

To further demonstrate the sensitivity of scanning multiphoton photoionization microscopy, the photoelectron emission from nanostructures has been studied under conditions where resonant plasmonic enhancement is absent. Specifically, 40 nm diameter silver nanoparticles have been imaged by four-photon photoionization using 840 nm excitation. What makes these particles interesting is that they exhibit a narrow (66 nm FWHM) dipolar plasmon resonance at 413 nm in aqueous solution, without any further strong absorption features in the visible / near-infrared (NIR) range [see Figure 9.5(a)]. In the substrate / vacuum sample

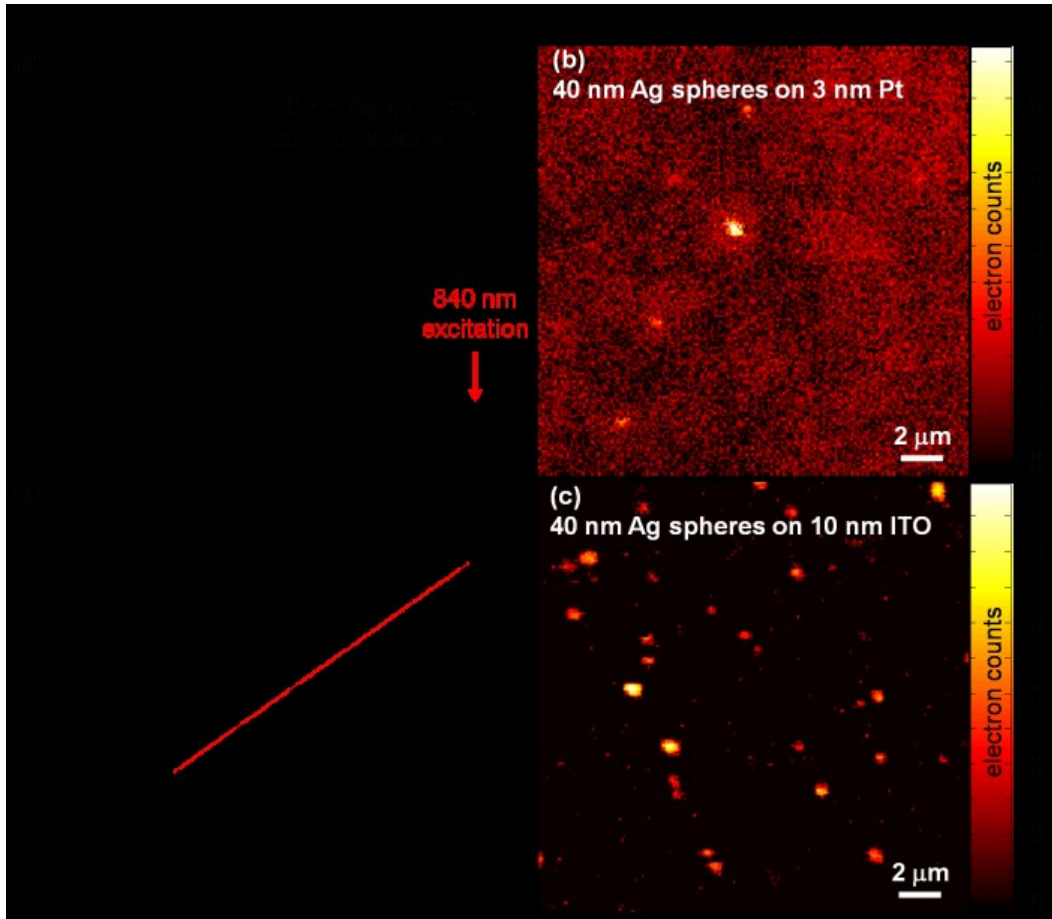


Figure 9.5: Silver spheres data. (a) Solution absorption spectrum of 40 nm diameter Ag spheres with the dominant dipolar plasmon resonance located at 413 nm. (b), (c) Logarithmic SPIM images of silver nanoparticles on 3 nm thick Pt substrate and 10 nm thick ITO, respectively, excited with linearly polarized light at 830 nm. The ITO substrate exhibits a significantly lower photoionization background, revealing a coverage with Ag nanospheres that is consistent with that observed from AFM images of identically prepared samples. In contrast, the higher background from the Pt substrate (b) masks the emission from weaker particles, leading to a lower signal-to-background ratio and a lower apparent coverage. (d) Logarithmic plot of photoemission from Ag particles on ITO as a function of laser intensity.

environment probed in these SPIM studies, this plasmon resonance at 413 nm is expected to shift to the blue. Due to low absorbance values, such a blue shift could not be independently confirmed by measuring an ensemble absorption spectrum of Ag spheres spin-coated onto substrates. However, consistent with these expectations, Mie scattering calculations<sup>82</sup> predict a plasmon resonance around 360 nm for 40 nm diameter Ag spheres in vacuum, and 380 nm in a



medium with a dielectric constant that is between that of vacuum and that of platinum.<sup>83</sup> In any case, excitation at 840 nm is far away from any such plasmonic resonance. Thus, the photoemission process from Ag spheres at this wavelength is not expected to be assisted by the plasmonic field enhancement.

In agreement with expectations, SPIM signals from Ag spheres at 840 nm are consequently quite weak compared to the Au nanorods. Nevertheless, photoelectron emission from individual Ag nanospheres on Pt substrates is sufficiently strong to distinguish these particles from background [Figure 9.5 (b)] despite the absence of any direct plasmon-resonant enhancement. It is interesting to note that the apparent coverage of Ag spheres determined by SPIM ( $\sim 5$  spheres in a  $20 \times 20 \mu\text{m}^2$  area), is substantially lower than that observed in the corresponding AFM images ( $\sim 20$  spheres in a  $20 \times 20 \mu\text{m}^2$  area). In fact, most spheres in Figure 9.5(b) are barely distinguishable from the Pt substrate background. Thus, it is likely that a significant fraction of spheres does not produce intense enough photoemission signal to stand out above the background.

We consequently explored the viability of an alternative conductive substrate with a potentially lower photoemissivity, i.e., 10 nm thick ITO films on glass coverslips. Under 800 nm illumination, ITO produces approximately three orders of magnitude lower background photoemission signals than the Pt substrate. Indeed, with much lower background, signal from even weakly emitting Ag spheres can now be observed, as shown in Figure 9.5(c), yielding an apparent coverage that is consistent with that determined by AFM. The average signal-to-background ratio for Ag spheres on ITO observed in Figure 9.5(c) is approximately  $S/B \sim 800$ , with some of the brightest spheres even yielding a  $S/B \sim 10^4$ . Such large signals are obtained

despite the fact that 40 nm diameter Ag spheres typically represent only  $2.5 \times 10^{-3}$  of the 4-photon excitation spot area.

The photoelectron signal from individual silver spheres follows the expected power dependence on excitation intensity  $I_{\text{peak}}$  (signal  $\sim I_{\text{peak}}^m$ ) [Figure 9.5(d)]. The value of  $m$  is observed to vary in the range  $3 \leq m \leq 4$  for different spheres, with the ensemble-averaged value (standard deviation) for  $N = 14$  particles being  $\langle m \rangle = 3.8(6)$ . The variability in  $m$  for different nanospheres may arise due to the fact that the work function of silver ranges between 4.2 - 4.8 eV, depending on the crystal facet from which emission occurs and the surface preparation method employed.<sup>84</sup> Thus, photoemission resulting from excitation with 1.47 eV (840 nm) photons may proceed via a third order process for work functions  $\Phi < 4.4$  eV and via a fourth order process for  $\Phi > 4.4$  eV. In previous work, non-integer power dependence of photoemission intensity, with the exponent varying between 2.9 and 3.7 at different points on the sample, has been observed in an ensemble-measurement study of silver nanoparticles on a silicon substrate upon excitation with  $\sim 1.5$  eV light.<sup>67</sup> These observations were explained by additional emission pathways co-existing with multi-photon photoemission.

We note that despite the high S/B ratio observed on ITO, silver spheres are about 100 times weaker emitters than gold nanorods on Pt. Qualitatively this is to be expected, given the absence of a nominal plasmonic enhancement in Ag spheres around 840 nm. However, we find it surprising that these Ag spheres are even as strong an electron emitter as experimentally observed. A simple estimate of nanoparticle's emission strength takes into account three major contributions: (1) the particle's linear absorption cross section at the excitation wavelength, (2) the material's bulk emissivity, (3) and the electric field enhancement due to the nanoparticle geometry, e.g., the "lightning-rod" effect. We next consider these three contributions separately.

First of all, the linear absorption cross section of 40 nm Ag spheres at 840 nm is 40 times smaller than that of Au rods at the same wavelength, i.e.  $\sigma_{\text{Ag}}/\sigma_{\text{Au}}=1/40$ . The excitation probability of an m-plasmon excited state ( $m = 4$  for plasmonic processes contributing to four-photon photoemission) should thus scale as the  $m^{\text{th}}$  power of the probability for a single excitation, i.e. in this case as  $(\sigma_{\text{Ag}}/\sigma_{\text{Au}})^4$ .<sup>71</sup> Secondly, we are unaware of any measurement of bulk four-photon photoemission properties of Ag and Au. However, there is no reason to expect them to be very different in strength. For example, the reported bulk *two-photon* photoemission strengths from flat Ag and Au surfaces are very similar.<sup>85,86</sup> Thirdly, the electric field enhancement for a sphere due to the lightning-rod effect proves to be independent of the particle's radius of curvature. In the dipole approximation, the incident electric field  $E_0$ , induces a dipole  $d = \alpha E_0$  in the metal particle, where  $\alpha$  denotes the particle's polarizability. The induced electric field  $E_{\text{ind}}$ , in turn, scales as  $E_{\text{ind}} \sim \alpha E_0/r^3$ , where  $r$  is the radial distance from the particle's center. For a particle of size  $a$ ,  $\alpha \sim a^3$ ; thus at the particle surface, where photoionization occurs, the induced electric field  $E_{\text{ind}}$ , is independent of the radius,  $a$ . By combining the three contributing factors, the ratio of four-photon photoemissive strength from Ag nanospheres and Au nanorods is thus predicted to be  $\sim(\sigma_{\text{Ag}}/\sigma_{\text{Au}})^4 = 10^{-6}$ , i.e., four orders of magnitude smaller than experimentally observed.

It is worth considering whether this unexpectedly strong photoemission from Ag spheres could arise from an *indirect* plasmonic enhancement, such as from a possible two-photon excitation of the dipolar plasmon resonance. Nonlinear effects, such as enhanced two-photon fluorescence from nanostructured metals, have been observed.<sup>81,87</sup> In a similar manner, one might speculate that four-photon excitation around 800 nm may benefit from nonlinear enhancements associated with the plasmon resonance (e.g., via two-photon excitation of the

plasmon resonance). To test for a possible two-photon excitation of the plasmon resonance, we compared photoemission at two different excitation wavelengths, 760 nm and 860 nm (data not shown). While there is a roughly three-fold increase in the overall signal levels for 760 nm vs 860 nm excitation, almost all Ag spheres are clearly visible at both wavelengths. This relative insensitivity to the excitation wavelength rules out any spectrally narrow resonant contribution to photoemission.

#### *9.5a Laser polarization-dependence of photoemission from Ag spheres*

In the absence of either direct or nonlinear plasmonic enhancements, one would predict fairly uniform photoelectron emission strengths from a spin-coated ensemble of Ag spheres. Very much to the contrary, however, Ag spheres on the ITO substrate in Figure 9.5 (c) exhibit factors of up to a 1000-fold difference in photoelectron emissivity when excited with light of a fixed linear polarization at 840 nm [Figure 9.7(c)]. To understand these large variations between Ag spheres, we tested for a dependence of their photoemissivity on laser polarization at 840 nm. Based on our studies of Au nanorods, one would expect a complete absence of any polarization dependence for these nominally spherical nano-objects. Rather surprisingly, a strongly peaked polarization dependence is observed for almost all spheres. Furthermore, in most cases only a small background signal was detected at a polarization orthogonal to the peak emission, similar to the case of Au nanorods. However, in contrast to Au nanorods, which all consistently produced an  $\approx \cos^8(\theta-\theta_0)$  polarization dependence arising from four-photon photoemission from a dipolar source, a much wider variety of phenomena is encountered for Ag spheres. Specifically, while the polarization-dependence for many of the brightest Ag spheres is consistent with four-photon photoemission from a dipolar emission source [see Figure 9.6(b)],

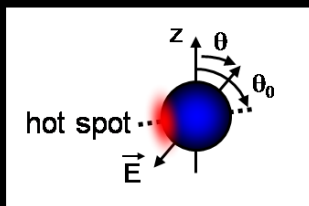


Figure 9.6: Polarization dependence for silver spheres. Many nominally spherical silver nanoparticles exhibit strong polarization dependent photoionization yield. (a) Such anisotropy, for example, could be associated with variations in electron emissivity of the different crystal facets that are exposed in the polycrystalline particles, as well as possible localized electric field hot-spots at grain boundaries and microscopic structural defects. (b) The brightest spheres show a strong polarization-dependent behavior, consistent with a four-photon photoemission from a dipolar emission source. (c) More weakly-emitting nanospheres tend to exhibit less pronounced polarization-dependent behavior. (d) Some of the weakest-emitting spheres display almost no polarization dependence. Dashed lines mark limits for 90% confidence levels.

many of the less emissive spheres display a distinctly weaker polarization dependence [see Figure 9.6(c)]. Photoemission from a few (6 out of 26) spheres, predominantly the most weakly emitting ones, can be observed at all angles, with only a weak polarization-dependent trend on top of a polarization-independent background [see Figure 9.6(d)]. However, even this surprisingly strong polarization dependence still does not fully explain the observed variations in photoemissivity between different Ag spheres. Indeed, while they exhibit  $10^3$ -fold variation at a

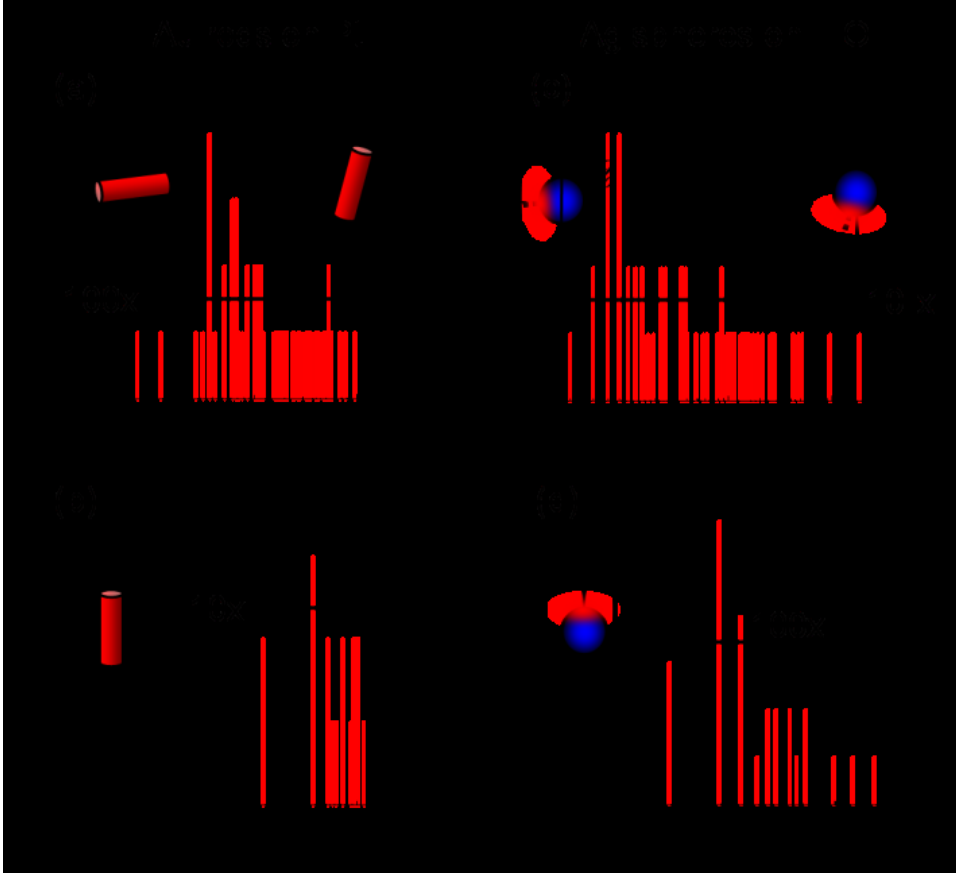


Figure 9.7: Photoemission yield from various nanostructures. Distributions in photoemission strength from (a, b) single Au rods on Pt, and (c, d) Ag spheres on ITO. (a), (c) Distribution of photoemissivity at a fixed linear polarization. Bright (weak) emitters presumably have their long axis, or a local hot-spot, aligned with (orthogonal to) the laser polarization. (b), (d) Distributions of the *peak* photoemissivity, i.e. emissivity value at the peak of each particle's polarization dependence, are much narrower than in (a) and (c). Ag spheres represent a much more heterogeneous sample (100x peak emissivity variation) than Au rods (10x variation)

fixed

laser polarization, the Ag spheres still show a significant 100-fold variation in peak photoemissivities. [Figure 9.7(c) and Figure 9.7(d)]. In particular, this contrasts with the much smaller factor of  $\sim 10$  in variability of the peak photoemission strength observed for gold nanorods [Figure 9.7(b)].

The (i) unexpected polarization dependence of photoemission from nominally spherical objects and (ii) large differences in the peak emissivity between Ag nanospheres, provoke

interesting questions regarding the underlying photoionization mechanism. One explanation that must be considered is the possibility of significant particle aggregation. This is relevant since such closely-spaced particle aggregates could potentially form red-shifted, coupled plasmon resonances in our excitation wavelength range and thus potentially lead to anisotropic photoemission. From multiple SPIM scans, we estimate average coverages of  $\sim 20$  particles in a  $20 \times 20 \mu\text{m}^2$  area, which is statistically low enough to ensure single emitting objects per diffraction limited spot. More critically, however, AFM images of identically prepared samples reveal coverages that are consistent with those observed in SPIM images, indicating that essentially all spheres exhibit detectable electron emission. If the observed photoemission signal originated only from aggregates, in contrast one would expect significantly lower apparent coverage in SPIM.

Another possible interpretation of our data is that multi-photon photoemission from solution-synthesized, *polycrystalline*, silver spheres is dominated by strong local variations in photoemission propensity arising from the microscopic features in their structure. For example, such local variations could be a consequence of the different work functions associated with the various crystal facets in the nanoparticle. Alternatively, localized regions of strong electric fields that may be expected near grain boundaries and structural defects in these polycrystalline particles could give rise to locally enhanced photoemissivity. Related effects have been observed in recent experiments on *evaporated* metal nanostructures. For example, strongly polarization-dependent electron emission has been detected from 140 nm Pb clusters on a silicon substrate.<sup>73</sup> Furthermore, recent observations of locations of strongly enhanced electron emission on evaporated silver gratings<sup>25</sup> and lithographically patterned silver nanodisks,<sup>88</sup> have all been tentatively explained by local electric-field hot-spots.

### 9.5b *Temporal fluctuations in the photoelectron emission from Ag spheres*

Additional important information regarding the photoemission mechanism comes from the surprising observation that the electron signals from individual Ag spheres, in contrast to Au rods, are time-dependent. In Figure 9.8, the photoemission signal from a few representative individual spheres in a sequence of scans under identical excitation conditions is shown. Photoemission signals are observed to rise or decay with time, as shown in Figure 9.8(a) and 9.8(b), respectively. Transient spikes or dips are occasionally encountered as well. Furthermore, some spheres exhibit abrupt jumps between more or less constant initial and final emission levels, as shown in Figure 9.8 (c) and (d). In contrast, such striking time-dependence was not observed for any of the studied gold rods. Interestingly, measurements of the polarization dependence of photoemission from Ag spheres prior and after abrupt jumps in signal levels suggest that these jumps are not accompanied by drastic changes in the polarization angle at which peak emission occurs [see Figure 9.8(e) and Figure 9.8(f)].

Both the observed anisotropies and the temporal variations in photoemission appear to suggest that photoemission is strongly influenced by microscopic structural features in these polycrystalline particles, rather than being driven by the lowest-order dipolar electron oscillation. These microscopic features may be very sensitive to small light-induced structural rearrangements, as has been observed by Jin and coworkers<sup>8</sup> in the conversion of silver nanospheres to nanoprisms, which could explain the observed dramatic time-dependent signals. A more detailed study of the photoemission mechanism of *individual* Ag nanospheres (as opposed to particle aggregates) is clearly worthwhile, but is beyond the scope of the current work.



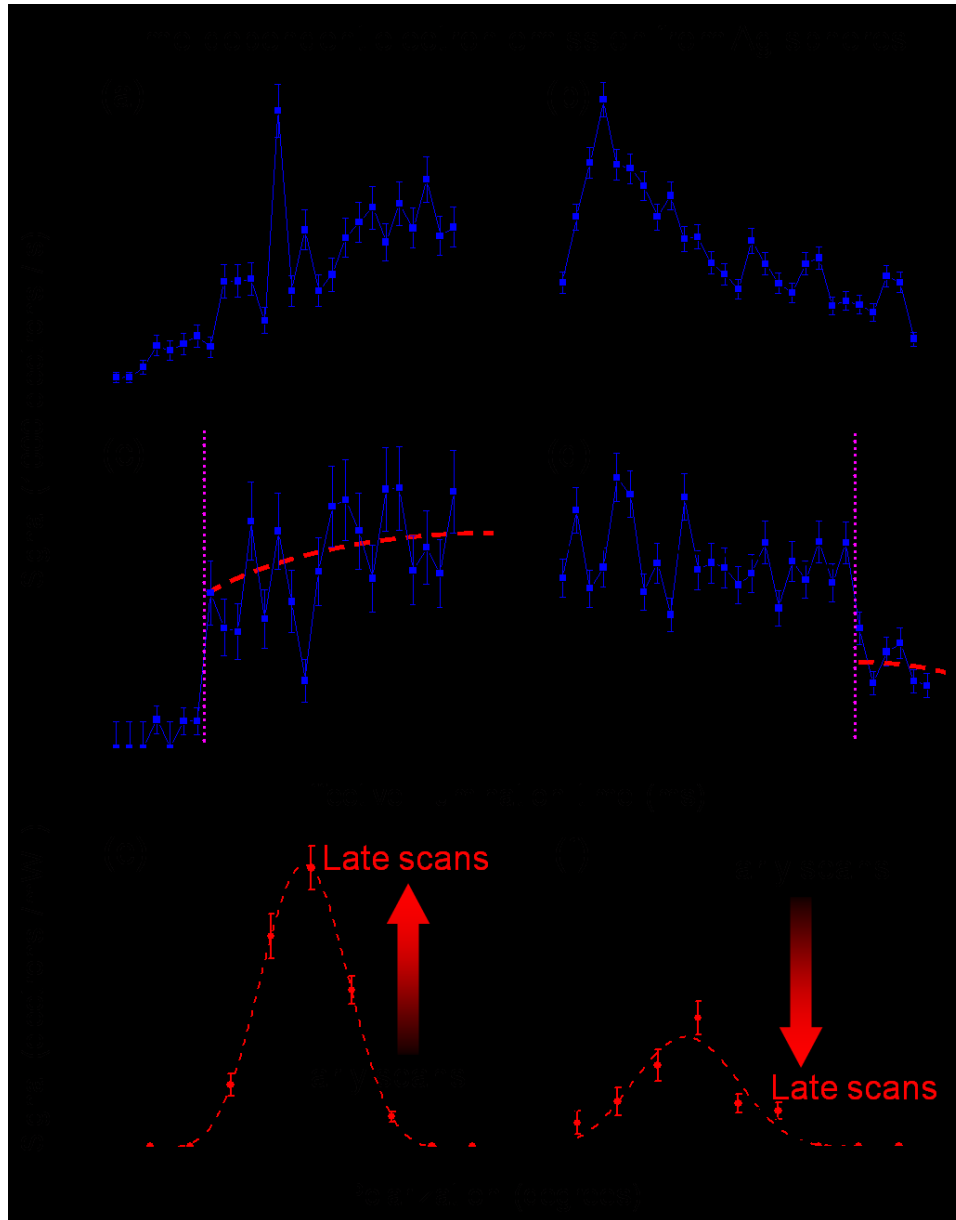


Figure 9.8: Time dependence of photoemission observed for Ag spheres. (a-d) Time sequences of the emission from individual Ag spheres recorded by repeatedly scanning the same sample area. Emission from individual spheres is plotted vs. the time that each sphere spends under illumination ( $\sim 50$  ms per scan). Emission from single particles may gradually (a) increase with time, exhibit sudden spikes, or (b) decrease gradually (dashed lines serve to guide the eye). (c) Abrupt increases or (d) decreases between more or less constant initial and final emission intensity are observed. (e), (f) Before and after such jumps, the polarization dependence is found to remain approximately unchanged [“early scans” and “late scans” in (e) and (f)]. For (a-d) the excitation intensity was  $1.9 \times 10^9$  W/cm<sup>2</sup>, while for (e) and (f) it was  $3.6 \times 10^9$  W/cm<sup>2</sup>.

## 9.6 Summary and Conclusions

We have demonstrated that scanning multi-photon photoionization microscopy is a viable technique for single-particle studies of heterogeneous samples of colloidal metal nanoparticles as well as photolithographically fabricated metal nanostructures. Four-photon photoemission from Au nanorods on Pt substrate was studied under 840 nm excitation. Individual nanoparticles exhibit strong,  $\cos^8(\theta-\theta_0)$  dependence of photoemission strength on the angle between laser polarization ( $\theta$ ) and the rod axis ( $\theta_0$ ), suggesting that four-photon photoemission is initiated by excitation of the long-axis dipolar plasmon resonance. For on-axis excitation, the photoemission strengths of different rods vary less than 10-fold. Such a small factor is remarkable given the fourth order photoemission dependence on local electric field strength surrounding the emitter, thus suggesting a relatively high degree of homogeneity among the Au nanorods.

Moreover, four-photon photoemission from polycrystalline Ag nanospheres on both Pt and ITO substrates have also been studied under 840 nm excitation. Surprisingly, strongly polarization-dependent photoelectron signals are also observed for these nominally spherical particles. However, different particles exhibit very different degrees of anisotropy with some showing strongly polarization-dependent behavior akin to the one observed in case of Au nanorods, whereas others exhibit almost none. Just as surprisingly, the observed photoelectron signals from Ag spheres, in contrast to Au rods, display striking time-dependence. More work is clearly necessary to elucidate the precise mechanisms underlying these observations.

The results suggest that the image contrast in SPIM can arise from a variety of different mechanisms, i.e., intrinsic differences in the strength of photoemission from different chemical species, photoemission enhancements due to plasmon resonances, and lightning-rod effects associated with concentrated electric fields near nanoscale structural features. Single-particle

studies of polarization-, intensity-, excitation-wavelength-, and even time-dependence of photoemission signals provide powerful means to unravel the contributions of these different mechanisms, even in strongly heterogeneous samples of particles. These studies thus establish the SPIM technique as a valuable, new approach to the study of local electronic properties of individual metallic nanostructures. Specifically, in the next chapter, SPIM studies of the local electric fields surrounding metal nanoholes will be presented.

## References

- (1) Yin, Y.; Alivisatos, A. P. *Nature* **2005**, *437*, 664.
- (2) Choi, C. L.; Alivisatos, A. P. *Annu. Rev. Phys. Chem.* **2010**, *61*, 369.
- (3) Pelton, M.; Aizpurua, J.; Bryant, G. *Laser Photonics Rev.* **2008**, *2*, 136.
- (4) Alekseeva, A. V.; Bogatyrev, V. A.; Khlebtsov, B. N.; Mel'nikov, A. G.; Dykman, L. A.; Khlebtsov, N. G. *Colloid J.* **2006**, *68*, 661.
- (5) Murphy, C. J.; San, T. K.; Gole, A. M.; Orendorff, C. J.; Gao, J. X.; Gou, L.; Hunyadi, S. E.; Li, T. *J. Phys. Chem. B* **2005**, *109*, 13857.
- (6) Sun, Y.; Xia, Y. *Science* **2002**, *298*, 2176.
- (7) Maillard, M.; Giorgio, S.; Pileni, M. P. *Adv. Mater.* **2002**, *14*, 1084.
- (8) Jin, R.; Cao, Y.; Mirkin, C. A.; Kelly, K. L.; Schatz, G. C.; Zheng, J. G. *Science* **2001**, *294*, 1901.
- (9) Brus, L. *Accounts Chem. Res.* **2008**, *41*, 1742.
- (10) Haes, A. J.; Haynes, C. L.; McFarland, A. D.; Schatz, G. C.; Van Duyne, R. R.; Zou, S. L. *MRS Bull.* **2005**, *30*, 368.

- (11) Halas, N. J. *MRS Bull.* **2005**, *30*, 362.
- (12) Callegari, A.; Tonti, D.; Chergui, M. *Nano Lett.* **2003**, *3*, 1565.
- (13) Seo, W. S.; Kim, S. M.; Kim, Y.-M.; Sun, X.; Dai, H. *Small* **2008**, *4*, 1968.
- (14) Sun, S.; Zeng, H.; Robinson, D. B.; Raoux, S.; Rice, P. M.; Wang, S. X. *J. Am. Chem. Soc.* **2004**, *126*, 273.
- (15) Watanabe, K.; Menzel, D.; Nilius, N.; Freund, H. J. *Chem. Rev.* **2006**, *106*, 4301.
- (16) Somorjai, G. A.; York, R. L.; Butcher, D.; Park, J. Y. *Phys. Chem. Chem. Phys.* **2007**, *9*, 3500.
- (17) Pillai, S.; Catchpole, K. R.; Trupke, T.; Green, M. A. *J. Appl. Phys.* **2007**, *101*, 093105.
- (18) Anker, J. N.; Hall, W. P.; Lyandres, O.; Shah, N. C.; Zhao, J.; Van Duyne, R. P. *Nature Mater.* **2008**, *7*, 442.
- (19) Konstantatos, G.; Sargent, E. H. *Nature Nanotech.* **2010**, *5*, 391.
- (20) Chen, W.; Zhang, J. Z.; Joly, A. G. *J Nanosci. Nanotechno.* **2004**, *4*, 919.
- (21) Barnes, W. L.; Dereux, A.; Ebbesen, T. W. *Nature* **2003**, *424*, 824.
- (22) Ozbay, E. *Science* **2006**, *311*, 189.
- (23) Rosi, N. L.; Mirkin, C. A. *Chem. Rev.* **2005**, *105*, 1547.
- (24) Mohamed, M. B.; Volkov, V.; Link, S.; El-Sayed, M. A. *Chem. Phys. Lett.* **2000**, *317*, 517.
- (25) Kubo, A.; Onda, K.; Petek, H.; Sun, Z.; Jung, Y. S.; Kim, H. K. *Nano Lett.* **2005**, *5* 1123.

- (26) Kubo, A.; Jung, Y. S.; Kim, H. K.; Petek, H. *J. Phys. B-At. Mol. Opt. Phys.* **2007**, *40*, S259.
- (27) Kubo, A.; Pontius, N.; Petek, H. *Nano Lett.* **2007**, *7*, 470.
- (28) Kubo, A.; Onda, K.; Petek, H.; Sun, Z. J.; Jung, Y. S.; Kim, H. K. *Nano Lett.* **2005**, *5*, 1123.
- (29) Kelly, K. L.; Coronado, E.; Zhao, L. L.; Schatz, G. C. *J. Phys. Chem. B* **2003**, *107*, 668.
- (30) Kreibig, U.; Vollmer, M. *Optical Properties of Metal Clusters*; Springer-Verlag: Heidelberg, 1995; Vol. 25.
- (31) Mock, J. J.; Barbic, M.; Smith, D. R.; Schultz, D. A.; Schultz, S. *J. Chem. Phys.* **2002**, *116*, 6755.
- (32) Willets, K. A.; Van Duyne, R. P. *Annu. Rev. Phys. Chem.* **2007**, *58*, 267.
- (33) Xia, Y. N.; Halas, N. J. *MRS Bull.* **2005**, *30*, 338.
- (34) West, J. L.; Halas, N. J. *Annu. Rev. Biomed. Eng.* **2003**, *5*, 285.
- (35) Link, S.; El-Sayed, M. A. *Int. Rev. Phys. Chem.* **2000**, *19*, 409.
- (36) Bardhan, R.; Grady, N. K.; Cole, J. R.; Joshi, A.; Halas, N. J. *ACS Nano* **2009**, *3*, 744.
- (37) Prodan, E.; Radloff, C.; Halas, N. J.; Nordlander, P. *Science* **2003**, *302*, 419.
- (38) McFarland, A. D.; Van Duyne, R. P. *Nano Lett.* **2003**, *3*, 1057.
- (39) Sherry, L. J.; Chang, S. H.; Schatz, G. C.; Van Duyne, R. P.; Wiley, B. J.; Xia, Y. N. *Nano Lett.* **2005**, *5*, 2034.
- (40) Moerner, W. E. *Science* **1994**, *265*, 46.

- (41) Nirmal, M.; Dabbousi, B. O.; Bawendi, M. G.; Macklin, J. J.; Trautman, J. K.; Harris, T. D.; Brus, L. E. *Nature* **1996**, *383*, 802.
- (42) Kuno, M.; Fromm, D. P.; Hamann, H. F.; Gallagher, A.; Nesbitt, D. J. *J. Chem. Phys.* **2001**, *115*, 1028.
- (43) Frantsuzov, P.; Kuno, M.; Janko, B.; Marcus, R. A. *Nature Physics* **2008**, *4*, 519.
- (44) Shaevitz, J. W.; Block, S. M.; Schnitzer, M. J. *Biophys. J.* **2005**, *89*, 2277.
- (45) Moerner, W. E.; Fromm, D. P. *Rev. Sci. Instrum.* **2003**, *74*, 3597.
- (46) Sönnichsen, C.; Franzl, T.; Wilk, T.; von Plessen, G.; Feldmann, J.; Wilson, O.; Mulvaney, P. *Phys. Rev. Lett.* **2002**, *88*, 077402.
- (47) Novo, C.; Funston, A. M.; Mulvaney, P. *Nature Nano* **2008**, *3*, 598.
- (48) Nie, S.; Emery, S. R. *Science* **1997**, *275*, 1102.
- (49) Muskens, O. L.; Bachelier, G.; Fatti, N. D.; Vallée, F.; Brioude, A.; Jiang, X.; Pileni, M.-P. *J. Phys. Chem. C* **2008**, *112*, 8917.
- (50) Muskens, O. L.; Billaud, P.; Broyer, M.; Fatti, N. D.; Vallée, F. *Phys. Rev. B* **2008**, *78*, 205410.
- (51) Billaud, P.; Marhaba, S.; Grillet, N.; Cottancin, E.; Bonnet, C.; Lermé, J.; Vialle, J.-L.; Broyer, M.; Pellarin, M. *Rev. Sci. Instr.* **2010**, *81*, 043101.
- (52) Yildiz, A.; Selvin, P. R. *Accounts Chem. Res.* **2005**, *38*, 574.
- (53) Lacoste, T. D.; Michalet, X.; Pinaud, F.; Chemla, D. S.; Alivisatos, A. P.; Weiss, S. *Proc. Natl. Acad. Sci.* **2000**, *97*, 9461.
- (54) Betzig, E.; Patterson, G. H.; Sougrat, R.; Lindwasser, O. W.; Olenych, S.; Bonifacino, J. S.; Davidson, M. W.; Lippincott-Schwartz, J.; Hess, H. F. *Science* **2006**, *313*, 1642.

- (55) Rust, M. J.; Bates, M.; Zhuang, X. *Nature Meth.* **2006**, *3*, 793.
- (56) Hess, S. T.; Girirajan, T. P. K.; Mason, M. D. *Biophys. J.* **2006**, *91*, 4258.
- (57) Hell, S. W.; Wichmann, J. *Opt. Lett.* **1994**, *19*, 780.
- (58) Lord, S. J.; Lee, H. D.; Moerner, W. E. *Anal. Chem.* **2010**, *82*, 2192.
- (59) Kohei, I.; Tetsuhiko, N.; Hiromi, O. *J. Chem. Phys.* **2005**, *122*, 154701.
- (60) Axelrod, D. *Method Cell Biol.* **2008**, *89*, 169.
- (61) Hamann, H. F.; Gallagher, A.; Nesbitt, D. J. *Appl. Phys. Lett.* **1998**, *73*, 1469.
- (62) Farahani, J.; Eisler, H.-J.; Pohl, D. W.; Hecht, B. *Phys. Rev. Lett.* **2005**, *95*, 017402.
- (63) Fort, E.; Gresillon, S. *J. Appl. Phys. D Appl. Phys.* **2008**, *41*, 013001 (31pp).
- (64) Zhao, J.; Pontius, N.; Winkelmann, A.; Sametoglu, V.; Kubo, A.; Borisov, A. G.; Sanchez-Portal, D.; Silkin, V. M.; Chulkov, E. V.; Echenique, P.; Petek, H. *Phys. Rev. B* **2008**, *78*, 085419.
- (65) Evers, F.; Rakete, C.; Watanabe, K.; Menzel, D.; Freund, H. J. *Surf. Sci.* **2005**, *593* 43.
- (66) Pfeiffer, W.; Kennerknecht, C.; Mershdorf, M. *Appl. Phys. A* **2004**, *78*, 1011.
- (67) Gloskovskii, A.; Valdaitsev, D.; Nepijko, S. A.; Schoenhense, G.; Rethfeld, B. *Surf. Sci.* **2007**, *601* 4706.
- (68) Kennerknecht, C.; Hövel, H.; Mershdorf, M.; Voll, S.; Pfeiffer, W. *Appl. Phys. B - Lasers O* **2001**, *73*, 425.
- (69) Mershdorf, M.; Pfeiffer, W.; Thon, A.; Voll, S.; Gerber, G. *Appl. Phys. A - Mater.* **2000**, *71*, 547.

- (70) Bauer, M.; Wiemann, C.; Lange, J.; Bayer, D.; Rohmer, M.; Aeschlimann, M. *Appl. Phys. A - Mater.* **2007**, *88*, 473.
- (71) Lehmann, J.; Merschdorf, M.; Pfeiffer, W.; Thon, A.; Voll, S.; Gerber, G. *Phys. Rev. Lett.* **2000**, *85*, 2921.
- (72) Munakata, T.; Masuda, T.; Ueno, N.; Sakaya, S.; Sugiyama, T.; Takehiro, N.; Sonoda, Y. *Surf. Sci.* **2003**, 532–535 1140.
- (73) Fecher, G. H.; Oliver Schmidt, O.; Hwu, Y.; Schonhense, G. *J. Electron Spectrosc.* **2002**, *126*, 77.
- (74) Monti, O. L. A.; Baker, T. A.; Nesbitt, D. J. *J. Chem. Phys.* **2006**, *125*, 154709.
- (75) Rohmer, M.; Bauer, M.; Leissner, T.; Schneider, C.; Fischer, A.; Niedner-Schatteburg, G.; Issendorff, B. v.; Aeschlimann, M. *Phys. Status Solidi B* **2010**, *247*, 1132.
- (76) Stockman, M. I.; Kling, M. F.; Kleineberg, U.; Krausz, F. *Nature Photonics* **2007**, *1*, 539.
- (77) Douillard, L.; Charra, F.; Korczak, Z.; Bachelot, R.; Kostcheev, S.; Lerondel, G.; Adam, P.-M.; Royer, P. *Nano Lett.* **2008**, *8*, 935.
- (78) Word, R. C.; Dornan, T.; Könenkamp, R. *Appl. Phys. Lett.* **2010**, *96*, 251110
- (79) Cinchetti, M.; Gloskovskii, A.; Nepijko, S. A.; Schoenhense, G.; Rochholz, H.; Kreiter, M. *Phys. Rev. Lett.* **2005**, *95*, 047601.
- (80) We note that mention of commercial product names is for information only; it does not imply National Institute of Standards and Technology recommendation or endorsement, nor does it imply that products mentioned are necessarily the best available for the purpose
- (81) Boyd, G. T.; Yu, Z. H.; Shen, Y. R. *Phys. Rev. B* **1986**, *33*, 7923.
- (82) Bohren, C. F.; Huffman, D. R. *Absorption and Scattering of Light by Small Particles*; Wiley VCH: Weinheim, 1983.



- (83) Xu, G.; Chen, Y.; Tazawa, M.; Jin, P. **2006**, 88, 043114
- (84) Chelvayohan, M.; C. H. B. Mee, C. H. B. *J. Phys. C Solid State* **1982**, 15, 2305.
- (85) Stuckless, J. T.; Moskovits, M. *Phys. Rev. B* **1989**, 40, 9997.
- (86) Sohn, Y.; Richter, J.; Ament, J., Stuckless, J.T. *Appl. Phys. Lett.* **2004**, 84, 76.
- (87) Schuck, P. J.; Fromm, D. P.; Sundaramurthy, A.; Kino, G. S.; Moerner, W. E. *Phys. Rev. Lett.* **2005**, 94, 017402.
- (88) Wiemann, C.; Bayer, D.; Rohmer, M.; Aeschlimann, M.; Bauer, M. *Surf. Sci.* **2007**, 601, 4714.

## Chapter 10

### Plasmonic Electron Photoemission Microscopy of Au Nanoholes and Nanohole Dimers

#### 10.1 Introduction

Metallic nanoparticle systems display qualitatively different optical properties from that observed in the bulk. In particular, optical extinction spectra of nanoparticles can reveal highly structured resonance behavior, in spite of a complete absence observed for corresponding samples of macroscopic dimensions. These nanoscale metal materials also possess many interesting electronic properties in addition to their unique optical properties. Synthetic and sample preparation techniques have progressed to a degree that permit study of the size and shape dependence for ensemble properties such as absorption and fluorescence emission spectra of noble metal nanoparticles.<sup>1-4</sup> The choice of the noble metals, predominately silver and gold, is motivated by the presence of strong surface plasmon resonances (SPR), which reflect excitation of a collective electron oscillation in the near ultraviolet and visible range. The convenience of visible laser excitation in this region, coupled with the strong size, shape and proximity dependence of the spectral properties, make these metal nanoparticles a logical target for a broad spectrum of research and commercial applications.<sup>5-10</sup>

Such plasmonic behavior not only influences far field measurements such as absorption and scattering, but also impacts the highly local electric fields in the sub-diffraction limited vicinity of the nanoparticle. This local enhancement of electric fields has been used to enable Raman characterization at the single molecule limit by surface enhanced Raman scattering (SERS).<sup>9,11-15</sup> The influence of plasmonic excitation on multi-photon processes has also been

studied. For example, second harmonic generation has been observed to be enhanced by metal nanostructures due to the intense local electric fields generated upon excitation<sup>16-19</sup>. Indeed, multiphoton processes are intrinsically more sensitive to such nanoscale enhancements due to the highly non-linear dependence on incident electric field. However, isolation of such plasmonic effects specifically from other nanoparticle contributions (e.g., geometry, surface roughness, laser frequency, etc.) has remained an ongoing challenge.

It has been long established that plasmonic resonances can significantly increase the rate of *single photon* photoemission from metal surfaces and particles.<sup>20-22</sup> Recently, *multiple photon* photoemission (MPPE) studies have begun to examine the role of plasmons in enhancing photoelectron yield from nanostructured materials.<sup>23,24</sup> Indeed, MPPE from metal nanoparticles removes several complications present in other studies (e.g., second harmonic generation), due to the absence of i) rigorous surface selection rules and ii) the need for high order electric field susceptibility materials. Specifically, MPPE has been shown to depend on the local electric field enhancements in the near field of the nanoparticle, which in turn can be rigorously modeled by plasmonic excitation theory.<sup>25-27</sup> This relatively simple combination of MPPE and optical microscopy, therefore, provides a novel access to probing single nanostructures with single electron counting sensitivity. A variety of nanostructures have been studied in SPIM, e.g. nanorods,<sup>25,26</sup> nanoshells, and nanocubes,<sup>25,27</sup> which has provided insights into the link between the local electric field and the photoemission yield. Most importantly, it is this powerful connection between i) near electric field distributions and ii) number of photoelectrons emitted that enables probing of sub-diffraction limited *near-field* effects due to nanostructures from an intrinsically *far-field* detection experiment.

By the superposition principle, one can readily extend these ideas of electric field enhancements due to the *presence* of isolated plasmonic nanostructures, to those of plasmonics explicitly arising from the *absence* of nanostructured materials. As the central focus of the present work, we have explored scanning electron photoemission microscopy dynamics of metal “anti-nanoparticles,” *i.e.*, strongly plasmonic 2D objects made by shadow lithographic formation of nanoscale *holes* in a thin Au metal film. By simple superposition arguments, the resulting vector fields arising from the Au nanohole should be similar in magnitude but opposite in sign for a nanodisk of the same diameter. Indeed, the general linear and non-linear optical properties of a nanoparticle and the associated “anti-nanoparticle” (*i.e.*, “nanohole”) are clearly intimately related.<sup>28,29</sup> Onuta *et al.* first took advantage of these superposition arguments and non-linear spectroscopy to investigate large monomer and dimer holes (300-1000 nm diameter) in relatively thick Au films (100-300 nm).<sup>30</sup> In particular, the absence of centrosymmetry at the Au thin film/nanohole interface could be exploited for second harmonic generation, which yielded spatially localized second harmonic generation (SHG) signals with strong polarization dependences for both monomer and dimer species.

The present work significantly extends both the concept and sensitivity of such studies into the ultrafast microscopy domain, specifically probing the plasmonic properties of nanohole monomers and dimers by multiphoton photoemission microscopy (MPPE). Specifically, we fabricate a thin film (height,  $h \approx 25$  nm) Au substrate containing holes with diameters both below ( $d \approx 60$  nm) and near ( $d \approx 500$  nm) the diffraction limit ( $\approx 700$  nm) by shadow mask lithography and spun cast polystyrene spheres. The sizes are chosen to explore how nanohole size and corresponding plasmonic properties influence the photoemission signals, as well as take advantage of the spatially resolved photoemission microscopy capabilities of the apparatus.

Complimentary vector information on local electric field enhancements is then also attained by studies as a function of laser polarization. In addition, both small ( $d \approx 60$  nm) and large ( $d \approx 500$  nm) nanohole dimers are investigated, which therefore probes the role of diffraction limit on spatial, frequency and polarization sensitivity of the photoemission event.

The paper is organized as follows. Section 10.2 presents details of the experimental and theoretical methods, while Sec. 10.3 describes photoemission results obtained from isolated nanohole monomers and comparison to computational modeling of the plasmonic electric field enhancement. Sec. 10.4 presents the corresponding results for spatial and polarization dependent photoemission from nanohole dimers, again correlated with computational predictions of the electric field enhancements. In addition, the observed polarization and spatial dependences are interpreted in the context of a simple model, which assumes appropriate 4-photon scaling of the photoemission signals with i) local volume and ii)  $8^{\text{th}}$  power of the local electric field enhancement. Sec. 10.5 presents further discussion about the similarities and difference from related geometries, while Sec. 10.6 summarizes the conclusions and suggests directions for future work.

## 10.2 Experiment

Isolated nanoholes are prepared by a simple shadow mask lithography procedure pictorially represented in Fig. 10.1. Low concentrations ( $10^8$  #/mL) of carboxylate functionalized polystyrene spheres (Invitrogen) of two different diameters ( $d = 60$  nm and  $500$  nm) are first spun cast on an ITO coated glass coverslip (Thin Film Devices, Inc). An uncoated copper TEM finder grid (EMS, LF400CU) is then secured on top of the coverslip and held in place with magnets. The sample is subsequently placed in a vacuum deposition chamber,

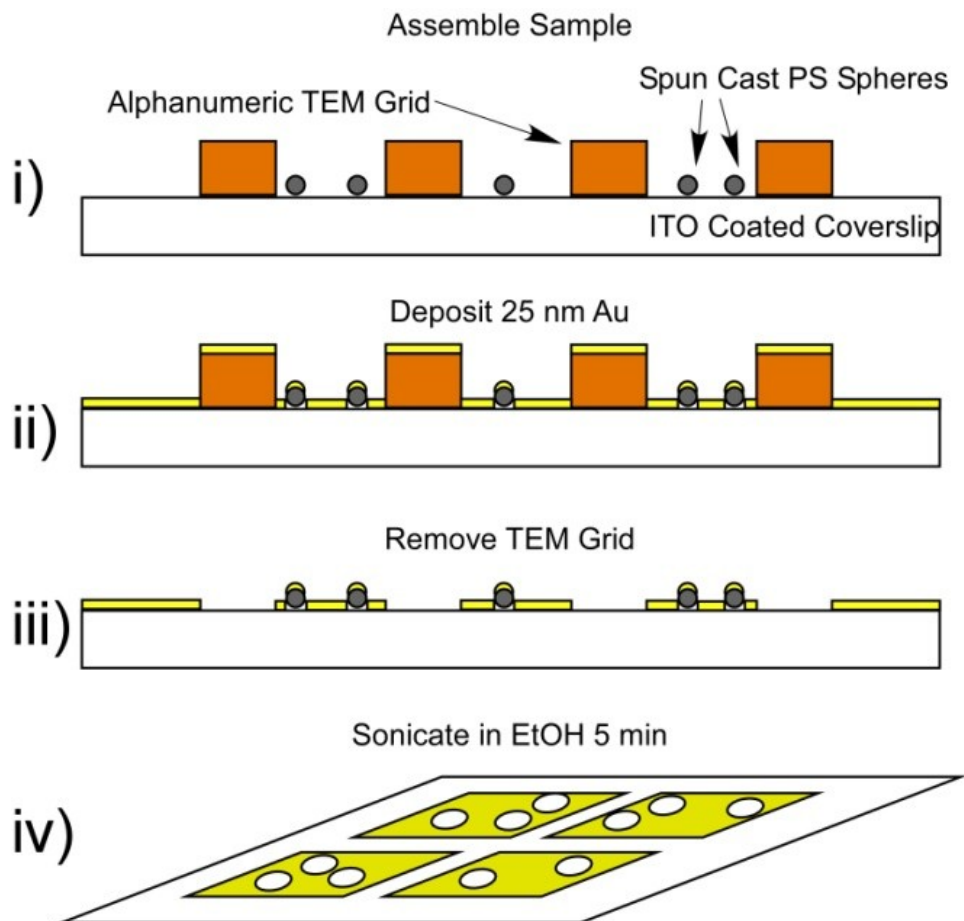


Figure 10.1: Sample preparation via shadow mask lithography. i) Polystyrene spheres (PS) are spin cast on an ITO coated coverslip. ii) Indexed TEM grid is placed on top and 25 nm of gold are deposited onto the sample. iii) TEM grid is then removed to expose the registration pattern. iv) Substrate is sonicated in ethanol for 5 minutes to remove the PS and leave nanohole monomers (and occasional dimers) in an indexed gold film.

where a 25 nm layer of gold is deposited via e-beam assisted vaporization at approximately 1 Å/s. The TEM grid is then carefully removed, with the resulting sample sonicated in ethanol for 5 minutes to detach the Au-capped PS spheres. The resultant substrate therefore contains isolated Au “nanohole” (and occasional “nanohole dimer”) shadows in the Au film, spatially registered with an easily addressable grid. The sample is checked for sufficiently low coverage (typically 0.7 objects /  $\mu\text{m}^2$ ) by dark field scattering before being loaded into the SPIM chamber.

The scanning photoionization microscopy (SPIM) technique is described here in brief, with more detailed descriptions available in the literature.<sup>31,32</sup> The fundamental frequency output from an ultrafast Ti:Sapphire laser system ( $\lambda \approx 800$  nm, 40 fs pulse width, 90 MHz repetition rate) is focused by an all-reflective microscope objective (NA = 0.65) inside a vacuum chamber maintained at  $\sim 5 \times 10^{-7}$  Torr. The focus ( $D \approx \lambda/(2NA) \approx 700$  nm) provides a diffraction limited spatial region in which the laser intensity (typically  $10^9$  W/cm<sup>2</sup> peak) is sufficient to eject electrons via multiphoton photoemission (MPPE). These electrons are then detected by a channeltron electron multiplier situated  $\sim 1$  cm above the nanosample platform, with the spatial region of interest raster scanned *in vacuo* by an open loop piezoelectric stage. The reported work function<sup>33</sup> of gold varies considerably in the literature ( $\Phi_{\text{Au}} = 4.6 - 5.1$  eV) due to surface preparation. However, for a typical estimate for clean, evaporated Au ( $\Phi_{\text{Au}} \approx 5$  eV), emission of single photoelectrons energetically requires absorption of 4 photons, which is confirmed by observation of a 4<sup>th</sup> order dependence of SPIM signal on laser intensity. Tapping mode AFM images of the samples are acquired using a 2-5 nm radius of curvature tip, which provide an invaluable one-to-one correspondence between nanostructure morphology and the observed SPIM signals.

The near-field distribution of electric fields of Au nanoholes and nanodimers are calculated via finite element methods in COMSOL (v4.2), with the predicted local electric field enhancements used to interpret the experimental results. The calculations are based on a three layer slab model comprised of i) a thin Au film containing the desired nanohole architecture, surrounded below and above by ii) a glass coverslip substrate and iii) vacuum, respectively. The nanostructured Au film is defined to be oriented in the xy-plane and has a thickness of  $h = 25$  nm to match the actual AFM measurements of the sample. The system is discretized using the built-

in free meshing algorithm, which defines elements as small tetrahedral regions and produces a mesh based on various user supplied constraints on the sample dimensions. The minimum element edge length is 2 nm in the 60 nm nanohole systems and 5 nm for the 500 nm systems, for a nanostructure radius of curvature to element ratio between 30:1 and 100:1. For all systems, the maximum element edge lengths were chosen to be 12 nm with a growth rate of 1.2, i.e., adjacent elements could grow at most by 20%. Convergence in these COMSOL predictions has been tested by calculations as a function of mesh sizes (e.g., 2 nm vs 3 nm) for the 60 nm nanoholes. As expected, such comparisons yield uniformly higher electric field enhancement factors for the more well defined edges, but are indistinguishable as a function of 3D spatial coordinate after renormalization. Finally, it is worth noting that the current choice of  $> 30:1$  radius of curvature to element ratios represents an order of magnitude improvement over previous studies, based on 8-10 nm minimum edge lengths for nanostructures with as small as 30 nm radii.<sup>30,34</sup> The bulk dielectric properties for gold are taken from previously reported tables.<sup>35</sup> Laser excitation at  $\lambda \approx 800$  nm is modeled as a linearly polarized plane wave starting in the glass surface and propagating towards vacuum in the z-direction. Due to the nanohole monomer/dimer architectural point group, only a single quadrant ( $x > 0, y > 0$ ) needs to be calculated, with the other three quadrants given by symmetry considerations. Even higher cylindrical point group symmetry is clearly available for the nanohole monomer structures, but we choose the lower point group to facilitate self consistent comparison between monomer and dimer nanohole behavior. The boundary conditions for the four sides are each set to properly match the linearly polarized plane wave excitation by being set as either a perfect electrical conductor (PEC) or perfect magnetic conductor (PMC).



The simulation proceeds in two stages, similar to a previous study of 3D nanocavities in a solid.<sup>36</sup> In the first step, the electric field is solved for a system comprising only a thin continuous Au film, with the grid mesh points defined as if the nanoholes were present. The resulting solution is found to match the analytic solution for a plane wave impinging on a thin film. The advantage of performing the simulation this way is to guarantee that the incident field is self-consistent at every mesh point, with no numerical artifacts that might arise from an analytic solution being applied to an arbitrary discrete mesh. The resulting electric field is then used as the background field in a second scattering calculation, which thereby determines the spatial dependence of the electric field enhancement due to the nanohole architecture. The exterior boundary condition for this second simulation step is represented by perfectly absorbing layers that absorb all out going waves without reflections. The resulting field enhancements are extracted as 2D slices through relevant planes, typically the top most surface of the film, and analyzed/processed in Matlab.

### **10.3 Nanohole Monomers**

#### *10.3a Experiment*

A sample AFM of an Au thin film section containing  $d = 60$  nm nanoholes is shown in Fig. 10.2A, with a scan at higher spatial resolution of an individual nanohole displayed as inset in the upper left corner. The corresponding SPIM image (with circularly polarized light) is shown below in Fig. 10.2B, which confirms that the photoemission signal arises primarily from the nanoholes, with a 100-fold lower background signal emitted from the gold film itself. As mentioned above, signals from the nanoholes are found to scale quite closely as  $I^4$  (inset Fig. 10.2B), consistent with the four 800 nm photons needed to overcome the work function for Au

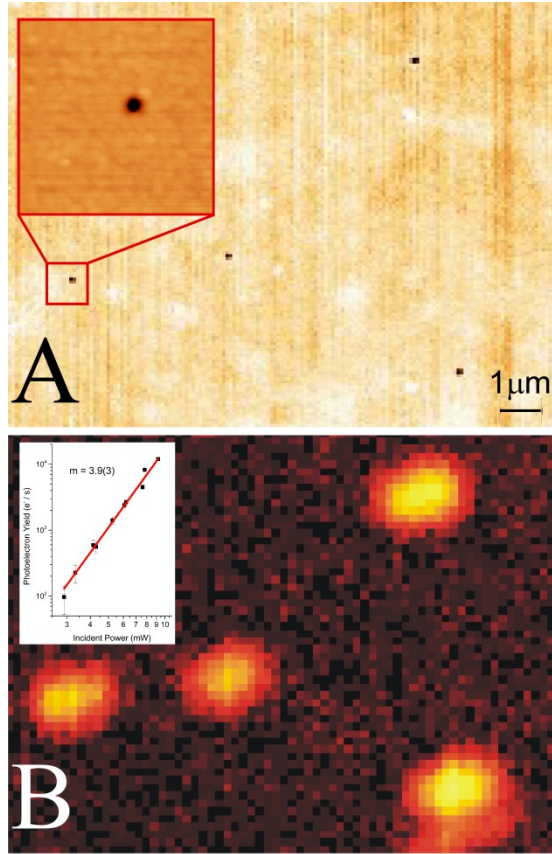


Figure 10.2: Sample AFM and SPIM images of *small* nanohole monomers *below* the diffraction limit ( $d \approx 60 \text{ nm} \ll \lambda$ ). A) AFM image: dark and light represent bare ITO substrate and 25 nm thick Au. (inset)  $1 \mu\text{m} \times 1 \mu\text{m}$  zoom of an individual nanohole. B) Correlated SPIM image from this same set of nanoholes, with peak signals and background of  $10^8 \text{ e}^-/\text{s}$  and  $10^2 \text{ e}^-/\text{s}$ , respectively  $1.4 \times 10^{10} \text{ W}/\text{cm}^2$ .

( $\Phi_{\text{Au}} \approx 5 \text{ eV}$ ). The spatial FWHM of the photoemission signal, obtained from a two dimensional Gaussian fit to the data, is  $445(8) \text{ nm}$ . The one photon diffraction limit of  $D = 1.22\lambda / 2NA \approx 750 \text{ nm}$  ( $NA = 0.65$ ,  $\lambda = 800 \text{ nm}$ ) is 67% larger than observed experimentally, due to the multiphoton nature of the excitation event. Specifically, a Gaussian spot size for an N-photon process scaling with  $I^N$  should be approximately  $D_n = D / \sqrt{N} \approx 375 \text{ nm}$ , which is much closer to and even slightly smaller (19%) than the observed experimental value.

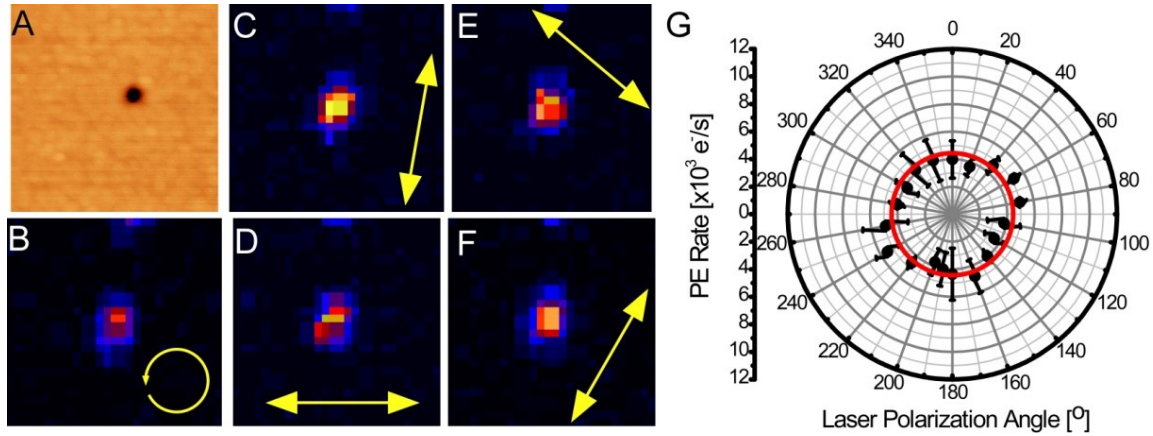


Figure 10.3: Sample polarization data from a *small* nanohole monomer ( $d \approx 60$  nm). A)  $1 \mu\text{m} \times 1 \mu\text{m}$  AFM of a 60 nm diameter nanohole. SPIM images for circular (B) and a series of linear (C-F) polarizations. G) Polar plot of photoelectron yield as a function of incident polarization angle, revealing a nearly isotropic dependence on laser excitation.

As a result of the shadow mask lithography method and uniformity of the polystyrene spheres, the nanohole monomers exhibit a high degree of cylindrical symmetry. By way of confirmation, the photoemission signal strengths for the nanoholes have been explored as a function of incident laser polarization. A subset of these data for  $d = 60$  nm nanoholes is shown in Fig. 10.3 for both circular (B) as well as four different linear polarizations (C-F), which indicates no preferred dependence on polarization for photoemission strength. More quantitatively, we can integrate up these signals for the full set of data to obtain the total photoemission rate. The polar plot (in Fig 10.3G) represents the full polarization data set as a function of linear polarization, which within uncertainty confirms that the emission is independent of the incident laser polarization angle, as expected for a 2D azimuthally symmetric object.

Corresponding studies of the much larger (i.e., non-diffraction limited)  $d = 500$  nm nanoholes provide an even more interesting behavior as a function of laser polarization. First of all, the AFM images of now are sufficiently high resolution to reveal, as anticipated, a nearly

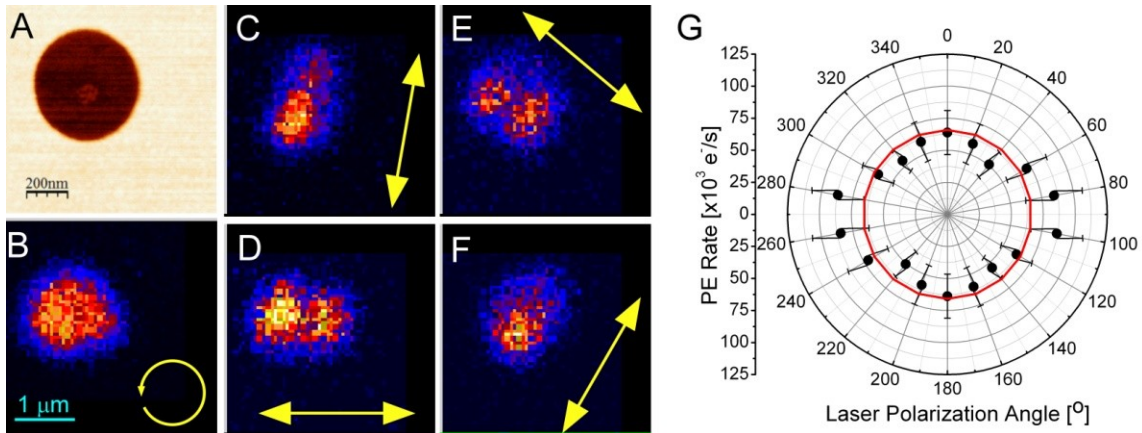


Figure 10.4: Sample polarization data from a *large* nanohole monomer *comparable* to the diffraction limit ( $d \approx 500 \text{ nm} \approx \lambda$ ). A)  $1 \mu\text{m} \times 1 \mu\text{m}$  AFM of a 500 nm diameter hole. B) SPIM image with circularly polarized incident excitation. C-F) SPIM images with linear polarization. Note that the integrated photoelectron yield as a function of incident polarization (G) is insensitive to the laser axis, despite the clear anisotropy evident in the spatial images.

perfect circular shape with edges that appear quite smooth down to  $< 5 \text{ nm}$  scale. A SPIM image taken with circularly polarized light is presented immediately below (Fig 10.4B) and reveals a single broad, cylindrically symmetric feature with a spatial FWHM of  $900(30) \text{ nm}$ . This is in reasonably good agreement with expectations, as the SPIM signal arises from the convolution of a cylindrically symmetric top hat function of width 500 nm with a diffraction limited spot size of  $\text{FWHM} \sim 400 \text{ nm}$ . However, a qualitatively different spatial image is observed when this same nanohole feature is investigated with linearly polarized light. Specifically, sample images (shown in Figs. 10.4 B-D) reveal that the photoemission signals split into two lobes localized i) on opposing sides of the 500 nm nanohole and ii) with near diffraction limited FWHMs comparable to 60 nm nanoholes. Interestingly, the two lobes in the SPIM images are always oriented *parallel* to and therefore always *rotate with* the incident linear laser polarization, which will be explored further below with theoretical model simulations. Nevertheless, the *integrated*

photoemission signal (Fig. 10.4G) is still best described by a perfectly isotropic distribution, which is again similar to our previous observation in Fig 10.3 for the 60 nm nanohole samples.

### 10.3b Theory

In order to interpret these results, we have implemented a detailed numerical modelling of the experimental signals based on finite element simulations, which permit us to explicitly incorporate plasmonic, laser polarization and finite spatial resolution effects of the experiment. First of all, the expectation from simple superposition arguments is that the spatial distribution of the plasmon (and thus electric field enhancement) around a nanohole should be closely related to that of a nanodisk. Indeed, experiments have shown that the resonances of comparable sized nanodisk and nanohole structures do have similar resonance wavelengths.<sup>28</sup> However, it is worth stressing that this is only rigorously true in the thin film limit for a dipolar plasmon mode. For example, Käll and coworkers have done several optical characterizations of different disk/hole systems and compared their results to a simple electrostatic theory for an oblate spheroid.<sup>28,29,37</sup> In actuality, they find that the true inverse of a *nanodisk* would be a *nanocavity* embedded in a 3D solid, for which the plasmon resonance is strongly *blue-shifted* to higher frequencies. Furthermore, their work has determined that nanoholes and nanodisks have similar resonances simply because the nanohole is unable to support significant polarization in the z-direction due to its 2D geometry. This absence of polarizability leads to a correspondingly strong *red shift* in the plasmon peak, which tends to make thin nanodisks and 3D nanoholes resonate with a more similar plasmon frequency.

Interestingly, the Käll studies also point out that nanoholes should have much *broader* resonances than nanodisks of the same size, which can be attributed to surface plasmon

polaritons (SPPs) that provide an additional relaxation pathway present only in nanoholes. SPPs have a decay length that can exceed 10  $\mu\text{m}$  in some 3D systems; however in thin 2D films, the decay length is found to be much less than 1  $\mu\text{m}$  due to scattering off the nearby glass surface.<sup>37</sup> The presence of a SPP has been found to be particularly relevant for experiments at high nanohole spatial density, where the average distances between objects is less than 500 nm and therefore the holes are optically coupled.<sup>38</sup> In the present samples, however, the average experimental distances between nanoholes is in considerably excess of 1  $\mu\text{m}$ ; thus SPP coupling between nanoholes can be neglected, though the spectral resonance of an isolated nanohole should still be slightly broadened.<sup>28</sup>

In order to facilitate a more detailed comparison with experiment, we accurately model such plasmonic multiphoton photoemission properties with finite element simulations for electric fields in the vicinity of a nanohole. In particular, we are interested in the spatial dependence of the local electric field *enhancement*,  $\eta_{ENH} = |E/E_0|$ , i.e., the ratio of field in the presence of the nanohole to the reference field for a continuous film<sup>39-41</sup>. These enhancement factors at 800 nm for small ( $d = 60$  nm) and large ( $d = 500$  nm) nanoholes are calculated in COMSOL and shown in Figs. 10.5 A and C, respectively, for an xy-slice through the top surface of the film (i.e.,  $h = 25$  nm) under horizontally polarized laser excitation conditions. Interestingly, the plasmonic enhancements are quite similar in each of the two cases, i.e., approximately  $\eta_{ENH}$  is 5-fold larger at opposite edges of the circle where the local tangent is *perpendicular* to the incident polarization compared to edges for which the local tangent is *parallel* to the incident polarization (Table 10.1). This immediately explains the lack of any laser polarization sensitivity to the integrated photoemission signals for both nanohole sizes, since circular symmetry always provides nanohole tangent edges pointing in the right direction for such enhancements to

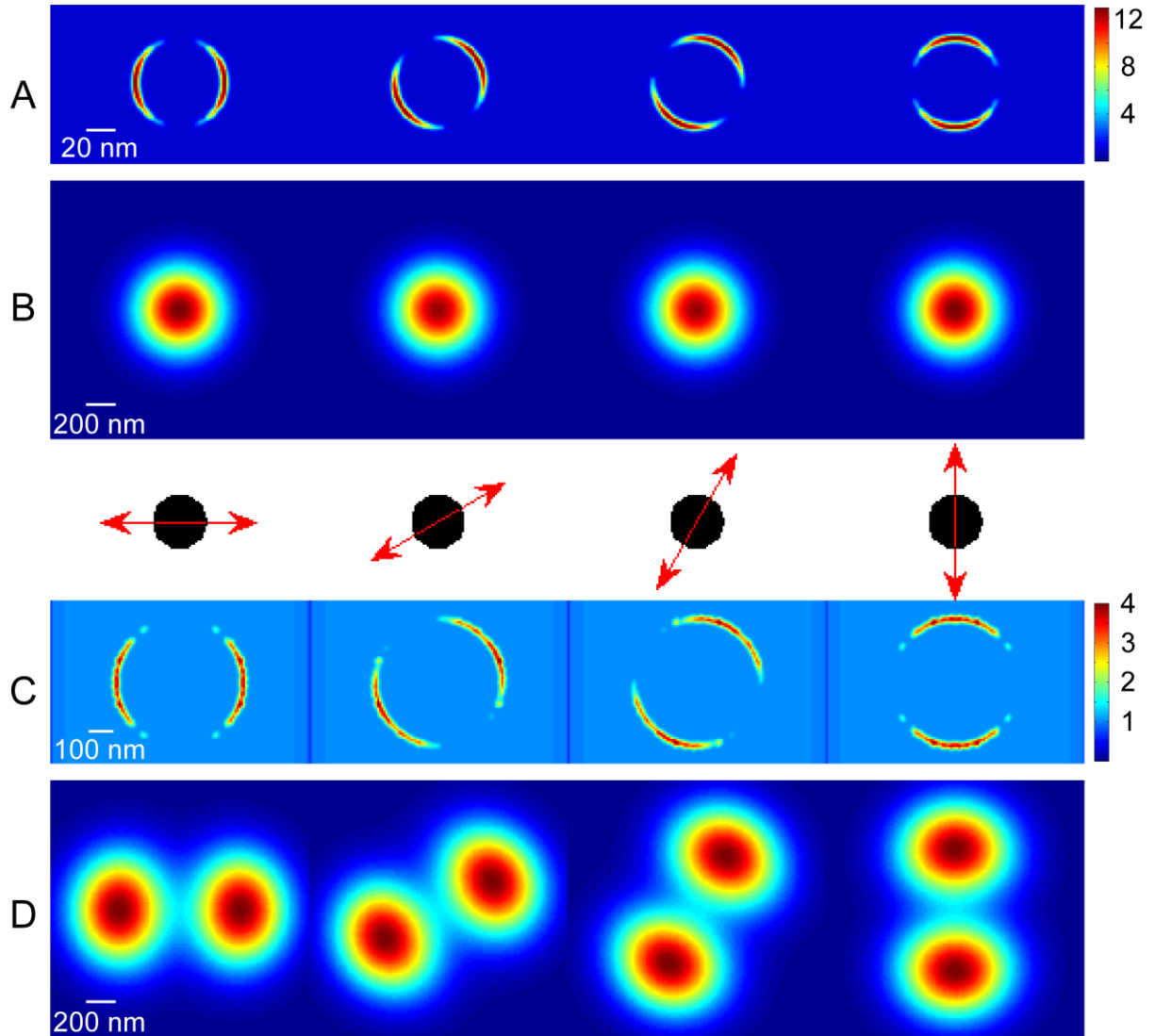


Fig 10.5: COMSOL predictions for polarization dependence of a *small* ( $d \approx 60 \text{ nm} \ll \lambda$ ) nanohole monomer (upper panels A,B) and a *large* ( $d \approx 500 \text{ nm} \approx \lambda$ ) nanohole monomer (lower panels C,D) for the selected polarizations shown in the middle. (A) For small nanohole monomers, the field enhancement factor ( $\eta_{\text{ENH}}$ ) remains perfectly aligned parallel with the incident laser. Color scale is identical for each row, with  $\max \eta_{\text{ENH}} = 25$  for A. However, when modeled by  $\eta_{\text{ENH}}^8$  averaged over the incident electric field distribution, the SPIM predictions (B) correctly reveal no anisotropic dependence on laser polarization. For large nanohole monomers both  $\eta_{\text{ENH}}$  (C), with  $\max \eta_{\text{ENH}} = 7$ , and SPIM (D) signals reveal spatially resolved variations in the images, but still yield the same integrated total intensity at each polarization, as expected for any azimuthally symmetric nanostructure.

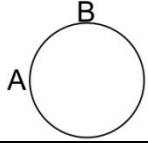
Nanohole		
		
Size	Left/Right Edge (A)	Top/Bottom Edge (B)
Small	26	5
Large	7	2

Table 10.1: COMSOL enhancement factors for small ( $d \approx 60 \text{ nm} \ll \lambda$ ) and large ( $d \approx 500 \text{ nm} \approx \lambda$ ) nanohole monomers at specific locations upon laser polarization perpendicular to the nanohole tangent edge at point A.

promote photoemission. Secondly, it provides a simple explanation for why the alignment in the spatial images for the larger nanoholes rotates with the laser polarization. Finally, it clearly identifies the essential reason for the absence ( $d = 60 \text{ nm}$ ) or presence ( $d = 500 \text{ nm}$ ) of spatial variation in the corresponding SPIM images. Specifically, the opposing regions of peak enhancement ( $\eta_{ENH} \approx 25$ ) for the small nanoholes are too close to be resolved, whereas for the larger nanohole species, the photoemission signals are sufficiently far apart to begin to contribute independently.

In order to interpret the observed spatial dependence of the nanohole MPPE images more quantitatively, we propose a model based on the multi-photon nature of the emission that also includes the spatial dependence of the plasmon excitation. In the simplest picture, the observed photoemission yield will be proportional to the *local* enhancement field raised to the  $(2n)^{\text{th}}$  power ( $PE \propto \eta_{ENH}^{2n}$ ), where  $n$  is the order of the photoemission process, times the differential area over which this field enhancement is maintained.<sup>26,27</sup> Therefore, 2D images can be simulated by a series of calculations at each point in the image. First, the enhancement factor ( $\eta_{ENH}$ ) image is multiplied by a Gaussian centered at a given  $xy$ -coordinate which represents the incident laser electric field to yield the map of the local electric field under illumination. Each pixel in this



image map is raised to the 8<sup>th</sup> power, due to the 4 photon nature of the photoemission process, and then the image is integrated to obtain the expected photoemission yield for the laser centered on that xy-coordinate. This procedure is repeated on a 2D grid across the feature to generate a map of the expected MPPE images. This process is equivalent to convolution of the electric field enhancement factor raised to the 8<sup>th</sup> power with the Gaussian instrument response function for a diffraction limited 4-photon process (FWHM = 375 nm), which is computationally faster and thus used for the generation of all simulated MPPE spatial images.

The results of these calculations are summarized in Figure 10.5 for the two different sized nanoholes. In Fig. 10.5A, we present spatial heat maps of  $\eta_{ENH}(x,y)$  for small ( $d = 60$  nm) nanoholes at a series of incident laser polarizations, which clearly reveals the synchronous rotation of the field enhanced region with polarization angle. By way of contrast, however, Fig. 10.5B illustrates the spatial convolution of  $\eta_{ENH}^8(x,y)$  over the instrument response function. Note that the spatial extent of the “hot spot” ridge regions ( $\eta_{ENH} \approx 20$ ) for a  $d = 60$  nm nanohole are considerably smaller than the diffraction limit, and thus the image appears as a single diffraction limited, nearly isotropic spot. For the larger nanoholes, on the other hand, the distance between the opposing hot spot ridge regions in  $\eta_{ENH}(x,y)$  is  $\approx 500$  nm (see Fig. 10.5C), which makes the predicted photoemission images appear as two nearly resolved peaks when excited with a linearly polarized focused laser beam at 800 nm. Once again, the directional alignment of the two “hot spots” in the enhancement field directly tracks the incident polarization, but which are now at sufficiently large distances to survive convolution of  $\eta_{ENH}^8(x,y)$  over the instrument response. Thus, the SPIM images themselves are also bi-lobal and rotate synchronously with laser polarization, as experimentally observed. Furthermore, the separation between peaks is quite uniformly 530(5) nm, which is of course consistent with the

500 nm nanohole size monitored by AFM. In summary, these results clearly indicate that photoemission for both small and large nanohole monomers occurs from the edge regions aligned *parallel* to the incident laser polarization, where the electric field enhancement factor is largest.

## 10.4 Nanohole Dimers

### 10.4a Experiment

As a rare but welcome accident, two spheres occasionally adhere in the spin coating process and fortuitously result in a “nanohole dimer” after deposition. While conditions are such that this is an intentionally low probability Poisson occurrence ( $\lambda < 0.01$ ), registry of the sample permits convenient return to and study of specific nanodimers identified by dark field images or AFM. By way of example, an AFM image of such a nanohole dimer formed from two 60 nm nanoholes is shown in Fig. 10.6A, along with the corresponding SPIM images of the same dimer under a variety of circular (B) and linear (C-F) polarization conditions. Due to the lower point group symmetry of the dimer, a strong polarization dependence is now observed, in which the photoemission signal peaks for laser polarization *perpendicular* to the dimer axis. This dependence is more quantitatively captured in the right most panel (Fig. 10.6G), which reveals a sharply peaked angular distribution well described by  $\cos^8(\theta)$ . This is of course entirely consistent with i) an  $|E_0| \cos(\theta)$  projection of the incident field along the preferred dimer axis, in conjunction with ii) sensitivity in photoemission to the 8<sup>th</sup> power of the laser electric field enhancement factor  $\eta_{\text{ENH}}(x,y)$ . This angular behavior is also similar to the polarization dependence noted for gold nanorods, where the photoemission event is dominated by resonant plasmonic excitation along the long axis<sup>25</sup>.

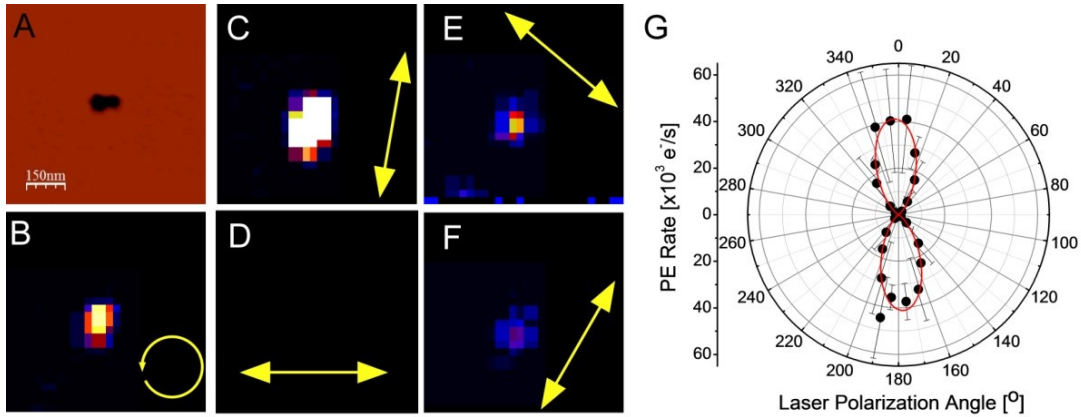


Figure 10.6: Sample correlated AFM and SPIM data for a *small* ( $d \approx 60 \text{ nm} \ll \lambda$ ) nanohole dimer. A) 600 nm x 600 nm AFM. SPIM images with circular (B) and various linear (C-F) polarizations of incident excitation, each spatially *isotropic* with respect to the nanohole dimer axis. G) Integrated photoelectron yield as a function of incident laser polarization, demonstrating a strong  $\cos^8(\theta)$  sensitivity *perpendicular* to the nanohole dimer axis.

Although the exact same plasmonic considerations are at play, the corresponding behavior for larger nanohole dimers ( $d = 500 \text{ nm}$ ) is fundamentally different, as summarized in Fig. 10.7 for a near horizontal dimer alignment. Indeed, guided by the previous nanohole monomer studies, the reasonable expectation might be that for circularly polarized excitation, the photoemission feature would cover the entire dimer structure and therefore be broadened *horizontally* by almost  $2 \times 500 \text{ nm} = 1000 \text{ nm}$ . Instead, we experimentally see a *vertically* elongated feature, *perpendicular* to the dimer axis that is considerably smaller than the entire nanohole structure, with a horizontal FWHM closer to 450 nm (see Fig. 10.7B). Secondly, similar to behavior of the large nanohole monomers, two peaks in the images are observed for linearly polarized excitation. Interestingly, however, these two peaks now maintain a *fixed* relative orientation *perpendicular* to the dimer axis, which *does not rotate* with the incident laser polarization, as illustrated in Fig. 10.7C-F. However, the most dramatic change is in the integrated SPIM intensity as a function of incident laser polarization, as summarized in a polar

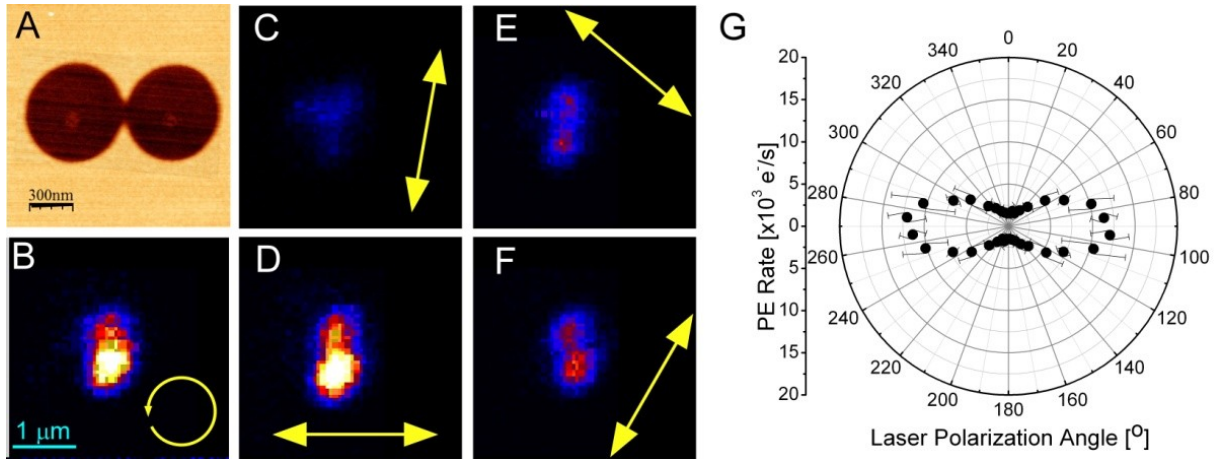


Figure 10.7: Sample data for a *large* ( $d \approx 500 \text{ nm} \approx \lambda$ ) nanohole dimer. A)  $1.2 \mu\text{m} \times 1.2 \mu\text{m}$  AFM of a 500 nm hole dimer. SPIM image with circular (B) and various linear (C-F) polarization, each spatially *perpendicular* to the nanohole dimer axis. G) Integrated photoelectron yield as a function of incident laser polarization which reveals a strong  $\cos^8(\theta)$  sensitivity *parallel* to the nanohole dimer axis.

plot in Fig. 10.7G. Note that the AFM of this exact dimer is shown explicitly in Fig. 10.7A, which is also in the same sample orientation as the subsequent SPIM images in Fig. 10.7B-G. Remarkably, now the alignment producing the largest electron photoemission yield for the larger nanohole dimers is *parallel* to the dimer axis, i.e., exactly *opposite* to what was witnessed for the smaller nanohole dimers. Furthermore, the corresponding SPIM images reveal a clear propensity for spatial photoemission i) from the *central region* and ii) along an axis *perpendicular* to the nanohole dimer. Such a major reversal in MPPE angular behavior for the larger ( $d = 500 \text{ nm}$ ) vs. smaller ( $d = 60 \text{ nm}$ ) nanohole dimers suggests a qualitative difference in the physical site for electron photoemission, which we explore further below with COMSOL simulations.

#### 10.4b Theory

Details of the dimer theoretical analysis are the same as previously discussed with respect to the nanohole monomers. Simulation of the local electric fields reveals the origin of the

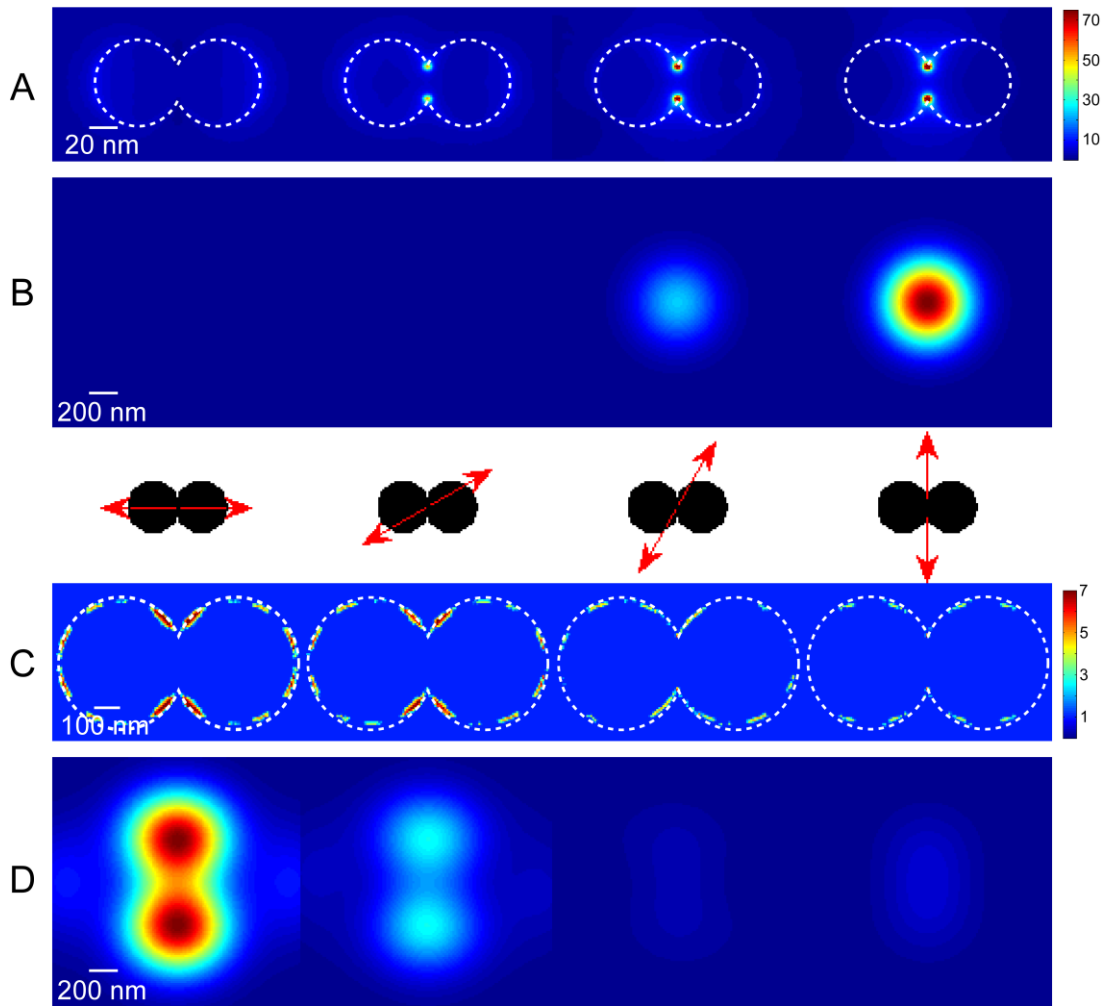


Figure 10.8: COMSOL simulations for a *small* ( $d \approx 60 \text{ nm} \ll \lambda$ ) nanohole dimer (upper panels) and a *large* ( $d \approx 500 \text{ nm} \approx \lambda$ ) nanohole dimer (lower panels) for the selected polarizations shown in the middle. (A) Spatial images of the enhancement field ( $\eta_{\text{ENH}}$ ) as a function of incident polarization. Color scale is identical for each row, with  $\max \eta_{\text{ENH}} = 200$  in the vicinity of the interstitial cusps for *perpendicular* excitation. (B) SPIM signal predictions (based on  $\eta_{\text{ENH}}^8$  convoluted over the incident laser electric field) reveal strong intensity variation with incident polarization but no anisotropy in the spatial image. (C) Spatial images of enhancement field dimers ( $\eta_{\text{ENH}}$ ) for large nanohole dimers as a function of incident laser polarization. Color scale with  $\max \eta_{\text{ENH}} = 10$  in the vicinity of the wedges for *parallel* excitation. (D) SPIM predictions, which predict strong intensity variations with polarization *opposite* to those of the small nanohole dimers, as well as anisotropy in the spatial image *perpendicular* to the nanohole dimer axis.

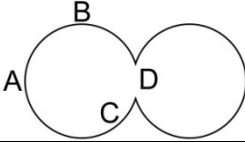
Nanohole Dimer					
					
Size	Incident Polarization (Relative to Dimer Axis)	Left/Right Edge (A)	Top/Bottom Edge (B)	Wedge (C)	Cusp (D)
Small	Parallel	15	4	4	<1
	Perpendicular	1.5	5	15	180
Large	Parallel	7	4	12	2
	Perpendicular	1	2	2	9

Table 10.2: COMSOL enhancement factors for small ( $d \approx 60 \text{ nm} \ll \lambda$ ) and large ( $d \approx 500 \text{ nm} \approx \lambda$ ) nanohole dimers upon two orthogonal laser polarizations: parallel or perpendicular to the dimer axis. A and B are locations of local curvature similar to the monomer in Table 1. C (wedge) and D (cusp) are curvature unique to dimers and where the enhancements are found to be largest. Note that for small dimers the largest value is observed at the cusp under *perpendicular* excitation, while for large dimers the largest enhancement is located at the wedge under *parallel* excitation.

profound differences observed between small and large dimers (Table 10.2). Fig. 10.8A displays the calculated electric field enhancement for a small nanohole dimer, upon excitation with various incident polarization directions relative to the dimer axis. Note that the color scales are all substantially expanded from those in Fig. 10.5 (see caption). Enhancement factors for laser excitation parallel to the dimer axis (left most panel in Fig. 10.8A) are  $\approx 40$ , which are larger than, although still comparable to, the maximum values observed in the corresponding nanohole monomers.

However, what is even more remarkable is the dramatic increase in electric field enhancement as a function of laser polarization. For the case of perpendicular excitation, the COMSOL calculations predict an order of magnitude greater enhancement factor of  $\eta_{\text{ENH}} \approx 400$ . For a 4-photon photoemission process and a 10-fold difference in electric field enhancement factor, one therefore already predicts a  $10^8$ -fold modulation in SPIM signals between horizontal and vertical polarization. This is nicely demonstrated in Fig. 10.8B, which presents a spatial convolution of  $\eta_{\text{ENH}}^8(x,y)$  over the instrument response function, and thereby illustrates the

enormous contrast in signal for excitation *perpendicular* vs. *parallel* to the nanohole dimer axis. We note that this behavior is in excellent agreement with the polar SPIM data plot in Fig. 10.6G, which is consistent with a perpendicular/parallel contrast in excess of 100:1.

The enhancement fields for the  $d = 500$  nm nanohole dimers (Fig. 10.8C) reveal many qualitative differences and similarities with respect to the  $d = 60$  nm diffraction limited counterparts. Most importantly, the electric field enhancement factors are now maximized for excitation *parallel* to the dimer axis and in excellent agreement with what is observed experimentally. Secondly, when the polarization is parallel to the dimer axis, the enhancement is no longer localized at opposite edges of the dimer. Indeed, although there are clearly much more broadly distributed regions of enhancement predicted than for the  $d = 60$  nm nanodimer species, the region of greatest electric field enhancement is still very much dominated near the dimer cusps. The regions along the sides of cusp (*i.e.* wedges) become the source of strongest enhancement and are comparable to that observed at the cusps in the orthogonal polarization. Additionally, the region over which the enhancement occurs is significantly larger in area, which results in a much greater contribution to photoemission yield for incident field parallel to the dimer axis. These two quantities, i)  $\eta_{\text{ENH}}$  and ii) active area, are incorporated by the convolution step in our model for photoemission images, as shown in the lower half of Fig. 10.8D. The predicted images agree well with the data presented in Fig. 10.7, which results in two peaks that do not rotate with incident polarization. Furthermore, photoemission signals with perpendicular excitation are predicted to be diminished with respect to parallel excitation, as indeed seen in the actual SPIM data images.

## 10.5 Discussion

The multiphoton photoionization of isolated nanoholes provides many interesting results that reveal details on the local electric field enhancements of various structures. The easiest understood system is the nanohole monomer, as summarized in Figs. 10.3-4. These simple structures reveal considerable differences in the MPPE spatial maps between small and large sizes, indicating significant spatial differences in the underlying enhancement fields. As expected, however, the total electron yield is experimentally found to be independent of incident polarization. Finite element simulations reveal identical polarization dependences for the enhancement fields for both small and large sizes. A clear spatial dependence upon changing polarization arises when the physical size of the nanohole monomer is included relative to the diffraction limited resolution. The same spatial dependence has also been observed in related experiments using SHG in thick films ( $> 100$  nm Au) containing large ( $> 500$  nm diameter) holes.<sup>30</sup> Specifically, they observe quite similar spatial maps, with peaks in signal parallel to the incident polarization, though with less sharpness due to their technique being two photon and thus only proportional to  $\eta_{\text{ENH}}^4$  compared to our  $\eta_{\text{ENH}}^8$ . As expected, the difference between small and large nanohole monomers is found to be quite minimal.

Nanohole dimers, on the other hand, provide a richer and more complex architecture with qualitative differences in the polarization dependences observed both experimentally and theoretically. First of all, a strong dependence of total electron yield on laser polarization is experimentally observed for both small and large nanohole dimers, as identified in Figs. 10.6 and 10.7. However, this dependence on laser polarization angle is clearly qualitatively different (specifically shifted by 90 degrees) for the small vs. large nanohole dimer architecture, as also evident in Figs. 10.6G and 10.7G. We can make a more quantitative comparison between our



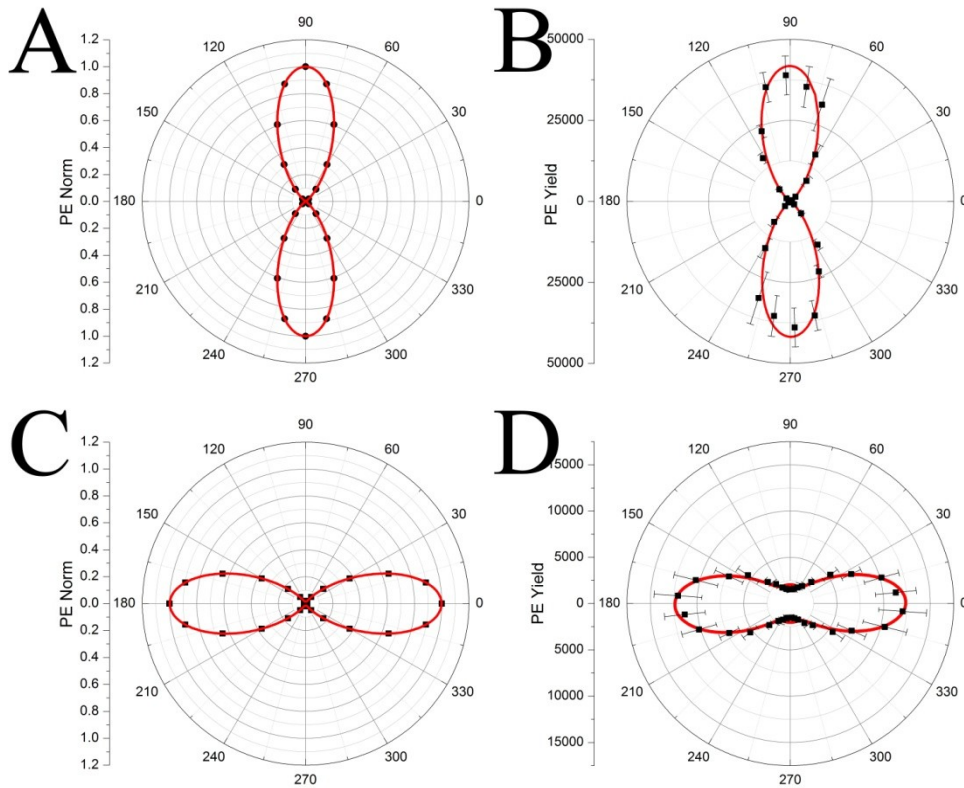


Figure 10.9: Theoretical (A,C) and experimental (B, D) polarization dependences for horizontally aligned nanohole dimers. Small nanohole dimers (60 nm, A) reveal a strongly *perpendicular* anisotropy, in excellent agreement with experiment (B). For the larger nanohole dimers (500 nm), theory (C) correctly predicts a predominantly *parallel* anisotropy in agreement with experiment (D), but underpredicts small non-zero contributions at *perpendicular* geometries.

theoretical modeling and experimental results by closer inspection of the polarization dependence of the total photoelectron yield relative to the dimer axis. To be consistent with experiment, the theoretical images are integrated at each angle to determine the total signal level from an individual nanohole dimer as a function of incident polarization, with the theoretical and experimental results summarized in Fig. 10.9A,C and B,D, respectively. From a least square fit to  $\cos^n(\theta)$ , theoretical results for the small nanohole dimers (Fig. 10.9A) are found to be very closely proportional to  $\cos^8(\theta)$ , with a parallel/perpendicular contrast ratio in excess of  $\sim 10^5$  between the two orthogonal directions. This is in excellent agreement with the experimental data

(Fig. 10.9B), which can also be nicely fit by a  $\cos^8(\theta)$  distribution, as shown in the upper right panel. This can be most simply interpreted as arising from two facts: i) that the photoionization process scales with the 8<sup>th</sup> power of the local electric field and ii) that the plasmonic excitation for a small nanohole dimer below the diffraction limit arises from a single dipole-like excitation, similar to that previously observed in gold nanorods<sup>26</sup>.

The results for the large nanohole dimers are qualitatively similar but differ in two important ways. In the case of large nanohole dimers, the least squares fits to the theoretical results predict a polarization dependence slightly better described by a  $\cos^7(\theta)$  instead of  $\cos^8(\theta)$  distribution. Simply stated, this is due to the longer range spatial extent of the predicted electric field enhancements, which brings the system further away from the strict dipole-like excitation limit and therefore slightly softens or blurs the angular dependence. This blurring is of course also true for excitation at the orthogonal polarization, which for any purely dipole-like dependence would be identically zero but in fact is now finite. Indeed, as shown in Fig. 10.8C, this is due to the presence of non-zero electric field enhancement factors for both polarizations. We can take this into account by summing a constant isotropic term into our  $\cos^7(\theta)$  model, which yields theoretical contrast between the two orthogonal directions only on the order of  $\sim 50:1$ . Though small, the presence of such an isotropic term is clearly real, as can be seen in the experimental data for the large nanohole dimer in Fig. 10.9D. Consistent with our treatment of the theoretical predictions, the red line represents a similar fit to a  $\cos^7(\theta)$  distribution superposed with an additional angle independent term. Note that the magnitude of the isotropic offset observed experimentally is considerably larger (approximately a factor of 10) than that predicted by the theory, but the  $\cos^7(\theta)$  angular dependence is described relatively well.

In contrast with monomer-based architectures, the corresponding nanoparticle dimers are often found to behave rather uniquely in many experimental venues, such as luminescence<sup>42</sup>, fluorescence enhancement of molecules<sup>43</sup>, or surface enhance Raman scattering<sup>9,14,44,45</sup>. One often quoted reason for the unusually high photophysical activity of dimers is that the physical gap between dimers is where the largest enhancement fields are predicted to be observed<sup>46-48</sup>. Moerner and coworkers exploited this local electric field enhancement in bowtie nanoantennas to detect single molecule fluorescence which showed an enhancement as large as a factor of 1340 times<sup>43</sup>. The high local electric fields have also been used to generate high-harmonic (17<sup>th</sup> harmonic,  $\lambda=47$  nm) of the incident light in the extreme-ultraviolet using an array of bowtie nanoantennas<sup>49</sup>. Other closely related systems are the triangular “bowtie apertures,” which have been studied thoroughly by Xu and coworkers with near-field methods and which reveal maximal electric field when the laser polarization is aligned across the gap<sup>50-53</sup>. One common feature in all these previous studies is the nanoparticle size; these bowtie structures typically with less than 100 nm edge lengths are most comparable to our 60 nm nanohole dimers. One might therefore expect a similar electric field enhancement dynamics in the 60 nm nanohole dimers to those seen in bowtie systems, where in our architectures the effective bowtie is formed by the gap structure located at the cusps. From such a picture, the most intense local electric field enhancement factors would be achieved when the incident polarization is *perpendicular* to the dimer axis, and therefore aligned with the gap, which is in excellent agreement with both experiment photoemission yields and theoretical predictions.

Though clearly governed by the same plasmonic physics, the larger nanohole dimers behave quite differently, where now the strongest total electron yield occurs when the incident electric field is *parallel* rather than perpendicular to the dimer axis. It is still the case that the

bowtie type excitation of the cusp regions is present for excitation perpendicular to the dimer axis; however excitation *parallel* to the large nanohole dimer axis results in enhancement factors of at least comparable magnitude. Furthermore, as discussed previously, the total electron yield is not merely determined by the absolute magnitude of these enhancement factors, but also by the effective photoemission area over which this occurs. Indeed, this latter contribution proves to be the dominant reason why the large and small nanohole dimers show a different polarization dependence. This is beautifully confirmed from the COMSOL calculations shown in Fig. 10.8C, which reveal a very strong and highly localized “hot spot” in electric field enhancement precisely at the bowtie-like cusps for perpendicular excitation (right side panel), but which is simply overwhelmed by the much larger areas of comparable electric field enhancement as the wedges obtained for parallel excitation (left side panel). This is in good agreement with effect observed in second harmonic generation (SHG) studies from large ( $> 500$  nm diameter) dimers in thick films by Onuta et al.<sup>30</sup> In these studies, nearly equal signal intensities were noted for both parallel and perpendicular excitation for a two photon process such as SHG, with similar spatial maps to those in Fig. 10.8C. This further supports that nanohole dimer structures with dimensions near or above the diffraction limit can lead to local field enhancement patterns fundamentally quite different from those of smaller nanohole dimers with more purely dipole like excitation patterns.

As a final comment, it is also worth noting that neither small nor large nanohole dimers behaves as a simple linear combination of two nanohole monomers. By way of example, consider two touching nanoholes aligned horizontally, as shown in Table 10.2. For vertically polarized excitation, i.e., perpendicular to the dimer axis, the simple superposition of two monomers would lead to a pair of enhancement fields located at the upper and lower curved

regions and displaced by the nanohole diameter (i.e., region B with suitable symmetry reflections). By way of contrast, the COMSOL simulations predict the region of maximum electric field enhancements to be at the cusps (region D) for small dimers or an expanded area (regions D and C) for the larger dimers. In neither size limit is the maximum enhancement localized around region B. Alternatively, if we consider excitation *parallel* to the dimer axis, a simple superposition expectation would be for the left/right edges (region A and its mirror image) to be most intense. For the small nanohole dimer, this is indeed where the local electric fields are maximal – albeit at approximately half of the isolated nanohole value. On the other hand, the left/right electric field enhancement regions for the large nanohole dimers are now considerably weaker than the cusp regions and thus do not contribute significantly to the spatial photoemission images observed. Of course, this is not any violation of the superposition principle, which is exact for static fields, but simply a matter of retardation effects for optical fields with nanoarchitectures near or above the diffraction limit. Nevertheless, this clearly supports that overlapping dimer structures can be quite different from non-overlapping dimer structures. In fact, studies have confirmed that the transition in electric field behavior from nearly touching to electrically contacted nanoobjects can even be discontinuous and therefore lead to unusual plasmonic behavior.<sup>54,55</sup> In any event, the present comparison between scanning photoelectron emission microscopy and COMSOL calculational results for nanohole monomers and dimers provides benchmark examples of the underlying electric field enhancement dynamics of such simple and yet novel plasmonic architectures.

## 10.6 Summary

Metal nanoholes and nanohole dimers formed by shadow mask lithography on Au films have been exploited as unique nanoobjects for investigating multiphoton photoemission (MPPE) from plasmonic materials, as well as simple yet tractable test systems for direct calculation of plasmonic field enhancements. Small nanoholes substantially below the diffraction limit ( $d \ll \lambda$ ) are found to yield significant electric field enhancements both parallel ( $\eta_{\text{ENH}} \approx 20$ ) and perpendicular ( $\eta_{\text{ENH}} \approx 5$ ) to the laser polarization axis. These enhancements are responsible for producing strong scanning photoionization microscopy (SPIM) signals under conditions of ultrafast laser excitation, but which display an isotropic photoemission yield dependence on laser polarization due to a combination of i) sub diffraction limited size and ii) near perfect azimuthal symmetry. Corresponding studies of nanoholes with sizes near the diffraction limit ( $d \approx \lambda$ ) also reveal large electric field enhancements near tangent edges of the cylindrical hole *parallel* with the laser polarization. Since the larger nanohole diameters are now comparable to the excitation wavelength, this yields strong photoemission lobes i) parallel to and ii) rotating with the incident electric field polarization. However, the *integrated* SPIM photoemission signal magnitudes for both small and large nanohole monomers remain completely isotropic with respect to polarization angle by virtue of azimuthal symmetry. Comparison with detailed COMSOL predictions and a simple model based on  $\eta_{\text{ENH}}$  raised to the  $(2n)^{\text{th}}$  for a 4-photon photoemission process ( $n=4$ ) and convoluted over the instrument response function proves to be in outstanding agreement with the experimental data.

Subsequent reduction of the azimuthal symmetry for nanohole dimers reveals a significantly richer spectrum of plasmonic and photoemission behavior, which we have explored or the two limiting cases of small ( $d \ll \lambda$ ) and large ( $d \approx \lambda$ ) holes. COMSOL simulations of the

electric fields around these dimer nanostructures reveal strongly spatially dependent enhancement fields that vary sensitively with incident polarization. Small nanohole dimers below the diffraction limit are found to behave qualitatively like “bowtie” nano-antennas of Moerner and coworkers, whereby the enhancement field is largest at the central cusps for laser polarization *perpendicular* to the dimer axis.<sup>43</sup> This is in clear contrast to the larger nanohole dimers, which exhibit pronounced photoemission signals from regions around the cusp edges, but which are primarily excited for polarization fields *parallel* to the dimer axis. In all cases, the same model of field enhancement raised to the 8<sup>th</sup> power ( $\eta_{\text{ENH}}^8$ ) and convolved over the instrument response function yields excellent agreement with experimental data and laser polarization dependences. As one critical factor in these image predictions, maximum photoemission yield is found to depend not only on the *magnitude* of the local field enhancement to the 8<sup>th</sup> power, but also on the relative areas for potential electron photoemission over which this enhancement occurs.

Directions for future studies include experimental and theoretical studies into the size regime between small (60 nm) and large (500 nm) dimers, where the polarization dependence of the maximum photoemission signals is found to transition from *perpendicular* to *parallel* with respect to the dimer axis. Additionally, it would be quite interesting to study the wavelength dependence of the SPIM signals, in order to correlate with i) near field MPPE with ii) the far field scattering spectra and thereby further investigate the synergism between near field electric enhancement, photoemission signals and far field optical properties. Lastly, these nanohole lithography methods can be simply extended with off axis metallic film deposition to formation of nearly perfect elliptical holes, which should of course exhibit additional sensitivity to wavelength and polarization of the photoemission laser light. In summary, the ability to both i)

measure photoemission from nanoobjects with SPIM studies and ii) model the detailed plasmonic response of these species from first principles electrodynamic calculations opens a wealth of new opportunities for exploring microscopy of nanoobjects with spatial resolution that extends far below the conventional diffraction limit.

## References

- (1) Mock, J. J.; Barbic, M.; Smith, D. R.; Schultz, D. A.; Schultz, S. *J. Chem. Phys.* **2002**, *116*, 6755.
- (2) Emory, S. R.; Nie, S. *J. Phys. Chem. B* **1998**, *102*, 493.
- (3) Kelly, K. L.; Coronado, E.; Zhao, L. L.; Schatz, G. C. *J. Phys. Chem. B* **2003**, *107*, 668.
- (4) Wiley, B. J.; Im, S. H.; Li, Z. Y.; McLellan, J.; Siekkinen, A.; Xia, Y. A. *J. Phys. Chem. B* **2006**, *110*, 15666.
- (5) Brolo, A. G.; Gordon, R.; Leathem, B.; Kavanagh, K. L. *Langmuir* **2004**, *20*, 4813.
- (6) Charbonneau, R.; Lahoud, N. *Opt. Express* **2005**, *13*, 977.
- (7) Haes, A. J.; Zou, S. L.; Schatz, G. C.; Van Duyne, R. P. *J. Phys. Chem. B* **2004**, *108*, 6961.
- (8) Lee, K. S.; El-Sayed, M. A. *J. Phys. Chem. B* **2006**, *110*, 19220.
- (9) Michaels, A. M.; Nirmal, M.; Brus, L. E. *J. Am. Chem. Soc.* **1999**, *121*, 9932.
- (10) Srituravanich, W.; Fang, N.; Sun, C.; Luo, Q.; Zhang, X. *Nano Lett.* **2004**, *4*, 1085.
- (11) Camden, J. P.; Dieringer, J. A.; Wang, Y. M.; Masiello, D. J.; Marks, L. D.; Schatz, G. C.; Van Duyne, R. P. *J. Am. Chem. Soc.* **2008**, *130*, 12616.
- (12) Ciou, S. H.; Cao, Y. W.; Huang, H. C.; Su, D. Y.; Huang, C. L. *J. Phys. Chem. C* **2009**, *113*, 9520.
- (13) Dieringer, J. A.; Wustholz, K. L.; Masiello, D. J.; Camden, J. P.; Kleinman, S. L.; Schatz, G. C.; Van Duyne, R. P. *J. Am. Chem. Soc.* **2009**, *131*, 849.
- (14) Jiang, J.; Bosnick, K.; Maillard, M.; Brus, L. *J. Phys. Chem. B* **2003**, *107*, 9964.



- (15) Moskovits, M. Surface-enhanced Raman spectroscopy: a brief perspective. In *Surface-Enhanced Raman Scattering: Physics And Applications*, 2006; Vol. 103; pp 1.
- (16) Berthelot, J.; Bachelier, G.; Song, M. X.; Rai, P.; des Francs, G. C.; Dereux, A.; Bouhelier, A. *Opt. Express* **2012**, *20*, 10498.
- (17) Kroo, N.; Farkas, G.; Dombi, P.; Varro, S. *Opt. Express* **2008**, *16*, 21656.
- (18) Park, S.; Hahn, J. W.; Lee, J. Y. *Opt. Express* **2012**, *20*, 4856.
- (19) Slablab, A.; Le Xuan, L.; Zielinski, M.; de Wilde, Y.; Jacques, V.; Chauvat, D.; Roch, J. F. *Opt. Express* **2012**, *20*, 220.
- (20) Aers, G. C.; Inglesfield, J. E. *J. Phys. F Met Phys.* **1983**, *13*, 1743.
- (21) Endriz, J. G. *Phys. Rev. B* **1973**, *7*, 3464.
- (22) Endriz, J. G.; Spicer, W. E. *Phys. Rev. B.* **1971**, *4*, 4159.
- (23) Douillard, L.; Charra, F. *J. Phys. D Appl. Phys.* **2011**, *44*.
- (24) Gloskovskii, A.; Valdaitsev, D. A.; Cinchetti, M.; Nepijko, S. A.; Lange, J.; Aeschlimann, M.; Bauer, M.; Klimenkov, M.; Viduta, L. V.; Tomchuk, P. M.; Schonhense, G. *Phys. Rev. B* **2008**, *77*.
- (25) Schweikhard, V.; Grubisic, A.; Baker, T. A.; Thomann, I.; Nesbitt, D. J. *ACS Nano* **2011**, *5*, 3724.
- (26) Grubisic, A.; Schweikhard, V.; Baker, T. A.; Nesbitt, D. J. *ACS Nano* **2012**, *7*, 87.
- (27) Grubisic, A.; Ringe, E.; Cogley, C. M.; Xia, Y.; Marks, L. D.; Van Duyne, R. P.; Nesbitt, D. J. *Nano Lett.* **2012**, *12*, 4823.
- (28) Prikulis, J.; Hanarp, P.; Olofsson, L.; Sutherland, D.; Kall, M. *Nano Lett.* **2004**, *4*, 1003.
- (29) Sepulveda, B.; Alaverdyan, Y.; Alegret, J.; Kall, M.; Johansson, P. *Opt. Exp.* **2008**, *16*, 5609.
- (30) Onuta, T.-D.; Waegele, M.; DuFort, C. C.; Schaich, W. L.; Dragnea, B. *Nano Lett.* **2007**, *7*, 557.
- (31) Monti, O. L. A.; Baker, T. A.; Nesbitt, D. J. *J. Chem. Phys.* **2006**, *125*.
- (32) Schweikhard, V.; Grubisic, A.; Baker, T. A.; Nesbitt, D. J. *J. Phys. Chem. C* **2011**, *115*, 83.
- (33) Michaelson, H. B. *J. Appl. Phys.* **1977**, *48*, 4729.

- (34) Goncalves, M. R.; Marti, O. Influence of the roughness of metal templates on surface enhanced Raman scattering. In *Nanophotonics Iii*; Andrews, D. L., Nunzi, J. M., Ostendorf, A., Eds., 2010; Vol. 7712.
- (35) Johnson, P. B.; Christy, R. W. *Phys. Rev. B* **1972**, *6*, 4370.
- (36) Pors, A.; Albrektsen, O.; Bozhevolnyi, S. I.; Willatzen, M. *Proc. COMSOL Conf.* **2009**.
- (37) Rindzevicius, T.; Alaverdyan, Y.; Sepulveda, B.; Pakizeh, T.; Kall, M.; Hillenbrand, R.; Aizpurua, J.; Garcia de Abajo, F. J. *J. Phys. Chem. C* **2007**, *111*, 1207.
- (38) Schwind, M.; Kasemo, B.; Zoric, I. *Nano Lett.* **2013**, *13*, 1743.
- (39) Dreier, J.; Eriksen, R. L.; Albrektsen, O.; Pors, A.; Simonsen, A. C. *J. Phys. Chem. Lett.* **2009**, *1*, 260.
- (40) Mark, W. K.; Naomi, J. H. *New J. Phys.* **2008**, *10*, 105006.
- (41) Wu, L. Y.; Ross, B. M.; Lee, L. P. *Nano Lett.* **2009**, *9*, 1956.
- (42) Wu, E.; Chi, Y.; Wu, B.; Xia, K.; Yokota, Y.; Ueno, K.; Misawa, H.; Zeng, H. *J. Lumin.* **2011**, *131*, 1971.
- (43) Kinkhabwala, A.; Yu, Z.; Fan, S.; Avlasevich, Y.; Muellen, K.; Moerner, W. E. *Nature Photonics* **2009**, *3*, 654.
- (44) Michaels, A. M.; Jiang, J.; Brus, L. *J. Phys. Chem. B* **2000**, *104*, 11965.
- (45) Xu, H.; Käll, M. *Chem. Phys. Chem.* **2003**, *4*, 1001.
- (46) Zhang, X. Y.; Hicks, E. M.; Zhao, J.; Schatz, G. C.; Van Duyne, R. P. *Nano Lett.* **2005**, *5*, 1503.
- (47) Hao, E.; Schatz, G. C. *J. Chem. Phys.* **2004**, *120*, 357.
- (48) McMahon, J. M.; Henry, A. I.; Wustholz, K. L.; Natan, M. J.; Freeman, R. G.; Van Duyne, R. P.; Schatz, G. C. *Anal. Bioanal. Chem.* **2009**, *394*, 1819.
- (49) Kim, S.; Jin, J.; Kim, Y.-J.; Park, I.-Y.; Kim, Y.; Kim, S.-W. *Nature* **2008**, *453*, 757.
- (50) Jin, E. X.; Xu, X. F. *Appl. Phys. Lett.* **2006**, *88*.
- (51) Jin, E. X.; Xu, X. *J. Comp. and Theo. Nano.* **2008**, *5*, 214.
- (52) Jin, E. X.; Xu, X. *Appl. Phys. B* **2006**, *84*, 3.
- (53) Sendur, K.; Challener, W. *J. Microscopy* **2003**, *210*, 279.

- (54) Atay, T.; Song, J. H.; Nurmikko, A. V. *Nano Lett.* **2004**, *4*, 1627.
- (55) Romero, I.; Aizpurua, J.; Bryant, G. W.; Garcia de Abajo, F. J. *Opt. Exp.* **2006**, *14*, 9988.

## Bibliography

1. Aers, G.C. and J.E. Inglesfield, *Photoyield enhancement from small metal particles*. J. Phys. F Met Phys., 1983. **13**(8): p. 1743.
2. Aggarwal, R.L., L.W. Farrar, E.D. Diebold, and D.L. Polla, *Measurement of the absolute Raman scattering cross section of the 1584-cm(-1) band of benzenethiol and the surface-enhanced Raman scattering cross section enhancement factor for femtosecond laser-nanostructured substrates*. J. Raman Spectrosc., 2009. **40**(9): p. 1331-1333.
3. Ahern, A.M. and R.L. Garrell, *Insitu Photoreduced Silver-Nitrate As A Substrate For Surface-Enhanced Raman-Spectroscopy*. Anal. Chem., 1987. **59**(23): p. 2813-2816.
4. Akimov, A.V., A. Mukherjee, C.L. Yu, D.E. Chang, A.S. Zibrov, P.R. Hemmer, H. Park, and M.D. Lukin, *Generation of single optical plasmons in metallic nanowires coupled to quantum dots*. Nature, 2007. **450**: p. 402-406.
5. Alekseeva, A.V., V.A. Bogatyrev, B.N. Khlebtsov, A.G. Mel'nikov, L.A. Dykman, and N.G. Khlebtsov, *Gold Nanorods: Synthesis and Optical Properties*. Colloid J., 2006. **68**: p. 661-678.
6. Anderson, D.J. and M. Moskovits, *A SERS-active system based on silver nanoparticles tethered to a deposited silver film*. J. Phys. Chem. B, 2006. **110**(28): p. 13722-13727.
7. Anker, J.N., W.P. Hall, O. Lyandres, N.C. Shah, J. Zhao, and R.P. Van Duyne, *Biosensing with plasmonic nanosensors*. Nature Mater., 2008. **7**(6): p. 442.
8. Antelman, J., Y. Ebenstein, T. Dertinger, X. Michalet, and S. Weiss, *Suppression of Quantum Dot Blinking in DTT-Doped Polymer Films†*. J. Phys. Chem. C, 2009. **113**(27): p. 11541-11545.
9. Armelao, L., R. Bertozello, and M. DeDominicis, *Silver nanocluster formation in silica coatings by the sol-gel route*. Adv. Mater., 1997. **9**(9): p. 736-741.
10. Atay, T., J.H. Song, and A.V. Nurmikko, *Strongly interacting plasmon nanoparticle pairs: From dipole-dipole interaction to conductively coupled regime*. Nano Lett., 2004. **4**(9): p. 1627-1631.
11. Avrami, M., *Kinetics of Phase Change: I - General Theory*. J. Chem. Phys., 1939. **7**: p. 1103-1112.
12. Avrami, M., *Kinetics of Phase Change: II - Transformation-Time Relations for Random Distribution of Nuclei*. J. Chem. Phys., 1940. **8**: p. 212-224.
13. Avrami, M., *Kinetics of Phase Change: III - Granulation, Phase Change, and Microstructure*. J. Chem. Phys., 1941. **9**: p. 177-184.

14. Axelrod, D., *Total Internal Reflection Fluorescence Microscopy*. Method Cell Biol., 2008. **89**: p. 169-221.
15. Bachir, A.I., N. Durisic, B. Hebert, P. Grutter, and P.W. Wiseman, *Characterization of blinking dynamics in quantum dot ensembles using image correlation spectroscopy*. J Appl Phys, 2006. **99**(6).
16. Baker, T.A., O.L.A. Monti, and D.J. Nesbitt, *Kinetic Studies of the Photogeneration of Silver Nanoparticles*. J Phys Chem B, 2011. **115**(20): p. 9861-9870.
17. Baker, T.A., J.L. Rouge, and D.J. Nesbitt, *Single molecule studies of quantum dot fluorescence intermittency: evidence for both dark and light-assisted blinking dynamics*. Mol Phys, 2009. **107**(18): p. 1867-1878.
18. Banin, U., M. Bruchez, A.P. Alivisatos, T. Ha, S. Weiss, and D.S. Chemla, *Evidence for a thermal contribution to emission intermittency in single CdSe/CdS core/shell nanocrystals*. J. Chem. Phys., 1999. **110**(2): p. 1195-1201.
19. Barashev, P.P., *Multiquantum Photoemissive Effect In Condensed Media And Statistical Characteristics Of Multiquantum Photocurrent .I*. Phys. Status Solidi A, 1972. **9**(1): p. 9-&.
20. Bardhan, R., N.K. Grady, J.R. Cole, A. Joshi, and N.J. Halas, *Fluorescence Enhancement by Au Nanostructures: Nanoshells and Nanorods*. ACS Nano, 2009. **3**: p. 744-752.
21. Barnes, W.L., A. Dereux, and T.W. Ebbesen, *Surface plasmon subwavelength optics*. Nature, 2003. **424**: p. 824-830.
22. Basche, T., S. Kummer, and C. Brauchle, *Direct spectroscopic observation of quantum jumps of a single molecule*. Nature, 1995. **373**(6510): p. 132-134.
23. Basche, T., S. Kummer, and C. Brauchle, *Direct Spectroscopic Observation Of Quantum Jumps Of A Single-Molecule*. Nature, 1995. **373**(6510): p. 132-134.
24. Bauer, M., C. Wiemann, J. Lange, D. Bayer, M. Rohmer, and M. Aeschlimann, *Phase propagation of localized surface plasmons probed by time-resolved photoemission electron microscopy* Appl. Phys. A - Mater., 2007. **88**(3): p. 473-480.
25. Bechtel, J.H., W.L. Smith, and N. Bloembergen, *2-Photon Photoemission From Metals Induced By Picosecond Laser-Pulses*. Phys. Rev. B, 1977. **15**(10): p. 4557-4563.
26. Bericaud, S., L. Cognet, P. Tamarat, and B. Lounis, Nano Lett., 2005. **5**: p. 515.
27. Bernabò, M., A. Pucci, F. Galembeck, C.A.d.P. Leite, and G. Ruggeri, *Thermal- and Sun-Promoted Generation of Silver Nanoparticles Embedded into Poly(vinyl alcohol) Films*. Macromol. Mater. Eng., 2009. **294**(4): p. 256-264.

28. Berthelot, J., G. Bachelier, M.X. Song, P. Rai, G.C. des Francs, A. Dereux, and A. Bouhelier, *Silencing and enhancement of second-harmonic generation in optical gap antennas*. Opt. Exp., 2012. **20**(10): p. 10498-10508.
29. Besocke, K., *An easily operable scanning tunneling microscope*. Surf. Sci., 1987. **181**(1-2): p. 145-153.
30. Betzig, E., G.H. Patterson, R. Sougrat, O.W. Lindwasser, S. Olenych, J.S. Bonifacino, M.W. Davidson, J. Lippincott-Schwartz, and H.F. Hess, *Imaging Intracellular Fluorescent Proteins at Nanometer Resolution*. Science, 2006. **313**(5793): p. 1642-1645.
31. Bharadwaj, P. and L. Novotny, *Robustness of Quantum Dot Power-Law Blinking*. Nano Lett., 2011. **11**(5): p. 2137-2141.
32. Billaud, P., S. Marhaba, N. Grillet, E. Cottancin, C. Bonnet, J. Lermé, J.-L. Vialle, M. Broyer, and M. Pellarin, *Absolute optical extinction measurements of single nano-objects by spatial modulation spectroscopy using a white lamp*. Rev. Sci. Instr., 2010. **81**: p. 043101.
33. Blackie, E.J., E.C.L. Ru, and P.G. Etchegoin, *Single-Molecule Surface-Enhanced Raman Spectroscopy of Nonresonant Molecules*. J. Am. Chem. Soc., 2009. **131**(40): p. 14466-14472.
34. Bohren, C.F. and D.R. Huffman, *Absorption and Scattering of Light by Small Particles*. 1 ed1983, New York: John Wiley & Sons. 530.
35. Bohren, C.F. and D.R. Huffman, *Absorption and Scattering of Light by Small Particles*. Absorption and Scattering of Light by Small Particles2007: Wiley-VCH Verlag GmbH.
36. Bopp, M.A., A.J. Meixner, G. Tarrach, I. ZschokkeGranacher, and L. Novotny, *Direct imaging single molecule diffusion in a solid polymer host*. Chem. Phys. Lett., 1996. **263**(6): p. 721-726.
37. Born, M. and E. Wolf, *Principles of Optics : Electromagnetic Theory of Propagation, Interference and Diffraction of Light*. 6th ed1980, Oxford ; New York: Pergamon Press. xxviii, 808 p.
38. Bosbach, J., C. Hendrich, F. Stietz, T. Vartanyan, and F. Träger, *Ultrafast Dephasing of Surface Plasmon Excitation in Silver Nanoparticles: Influence of Particle Size, Shape, and Chemical Surrounding*. Phys. Rev. Lett., 2002. **89**(25): p. 257404.
39. Boulesbaa, A., A. Issac, D. Stockwell, Z. Huang, J. Huang, J. Guo, and T. Lian, *Ultrafast charge separation at CdS quantum dot/rhodamine B molecule interface*. J. Am. Chem. Soc., 2007. **129**(49): p. 15132-+.
40. Boyd, G.T., Z.H. Yu, and Y.R. Shen, *Photoinduced luminescence from the noble metals and its enhancement on roughened surfaces*. PRB, 1986. **33**: p. 7923-7935.

41. Brewer, S.H. and S. Franzen, *Indium Tin Oxide Plasma Frequency Dependence on Sheet Resistance and Surface Adlayers Determined by Reflectance FTIR Spectroscopy*. JPC B, 2002. **106**: p. 12986-12992.
42. Brolo, A.G., R. Gordon, B. Leathem, and K.L. Kavanagh, *Surface plasmon sensor based on the enhanced light transmission through arrays of nanoholes in gold films*. Langmuir, 2004. **20**(12): p. 4813-4815.
43. Brus, L., *Noble Metal Nanocrystals: Plasmon Electron Transfer Photochemistry and Single-Molecule Raman Spectroscopy*. Accounts Chem. Res., 2008. **41**(12): p. 1742-1749.
44. Burle, *Channeltron Electron Multiplier Handbook for Mass Spectroscopy Applications*.
45. Callegari, A., D. Tonti, and M. Chergui, *Photochemically Grown Silver Nanoparticles with Wavelength-Controlled Size and Shape*. Nano Lett., 2003. **3**(11): p. 1565-1568.
46. Camden, J.P., J.A. Dieringer, Y.M. Wang, D.J. Masiello, L.D. Marks, G.C. Schatz, and R.P. Van Duyne, *Probing the structure of single-molecule surface-enhanced Raman scattering hot spots*. J. Am. Chem. Soc., 2008. **130**(38): p. 12616-+.
47. Canamares, M.V., J.V. Garcia-Ramos, J.D. Gomez-Varga, C. Domingo, and S. Sanchez-Cortes, *Ag nanoparticles prepared by laser photoreduction as substrates for in situ surface-enhanced raman scattering analysis of dyes*. Langmuir, 2007. **23**(9): p. 5210-5215.
48. Cardona, M. and L. Ley, *Introduction*, in *Photoemission in solids*, M. Cardona and L. Ley, Editors. 1978, Springer-Verlag: Berlin ; New York. p. 1-104.
49. Chang, C.F., C.Y. Chen, F.H. Chang, S.P. Tai, C.Y. Chen, C.H. Yu, Y.B. Tseng, T.H. Tsai, I.S. Liu, W.F. Su, and C.K. Sun, *Cell tracking and detection of molecular expression in live cells using lipid-enclosed CdSe quantum dots as contrast agents for epi-third harmonic generation microscopy*. Opt. Exp., 2008. **16**(13): p. 9534-9548.
50. Chang, D.E., A.S. Sorensen, P.R. Hemmer, and M.D. Lukin, *Quantum Optics with Surface Plasmons*. PRL, 2006. **97**: p. 053002.
51. Chang, S.-H., S. Gray, and G. Schatz, *Surface plasmon generation and light transmission by isolated nanoholes and arrays of nanoholes in thin metal films*. Opt. Express, 2005. **13**(8): p. 3150-3165.
52. Chang, Y.P., F. Pinaud, J. Antelman, and S. Weiss, *Tracking bio-molecules in live cells using quantum dots*. J Biophotonics, 2008. **1**(4): p. 287-298.
53. Charbonneau, R. and N. Lahoud, *Demonstration of integrated optics elements based on long-ranging surface plasmon polaritons*. Opt. Exp., 2005. **13**(3): p. 977-984.

54. Chelvayohan, M. and C.H.B. C. H. B. Mee, *J. Phys. C Solid State*, 1982. **15**: p. 2305-2312.
55. Chen, C.J., *Electromechanical deflections of piezoelectric tubes with quartered electrodes*. *Appl. Phys. Lett.*, 1992. **60**(1): p. 132-134.
56. Chen, W., J.Z. Zhang, and A.G. Joly, *Optical properties and potential applications of doped semiconductor nanoparticles*. *J Nanosci. Nanotechnol.*, 2004. **4**(8): p. 919-947.
57. Chen, Y., J. Vela, H. Htoon, J.L. Casson, D.J. Werder, D.A. Bussian, V.I. Klimov, and J.A. Hollingsworth, *"Giant" multishell CdSe nanocrystal quantum dots with suppressed blinking*. *J. Am. Chem. Soc.*, 2008. **130**(15): p. 5026+.
58. Chepic, D.I., A.L. Efros, A.I. Ekimov, M.G. Vanov, V.A. Kharchenko, I.A. Kudriavtsev, and T.V. Yazeva, *Auger Ionization Of Semiconductor Quantum Drops In A Glass Matrix*. *J. Lumines.*, 1990. **47**(3): p. 113-127.
59. Choi, C.L. and A.P. Alivisatos, *From Artificial Atoms to Nanocrystal Molecules: Preparation and Properties of More Complex Nanostructures*. *Annu. Rev. Phys. Chem.*, 2010. **61**: p. 369-389.
60. Chon, B., S.J. Lim, W. Kim, J. Seo, H. Kang, T. Joo, J. Hwang, and S.K. Shin, *Shell and ligand-dependent blinking of CdSe-based core/shell nanocrystals*. *Phys. Chem. Chem. Phys.*, 2010. **12**(32): p. 9312-9319.
61. Christensen, N.E., *High-energy band structure of gold*. *PRB*, 1976. **13**: p. 2698-2701.
62. Christian, J.W., *The Theory of Transformations in Metals and Alloys*. 2nd ed 1975: Pergamon Press.
63. Chung, I., J.B. Witkoskie, J.S. Cao, and M.G. Bawendi, *Description of the fluorescence intensity time trace of collections of CdSe nanocrystal quantum dots based on single quantum dot fluorescence blinking statistics*. *Phys Rev E*, 2006. **73**(1).
64. Chung, I., J.B. Witkoskie, J.P. Zimmer, J. Cao, and M.G. Bawendi, *Extracting the number of quantum dots in a microenvironment from ensemble fluorescence intensity fluctuations*. *Phys. Rev. B*, 2007. **75**(4).
65. Chung, I.H. and M.G. Bawendi, *Relationship between single quantum-dot intermittency and fluorescence intensity decays from collections of dots*. *Phys. Rev. B*, 2004. **70**(16): p. 165304.
66. Cichos, F., C. von Borczyskowski, and M. Orrit, *Power-law intermittency of single emitters*. *Curr. Opin. Colloid Interface Sci.*, 2007. **12**(6): p. 272-284.
67. Cinchetti, M., A. Gloskovskii, S.A. Nepijko, G. Schoenhense, H. Rochholz, and M. Kreiter, *Photoemission Electron Microscopy as a Tool for the Investigation of Optical Near Fields*. *PRL*, 2005. **95**: p. 047601.



68. Ciou, S.H., Y.W. Cao, H.C. Huang, D.Y. Su, and C.L. Huang, *SERS Enhancement Factors Studies of Silver Nanoprism and Spherical Nanoparticle Colloids in The Presence of Bromide Ions*. J Phys Chem B, 2009. **113**(22): p. 9520-9525.
69. Clauset, A., C.R. Shalizi, and M.E.J. Newman, *Power-Law Distributions in Empirical Data*. Siam Rev, 2009. **51**(4): p. 661-703.
70. Clifford, J.N., T.D.M. Bell, P. Tinnefeld, M. Heilemann, S.M. Melnikov, J. Hotta, M. Sliwa, P. Dedecker, M. Sauer, J. Hofkens, and E.K.L. Yeow, *Fluorescence of single molecules in polymer films: Sensitivity of blinking to local environment*. J. Phys. Chem. B, 2007. **111**(25): p. 6987-6991.
71. Conchello, J.-A. and J.W. Lichtman, *Optical sectioning microscopy*. Nature Methods, 2005. **2**(12): p. 920-931.
72. Crouch, C.H., R. Mohr, T. Emmons, S. Wang, and M. Drndic, *Excitation Energy Dependence of Fluorescence Intermittency in CdSe/ZnS Core-Shell Nanocrystals*. J Phys Chem B, 2009. **113**(28): p. 12059-12066.
73. Crouch, C.H., O. Sauter, X. Wu, R. Purcell, C. Querner, M. Drndic, and M. Pelton, *Facts and Artifacts in the Blinking Statistics of Semiconductor Nanocrystals*. Nano Lett., 2010. **10**(5): p. 1692-1698.
74. Cumbreira, F.L. and F. SanchezBajo, *The use of the JMAYK kinetic equation for the analysis of solid-state reactions: Critical considerations and recent interpretations*. Thermochim. Acta, 1995. **266**: p. 315-330.
75. Dahan, M., S. Levi, C. Luccardini, P. Rostaing, B. Riveau, and A. Triller, *Diffusion dynamics of glycine receptors revealed by single-quantum dot tracking*. Science, 2003. **302**(5644): p. 442-445.
76. Dieringer, J.A., K.L. Wustholz, D.J. Masiello, J.P. Camden, S.L. Kleinman, G.C. Schatz, and R.P. Van Duyne, *Surface-Enhanced Raman Excitation Spectroscopy of a Single Rhodamine 6G Molecule*. J. Am. Chem. Soc., 2009. **131**(2): p. 849-854.
77. Ditlbacher, H., A. Hohenau, D. Wagner, U. Kreibig, M. Rogers, F. Hofer, F.R. Aussenegg, and J.R. Krenn, *Silver Nanowires as Surface Plasmon Resonators*. PRL, 2005. **95**: p. 257403.
78. Douillard, L. and F. Charra, *High-resolution mapping of plasmonic modes: photoemission and scanning tunnelling luminescence microscopies*. J. Phys. D Appl. Phys., 2011. **44**(46).
79. Douillard, L., F. Charra, Z. Korczak, R. Bachelot, S. Kostcheev, G. Lerondel, P.-M. Adam, and P. Royer, *Short Range Plasmon Resonators Probed by Photoemission Electron Microscopy*. Nano Lett., 2008. **8**(3): p. 935.

80. Dreier, J., R.L. Eriksen, O. Albrektsen, A. Pors, and A.C. Simonsen, *Gold Films with Imprinted Cavities*. The Journal of Physical Chemistry Letters, 2009. **1**(1): p. 260-264.
81. Dulkeith, E., T. Niedereichholz, T.A. Klar, J. Feldmann, G. von Plessen, D.I. Gittins, K.S. Mayya, and F. Caruso, *Plasmon emission in photoexcited gold nanoparticles*. Phys. Rev. B, 2004. **70**(20): p. 205424.
82. D'Urso, L., V. Nicolosi, G. Compagnini, and O. Puglisi, *Size distribution of silver nanoclusters induced by ion, electron, laser beams and thermal treatments of an organometallic precursor*. Appl. Surf. Sci., 2004. **226**(1-3): p. 131-136.
83. Early, K.T., K.D. McCarthy, N.I. Hammer, M.Y. Odoi, R. Tangirala, T. Emrick, and M.D. Barnes, *Blinking suppression and intensity recurrences in single CdSe-oligo(phenylene vinylene) nanostructures: experiment and kinetic model*. Nanotechnology, 2007. **18**(42): p. 424027.
84. Eastman, D.E., *Photoelectric Work Functions Of Transition, Rare-Earth, And Noble Metals*. Phys. Rev. B, 1970. **2**(1): p. 1-&.
85. Efros, A.L. and M. Rosen, *Random telegraph signal in the photoluminescence intensity of a single quantum dot*. Phys. Rev. Lett., 1997. **78**(6): p. 1110-1113.
86. Eggeling, C., J.R. Fries, L. Brand, R. Günther, and C.A.M. Seidel, *Monitoring conformational dynamics of a single molecule by selective fluorescence spectroscopy*. Proc. Nat. Acad. Sci., 1998. **95**(4): p. 1556-1561.
87. Eland, J.H.D., *Photoelectron Spectroscopy : An Introduction to Ultraviolet Photoelectron Spectroscopy in the Gas Phase*. 2 ed1984, London: Butterworths.
88. Emory, S.R., R.A. Jensen, T. Wenda, M. Han, and S. Nie, *Re-examining the origins of spectral blinking in single-molecule and single-nanoparticle SERS*. Faraday Discuss., 2006. **132**: p. 249-259.
89. Emory, S.R. and S. Nie, *Near-Field Surface-Enhanced Raman Spectroscopy on Single Silver Nanoparticles*. Anal. Chem., 1997. **69**(14): p. 2631-2635.
90. Emory, S.R. and S. Nie, *Screening and enrichment of metal nanoparticles with novel optical properties*. J. Phys. Chem. B, 1998. **102**(3): p. 493-497.
91. Endriz, J.G., *Calculation of the Surface Photoelectric Effect*. Phys. Rev. B, 1973. **7**(8): p. 3464-3481.
92. Endriz, J.G. and W.E. Spicer, *Study of Aluminum Films. II. Photoemission Studies of Surface-Plasmon Oscillations on Controlled-Roughness Films*. Phys. Rev. B, 1971. **4**(12): p. 4159-4184.

93. Eustis, S., H.Y. Hsu, and M.A. El-Sayed, *Gold nanoparticle formation from photochemical reduction of Au<sup>3+</sup> by continuous excitation in colloidal solutions. A proposed molecular mechanism*. J. Phys. Chem. B, 2005. **109**(11): p. 4811-4815.
94. Eustis, S., G. Krylova, N. Smirnova, A. Eremenko, C. Tabor, W.Y. Huang, and M.A. El-Sayed, *Using silica films and powders modified with benzophenone to photoreduce silver nanoparticles*. J. Photochem. Photobiol. A-Chem., 2006. **181**(2-3): p. 385-393.
95. Evanoff, D.D. and G. Chumanov, *Size-controlled synthesis of nanoparticles. 1. "Silver-only" aqueous suspensions via hydrogen reduction*. J. Phys. Chem. B, 2004. **108**(37): p. 13948-13956.
96. Evanoff, D.D. and G. Chumanov, *Size-controlled synthesis of nanoparticles. 2. Measurement of extinction, scattering, and absorption cross sections*. J. Phys. Chem. B, 2004. **108**(37): p. 13957-13962.
97. Evers, F., C. Rakete, K. Watanabe, D. Menzel, and H.J. Freund, *Two-photon photoemission from silver nanoparticles on thin alumina films: Role of plasmon excitation*. Surf. Sci., 2005. **593** p. 43-48.
98. Faraday, M., *The Bakerian Lecture: Experimental Relations of Gold (and Other Metals) to Light*. Philos. T. Roy. Soc., 1857. **147**(0): p. 145-181.
99. Farahani, J., H.-J. Eisler, D.W. Pohl, and B. Hecht, *Single Quantum Dot Coupled to a Scanning Optical Antenna: A Tunable Superemitter*. Phys. Rev. Lett., 2005. **95**: p. 017402.
100. Fecher, G.H., O. Oliver Schmidt, Y. Hwu, and G. Schonhense, *Multiphoton photoemission electron microscopy using femtosecond laser radiation*. J. Electron Spectrosc., 2002. **126**: p. 77-87.
101. Fisher, B.R., H.J. Eisler, N.E. Stott, and M.G. Bawendi, *Emission intensity dependence and single-exponential behavior in single colloidal quantum dot fluorescence lifetimes*. J. Phys. Chem. B, 2004. **108**(1): p. 143-148.
102. Fomenko, V. and D.J. Nesbitt, *Solution Control of Radiative and Nonradiative Lifetimes: A Novel Contribution to Quantum Dot Blinking Suppression*. Nano Lett., 2007. **8**(1): p. 287-293.
103. Fomenko, V. and D.J. Nesbitt, *Solution control of radiative and nonradiative lifetimes: A novel contribution to quantum dot blinking suppression*. Nano Lett., 2008. **8**(1): p. 287-293.
104. Fort, E. and S. Gresillon, *Surface Enhanced Fluorescence*. J. Appl. Phys. D Appl. Phys., 2008. **41**: p. 013001 (31pp).
105. Frantsuzov, P., M. Kuno, B. Janko, and R.A. Marcus, *Universal emission intermittency in quantum dots, nanorods and nanowires*. Nat. Phys., 2008. **4**(7): p. 519-522.

106. Frantsuzov, P.A. and R.A. Marcus, *Explanation of quantum dot blinking without the long-lived trap hypothesis*. Phys. Rev. B, 2005. **72**(15): p. 155321.
107. Frantsuzov, P.A., S. Volkan-Kacso, and B. Janko, *Model of Fluorescence Intermittency of Single Colloidal Semiconductor Quantum Dots Using Multiple Recombination Centers*. Phys. Rev. Lett., 2009. **103**(20).
108. Frantsuzov, P.A., S. Volkan-Kacso, and B. Janko, *Universality of the Fluorescence Intermittency in Nanoscale Systems: Experiment and Theory*. Nano Lett., 2013. **13**(2): p. 402-408.
109. Fromm, D.P., A. Sundaramurthy, P.J. Schuck, G. Kino, and W.E. Moerner, *Gap-dependent optical coupling of single "Bowtie" nanoantennas resonant in the visible*. Nano Lett., 2004. **4**(5): p. 957-961.
110. Gaddy, G.A., A.S. Korchev, J.L. McLain, B.L. Slaten, E.S. Steigerwalt, and G. Mills, *Light-induced formation of silver particles and clusters in crosslinked PVA/PAA films*. J. Phys. Chem. B, 2004. **108**(39): p. 14850-14857.
111. Gaddy, G.A., J.L. McLain, A.S. Korchev, B.L. Slaten, and G. Mills, *Kinetics of silver particle photogeneration in crosslinked PVA/PAA films*. J. Phys. Chem. B, 2004. **108**(39): p. 14858-14865.
112. Gaddy, G.A., J.L. McLain, S.V. Ruggs, B.L. Slaten, and G. Mills, *Characterization and kinetics of the photoinduced formation of silver particles*. Abstracts Of Papers Of The American Chemical Society, 2001. **221**: p. U355-U355.
113. Gaddy, G.A., J.L. McLain, E.S. Steigerwalt, R. Broughton, B.L. Slaten, and G. Mills, *Photogeneration of silver particles in PVA fibers and films*. J. Clust. Sci., 2001. **12**(3): p. 457-471.
114. Galland, C., Y. Ghosh, A. Steinbruck, M. Sykora, J.A. Hollingsworth, V.I. Klimov, and H. Htoon, *Two types of luminescence blinking revealed by spectroelectrochemistry of single quantum dots*. Nature, 2011. **479**(7372): p. 203-U75.
115. Gan, Y.J., W.P. Cai, G.H. Fu, and G.L. Hu, *Water vapour-induced enhancement of the surface plasmon resonance for Ag nanoparticles dispersed within pores of mesoporous silica*. J. Phys.-Condes. Matter, 2004. **16**(13): p. L201-L206.
116. Gao, H., J. Henzie, and T.W. Odom, *Direct Evidence for Surface Plasmon-Mediated Enhanced Light Transmission through Metallic Nanohole Arrays*. Nano Lett., 2006. **6**(9): p. 2104-2108.
117. Gi, X., M. Ma, J.F. Zhang, Y. Lu, and K.T. Carron, *Sers And Xps Studies Of The Molecular-Orientation Of Thiophenols From The Gaseous State Onto Silver*. J. Colloid Interface Sci., 1992. **150**(1): p. 1-6.

118. Gloskovskii, A., D. Valdaitsev, S.A. Nepijko, G. Schoenhense, and B. Rethfeld, *Coexisting electron emission mechanisms in small metal particles observed in fs-laser excited PEEM*. Surf. Sci., 2007. **601** p. 4706–4713.
119. Gloskovskii, A., D.A. Valdaitsev, M. Cinchetti, S.A. Nepijko, J. Lange, M. Aeschlimann, M. Bauer, M. Klimenkov, L.V. Viduta, P.M. Tomchuk, and G. Schonhense, *Electron emission from films of Ag and Au nanoparticles excited by a femtosecond pump-probe laser*. Physical Review B (Condensed Matter and Materials Physics), 2008. **77**(19): p. 195427.
120. Gobin, A.M., M.H. Lee, N.J. Halas, W.D. James, R.A. Drezek, and J.L. West, *Near-infrared resonant nanoshells for combined optical imaging and photothermal cancer therapy*. Nano Lett., 2007. **7**(7): p. 1929-1934.
121. Gomez, D.E., M. Califano, and P. Mulvaney, *Optical properties of single semiconductor nanocrystals*. Phys. Chem. Chem. Phys., 2006. **8**(43): p. 4989-5011.
122. Goncalves, M.R. and O. Marti, *Influence of the roughness of metal templates on surface enhanced Raman scattering*, in *Nanophotonics Iii*, D.L. Andrews, J.M. Nunzi, and A. Ostendorf, Editors. 2010.
123. Greytak, A.B., P.M. Allen, W. Liu, J. Zhao, E.R. Young, Z. Popovic, B.J. Walker, D.G. Nocera, and M.G. Bawendi, *Alternating layer addition approach to CdSe/CdS core/shell quantum dots with near-unity quantum yield and high on-time fractions*. Chem. Sci., 2012. **3**(6): p. 2028-2034.
124. Greytak, A.B., P.M. Allen, W.H. Liu, J. Zhao, E.R. Young, Z. Popovic, B.J. Walker, D.G. Nocera, and M.G. Bawendi, *Alternating layer addition approach to CdSe/CdS core/shell quantum dots with near-unity quantum yield and high on-time fractions*. Chem. Sci., 2012. **3**(6): p. 2028-2034.
125. Grubisic, A., E. Ringe, C.M. Cobley, Y. Xia, L.D. Marks, R.P. Van Duyne, and D.J. Nesbitt, *Plasmonic Near-Electric Field Enhancement Effects in Ultrafast Photoelectron Emission: Correlated Spatial and Laser Polarization Microscopy Studies of Individual Ag Nanocubes*. Nano Lett., 2012. **12**(9): p. 4823-4829.
126. Grubisic, A., V. Schweikhard, T.A. Baker, and D.J. Nesbitt, *Coherent Multiphoton Photoelectron Emission from Single Au Nanorods: The Critical Role of Plasmonic Electric Near-Field Enhancement*. ACS Nano, 2012. **7**(1): p. 87-99.
127. Ha, T., T. Enderle, D.S. Chemla, P.R. Selvin, and S. Weiss, *Single Molecule Dynamics Studied by Polarization Modulation*. Phys. Rev. Lett., 1996. **77**(19): p. 3979-3982.
128. Hada, H., Y. Yonezawa, A. Yoshida, and A. Kurakake, *PHOTOREDUCTION OF SILVER ION IN AQUEOUS AND ALCOHOLIC SOLUTIONS*. J. Phys. Chem., 1976. **80**(25): p. 2728-2731.

129. Haes, A.J., C.L. Haynes, A.D. McFarland, G.C. Schatz, R.R. Van Duyne, and S.L. Zou, *Plasmonic materials for surface-enhanced sensing and spectroscopy* MRS Bull., 2005. **30**(5): p. 368-375.
130. Haes, A.J., S.L. Zou, G.C. Schatz, and R.P. Van Duyne, *Nanoscale optical biosensor: Short range distance dependence of the localized surface plasmon resonance of noble metal nanoparticles*. J. Phys. Chem. B, 2004. **108**(22): p. 6961-6968.
131. Halas, N.J., *Playing with Plasmons: Tuning the Optical Resonant Properties of Metallic Nanoshells*. MRS Bull., 2005. **30**: p. 362-367.
132. Hamann, H.F., A. Gallagher, and D.J. Nesbitt, *Enhanced sensitivity near-field scanning optical microscopy at high spatial resolution*. Appl. Phys. Lett., 1998. **73**(11): p. 1469-1471.
133. Hao, E. and G.C. Schatz, *Electromagnetic fields around silver nanoparticles and dimers*. J. Chem. Phys., 2004. **120**(1): p. 357-366.
134. Haynes, C.L., A.D. McFarland, M.T. Smith, J.C. Hulteen, and R.P. Van Duyne, *Angle-resolved nanosphere lithography: Manipulation of nanoparticle size, shape, and interparticle spacing*. J. Phys. Chem. B, 2002. **106**(8): p. 1898-1902.
135. Haynes, C.L., A.D. McFarland, L.L. Zhao, R.P. Van Duyne, G.C. Schatz, L. Gunnarsson, J. Prikulis, B. Kasemo, and M. Kall, *Nanoparticle optics: The importance of radiative dipole coupling in two-dimensional nanoparticle arrays*. J. Phys. Chem. B, 2003. **107**(30): p. 7337-7342.
136. Haynes, C.L. and R.P. Van Duyne, *Nanosphere lithography: A versatile nanofabrication tool for studies of size-dependent nanoparticle optics*. J. Phys. Chem. B, 2001. **105**(24): p. 5599-5611.
137. Haynes, C.L. and R.P. Van Duyne, *Plasmon-sampled surface-enhanced Raman excitation spectroscopy*. J. Phys. Chem. B, 2003. **107**(30): p. 7426-7433.
138. Hell, S.W. and J. Wichmann, *BREAKING THE DIFFRACTION RESOLUTION LIMIT BY STIMULATED-EMISSION - STIMULATED-EMISSION-DEPLETION FLUORESCENCE MICROSCOPY*. Opt. Lett., 1994. **19**(11): p. 780-782.
139. Henley, S.J. and S.R.P. Silva, *Laser direct write of silver nanoparticles from solution onto glass substrates for surface-enhanced Raman spectroscopy*. Appl. Phys. Lett., 2007. **91**(2).
140. Hess, S.T., T.P.K. Girirajan, and M.D. Mason, *Ultra-High Resolution Imaging by Fluorescence Photoactivation Localization Microscopy*. Biophys. J., 2006. **91**: p. 4258-4272.

141. Hess, S.T. and W.W. Webb, *Focal Volume Optics and Experimental Artifacts in Confocal Fluorescence Correlation Spectroscopy*. Biophys. J., 2002. **83**(4): p. 2300-2317.
142. Hill, A.E., *The distribution of a strong electrolyte between benzene and water*. J. Am. Chem. Soc., 1921. **43**: p. 254-268.
143. Hill, A.E., *The system, silver perchlorate-water-benzene*. J. Am. Chem. Soc., 1922. **44**: p. 1163-1193.
144. Hodak, J.H., J.L. Fiore, D.J. Nesbitt, C.D. Downey, and A. Pardi, *Docking kinetics and equilibrium of a GAAA tetraloop-receptor motif probed by single-molecule FRET (vol 102, pg 10505, 2005)*. Proc. Nat. Acad. Sci., 2005. **102**(37): p. 13351-13351.
145. Hohng, S. and T. Ha, *Near-complete suppression of quantum dot blinking in ambient conditions*. J. Am. Chem. Soc., 2004. **126**(5): p. 1324-1325.
146. Hoogenboom, J.P., W.K. den Otter, and H.L. Offerhaus, *Accurate and unbiased estimation of power-law exponents from single-emitter blinking data*. J. Chem. Phys., 2006. **125**(20).
147. Hoogenboom, J.P., J. Hernando, E.M.H.R. van Dijk, N.F. van Hulst, and M.F. Garcia-Parajo, *Power-law blinking in the fluorescence of single organic molecules*. Chemphyschem, 2007. **8**(6): p. 823-833.
148. Hsiao, J.K., C.P. Tsai, T.H. Chung, Y. Hung, M. Yao, H.M. Liu, C.Y. Mou, C.S. Yang, Y.C. Chen, and D.M. Huang, *Mesoporous silica nanoparticles as a delivery system of gadolinium for effective human stem cell tracking*. Small, 2008. **4**(9): p. 1445-1452.
149. Hwa, T. and M. Kardar, *Avalanches, hydrodynamics, and discharge events in models of sandpiles*. Phys Rev A, 1992. **45**(10): p. 7002-7023.
150. Isnaeni, K.H. Kim, D.L. Nguyen, H. Lim, T.N. Pham, and Y.H. Cho, *Shell layer dependence of photoblinking in CdSe/ZnSe/ZnS quantum dots*. Appl. Phys. Lett., 2011. **98**(1).
151. Issac, A., C. von Borczyskowski, and F. Cichos, *Correlation between photoluminescence intermittency of CdSe quantum dots and self-trapped states in dielectric media*. Phys. Rev. B, 2005. **71**(16): p. 161302.
152. Iyer, G., X. Michalet, Y.P. Chang, F.F. Pinaud, S.E. Matyas, G. Payne, and S. Weiss, *High Affinity scFv-Hapten Pair as a Tool for Quantum Dot Labeling and Tracking of Single Proteins in Live Cells*. Nano Lett., 2008. **8**(12): p. 4618-4623.
153. Jackson, J.D., *Classical Electrodynamics* 1962, New York: John Wiley and Sons.

154. Jacob, J.A., S. Kapoor, N. Biswas, and T. Mukherjee, *Size tunable synthesis of silver nanoparticles in water-ethylene glycol mixtures*. Colloid Surf. A-Physicochem. Eng. Asp., 2007. **301**(1-3): p. 329-334.
155. Jaczewska, J., A. Budkowski, A. Bernasik, I. Raptis, J. Raczowska, D. Goustoruidis, J. Rysz, and M. Sanopoulou, *Humidity and solvent effects in spin-coated polythiophene-polystyrene blends*. J. Appl. Polym. Sci., 2007. **105**(1): p. 67-79.
156. Janesick, J.R., K.P. Klaasen, and T. Elliott, *CHARGE-COUPLED-DEVICE CHARGE-COLLECTION EFFICIENCY AND THE PHOTON-TRANSFER TECHNIQUE*. Opt. Eng., 1987. **26**(10): p. 972-980.
157. Jeanmaire, D.L. and R.P. Van Duyne, *Surface Raman Spectroelectrochemistry .I. Heterocyclic, Aromatic, and Aliphatic-Amines Adsorbed on Anodized Silver Electrode*. J. Electroanal. Chem., 1977. **84**(1): p. 1-20.
158. Jensen, H.J., K. Christensen, and H.C. Fogedby, *1/f noise, distribution of lifetimes, and a pile of sand*. Phys. Rev. B, 1989. **40**(10): p. 7425-7427.
159. Ji, X., G. Palui, T. Avellini, H.B. Na, C.Y. Yi, K.L. Knappenberger, and H. Mattoussi, *On the pH-Dependent Quenching of Quantum Dot Photoluminescence by Redox Active Dopamine*. J. Am. Chem. Soc., 2012. **134**(13): p. 6006-6017.
160. Jiang, J., K. Bosnick, M. Maillard, and L. Brus, *Single molecule Raman spectroscopy at the junctions of large Ag nanocrystals*. J. Phys. Chem. B, 2003. **107**(37): p. 9964-9972.
161. Jin, E.X. and X. Xu, *Plasmonic effects in near-field optical transmission enhancement through a single bowtie-shaped aperture*. Appl. Phys. B, 2006. **84**(1-2): p. 3-9.
162. Jin, E.X. and X. Xu, *Optical resonance in bowtie-shaped nanoapertures*. J. Comp. and Theo. Nano., 2008. **5**(2): p. 214-220.
163. Jin, E.X. and X.F. Xu, *Enhanced optical near field from a bowtie aperture*. Appl. Phys. Lett., 2006. **88**(15).
164. Jin, R., Y. Cao, C.A. Mirkin, K.L. Kelly, G.C. Schatz, and J.G. Zheng, *Photoinduced Conversion of Silver Nanospheres to Nanoprisms*. Science, 2001. **294**(5548): p. 1901-1903.
165. Jin, R.C., Y.W. Cao, C.A. Mirkin, K.L. Kelly, G.C. Schatz, and J.G. Zheng, *Photoinduced conversion of silver nanospheres to nanoprisms*. Science, 2001. **294**(5548): p. 1901-1903.
166. Johnson, P.B. and R.W. Christy, *Optical Constants of the Noble Metals*. Phys. Rev. B, 1972. **6**(12): p. 4370-4379.
167. Joo, T.H., M.S. Kim, and K. Kim, *Surface-Enhanced Raman-Scattering Of Benzenethiol In Silver Sol*. J. Raman Spectrosc., 1987. **18**(1): p. 57-60.



168. Kapoor, S., D. Lawless, P. Kennepohl, D. Meisel, and N. Serpone, *Reduction And Aggregation Of Silver Ions In Aqueous Gelatin Solutions*. Langmuir, 1994. **10**(9): p. 3018-3022.
169. Kelly, K.L., E. Coronado, L.L. Zhao, and G.C. Schatz, *The Optical Properties of Metal Nanoparticles: The Influence of Size, Shape, and Dielectric Environment*. J. Phys. Chem. B, 2002. **107**(3): p. 668-677.
170. Kelly, K.L., E. Coronado, L.L. Zhao, and G.C. Schatz, *The optical properties of metal nanoparticles: The influence of size, shape, and dielectric environment*. J. Phys. Chem. B, 2003. **107**(3): p. 668-677.
171. Kelly, K.L. and K. Yamashita, *Nanostructure of silver metal produced photocatalytically in TiO<sub>2</sub> films and the mechanism of the resulting photochromic behavior*. J. Phys. Chem. B, 2006. **110**(15): p. 7743-7749.
172. Kennerknecht, C., H. Hövel, M. Merschorf, S. Voll, and W. Pfeiffer, *Surface plasmon assisted photoemission from Au nanoparticles on graphite* Appl. Phys. B - Lasers O, 2001. **73**(4): p. 425-429.
173. Kerker, M., *The Optics Of Colloidal Silver - Something Old And Something New*. J. Colloid Interface Sci., 1985. **105**(2): p. 297-314.
174. Kim, S., J. Jin, Y.-J. Kim, I.-Y. Park, Y. Kim, and S.-W. Kim, *High-harmonic generation by resonant plasmon field enhancement*. Nature, 2008. **453**(7196): p. 757-760.
175. Kim, Y., N.W. Song, H. Yu, D.W. Moon, S.J. Lim, W. Kim, H.J. Yoon, and S.K. Shin, *Ligand-dependent blinking of zinc-blende CdSe/ZnS core/shell nanocrystals*. Phys. Chem. Chem. Phys., 2009. **11**(18): p. 3497-3502.
176. Kinkhabwala, A., Z. Yu, S. Fan, Y. Avlasevich, K. Muellen, and W.E. Moerner, *Large single-molecule fluorescence enhancements produced by a bowtie nanoantenna*. Nature Photonics, 2009. **3**(11): p. 654-657.
177. Klimov, V.I., *Semiconductor and Metal Nanocrystals: Synthesis and Electronic and Optical Properties* 2003: CRC Press.
178. Klimov, V.I., D.W. McBranch, C.A. Leatherdale, and M.G. Bawendi, *Electron and hole relaxation pathways in semiconductor quantum dots*. Phys. Rev. B, 1999. **60**(19): p. 13740-13749.
179. Klimov, V.I., A.A. Mikhailovsky, D.W. McBranch, C.A. Leatherdale, and M.G. Bawendi, *Quantization of multiparticle Auger rates in semiconductor quantum dots*. Science, 2000. **287**(5455): p. 1011-1013.
180. Knappenberger, K.L., D.B. Wong, Y.E. Romanyuk, and S.R. Leone, *Excitation wavelength dependence of fluorescence intermittency in CdSe/ZnS core/shell quantum dots*. Nano Lett., 2007. **7**(12): p. 3869-3874.

181. Knappenberger, K.L., Jr., D.B. Wong, Y.E. Romanyuk, and S.R. Leone, *Excitation wavelength dependence of fluorescence intermittency in CdSe/ZnS core/shell quantum dots*. Nano Lett., 2007. **7**(12): p. 3869-3874.
182. Knappenberger, K.L., Jr., D.B. Wong, W. Xu, A.M. Schwartzberg, A. Wolcott, J.Z. Zhang, and S.R. Leone, *Excitation-Wavelength Dependence of Fluorescence Intermittency in CdSe Nanorods*. ACS Nano, 2008. **2**(10): p. 2143-2153.
183. Kneipp, K., Y. Wang, H. Kneipp, L.T. Perelman, I. Itzkan, R. Dasari, and M.S. Feld, *Single molecule detection using surface-enhanced Raman scattering (SERS)*. Phys. Rev. Lett., 1997. **78**(9): p. 1667-1670.
184. Knight, M.W., Y. Wu, J.B. Lassiter, P. Nordlander, and N.J. Halas, *Substrates Matter: Influence of an Adjacent Dielectric on an Individual Plasmonic Nanoparticle*. Nano Lett., 2009.
185. Kohei, I., N. Tetsuhiko, and O. Hiromi, *Near-field optical imaging of plasmon modes in gold nanorods*. The Journal of Chemical Physics, 2005. **122**(15): p. 154701.
186. Konstantatos, G. and E.H. Sargent, *Nanostructured materials for photon detection*. Nature Nanotech., 2010. **5**(6): p. 391.
187. Kuposov, A.Y., P. Szymanski, T. Cardolaccia, T.J. Meyer, V.I. Klimov, and M. Sykora, *Electronic Properties and Structure of Assemblies of CdSe Nanocrystal Quantum Dots and Ru-Polypyridine Complexes Probed by Steady State and Time-Resolved Photoluminescence*. Adv. Fund. Mater., 2011. **21**(16): p. 3159-3168.
188. Korchev, A.S., T. Konovalova, V. Cammarata, L. Kispert, L. Slaten, and G. Mills, *Radical-induced generation of small silver particles in SPEEK/PVA polymer films and solutions: UV-vis, EPR, and FT-IR studies*. Langmuir, 2006. **22**(1): p. 375-384.
189. Kraus, R.M., P.G. Lagoudakis, J. Muller, A.L. Rogach, J.M. Lupton, J. Feldmann, D.V. Talapin, and H. Weller, *Interplay between auger and ionization processes in nanocrystal quantum dots*. J. Phys. Chem. B, 2005. **109**(39): p. 18214-18217.
190. Krauss, T.D., S. O'Brien, and L.E. Brus, *Charge and photoionization properties of single semiconductor nanocrystals*. J. Phys. Chem. B, 2001. **105**(9): p. 1725-1733.
191. Kreibig, U. and M. Vollmer, *Optical Properties of Metal Clusters*. Springer Series in Materials Science. Vol. 25. 1995, Heidelberg: Springer-Verlag. 532.
192. Krogmeier, J.R. and J. Hwang, *Data analysis considerations in probing single quantum dot fluorescence intermittency*, in *Nanobiophotonics and Biomedical Applications II*, A.N. Cartwright and M. Osinski, Editors. 2005. p. 255-262.
193. Kroo, N., G. Farkas, P. Dombi, and S. Varro, *Nonlinear processes induced by the enhanced, evanescent field of surface plasmons excited by femtosecond laser pulses*. Opt. Exp., 2008. **16**(26): p. 21656-21661.

194. Kubo, A., Y.S. Jung, H.K. Kim, and H. Petek, *Femtosecond microscopy of localized and propagating surface plasmons in silver gratings*. J. Phys. B-At. Mol. Opt. Phys., 2007. **40**(11): p. S259-S272.
195. Kubo, A., K. Onda, H. Petek, Z. Sun, Y.S. Jung, and H.K. Kim, *Femtosecond imaging of surface plasmon dynamics in a nanostructured silver film*. Nano Lett., 2005. **5** (6): p. 1123-1127.
196. Kubo, A., K. Onda, H. Petek, Z.J. Sun, Y.S. Jung, and H.K. Kim, *Femtosecond imaging of surface plasmon dynamics in a nanostructured silver film*. Nano Lett., 2005. **5**(6): p. 1123-1127.
197. Kubo, A., N. Pontius, and H. Petek, *Femtosecond microscopy of surface plasmon polariton wave packet evolution at the silver/vacuum interface*. Nano Lett., 2007. **7**(2): p. 470-475.
198. Kudelski, A. and B. Pettinger, *SERS on carbon chain segments: monitoring locally surface chemistry*. Chem. Phys. Lett., 2000. **321**(5-6): p. 356-362.
199. Kuehn, S., U. Hakanson, L. Rogobete, and V. Sandoghdar, *Enhancement of single-molecule fluorescence using a gold nanoparticle as an optical nanoantenna*. PRL, 2006. **97**: p. 017402.
200. Kuno, M., D.P. Fromm, A. Gallagher, D.J. Nesbitt, O.I. Micic, and A.J. Nozik, *Fluorescence intermittency in single InP quantum dots*. Nano Lett., 2001. **1**(10): p. 557-564.
201. Kuno, M., D.P. Fromm, H.F. Hamann, A. Gallagher, and D.J. Nesbitt, *Nonexponential "blinking" kinetics of single CdSe quantum dots: A universal power law behavior*. J. Chem. Phys., 2000. **112**(7): p. 3117-3120.
202. Kuno, M., D.P. Fromm, H.F. Hamann, A. Gallagher, and D.J. Nesbitt, *"On"/"off" fluorescence intermittency of single semiconductor quantum dots*. J. Chem. Phys., 2001. **115**(2): p. 1028-1040.
203. Kuno, M., D.P. Fromm, S.T. Johnson, A. Gallagher, and D.J. Nesbitt, *Modeling distributed kinetics in isolated semiconductor quantum dots*. Phys. Rev. B, 2003. **67**(12): p. 125304
204. Kurpick, U., J. Westhof, G. Meister, and A. Goldmann, *Ultraviolet Photoelectron-Spectroscopy With Energy-Resolved Imaging*. J. Electron Spectrosc., 1993. **63**(4): p. 311-326.
205. Lacoste, T.D., X. Michalet, F. Pinaud, D.S. Chemla, A.P. Alivisatos, and S. Weiss, *Ultra-high-resolution multicolor colocalization of single fluorescent probes*. Proc. Natl. Acad. Sci., 2000. **97**(17): p. 9461-9466.

206. Lal, S., S. Link, and N.J. Halas, *Nano-optics from sensing to waveguiding*. Nature Photonics, 2007. **1**: p. 641-648.
207. Lalanne, P., J.C. Rodier, and J.P. Hugonin, *Surface plasmons of metallic surfaces perforated by nanohole arrays*. J. Optics A, 2005. **7**(8): p. 422.
208. Lange, J., D. Bayer, C. Rohmer, C. Wiemann, O. Gaier, M. Aeschlimann, and M. Bauer, *Probing Femtosecond plasmon dynamics with nanometer resolution*. Proc. SPIE, 2006. **6195**: p. 61950Z.
209. Larson, D.R., W.R. Zipfel, R.M. Williams, S.W. Clark, M.P. Bruchez, F.W. Wise, and W.W. Webb, *Water-soluble quantum dots for multiphoton fluorescence imaging in vivo*. Science, 2003. **300**(5624): p. 1434-1436.
210. Laurence, T.A., S. Fore, and T. Huser, *Fast, flexible algorithm for calculating photon correlations*. Opt Lett, 2006. **31**(6): p. 829-831.
211. Lawless, D., S. Kapoor, P. Kennepohl, D. Meisel, and N. Serpone, *Reduction And Aggregation Of Silver Ions At The Surface Of Colloidal Silica*. J. Phys. Chem., 1994. **98**(38): p. 9619-9625.
212. Lee, D.-H., C.-T. Yuan, M. Tachiya, and J. Tang, *Influence of bin time and excitation intensity on fluorescence lifetime distribution and blinking statistics of single quantum dots*. Appl. Phys. Lett., 2009. **95**(16).
213. Lee, J., *New electrostatic energy analyzer for ESCA*. Rev. Sci. Instr., 1972. **43**(9): p. 1291-&.
214. Lee, K.S. and M.A. El-Sayed, *Gold and silver nanoparticles in sensing and imaging: Sensitivity of plasmon response to size, shape, and metal composition*. J. Phys. Chem. B, 2006. **110**(39): p. 19220-19225.
215. Lee, K.-S. and M.A. El-Sayed, *Gold and Silver Nanoparticles in Sensing and Imaging: Sensitivity of Plasmon Response to Size, Shape, and Metal Composition*. J. Phys. Chem. B, 2006. **110**(39): p. 19220-19225.
216. Lehmann, J., M. Merschdorf, W. Pfeiffer, A. Thon, S. Voll, and G. Gerber, *Surface Plasmon Dynamics in Silver Nanoparticles Studied by Femtosecond Time-Resolved Photoemission*. PRL, 2000. **85**: p. 2921-2924.
217. Li, Y.Y., H. Cheng, Z.G. Zhang, C. Wang, J.L. Zhu, Y. Liang, K.L. Zhang, S.X. Cheng, X.Z. Zhang, and R.X. Zhuo, *Cellular internalization and in vivo tracking of thermosensitive luminescent micelles based on luminescent lanthanide chelate*. ACS Nano, 2008. **2**(1): p. 125-133.
218. Lindquist, N.C., A. Lesuffleur, H. Im, and S.-H. Oh, *Sub-micron resolution surface plasmon resonance imaging enabled by nanohole arrays with surrounding Bragg mirrors for enhanced sensitivity and isolation*. Lab on a Chip, 2009. **9**(3): p. 382-387.

219. Link, S. and M.A. El-Sayed, *Spectral properties and relaxation dynamics of surface plasmon electronic oscillations in gold and silver nanodots and nanorods*. J. Phys. Chem. B, 1999. **103**(40): p. 8410-8426.
220. Link, S. and M.A. El-Sayed, *Shape and size dependence of radiative, non-radiative and photothermal properties of gold nanocrystals*. Int. Rev. Phys. Chem., 2000. **19**(3): p. 409-453.
221. Link, S., Z.L. Wang, and M.A. El-Sayed, *Alloy formation of gold-silver nanoparticles and the dependence of the plasmon absorption on their composition*. J. Phys. Chem. B, 1999. **103**(18): p. 3529-3533.
222. Lippitz, M., F. Kulzer, and M. Orrit, *Statistical evaluation of single nano-object fluorescence*. Chemphyschem, 2005. **6**(5): p. 770-789.
223. Logothetis, E.M. and P.L. Hartman, *Laser-Induced Electron Emission From Solids . Many-Photon Photoelectric Effects And Thermionic Emission*. Phys. Rev., 1969. **187**(2): p. 460-&.
224. Loo, C., A. Lowery, N. Halas, J. West, and R. Drezek, *Immunotargeted nanoshells for integrated cancer imaging and therapy*. Nano Lett., 2005. **5**(4): p. 709-711.
225. Lord, S.J., H.D. Lee, and W.E. Moerner, *Single-Molecule Spectroscopy and Imaging of Biomolecules in Living Cells*. Anal. Chem., 2010. **82**: p. 2192-2203.
226. Lott, K.F., B.D. Ghosh, and J.E. Ritchie, *Understanding the mechanism of ionic conductivity in an anhydrous proton-conducting electrolyte through measurements of single-ion diffusion coefficients*. J. Electrochem. Soc., 2006. **153**(11): p. A2044-A2048.
227. Mahler, B., P. Spinicelli, S. Buil, X. Quelin, J.-P. Hermier, and B. Dubertret, *Towards non-blinking colloidal quantum dots*. Nature Mat., 2008. **7**(8): p. 659-664.
228. Maillard, M., S. Giorgio, and M.P. Pileni, *Silver Nanodisks*. Adv. Mater., 2002. **14**(15): p. 1084-1086.
229. Malone, K., S. Weaver, D. Taylor, H. Cheng, K.P. Sarathy, and G. Mills, *Formation kinetics of small gold crystallites in photoresponsive polymer gels*. J. Phys. Chem. B, 2002. **106**(30): p. 7422-7431.
230. Mao, H.B., J. Chen, J.Q. Wang, Z.F. Li, N. Dai, and Z.Q. Zhu, *Photoluminescence investigation of CdSe quantum dots and the surface state effect*. Physica E, 2005. **27**(1-2): p. 124-128.
231. Marinchuk, M.E., *Value of Multiquantum Photocurrent*. Phys. Lett. A, 1971. **A 34**(2): p. 97.

232. Mark, W.K. and J.H. Naomi, *Nanoshells to nanoeggs to nanocups: optical properties of reduced symmetry core-shell nanoparticles beyond the quasistatic limit*. *New J Phys*, 2008. **10**(10): p. 105006.
233. Marthandam, P., A.G. Brolo, D. Sinton, K.L. Kavanagh, M.G. Moffitt, and R. Gordon, *Nanoholes in metals with applications to sensors and spectroscopy*. *Int. J. Nanotech.*, 2008. **5**(9-10): p. 1058-1081.
234. McFarland, A.D. and R.P. Van Duyne, *Single silver nanoparticles as real-time optical sensors with zeptomole sensitivity*. *Nano Lett.*, 2003. **3**(8): p. 1057-1062.
235. McGuire, J.A., M. Sykora, I. Robel, L.A. Padilha, J. Joo, J.M. Pietryga, and V.I. Klimov, *Spectroscopic Signatures of Photocharging due to Hot-Carrier Transfer in Solutions of Semiconductor Nanocrystals under Low-Intensity Ultraviolet Excitation*. *ACS Nano*, 2010. **4**(10): p. 6087-6097.
236. McMahon, J.M., A.I. Henry, K.L. Wustholz, M.J. Natan, R.G. Freeman, R.P. Van Duyne, and G.C. Schatz, *Gold nanoparticle dimer plasmonics: finite element method calculations of the electromagnetic enhancement to surface-enhanced Raman spectroscopy*. *Anal. Bioanal. Chem.*, 2009. **394**(7): p. 1819-1825.
237. Medintz, I.L., H.T. Uyeda, E.R. Goldman, and H. Mattoussi, *Quantum dot bioconjugates for imaging, labelling and sensing*. *Nature Mat.*, 2005. **4**(6): p. 435-446.
238. Meister, G. and A. Goldmann, *Angle-resolved ultraviolet photoelectron microspectroscopy*. *J. Electron Spectrosc.*, 1997. **84**(1-3): p. 1-7.
239. Merschdorf, M., W. Pfeiffer, A. Thon, S. Voll, and G. Gerber, *Photoemission from multiply excited surface plasmons in Ag nanoparticles* *Appl. Phys. A - Mater.*, 2000. **71**(5): p. 547-552.
240. Mertens, H., A.F. Koenderink, and A. Polman, *Phys. Rev. B*, 2007. **75**: p. 115123
241. Messin, G., J.P. Hermier, E. Giacobino, P. Desbiolles, and M. Dahan, *Bunching and antibunching in the fluorescence of semiconductor nanocrystals*. *Opt Lett*, 2001. **26**(23): p. 1891-1893.
242. Meyer, E.R. and J.L. Bohn, *Influence of a humidior on the aerodynamics of baseballs*. *Am. J. Phys.*, 2008. **76**(11): p. 1015-1021.
243. Michaels, A.M., J. Jiang, and L. Brus, *Ag nanocrystal junctions as the site for surface-enhanced Raman scattering of single Rhodamine 6G molecules*. *J. Phys. Chem. B*, 2000. **104**(50): p. 11965-11971.
244. Michaels, A.M., M. Nirmal, and L.E. Brus, *Surface enhanced Raman spectroscopy of individual rhodamine 6G molecules on large Ag nanocrystals*. *J. Am. Chem. Soc.*, 1999. **121**(43): p. 9932-9939.

245. Michaelson, H., *Work Function of elements and its periodicity*. J Appl Phys, 1977. **48**(11): p. 4729-4733.
246. Michaelson, H.B., *The work function of the elements and its periodicity*. J Appl Phys, 1977. **48**(11): p. 4729-4733.
247. Michler, P., A. Imamoglu, M.D. Mason, P.J. Carson, G.F. Strouse, and S.K. Buratto, *Quantum correlation among photons from a single quantum dot at room temperature*. Nature, 2000. **406**(6799): p. 968-970.
248. Mie, G., *Beiträge zur Optik trüber Medien, speziell kolloidaler Metallösungen*. Ann. Phys., 1908. **330**(3): p. 377-445.
249. Miyama, T. and Y. Yonezawa, *Photoinduced formation and aggregation of silver nanoparticles at the surface of carboxymethylcellulose films*. J. Nanopart. Res., 2004. **6**(5): p. 457-465.
250. Mock, J.J., M. Barbic, D.R. Smith, D.A. Schultz, and S. Schultz, *Shape effects in plasmon resonance of individual colloidal silver nanoparticles*. J. Chem. Phys., 2002. **116**(15): p. 6755-6759.
251. Mock, J.J., R.T. Hill, A. Degiron, S. Zauscher, A. Chilkoti, and D.R. Smith, *Distance-Dependent Plasmon Resonant Coupling between a Gold Nanoparticle and Gold Film*. Nano Lett., 2008. **8**(8): p. 2245.
252. Moerner, W.E., *Examining Nanoenvironments in Solids on the Scale of a Single, Isolated Impurity Molecule*. Science, 1994. **265**(5168): p. 46-53.
253. Moerner, W.E. and D.P. Fromm, *Methods of single-molecule fluorescence spectroscopy and microscopy*. Rev. Sci. Instr., 2003. **74**(8): p. 3597-3619.
254. Moerner, W.E. and L. Kador, *Optical detection and spectroscopy of single molecules in a solid*. Phys. Rev. Lett., 1989. **62**(21): p. 2535-2538.
255. Mohamed, M.B., V. Volkov, S. Link, and M.A. El-Sayed, *The 'lightning' gold nanorods: fluorescence enhancement of over a million compared to the gold metal*. Chem. Phys. Lett., 2000. **317**(6): p. 517.
256. Monti, O.L.A., T.A. Baker, and D.J. Nesbitt, *Imaging nanostructures with scanning photoionization microscopy*. JCP, 2006. **125**: p. 154709.
257. Monti, O.L.A., J.T. Fourkas, and D.J. Nesbitt, *Diffraction-limited photogeneration and characterization of silver nanoparticles*. J. Phys. Chem. B, 2004. **108**(5): p. 1604-1612.
258. Moskovits, M., *Surface-enhanced Raman spectroscopy: a brief retrospective*. J. Raman Spectrosc., 2005. **36**(6-7): p. 485-496.

259. Moskovits, M., *Surface-enhanced Raman spectroscopy: a brief perspective*, in *Surface-Enhanced Raman Scattering: Physics And Applications* 2006. p. 1-17.
260. Muehlschlegel, P., H.-J. Eisler, O.J.F. Martin, B. Hecht, and D.W. Pohl, *Resonant Optical Antennas*. Science, 2005. **308**: p. 1607-1609.
261. Mulvaney, P., J. Perez-Juste, M. Giersig, L.M. Liz-Marzan, and C. Pecharroman, *Drastic Surface Plasmon Mode Shifts in Gold Nanorods Due to Electron Charging*. Plasmonics, 2006. **1**: p. 61–66.
262. Munakata, T., T. Masuda, N. Ueno, A. Abdureyim, and Y. Sonoda, *Time-resolved photoemission microspectroscopy based on fs-VUV laser light*. Surf. Sci., 2002. **507**: p. 434-440.
263. Munakata, T., T. Masuda, N. Ueno, S. Sakaya, T. Sugiyama, N. Takehiro, and Y. Sonoda, *Microspot photoemission spectrometer based on FS-VUV radiation*. Surf. Sci., 2003. **532**: p. 1140-1144.
264. Munakata, T., T. Masuda, N. Ueno, S. Sakaya, T. Sugiyama, N. Takehiro, and Y. Sonoda, *Microspot photoemission spectrometer based on FS-VUV radiation*. Surf. Sci., 2003. **532–535** p. 1140–1144.
265. Munakata, T., T. Sugiyama, and Y. Sonoda, *Laser-based photoemission microspectroscopy for occupied and unoccupied states of inhomogeneous surfaces*. Surf. Sci., 2005. **593**(1-3): p. 38-42.
266. Muniz-Miranda, M., *SERS effect from silver photoreduced on to silica colloidal nanoparticles*. J. Raman Spectrosc., 2002. **33**(4): p. 295-297.
267. Muniz-Miranda, M., *Silver clusters onto nanosized colloidal silica as novel surface-enhanced Raman scattering active substrates*. Appl. Spectrosc., 2003. **57**(6): p. 655-660.
268. Muniz-Miranda, M., *SERS-active Ag/SiO<sub>2</sub> colloids: photoreduction mechanism of the silver ions and catalytic activity of the colloidal nanoparticles*. J. Raman Spectrosc., 2004. **35**(10): p. 839-842.
269. Muniz-Miranda, M. and M.F. Ottaviani, *Silver nanoclusters in mesoporous silica, as obtained by visible-laser irradiation*. Laser Phys., 2004. **14**(12): p. 1533-1538.
270. Murphy, C.J., T.K. San, A.M. Gole, C.J. Orendorff, J.X. Gao, L. Gou, S.E. Hunyadi, and T. Li, *Anisotropic metal nanoparticles: Synthesis, assembly, and optical applications*. J. Phys. Chem. B, 2005. **109**(29): p. 13857-13870.
271. Muskens, O.L., G. Bachelier, N.D. Fatti, F. Valleè, A. Brioude, X. Jiang, and M.-P. Pileni, *Quantitative Absorption Spectroscopy of a Single Gold Nanorod*. J. Phys. Chem. C, 2008. **112**(24): p. 8917.



272. Muskens, O.L., P. Billaud, M. Broyer, N.D. Fatti, and F. Vallée, *Optical extinction spectrum of a single metal nanoparticle: Quantitative characterization of a particle and of its local environment*. Phys. Rev. B, 2008. **78**(20): p. 205410.
273. Myroshnychenko, V., J. Rodriguez-Fernandez, I. Pastoriza-Santos, A.M. Funston, C. Novo, P. Mulvaney, L.M. Liz-Marzan, and F.J. Garcia de Abajo, *Modelling the optical response of gold nanoparticles*. Chem. Soc. Rev., 2008. **37**(9): p. 1792-1805.
274. Naaman, O. and J. Aumentado, *Poisson transition rates from time-domain measurements with a finite bandwidth*. Phys. Rev. Lett., 2006. **96**(10).
275. Neher, E., B. Sakmann, and J.H. Steinbach, *The extracellular patch clamp: A method for resolving currents through individual open channels in biological membranes*. Euro. J. Physiol., 1978. **375**(2): p. 219-228.
276. Neuman, K.C. and A. Nagy, *Single-molecule force spectroscopy: optical tweezers, magnetic tweezers and atomic force microscopy*. Nature Methods, 2008. **5**(6): p. 491-505.
277. Nie, S. and S.R. Emery, Science, 1997. **275**: p. 1102.
278. Nie, S.M. and S.R. Emory, *Probing single molecules and single nanoparticles by surface-enhanced Raman scattering*. Science, 1997. **275**(5303): p. 1102-1106.
279. Niemann, M., H. Kantz, and E. Barkai, *Fluctuations of 1/f Noise and the Low-Frequency Cutoff Paradox*. Phys. Rev. Lett., 2013. **110**(14): p. 140603.
280. Nirmal, M., B.O. Dabbousi, M.G. Bawendi, J.J. Macklin, J.K. Trautman, T.D. Harris, and L.E. Brus, *Fluorescence intermittency in single cadmium selenide nanocrystals*. Nature, 1996. **383**(6603): p. 802-804.
281. Nirmal, M., B.O. Dabbousi, M.G. Bawendi, J.J. Macklin, J.K. Trautman, T.D. Harris, and L.E. Brus, *Fluorescence intermittency of single cadmium selenide nanocrystals*. Nature, 1996. **383**: p. 802-804.
282. Nolte, A.J., N.D. Treat, R.E. Cohen, and M.F. Rubner, *Effect of relative humidity on the Young's modulus of polyelectrolyte multilayer films and related nonionic polymers*. Macromolecules, 2008. **41**(15): p. 5793-5798.
283. Norrod, K.L. and K.L. Rowlen, *Removal of carbonaceous contamination from SERS-active silver by self-assembly of decanethiol*. Anal. Chem., 1998. **70**(19): p. 4218-4221.
284. Novo, C., A.M. Funston, and P. Mulvaney, *Direct observation of chemical reactions on single gold nanocrystals using surface plasmon spectroscopy*. Nature Nano, 2008. **3**(10): p. 598.
285. Novo, C., D. Gomez, J. Perez-Juste, Z. Zhang, H. Petrova, M. Reismann, P. Mulvaney, and G.V. Hartland, *Contributions from radiation damping and surface scattering to the*

- linewidth of the longitudinal plasmon band of gold nanorods: a single particle study.* Phys. Chem. Chem. Phys., 2006. **8**: p. 3540.
286. Novotny, L., *Effective wavelength scaling for optical antennas.* PRL, 2007. **98**: p. 266802.
287. Odoi, M.Y., N.I. Hammer, K.T. Early, K.D. McCarthy, R. Tangirala, T. Emrick, and M.D. Barnes, *Fluorescence lifetimes and correlated photon statistics from single CdSe/oligo(phenylene vinylene) composite nanostructures.* Nano Lett., 2007. **7**(9): p. 2769-2773.
288. Oldenburg, S.J., R.D. Averitt, S.L. Westcott, and N.J. Halas, *Nanoengineering of optical resonances.* Chem. Phys. Lett., 1998. **288**(2-4): p. 243-247.
289. Onuta, T.-D., M. Waegele, C.C. DuFort, W.L. Schaich, and B. Dragnea, *Optical Field Enhancement at Cusps between Adjacent Nanoapertures.* Nano Lett., 2007. **7**(3): p. 557-564.
290. Orendorff, C.J., L. Gearheart, N.R. Janaz, and C.J. Murphy, *Aspect ratio dependence on surface enhanced Raman scattering using silver and gold nanorod substrates.* PCCP, 2005. **8**: p. 165–170.
291. Orrit, M. and J. Bernard, *Single pentacene molecules detected by fluorescence excitation in a p-terphenyl crystal.* Phys. Rev. Lett., 1990. **65**(21): p. 2716-2719.
292. Ozbay, E., *Plasmonics: Merging photonics and electronics at nanoscale dimensions.* Science, 2006. **311**(5758): p. 189-193.
293. Paje, S.E., M.A. Garcia, J. Llopis, and M.A. Villegas, *Optical spectroscopy of silver ion-exchanged As-doped glass.* J. Non-Cryst. Solids, 2003. **318**(3): p. 239-247.
294. Palik, e., *Handbook of optical constants of solids.* 1985.
295. Palik, E.D. and G. Ghosh, *Handbook of Optical Constants of Solids* 1998, San Diego: Academic Press.
296. Park, S., J.W. Hahn, and J.Y. Lee, *Doubly resonant metallic nanostructure for high conversion efficiency of second harmonic generation.* Opt. Exp., 2012. **20**(5): p. 4856-4870.
297. Park, T.-H., N. Mirin, J.B. Lassiter, C.L. Nehl, N.J. Halas, and P. Nordlander, *Optical Properties of a Nanosized Hole in a Thin Metallic Film.* ACS Nano, 2008. **2**(1): p. 25-32.
298. Patterson, G., M. Davidson, S. Manley, and J. Lippincott-Schwartz, *Superresolution Imaging using Single-Molecule Localization.* Ann. Rev. Phys. Chem., 2010. **61**(1): p. 345-367.

299. Peck, K., L. Stryer, A.N. Glazer, and R.A. Mathies, *Single-molecule fluorescence detection - auto-correlation criterion and experimental realization with phycoerythrin*. Proc. Nat. Acad. Sci., 1989. **86**(11): p. 4087-4091.
300. Pelton, M., J. Aizpurua, and G. Bryant, *Metal-nanoparticle plasmonics*. Laser Photonics Rev., 2008. **2**(3): p. 136-159.
301. Pelton, M., D.G. Grier, and P. Guyot-Sionnest, *Characterizing quantum-dot blinking using noise power spectra*. Appl. Phys. Lett., 2004. **85**(5): p. 819-821.
302. Pelton, M., M. Liu, H.Y. Kim, G. Smith, P. Guyot-Sionnest, and N.F. Scherer, *Optical trapping and alignment of single gold nanorods by using plasmon resonances*. Opt Lett, 2006. **31**: p. 2075-2077.
303. Pelton, M., M. Liu, S.S. Sungnam Park, N. F. , and P. Guyot-Sionnest, *Ultrafast resonant optical scattering from single gold nanorods: Large nonlinearities and plasmon saturation*. PRB, 2006. **73**: p. 155419.
304. Pelton, M., G. Smith, N.F. Scherer, and R.A. Marcus, *Evidence for a diffusion-controlled mechanism for fluorescence blinking of colloidal quantum dots*. Proc. Nat. Acad. Sci., 2007. **104**(36): p. 14249-14254.
305. Perroud, T.D., B. Huang, and R.N. Zare, *Effect of Bin Time on the Photon Counting Histogram for One-Photon Excitation*. Chemphyschem, 2005. **6**(5): p. 905-912.
306. Petek, H. and S. Ogawa, *Femtosecond time-resolved two-photon photoemission studies of electron dynamics in metals*. Prog. Surf. Sci., 1997. **56**(4): p. 239-310.
307. Peterson, J.J. and D.J. Nesbitt, *Modified Power Law Behavior in Quantum Dot Blinking: A Novel Role for Biexcitons and Auger Ionization*. Nano Lett., 2008: p. in press.
308. Peterson, J.J. and D.J. Nesbitt, *Modified Power Law Behavior in Quantum Dot Blinking: A Novel Role for Biexcitons and Auger Ionization*. Nano Lett., 2009. **9**(1): p. 338-345.
309. Petterson, J.J. and D.J. Nesbitt, *Modified Power Law Behavior in Quantum Dot Blinking: A Novel Role for Biexcitons and Auger Ionization*. Nano Lett., 2008: p. in press.
310. Peyser, L.A., T.H. Lee, and R.M. Dickson, *Mechanism of Ag-n nanocluster photoproduction from silver oxide films*. J. Phys. Chem. B, 2002. **106**(32): p. 7725-7728.
311. Peyser, L.A., A.E. Vinson, A.P. Bartko, and R.M. Dickson, *Photoactivated fluorescence from individual silver nanoclusters*. Science, 2001. **291**(5501): p. 103-106.
312. Peyser-Capadona, L., J. Zheng, J.I. Gonzalez, T.H. Lee, S.A. Patel, and R.M. Dickson, *Nanoparticle-free single molecule anti-Stokes Raman spectroscopy (vol 94, art no 058301, 2005)*. Phys. Rev. Lett., 2005. **94**(5): p. 058301

313. Pfeiffer, W., C. Kennerknecht, and M. Merschdorf, *Electron dynamics in supported metal nanoparticles: relaxation and charge transfer studied by time-resolved photoemission*. Appl. Phys. A, 2004. **78**: p. 1011–1028.
314. Pillai, S., K.R. Catchpole, T. Trupke, and M.A. Green, *Surface plasmon enhanced silicon solar cells*. J Appl Phys, 2007. **101**: p. 093105.
315. Pillai, Z.S. and P.V. Kamat, *What factors control the size and shape of silver nanoparticles in the citrate ion reduction method?* J. Phys. Chem. B, 2004. **108**(3): p. 945-951.
316. Podhorodecki, A., J. Misiewicz, and K. Nauka, *Photoluminescence and photoluminescence excitation spectroscopy of CdSe/ZnS core-shell free standing nanocrystals in the ultraviolet spectral range*. Phys Status Solidi (C), 2006. **3**(11): p. 3836-3839.
317. Pons, T., I.L. Medintz, D. Farrell, X. Wang, A.F. Grimes, D.S. English, L. Berti, and H. Mattoussi, *Single-Molecule Colocalization Studies Shed Light on the Idea of Fully Emitting versus Dark Single Quantum Dots*. Small, 2011. **7**(14): p. 2101-2108.
318. Pors, A., O. Albrektsen, S.I. Bozhevolnyi, and M. Willatzen, *The Optical Properties of a Truncated Spherical Cavity Embedded in Gold*. Proc. COMSOL Conf., 2009.
319. Prikulis, J., P. Hanarp, L. Olofsson, D. Sutherland, and M. Käll, *Optical spectroscopy of nanometric holes in thin gold films*. Nano Lett., 2004. **4**(6): p. 1003-1007.
320. Prodan, E., C. Radloff, N.J. Halas, and P. Nordlander, *A hybridization model for the plasmon response of complex nanostructures*. Science, 2003. **302**(5644): p. 419-422.
321. Ranganathan, S. and M. Vonheimendahl, *The 3 Activation-Energies With Isothermal Transformations - Applications To Metallic Glasses*. J. Mater. Sci., 1981. **16**(9): p. 2401-2404.
322. Rao, C.N.R. and K.J. Rao, *Phase Transitions in Solids*: McGraw-Hill.
323. Reilly, T.H., R.C. Tenent, T.M. Barnes, K.L. Rowlen, and J. van de Lagemaat, *Controlling the Optical Properties of Plasmonic Disordered Nanohole Silver Films*. ACS Nano, 2010. **4**(2): p. 615-624.
324. Rindzevicius, T., Y. Alaverdyan, B. Sepulveda, T. Pakizeh, M. Käll, R. Hillenbrand, J. Aizpurua, and F.J. Garcia de Abajo, *Nanohole plasmons in optically thin gold films*. J Phys Chem B, 2007. **111**(3): p. 1207-1212.
325. Rindzevicius, T., Y. Alaverdyan, B. Sepulveda, T. Pakizeh, M. Käll, R. Hillenbrand, J. Aizpurua, and F.J. García de Abajo, *Nanohole Plasmons in Optically Thin Gold Films*. J. Phys. Chem. C, 2006. **111**(3): p. 1207-1212.

326. Robel, I., M. Kuno, and P.V. Kamat, *Size-Dependent Electron Injection from Excited CdSe Quantum Dots into TiO<sub>2</sub> Nanoparticles*. J. Am. Chem. Soc., 2007. **129**(14): p. 4136-4137.
327. Roduner, E., *Size matters: why nanomaterials are different*. Chem. Soc. Rev., 2006. **35**(7): p. 583-592.
328. Rohmer, M., M. Bauer, T. Leissner, C. Schneider, A. Fischer, G. Niedner-Schatteburg, B.v. Issendorff, and M. Aeschlimann, *Time-resolved photoelectron nano-spectroscopy of individual silver particles: Perspectives and limitations*. Phys. Status Solidi B, 2010. **247**(5): p. 1132-1138.
329. Rombach-Riegraf, V., P. Oswald, R. Bienert, J. Petersen, M.P. Domingo, J. Pardo, P. Graeber, and E.M. Galvez, *Blinking effect and the use of quantum dots in single molecule spectroscopy*. Biochem Biophys Res Commun, 2013. **430**(1): p. 260-264.
330. Romero, I., J. Aizpurua, G.W. Bryant, and F.J. Garcia de Abajo, *Plasmons in nearly touching metallic nanoparticles: singular response in the limit of touching dimers*. Opt. Exp., 2006. **14**(21): p. 9988-9999.
331. Ropers, C., D.R. Solli, C.P. Schulz, C. Lienau, and T. Elsaesser, *Localized Multiphoton Emission of Femtosecond Electron Pulses from Metal Nanotips*. Phys. Rev. Lett., 2007. **98**(4): p. 043907.
332. Rosi, N.L. and C.A. Mirkin, *Nanostructures in Biomedicine*. Chem. Rev., 2005. **105**: p. 1547-1562.
333. Rotermund, H.H., *Imaging of dynamic processes on surfaces by light*. Surf. Sci. Rep., 1997. **29**(7-8): p. 267-364.
334. Rotermund, H.H., G. Ertl, and W. Sesselmann, *Scanning Photoemission Microscopy Of Surfaces*. Surf. Sci., 1989. **217**(3): p. L383-L390.
335. Rotermund, H.H., S. Jakubith, S. Kubala, A. Vonoertzen, and G. Ertl, *Investigation Of Surfaces By Scanning Photoemission Microscopy*. J. Electron Spectrosc., 1990. **52**: p. 811-819.
336. Roy, R., S. Hohng, and T. Ha, *A practical guide to single-molecule FRET*. Nature Methods, 2008. **5**(6): p. 507-516.
337. Rueda, D., G. Bokinsky, M.M. Rhodes, M.J. Rust, X. Zhuang, and N.G. Walter, *Single-molecule enzymology of RNA: Essential functional groups impact catalysis from a distance*. Proc. Nat. Acad. Sci., 2004. **101**(27): p. 10066-10071.
338. Rust, M.J., M. Bates, and X. Zhuang, *Sub-diffraction-limit imaging by stochastic optical reconstruction microscopy (STORM)*. Nature Meth., 2006. **3**: p. 793-795.

339. Sandstrom, M., G.W. Neilson, G. Johansson, and T. Yamaguchi, *Ag + hydration in perchlorate solution*. J. Phys. C, 1985. **18**(36): p. L1115.
340. Schaller, R.D., M. Sykora, S. Jeong, and V.I. Klimov, *High-efficiency carrier multiplication and ultrafast charge separation in semiconductor nanocrystals studied via time-resolved photoluminescence*. J. Phys. Chem. B, 2006. **110**(50): p. 25332-25338.
341. Schlegel, G., J. Bohnenberger, I. Potapova, and A. Mews, *Fluorescence decay time of single semiconductor nanocrystals*. Phys. Rev. Lett., 2002. **88**(13).
342. Schuck, P.J., D.P. Fromm, A. Sundaramurthy, G.S. Kino, and W.E. Moerner, *Improving the Mismatch between Light and Nanoscale Objects with Gold Bowtie Nanoantennas*. Phys. Rev. Lett., 2005. **94**(1): p. 017402.
343. Schweikhard, V., T.A. Baker, and D.J. Nesbitt, to be published.
344. Schweikhard, V., A. Grubisic, T.A. Baker, and D.J. Nesbitt, *Multiphoton Scanning Photoionization Imaging Microscopy for Single-Particle Studies of Plasmonic Metal Nanostructures*. J Phys Chem B, 2011. **115**(1): p. 83-91.
345. Schweikhard, V., A. Grubisic, T.A. Baker, I. Thomann, and D.J. Nesbitt, *Polarization-Dependent Scanning Photoionization Microscopy: Ultrafast Plasmon-Mediated Electron Ejection Dynamics in Single Au Nanorods*. ACS Nano, 2011. **5**(5): p. 3724-3735.
346. Schwind, M., B. Kasemo, and I. Zoric, *Localized and Propagating Plasmons in Metal Films with Nanoholes*. Nano Lett., 2013. **13**(4): p. 1743-1750.
347. Sendur, K. and W. Challener, *Near-field radiation of bow-tie antennas and apertures at optical frequencies*. J. Microscopy, 2003. **210**: p. 279-283.
348. Seo, W.S., S.M. Kim, Y.-M. Kim, X. Sun, and H. Dai, *Synthesis of Ultrasmall Ferromagnetic Face-Centered Tetragonal FePt-Graphite Core-Shell Nanocrystals*. Small, 2008. **4**: p. 1968-1971.
349. Sepulveda, B., Y. Alaverdyan, J. Alegret, M. Kall, and P. Johansson, *Shape effects in the localized surface plasmon resonance of single nanoholes in thin metal films*. Opt. Exp., 2008. **16**(8): p. 5609-5616.
350. Shaevitz, J.W., S.M. Block, and M.J. Schnitzer, *Statistical Kinetics of Macromolecular Dynamics*. Biophys. J., 2005. **89**: p. 2277-2285.
351. Shalaev, V.M., C. Douketis, T. Haslett, T. Stuckless, and M. Moskovits, *Two-photon-electron emission from smooth and rough metal films in the threshold region*. Phys. Rev. B, 1996. **53**(16): p. 11193-11206.
352. Sheng, J.W., J.W. Zheng, J. Zhang, C.H. Zhou, and L.Q. Jiang, *UV-laser-induced nanoclusters in silver ion-exchanged soda-lime silicate glass*. Physica B, 2007. **387**(1-2): p. 32-35.

353. Sherry, L.J., S.H. Chang, G.C. Schatz, R.P. Van Duyne, B.J. Wiley, and Y.N. Xia, *Localized surface plasmon resonance spectroscopy of single silver nanocubes*. Nano Lett., 2005. **5**(10): p. 2034-2038.
354. Shimizu, K.T., R.G. Neuhauser, C.A. Leatherdale, S.A. Empedocles, W.K. Woo, and M.G. Bawendi, *Blinking statistics in single semiconductor nanocrystal quantum dots*. Phys. Rev. B, 2001. **63**(20): p. 205316.
355. Shuford, K.L., S.K. Gray, M.A. Ratner, and G.C. Schatz, *Substrate effects on surface plasmons in single nanoholes*. Chem. Phys. Lett., 2007. **435**(1-3): p. 123-126.
356. Slablab, A., L. Le Xuan, M. Zielinski, Y. de Wilde, V. Jacques, D. Chauvat, and J.F. Roch, *Second-harmonic generation from coupled plasmon modes in a single dimer of gold nanospheres*. Opt. Exp., 2012. **20**(1): p. 220-227.
357. Smith, R.L., *2-Photon Photoelectric Effect*. Phys. Rev., 1962. **128**(5): p. 2225-&.
358. Sohn, Y., J. Richter, and J. Ament, Stuckless, J.T., *Two-photon photoelectron spectroscopy of conjugated polymer thin films on gold*. Appl. Phys. Lett., 2004. **84**: p. 76-78.
359. Somorjai, G.A., R.L. York, D. Butcher, and J.Y. Park, *The evolution of model catalytic systems; studies of structure, bonding and dynamics from single crystal metal surfaces to nanoparticles, and from low pressure (< 10<sup>-3</sup> Torr) to high pressure (> 10<sup>-3</sup> Torr) to liquid interfaces*. Phys. Chem. Chem. Phys., 2007. **9**(27): p. 3500-3513.
360. Son, D.H., J.S. Wittenberg, and A.P. Alivisatos, *Multielectron ionization of CdSe quantum dots in intense femtosecond ultraviolet light*. Phys. Rev. Lett., 2004. **92**(12).
361. Song, N.H., H.M. Zhu, S.Y. Jin, and T.Q. Lian, *Hole Transfer from Single Quantum Dots*. ACS Nano, 2011. **5**(11): p. 8750-8759.
362. Sönnichsen, C., T. Franzl, T. Wilk, G. von Plessen, J. Feldmann, O. Wilson, and P. Mulvaney, *Drastic Reduction of Plasmon Damping in Gold Nanorods*. Phys. Rev. Lett., 2002. **88**(7): p. 077402.
363. Srituravanich, W., N. Fang, C. Sun, Q. Luo, and X. Zhang, *Plasmonic nanolithography*. Nano Lett., 2004. **4**(6): p. 1085-1088.
364. Stefani, F.D., J.P. Hoogenboom, and E. Barkai, *Beyond quantum jumps: Blinking nanoscale light emitters*. Phys Today, 2009. **62**(2): p. 34-39.
365. Stefani, F.D., W. Knoll, M. Kreiter, X. Zhong, and M.Y. Han, *Quantification of photoinduced and spontaneous quantum-dot luminescence blinking*. Phys. Rev. B, 2005. **72**(12): p. 125304.
366. Stefani, F.D., K. Vasilev, N. Bocchio, F. Gaul, A. Pomozzi, and M. Kreiter, *Photonic mode density effects on single-molecule fluorescence blinking*. New J Phys, 2007. **9**.

367. Stefani, F.D., X.H. Zhong, W. Knoll, M.Y. Han, and M. Kreiter, *Memory in quantum-dot photoluminescence blinking*. *New J Phys*, 2005. **7**.
368. Stockman, M.I., M.F. Kling, U. Kleineberg, and F. Krausz, *Attosecond nanoplasmonic-field microscope*. *Nature Photonics*, 2007. **1**: p. 539-544.
369. Stranahan, S.M. and K.A. Willets, *Super-resolution Optical Imaging of Single-Molecule SERS Hot Spots*. *Nano Lett.*, 2010. **10**(9): p. 3777-3784.
370. Stuckless, J.T. and M. Moskovits, *Enhanced 2-Photon Photoemission from Coldly Deposited Silver Films*. *Phys. Rev. B*, 1989. **40**(14): p. 9997-9998.
371. Stuckless, J.T. and M. Moskovits, *Enhanced two-photon photoemission from coldly deposited silver films*. *PRB*  
1989. **40**: p. 9997-9998.
372. Sun, S., H. Zeng, D.B. Robinson, S. Raoux, P.M. Rice, and S.X. Wang, *Monodisperse  $MFe_2O_4$  ( $M=Fe, Co, Mn$ ) nanoparticles*. *J. Am. Chem. Soc.*, 2004. **126**: p. 273-279.
373. Sun, Y. and Y. Xia, *Shape-controlled synthesis of gold and silver nanoparticles*. *Science*, 2002. **298**(5601): p. 2176-2179.
374. Sykora, M., M.A. Petruska, J. Alstrum-Acevedo, I. Bezel, T.J. Meyer, and V.I. Klimov, *Photoinduced charge transfer between CdSe nanocrystal quantum dots and Ru-polypyridine complexes*. *J. Am. Chem. Soc.*, 2006. **128**(31): p. 9984-9985.
375. Sykora, M., M.A. Petruska, J.H. Alstrum-Acevedo, J. Leonard, T.J. Meyer, and V. Klimov, *Interfacial energy and charge transfer in assemblies consisting of CdSe nanocrystal quantum dots and Ru-polypyridine complexes*. *Abstracts of Papers of the American Chemical Society*, 2007. **234**.
376. Talley, C.E., J.B. Jackson, C. Oubre, N.K. Grady, C.W. Hollars, S.M. Lane, T.R. Huser, P. Nordlander, and N.J. Halas, *Surface-enhanced Raman scattering from individual Au nanoparticles and nanoparticle dimer substrates*. *Nano Lett.*, 2005. **5**(8): p. 1569-1574.
377. Taminiau, T., F.D. Stefani, F.B. Segerink, and N.F. Van Hulst, *Optical Antennas direct single-molecule emission*. *Nature Photonics*, 2008.
378. Tanabe, K., *Field Enhancement around Metal Nanoparticles and Nanoshells: A Systematic Investigation*. *J. Phys. Chem. C*, 2008. **112**(40): p. 15721.
379. Tang, J. and R.A. Marcus, *Mechanisms of fluorescence blinking in semiconductor nanocrystal quantum dots*. *J. Chem. Phys.*, 2005. **123**(5): p. 054704.
380. Tang, J. and R.A. Marcus, *Diffusion-controlled electron transfer processes and power-law statistics of fluorescence intermittency of nanoparticles*. *Phys. Rev. Lett.*, 2005. **95**(10): p. 107401



381. Tang, J. and R.A. Marcus, *Single particle versus ensemble average: From power-law intermittency of a single quantum dot to quasistretched exponential fluorescence decay of an ensemble*. J. Chem. Phys., 2005. **123**(20).
382. Taylor, C.E., S.D. Garvey, and J.E. Pemberton, *Carbon contamination at silver surfaces: Surface preparation procedures evaluated by Raman spectroscopy and X-ray photoelectron spectroscopy*. Anal. Chem., 1996. **68**(14): p. 2401-2408.
383. Taylor, C.E., J.E. Pemberton, G.G. Goodman, and M.H. Schoenfish, *Surface enhancement factors for Ag and Au surfaces relative to Pt surfaces for monolayers of thiophenol*. Appl. Spectrosc., 1999. **53**(10): p. 1212-1221.
384. Texter, J., J.J. Hastreiter, and J.L. Hall, *Spectroscopic confirmation of the tetrahedral geometry of tetraaquasilver(+) ion (Ag(H<sub>2</sub>O)<sub>4</sub><sup>+</sup>)*. The Journal of Physical Chemistry, 1983. **87**(23): p. 4690-4693.
385. Theye, M.L., *Investigation of the optical properties of Au by means of thin semitransparent films*. Phys. Rev. B, 1970. **2**(8): p. 3060-3081.
386. Tomov, Toma E., R. Tsukanov, R. Masoud, M. Liber, N. Plavner, and E. Nir, *Disentangling Subpopulations in Single-Molecule FRET and ALEX Experiments with Photon Distribution Analysis*. Biophys. J., 2012. **102**(5): p. 1163-1173.
387. Tompkins, H.G., S. Tasic, J. Baker, and D. Convey, *Spectroscopic ellipsometry measurements of thin metal films*. Surf. Interface Anal., 2000. **29**(3): p. 179-187.
388. Turkevich, J., P.C. Stevenson, and J. Hillier, *A Study Of The Nucleation And Growth Processes In The Synthesis Of Colloidal Gold*. Discuss Faraday Soc, 1951(11): p. 55-&.
389. Uchaikin, V.V. and R.T. Sibatov, *Statistical model of fluorescence blinking*. J Exp Theo Phys, 2009. **109**(4): p. 537-546.
390. Verberk, R., J.W.M. Chon, M. Gu, and M. Orrit, *Environment-dependent blinking of single semiconductor nanocrystals and statistical aging of ensembles*. Physica E, 2005. **26**(1-4): p. 19-23.
391. Verberk, R. and M. Orrit, *Photon statistics in the fluorescence of single molecules and nanocrystals: Correlation functions versus distributions of on- and off-times*. J. Chem. Phys., 2003. **119**(4): p. 2214-2222.
392. Verberk, R., A.M. van Oijen, and M. Orrit, *Simple model for the power-law blinking of single semiconductor nanocrystals*. Phys. Rev. B, 2002. **66**(23): p. 233202
393. Verneker, V.R. and J.N. Maycock, *PHOTOCHEMICAL DECOMPOSITION OF SILVER PERCHLORATE*. J. Phys. Chem., 1968. **72**(8): p. 2798-&.

394. Vitukhnovskii, A.G., A.Y. Pereverzev, V.V. Fedyanin, S.A. Ambrozevich, R.B. Vasiliev, and D.N. Dirin, *Correlation between photon-emission intervals in blinking luminescence of single CdSe/CdS nanocrystals*. *Jetp Lett*, 2012. **96**(1): p. 17-20.
395. Vlckova, B., P. Matejka, J. Simonova, K. Cermakova, P. Pancoska, and V. Baumruk, *Surface-Enhanced Resonance Raman-Spectra Of Free-Base 5,10,15,20-Tetrakis(4-Carboxyphenyl)Porphyrin And Its Silver Complex In Systems With Silver Colloid - Direct Adsorption In Comparison To Adsorption Via Molecular Spacer*. *J. Phys. Chem.*, 1993. **97**(38): p. 9719-9729.
396. Vogel, M., A. Gruber, J. Wrachtrup, and C. Vonborczyskowski, *Determination Of Intersystem Crossing Parameters Via Observation Of Quantum Jumps On Single Molecules*. *J. Phys. Chem.*, 1995. **99**(41): p. 14915-14917.
397. Vonoertzen, A., H.H. Rotermund, S. Jakubith, and G. Ertl, *The Scanning Photoemission Microscope - A Novel Tool In Surface Science*. *Ultramicroscopy*, 1991. **36**(1-3): p. 107-116.
398. Wang, S., C. Querner, T. Emmons, M. Drndic, and C.H. Crouch, *Fluorescence blinking statistics from CdSe core and core/shell nanorods*. *J. Phys. Chem. B*, 2006. **110**(46): p. 23221-23227.
399. Wang, S., C. Querner, M.D. Fischbein, L. Willis, D.S. Novikov, C.H. Crouch, and M. Drndic, *Blinking Statistics Correlated with Nanoparticle Number*. *Nano Lett.*, 2008. **8**(11): p. 4020-4026.
400. Wang, X., X. Ren, K. Kahen, M.A. Hahn, M. Rajeswaran, S. Maccagnano-Zacher, J. Silcox, G.E. Cragg, A.L. Efros, and T.D. Krauss, *Non-blinking semiconductor nanocrystals*. *Nature*, 2009. **459**(7247): p. 686-689.
401. Watanabe, K., D. Menzel, N. Nilius, and H.J. Freund, *Photochemistry on metal nanoparticles*. *Chem. Rev.*, 2006. **106**: p. 4301-4320.
402. Watkins, L.P. and H. Yang, *Detection of intensity change points in time-resolved single-molecule measurements*. *J. Phys. Chem. B*, 2005. **109**(1): p. 617-628.
403. Weber, M.L., J.P. Litz, D.J. Masiello, and K.A. Willets, *Super-Resolution Imaging Reveals a Difference between SERS and Luminescence Centroids*. *ACS Nano*, 2012. **6**(2): p. 1839-1848.
404. Weber, M.L. and K.A. Willets, *Correlated Super-Resolution Optical and Structural Studies of Surface-Enhanced Raman Scattering Hot Spots in Silver Colloid Aggregates*. *J. Phys. Chem. Lett.*, 2011. **2**(14): p. 1766-1770.
405. Weiss, S., *Fluorescence Spectroscopy of Single Biomolecules*. *Science*, 1999. **283**(5408): p. 1676-1683.

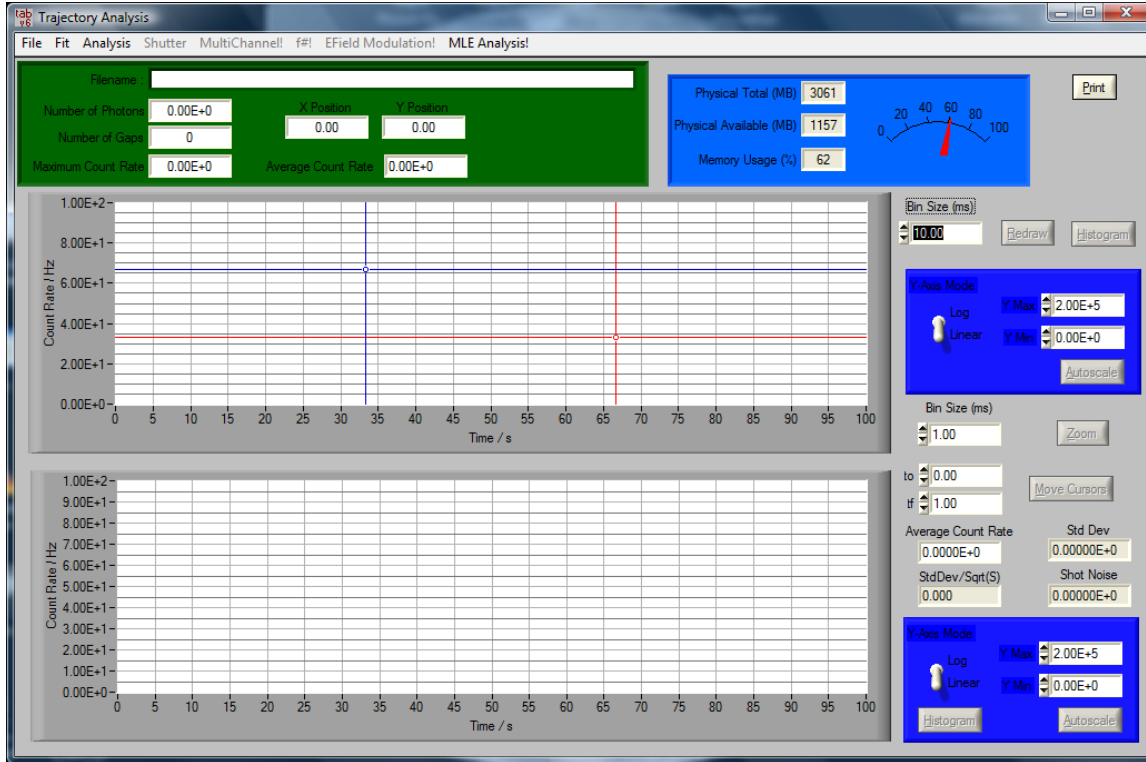
406. Wenzel, T., J. Bosbach, A. Goldmann, F. Stietz, and F. Träger, *Shaping nanoparticles and their optical spectra with photons*. Appl. Phys. B, 1999. **69**(5): p. 513.
407. West, J.L. and N.J. Halas, *Engineered nanomaterials for biophotonics applications: Improving sensing, imaging, and therapeutics*. Annu. Rev. Biomed. Eng., 2003. **5**: p. 285-292.
408. Weston, K.D., M. Dyck, P. Tinnefeld, C. Müller, D.P. Herten, and M. Sauer, *Measuring the Number of Independent Emitters in Single-Molecule Fluorescence Images and Trajectories Using Coincident Photons*. Anal. Chem., 2002. **74**(20): p. 5342-5349.
409. Whitney, A.V., J.W. Elam, S.L. Zou, A.V. Zinovev, P.C. Stair, G.C. Schatz, and R.P. Van Duyne, *Localized surface plasmon resonance nanosensor: A high-resolution distance-dependence study using atomic layer deposition*. J. Phys. Chem. B, 2005. **109**(43): p. 20522-20528.
410. Wiemann, C., D. Bayer, M. Rohmer, M. Aeschlimann, and M. Bauer, *Local 2PPE-yield enhancement in a defined periodic silver nanodisk array*. Surf. Sci., 2007. **601**: p. 4714-4721.
411. Wiley, B.J., S.H. Im, Z.Y. Li, J. McLellan, A. Siekkinen, and Y.A. Xia, *Maneuvering the surface plasmon resonance of silver nanostructures through shape-controlled synthesis*. J. Phys. Chem. B, 2006. **110**(32): p. 15666-15675.
412. Willets, K.A. and R.P. Van Duyne, *Localized surface plasmon resonance spectroscopy and sensing*. Ann. Rev. Phys. Chem., 2007. **58**: p. 267-297.
413. Word, R.C., T. Dornan, and R. Könenkamp, *Photoemission from localized surface plasmons in fractal metal nanostructures*. Appl. Phys. Lett., 2010. **96**: p. 251110
414. Wu, E., Y. Chi, B. Wu, K. Xia, Y. Yokota, K. Ueno, H. Misawa, and H. Zeng, *Spatial polarization sensitivity of single Au bowtie nanostructures*. J. Lumines., 2011. **131**(9): p. 1971-1974.
415. Wu, L.Y., B.M. Ross, and L.P. Lee, *Optical Properties of the Crescent-Shaped Nanohole Antenna*. Nano Lett., 2009. **9**(5): p. 1956-1961.
416. Wu, P.W., B. Dunn, V. Doan, B.J. Schwartz, E. Yablonovitch, and M. Yamane, *Controlling the spontaneous precipitation of silver nanoparticles in sol-gel materials*. J. Sol-Gel Sci. Technol., 2000. **19**(1-3): p. 249-252.
417. Wustholz, K.L., E.D. Bott, B. Kahr, and P.J. Reid, *Memory and spectral diffusion in single-molecule emission*. J Phys Chem B, 2008. **112**(21): p. 7877-7885.
418. Xia, Y.N. and N.J. Halas, *Shape-controlled synthesis and surface plasmonic properties of metallic nanostructures*. MRS Bull., 2005. **30**(5): p. 338-344.

419. Xie, X. and J. Trautman, *Optical studies of single molecules at room temperature*. Ann. Rev. Phys. Chem., 1998. **49**: p. 441-480.
420. Xu, H. and M. Käll, *Polarization-Dependent Surface-Enhanced Raman Spectroscopy of Isolated Silver Nanoaggregates*. Chemphyschem, 2003. **4**(9): p. 1001-1005.
421. Xu, X.S., T. Yamada, and S. Yokoyama, *Correlations between antibunching and blinking of photoluminescence from a single CdSe quantum dot*. Eu Phys J D, 2009. **55**(3): p. 691-697.
422. Yao, J., D.R. Larson, H.D. Vishwasrao, W.R. Zipfel, and W.W. Webb, *Blinking and nonradiant dark fraction of water-soluble quantum dots in aqueous solution*. Proc. Nat. Acad. Sci., 2005. **102**(40): p. 14284-14289.
423. Yildiz, A., J.N. Forkey, S.A. McKinney, T. Ha, Y.E. Goldman, and P.R. Selvin, *Myosin V Walks Hand-Over-Hand: Single Fluorophore Imaging with 1.5-nm Localization*. Science, 2003. **300**(5628): p. 2061-2065.
424. Yildiz, A. and P.R. Selvin, *Fluorescence imaging with one nanometer accuracy: Application to molecular motors*. Accounts Chem. Res., 2005. **38**(7): p. 574-582.
425. Yin, L., V.K. Vlasko-Vlasov, A. Rydh, J. Pearson, U. Welp, S.H. Chang, S.K. Gray, G.C. Schatz, D.B. Brown, and C.W. Kimball, *Surface plasmons at single nanoholes in Au films*. Appl. Phys. Lett., 2004. **85**(3): p. 467-469.
426. Yin, Y. and A.P. Alivisatos, *Colloidal nanocrystal synthesis and the organic-inorganic interface*. Nature, 2005. **437**: p. 664-670.
427. Yu, M. and A. Van Orden, *Enhanced fluorescence intermittency of CdSe-ZnS quantum-dot clusters*. Phys. Rev. Lett., 2006. **97**(23).
428. Zhang, J.G., S.Q. Xu, and E. Kumacheva, *Photogeneration of fluorescent silver nanoclusters in polymer microgels*. Adv. Mater., 2005. **17**(19): p. 2336-+.
429. Zhang, K., H.Y. Chang, A.H. Fu, A.P. Alivisatos, and H. Yang, *Continuous distribution of emission states from single CdSe/ZnS quantum dots*. Nano Lett., 2006. **6**(4): p. 843-847.
430. Zhang, L.Z., J.C. Yu, H.Y. Yip, Q. Li, K.W. Kwong, A.W. Xu, and P.K. Wong, *Ambient light reduction strategy to synthesize silver nanoparticles and silver-coated TiO<sub>2</sub> with enhanced photocatalytic and bactericidal activities*. Langmuir, 2003. **19**(24): p. 10372-10380.
431. Zhang, X.Y., E.M. Hicks, J. Zhao, G.C. Schatz, and R.P. Van Duyne, *Electrochemical tuning of silver nanoparticles fabricated by nanosphere lithography*. Nano Lett., 2005. **5**(7): p. 1503-1507.

432. Zhang, X.Y., A.V. Whitney, J. Zhao, E.M. Hicks, and R.P. Van Duyne, *Advances in contemporary nanosphere lithographic techniques*. J. Nanosci. Nanotechnol., 2006. **6**(7): p. 1920-1934.
433. Zhao, J., O. Chen, D.B. Strasfeld, and M.G. Bawendi, *Biexciton Quantum Yield Heterogeneities in Single CdSe (CdS) Core (Shell) Nanocrystals and Its Correlation to Exciton Blinking*. Nano Lett., 2012. **12**(9): p. 4477-4483.
434. Zhao, J., N. Pontius, A. Winkelmann, V. Sametoglu, A. Kubo, A.G. Borisov, D. Sanchez-Portal, V.M. Silkin, E.V. Chulkov, P. Echenique, and H. Petek, *Electronic potential of a chemisorption surface*. PRB, 2008. **78**: p. 085419.
435. Zheng, X., W. Xu, C. Corredor, S. Xu, J. An, B. Zhao, and J.R. Lombardi, *Laser-Induced Growth of Monodisperse Silver Nanoparticles with Tunable Surface Plasmon Resonance Properties and a Wavelength Self-Limiting Effect*. J. Phys. Chem. C, 2007. **111**(41): p. 14962.
436. Zheng, X.L., D.W. Guo, Y.L. Shao, S.J. Jia, S.P. Xu, B. Zhao, W.Q. Xu, C. Corredor, and J.R. Lombardi, *Photochemical modification of an optical fiber tip with a silver nanoparticle film: A SERS chemical sensor*. Langmuir, 2008. **24**(8): p. 4394-4398.
437. Zhu, H.M., N.H. Song, and T.Q. Lian, *Wave Function Engineering for Ultrafast Charge Separation and Slow Charge Recombination in Type II Core/Shell Quantum Dots*. J. Am. Chem. Soc., 2011. **133**(22): p. 8762-8771.
438. Zhu, X.Y., *Electron transfer at molecule-metal interfaces: A two-photon photoemission study*. Ann. Rev. Phys. Chem., 2002. **53**: p. 221-247.
439. Zhu, X.Y., *Charge transport at metal-molecule interfaces: A spectroscopic view*. J. Phys. Chem. B, 2004. **108**(26): p. 8778-8793.

# Appendix A: TAB Analysis

## A.1 Main Panel and Functions





```
1 #include "pch.h"
2 #include <QGLWidget>
3 #include <QGuiApplication>
4 #include <QColor>
5 #include <QPainter>
6 #include <QTextStream>
7 #include <QTextStream>
8 #include <QTextStream>
9 #include <QTextStream>
10 #include <QTextStream>
11 #include <QTextStream>
12 #include <QTextStream>
13 #include <QTextStream>
14 #include <QTextStream>
15 #include <QTextStream>
16 #include <QTextStream>
17 #include <QTextStream>
18 #include <QTextStream>
19 #include <QTextStream>
20 #include <QTextStream>
21 #include <QTextStream>
22 #include <QTextStream>
23
24 #define WINDOW_WIDTH 1024
25 #define WINDOW_HEIGHT 768
26 #define COLOR_COUNT 256
27
28 int main(int argc, char *argv[])
29 {
30     // Create application
31     QGuiApplication app(argc, argv);
32
33     // Create window
34     QWidget widget(WINDOW_WIDTH, WINDOW_HEIGHT);
35
36     // Create widget
37     QWidget *w = new QWidget(&widget);
38
39     // Create widget
40     QWidget *w2 = new QWidget(w);
41
42     // Create widget
43     QWidget *w3 = new QWidget(w2);
44
45     // Create widget
46     QWidget *w4 = new QWidget(w3);
47
48     // Create widget
49     QWidget *w5 = new QWidget(w4);
50
51     // Create widget
52     QWidget *w6 = new QWidget(w5);
53
54     // Create widget
55     QWidget *w7 = new QWidget(w6);
56
57     // Create widget
58     QWidget *w8 = new QWidget(w7);
59
60     // Create widget
61     QWidget *w9 = new QWidget(w8);
62
63     // Create widget
64     QWidget *w10 = new QWidget(w9);
65
66     // Create widget
67     QWidget *w11 = new QWidget(w10);
68
69     // Create widget
70     QWidget *w12 = new QWidget(w11);
71
72     // Create widget
73     QWidget *w13 = new QWidget(w12);
74
75     // Create widget
76     QWidget *w14 = new QWidget(w13);
77
78     // Create widget
79     QWidget *w15 = new QWidget(w14);
80
81     // Create widget
82     QWidget *w16 = new QWidget(w15);
83
84     // Create widget
85     QWidget *w17 = new QWidget(w16);
86
87     // Create widget
88     QWidget *w18 = new QWidget(w17);
89
90     // Create widget
91     QWidget *w19 = new QWidget(w18);
92
93     // Create widget
94     QWidget *w20 = new QWidget(w19);
95
96     // Create widget
97     QWidget *w21 = new QWidget(w20);
98
99     // Create widget
100     QWidget *w22 = new QWidget(w21);
101
102     // Create widget
103     QWidget *w23 = new QWidget(w22);
104
105     // Create widget
106     QWidget *w24 = new QWidget(w23);
107
108     // Create widget
109     QWidget *w25 = new QWidget(w24);
110
111     // Create widget
112     QWidget *w26 = new QWidget(w25);
113
114     // Create widget
115     QWidget *w27 = new QWidget(w26);
116
117     // Create widget
118     QWidget *w28 = new QWidget(w27);
119
120     // Create widget
121     QWidget *w29 = new QWidget(w28);
122
123     // Create widget
124     QWidget *w30 = new QWidget(w29);
125
126     // Create widget
127     QWidget *w31 = new QWidget(w30);
128
129     // Create widget
130     QWidget *w32 = new QWidget(w31);
131
132     // Create widget
133     QWidget *w33 = new QWidget(w32);
134
135     // Create widget
136     QWidget *w34 = new QWidget(w33);
137
138     // Create widget
139     QWidget *w35 = new QWidget(w34);
140
141     // Create widget
142     QWidget *w36 = new QWidget(w35);
143
144     // Create widget
145     QWidget *w37 = new QWidget(w36);
146
147     // Create widget
148     QWidget *w38 = new QWidget(w37);
149
150     // Create widget
151     QWidget *w39 = new QWidget(w38);
152
153     // Create widget
154     QWidget *w40 = new QWidget(w39);
155
156     // Create widget
157     QWidget *w41 = new QWidget(w40);
158
159     // Create widget
160     QWidget *w42 = new QWidget(w41);
161
162     // Create widget
163     QWidget *w43 = new QWidget(w42);
164
165     // Create widget
166     QWidget *w44 = new QWidget(w43);
167
168     // Create widget
169     QWidget *w45 = new QWidget(w44);
170
171     // Create widget
172     QWidget *w46 = new QWidget(w45);
173
174     // Create widget
175     QWidget *w47 = new QWidget(w46);
176
177     // Create widget
178     QWidget *w48 = new QWidget(w47);
179
180     // Create widget
181     QWidget *w49 = new QWidget(w48);
182
183     // Create widget
184     QWidget *w50 = new QWidget(w49);
185
186     // Create widget
187     QWidget *w51 = new QWidget(w50);
188
189     // Create widget
190     QWidget *w52 = new QWidget(w51);
191
192     // Create widget
193     QWidget *w53 = new QWidget(w52);
194
195     // Create widget
196     QWidget *w54 = new QWidget(w53);
197
198     // Create widget
199     QWidget *w55 = new QWidget(w54);
200
201     // Create widget
202     QWidget *w56 = new QWidget(w55);
203
204     // Create widget
205     QWidget *w57 = new QWidget(w56);
206
207     // Create widget
208     QWidget *w58 = new QWidget(w57);
209
210     // Create widget
211     QWidget *w59 = new QWidget(w58);
212
213     // Create widget
214     QWidget *w60 = new QWidget(w59);
215
216     // Create widget
217     QWidget *w61 = new QWidget(w60);
218
219     // Create widget
220     QWidget *w62 = new QWidget(w61);
221
222     // Create widget
223     QWidget *w63 = new QWidget(w62);
224
225     // Create widget
226     QWidget *w64 = new QWidget(w63);
227
228     // Create widget
229     QWidget *w65 = new QWidget(w64);
230
231     // Create widget
232     QWidget *w66 = new QWidget(w65);
233
234     // Create widget
235     QWidget *w67 = new QWidget(w66);
236
237     // Create widget
238     QWidget *w68 = new QWidget(w67);
239
240     // Create widget
241     QWidget *w69 = new QWidget(w68);
242
243     // Create widget
244     QWidget *w70 = new QWidget(w69);
245
246     // Create widget
247     QWidget *w71 = new QWidget(w70);
248
249     // Create widget
250     QWidget *w72 = new QWidget(w71);
251
252     // Create widget
253     QWidget *w73 = new QWidget(w72);
254
255     // Create widget
256     QWidget *w74 = new QWidget(w73);
257
258     // Create widget
259     QWidget *w75 = new QWidget(w74);
260
261     // Create widget
262     QWidget *w76 = new QWidget(w75);
263
264     // Create widget
265     QWidget *w77 = new QWidget(w76);
266
267     // Create widget
268     QWidget *w78 = new QWidget(w77);
269
270     // Create widget
271     QWidget *w79 = new QWidget(w78);
272
273     // Create widget
274     QWidget *w80 = new QWidget(w79);
275
276     // Create widget
277     QWidget *w81 = new QWidget(w80);
278
279     // Create widget
280     QWidget *w82 = new QWidget(w81);
281
282     // Create widget
283     QWidget *w83 = new QWidget(w82);
284
285     // Create widget
286     QWidget *w84 = new QWidget(w83);
287
288     // Create widget
289     QWidget *w85 = new QWidget(w84);
290
291     // Create widget
292     QWidget *w86 = new QWidget(w85);
293
294     // Create widget
295     QWidget *w87 = new QWidget(w86);
296
297     // Create widget
298     QWidget *w88 = new QWidget(w87);
299
300     // Create widget
301     QWidget *w89 = new QWidget(w88);
302
303     // Create widget
304     QWidget *w90 = new QWidget(w89);
305
306     // Create widget
307     QWidget *w91 = new QWidget(w90);
308
309     // Create widget
310     QWidget *w92 = new QWidget(w91);
311
312     // Create widget
313     QWidget *w93 = new QWidget(w92);
314
315     // Create widget
316     QWidget *w94 = new QWidget(w93);
317
318     // Create widget
319     QWidget *w95 = new QWidget(w94);
320
321     // Create widget
322     QWidget *w96 = new QWidget(w95);
323
324     // Create widget
325     QWidget *w97 = new QWidget(w96);
326
327     // Create widget
328     QWidget *w98 = new QWidget(w97);
329
330     // Create widget
331     QWidget *w99 = new QWidget(w98);
332
333     // Create widget
334     QWidget *w100 = new QWidget(w99);
335
336     // Create widget
337     QWidget *w101 = new QWidget(w100);
338
339     // Create widget
340     QWidget *w102 = new QWidget(w101);
341
342     // Create widget
343     QWidget *w103 = new QWidget(w102);
344
345     // Create widget
346     QWidget *w104 = new QWidget(w103);
347
348     // Create widget
349     QWidget *w105 = new QWidget(w104);
350
351     // Create widget
352     QWidget *w106 = new QWidget(w105);
353
354     // Create widget
355     QWidget *w107 = new QWidget(w106);
356
357     // Create widget
358     QWidget *w108 = new QWidget(w107);
359
360     // Create widget
361     QWidget *w109 = new QWidget(w108);
362
363     // Create widget
364     QWidget *w110 = new QWidget(w109);
365
366     // Create widget
367     QWidget *w111 = new QWidget(w110);
368
369     // Create widget
370     QWidget *w112 = new QWidget(w111);
371
372     // Create widget
373     QWidget *w113 = new QWidget(w112);
374
375     // Create widget
376     QWidget *w114 = new QWidget(w113);
377
378     // Create widget
379     QWidget *w115 = new QWidget(w114);
380
381     // Create widget
382     QWidget *w116 = new QWidget(w115);
383
384     // Create widget
385     QWidget *w117 = new QWidget(w116);
386
387     // Create widget
388     QWidget *w118 = new QWidget(w117);
389
390     // Create widget
391     QWidget *w119 = new QWidget(w118);
392
393     // Create widget
394     QWidget *w120 = new QWidget(w119);
395
396     // Create widget
397     QWidget *w121 = new QWidget(w120);
398
399     // Create widget
400     QWidget *w122 = new QWidget(w121);
401
402     // Create widget
403     QWidget *w123 = new QWidget(w122);
404
405     // Create widget
406     QWidget *w124 = new QWidget(w123);
407
408     // Create widget
409     QWidget *w125 = new QWidget(w124);
410
411     // Create widget
412     QWidget *w126 = new QWidget(w125);
413
414     // Create widget
415     QWidget *w127 = new QWidget(w126);
416
417     // Create widget
418     QWidget *w128 = new QWidget(w127);
419
420     // Create widget
421     QWidget *w129 = new QWidget(w128);
422
423     // Create widget
424     QWidget *w130 = new QWidget(w129);
425
426     // Create widget
427     QWidget *w131 = new QWidget(w130);
428
429     // Create widget
430     QWidget *w132 = new QWidget(w131);
431
432     // Create widget
433     QWidget *w133 = new QWidget(w132);
434
435     // Create widget
436     QWidget *w134 = new QWidget(w133);
437
438     // Create widget
439     QWidget *w135 = new QWidget(w134);
440
441     // Create widget
442     QWidget *w136 = new QWidget(w135);
443
444     // Create widget
445     QWidget *w137 = new QWidget(w136);
446
447     // Create widget
448     QWidget *w138 = new QWidget(w137);
449
450     // Create widget
451     QWidget *w139 = new QWidget(w138);
452
453     // Create widget
454     QWidget *w140 = new QWidget(w139);
455
456     // Create widget
457     QWidget *w141 = new QWidget(w140);
458
459     // Create widget
460     QWidget *w142 = new QWidget(w141);
461
462     // Create widget
463     QWidget *w143 = new QWidget(w142);
464
465     // Create widget
466     QWidget *w144 = new QWidget(w143);
467
468     // Create widget
469     QWidget *w145 = new QWidget(w144);
470
471     // Create widget
472     QWidget *w146 = new QWidget(w145);
473
474     // Create widget
475     QWidget *w147 = new QWidget(w146);
476
477     // Create widget
478     QWidget *w148 = new QWidget(w147);
479
480     // Create widget
481     QWidget *w149 = new QWidget(w148);
482
483     // Create widget
484     QWidget *w150 = new QWidget(w149);
485
486     // Create widget
487     QWidget *w151 = new QWidget(w150);
488
489     // Create widget
490     QWidget *w152 = new QWidget(w151);
491
492     // Create widget
493     QWidget *w153 = new QWidget(w152);
494
495     // Create widget
496     QWidget *w154 = new QWidget(w153);
497
498     // Create widget
499     QWidget *w155 = new QWidget(w154);
500
501     // Create widget
502     QWidget *w156 = new QWidget(w155);
503
504     // Create widget
505     QWidget *w157 = new QWidget(w156);
506
507     // Create widget
508     QWidget *w158 = new QWidget(w157);
509
510     // Create widget
511     QWidget *w159 = new QWidget(w158);
512
513     // Create widget
514     QWidget *w160 = new QWidget(w159);
515
516     // Create widget
517     QWidget *w161 = new QWidget(w160);
518
519     // Create widget
520     QWidget *w162 = new QWidget(w161);
521
522     // Create widget
523     QWidget *w163 = new QWidget(w162);
524
525     // Create widget
526     QWidget *w164 = new QWidget(w163);
527
528     // Create widget
529     QWidget *w165 = new QWidget(w164);
529
```



```

443 unsigned long ubin_size, ul;
444 int i=0, ibin = 0, di;
445 double curbin_time;
446 int count = 0;
447 unsigned int *i;
448 double acti;
449 double mean = 0.0;
450
451 ubin_size = (unsigned long) ceil((double) (numMacrof[binMacrof-1]) * prec * 1.05 / (bin_time));
452 int *bin = (int *) malloc(ubin_size);
453 if (!bin) {
454     fprintf(stderr, "Error: out of memory\n");
455     return 1;
456 }
457
458 // Bin the MCS data
459 int i;
460 for (i = 0; i < ubin_size; i++) {
461     bin[i] = 0;
462 }
463
464 // Returns the bin count rate in Hz
465 double bin_count_rate;
466 double curbin_time;
467 double acti;
468 double mean = 0.0;
469
470 // MCS data
471 int i;
472 for (i = 0; i < ubin_size; i++) {
473     bin[i] = 0;
474 }
475
476 // Compute the bin count rate in Hz
477 double bin_count_rate;
478 double curbin_time;
479 double acti;
480 double mean = 0.0;
481
482 // MCS data
483 int i;
484 for (i = 0; i < ubin_size; i++) {
485     bin[i] = 0;
486 }
487
488 // Returns the bin count rate in Hz
489 double bin_count_rate;
490 double curbin_time;
491 double acti;
492 double mean = 0.0;
493
494 // MCS data
495 int i;
496 for (i = 0; i < ubin_size; i++) {
497     bin[i] = 0;
498 }
499
500 // Returns the bin count rate in Hz
501 double bin_count_rate;
502 double curbin_time;
503 double acti;
504 double mean = 0.0;
505
506 // MCS data
507 int i;
508 for (i = 0; i < ubin_size; i++) {
509     bin[i] = 0;
510 }
511
512 // Returns the bin count rate in Hz
513 double bin_count_rate;
514 double curbin_time;
515 double acti;
516 double mean = 0.0;
517
518 // MCS data
519 int i;
520 for (i = 0; i < ubin_size; i++) {
521     bin[i] = 0;
522 }
523
524 // Returns the bin count rate in Hz
525 double bin_count_rate;
526 double curbin_time;
527 double acti;
528 double mean = 0.0;
529
530 // MCS data
531 int i;
532 for (i = 0; i < ubin_size; i++) {
533     bin[i] = 0;
534 }
535
536 // Returns the bin count rate in Hz
537 double bin_count_rate;
538 double curbin_time;
539 double acti;
540 double mean = 0.0;
541
535 // MCS data
536 int i;
537 for (i = 0; i < ubin_size; i++) {
538     bin[i] = 0;
539 }
540
541 // Returns the bin count rate in Hz
542 double bin_count_rate;
543 double curbin_time;
544 double acti;
545 double mean = 0.0;
546
547 // MCS data
548 int i;
549 for (i = 0; i < ubin_size; i++) {
550     bin[i] = 0;
551 }
552
553 // Returns the bin count rate in Hz
554 double bin_count_rate;
555 double curbin_time;
556 double acti;
557 double mean = 0.0;
558
559 // MCS data
560 int i;
561 for (i = 0; i < ubin_size; i++) {
562     bin[i] = 0;
563 }
564
565 // Returns the bin count rate in Hz
566 double bin_count_rate;
567 double curbin_time;
568 double acti;
569 double mean = 0.0;
570
571 // MCS data
572 int i;
573 for (i = 0; i < ubin_size; i++) {
574     bin[i] = 0;
575 }
576
577 // Returns the bin count rate in Hz
578 double bin_count_rate;
579 double curbin_time;
580 double acti;
581 double mean = 0.0;
582
583 // MCS data
584 int i;
585 for (i = 0; i < ubin_size; i++) {
586     bin[i] = 0;
587 }
588
589 // Returns the bin count rate in Hz
590 double bin_count_rate;
591 double curbin_time;
592 double acti;
593 double mean = 0.0;
594
595 // MCS data
596 int i;
597 for (i = 0; i < ubin_size; i++) {
598     bin[i] = 0;
599 }
600
601 // Returns the bin count rate in Hz
602 double bin_count_rate;
603 double curbin_time;
604 double acti;
605 double mean = 0.0;
606
607 // MCS data
608 int i;
609 for (i = 0; i < ubin_size; i++) {
610     bin[i] = 0;
611 }
612
613 // Returns the bin count rate in Hz
614 double bin_count_rate;
615 double curbin_time;
616 double acti;
617 double mean = 0.0;
618
619 // MCS data
620 int i;
621 for (i = 0; i < ubin_size; i++) {
622     bin[i] = 0;
623 }
624
625 // Returns the bin count rate in Hz
626 double bin_count_rate;
627 double curbin_time;
628 double acti;
629 double mean = 0.0;
630
631 // MCS data
632 int i;
633 for (i = 0; i < ubin_size; i++) {
634     bin[i] = 0;
635 }
636
637 // Returns the bin count rate in Hz
638 double bin_count_rate;
639 double curbin_time;
640 double acti;
641 double mean = 0.0;
642
643 // MCS data
644 int i;
645 for (i = 0; i < ubin_size; i++) {
646     bin[i] = 0;
647 }
648
649 // Returns the bin count rate in Hz
650 double bin_count_rate;
651 double curbin_time;
652 double acti;
653 double mean = 0.0;
654
655 // MCS data
656 int i;
657 for (i = 0; i < ubin_size; i++) {
658     bin[i] = 0;
659 }
660
661 // Returns the bin count rate in Hz
662 double bin_count_rate;
663 double curbin_time;
664 double acti;
665 double mean = 0.0;
666
667 // MCS data
668 int i;
669 for (i = 0; i < ubin_size; i++) {
670     bin[i] = 0;
671 }
672
673 // Returns the bin count rate in Hz
674 double bin_count_rate;
675 double curbin_time;
676 double acti;
677 double mean = 0.0;
678
679 // MCS data
680 int i;
681 for (i = 0; i < ubin_size; i++) {
682     bin[i] = 0;
683 }
684
685 // Returns the bin count rate in Hz
686 double bin_count_rate;
687 double curbin_time;
688 double acti;
689 double mean = 0.0;
690
691 // MCS data
692 int i;
693 for (i = 0; i < ubin_size; i++) {
694     bin[i] = 0;
695 }
696
697 // Returns the bin count rate in Hz
698 double bin_count_rate;
699 double curbin_time;
700 double acti;
701 double mean = 0.0;
702
703 // MCS data
704 int i;
705 for (i = 0; i < ubin_size; i++) {
706     bin[i] = 0;
707 }
708
709 // Returns the bin count rate in Hz
710 double bin_count_rate;
711 double curbin_time;
712 double acti;
713 double mean = 0.0;
714
715 // MCS data
716 int i;
717 for (i = 0; i < ubin_size; i++) {
718     bin[i] = 0;
719 }
720
721 // Returns the bin count rate in Hz
722 double bin_count_rate;
723 double curbin_time;
724 double acti;
725 double mean = 0.0;
726
727 // MCS data
728 int i;
729 for (i = 0; i < ubin_size; i++) {
730     bin[i] = 0;
731 }
732
733 // Returns the bin count rate in Hz
734 double bin_count_rate;
735 double curbin_time;
736 double acti;
737 double mean = 0.0;
738
739 // MCS data
740 int i;
741 for (i = 0; i < ubin_size; i++) {
742     bin[i] = 0;
743 }
744
745 // Returns the bin count rate in Hz
746 double bin_count_rate;
747 double curbin_time;
748 double acti;
749 double mean = 0.0;
750
751 // MCS data
752 int i;
753 for (i = 0; i < ubin_size; i++) {
754     bin[i] = 0;
755 }
756
757 // Returns the bin count rate in Hz
758 double bin_count_rate;
759 double curbin_time;
760 double acti;
761 double mean = 0.0;
762
763 // MCS data
764 int i;
765 for (i = 0; i < ubin_size; i++) {
766     bin[i] = 0;
767 }
768
769 // Returns the bin count rate in Hz
770 double bin_count_rate;
771 double curbin_time;
772 double acti;
773 double mean = 0.0;
774
775 // MCS data
776 int i;
777 for (i = 0; i < ubin_size; i++) {
778     bin[i] = 0;
779 }
780
781 // Returns the bin count rate in Hz
782 double bin_count_rate;
783 double curbin_time;
784 double acti;
785 double mean = 0.0;
786
787 // MCS data
788 int i;
789 for (i = 0; i < ubin_size; i++) {
790     bin[i] = 0;
791 }
792
793 // Returns the bin count rate in Hz
794 double bin_count_rate;
795 double curbin_time;
796 double acti;
797 double mean = 0.0;
798
799 // MCS data
800 int i;
801 for (i = 0; i < ubin_size; i++) {
802     bin[i] = 0;
803 }
804
805 // Returns the bin count rate in Hz
806 double bin_count_rate;
807 double curbin_time;
808 double acti;
809 double mean = 0.0;
810
811 // MCS data
812 int i;
813 for (i = 0; i < ubin_size; i++) {
814     bin[i] = 0;
815 }
816
817 // Returns the bin count rate in Hz
818 double bin_count_rate;
819 double curbin_time;
820 double acti;
821 double mean = 0.0;
822
823 // MCS data
824 int i;
825 for (i = 0; i < ubin_size; i++) {
826     bin[i] = 0;
827 }
828
829 // Returns the bin count rate in Hz
830 double bin_count_rate;
831 double curbin_time;
832 double acti;
833 double mean = 0.0;
834
835 // MCS data
836 int i;
837 for (i = 0; i < ubin_size; i++) {
838     bin[i] = 0;
839 }
840
841 // Returns the bin count rate in Hz
842 double bin_count_rate;
843 double curbin_time;
844 double acti;
845 double mean = 0.0;
846
847 // MCS data
848 int i;
849 for (i = 0; i < ubin_size; i++) {
850     bin[i] = 0;
851 }
852
853 // Returns the bin count rate in Hz
854 double bin_count_rate;
855 double curbin_time;
856 double acti;
857 double mean = 0.0;
858
859 // MCS data
860 int i;
861 for (i = 0; i < ubin_size; i++) {
862     bin[i] = 0;
863 }
864
865 // Returns the bin count rate in Hz
866 double bin_count_rate;
867 double curbin_time;
868 double acti;
869 double mean = 0.0;
870
871 // MCS data
872 int i;
873 for (i = 0; i < ubin_size; i++) {
874     bin[i] = 0;
875 }
876
877 // Returns the bin count rate in Hz
878 double bin_count_rate;
879 double curbin_time;
880 double acti;
881 double mean = 0.0;
882
883 // MCS data
884 int i;
885 for (i = 0; i < ubin_size; i++) {
886     bin[i] = 0;
887 }
888
889 // Returns the bin count rate in Hz
890 double bin_count_rate;
891 double curbin_time;
892 double acti;
893 double mean = 0.0;
894
895 // MCS data
896 int i;
897 for (i = 0; i < ubin_size; i++) {
898     bin[i] = 0;
899 }
900
901 // Returns the bin count rate in Hz
902 double bin_count_rate;
903 double curbin_time;
904 double acti;
905 double mean = 0.0;
906
907 // MCS data
908 int i;
909 for (i = 0; i < ubin_size; i++) {
910     bin[i] = 0;
911 }
912
913 // Returns the bin count rate in Hz
914 double bin_count_rate;
915 double curbin_time;
916 double acti;
917 double mean = 0.0;
918
919 // MCS data
920 int i;
921 for (i = 0; i < ubin_size; i++) {
922     bin[i] = 0;
923 }
924
925 // Returns the bin count rate in Hz
926 double bin_count_rate;
927 double curbin_time;
928 double acti;
929 double mean = 0.0;
930
931 // MCS data
932 int i;
933 for (i = 0; i < ubin_size; i++) {
934     bin[i] = 0;
935 }
936
937 // Returns the bin count rate in Hz
938 double bin_count_rate;
939 double curbin_time;
940 double acti;
941 double mean = 0.0;
942
943 // MCS data
944 int i;
945 for (i = 0; i < ubin_size; i++) {
946     bin[i] = 0;
947 }
948
949 // Returns the bin count rate in Hz
950 double bin_count_rate;
951 double curbin_time;
952 double acti;
953 double mean = 0.0;
954
955 // MCS data
956 int i;
957 for (i = 0; i < ubin_size; i++) {
958     bin[i] = 0;
959 }
960
961 // Returns the bin count rate in Hz
962 double bin_count_rate;
963 double curbin_time;
964 double acti;
965 double mean = 0.0;
966
967 // MCS data
968 int i;
969 for (i = 0; i < ubin_size; i++) {
970     bin[i] = 0;
971 }
972
973 // Returns the bin count rate in Hz
974 double bin_count_rate;
975 double curbin_time;
976 double acti;
977 double mean = 0.0;
978
979 // MCS data
980 int i;
981 for (i = 0; i < ubin_size; i++) {
982     bin[i] = 0;
983 }
984
985 // Returns the bin count rate in Hz
986 double bin_count_rate;
987 double curbin_time;
988 double acti;
989 double mean = 0.0;
990
991 // MCS data
992 int i;
993 for (i = 0; i < ubin_size; i++) {
994     bin[i] = 0;
995 }
996
997 // Returns the bin count rate in Hz
998 double bin_count_rate;
999 double curbin_time;
1000 double acti;
1001 double mean = 0.0;

```

```

659 }
660
661 int OYCOLLBACK Quedist (int panel, int control, int event,
662 int callbackData, int eventData1, int eventData2)
663 {
664     double yain, ymax;
665     double ibin;
666     double *Xaxis;
667     int *CHRlistogram;
668     switch (event)
669     {
670         case EVENT_COMMENT:
671             DisplayForm3 (panel2);
672             GetCtrlVal (panel0, FRAME_0_NUMERIC_BUTTON, edbinbin);
673             GetCtrlVal (panel0, FRAME_0_NUMERIC_BUTTON, edbinmax);
674             double yain = edbinbin * 1E-3;
675             double ymax = edbinmax * 1E-3;
676             SetCtrlVal (panel2, FRAME_2_NUMERIC_MAIN_YAIN, yain);
677             SetCtrlVal (panel2, FRAME_2_NUMERIC_MAIN_YSUM, ysum);
678             SetCtrlVal (panel2, FRAME_2_NUMERIC_MAIN_IBIN, ibin);
679             SetCtrlVal (panel2, FRAME_2_NUMERIC_MAIN_IX, ix);
680             SetCtrlVal (panel2, FRAME_2_NUMERIC_MAIN_IZ, iz);
681             SetCtrlVal (panel2, FRAME_2_NUMERIC_MAIN_IZ, iz);
682             SetCtrlVal (panel2, FRAME_2_NUMERIC_MAIN_IZ, iz);
683             SetCtrlVal (panel2, FRAME_2_NUMERIC_MAIN_IZ, iz);
684             SetCtrlVal (panel2, FRAME_2_NUMERIC_MAIN_IZ, iz);
685             SetCtrlVal (panel2, FRAME_2_NUMERIC_MAIN_IZ, iz);
686             SetCtrlVal (panel2, FRAME_2_NUMERIC_MAIN_IZ, iz);
687             SetCtrlVal (panel2, FRAME_2_NUMERIC_MAIN_IZ, iz);
688             SetCtrlVal (panel2, FRAME_2_NUMERIC_MAIN_IZ, iz);
689             SetCtrlVal (panel2, FRAME_2_NUMERIC_MAIN_IZ, iz);
690             Histogram (edbinbin, yain, ymax, CHRlistogram, Xaxis, ibin);
691             Deallocate (panel2, FRAME_2_GRAPH_HIST, -1, VAL_IMMEDIATE_DRAW);
692             PLOTT (panel2, FRAME_2_GRAPH_HIST, Xaxis, CHRlistogram, ibin, VAL_DOUBLE, VAL_DOUBLE, VAL_INTEGER, VAL_SCATTER,
693                 VAL_FONT_NORMAL, VAL_BOLD, 1, VAL_BLACK);
694             Free (Xaxis);
695             Free (CHRlistogram);
696             return 0;
697         case EVENT_COMMENT:
698             return 0;
699         case EVENT_COMMENT:
700             return 0;
701         case EVENT_COMMENT:
702             return 0;
703     }
704     int OYCOLLBACK Quedist (int panel, int control, int event,
705     int callbackData, int eventData1, int eventData2)
706     {
707         double yain, ymax;
708         double cmax, cmin;
709         int ix, iy;
710         switch (event)
711         {
712             case EVENT_COMMENT:
713                 HidePanel (panel2);
714                 return 0;
715         }
716     }
717     int OYCOLLBACK ReHist (int panel, int control, int event,
718     int callbackData, int eventData1, int eventData2)
719     {
720         double yain, ymax;
721         double ibin;
722         double *Xaxis;
723         int *CHRlistogram;
724         switch (event)
725         {
726             case EVENT_COMMENT:
727                 DisplayForm3 (panel2);
728                 GetCtrlVal (panel0, FRAME_0_NUMERIC_BUTTON, edbinbin);
729                 GetCtrlVal (panel0, FRAME_0_NUMERIC_BUTTON, edbinmax);
730                 double yain = edbinbin * 1E-3;
731                 double ymax = edbinmax * 1E-3;
732                 SetCtrlVal (panel2, FRAME_2_NUMERIC_MAIN_YAIN, yain);
733                 SetCtrlVal (panel2, FRAME_2_NUMERIC_MAIN_YSUM, ysum);
734                 SetCtrlVal (panel2, FRAME_2_NUMERIC_MAIN_IBIN, ibin);
735                 SetCtrlVal (panel2, FRAME_2_NUMERIC_MAIN_IX, ix);
736                 SetCtrlVal (panel2, FRAME_2_NUMERIC_MAIN_IZ, iz);
737                 SetCtrlVal (panel2, FRAME_2_NUMERIC_MAIN_IZ, iz);
738                 SetCtrlVal (panel2, FRAME_2_NUMERIC_MAIN_IZ, iz);
739                 SetCtrlVal (panel2, FRAME_2_NUMERIC_MAIN_IZ, iz);
740                 SetCtrlVal (panel2, FRAME_2_NUMERIC_MAIN_IZ, iz);
741                 SetCtrlVal (panel2, FRAME_2_NUMERIC_MAIN_IZ, iz);
742                 SetCtrlVal (panel2, FRAME_2_NUMERIC_MAIN_IZ, iz);
743                 SetCtrlVal (panel2, FRAME_2_NUMERIC_MAIN_IZ, iz);
744                 SetCtrlVal (panel2, FRAME_2_NUMERIC_MAIN_IZ, iz);
745                 Histogram (edbinbin, yain, ymax, CHRlistogram, Xaxis, ibin);
746                 Deallocate (panel2, FRAME_2_GRAPH_HIST, -1, VAL_IMMEDIATE_DRAW);
747                 PLOTT (panel2, FRAME_2_GRAPH_HIST, Xaxis, CHRlistogram, ibin, VAL_DOUBLE, VAL_DOUBLE, VAL_INTEGER, VAL_SCATTER,
748                     VAL_FONT_NORMAL, VAL_BOLD, 1, VAL_BLACK);
749                 Free (Xaxis);
750                 Free (CHRlistogram);
751                 return 0;
752         }
753     }
754     int OYCOLLBACK ReHist (int panel, int control, int event,
755     int callbackData, int eventData1, int eventData2)
756     {
757         double yain, ymax;
758         double cmax, cmin;
759         int ix, iy;
760         switch (event)
761         {
762             case EVENT_COMMENT:
763                 HidePanel (panel2);
764                 return 0;
765         }
766     }
767     int OYCOLLBACK ReHist (int panel, int control, int event,
768     int callbackData, int eventData1, int eventData2)
769     {
770         double yain, ymax;
771         double cmax, cmin;
772         int ix, iy;
773         switch (event)
774         {
775             case EVENT_COMMENT:
776                 HidePanel (panel2);
777                 return 0;
778         }
779     }
780     int OYCOLLBACK ReHist (int panel, int control, int event,
781     int callbackData, int eventData1, int eventData2)
782     {
783         double yain, ymax;
784         double cmax, cmin;
785         int ix, iy;
786         switch (event)
787         {
788             case EVENT_COMMENT:
789                 HidePanel (panel2);
790                 return 0;
791         }
792     }
793     int OYCOLLBACK ReHist (int panel, int control, int event,
794     int callbackData, int eventData1, int eventData2)
795     {
796         double yain, ymax;
797         double cmax, cmin;
798         int ix, iy;
799         switch (event)
800         {
801             case EVENT_COMMENT:
802                 HidePanel (panel2);
803                 return 0;
804         }
805     }
806     int OYCOLLBACK ReHist (int panel, int control, int event,
807     int callbackData, int eventData1, int eventData2)
808     {
809         double yain, ymax;
810         double cmax, cmin;
811         int ix, iy;
812         switch (event)
813         {
814             case EVENT_COMMENT:
815                 HidePanel (panel2);
816                 return 0;
817         }
818     }
819     int OYCOLLBACK ReHist (int panel, int control, int event,
820     int callbackData, int eventData1, int eventData2)
821     {
822         double yain, ymax;
823         double cmax, cmin;
824         int ix, iy;
825         switch (event)
826         {
827             case EVENT_COMMENT:
828                 HidePanel (panel2);
829                 return 0;
830         }
831     }
832     int OYCOLLBACK ReHist (int panel, int control, int event,
833     int callbackData, int eventData1, int eventData2)
834     {
835         double yain, ymax;
836         double cmax, cmin;
837         int ix, iy;
838         switch (event)
839         {
840             case EVENT_COMMENT:
841                 HidePanel (panel2);
842                 return 0;
843         }
844     }
845     int OYCOLLBACK ReHist (int panel, int control, int event,
846     int callbackData, int eventData1, int eventData2)
847     {
848         double yain, ymax;
849         double cmax, cmin;
850         int ix, iy;
851         switch (event)
852         {
853             case EVENT_COMMENT:
854                 HidePanel (panel2);
855                 return 0;
856         }
857     }
858     int OYCOLLBACK ReHist (int panel, int control, int event,
859     int callbackData, int eventData1, int eventData2)
860     {
861         double yain, ymax;
862         double cmax, cmin;
863         int ix, iy;
864         switch (event)
865         {
866             case EVENT_COMMENT:
867                 HidePanel (panel2);
868                 return 0;
869         }
870     }
871     int OYCOLLBACK ReHist (int panel, int control, int event,
872     int callbackData, int eventData1, int eventData2)
873     {
874         double yain, ymax;
875         double cmax, cmin;
876         int ix, iy;
877         switch (event)
878         {
879             case EVENT_COMMENT:
880                 HidePanel (panel2);
881                 return 0;
882         }
883     }
884     int OYCOLLBACK ReHist (int panel, int control, int event,
885     int callbackData, int eventData1, int eventData2)
886     {
887         double yain, ymax;
888         double cmax, cmin;
889         int ix, iy;
890         switch (event)
891         {
892             case EVENT_COMMENT:
893                 HidePanel (panel2);
894                 return 0;
895         }
896     }
897     int OYCOLLBACK ReHist (int panel, int control, int event,
898     int callbackData, int eventData1, int eventData2)
899     {
900         double yain, ymax;
901         double cmax, cmin;
902         int ix, iy;
903         switch (event)
904         {
905             case EVENT_COMMENT:
906                 HidePanel (panel2);
907                 return 0;
908         }
909     }
910     int OYCOLLBACK ReHist (int panel, int control, int event,
911     int callbackData, int eventData1, int eventData2)
912     {
913         double yain, ymax;
914         double cmax, cmin;
915         int ix, iy;
916         switch (event)
917         {
918             case EVENT_COMMENT:
919                 HidePanel (panel2);
920                 return 0;
921         }
922     }
923     int OYCOLLBACK ReHist (int panel, int control, int event,
924     int callbackData, int eventData1, int eventData2)
925     {
926         double yain, ymax;
927         double cmax, cmin;
928         int ix, iy;
929         switch (event)
930         {
931             case EVENT_COMMENT:
932                 HidePanel (panel2);
933                 return 0;
934         }
935     }
936     int OYCOLLBACK ReHist (int panel, int control, int event,
937     int callbackData, int eventData1, int eventData2)
938     {
939         double yain, ymax;
940         double cmax, cmin;
941         int ix, iy;
942         switch (event)
943         {
944             case EVENT_COMMENT:
945                 HidePanel (panel2);
946                 return 0;
947         }
948     }
949     int OYCOLLBACK ReHist (int panel, int control, int event,
950     int callbackData, int eventData1, int eventData2)
951     {
952         double yain, ymax;
953         double cmax, cmin;
954         int ix, iy;
955         switch (event)
956         {
957             case EVENT_COMMENT:
958                 HidePanel (panel2);
959                 return 0;
960         }
961     }
962     int OYCOLLBACK ReHist (int panel, int control, int event,
963     int callbackData, int eventData1, int eventData2)
964     {
965         double yain, ymax;
966         double cmax, cmin;
967         int ix, iy;
968         switch (event)
969         {
970             case EVENT_COMMENT:
971                 HidePanel (panel2);
972                 return 0;
973         }
974     }
975     int OYCOLLBACK ReHist (int panel, int control, int event,
976     int callbackData, int eventData1, int eventData2)
977     {
978         double yain, ymax;
979         double cmax, cmin;
980         int ix, iy;
981         switch (event)
982         {
983             case EVENT_COMMENT:
984                 HidePanel (panel2);
985                 return 0;
986         }
987     }
988     int OYCOLLBACK ReHist (int panel, int control, int event,
989     int callbackData, int eventData1, int eventData2)
990     {
991         double yain, ymax;
992         double cmax, cmin;
993         int ix, iy;
994         switch (event)
995         {
996             case EVENT_COMMENT:
997                 HidePanel (panel2);
998                 return 0;
999         }
1000     }

```

```
880 ReadCheck1);
881
882 SetMenuAttributes (hmenu, MENU_FILE_SaveloadSIZI, APPEND_DIALOG, 0);
883 return 0;
884
885
886 int CYCLONAMEK AutoScale MCS_Zoom (int panel, int control, int event,
887 void *callbackData, int eventData1, int eventData2)
888 {
889     double cmx, cmy;
890     int i;
891     switch (event)
892     {
893         case EVENT_COMMIT:
894             MAXIMUMID (eMCS_Zoom, ulzombinMSC-1, cmx, cmy, kMin, kMax);
895             SetCtrlVal (panel, PARAM_0_NUMERIC_Min_Z, 0.0);
896             SetCtrlVal (panel, PARAM_0_NUMERIC_Max_Z, 1.0*cmx);
897             break;
898     }
899     return 0;
900 }
901
902 int CYCLONAMEK Plot_Scale (int panel, int control, int event,
903 void *callbackData, int eventData1, int eventData2)
904 {
905     switch (event)
906     {
907         case EVENT_COMMIT:
908             PrintPanel (panel, "1", 0, VAL_PLOT, PARAM_1);
909             break;
910     }
911     return 0;
912 }
913
914 int CYCLONAMEK Move Cursors (int panel, int control, int event,
915 void *callbackData, int eventData1, int eventData2)
916 {
917     double dMin_Like;
918     dMin_Like = dMin;
919     PlotBand1d_1 (plotband1d, plotband1d);
920     switch (event)
921     {
922         case EVENT_COMMIT:
923             SetCtrlVal (panel, PARAM_0_NUMERIC_Min_Z, dMin);
924             SetCtrlVal (panel, PARAM_0_NUMERIC_Max_Z, dMin_Like);
925             break;
926     }
927     return 0;
928 }
929
930 GetMouseCoordinates (panel0, PARAM_0_NUMERIC_Min_Z, 1, plotband1d, kMindest);
931
932
933
934
935
936
937
938
939
940
941
942
943
944
945
946
947
948
949
950 int CYCLONAMEK Behave_Zoom (int panel, int control, int event,
951 void *callbackData, int eventData1, int eventData2)
952 {
953     double yMin, yMax;
954     int i;
955     switch (event)
956     {
957         case EVENT_COMMIT:
958             SetCtrlVal (panel, PARAM_3_NUMERIC_Min_AbsIncr);
959             SetCtrlVal (panel, PARAM_3_NUMERIC_Max_AbsIncr);
960             SetCtrlVal (panel, PARAM_3_NUMERIC_Min_Sym);
961             SetCtrlVal (panel, PARAM_3_NUMERIC_Max_Sym);
962             XAxis = malloc (sizeof (double));
963             YAxis = malloc (sizeof (double));
964             memset (XAxis, 0.0, sizeof (double));
965             memset (YAxis, 0.0, sizeof (double));
966             Histogram (eMCS_Zoom, ulzombinMSC-1, yMin, yMax, CHR_Histogram, XAxis, YAxis);
967             break;
968     }
969     return 0;
970 }
971
972 Plot_Scale (panel, PARAM_3_NUMERIC_Min_AbsIncr, -1, VAL_HORIZONTAL_SCROLL);
973 Plot_Scale (panel, PARAM_3_NUMERIC_Max_AbsIncr, -1, VAL_HORIZONTAL_SCROLL);
974 Plot_Scale (panel, PARAM_3_NUMERIC_Min_Sym, -1, VAL_HORIZONTAL_SCROLL);
975 Plot_Scale (panel, PARAM_3_NUMERIC_Max_Sym, -1, VAL_HORIZONTAL_SCROLL);
976 free (XAxis);
977 free (YAxis);
978 break;
979 }
980 }
981 return 0;
982
983 int CYCLONAMEK Closest_Zoom (int panel, int control, int event,
984 void *callbackData, int eventData1, int eventData2)
985 {
986     switch (event)
987     {
988     }
989 }
```

```

986
987
988
989
990
991
992
993
994
995
996
997
998
999
1000
1001
1002
1003
1004
1005
1006
1007
1008
1009
1010
1011
1012
1013
1014
1015
1016
1017
1018
1019
1020
1021
1022
1023
1024
1025
1026
1027
1028
1029
1030
1031
1032
1033
1034
1035
1036
1037
1038
1039
1040
1041
1042
1043
1044
1045
1046
1047
1048
1049
1050
1051
1052
1053
1054
1055
1056
1057
1058
1059
1060
1061
1062
1063
1064
1065
1066
1067
1068
1069
1070
1071
1072
1073
1074
1075
1076
1077
1078
1079
1080
1081
1082
1083
1084
1085
1086
1087
1088
1089
1090
1091
1092
1093
1094
1095
1096
1097
1098
1099
1100
1101
1102
1103
1104
1105
1106
1107
1108
1109
1110
1111
1112
1113
1114
1115
1116
1117
1118
1119
1120
1121
1122
1123
1124
1125
1126
1127
1128
1129
1130
1131
1132
1133
1134
1135
1136
1137
1138
1139
1140
1141
1142
1143
1144
1145
1146
1147
1148
1149
1150
1151
1152
1153
1154
1155
1156
1157
1158
1159
1160
1161
1162
1163
1164
1165
1166
1167
1168
1169
1170
1171
1172
1173
1174
1175
1176
1177
1178
1179
1180
1181
1182
1183
1184
1185
1186
1187
1188
1189
1190
1191
1192
1193
1194
1195
1196
1197
1198
1199
1200
1201
1202
1203
1204
1205
1206
1207
1208
1209
1210
1211
1212
1213
1214
1215
1216
1217
1218
1219
1220
1221
1222
1223
1224
1225
1226
1227
1228
1229
1230
1231
1232
1233
1234
1235
1236
1237
1238
1239
1240
1241
1242
1243
1244
1245
1246
1247
1248
1249
1250
1251
1252
1253
1254
1255
1256
1257
1258
1259
1260
1261
1262
1263
1264
1265
1266
1267
1268
1269
1270
1271
1272
1273
1274
1275
1276
1277
1278
1279
1280
1281
1282
1283
1284
1285
1286
1287
1288
1289
1290
1291
1292
1293
1294
1295
1296
1297
1298
1299
1300
1301
1302
1303
1304
1305
1306
1307
1308
1309
1310
1311
1312
1313
1314
1315
1316
1317
1318
1319
1320
1321
1322
1323
1324
1325
1326
1327
1328
1329
1330
1331
1332
1333
1334
1335
1336
1337
1338
1339
1340
1341
1342
1343
1344
1345
1346
1347
1348
1349
1350
1351
1352
1353
1354
1355
1356
1357
1358
1359
1360
1361
1362
1363
1364
1365
1366
1367
1368
1369
1370
1371
1372
1373
1374
1375
1376
1377
1378
1379
1380
1381
1382
1383
1384
1385
1386
1387
1388
1389
1390
1391
1392
1393
1394
1395
1396
1397
1398
1399
1400
```

```

1046
1047
1048
1049
1050
1051
1052
1053
1054
1055
1056
1057
1058
1059
1060
1061
1062
1063
1064
1065
1066
1067
1068
1069
1070
1071
1072
1073
1074
1075
1076
1077
1078
1079
1080
1081
1082
1083
1084
1085
1086
1087
1088
1089
1090
1091
1092
1093
1094
1095
1096
1097
1098
1099
1100
1101
1102
1103
1104
1105
1106
1107
1108
1109
1110
1111
1112
1113
1114
1115
1116
1117
1118
1119
1120
1121
1122
1123
1124
1125
1126
1127
1128
1129
1130
1131
1132
1133
1134
1135
1136
1137
1138
1139
1140
1141
1142
1143
1144
1145
1146
1147
1148
1149
1150
1151
1152
1153
1154
1155
1156
1157
1158
1159
1160
1161
1162
1163
1164
1165
1166
1167
1168
1169
1170
1171
1172
1173
1174
1175
1176
1177
1178
1179
1180
1181
1182
1183
1184
1185
1186
1187
1188
1189
1190
1191
1192
1193
1194
1195
1196
1197
1198
1199
1200
1201
1202
1203
1204
1205
1206
1207
1208
1209
1210
1211
1212
1213
1214
1215
1216
1217
1218
1219
1220
1221
1222
1223
1224
1225
1226
1227
1228
1229
1230
1231
1232
1233
1234
1235
1236
1237
1238
1239
1240
1241
1242
1243
1244
1245
1246
1247
1248
1249
1250
1251
1252
1253
1254
1255
1256
1257
1258
1259
1260
1261
1262
1263
1264
1265
1266
1267
1268
1269
1270
1271
1272
1273
1274
1275
1276
1277
1278
1279
1280
1281
1282
1283
1284
1285
1286
1287
1288
1289
1290
1291
1292
1293
1294
1295
1296
1297
1298
1299
1300
1301
1302
1303
1304
1305
1306
1307
1308
1309
1310
1311
1312
1313
1314
1315
1316
1317
1318
1319
1320
1321
1322
1323
1324
1325
1326
1327
1328
1329
1330
1331
1332
1333
1334
1335
1336
1337
1338
1339
1340
1341
1342
1343
1344
1345
1346
1347
1348
1349
1350
1351
1352
1353
1354
1355
1356
1357
1358
1359
1360
1361
1362
1363
1364
1365
1366
1367
1368
1369
1370
1371
1372
1373
1374
1375
1376
1377
1378
1379
1380
1381
1382
1383
1384
1385
1386
1387
1388
1389
1390
1391
1392
1393
1394
1395
1396
1397
1398
1399
1400
```





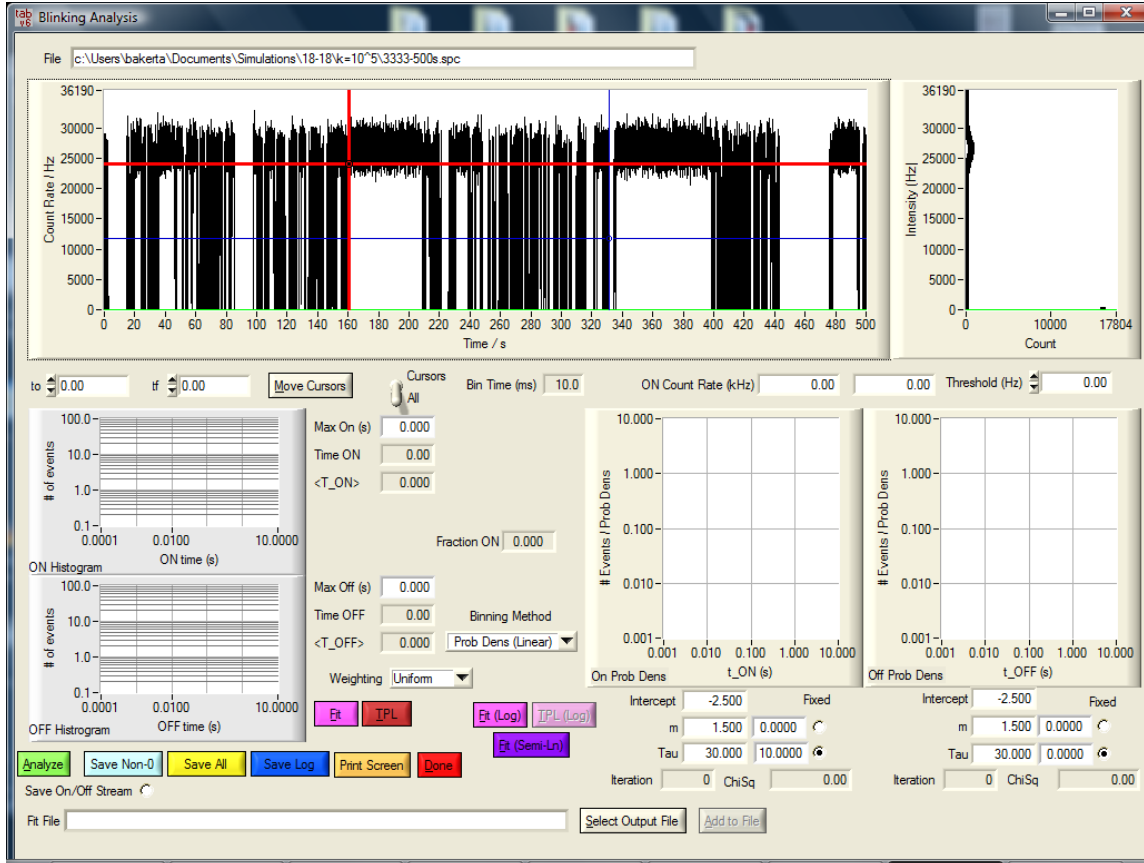


```

402 }
403 }
404 }
405 }
406 }
407 }
408 }
409 }
410 }
411 }
412 }
413 }
414 }
415 }
416 }
417 }
418 }
419 }
420 }
421 }
422 }
423 }
424 }
425 }
426 }
427 }
428 }
429 }
430 }
431 }
432 }
433 }
434 }
435 }
436 }
437 }
438 }
439 }
440 }
441 }
442 }
443 }
444 }
445 }
446 }
447 }
448 }
449 }
450 }
451 }
452 }
453 }
454 }
455 }
456 }
457 }
458 }
459 }
460 }
461 }
462 }
463 }
464 }
465 }
466 }
467 }
468 }
469 }
470 }
471 }
472 }
473 }

```

## A.2 Blinking Analysis















```

1192     f=fopen(FILE_PATH, "rb");
1193     fclose(f);
1194     if (!f) return 0;
1195     fread(data, sizeof(int), 1, f);
1196     fclose(f);
1197     fread(data, sizeof(int), 1, f);
1198     fclose(f);
1199     fread(data, sizeof(int), 1, f);
1200     fclose(f);
1201     fread(data, sizeof(int), 1, f);
1202     fclose(f);
1203     fread(data, sizeof(int), 1, f);
1204     fclose(f);
1205     fread(data, sizeof(int), 1, f);
1206     fclose(f);
1207     fread(data, sizeof(int), 1, f);
1208     fclose(f);
1209     fread(data, sizeof(int), 1, f);
1210     fclose(f);
1211     fread(data, sizeof(int), 1, f);
1212     fclose(f);
1213     fread(data, sizeof(int), 1, f);
1214     fclose(f);
1215     fread(data, sizeof(int), 1, f);
1216     fclose(f);
1217     fread(data, sizeof(int), 1, f);
1218     fclose(f);
1219     fread(data, sizeof(int), 1, f);
1220     fclose(f);
1221     fread(data, sizeof(int), 1, f);
1222     fclose(f);
1223     fread(data, sizeof(int), 1, f);
1224     fclose(f);
1225     fread(data, sizeof(int), 1, f);
1226     fclose(f);
1227     fread(data, sizeof(int), 1, f);
1228     fclose(f);
1229     fread(data, sizeof(int), 1, f);
1230     fclose(f);
1231     fread(data, sizeof(int), 1, f);
1232     fclose(f);
1233     fread(data, sizeof(int), 1, f);
1234     fclose(f);
1235     fread(data, sizeof(int), 1, f);
1236     fclose(f);
1237     fread(data, sizeof(int), 1, f);
1238     fclose(f);
1239     fread(data, sizeof(int), 1, f);
1240     fclose(f);
1241     fread(data, sizeof(int), 1, f);
1242     fclose(f);
1243     fread(data, sizeof(int), 1, f);
1244     fclose(f);
1245     fread(data, sizeof(int), 1, f);
1246     fclose(f);
1247     fread(data, sizeof(int), 1, f);
1248     fclose(f);
1249     fread(data, sizeof(int), 1, f);
1250     fclose(f);
1251     fread(data, sizeof(int), 1, f);
1252     fclose(f);
1253     fread(data, sizeof(int), 1, f);
1254     fclose(f);

```

```

1255     fclose(f);
1256     fread(data, sizeof(int), 1, f);
1257     fclose(f);
1258     fread(data, sizeof(int), 1, f);
1259     fclose(f);
1260     fread(data, sizeof(int), 1, f);
1261     fclose(f);
1262     fread(data, sizeof(int), 1, f);
1263     fclose(f);
1264     fread(data, sizeof(int), 1, f);
1265     fclose(f);
1266     fread(data, sizeof(int), 1, f);
1267     fclose(f);
1268     fread(data, sizeof(int), 1, f);
1269     fclose(f);
1270     fread(data, sizeof(int), 1, f);
1271     fclose(f);
1272     fread(data, sizeof(int), 1, f);
1273     fclose(f);
1274     fread(data, sizeof(int), 1, f);
1275     fclose(f);
1276     fread(data, sizeof(int), 1, f);
1277     fclose(f);
1278     fread(data, sizeof(int), 1, f);
1279     fclose(f);
1280     fread(data, sizeof(int), 1, f);
1281     fclose(f);
1282     fread(data, sizeof(int), 1, f);
1283     fclose(f);
1284     fread(data, sizeof(int), 1, f);
1285     fclose(f);
1286     fread(data, sizeof(int), 1, f);
1287     fclose(f);
1288     fread(data, sizeof(int), 1, f);
1289     fclose(f);
1290     fread(data, sizeof(int), 1, f);
1291     fclose(f);
1292     fread(data, sizeof(int), 1, f);
1293     fclose(f);
1294     fread(data, sizeof(int), 1, f);
1295     fclose(f);
1296     fread(data, sizeof(int), 1, f);
1297     fclose(f);
1298     fread(data, sizeof(int), 1, f);
1299     fclose(f);
1300     fread(data, sizeof(int), 1, f);
1301     fclose(f);
1302     fread(data, sizeof(int), 1, f);
1303     fclose(f);
1304     fread(data, sizeof(int), 1, f);
1305     fclose(f);
1306     fread(data, sizeof(int), 1, f);
1307     fclose(f);
1308     fread(data, sizeof(int), 1, f);
1309     fclose(f);

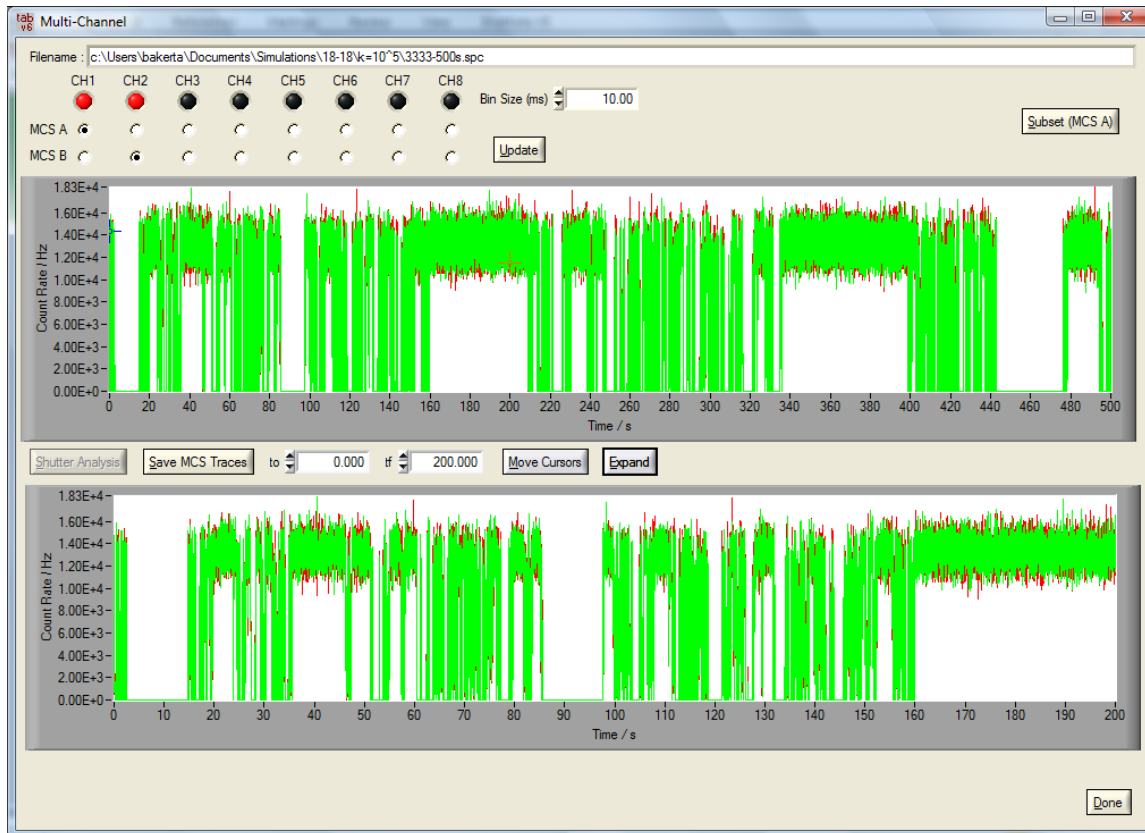
```







### A.3 Multichannel Analysis





```

221 if (i <= iMaxCS)
222 MessagePop ("memory allocation failure", "Insufficient Memory");
223 return 0;
224 }
225 }
226 }
227 }
228 }
229 }
230 }
231 }
232 }
233 }
234 }
235 }
236 }
237 }
238 }
239 }
240 }
241 }
242 }
243 }
244 }
245 }
246 }
247 }
248 }
249 }
250 }
251 }
252 }
253 }
254 }
255 }
256 }
257 }
258 }
259 }
260 }
261 }
262 }
263 }
264 }
265 }
266 }
267 }
268 }
269 }
270 }
271 }
272 }
273 }
274 }
275 }
276 }
277 }
278 }
279 }
280 }
281 }
282 }
283 }
284 }
285 }
286 }
287 }
288 }
289 }
290 }
291 }
292 }
293 }
294 }
295 }
296 }
297 }
298 }
299 }
300 }
301 }
302 }
303 }
304 }
305 }
306 }
307 }
308 }
309 }
310 }
311 }
312 }
313 }
314 }
315 }
316 }
317 }
318 }
319 }
320 }
321 }
322 }
323 }
324 }
325 }
326 }
327 }
328 }
329 }
330 }
331 }
332 }
333 }
334 }
335 }
336 }
337 }
338 }
339 }
340 }
341 }
342 }
343 }
344 }
345 }
346 }
347 }
348 }
349 }
350 }
351 }
352 }
353 }
354 }
355 }
356 }
357 }
358 }
359 }
360 }
361 }
362 }
363 }
364 }
365 }
366 }
367 }
368 }
369 }
370 }
371 }
372 }
373 }
374 }
375 }
376 }
377 }
378 }
379 }
380 }
381 }
382 }
383 }
384 }
385 }
386 }
387 }
388 }
389 }
390 }
391 }
392 }
393 }
394 }
395 }
396 }
397 }
398 }
399 }
400 }
401 }
402 }
403 }
404 }
405 }
406 }
407 }
408 }
409 }
410 }
411 }
412 }
413 }
414 }
415 }
416 }
417 }
418 }
419 }
420 }
421 }
422 }
423 }
424 }
425 }
426 }
427 }
428 }
429 }
430 }
431 }
432 }
433 }
434 }
435 }
436 }
437 }
438 }
439 }
440 }
441 }
442 }
443 }
444 }
445 }
446 }
447 }
448 }
449 }
450 }
451 }
452 }
453 }
454 }
455 }
456 }
457 }
458 }
459 }
460 }
461 }
462 }
463 }
464 }
465 }
466 }
467 }
468 }
469 }
470 }
471 }
472 }
473 }
474 }
475 }
476 }
477 }
478 }
479 }
480 }
481 }
482 }
483 }
484 }
485 }
486 }
487 }
488 }
489 }
490 }
491 }
492 }
493 }
494 }
495 }
496 }
497 }
498 }
499 }
500 }
501 }
502 }
503 }
504 }
505 }
506 }
507 }
508 }
509 }
510 }
511 }
512 }
513 }
514 }
515 }
516 }
517 }
518 }
519 }
520 }
521 }
522 }
523 }
524 }
525 }
526 }
527 }
528 }
529 }
530 }
531 }
532 }
533 }
534 }
535 }
536 }
537 }
538 }
539 }
540 }
541 }
542 }
543 }
544 }
545 }
546 }
547 }
548 }
549 }
550 }
551 }
552 }
553 }
554 }
555 }
556 }
557 }
558 }
559 }
560 }
561 }
562 }
563 }
564 }
565 }
566 }
567 }
568 }
569 }
570 }
571 }
572 }
573 }
574 }
575 }
576 }
577 }
578 }
579 }
580 }
581 }
582 }
583 }
584 }
585 }
586 }
587 }
588 }
589 }
590 }
591 }
592 }
593 }
594 }
595 }
596 }
597 }
598 }
599 }
600 }
601 }
602 }
603 }
604 }
605 }
606 }
607 }
608 }
609 }
610 }
611 }
612 }
613 }
614 }
615 }
616 }
617 }
618 }
619 }
620 }
621 }
622 }
623 }
624 }
625 }
626 }
627 }
628 }
629 }
630 }
631 }
632 }
633 }
634 }
635 }
636 }
637 }
638 }
639 }
640 }
641 }
642 }
643 }
644 }
645 }
646 }
647 }
648 }
649 }
650 }
651 }
652 }
653 }
654 }
655 }
656 }
657 }
658 }
659 }
660 }
661 }
662 }
663 }
664 }
665 }
666 }
667 }
668 }
669 }
670 }
671 }
672 }
673 }
674 }
675 }
676 }
677 }
678 }
679 }
680 }
681 }
682 }
683 }
684 }
685 }
686 }
687 }
688 }
689 }
690 }
691 }
692 }
693 }
694 }
695 }
696 }
697 }
698 }
699 }
700 }
701 }
702 }
703 }
704 }
705 }
706 }
707 }
708 }
709 }
710 }
711 }
712 }
713 }
714 }
715 }
716 }
717 }
718 }
719 }
720 }
721 }
722 }
723 }
724 }
725 }
726 }
727 }
728 }
729 }
730 }
731 }
732 }
733 }
734 }
735 }
736 }
737 }
738 }
739 }
740 }
741 }
742 }
743 }
744 }
745 }
746 }
747 }
748 }
749 }
750 }
751 }
752 }
753 }
754 }
755 }
756 }
757 }
758 }
759 }
760 }
761 }
762 }
763 }
764 }
765 }
766 }
767 }
768 }
769 }
770 }
771 }
772 }
773 }
774 }
775 }
776 }
777 }
778 }
779 }
780 }
781 }
782 }
783 }
784 }
785 }
786 }
787 }
788 }
789 }
790 }
791 }
792 }
793 }
794 }
795 }
796 }
797 }
798 }
799 }
800 }
801 }
802 }
803 }
804 }
805 }
806 }
807 }
808 }
809 }
810 }
811 }
812 }
813 }
814 }
815 }
816 }
817 }
818 }
819 }
820 }
821 }
822 }
823 }
824 }
825 }
826 }
827 }
828 }
829 }
830 }
831 }
832 }
833 }
834 }
835 }
836 }
837 }
838 }
839 }
840 }
841 }
842 }
843 }
844 }
845 }
846 }
847 }
848 }
849 }
850 }
851 }
852 }
853 }
854 }
855 }
856 }
857 }
858 }
859 }
860 }
861 }
862 }
863 }
864 }
865 }
866 }
867 }
868 }
869 }
870 }
871 }
872 }
873 }
874 }
875 }
876 }
877 }
878 }
879 }
880 }
881 }
882 }
883 }
884 }
885 }
886 }
887 }
888 }
889 }
890 }
891 }
892 }
893 }
894 }
895 }
896 }
897 }
898 }
899 }
900 }
901 }
902 }
903 }
904 }
905 }
906 }
907 }
908 }
909 }
910 }
911 }
912 }
913 }
914 }
915 }
916 }
917 }
918 }
919 }
920 }
921 }
922 }
923 }
924 }
925 }
926 }
927 }
928 }
929 }
930 }
931 }
932 }
933 }
934 }
935 }
936 }
937 }
938 }
939 }
940 }
941 }
942 }
943 }
944 }
945 }
946 }
947 }
948 }
949 }
950 }
951 }
952 }
953 }
954 }
955 }
956 }
957 }
958 }
959 }
960 }
961 }
962 }
963 }
964 }
965 }
966 }
967 }
968 }
969 }
970 }
971 }
972 }
973 }
974 }
975 }
976 }
977 }
978 }
979 }
980 }
981 }
982 }
983 }
984 }
985 }
986 }
987 }
988 }
989 }
990 }
991 }
992 }
993 }
994 }
995 }
996 }
997 }
998 }
999 }
1000 }

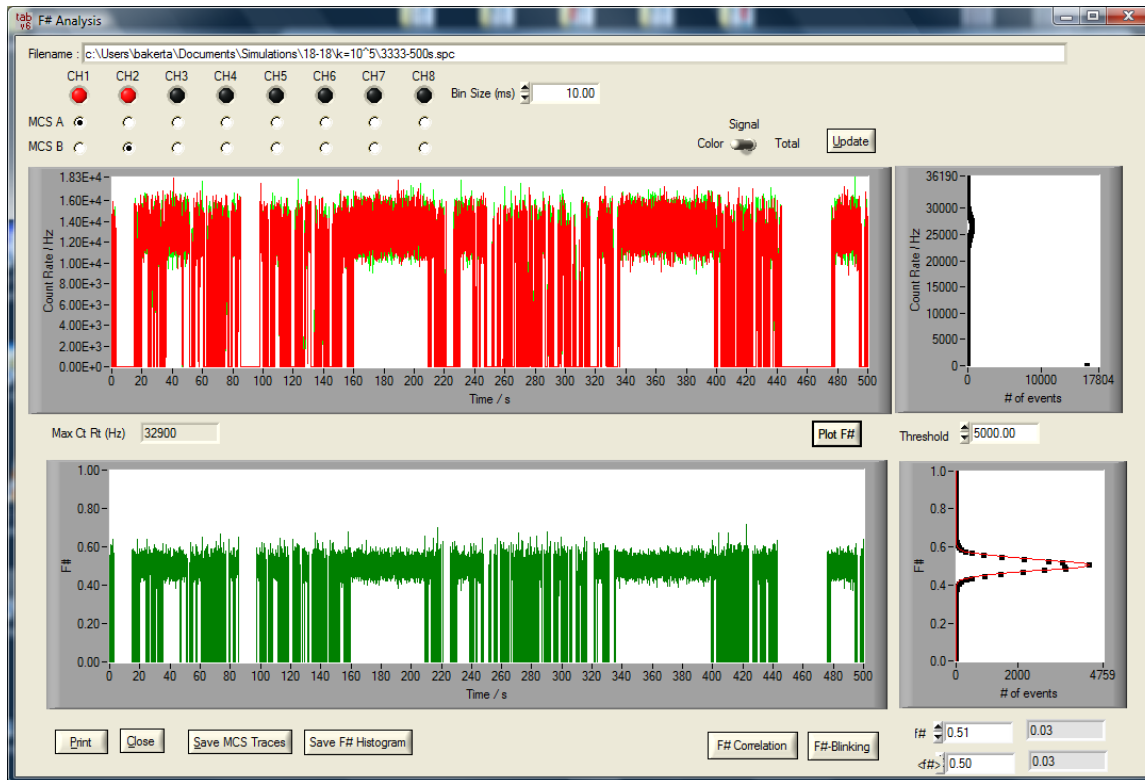
```

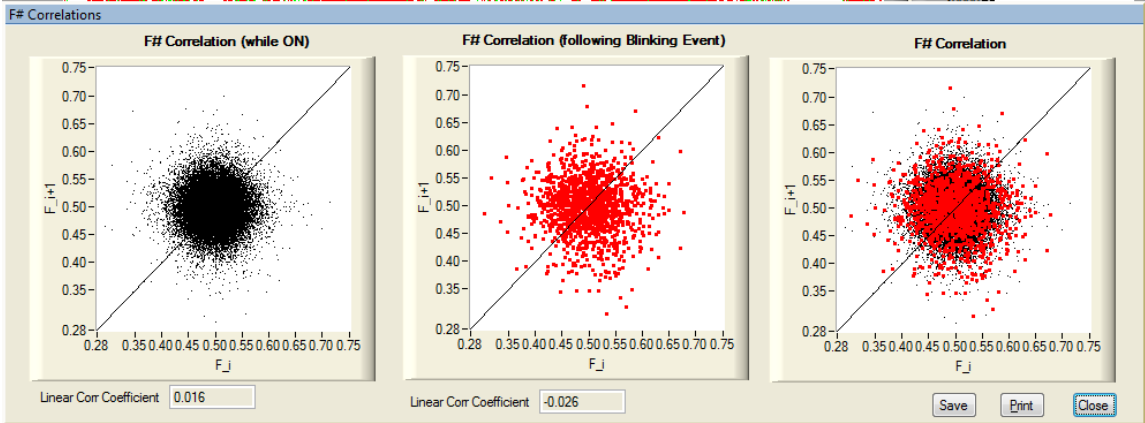
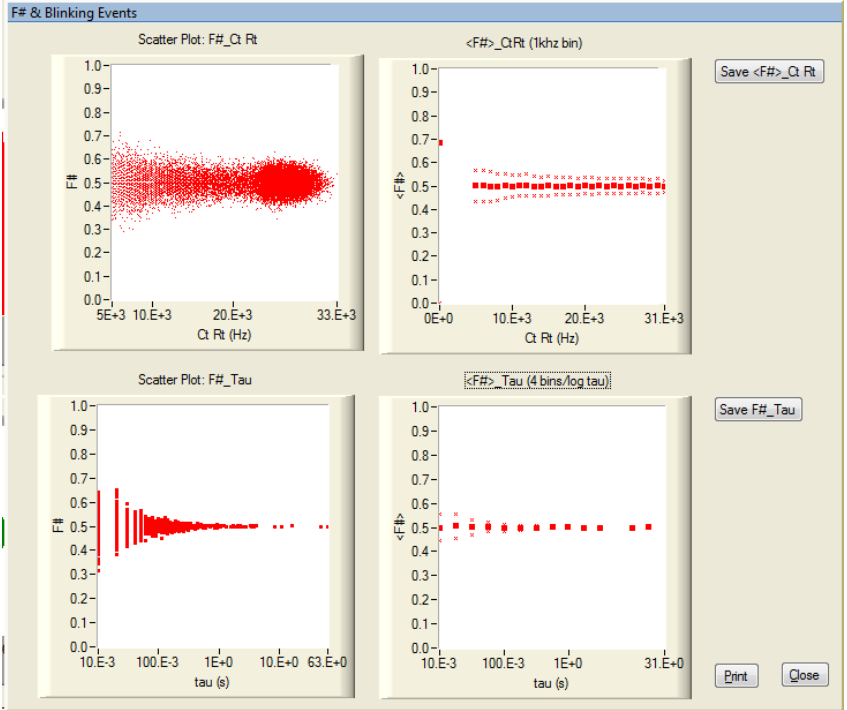
```

442         if ( !strcmp(auchChan[1])
443             !strcmp(auchChan[2]) ) = atoiRecord(1);
444             auchMicroSub[1] = atoiRecord(1);
445             auchChanSub[1] = atoiRecord(1);
446             }++;
447         }
448     }
449     SPCLoop = malloc(2*strlenof(assigned loop));
450     Record = FIFO_Enode(SPCLoop, auchMicroSub, auchMicroSub, auchChanSub, 3);
451     ArrayToFile (saveFile, SPCLoop, VAL_DESTINED_HEADERS, Record, 1, VAL_GROUPS_WO_HEADERS,
452                 VAL_GROUPS_NC_COLUMNS, VAL_CONST_WIDTH, 10, VAL_PRIMARY, VAL_TRUNCATES);
453     /* Here is the main loop:
454     Scanfile into file handle, *maskFile[pc] var[pc] var[pc], the files
455     thus, here is the writing form needed here:
456     FILE* = fopenFile (textFile, VAL_WRITE_ONLY, VAL_TRUNCATES, VAL_ASCII);
457     fprintf(FILE*,"%s-%s[pc]\n%[pc]\n%[pc]\n%[pc]", i,0,1,0,-1,-1);
458     fscanf(FILE*, "%s", information, 10*strlenof(mask)); /*the definition of the stored parameters*/
459     fclose(FILE*);
460     free(SPCLoop);
461     free(auchMicroSub);
462     free(auchChanSub);
463     free(auchChanSub);
464     }
465     }
466     }
467     }
468     }
469     }
470     }
471     }
472     }
473     return 0;

```

## A.4 F-Number Analysis













```

659 //k indexes each chart so it can be binned in 1000 intervals
660 int floor(int x) { return x/1000; }
661 int* advmg2f(int n) {
662     int* advmg2f = new int[n];
663     advmg2f[0] = 1;
664     for (int i=1; i<n; i++) advmg2f[i] = advmg2f[i-1]*i;
665 }
666
667 double* advmg2f(double* advmg2f, int n) {
668     double* advmg2f = new double[n];
669     advmg2f[0] = 1;
670     for (int i=1; i<n; i++) advmg2f[i] = advmg2f[i-1]*i;
671 }
672
673 //Create array with average/ndev # at each intensity level
674 for (int i=0; i<1000; i++)
675     advmg2f[i] = advmg2f[i]/i;
676
677
678
679
680
681
682
683
684
685
686
687
688
689
690
691
692
693
694
695
696
697
698
699
700
701
702
703
704
705
706
707
708
709
710
711
712
713
714
715
716
717
718
719
720
721
722
723
724
725
726
727
728
729
730
731
732
733
734
735
736
737
738
739
740
741
742
743
744
745
746
747
748
749
750
751
752
753
754
755
756
757
758
759
760
761
762
763
764
765
766
767
768
769
770
771
772
773
774
775
776
777
778
779
780
781
782
783
784
785
786
787
788
789
790
791
792
793
794
795
796
797
798
799
800
801
802
803
804
805
806
807
808
809
810
811
812
813
814
815
816
817
818
819
820
821
822
823
824
825
826
827
828
829
830
831
832
833
834
835
836
837
838
839
840
841
842
843
844
845
846
847
848
849
850
851
852
853
854
855
856
857
858
859
860
861
862
863
864
865
866
867
868
869
870
871
872
873
874
875

```



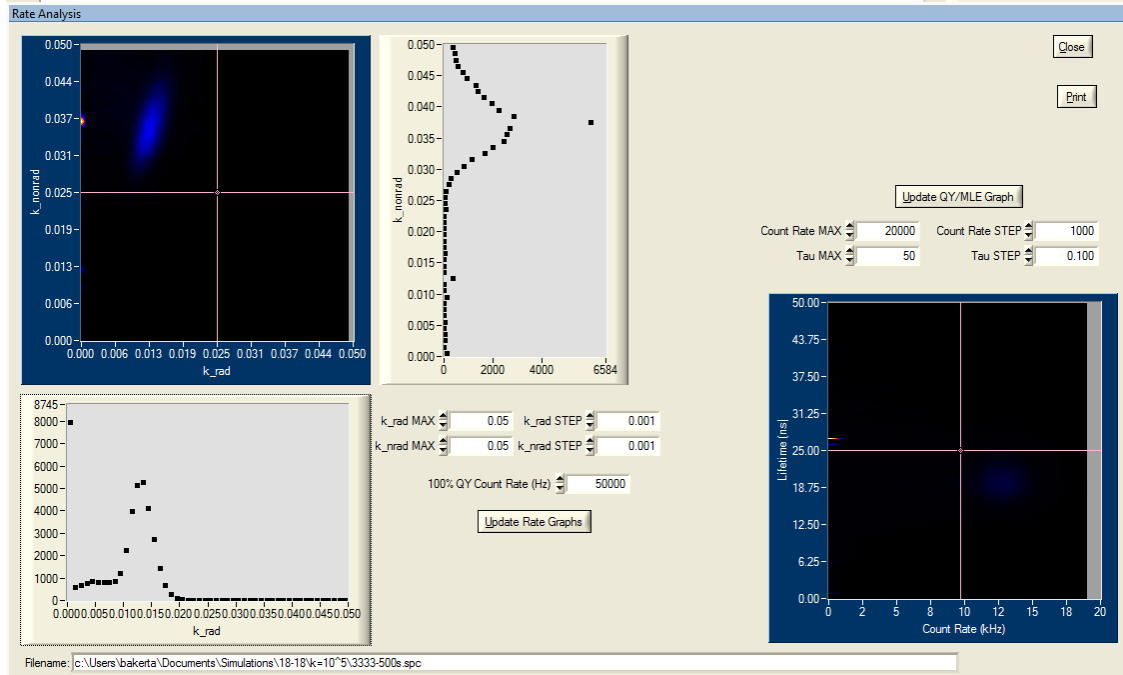
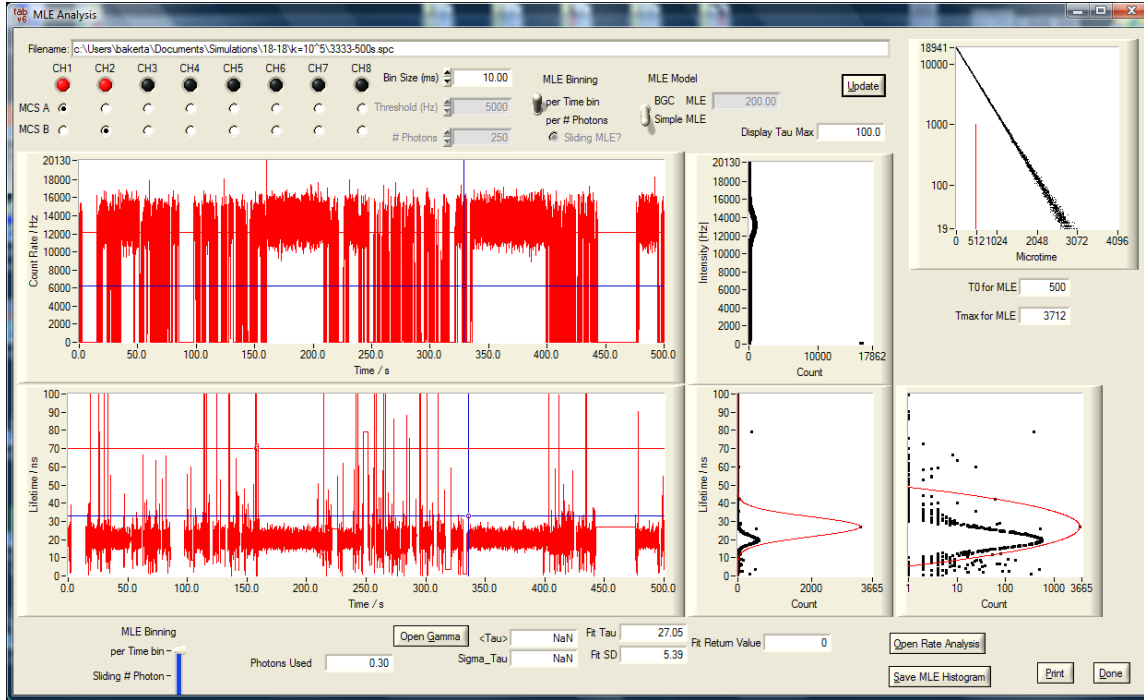




1538 return 0;  
1539 }

```
1530 Free(pEvent);  
1531 Free(pEvent);  
1532 Free(pEvent);  
1533 Free(pEvent);  
1534 }  
1535 }  
1536 }  
1537 }  
1538 }  
1539 }  
1540 }  
1541 }  
1542 }  
1543 }  
1544 }  
1545 }  
1546 }  
1547 }  
1548 }  
1549 }  
1550 }  
1551 }  
1552 }  
1553 }  
1554 }  
1555 }  
1556 }  
1557 }  
1558 }  
1559 }  
1560 }  
1561 }  
1562 }  
1563 }  
1564 }  
1565 }  
1566 }  
1567 }  
1568 }  
1569 }  
1570 }  
1571 }  
1572 }  
1573 }  
1574 }  
1575 }  
1576 }  
1577 }  
1578 }  
1579 }  
1580 }  
1581 }  
1582 }  
1583 }  
1584 }  
1585 }  
1586 }  
1587 }
```

## A.5 Maximum Likelihood Estimation









```

452 ubinvar(unaligned long) (ceil((double) (numMicroc(tNumPhotons-1)) * psize*1.0E5/dbin_time));
453 *total_binvar=ubinv;
454 //
455 int (admc2n);
456 //
457 int (admc3n);
458 //
459 //
460 //
461 //
462 //
463 //
464 //
465 //
466 //
467 //
468 //
469 //
470 //
471 //
472 //
473 //
474 //
475 //
476 //
477 //
478 //
479 //
480 //
481 //
482 //
483 //
484 //
485 //
486 //
487 //
488 //
489 //
490 //
491 //
492 //
493 //
494 //
495 //
496 //
497 //
498 //
499 //
500 //
501 //
502 //
503 //
504 //
505 //
506 //
507 //
508 //
509 //
510 //
511 //
512 //
513 //
514 //
515 //
516 //
517 //
518 //
519 //
520 //
521 //
522 //
523 //
524 //
525 //
526 //
527 //
528 //
529 //
530 //
531 //
532 //
533 //
534 //
535 //
536 //
537 //
538 //
539 //
540 //
541 //
542 //
543 //
544 //
545 //
546 //
547 //
548 //
549 //
550 //
551 //
552 //
553 //
554 //
555 //
556 //
557 //
558 //
559 //
560 //
561 //
562 //
563 //
564 //
565 //
566 //
567 //
568 //
569 //
570 //
571 //
572 //
573 //
574 //
575 //
576 //
577 //
578 //
579 //
580 //
581 //
582 //
583 //
584 //
585 //
586 //
587 //
588 //
589 //
590 //
591 //
592 //
593 //
594 //
595 //
596 //
597 //
598 //
599 //
600 //
601 //
602 //
603 //
604 //
605 //
606 //
607 //
608 //
609 //
610 //
611 //
612 //
613 //
614 //
615 //
616 //
617 //
618 //
619 //
620 //
621 //
622 //
623 //
624 //
625 //
626 //
627 //
628 //
629 //
630 //
631 //
632 //
633 //
634 //
635 //
636 //
637 //
638 //
639 //
640 //
641 //
642 //
643 //
644 //
645 //
646 //
647 //
648 //
649 //
650 //
651 //
652 //
653 //

```



```

875     if (j == 30) return 0.0;
876     }
877     sum += 1.0; // Not enough observations
878     *lambdaExponential = 0;
879     return 0.0;
880 }
881 }
882 }
883 }
884 return 0.0;
885 }
886 }
887 }
888 double WZ_FUNC(double dfn, int first, int last, double dh, double db, int Whotocn)
889 {
890     double dms, dms;
891     int i;
892     double dmi, dmi;
893     double dmi;
894     double dmi;
895     double dms;
896     double dChannelWidth, dChannelLength;
897     double dChannelWidth = 1. / 4096.;
898     double dChannelLength = 1.;
899     double dmi = ((double) (first - 1) + 1) / 4096.;
900     double dmi = 1. / dmi;
901     // Calculate IBS
902     dms = 0.0;
903     for (i = first; i <= last; i++)
904     {
905         if (random() >= 0.5)
906             i = random();
907         dmi = db * (1. - exp(-dChannelWidth * exp(dChannelWidth * dms + (1. - 1.))));
908         dmi = db * (1. - exp(-dChannelWidth * exp(-dChannelWidth * dmi + 1.)));
909         dms += dmi * dmi;
910         dmi = db * (1. - exp(-dChannelWidth * exp(-dChannelWidth * dmi + 1.)));
911         dmi = db * (1. - exp(-dChannelWidth * exp(dChannelWidth * dms + (1. - 1.))));
912         dmi = db * (1. - exp(-dChannelWidth * exp(-dChannelWidth * dmi + 1.)));
913     }
914     // Calculate IBS
915     dms = dms * dmi;
916     dms = dms * dmi;
917     dms = dms * dmi;
918     dms = dms * dmi;
919     dms = dms * dmi;
920     dms = dms * dmi;
921     dms = dms * dmi;
922     dms = dms * dmi;
923     dms = dms * dmi;
924     dms = dms * dmi;
925     dms = dms * dmi;
926     dms = dms * dmi;
927     dms = dms * dmi;
928     dms = dms * dmi;

```

```

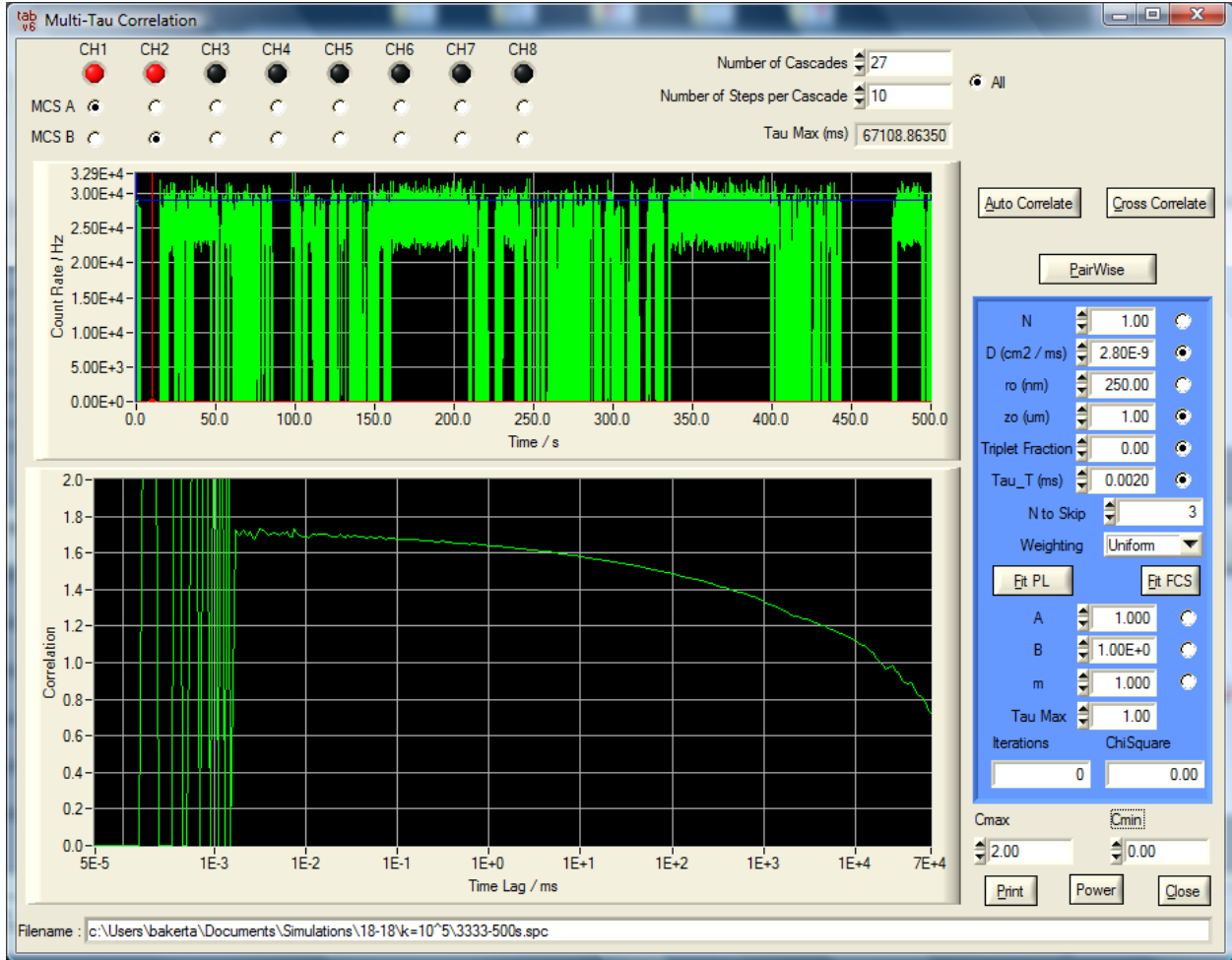
929     return dms - dms;
930 }
931 }
932 }
933 }
934 }
935 }
936 }
937 }
938 }
939 }
940 }
941 }
942 }
943 }
944 }
945 }
946 }
947 }
948 }
949 }
950 }
951 }
952 }
953 }
954 }
955 }
956 }
957 }
958 }
959 }
960 }
961 }
962 }
963 }
964 }
965 }
966 }
967 }
968 }
969 }
970 }
971 }
972 }
973 }
974 }
975 }
976 }
977 }
978 }
979 }
980 }
981 }
982 }
983 }
984 }
985 }
986 }
987 }
988 }
989 }
990 }
991 }
992 }
993 }
994 }
995 }
996 }
997 }
998 }
999 }
1000 }
1001 }
1002 }
1003 }
1004 }
1005 }
1006 }
1007 }
1008 }
1009 }
1010 }
1011 }
1012 }
1013 }
1014 }
1015 }
1016 }
1017 }
1018 }
1019 }
1020 }
1021 }
1022 }
1023 }
1024 }
1025 }
1026 }
1027 }
1028 }
1029 }
1030 }
1031 }
1032 }
1033 }
1034 }
1035 }
1036 }
1037 }
1038 }
1039 }
1040 }

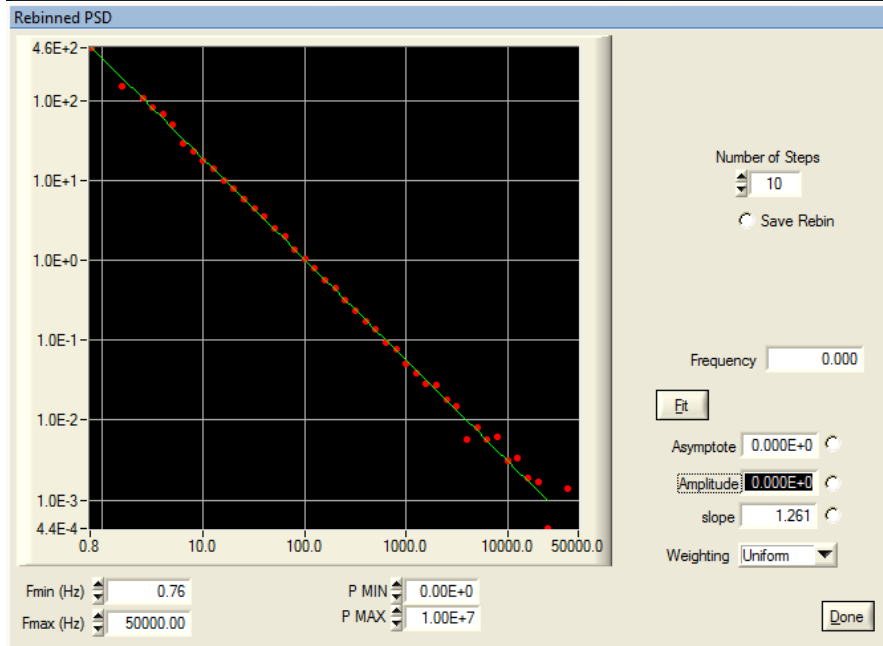
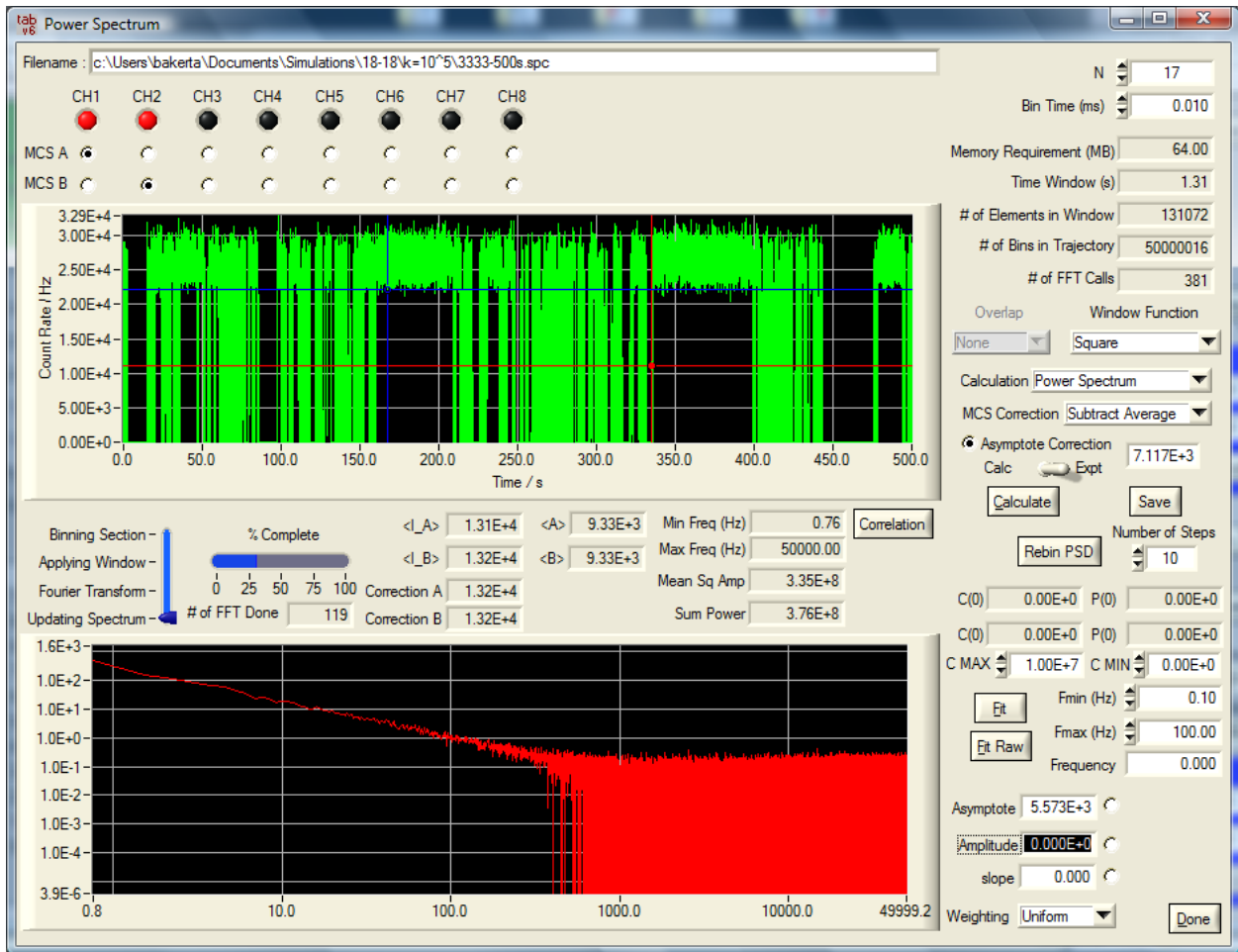
```



```
1308 Free(jcGame);
1309 Free(jcData);
1310 Free(CLRHistogram);
1311 }
1312
1313 } break;
1314
1315 } break;
1316 return 0;
1317 }
1318
1319 int CYCALLBACK CloseGame (int panel, int control, int event,
1320 void *callBackData, int eventData1, int eventData2)
1321 {
1322     switch (event)
1323     {
1324     case EVENT_COMMIT:
1325         HidePanel(panelCOMMON);
1326     }
1327     } break;
1328 return 0;
1329 }
1330
1331 }
```

## A.6 Correlation and Power Spectral Density







```

1 // Global Constants
2 #include <string.h>
3 #include <math.h>
4 #include <stdio.h>
5 #include <stdlib.h>
6 #include <string.h>
7 #include <math.h>
8 #include <string.h>
9 #include <math.h>
10 #include <string.h>
11 #include <string.h>
12 #include <string.h>
13 #include <string.h>
14 #include <string.h>
15 #include <string.h>
16 // Local Function Prototypes
17 void printMatrix(double **a, int n, int m);
18 void printMatrix(double **a, int n, int m, double **b);
19 void printMatrix(double **a, int n, int m, double **b, double **c);
20 void printMatrix(double **a, int n, int m, double **b, double **c, double **d);
21 void printMatrix(double **a, int n, int m, double **b, double **c, double **d, double **e);
22 void printMatrix(double **a, int n, int m, double **b, double **c, double **d, double **e, double **f);
23 void printMatrix(double **a, int n, int m, double **b, double **c, double **d, double **e, double **f, double **g);
24 void printMatrix(double **a, int n, int m, double **b, double **c, double **d, double **e, double **f, double **g, double **h);
25 void printMatrix(double **a, int n, int m, double **b, double **c, double **d, double **e, double **f, double **g, double **h, double **i);
26 void printMatrix(double **a, int n, int m, double **b, double **c, double **d, double **e, double **f, double **g, double **h, double **i, double **j);
27 void printMatrix(double **a, int n, int m, double **b, double **c, double **d, double **e, double **f, double **g, double **h, double **i, double **j, double **k);
28 void printMatrix(double **a, int n, int m, double **b, double **c, double **d, double **e, double **f, double **g, double **h, double **i, double **j, double **k, double **l);
29 void printMatrix(double **a, int n, int m, double **b, double **c, double **d, double **e, double **f, double **g, double **h, double **i, double **j, double **k, double **l, double **m);
30 void printMatrix(double **a, int n, int m, double **b, double **c, double **d, double **e, double **f, double **g, double **h, double **i, double **j, double **k, double **l, double **m, double **n);
31 // Local Constants
32 int n = 10;
33 int m = 10;
34 double **a;
35 double **b;
36 double **c;
37 double **d;
38 double **e;
39 double **f;
40 double **g;
41 double **h;
42 double **i;
43 double **j;
44 double **k;
45 double **l;
46 double **m;
47 double **n;
48 // Global Variables
49 int i;
50 int j;
51 int k;
52 int l;
53 int m;
54 int n;
55 // Main Function
56 int main() {
57     // Create matrix 'a'
58     a = (double **) malloc(n * sizeof(double *));
59     for (i = 0; i < n; i++)
60         a[i] = (double *) malloc(m * sizeof(double));
61     // Create matrix 'b'
62     b = (double **) malloc(n * sizeof(double *));
63     for (i = 0; i < n; i++)
64         b[i] = (double *) malloc(m * sizeof(double));
65     // Create matrix 'c'
66     c = (double **) malloc(n * sizeof(double *));
67     for (i = 0; i < n; i++)
68         c[i] = (double *) malloc(m * sizeof(double));
69     // Create matrix 'd'
70     d = (double **) malloc(n * sizeof(double *));
71     for (i = 0; i < n; i++)
72         d[i] = (double *) malloc(m * sizeof(double));
73     // Create matrix 'e'
74     e = (double **) malloc(n * sizeof(double *));
75     for (i = 0; i < n; i++)
76         e[i] = (double *) malloc(m * sizeof(double));
77     // Create matrix 'f'
78     f = (double **) malloc(n * sizeof(double *));
79     for (i = 0; i < n; i++)
80         f[i] = (double *) malloc(m * sizeof(double));
81     // Create matrix 'g'
82     g = (double **) malloc(n * sizeof(double *));
83     for (i = 0; i < n; i++)
84         g[i] = (double *) malloc(m * sizeof(double));
85     // Create matrix 'h'
86     h = (double **) malloc(n * sizeof(double *));
87     for (i = 0; i < n; i++)
88         h[i] = (double *) malloc(m * sizeof(double));
89     // Create matrix 'i'
90     i = (double **) malloc(n * sizeof(double *));
91     for (i = 0; i < n; i++)
92         i[i] = (double *) malloc(m * sizeof(double));
93     // Create matrix 'j'
94     j = (double **) malloc(n * sizeof(double *));
95     for (i = 0; i < n; i++)
96         j[i] = (double *) malloc(m * sizeof(double));
97     // Create matrix 'k'
98     k = (double **) malloc(n * sizeof(double *));
99     for (i = 0; i < n; i++)
100         k[i] = (double *) malloc(m * sizeof(double));
101     // Create matrix 'l'
102     l = (double **) malloc(n * sizeof(double *));
103     for (i = 0; i < n; i++)
104         l[i] = (double *) malloc(m * sizeof(double));
105     // Create matrix 'm'
106     m = (double **) malloc(n * sizeof(double *));
107     for (i = 0; i < n; i++)
108         m[i] = (double *) malloc(m * sizeof(double));
109     // Create matrix 'n'
110     n = (double **) malloc(n * sizeof(double *));
111     for (i = 0; i < n; i++)
112         n[i] = (double *) malloc(m * sizeof(double));
113     // Print matrix 'a'
114     printMatrix(a, n, m);
115     // Print matrix 'b'
116     printMatrix(b, n, m);
117     // Print matrix 'c'
118     printMatrix(c, n, m);
119     // Print matrix 'd'
120     printMatrix(d, n, m);
121     // Print matrix 'e'
122     printMatrix(e, n, m);
123     // Print matrix 'f'
124     printMatrix(f, n, m);
125     // Print matrix 'g'
126     printMatrix(g, n, m);
127     // Print matrix 'h'
128     printMatrix(h, n, m);
129     // Print matrix 'i'
129     printMatrix(i, n, m);
130     // Print matrix 'j'
130     printMatrix(j, n, m);
131     // Print matrix 'k'
131     printMatrix(k, n, m);
132     // Print matrix 'l'
132     printMatrix(l, n, m);
133     // Print matrix 'm'
133     printMatrix(m, n, m);
134     // Print matrix 'n'
134     printMatrix(n, n, m);
135     return 0;
136 }

```







```

882     s[i][k]++;
883     while ( ( ( numMicro[0][sin[k]] - ito) <= aItrun[k] ) && ( sin[k] < ulimmb-1 ) )
884         s[i][k]++;
885     }
886 }
887
888 // Update graph every 1000 photons //
889 if ( ( k % 1000) == 1 )
890 {
891     // Update graph every 1000 photons //
892     if ( ( k % 1000) == 1 )
893     {
894         deleteGraph(pPanel12, PANEL_12_GRAPH_Cover, -1, VAL_IMMEDIATE_DUMP);
895         Panel12_Cover_Admit;
896         VAL_THIN_LINE, VAL_NO_POINT, VAL_SOLID, 1, VAL_GREEN);
897         GetCtrlVal(pPanel12, PANEL_12_NUMERICAL_PROGRESS, (double) (i-1)*numStep/(double) i);
898         SetCtrlVal(pPanel12, PANEL_12_NUMERICAL_PROGRESS, (double) (i-1)*numStep/(double) i);
899     }
900 }
901
902 // Save correlation //
903 if ( saveCorrelation == "Save Correlation", VAL_SAVE_BUTTON, 0, 1, 1, 1, filename);
904 SetCtrlAttribute(pPanel12, PANEL_12_NUMERICAL_PROGRESS, ATTR_VISIBLE, 0);
905 // Save Correlation //
906 int i;
907 int j;
908 int k;
909 int l;
910 int m;
911 int n;
912 // Save Correlation //
913 int i;
914 int j;
915 int k;
916 int l;
917 int m;
918 int n;
919 int o;
920 int p;
921 int q;
922 int r;
923 int s;
924 int t;
925 int u;
926 int v;
927 int w;
928 int x;
929 int y;
930 int z;
931 int aa;
932 int ab;
933 int ac;
934 int ad;
935 int ae;
936 int af;
937 int ag;
938 int ah;
939 int ai;
940 int aj;
941 int ak;
942 int al;
943 int am;
944 int an;
945 int ao;
946 int ap;
947 int aq;
948 int ar;
949 int as;
950 int at;
951 int au;
952 int av;
953 int aw;
954 int ax;
955 int ay;
956 int az;
957 int ba;
958 int bb;
959 int bc;
960 int bd;
961 int be;
962 int bf;
963 int bg;
964 int bh;
965 int bi;
966 int bj;
967 int bk;
968 int bl;
969 int bm;
970 int bn;
971 int bo;
972 int bp;
973 int bq;
974 int br;
975 int bs;
976 int bt;
977 int bu;
978 int bv;
979 int bw;
980 int bx;
981 int by;
982 int bz;
983 int ca;
984 int cb;
985 int cc;
986 int cd;
987 int ce;
988 int cf;
989 int cg;
990 int ch;
991 int ci;
992 int cj;
993 int ck;
994 int cl;
995 int cm;
996 int cn;
997 int co;
998 int cp;
999 int cq;
1000 int cr;
1001 int cs;
1002 int ct;
1003 int cu;
1004 int cv;
1005 int cw;
1006 int cx;
1007 int cy;
1008 int cz;
1009 int da;
1010 int db;
1011 int dc;
1012 int dd;
1013 int de;
1014 int df;
1015 int dg;
1016 int dh;
1017 int di;
1018 int dj;
1019 int dk;
1020 int dl;
1021 int dm;
1022 int dn;
1023 int do;
1024 int dp;
1025 int dq;
1026 int dr;
1027 int ds;
1028 int dt;
1029 int du;
1030 int dv;
1031 int dw;
1032 int dx;
1033 int dy;
1034 int dz;
1035 int ea;
1036 int eb;
1037 int ec;
1038 int ed;
1039 int ee;
1040 int ef;
1041 int eg;
1042 int eh;
1043 int ei;
1044 int ej;
1045 int ek;
1046 int el;
1047 int em;
1048 int en;
1049 int eo;
1050 int ep;
1051 int eq;
1052 int er;
1053 int es;
1054 int et;
1055 int eu;
1056 int ev;
1057 int ew;
1058 int ex;
1059 int ey;
1060 int ez;
1061 int fa;
1062 int fb;
1063 int fc;
1064 int fd;
1065 int fe;
1066 int ff;
1067 int fg;
1068 int fh;
1069 int fi;
1070 int fj;
1071 int fk;
1072 int fl;
1073 int fm;
1074 int fn;
1075 int fo;
1076 int fp;
1077 int fq;
1078 int fr;
1079 int fs;
1080 int ft;
1081 int fu;
1082 int fv;
1083 int fw;
1084 int fx;
1085 int fy;
1086 int fz;
1087 int ga;
1088 int gb;
1089 int gc;
1090 int gd;
1091 int ge;
1092 int gf;
1093 int gg;
1094 int gh;
1095 int gi;
1096 int gj;
1097 int gk;
1098 int gl;
1099 int gm;
1100 int gn;
1101 int go;
1102 int gp;
1103 int gq;
1104 int gr;
1105 int gs;
1106 int gt;
1107 int gu;
1108 int gv;
1109 int gw;
1110 int gx;
1111 int gy;
1112 int gz;
1113 int ha;
1114 int hb;
1115 int hc;
1116 int hd;
1117 int he;
1118 int hf;
1119 int hg;
1120 int hh;
1121 int hi;
1122 int hj;
1123 int hk;
1124 int hl;
1125 int hm;
1126 int hn;
1127 int ho;
1128 int hp;
1129 int hq;
1130 int hr;
1131 int hs;
1132 int ht;
1133 int hu;
1134 int hv;
1135 int hw;
1136 int hx;
1137 int hy;
1138 int hz;
1139 int ia;
1140 int ib;
1141 int ic;
1142 int id;
1143 int ie;
1144 int if;
1145 int ig;
1146 int ih;
1147 int ii;
1148 int ij;
1149 int ik;
1150 int il;
1151 int im;
1152 int in;
1153 int io;
1154 int ip;
1155 int iq;
1156 int ir;
1157 int is;
1158 int it;
1159 int iu;
1160 int iv;
1161 int iw;
1162 int ix;
1163 int iy;
1164 int iz;
1165 int ja;
1166 int jb;
1167 int jc;
1168 int jd;
1169 int je;
1170 int jf;
1171 int jg;
1172 int jh;
1173 int ji;
1174 int jj;
1175 int jk;
1176 int jl;
1177 int jm;
1178 int jn;
1179 int jo;
1180 int jp;
1181 int jq;
1182 int jr;
1183 int js;
1184 int jt;
1185 int ju;
1186 int jv;
1187 int jw;
1188 int jx;
1189 int jy;
1190 int jz;
1191 int ka;
1192 int kb;
1193 int kc;
1194 int kd;
1195 int ke;
1196 int kf;
1197 int kg;
1198 int kh;
1199 int ki;
1200 int kj;
1201 int kk;
1202 int kl;
1203 int km;
1204 int kn;
1205 int ko;
1206 int kp;
1207 int kq;
1208 int kr;
1209 int ks;
1210 int kt;
1211 int ku;
1212 int kv;
1213 int kw;
1214 int kx;
1215 int ky;
1216 int kz;
1217 int la;
1218 int lb;
1219 int lc;
1220 int ld;
1221 int le;
1222 int lf;
1223 int lg;
1224 int lh;
1225 int li;
1226 int lj;
1227 int lk;
1228 int ll;
1229 int lm;
1230 int ln;
1231 int lo;
1232 int lp;
1233 int lq;
1234 int lr;
1235 int ls;
1236 int lt;
1237 int lu;
1238 int lv;
1239 int lw;
1240 int lx;
1241 int ly;
1242 int lz;
1243 int ma;
1244 int mb;
1245 int mc;
1246 int md;
1247 int me;
1248 int mf;
1249 int mg;
1250 int mh;
1251 int mi;
1252 int mj;
1253 int mk;
1254 int ml;
1255 int mn;
1256 int mo;
1257 int mp;
1258 int mq;
1259 int mr;
1260 int ms;
1261 int mt;
1262 int mu;
1263 int mv;
1264 int mw;
1265 int mx;
1266 int my;
1267 int mz;
1268 int na;
1269 int nb;
1270 int nc;
1271 int nd;
1272 int ne;
1273 int nf;
1274 int ng;
1275 int nh;
1276 int ni;
1277 int nj;
1278 int nk;
1279 int nl;
1280 int nm;
1281 int no;
1282 int np;
1283 int nq;
1284 int nr;
1285 int ns;
1286 int nt;
1287 int nu;
1288 int nv;
1289 int nw;
1290 int nx;
1291 int ny;
1292 int nz;
1293 int oa;
1294 int ob;
1295 int oc;
1296 int od;
1297 int oe;
1298 int of;
1299 int og;
1300 int oh;
1301 int oi;
1302 int oj;
1303 int ok;
1304 int ol;
1305 int om;
1306 int on;
1307 int oo;
1308 int op;
1309 int oq;
1310 int or;
1311 int os;
1312 int ot;
1313 int ou;
1314 int ov;
1315 int ow;
1316 int ox;
1317 int oy;
1318 int oz;
1319 int pa;
1320 int pb;
1321 int pc;
1322 int pd;
1323 int pe;
1324 int pf;
1325 int pg;
1326 int ph;
1327 int pi;
1328 int pj;
1329 int pk;
1330 int pl;
1331 int pm;
1332 int pn;
1333 int po;
1334 int pp;
1335 int pq;
1336 int pr;
1337 int ps;
1338 int pt;
1339 int pu;
1340 int pv;
1341 int pw;
1342 int px;
1343 int py;
1344 int pz;
1345 int qa;
1346 int qb;
1347 int qc;
1348 int qd;
1349 int qe;
1350 int qf;
1351 int qg;
1352 int qh;
1353 int qi;
1354 int qj;
1355 int qk;
1356 int ql;
1357 int qm;
1358 int qn;
1359 int qo;
1360 int qp;
1361 int qq;
1362 int qr;
1363 int qs;
1364 int qt;
1365 int qu;
1366 int qv;
1367 int qw;
1368 int qx;
1369 int qy;
1370 int qz;
1371 int ra;
1372 int rb;
1373 int rc;
1374 int rd;
1375 int re;
1376 int rf;
1377 int rg;
1378 int rh;
1379 int ri;
1380 int rj;
1381 int rk;
1382 int rl;
1383 int rm;
1384 int rn;
1385 int ro;
1386 int rp;
1387 int rq;
1388 int rr;
1389 int rs;
1390 int rt;
1391 int ru;
1392 int rv;
1393 int rw;
1394 int rx;
1395 int ry;
1396 int rz;
1397 int sa;
1398 int sb;
1399 int sc;
1400 int sd;
1401 int se;
1402 int sf;
1403 int sg;
1404 int sh;
1405 int si;
1406 int sj;
1407 int sk;
1408 int sl;
1409 int sm;
1410 int sn;
1411 int so;
1412 int sp;
1413 int sq;
1414 int sr;
1415 int ss;
1416 int st;
1417 int su;
1418 int sv;
1419 int sw;
1420 int sx;
1421 int sy;
1422 int sz;
1423 int ta;
1424 int tb;
1425 int tc;
1426 int td;
1427 int te;
1428 int tf;
1429 int tg;
1430 int th;
1431 int ti;
1432 int tj;
1433 int tk;
1434 int tl;
1435 int tm;
1436 int tn;
1437 int to;
1438 int tp;
1439 int tq;
1440 int tr;
1441 int ts;
1442 int tt;
1443 int tu;
1444 int tv;
1445 int tw;
1446 int tx;
1447 int ty;
1448 int tz;
1449 int ua;
1450 int ub;
1451 int uc;
1452 int ud;
1453 int ue;
1454 int uf;
1455 int ug;
1456 int uh;
1457 int ui;
1458 int uj;
1459 int uk;
1460 int ul;
1461 int um;
1462 int un;
1463 int uo;
1464 int up;
1465 int uq;
1466 int ur;
1467 int us;
1468 int ut;
1469 int uu;
1470 int uv;
1471 int uw;
1472 int ux;
1473 int uy;
1474 int uz;
1475 int va;
1476 int vb;
1477 int vc;
1478 int vd;
1479 int ve;
1480 int vf;
1481 int vg;
1482 int vh;
1483 int vi;
1484 int vj;
1485 int vk;
1486 int vl;
1487 int vm;
1488 int vn;
1489 int vo;
1490 int vp;
1491 int vq;
1492 int vr;
1493 int vs;
1494 int vt;
1495 int vu;
1496 int vv;
1497 int vw;
1498 int vx;
1499 int vy;
1500 int vz;
1501 int wa;
1502 int wb;
1503 int wc;
1504 int wd;
1505 int we;
1506 int wf;
1507 int wg;
1508 int wh;
1509 int wi;
1510 int wj;
1511 int wk;
1512 int wl;
1513 int wm;
1514 int wn;
1515 int wo;
1516 int wp;
1517 int wq;
1518 int wr;
1519 int ws;
1520 int wt;
1521 int wu;
1522 int wv;
1523 int ww;
1524 int wx;
1525 int wy;
1526 int wz;
1527 int xa;
1528 int xb;
1529 int xc;
1530 int xd;
1531 int xe;
1532 int xf;
1533 int xg;
1534 int xh;
1535 int xi;
1536 int xj;
1537 int xk;
1538 int xl;
1539 int xm;
1540 int xn;
1541 int xo;
1542 int xp;
1543 int xq;
1544 int xr;
1545 int xs;
1546 int xt;
1547 int xu;
1548 int xv;
1549 int xw;
1550 int xx;
1551 int xy;
1552 int xz;
1553 int ya;
1554 int yb;
1555 int yc;
1556 int yd;
1557 int ye;
1558 int yf;
1559 int yg;
1560 int yh;
1561 int yi;
1562 int yj;
1563 int yk;
1564 int yl;
1565 int ym;
1566 int yn;
1567 int yo;
1568 int yp;
1569 int yq;
1570 int yr;
1571 int ys;
1572 int yt;
1573 int yu;
1574 int yv;
1575 int yw;
1576 int yx;
1577 int yy;
1578 int yz;
1579 int za;
1580 int zb;
1581 int zc;
1582 int zd;
1583 int ze;
1584 int zf;
1585 int zg;
1586 int zh;
1587 int zi;
1588 int zj;
1589 int zk;
1590 int zl;
1591 int zm;
1592 int zn;
1593 int zo;
1594 int zp;
1595 int zq;
1596 int zr;
1597 int zs;
1598 int zt;
1599 int zu;
1600 int zv;
1601 int zw;
1602 int zx;
1603 int zy;
1604 int zz;

```





```

1540  dramp= s[16];
1541
1542  dramp = cvo/dco/(4. * db);
1543  dalpha = cvo/dco;
1544
1545  dk = x / dramp;
1546
1547  dcm = (1./db) / ( 1.+ dk) * sqrt(1. + dalpha*dalpha*dk);
1548  dcs = 1. - dk + dk*exp(-x/dramp);
1549  *y = 1. + dk*dcm;
1550
1551  dcramp = - dk / dramp;
1552  dcrandco = dco / (2. * db);
1553  dcrandcm = dk / (2. * db);
1554  dalphaco = 1. / dco;
1555  dalphaco = - dco / (dco * dco);
1556
1557  dcdm1 = - dcm / (1.+dk);
1558  dcdm2 = - dalpha*dalpha*dcm / ( 2.*(1.-dalpha*dalpha*dk) );
1559  dcdm3 = - dalpha*dk*dcm / ( 1.-dalpha*dalpha*dk);
1560
1561  dcdm11 = -(dcm/db)*dk;
1562
1563  // d/dco
1564  dcdm12 = (dcdm1+dcdm2)*dcrandco+dcdm3*dalphaco*dk;
1565  dcdm13 = dcdm1 - dcdm12*dalphaco*dk;
1566
1567  // d/dcm
1568  dcdm14 = (dcdm1+dcdm2)*dcrandco+dcdm3*dalphaco*dk;
1569  dcdm15 = dcdm1 - dcdm14*dalphaco*dk;
1570
1571  // d/dk
1572  dcdm16 = [-1. + exp(-x/dramp)]*dcm;
1573
1574  dcdm17 = [-1. + exp(-x/dramp)]*dcm;
1575
1576  dcdm18 = (dcrandco+dcrandcm)*exp(-x/dramp)*dcm;
1577
1578  return;
1579
1580 }
1581
1582 int CYCLBACK PrintEtc (int panel, int control, int event,
1583 int *val, int *eventData, int *eventData2)
1584 {
1585     switch (event)
1586     {
1587     case EVENT_COMMIT:
1588         SetPrintAttribute (AFRQ_PRINT_ABA_WIDTH, VAL_INTEGERAL_SCROLL);
1589         SetPrintAttribute (AFRQ_PRINT_ABA_HEIGHT, VAL_USE_ENTIRE_PANEL);
1590         SetPrintAttribute ("*", VAL_VAL_PANEL, 1);
1591         break;
1592     }
1593 }
1594
1595
1596
1597
1598
1599
1600
1601
1602
1603
1604
1605
1606
1607
1608
1609
1610
1611
1612
1613
1614
1615
1616
1617
1618
1619
1620
1621
1622
1623
1624
1625
1626
1627
1628
1629
1630
1631
1632
1633
1634
1635
1636
1637
1638
1639
1640
1641
1642
1643
1644
1645
1646
1647
1648
1649
1650
1651
1652
1653
1654
1655
1656
1657
1658
1659
1660
1661
1662
1663
1664
1665
1666
1667
1668
1669
1670
1671
1672
1673
1674
1675
1676
1677
1678
1679
1680
1681
1682
1683
1684
1685
1686
1687
1688
1689
1690
1691
1692
1693
1694
1695
1696
1697
1698
1699
1700
1701
1702
1703
1704
1705
1706
1707
1708
1709
1710
1711
1712
1713
1714
1715
1716
1717
1718
1719
1720
1721
1722
1723
1724
1725
1726
1727
1728
1729
1730
1731
1732
1733
1734
1735
1736
1737
1738
1739
1740
1741
1742
1743
1744
1745
1746
1747
1748
1749
1750
1751
1752
1753
1754
1755
1756
1757
1758
1759
1760
1761
1762
1763
1764
1765
1766
1767
1768
1769
1770
1771
1772
1773
1774
1775
1776
1777
1778
1779
1780
1781
1782
1783
1784
1785
1786
1787
1788
1789
1790
1791
1792
1793
1794
1795
1796
1797
1798
1799
1800
1801
1802
1803
1804
1805
1806
1807
1808
1809
1810
1811
1812
1813
1814
1815
1816
1817
1818
1819
1820
1821
1822
1823
1824
1825
1826
1827
1828
1829
1830
1831
1832
1833
1834
1835
1836
1837
1838
1839
1840
1841
1842
1843
1844
1845
1846
1847
1848
1849
1850
1851
1852
1853
1854
1855
1856
1857
1858
1859
1860
1861
1862
1863
1864
1865
1866
1867
1868
1869
1870
1871
1872
1873
1874
1875
1876
1877
1878
1879
1880
1881
1882
1883
1884
1885
1886
1887
1888
1889
1890
1891
1892
1893
1894
1895
1896
1897
1898
1899
1900
1901
1902
1903
1904
1905
1906
1907
1908
1909
1910
1911
1912
1913
1914
1915
1916
1917
1918
1919
1920
1921
1922
1923
1924
1925
1926
1927
1928
1929
1930
1931
1932
1933
1934
1935
1936
1937
1938
1939
1940
1941
1942
1943
1944
1945
1946
1947
1948
1949
1950
1951
1952
1953
1954
1955
1956
1957
1958
1959
1960
1961
1962
1963
1964
1965
1966
1967
1968
1969
1970
1971
1972
1973
1974
1975
1976
1977
1978
1979
1980
1981
1982
1983
1984
1985
1986
1987
1988
1989
1990
1991
1992
1993
1994
1995
1996
1997
1998
1999
2000
2001
2002
2003
2004
2005
2006
2007
2008
2009
2010
2011
2012
2013
2014
2015
2016
2017
2018
2019
2020
2021
2022
2023
2024
2025
2026
2027
2028
2029
2030
2031
2032
2033
2034
2035
2036
2037
2038
2039
2040
2041
2042
2043
2044
2045
2046
2047
2048
2049
2050
2051
2052
2053
2054
2055
2056
2057
2058
2059
2060
2061
2062
2063
2064
2065
2066
2067
2068
2069
2070
2071
2072
2073
2074
2075
2076
2077
2078
2079
2080
2081
2082
2083
2084
2085
2086
2087
2088
2089
2090
2091
2092
2093
2094
2095
2096
2097
2098
2099
2100
2101
2102
2103
2104
2105
2106
2107
2108
2109
2110
2111
2112
2113
2114
2115
2116
2117
2118
2119
2120
2121
2122
2123
2124
2125
2126
2127
2128
2129
2130
2131
2132
2133
2134
2135
2136
2137
2138
2139
2140
2141
2142
2143
2144
2145
2146
2147
2148
2149
2150
2151
2152
2153
2154
2155
2156
2157
2158
2159
2160
2161
2162
2163
2164
2165
2166
2167
2168
2169
2170
2171
2172
2173
2174
2175
2176
2177
2178
2179
2180
2181
2182
2183
2184
2185
2186
2187
2188
2189
2190
2191
2192
2193
2194
2195
2196
2197
2198
2199
2200
2201
2202
2203
2204
2205
2206
2207
2208
2209
2210
2211
2212
2213
2214
2215
2216
2217
2218
2219
2220
2221
2222
2223
2224
2225
2226
2227
2228
2229
2230
2231
2232
2233
2234
2235
2236
2237
2238
2239
2240
2241
2242
2243
2244
2245
2246
2247
2248
2249
2250
2251
2252
2253
2254
2255
2256
2257
2258
2259
2260
2261
2262
2263
2264
2265
2266
2267
2268
2269
2270
2271
2272
2273
2274
2275
2276
2277
2278
2279
2280
2281
2282
2283
2284
2285
2286
2287
2288
2289
2290
2291
2292
2293
2294
2295
2296
2297
2298
2299
2300
2301
2302
2303
2304
2305
2306
2307
2308
2309
2310
2311
2312
2313
2314
2315
2316
2317
2318
2319
2320
2321
2322
2323
2324
2325
2326
2327
2328
2329
2330
2331
2332
2333
2334
2335
2336
2337
2338
2339
2340
2341
2342
2343
2344
2345
2346
2347
2348
2349
2350
2351
2352
2353
2354
2355
2356
2357
2358
2359
2360
2361
2362
2363
2364
2365
2366
2367
2368
2369
2370
2371
2372
2373
2374
2375
2376
2377
2378
2379
2380
2381
2382
2383
2384
2385
2386
2387
2388
2389
2390
2391
2392
2393
2394
2395
2396
2397
2398
2399
2400
2401
2402
2403
2404
2405
2406
2407
2408
2409
2410
2411
2412
2413
2414
2415
2416
2417
2418
2419
2420
2421
2422
2423
2424
2425
2426
2427
2428
2429
2430
2431
2432
2433
2434
2435
2436
2437
2438
2439
2440
2441
2442
2443
2444
2445
2446
2447
2448
2449
2450
2451
2452
2453
2454
2455
2456
2457
2458
2459
2460
2461
2462
2463
2464
2465
2466
2467
2468
2469
2470
2471
2472
2473
2474
2475
2476
2477
2478
2479
2480
2481
2482
2483
2484
2485
2486
2487
2488
2489
2490
2491
2492
2493
2494
2495
2496
2497
2498
2499
2500
2501
2502
2503
2504
2505
2506
2507
2508
2509
2510
2511
2512
2513
2514
2515
2516
2517
2518
2519
2520
2521
2522
2523
2524
2525
2526
2527
2528
2529
2530
2531
2532
2533
2534
2535
2536
2537
2538
2539
2540
2541
2542
2543
2544
2545
2546
2547
2548
2549
2550
2551
2552
2553
2554
2555
2556
2557
2558
2559
2560
2561
2562
2563
2564
2565
2566
2567
2568
2569
2570
2571
2572
2573
2574
2575
2576
2577
2578
2579
2580
2581
2582
2583
2584
2585
2586
2587
2588
2589
2590
2591
2592
2593
2594
2595
2596
2597
2598
2599
2600
2601
2602
2603
2604
2605
2606
2607
2608
2609
2610
2611
2612
2613
2614
2615
2616
2617
2618
2619
2620
2621
2622
2623
2624
2625
2626
2627
2628
2629
2630
2631
2632
2633
2634
2635
2636
2637
2638
2639
2640
2641
2642
2643
2644
2645
2646
2647
2648
2649
2650
2651
2652
2653
2654
2655
2656
2657
2658
2659
2660
2661
2662
2663
2664
2665
2666
2667
2668
2669
2670
2671
2672
2673
2674
2675
2676
2677
2678
2679
2680
2681
2682
2683
2684
2685
2686
2687
2688
2689
2690
2691
2692
2693
2694
2695
2696
2697
2698
2699
2700
2701
2702
2703
2704
2705
2706
2707
2708
2709
2710
2711
2712
2713
2714
2715
2716
2717
2718
2719
2720
2721
2722
2723
2724
2725
2726
2727
2728
2729
2730
2731
2732
2733
2734
2735
2736
2737
2738
2739
2740
2741
2742
2743
2744
2745
2746
2747
2748
2749
2750
2751
2752
2753
2754
2755
2756
2757
2758
2759
2760
2761
2762
2763
2764
2765
2766
2767
2768
2769
2770
2771
2772
2773
2774
2775
2776
2777
2778
2779
2780
2781
2782
2783
2784
2785
2786
2787
2788
2789
2790
2791
2792
2793
2794
2795
2796
2797
2798
2799
2800
2801
2802
2803
2804
2805
2806
2807
2808
2809
2810
2811
2812
2813
2814
2815
2816
2817
2818
2819
2820
2821
2822
2823
2824
2825
2826
2827
2828
2829
2830
2831
2832
2833
2834
2835
2836
2837
2838
2839
2840
2841
2842
2843
2844
2845
2846
2847
2848
2849
2850
2851
2852
2853
2854
2855
2856
2857
2858
2859
2860
2861
2862
2863
2864
2865
2866
2867
2868
2869
2870
2871
2872
2873
2874
2875
2876
2877
2878
2879
2880
2881
2882
2883
2884
2885
2886
2887
2888
2889
2890
2891
2892
2893
2894
2895
2896
2897
2898
2899
2900
2901
2902
2903
2904
2905
2906
2907
2908
2909
2910
2911
2912
2913
2914
2915
2916
2917
2918
2919
2920
2921
2922
2923
2924
2925
2926
2927
2928
2929
2930
2931
2932
2933
2934
2935
2936
2937
2938
2939
2940
2941
2942
2943
2944
2945
2946
2947
2948
2949
2950
2951
2952
2953
2954
2955
2956
2957
2958
2959
2960
2961
2962
2963
2964
2965
2966
2967
2968
2969
2970
2971
2972
2973
2974
2975
2976
2977
2978
2979
2980
2981
2982
2983
2984
2985
2986
2987
2988
2989
2990
2991
2992
2993
2994
2995
2996
2997
2998
2999
3000

```

















```

3270 {
3271     adbin[ibin-1] /= abins;
3272     ibin++;
3273     abins = 0;
3274     adbin[ibin-1] += adPower[i];
3275     abins++;
3276     }
3277 }
3278 }
3279 }
3280 }
3281 }
3282 }
3283 }
3284 }
3285 }
3286 }
3287 }
3288 }
3289 }
3290 }
3291 }
3292 }
3293 }
3294 }
3295 }
3296 }
3297 }
3298 }
3299 }
3300 }
3301 }
3302 }
3303 }
3304 }
3305 }
3306 }
3307 }
3308 }
3309 }
3310 }
3311 }
3312 }
3313 }
3314 }
3315 }
3316 }
3317 }
3318 }
3319 }
3320 }
3321 }
3322 }
3323 }
3324 }
3325 }
3326 }
3327 }
3328 }
3329 }
3330 }
3331 }
3332 }
3333 }
3334 }
3335 }
3336 }
3337 }
3338 }
3339 }
3340 }
3341 }
3342 }
3343 }
3344 }
3345 }
3346 }
3347 }
3348 }
3349 }
3350 }
3351 }
3352 }
3353 }
3354 }
3355 }
3356 }
3357 }
3358 }
3359 }
3360 }
3361 }
3362 }
3363 }
3364 }
3365 }
3366 }
3367 }
3368 }
3369 }
3370 }
3371 }
3372 }
3373 }
3374 }
3375 }
3376 }
3377 }
3378 }
3379 }
3380 }
3381 }
3382 }
3383 }
3384 }
3385 }
3386 }
3387 }
3388 }
3389 }
3390 }
3391 }
3392 }
3393 }
3394 }
3395 }
3396 }
3397 }
3398 }
3399 }
3400 }
3401 }
3402 }
3403 }
3404 }
3405 }
3406 }
3407 }
3408 }
3409 }
3410 }
3411 }
3412 }
3413 }
3414 }
3415 }
3416 }
3417 }
3418 }
3419 }
3420 }
3421 }
3422 }
3423 }
3424 }
3425 }
3426 }
3427 }
3428 }
3429 }
3430 }
3431 }

```

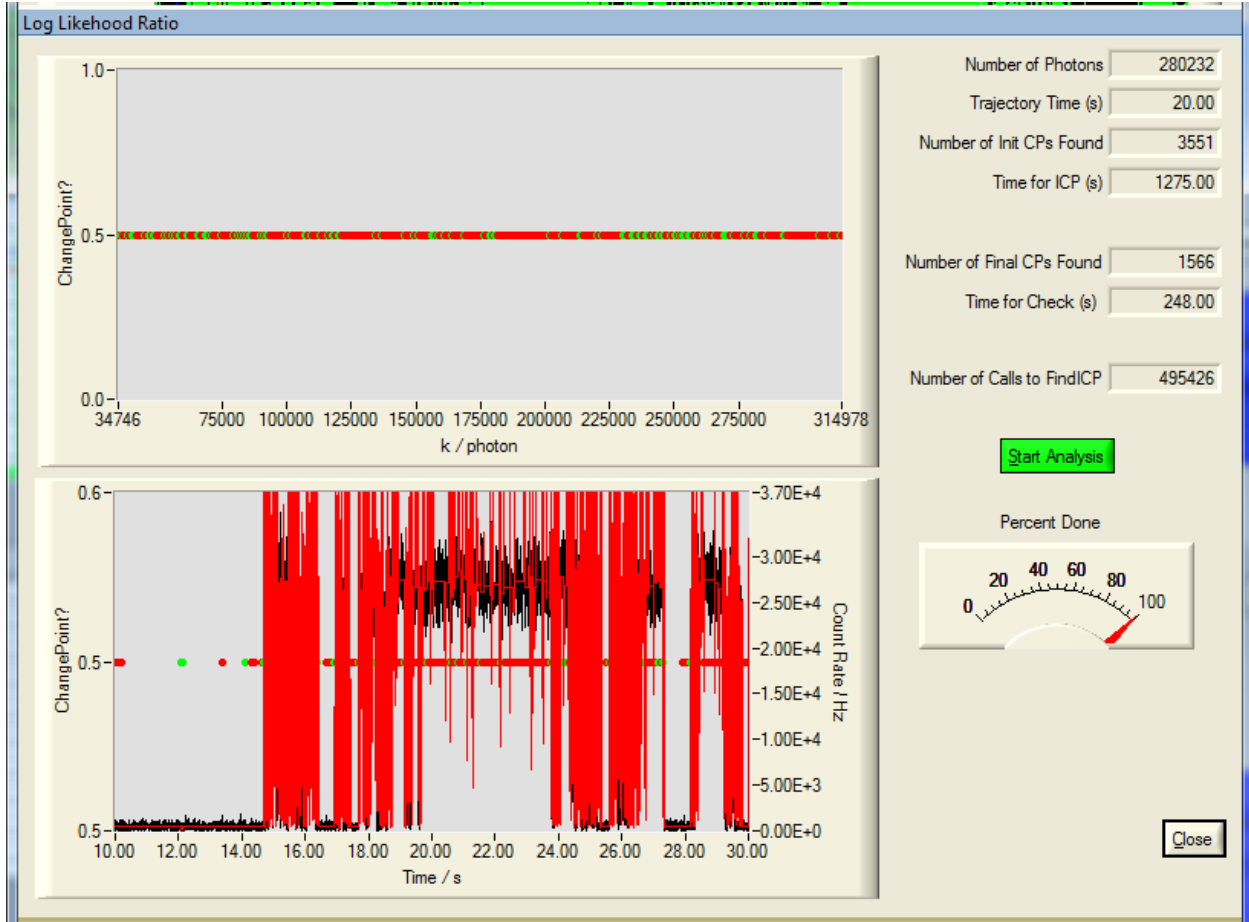
```

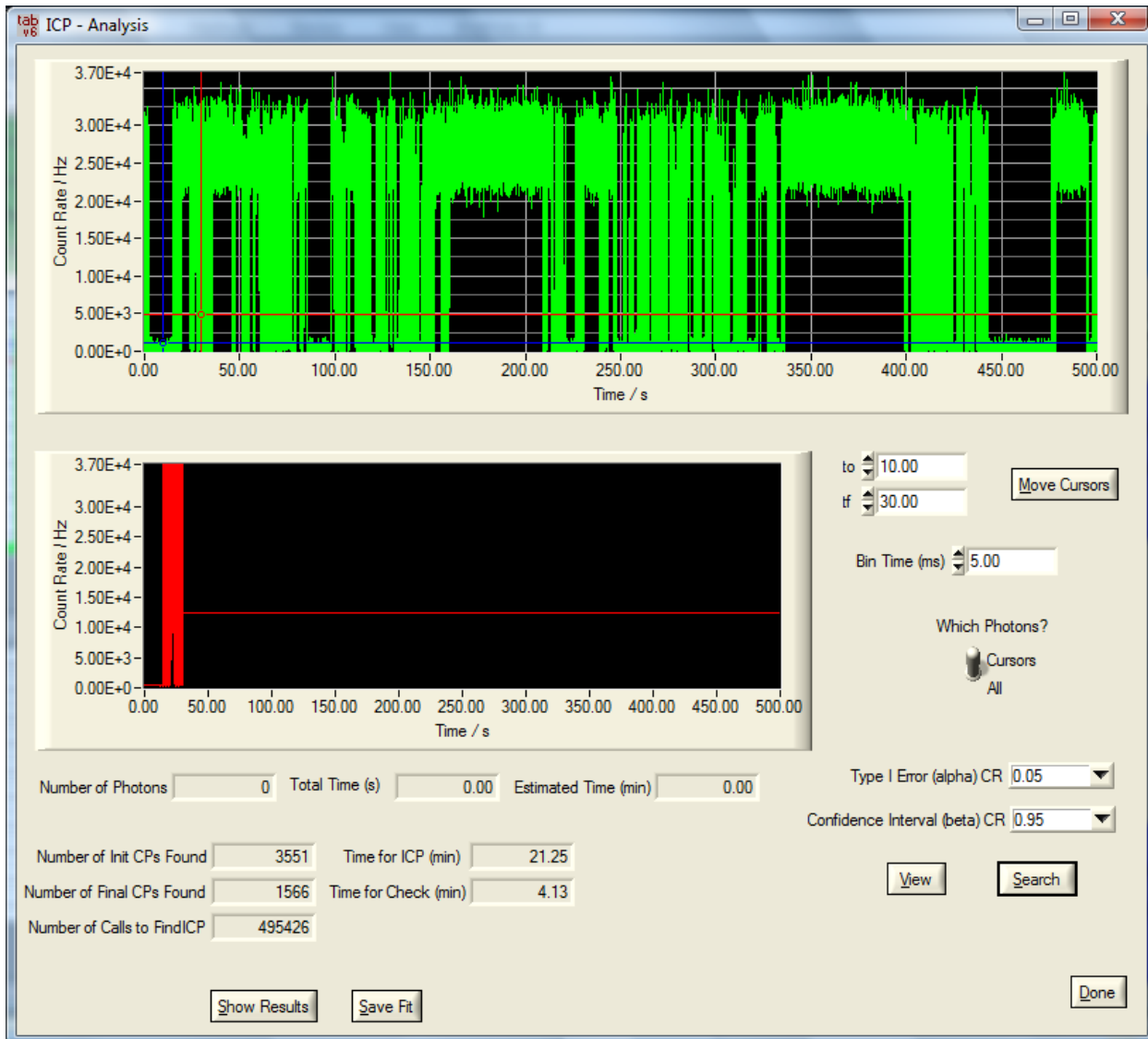
3222 }
3223 }
3224 }
3225 }
3226 }
3227 }
3228 }
3229 }
3230 }
3231 }
3232 }
3233 }
3234 }
3235 }
3236 }
3237 }
3238 }
3239 }
3240 }
3241 }
3242 }
3243 }
3244 }
3245 }
3246 }
3247 }
3248 }
3249 }
3250 }
3251 }
3252 }
3253 }
3254 }
3255 }
3256 }
3257 }
3258 }
3259 }
3260 }
3261 }
3262 }
3263 }
3264 }
3265 }
3266 }
3267 }
3268 }
3269 }
3270 }
3271 }
3272 }
3273 }
3274 }
3275 }
3276 }
3277 }
3278 }
3279 }
3280 }
3281 }
3282 }
3283 }
3284 }
3285 }
3286 }
3287 }
3288 }
3289 }
3290 }
3291 }
3292 }
3293 }
3294 }
3295 }
3296 }
3297 }
3298 }
3299 }
3300 }
3301 }
3302 }
3303 }
3304 }
3305 }
3306 }
3307 }
3308 }
3309 }
3310 }
3311 }
3312 }
3313 }
3314 }
3315 }
3316 }
3317 }
3318 }
3319 }
3320 }
3321 }
3322 }
3323 }
3324 }
3325 }
3326 }
3327 }
3328 }
3329 }
3330 }
3331 }
3332 }
3333 }
3334 }
3335 }
3336 }
3337 }
3338 }
3339 }
3340 }
3341 }
3342 }
3343 }
3344 }
3345 }
3346 }
3347 }
3348 }
3349 }
3350 }
3351 }
3352 }
3353 }
3354 }
3355 }
3356 }
3357 }
3358 }
3359 }
3360 }
3361 }
3362 }
3363 }
3364 }
3365 }
3366 }
3367 }
3368 }
3369 }
3370 }
3371 }
3372 }
3373 }
3374 }
3375 }
3376 }
3377 }
3378 }
3379 }
3380 }
3381 }
3382 }
3383 }
3384 }
3385 }
3386 }
3387 }
3388 }
3389 }
3390 }
3391 }
3392 }
3393 }
3394 }
3395 }
3396 }
3397 }
3398 }
3399 }
3400 }
3401 }
3402 }
3403 }
3404 }
3405 }
3406 }
3407 }
3408 }
3409 }
3410 }
3411 }
3412 }
3413 }
3414 }
3415 }
3416 }
3417 }
3418 }
3419 }
3420 }
3421 }
3422 }
3423 }
3424 }
3425 }
3426 }
3427 }
3428 }
3429 }
3430 }
3431 }

```



## A.7 Intensity Change Point Analysis





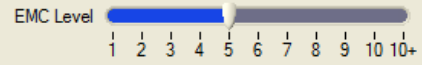
Tabular Results of ICP

Change Point Results

	LHB	ICP	RHB	Time (s)	Intensity
1	34746	34746	34746	10.0016	473.058
2	35706	35726	35731	12.0732	156.672
3	35730	35734	35763	12.1243	503.827
4	36697	36733	36753	14.1071	426.591
5	36973	36974	36977	14.6720	21900.475
6	37009	37010	37011	14.6737	153061.224
7	37015	37019	37020	14.6738	26528.903
8	37031	37038	37050	14.6745	7789.095
9	37050	37051	37055	14.6761	39780.521
10	37076	37080	37085	14.6769	6719.735
11	37092	37093	37099	14.6788	24987.487
12	37414	37415	37424	14.6917	87014.726
13	37425	37428	37429	14.6918	1958.672
14	37431	37432	37435	14.6939	26249.022
15	37755	37776	37777	14.7070	6706.908
16	37780	37782	37783	14.7079	274.683
17	37786	37787	37789	14.7261	8945.409
18	37822	37824	37833	14.7302	13436.249
19	37870	37871	37881	14.7337	24928.704
20	38108	38121	38176	14.7437	33592.512
21	38209	38210	38212	14.7464	390625.000
22	38212	38215	38218	14.7464	25248.730
23	38380	38383	38386	14.7531	1174.300
24	38388	38390	38392	14.7590	19136.961
25	38435	38441	38443	14.7617	1865.440
26	38444	38444	38444	14.7633	7485.030

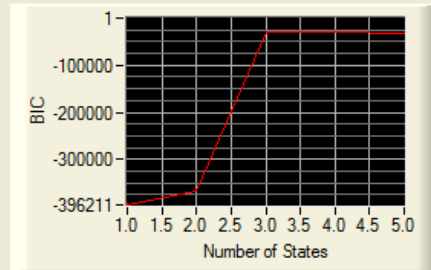
Maximum # of States

Time for AHC (s)



Time for EMC (s)

Time for BIC (s)



Most Likely # of Groups

```

1 /* Reverse binary from the source of Bar Yang */
2 #include <math.h>
3 #include <stdio.h>
4 #include <string.h>
5 #include <stdlib.h>
6 #include "toolbox.h"
7 #include "global.h"
8 #include "CP.h"
9 #include "ICP.h"
10 #include "Functions.h"
11 #include "STRUCT.h"
12 #include "UTIL.h"
13 #include "UTIL.h"
14 #include "UTIL.h"
15 // Constants used in the ICP search algorithm */
16 #define CP_OVERLAP 200 // Number of photon overlap between split regions */
17 #define CP_OVERLAP_FACTOR 20 // Number of photon overlap between split regions */
18 #define PARM 1.0E-10 // Polarsion for RM analysis */
19 #define PARM 2 // Number of Parameters in RIC analysis */
20 // User defined structures */
21 struct changepoint
22 {
23     unsigned long li; // Location of Changepoint */
24     unsigned long lr; // Right Hand Bound of Confidence Region */
25     unsigned long ll; // Left Hand Bound of Confidence Region */
26 }
27
28
29 struct group
30 {
31     unsigned long n; // Total number of photons in this group */
32     double T; // Total time duration of this group */
33     unsigned long m; // Total number of members of this group */
34     unsigned long *number; // Array containing the member's CP index of this group */
35 }
36
37
38 struct em_group
39 {
40     int **c; // Classification to which this point belongs */
41     double **intensity; // Estimated intensity value */
42     double **prob; // Posterior probability of this classification */
43 }
44
45
46 enum bool { false=0, true=1 };
47 // Local Function Prototypes */
48 void findInitialRegions(unsigned long *lph, unsigned long *rph, int col);
49 void findInitialRegions(void);
50 void findICP(void);
51 void findCP(void);
52 void findRM(void);
53 void findRM(void);
54 void delete(unsigned long *li, unsigned long *lj, struct group *g, int Ng);
55 void reconstruct(void);
56
57
58
59
60
61
62
63
64
65
66
67
68
69
70
71
72
73
74
75
76
77
78
79
80
81
82
83
84
85
86
87
88
89
90
91
92
93
94
95
96
97
98
99
100
101
102
103
104
105
106
107
108
109
110
111
112
113
114
115
116
117
118
119
120
121
122
123
124
125
126
127
128
129
130
131
132
133
134
135
136
137
138
139
140
141
142
143
144
145
146
147
148
149
150
151
152
153
154
155
156
157
158
159
160
161
162
163
164
165
166
167
168
169
170
171
172
173
174
175
176
177
178
179
180
181
182
183
184
185
186
187
188
189
190
191
192
193
194
195
196
197
198
199
200
201
202
203
204
205
206
207
208
209
210
211
212
213
214
215
216
217
218
219
220
221
222
223
224
225
226
227
228
229
230
231
232
233
234
235
236
237
238
239
240
241
242
243
244
245
246
247
248
249
250
251
252
253
254
255
256
257
258
259
260
261
262
263
264
265
266
267
268
269
270
271
272
273
274
275
276
277
278
279
280
281
282
283
284
285
286
287
288
289
290
291
292
293
294
295
296
297
298
299
300
301
302
303
304
305
306
307
308
309
310
311
312
313
314
315
316
317
318
319
320
321
322
323
324
325
326
327
328
329
330
331
332
333
334
335
336
337
338
339
340
341
342
343
344
345
346
347
348
349
350
351
352
353
354
355
356
357
358
359
360
361
362
363
364
365
366
367
368
369
370
371
372
373
374
375
376
377
378
379
380
381
382
383
384
385
386
387
388
389
390
391
392
393
394
395
396
397
398
399
400
401
402
403
404
405
406
407
408
409
410
411
412
413
414
415
416
417
418
419
420
421
422
423
424
425
426
427
428
429
430
431
432
433
434
435
436
437
438
439
440
441
442
443
444
445
446
447
448
449
450
451
452
453
454
455
456
457
458
459
460
461
462
463
464
465
466
467
468
469
470
471
472
473
474
475
476
477
478
479
480
481
482
483
484
485
486
487
488
489
490
491
492
493
494
495
496
497
498
499
500
501
502
503
504
505
506
507
508
509
510
511
512
513
514
515
516
517
518
519
520
521
522
523
524
525
526
527
528
529
530
531
532
533
534
535
536
537
538
539
540
541
542
543
544
545
546
547
548
549
550
551
552
553
554
555
556
557
558
559
560
561
562
563
564
565
566
567
568
569
570
571
572
573
574
575
576
577
578
579
580
581
582
583
584
585
586
587
588
589
590
591
592
593
594
595
596
597
598
599
600
601
602
603
604
605
606
607
608
609
610
611
612
613
614
615
616
617
618
619
620
621
622
623
624
625
626
627
628
629
630
631
632
633
634
635
636
637
638
639
640
641
642
643
644
645
646
647
648
649
650
651
652
653
654
655
656
657
658
659
660
661
662
663
664
665
666
667
668
669
670
671
672
673
674
675
676
677
678
679
680
681
682
683
684
685
686
687
688
689
690
691
692
693
694
695
696
697
698
699
700
701
702
703
704
705
706
707
708
709
710
711
712
713
714
715
716
717
718
719
720
721
722
723
724
725
726
727
728
729
730
731
732
733
734
735
736
737
738
739
740
741
742
743
744
745
746
747
748
749
750
751
752
753
754
755
756
757
758
759
760
761
762
763
764
765
766
767
768
769
770
771
772
773
774
775
776
777
778
779
780
781
782
783
784
785
786
787
788
789
790
791
792
793
794
795
796
797
798
799
800
801
802
803
804
805
806
807
808
809
810
811
812
813
814
815
816
817
818
819
820
821
822
823
824
825
826
827
828
829
830
831
832
833
834
835
836
837
838
839
840
841
842
843
844
845
846
847
848
849
850
851
852
853
854
855
856
857
858
859
860
861
862
863
864
865
866
867
868
869
870
871
872
873
874
875
876
877
878
879
880
881
882
883
884
885
886
887
888
889
890
891
892
893
894
895
896
897
898
899
900
901
902
903
904
905
906
907
908
909
910
911
912
913
914
915
916
917
918
919
920
921
922
923
924
925
926
927
928
929
930
931
932
933
934
935
936
937
938
939
940
941
942
943
944
945
946
947
948
949
950
951
952
953
954
955
956
957
958
959
960
961
962
963
964
965
966
967
968
969
970
971
972
973
974
975
976
977
978
979
980
981
982
983
984
985
986
987
988
989
990
991
992
993
994
995
996
997
998
999
1000

```

```

55 double *lphome; // Location of Changepoint */
56 void reconstruct(void);
57
58
59
60
61
62
63
64
65
66
67
68
69
70
71
72
73
74
75
76
77
78
79
80
81
82
83
84
85
86
87
88
89
90
91
92
93
94
95
96
97
98
99
100
101
102
103
104
105
106
107
108
109
110
111
112
113
114
115
116
117
118
119
120
121
122
123
124
125
126
127
128
129
130
131
132
133
134
135
136
137
138
139
140
141
142
143
144
145
146
147
148
149
150
151
152
153
154
155
156
157
158
159
160
161
162
163
164
165
166
167
168
169
170
171
172
173
174
175
176
177
178
179
180
181
182
183
184
185
186
187
188
189
190
191
192
193
194
195
196
197
198
199
200
201
202
203
204
205
206
207
208
209
210
211
212
213
214
215
216
217
218
219
220
221
222
223
224
225
226
227
228
229
230
231
232
233
234
235
236
237
238
239
240
241
242
243
244
245
246
247
248
249
250
251
252
253
254
255
256
257
258
259
260
261
262
263
264
265
266
267
268
269
270
271
272
273
274
275
276
277
278
279
280
281
282
283
284
285
286
287
288
289
290
291
292
293
294
295
296
297
298
299
300
301
302
303
304
305
306
307
308
309
310
311
312
313
314
315
316
317
318
319
320
321
322
323
324
325
326
327
328
329
330
331
332
333
334
335
336
337
338
339
340
341
342
343
344
345
346
347
348
349
350
351
352
353
354
355
356
357
358
359
360
361
362
363
364
365
366
367
368
369
370
371
372
373
374
375
376
377
378
379
380
381
382
383
384
385
386
387
388
389
390
391
392
393
394
395
396
397
398
399
400
401
402
403
404
405
406
407
408
409
410
411
412
413
414
415
416
417
418
419
420
421
422
423
424
425
426
427
428
429
430
431
432
433
434
435
436
437
438
439
440
441
442
443
444
445
446
447
448
449
450
451
452
453
454
455
456
457
458
459
460
461
462
463
464
465
466
467
468
469
470
471
472
473
474
475
476
477
478
479
480
481
482
483
484
485
486
487
488
489
490
491
492
493
494
495
496
497
498
499
500
501
502
503
504
505
506
507
508
509
510
511
512
513
514
515
516
517
518
519
520
521
522
523
524
525
526
527
528
529
530
531
532
533
534
535
536
537
538
539
540
541
542
543
544
545
546
547
548
549
550
551
552
553
554
555
556
557
558
559
560
561
562
563
564
565
566
567
568
569
570
571
572
573
574
575
576
577
578
579
580
581
582
583
584
585
586
587
588
589
590
591
592
593
594
595
596
597
598
599
600
601
602
603
604
605
606
607
608
609
610
611
612
613
614
615
616
617
618
619
620
621
622
623
624
625
626
627
628
629
630
631
632
633
634
635
636
637
638
639
640
641
642
643
644
645
646
647
648
649
650
651
652
653
654
655
656
657
658
659
660
661
662
663
664
665
666
667
668
669
670
671
672
673
674
675
676
677
678
679
680
681
682
683
684
685
686
687
688
689
690
691
692
693
694
695
696
697
698
699
700
701
702
703
704
705
706
707
708
709
710
711
712
713
714
715
716
717
718
719
720
721
722
723
724
725
726
727
728
729
730
731
732
733
734
735
736
737
738
739
740
741
742
743
744
745
746
747
748
749
750
751
752
753
754
755
756
757
758
759
760
761
762
763
764
765
766
767
768
769
770
771
772
773
774
775
776
777
778
779
780
781
782
783
784
785
786
787
788
789
790
791
792
793
794
795
796
797
798
799
800
801
802
803
804
805
806
807
808
809
810
811
812
813
814
815
816
817
818
819
820
821
822
823
824
825
826
827
828
829
830
831
832
833
834
835
836
837
838
839
840
841
842
843
844
845
846
847
848
849
850
851
852
853
854
855
856
857
858
859
860
861
862
863
864
865
866
867
868
869
870
871
872
873
874
875
876
877
878
879
880
881
882
883
884
885
886
887
888
889
890
891
892
893
894
895
896
897
898
899
900
901
902
903
904
905
906
907
908
909
910
911
912
913
914
915
916
917
918
919
920
921
922
923
924
925
926
927
928
929
930
931
932
933
934
935
936
937
938
939
940
941
942
943
944
945
946
947
948
949
950
951
952
953
954
955
956
957
958
959
960
961
962
963
964
965
966
967
968
969
970
971
972
973
974
975
976
977
978
979
980
981
982
983
984
985
986
987
988
989
990
991
992
993
994
995
996
997
998
999
1000

```





```

650     }
651     for (i = 1; i < lnumphot; i++)
652     {
653         sub(i,lnumphot-1) = sub(i,1);
654         sub2(i,lnumphot-1) = sub2(i,1);
655     }
656     dtime = E1(0.781/(E.0 - sub2(i,1)));
657     dl = (double) i;
658     sub2(i,1) = 4.0*dl*sub2(i,1) + 4.0*(dtime-dl)*(dtime-dl)*sub2(i,1)+4.0*dl*(dtime-dl)*dtime;
659     for (i=1; i<lnumphot;i++)
660     {
661         sub(i,1) = sqrt(sub2(i,1));
662     }
663     // Calculate the log of the likelihood ratio for every photon using Henderson's approach */
664     for (k = 0; k < lnumphot; k++)
665     {
666         dl = (double) k;
667         dtime = dtime / dtime;
668         dl = dtime / dtime;
669         // Henderson */
670         dtime = 0.5 * log(4.0 * dl * (dtime-dk) / dtime / dtime);
671         dtime = -2.0*(dtime-dk)*log(1.0/dk) + 2.0*(dtime-dk)*sub1(k);
672         subloglik(k) = (dtime + dtime3) / sub1(k) + dtime1;
673         if (subloglik(k) > dloglik_max)
674         {
675             dloglik_max = subloglik(k);
676             k_max = k;
677         }
678     }
679     // Clone for loop that evaluates loglik */
680     if (dloglik_max > sub1(lnumphot)) /* Change point found - Find Confidence Interval */
681     {
682         while ( (l > 0) && (dloglik(k)+sub1(lnumphot)-dloglik_max > 0) ) k--;
683         while ( (k < lnumphot) && (dloglik(k)+sub1(lnumphot)-dloglik_max > 0) ) k++;
684         lnum = k;
685         lnumb = k;
686         lnumc = k;
687         lnumd = k;
688         lnume = k;
689         lnumf = k;
690         lnumg = k;
691         lnumh = k;
692         lnumi = k;
693         lnumj = k;
694         lnumk = k;
695         lnuml = k;
696         lnumm = k;
697         lnumn = k;
698         lnumo = k;
699         lnump = k;
700         lnumq = k;
701         lnumr = k;
702         lnum_s = k;
703         lnumt = k;
704         lnumu = k;
705         lnumv = k;
706         lnumw = k;
707         lnumx = k;
708         lnumy = k;
709         lnumz = k;
710         lnumaa = k;
711         lnumab = k;
712         lnumac = k;
713         lnumad = k;
714         lnumae = k;
715         lnumaf = k;
716         lnumag = k;
717         lnumah = k;
718         lnumai = k;
719         lnumaj = k;
720         lnumak = k;
721         lnumal = k;
722         lnumam = k;
723         lnuman = k;
724         lnumao = k;
725         lnumap = k;
726         lnumaq = k;
727         lnumar = k;
728         lnumas = k;
729         lnumat = k;
730         lnumau = k;
731         lnumav = k;
732         lnumaw = k;
733         lnumax = k;
734         lnumay = k;
735         lnumaz = k;
736         lnumba = k;
737         lnumbb = k;
738         lnumbc = k;
739         lnumbd = k;
740         lnumbe = k;
741         lnumbf = k;
742         lnumbg = k;
743         lnumbh = k;
744         lnumbi = k;
745         lnumbj = k;
746         lnumbk = k;
747         lnumbl = k;
748         lnumbm = k;
749         lnumbn = k;
750         lnumbo = k;
751         lnumbp = k;
752         lnumbq = k;
753         lnumbr = k;
754         lnumbs = k;
755         lnumbt = k;
756         lnumbu = k;
757         lnumbv = k;
758         lnumbw = k;
759         lnumbx = k;
760         lnumby = k;
761         lnumbz = k;
762         lnumca = k;
763         lnumcb = k;
764         lnumcc = k;
765         lnumcd = k;
766         lnumce = k;
767         lnumcf = k;
768         lnumcg = k;
769         lnumch = k;
770         lnumci = k;
771         lnumcj = k;
772         lnumck = k;
773         lnumcl = k;
774         lnumcm = k;
775         lnumcn = k;
776         lnumco = k;
777         lnumcp = k;
778         lnumcq = k;
779         lnumcr = k;
780         lnumcs = k;
781         lnumct = k;
782         lnumcu = k;
783         lnumcv = k;
784         lnumcw = k;
785         lnumcx = k;
786         lnumcy = k;
787         lnumcz = k;
788         lnumda = k;
789         lnumdb = k;
790         lnumdc = k;
791         lnumdd = k;
792         lnumde = k;
793         lnumdf = k;
794         lnumdg = k;
795         lnumdh = k;
796         lnumdi = k;
797         lnumdj = k;
798         lnumdk = k;
799         lnumdl = k;
800         lnumdm = k;
801         lnumdn = k;
802         lnumdo = k;
803         lnumdp = k;
804         lnumdq = k;
805         lnumdr = k;
806         lnumds = k;
807         lnumdt = k;
808         lnumdu = k;
809         lnumdv = k;
810         lnumdw = k;
811         lnumdx = k;
812         lnumdy = k;
813         lnumdz = k;
814         lnumea = k;
815         lnumeb = k;
816         lnumec = k;
817         lnumed = k;
818         lnumee = k;
819         lnumef = k;
820         lnumeg = k;
821         lnumeh = k;
822         lnumei = k;
823         lnumej = k;
824         lnumek = k;
825         lnumel = k;
826         lnumem = k;
827         lnumen = k;
828         lnumeo = k;
829         lnumep = k;
830         lnumeq = k;
831         lnumer = k;
832         lnumes = k;
833         lnumet = k;
834         lnumeu = k;
835         lnumev = k;
836         lnumew = k;
837         lnumex = k;
838         lnumey = k;
839         lnumez = k;
840         lnumfa = k;
841         lnumfb = k;
842         lnumfc = k;
843         lnumfd = k;
844         lnumfe = k;
845         lnumff = k;
846         lnumfg = k;
847         lnumfh = k;
848         lnumfi = k;
849         lnumfj = k;
850         lnumfk = k;
851         lnumfl = k;
852         lnumfm = k;
853         lnumfn = k;
854         lnumfo = k;
855         lnumfp = k;
856         lnumfq = k;
857         lnumfr = k;
858         lnumfs = k;
859         lnumft = k;
860         lnumfu = k;
861         lnumfv = k;
862         lnumfw = k;
863         lnumfx = k;
864         lnumfy = k;
865         lnumfz = k;
866         lnumga = k;
867         lnumgb = k;
868         lnumgc = k;
869         lnumgd = k;
870         lnumge = k;
871         lnumgf = k;
872         lnumgg = k;
873         lnumgh = k;
874         lnumgi = k;
875         lnumgj = k;
876         lnumgk = k;
877         lnumgl = k;
878         lnumgm = k;
879         lnumgn = k;
880         lnumgo = k;
881         lnumgp = k;
882         lnumgq = k;
883         lnumgr = k;
884         lnumgs = k;
885         lnumgt = k;
886         lnumgu = k;
887         lnumgv = k;
888         lnumgw = k;
889         lnumgx = k;
890         lnumgy = k;
891         lnumgz = k;
892         lnumha = k;
893         lnumhb = k;
894         lnumhc = k;
895         lnumhd = k;
896         lnumhe = k;
897         lnumhf = k;
898         lnumhg = k;
899         lnumhi = k;
900         lnumhj = k;
901         lnumhk = k;
902         lnumhl = k;
903         lnumhm = k;
904         lnumhn = k;
905         lnumho = k;
906         lnumhp = k;
907         lnumhq = k;
908         lnumhr = k;
909         lnumhs = k;
910         lnumht = k;
911         lnumhu = k;
912         lnumhv = k;
913         lnumhw = k;
914         lnumhx = k;
915         lnumhy = k;
916         lnumhz = k;
917         lnumia = k;
918         lnumib = k;
919         lnumic = k;
920         lnumid = k;
921         lnumie = k;
922         lnumif = k;
923         lnumig = k;
924         lnumih = k;
925         lnumii = k;
926         lnumij = k;
927         lnumik = k;
928         lnumil = k;
929         lnumim = k;
930         lnumin = k;
931         lnumio = k;
932         lnumip = k;
933         lnumiq = k;
934         lnumir = k;
935         lnumis = k;
936         lnumit = k;
937         lnumiu = k;
938         lnumiv = k;
939         lnumiw = k;
940         lnumix = k;
941         lnumiy = k;
942         lnumiz = k;
943         lnumja = k;
944         lnumjb = k;
945         lnumjc = k;
946         lnumjd = k;
947         lnumje = k;
948         lnumjf = k;
949         lnumjg = k;
950         lnumjh = k;
951         lnumji = k;
952         lnumjj = k;
953         lnumjk = k;
954         lnumjl = k;
955         lnumjm = k;
956         lnumjn = k;
957         lnumjo = k;
958         lnumjp = k;
959         lnumjq = k;
960         lnumjr = k;
961         lnumjs = k;
962         lnumjt = k;
963         lnumju = k;
964         lnumjv = k;
965         lnumjw = k;
966         lnumjx = k;
967         lnumjy = k;
968         lnumjz = k;
969         lnumka = k;
970         lnumkb = k;
971         lnumkc = k;
972         lnumkd = k;
973         lnumke = k;
974         lnumkf = k;
975         lnumkg = k;
976         lnumkh = k;
977         lnumki = k;
978         lnumkj = k;
979         lnumkk = k;
980         lnumkl = k;
981         lnumkm = k;
982         lnumkn = k;
983         lnumko = k;
984         lnumkp = k;
985         lnumkq = k;
986         lnumkr = k;
987         lnumks = k;
988         lnumkt = k;
989         lnumku = k;
990         lnumkv = k;
991         lnumkw = k;
992         lnumkx = k;
993         lnumky = k;
994         lnumkz = k;
995         lnumla = k;
996         lnumlb = k;
997         lnumlc = k;
998         lnumld = k;
999         lnumle = k;
1000         lnumlf = k;
1001         lnumlg = k;
1002         lnumlh = k;
1003         lnumli = k;
1004         lnumlj = k;
1005         lnumlk = k;
1006         lnumll = k;
1007         lnumlm = k;
1008         lnumln = k;
1009         lnumlo = k;
1010         lnumlp = k;
1011         lnumlq = k;
1012         lnumlr = k;
1013         lnumls = k;
1014         lnumlt = k;
1015         lnumlu = k;
1016         lnumlv = k;
1017         lnumlw = k;
1018         lnumlx = k;
1019         lnumly = k;
1020         lnumlz = k;
1021         lnumma = k;
1022         lnummb = k;
1023         lnummc = k;
1024         lnummd = k;
1025         lnumme = k;
1026         lnummf = k;
1027         lnummg = k;
1028         lnummh = k;
1029         lnummi = k;
1030         lnummj = k;
1031         lnummk = k;
1032         lnumml = k;
1033         lnummm = k;
1034         lnummn = k;
1035         lnummo = k;
1036         lnummp = k;
1037         lnummq = k;
1038         lnummr = k;
1039         lnumms = k;
1040         lnummt = k;
1041         lnummu = k;
1042         lnummv = k;
1043         lnummw = k;
1044         lnummx = k;
1045         lnummy = k;
1046         lnummz = k;
1047         lnumna = k;
1048         lnumnb = k;
1049         lnumnc = k;
1050         lnumnd = k;
1051         lnumne = k;
1052         lnumnf = k;
1053         lnumng = k;
1054         lnumnh = k;
1055         lnumni = k;
1056         lnumnj = k;
1057         lnumnk = k;
1058         lnumnl = k;
1059         lnumnm = k;
1060         lnumnn = k;
1061         lnumno = k;
1062         lnumnp = k;
1063         lnumnq = k;
1064         lnumnr = k;
1065         lnumns = k;
1066         lnumnt = k;
1067         lnumnu = k;
1068         lnumnv = k;
1069         lnumnw = k;
1070         lnumnx = k;
1071         lnumny = k;
1072         lnumnz = k;
1073         lnumoa = k;
1074         lnumob = k;
1075         lnumoc = k;
1076         lnumod = k;
1077         lnumoe = k;
1078         lnumof = k;
1079         lnumog = k;
1080         lnumoh = k;
1081         lnumoi = k;
1082         lnumoj = k;
1083         lnumok = k;
1084         lnumol = k;
1085         lnumom = k;
1086         lnumon = k;
1087         lnumoo = k;
1088         lnumop = k;
1089         lnumoq = k;
1090         lnumor = k;
1091         lnumos = k;
1092         lnumot = k;
1093         lnumou = k;
1094         lnumov = k;
1095         lnumow = k;
1096         lnumox = k;
1097         lnumoy = k;
1098         lnumoz = k;
1099         lnumpa = k;
1100         lnumpb = k;
1101         lnumpc = k;
1102         lnumpd = k;
1103         lnumpe = k;
1104         lnumpf = k;
1105         lnumpg = k;
1106         lnumph = k;
1107         lnumpi = k;
1108         lnumpj = k;
1109         lnumpk = k;
1110         lnumpl = k;
1111         lnumpm = k;
1112         lnumpn = k;
1113         lnumpo = k;
1114         lnumpp = k;
1115         lnumpq = k;
1116         lnumpr = k;
1117         lnumps = k;
1118         lnumpt = k;
1119         lnumpu = k;
1120         lnumpv = k;
1121         lnumpw = k;
1122         lnumpx = k;
1123         lnumpy = k;
1124         lnumpz = k;
1125         lnumqa = k;
1126         lnumqb = k;
1127         lnumqc = k;
1128         lnumqd = k;
1129         lnumqe = k;
1130         lnumqf = k;
1131         lnumqg = k;
1132         lnumqh = k;
1133         lnumqi = k;
1134         lnumqj = k;
1135         lnumqk = k;
1136         lnumql = k;
1137         lnumqm = k;
1138         lnumqn = k;
1139         lnumqo = k;
1140         lnumqp = k;
1141         lnumqq = k;
1142         lnumqr = k;
1143         lnumqs = k;
1144         lnumqt = k;
1145         lnumqu = k;
1146         lnumqv = k;
1147         lnumqw = k;
1148         lnumqx = k;
1149         lnumqy = k;
1150         lnumqz = k;
1151         lnumra = k;
1152         lnumrb = k;
1153         lnumrc = k;
1154         lnumrd = k;
1155         lnumre = k;
1156         lnumrf = k;
1157         lnumrg = k;
1158         lnumrh = k;
1159         lnumri = k;
1160         lnumrj = k;
1161         lnumrk = k;
1162         lnumrl = k;
1163         lnumrm = k;
1164         lnumrn = k;
1165         lnumro = k;
1166         lnumrp = k;
1167         lnumrq = k;
1168         lnumrr = k;
1169         lnumrs = k;
1170         lnumrt = k;
1171         lnumru = k;
1172         lnumrv = k;
1173         lnumrw = k;
1174         lnumrx = k;
1175         lnumry = k;
1176         lnumrz = k;
1177         lnumsa = k;
1178         lnumsb = k;
1179         lnumsc = k;
1180         lnumsd = k;
1181         lnumse = k;
1182         lnumsf = k;
1183         lnumsg = k;
1184         lnumsh = k;
1185         lnumsi = k;
1186         lnumsj = k;
1187         lnumsk = k;
1188         lnumsl = k;
1189         lnumsm = k;
1190         lnumsn = k;
1191         lnumso = k;
1192         lnumsp = k;
1193         lnumsq = k;
1194         lnumsr = k;
1195         lnumss = k;
1196         lnumst = k;
1197         lnumsu = k;
1198         lnumsv = k;
1199         lnumsw = k;
1200         lnumsx = k;
1201         lnumsy = k;
1202         lnumsz = k;
1203         lnumta = k;
1204         lnumtb = k;
1205         lnumtc = k;
1206         lnumtd = k;
1207         lnumte = k;
1208         lnumtf = k;
1209         lnumtg = k;
1210         lnumth = k;
1211         lnumti = k;
1212         lnumtj = k;
1213         lnumtk = k;
1214         lnumtl = k;
1215         lnumtm = k;
1216         lnumtn = k;
1217         lnumto = k;
1218         lnumtp = k;
1219         lnumtq = k;
1220         lnumtr = k;
1221         lnumts = k;
1222         lnumtt = k;
1223         lnumtu = k;
1224         lnumtv = k;
1225         lnumtw = k;
1226         lnumtx = k;
1227         lnumty = k;
1228         lnumtz = k;
1229         lnumua = k;
1230         lnumub = k;
1231         lnumuc = k;
1232         lnumud = k;
1233         lnumue = k;
1234         lnumuf = k;
1235         lnumug = k;
1236         lnumuh = k;
1237         lnumui = k;
1238         lnumuj = k;
1239         lnumuk = k;
1240         lnumul = k;
1241         lnumum = k;
1242         lnumun = k;
1243         lnumuo = k;
1244         lnumup = k;
1245         lnumuq = k;
1246         lnumur = k;
1247         lnumus = k;
1248         lnumut = k;
1249         lnumuu = k;
1250         lnumuv = k;
1251         lnumuw = k;
1252         lnumux = k;
1253         lnumuy = k;
1254         lnumuz = k;
1255         lnumva = k;
1256         lnumvb = k;
1257         lnumvc = k;
1258         lnumvd = k;
1259         lnumve = k;
1260         lnumvf = k;
1261         lnumvg = k;
1262         lnumvh = k;
1263         lnumvi = k;
1264         lnumvj = k;
1265         lnumvk = k;
1266         lnumvl = k;
1267         lnumvm = k;
1268         lnumvn = k;
1269         lnumvo = k;
1270         lnumvp = k;
1271         lnumvq = k;
1272         lnumvr = k;
1273         lnumvs = k;
1274         lnumvt = k;
1275         lnumvu = k;
1276         lnumvv = k;
1277         lnumvw = k;
1278         lnumvx = k;
1279         lnumvy = k;
1280         lnumvz = k;
1281         lnumwa = k;
1282         lnumwb = k;
1283         lnumwc = k;
1284         lnumwd = k;
1285         lnumwe = k;
1286         lnumwf = k;
1287         lnumwg = k;
1288         lnumwh = k;
1289         lnumwi = k;
1290         lnumwj = k;
1291         lnumwk = k;
1292         lnumwl = k;
1293         lnumwm = k;
1294         lnumwn = k;
1295         lnumwo = k;
1296         lnumwp = k;
1297         lnumwq = k;
1298         lnumwr = k;
1299         lnumws = k;
1300         lnumwt = k;
1301         lnumwu = k;
1302         lnumwv = k;
1303         lnumww = k;
1304         lnumwx = k;
1305         lnumwy = k;
1306         lnumwz = k;
1307         lnumxa = k;
1308         lnumxb = k;
1309         lnumxc = k;
1310         lnumxd = k;
1311         lnumxe = k;
1312         lnumxf = k;
1313         lnumxg = k;
1314         lnumxh = k;
1315         lnumxi = k;
1316         lnumxj = k;
1317         lnumxk = k;
1318         lnumxl = k;
1319         lnumxm = k;
1320         lnumxn = k;
1321         lnumxo = k;
1322         lnumxp = k;
1323         lnumxq = k;
1324         lnumxr = k;
1325         lnumxs = k;
1326         lnumxt = k;
1327         lnumxu = k;
1328         lnumxv = k;
1329         lnumxw = k;
1330         lnumxx = k;
1331         lnumxy = k;
1332         lnumxz = k;
1333         lnumya = k;
1334         lnumyb = k;
1335         lnumyc = k;
1336         lnumyd = k;
1337         lnumye = k;
1338         lnumyf = k;
1339         lnumyg = k;
1340         lnumyh = k;
1341         lnumyi = k;
1342         lnumyj = k;
1343         lnumyk = k;
1344         lnumyl = k;
1345         lnumym = k;
1346         lnumyn = k;
1347         lnumyo = k;
1348         lnumyp = k;
1349         lnumyq = k;
1350         lnumyr = k;
1351         lnumys = k;
1352         lnumyt = k;
1353         lnumyu = k;
1354         lnumyv = k;
1355         lnumyw = k;
1356         lnumyx = k;
1357         lnumyy = k;
1358         lnumyz = k;
1359         lnumza = k;
1360         lnumzb = k;
1361         lnumzc = k;
1362         lnumzd = k;
1363         lnumze = k;
1364         lnumzf = k;
1365         lnumzg = k;
1366         lnumzh = k;
1367         lnumzi = k;
1368         lnumzj = k;
1369         lnumzk = k;
1370         lnumzl = k;
1371         lnumzm = k;
1372         lnumzn = k;
1373         lnumzo = k;
1374         lnumzp = k;
1375         lnumzq = k;
1376         lnumzr = k;
1377         lnumzs = k;
1378         lnumzt = k;
1379         lnumzu = k;
1380         lnumzv = k;
1381         lnumzw = k;
1382         lnumzx = k;
1383         lnumzy = k;
1384         lnumzz = k;

```





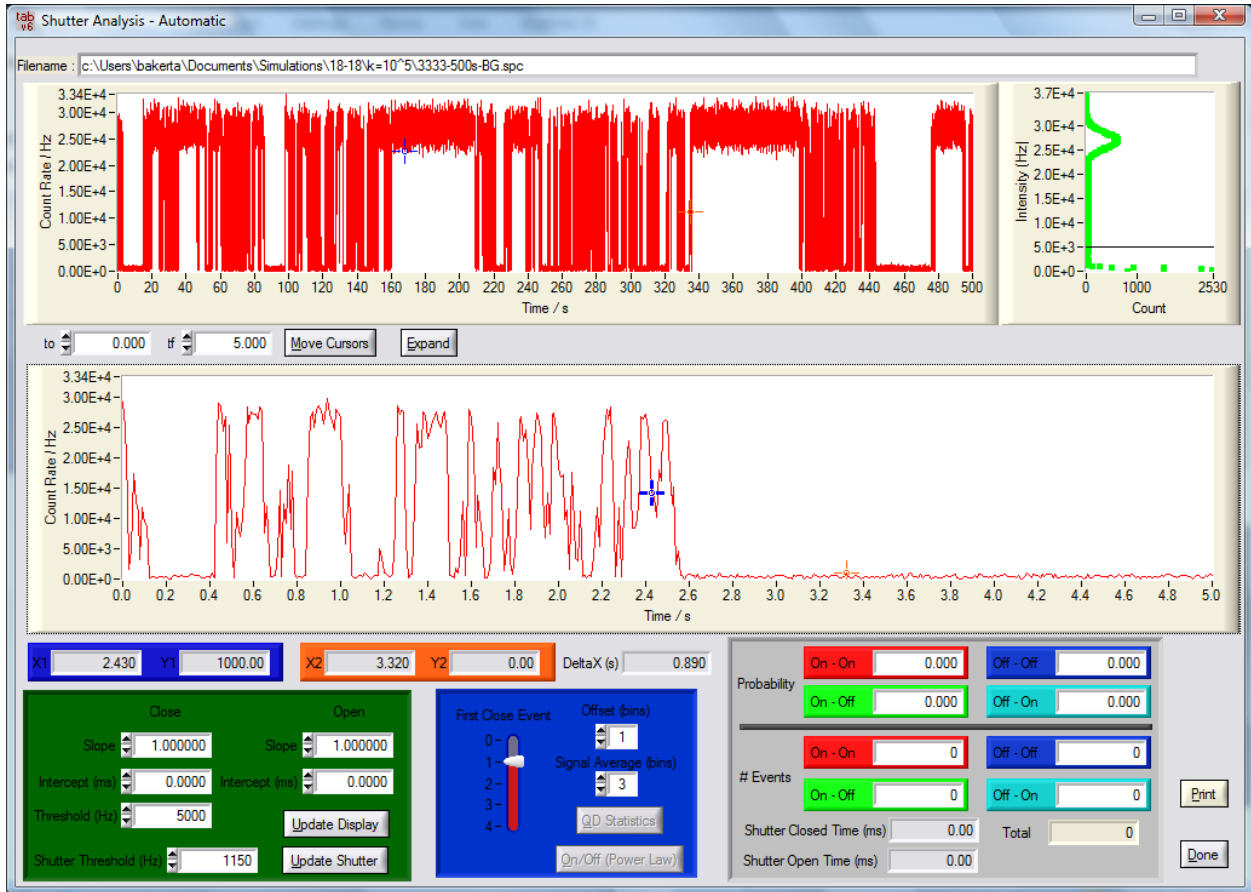








## A.8 Shutter Analysis



```

1 #include <omp.h>
2 #include <stdio.h>
3 #include <math.h>
4 #include <string.h>
5 #include <stdlib.h>
6 #include "A_Functions.h"
7 #include "Global.h"
8 #include "Shutter.h"
9 #include "ShutterCoord.h"
10 #include "ShutterCoord.h"
11 #include "ShutterCoord.h"
12 #include "ShutterCoord.h"
13 // From RM (CB)
14 #include "ShutterCoord.h"
15 #include "ShutterCoord.h"
16 #include "ShutterCoord.h"
17 #include "ShutterCoord.h"
18 #include "ShutterCoord.h"
19 // From RC (Internal Clock)
20 #include "ShutterCoord.h"
21 #include "ShutterCoord.h"
22 #include "ShutterCoord.h"
23 #include "ShutterCoord.h"
24 #include "ShutterCoord.h"
25 #include "ShutterCoord.h"
26 #include "ShutterCoord.h"
27 #include "ShutterCoord.h"
28 #include "ShutterCoord.h"
29 #include "ShutterCoord.h"
30 #include "ShutterCoord.h"
31 #include "ShutterCoord.h"
32 #include "ShutterCoord.h"
33 #include "ShutterCoord.h"
34 #include "ShutterCoord.h"
35 #include "ShutterCoord.h"
36 #include "ShutterCoord.h"
37 #include "ShutterCoord.h"
38 void OTTOLOCKER_OpenSHA (int number, int memSize, void *callback,
39 {
40     int i;
41     int j;
42     int k;
43     int l;
44     int m;
45     int n;
46     int o;
47     int p;
48     int q;
49     int r;
50     int s;
51     int t;
52     int u;
53     int v;
54     int w;
55     int x;
56     int y;
57     int z;
58     int aa;
59     int bb;
60     int cc;
61     int dd;
62     int ee;
63     int ff;
64     int gg;
65     int hh;
66     int ii;
67     int jj;
68     int kk;
69     int ll;
70     int mm;
71     int nn;
72     int oo;
73     int pp;
74     int qq;
75     int rr;
76     int ss;
77     int tt;
78     int uu;
79     int vv;
80     int ww;
81     int xx;
82     int yy;
83     int zz;
84     int aaa;
85     int bbb;
86     int ccc;
87     int ddd;
88     int eee;
89     int fff;
90     int ggg;
91     int hhh;
92     int iii;
93     int jjj;
94     int kkk;
95     int lll;
96     int mmm;
97     int nnn;
98     int ooo;
99     int ppp;
100     int qqq;
101     int rrr;
102     int sss;
103     int ttt;
104     int uuu;
105     int vvv;
106     int www;
107     int xxx;
108     int yyy;
109     int zzz;
110     int aaa;
111     int bbb;
112     int ccc;
113     int ddd;
114     int eee;
115     int fff;
116     int ggg;
117     int hhh;
118     int iii;
119     int jjj;
120     int kkk;
121     int lll;
122     int mmm;
123     int nnn;
124     int ooo;
125     int ppp;
126     int qqq;
127     int rrr;
128     int sss;
129     int ttt;
130     int uuu;
131     int vvv;
132     int www;
133     int xxx;
134     int yyy;
135     int zzz;
136     int aaa;
137     int bbb;
138     int ccc;
139     int ddd;
140     int eee;
141     int fff;
142     int ggg;
143     int hhh;
144     int iii;
145     int jjj;
146     int kkk;
147     int lll;
148     int mmm;
149     int nnn;
150     int ooo;
151     int ppp;
152     int qqq;
153     int rrr;
154     int sss;
155     int ttt;
156     int uuu;
157     int vvv;
158     int www;
159     int xxx;
160     int yyy;
161     int zzz;
162     int aaa;
163     int bbb;
164     int ccc;
165     int ddd;
166     int eee;
167     int fff;
168     int ggg;
169     int hhh;
170     int iii;
171     int jjj;
172     int kkk;
173     int lll;
174     int mmm;
175     int nnn;
176     int ooo;
177     int ppp;
178     int qqq;
179     int rrr;
180     int sss;
181     int ttt;
182     int uuu;
183     int vvv;
184     int www;
185     int xxx;
186     int yyy;
187     int zzz;
188     int aaa;
189     int bbb;
190     int ccc;
191     int ddd;
192     int eee;
193     int fff;
194     int ggg;
195     int hhh;
196     int iii;
197     int jjj;
198     int kkk;
199     int lll;
200     int mmm;
201     int nnn;
202     int ooo;
203     int ppp;
204     int qqq;
205     int rrr;
206     int sss;
207     int ttt;
208     int uuu;
209     int vvv;
210     int www;
211     int xxx;
212     int yyy;
213     int zzz;
214     int aaa;
215     int bbb;
216     int ccc;
217     int ddd;
218     int eee;
219     int fff;
220     int ggg;
221     int hhh;
222     int iii;
223     int jjj;
224     int kkk;
225     int lll;
226     int mmm;
227     int nnn;
228     int ooo;
229     int ppp;
230     int qqq;
231     int rrr;
232     int sss;
233     int ttt;
234     int uuu;
235     int vvv;
236     int www;
237     int xxx;
238     int yyy;
239     int zzz;
240     int aaa;
241     int bbb;
242     int ccc;
243     int ddd;
244     int eee;
245     int fff;
246     int ggg;
247     int hhh;
248     int iii;
249     int jjj;
250     int kkk;
251     int lll;
252     int mmm;
253     int nnn;
254     int ooo;
255     int ppp;
256     int qqq;
257     int rrr;
258     int sss;
259     int ttt;
260     int uuu;
261     int vvv;
262     int www;
263     int xxx;
264     int yyy;
265     int zzz;
266     int aaa;
267     int bbb;
268     int ccc;
269     int ddd;
270     int eee;
271     int fff;
272     int ggg;
273     int hhh;
274     int iii;
275     int jjj;
276     int kkk;
277     int lll;
278     int mmm;
279     int nnn;
280     int ooo;
281     int ppp;
282     int qqq;
283     int rrr;
284     int sss;
285     int ttt;
286     int uuu;
287     int vvv;
288     int www;
289     int xxx;
290     int yyy;
291     int zzz;
292     int aaa;
293     int bbb;
294     int ccc;
295     int ddd;
296     int eee;
297     int fff;
298     int ggg;
299     int hhh;
300     int iii;
301     int jjj;
302     int kkk;
303     int lll;
304     int mmm;
305     int nnn;
306     int ooo;
307     int ppp;
308     int qqq;
309     int rrr;
310     int sss;
311     int ttt;
312     int uuu;
313     int vvv;
314     int www;
315     int xxx;
316     int yyy;
317     int zzz;
318     int aaa;
319     int bbb;
320     int ccc;
321     int ddd;
322     int eee;
323     int fff;
324     int ggg;
325     int hhh;
326     int iii;
327     int jjj;
328     int kkk;
329     int lll;
330     int mmm;
331     int nnn;
332     int ooo;
333     int ppp;
334     int qqq;
335     int rrr;
336     int sss;
337     int ttt;
338     int uuu;
339     int vvv;
340     int www;
341     int xxx;
342     int yyy;
343     int zzz;
344     int aaa;
345     int bbb;
346     int ccc;
347     int ddd;
348     int eee;
349     int fff;
350     int ggg;
351     int hhh;
352     int iii;
353     int jjj;
354     int kkk;
355     int lll;
356     int mmm;
357     int nnn;
358     int ooo;
359     int ppp;
360     int qqq;
361     int rrr;
362     int sss;
363     int ttt;
364     int uuu;
365     int vvv;
366     int www;
367     int xxx;
368     int yyy;
369     int zzz;
370     int aaa;
371     int bbb;
372     int ccc;
373     int ddd;
374     int eee;
375     int fff;
376     int ggg;
377     int hhh;
378     int iii;
379     int jjj;
380     int kkk;
381     int lll;
382     int mmm;
383     int nnn;
384     int ooo;
385     int ppp;
386     int qqq;
387     int rrr;
388     int sss;
389     int ttt;
390     int uuu;
391     int vvv;
392     int www;
393     int xxx;
394     int yyy;
395     int zzz;
396     int aaa;
397     int bbb;
398     int ccc;
399     int ddd;
400     int eee;
401     int fff;
402     int ggg;
403     int hhh;
404     int iii;
405     int jjj;
406     int kkk;
407     int lll;
408     int mmm;
409     int nnn;
410     int ooo;
411     int ppp;
412     int qqq;
413     int rrr;
414     int sss;
415     int ttt;
416     int uuu;
417     int vvv;
418     int www;
419     int xxx;
420     int yyy;
421     int zzz;
422     int aaa;
423     int bbb;
424     int ccc;
425     int ddd;
426     int eee;
427     int fff;
428     int ggg;
429     int hhh;
430     int iii;
431     int jjj;
432     int kkk;
433     int lll;
434     int mmm;
435     int nnn;
436     int ooo;
437     int ppp;
438     int qqq;
439     int rrr;
440     int sss;
441     int ttt;
442     int uuu;
443     int vvv;
444     int www;
445     int xxx;
446     int yyy;
447     int zzz;
448     int aaa;
449     int bbb;
450     int ccc;
451     int ddd;
452     int eee;
453     int fff;
454     int ggg;
455     int hhh;
456     int iii;
457     int jjj;
458     int kkk;
459     int lll;
460     int mmm;
461     int nnn;
462     int ooo;
463     int ppp;
464     int qqq;
465     int rrr;
466     int sss;
467     int ttt;
468     int uuu;
469     int vvv;
470     int www;
471     int xxx;
472     int yyy;
473     int zzz;
474     int aaa;
475     int bbb;
476     int ccc;
477     int ddd;
478     int eee;
479     int fff;
480     int ggg;
481     int hhh;
482     int iii;
483     int jjj;
484     int kkk;
485     int lll;
486     int mmm;
487     int nnn;
488     int ooo;
489     int ppp;
490     int qqq;
491     int rrr;
492     int sss;
493     int ttt;
494     int uuu;
495     int vvv;
496     int www;
497     int xxx;
498     int yyy;
499     int zzz;
500     int aaa;
501     int bbb;
502     int ccc;
503     int ddd;
504     int eee;
505     int fff;
506     int ggg;
507     int hhh;
508     int iii;
509     int jjj;
510     int kkk;
511     int lll;
512     int mmm;
513     int nnn;
514     int ooo;
515     int ppp;
516     int qqq;
517     int rrr;
518     int sss;
519     int ttt;
520     int uuu;
521     int vvv;
522     int www;
523     int xxx;
524     int yyy;
525     int zzz;
526     int aaa;
527     int bbb;
528     int ccc;
529     int ddd;
530     int eee;
531     int fff;
532     int ggg;
533     int hhh;
534     int iii;
535     int jjj;
536     int kkk;
537     int lll;
538     int mmm;
539     int nnn;
540     int ooo;
541     int ppp;
542     int qqq;
543     int rrr;
544     int sss;
545     int ttt;
546     int uuu;
547     int vvv;
548     int www;
549     int xxx;
550     int yyy;
551     int zzz;
552     int aaa;
553     int bbb;
554     int ccc;
555     int ddd;
556     int eee;
557     int fff;
558     int ggg;
559     int hhh;
560     int iii;
561     int jjj;
562     int kkk;
563     int lll;
564     int mmm;
565     int nnn;
566     int ooo;
567     int ppp;
568     int qqq;
569     int rrr;
570     int sss;
571     int ttt;
572     int uuu;
573     int vvv;
574     int www;
575     int xxx;
576     int yyy;
577     int zzz;
578     int aaa;
579     int bbb;
580     int ccc;
581     int ddd;
582     int eee;
583     int fff;
584     int ggg;
585     int hhh;
586     int iii;
587     int jjj;
588     int kkk;
589     int lll;
590     int mmm;
591     int nnn;
592     int ooo;
593     int ppp;
594     int qqq;
595     int rrr;
596     int sss;
597     int ttt;
598     int uuu;
599     int vvv;
600     int www;
601     int xxx;
602     int yyy;
603     int zzz;
604     int aaa;
605     int bbb;
606     int ccc;
607     int ddd;
608     int eee;
609     int fff;
610     int ggg;
611     int hhh;
612     int iii;
613     int jjj;
614     int kkk;
615     int lll;
616     int mmm;
617     int nnn;
618     int ooo;
619     int ppp;
620     int qqq;
621     int rrr;
622     int sss;
623     int ttt;
624     int uuu;
625     int vvv;
626     int www;
627     int xxx;
628     int yyy;
629     int zzz;
630     int aaa;
631     int bbb;
632     int ccc;
633     int ddd;
634     int eee;
635     int fff;
636     int ggg;
637     int hhh;
638     int iii;
639     int jjj;
640     int kkk;
641     int lll;
642     int mmm;
643     int nnn;
644     int ooo;
645     int ppp;
646     int qqq;
647     int rrr;
648     int sss;
649     int ttt;
650     int uuu;
651     int vvv;
652     int www;
653     int xxx;
654     int yyy;
655     int zzz;
656     int aaa;
657     int bbb;
658     int ccc;
659     int ddd;
660     int eee;
661     int fff;
662     int ggg;
663     int hhh;
664     int iii;
665     int jjj;
666     int kkk;
667     int lll;
668     int mmm;
669     int nnn;
670     int ooo;
671     int ppp;
672     int qqq;
673     int rrr;
674     int sss;
675     int ttt;
676     int uuu;
677     int vvv;
678     int www;
679     int xxx;
680     int yyy;
681     int zzz;
682     int aaa;
683     int bbb;
684     int ccc;
685     int ddd;
686     int eee;
687     int fff;
688     int ggg;
689     int hhh;
690     int iii;
691     int jjj;
692     int kkk;
693     int lll;
694     int mmm;
695     int nnn;
696     int ooo;
697     int ppp;
698     int qqq;
699     int rrr;
700     int sss;
701     int ttt;
702     int uuu;
703     int vvv;
704     int www;
705     int xxx;
706     int yyy;
707     int zzz;
708     int aaa;
709     int bbb;
710     int ccc;
711     int ddd;
712     int eee;
713     int fff;
714     int ggg;
715     int hhh;
716     int iii;
717     int jjj;
718     int kkk;
719     int lll;
720     int mmm;
721     int nnn;
722     int ooo;
723     int ppp;
724     int qqq;
725     int rrr;
726     int sss;
727     int ttt;
728     int uuu;
729     int vvv;
730     int www;
731     int xxx;
732     int yyy;
733     int zzz;
734     int aaa;
735     int bbb;
736     int ccc;
737     int ddd;
738     int eee;
739     int fff;
740     int ggg;
741     int hhh;
742     int iii;
743     int jjj;
744     int kkk;
745     int lll;
746     int mmm;
747     int nnn;
748     int ooo;
749     int ppp;
750     int qqq;
751     int rrr;
752     int sss;
753     int ttt;
754     int uuu;
755     int vvv;
756     int www;
757     int xxx;
758     int yyy;
759     int zzz;
760     int aaa;
761     int bbb;
762     int ccc;
763     int ddd;
764     int eee;
765     int fff;
766     int ggg;
767     int hhh;
768     int iii;
769     int jjj;
770     int kkk;
771     int lll;
772     int mmm;
773     int nnn;
774     int ooo;
775     int ppp;
776     int qqq;
777     int rrr;
778     int sss;
779     int ttt;
780     int uuu;
781     int vvv;
782     int www;
783     int xxx;
784     int yyy;
785     int zzz;
786     int aaa;
787     int bbb;
788     int ccc;
789     int ddd;
790     int eee;
791     int fff;
792     int ggg;
793     int hhh;
794     int iii;
795     int jjj;
796     int kkk;
797     int lll;
798     int mmm;
799     int nnn;
800     int ooo;
801     int ppp;
802     int qqq;
803     int rrr;
804     int sss;
805     int ttt;
806     int uuu;
807     int vvv;
808     int www;
809     int xxx;
810     int yyy;
811     int zzz;
812     int aaa;
813     int bbb;
814     int ccc;
815     int ddd;
816     int eee;
817     int fff;
818     int ggg;
819     int hhh;
820     int iii;
821     int jjj;
822     int kkk;
823     int lll;
824     int mmm;
825     int nnn;
826     int ooo;
827     int ppp;
828     int qqq;
829     int rrr;
830     int sss;
831     int ttt;
832     int uuu;
833     int vvv;
834     int www;
835     int xxx;
836     int yyy;
837     int zzz;
838     int aaa;
839     int bbb;
840     int ccc;
841     int ddd;
842     int eee;
843     int fff;
844     int ggg;
845     int hhh;
846     int iii;
847     int jjj;
848     int kkk;
849     int lll;
850     int mmm;
851     int nnn;
852     int ooo;
853     int ppp;
854     int qqq;
855     int rrr;
856     int sss;
857     int ttt;
858     int uuu;
859     int vvv;
860     int www;
861     int xxx;
862     int yyy;
863     int zzz;
864     int aaa;
865     int bbb;
866     int ccc;
867     int ddd;
868     int eee;
869     int fff;
870     int ggg;
871     int hhh;
872     int iii;
873     int jjj;
874     int kkk;
875     int lll;
876     int mmm;
877     int nnn;
878     int ooo;
879     int ppp;
880     int qqq;
881     int rrr;
882     int sss;
883     int ttt;
884     int uuu;
885     int vvv;
886     int www;
887     int xxx;
888     int yyy;
889     int zzz;
890     int aaa;
891     int bbb;
892     int ccc;
893     int ddd;
894     int eee;
895     int fff;
896     int ggg;
897     int hhh;
898     int iii;
899     int jjj;
900     int kkk;
901     int lll;
902     int mmm;
903     int nnn;
904     int ooo;
905     int ppp;
906     int qqq;
907     int rrr;
908     int sss;
909     int ttt;
910     int uuu;
911     int vvv;
912     int www;
913     int xxx;
914     int yyy;
915     int zzz;
916     int aaa;
917     int bbb;
918     int ccc;
919     int ddd;
920     int eee;
921     int fff;
922     int ggg;
923     int hhh;
924     int iii;
925     int jjj;
926     int kkk;
927     int lll;
928     int mmm;
929     int nnn;
930     int ooo;
931     int ppp;
932     int qqq;
933     int rrr;
934     int sss;
935     int ttt;
936     int uuu;
937     int vvv;
938     int www;
939     int xxx;
940     int yyy;
941     int zzz;
942     int aaa;
943     int bbb;
944     int ccc;
945     int ddd;
946     int eee;
947     int fff;
948     int ggg;
949     int hhh;
950     int iii;
951     int jjj;
952     int kkk;
953     int lll;
954     int mmm;
955     int nnn;
956     int ooo;
957     int ppp;
958     int qqq;
959     int rrr;
960     int sss;
961     int ttt;
962     int uuu;
963     int vvv;
964     int www;
965     int xxx;
966     int yyy;
967     int zzz;
968     int aaa;
969     int bbb;
970     int ccc;
971     int ddd;
972     int eee;
973     int fff;
974     int ggg;
975     int hhh;
976     int iii;
977     int jjj;
978     int kkk;
979     int lll;
980     int mmm;
981     int nnn;
982     int ooo;
983     int ppp;
984     int qqq;
985     int rrr;
986     int sss;
987     int ttt;
988     int uuu;
989     int vvv;
990     int www;
991     int xxx;
992     int yyy;
993     int zzz;
994     int aaa;
995     int bbb;
996     int ccc;
997     int ddd;
998     int eee;
999     int fff;
1000    int ggg;

```



```

432 maxm = intmax * dmin_time * 1.E-3;
433 double dthreshold;
434 int ioffset, lsum, iFirstClose;
435 double dclose=0, dclose0;
436 double dclose=0, dclose0;
437 int iclose, iopen;
438 double dpre, dpost;
439 double dclose=0, dclose0;
440 double dclose=0, dclose0;
441 int iResult(1)-(0,0,0); // 0 = On-On; 1 = On-Off; 2 = Off-Off; 3 = Off-On
442 double dclose=0, dclose0;
443 double dclose=0, dclose0;
444 double dclose=0, dclose0;
445 double dclose=0, dclose0;
446 double dclose=0, dclose0;
447 double dclose=0, dclose0;
448 double dclose=0, dclose0;
449 double dclose=0, dclose0;
450 double dclose=0, dclose0;
451 int iResult(1)-(0,0,0); // 0 = On-On; 1 = On-Off; 2 = Off-Off; 3 = Off-On
452 double dclose=0, dclose0;
453 double dclose=0, dclose0;
454 int i, i_max;
455 double dthreshold;
456 double dclose=0, dclose0;
457 double dclose=0, dclose0;
458 double dclose=0, dclose0;
459 double dclose=0, dclose0;
460 double dclose=0, dclose0;
461 double dclose=0, dclose0;
462 double dclose=0, dclose0;
463 double dclose=0, dclose0;
464 double dclose=0, dclose0;
465 double dclose=0, dclose0;
466 double dclose=0, dclose0;
467 double dclose=0, dclose0;
468 double dclose=0, dclose0;
469 double dclose=0, dclose0;
470 double dclose=0, dclose0;
471 double dclose=0, dclose0;
472 double dclose=0, dclose0;
473 double dclose=0, dclose0;
474 double dclose=0, dclose0;
475 double dclose=0, dclose0;
476 double dclose=0, dclose0;
477 double dclose=0, dclose0;
478 double dclose=0, dclose0;
479 double dclose=0, dclose0;
480 double dclose=0, dclose0;
481 double dclose=0, dclose0;
482 double dclose=0, dclose0;
483 double dclose=0, dclose0;
484 double dclose=0, dclose0;
485 double dclose=0, dclose0;
486 double dclose=0, dclose0;
487 double dclose=0, dclose0;
488 double dclose=0, dclose0;
489 double dclose=0, dclose0;
490 double dclose=0, dclose0;
491 double dclose=0, dclose0;
492 double dclose=0, dclose0;
493 double dclose=0, dclose0;
494 double dclose=0, dclose0;
495 double dclose=0, dclose0;
496 double dclose=0, dclose0;
497 double dclose=0, dclose0;
498 double dclose=0, dclose0;
499 double dclose=0, dclose0;
500 double dclose=0, dclose0;
501 double dclose=0, dclose0;
502 double dclose=0, dclose0;
503 double dclose=0, dclose0;
504 double dclose=0, dclose0;
505 double dclose=0, dclose0;
506 double dclose=0, dclose0;
507 double dclose=0, dclose0;
508 double dclose=0, dclose0;
509 double dclose=0, dclose0;
510 int i, i_max;
511 double dclose=0, dclose0;
512 int iLoop;
513 // Want 4 arrays that have the results in them, so they can be plotted color coded.
514 // Make xval = dClose/dOpen, and yval = maxc
515 //
516 //
517 //
518 //
519 //
520 //
521 //
522 //
523 //
524 //
525 //
526 //
527 //
528 //
529 //
530 //
531 //
532 //
533 //
534 //
535 //
536 //
537 //
538 //
539 //
540 //
541 //
542 //
543 //
544 //
545 //
546 //
547 //
548 //
549 //
550 //
551 //
552 //
553 //
554 //
555 //
556 //
557 //
558 //
559 //
560 //
561 //
562 //
563 //
564 //
565 //
566 //
567 //
568 //
569 //
570 //
571 //
572 //
573 //
574 //
575 //
576 //
577 //
578 //
579 //
580 //
581 //
582 //
583 //
584 //
585 //
586 //
587 //
588 //
589 //
590 //
591 //
592 //
593 //
594 //
595 //
596 //
597 //
598 //
599 //
600 //
601 //
602 //
603 //
604 //
605 //
606 //
607 //
608 //
609 //
610 //
611 //
612 //
613 //
614 //
615 //
616 //
617 //
618 //
619 //
620 //
621 //
622 //
623 //
624 //
625 //
626 //
627 //
628 //
629 //
630 //
631 //
632 //
633 //
634 //
635 //
636 //
637 //
638 //
639 //
640 //
641 //
642 //
643 //
644 //
645 //
646 //
647 //
648 //
649 //
650 //
651 //
652 //
653 //
654 //
655 //
656 //
657 //
658 //
659 //
660 //
661 //
662 //
663 //
664 //
665 //
666 //
667 //
668 //
669 //
670 //
671 //
672 //
673 //
674 //
675 //
676 //
677 //
678 //
679 //
680 //
681 //
682 //
683 //
684 //
685 //
686 //
687 //
688 //
689 //
690 //
691 //
692 //
693 //
694 //
695 //
696 //
697 //
698 //
699 //
700 //
701 //
702 //
703 //
704 //
705 //
706 //
707 //
708 //
709 //
710 //
711 //
712 //
713 //
714 //
715 //
716 //
717 //
718 //
719 //
720 //
721 //
722 //
723 //
724 //
725 //
726 //
727 //
728 //
729 //
730 //
731 //
732 //
733 //
734 //
735 //
736 //
737 //
738 //
739 //
740 //
741 //
742 //
743 //
744 //
745 //
746 //
747 //
748 //
749 //
750 //
751 //
752 //
753 //
754 //
755 //
756 //
757 //
758 //
759 //
760 //
761 //
762 //
763 //
764 //
765 //
766 //
767 //
768 //
769 //
770 //
771 //
772 //
773 //
774 //
775 //
776 //
777 //
778 //
779 //
780 //
781 //
782 //
783 //
784 //
785 //
786 //
787 //
788 //
789 //
790 //
791 //
792 //
793 //
794 //
795 //
796 //
797 //
798 //
799 //
800 //
801 //
802 //
803 //
804 //
805 //
806 //
807 //
808 //
809 //
810 //
811 //
812 //
813 //
814 //
815 //
816 //
817 //
818 //
819 //
820 //
821 //
822 //
823 //
824 //
825 //
826 //
827 //
828 //
829 //
830 //
831 //
832 //
833 //
834 //
835 //
836 //
837 //
838 //
839 //
840 //
841 //
842 //
843 //
844 //
845 //
846 //
847 //
848 //
849 //
850 //
851 //
852 //
853 //
854 //
855 //
856 //
857 //
858 //
859 //
860 //
861 //
862 //
863 //
864 //
865 //
866 //
867 //
868 //
869 //
870 //
871 //
872 //
873 //
874 //
875 //
876 //
877 //
878 //
879 //
880 //
881 //
882 //
883 //
884 //
885 //
886 //
887 //
888 //
889 //
890 //
891 //
892 //
893 //
894 //
895 //
896 //
897 //
898 //
899 //
900 //
901 //
902 //
903 //
904 //
905 //
906 //
907 //
908 //
909 //
910 //
911 //
912 //
913 //
914 //
915 //
916 //
917 //
918 //
919 //
920 //
921 //
922 //
923 //
924 //
925 //
926 //
927 //
928 //
929 //
930 //
931 //
932 //
933 //
934 //
935 //
936 //
937 //
938 //
939 //
940 //
941 //
942 //
943 //
944 //
945 //
946 //
947 //
948 //
949 //
950 //
951 //
952 //
953 //
954 //
955 //
956 //
957 //
958 //
959 //
960 //
961 //
962 //
963 //
964 //
965 //
966 //
967 //
968 //
969 //
970 //
971 //
972 //
973 //
974 //
975 //
976 //
977 //
978 //
979 //
980 //
981 //
982 //
983 //
984 //
985 //
986 //
987 //
988 //
989 //
990 //
991 //
992 //
993 //
994 //
995 //
996 //
997 //
998 //
999 //
1000 //

```









```
432 DeleteGraphPlot (panelID, PANEL_SRD_GRAPH_CLOSE, -1, VAL_IMMEDIATE_DRAIN);
433 PLOTXY (panelID, PANEL_SRD_GRAPH_OPEN, -1, VAL_IMMEDIATE_DRAIN);
434 VAL_DORIS, VAL_DORIS, VAL_THIS_LINE, VAL_NO_POINT, VAL_SOLID, 1, VAL_DSD);
435 PLOTXY (panelID, PANEL_SRD_GRAPH_CLOSE, -1, VAL_IMMEDIATE_DRAIN);
436 VAL_DORIS, VAL_DORIS, VAL_THIS_LINE, VAL_NO_POINT, VAL_SOLID, 1, VAL_DSD);
437 adPop = malloc (sizeof (double));
438 for (i = 0; i < ulimit - 1; i++)
439     *adPop++ = *adSubstr[i] * adSubstr[i];
440 //
441 //
442 //
443 PLOTXY (panelID, PANEL_SRD_GRAPH_OPEN, -1, VAL_IMMEDIATE_DRAIN);
444 VAL_DORIS, VAL_DORIS, VAL_THIS_LINE, VAL_NO_POINT, VAL_SOLID, 1, VAL_DSD);
445 //
446 //
447 //
448 //
449 //
450 //
451 //
452 //
453 //
454 //
455 //
456 //
457 //
458 //
459 //
460 //
461 //
462 //
463 //
464 //
465 //
466 //
467 //
468 //
469 //
470 //
471 //
472 //
473 //
474 //
475 //
476 //
477 //
478 //
479 //
480 //
481 //
482 //
483 //
484 //
485 //
486 //
487 //
488 //
489 //
490 //
491 //
492 //
493 //
494 //
495 //
496 //
497 //
498 //
499 //
500 //
501 //
502 //
503 //
504 //
505 //
506 //
507 //
508 //
509 //
510 //
511 //
512 //
513 //
514 //
515 //
516 //
517 //
518 //
519 //
520 //
521 //
522 //
523 //
524 //
525 //
526 //
527 //
528 //
529 //
530 //
531 //
532 //
533 //
534 //
535 //
536 //
537 //
538 //
539 //
540 //
541 //
542 //
543 //
544 //
545 //
546 //
547 //
548 //
```

```
604 int i;
605 int cycles;
606 int cycles;
607 int cycles;
608 int cycles;
609 int cycles;
610 int cycles;
611 int cycles;
612 int cycles;
613 int cycles;
614 int cycles;
615 int cycles;
616 int cycles;
617 int cycles;
618 int cycles;
619 int cycles;
620 int cycles;
621 int cycles;
622 int cycles;
623 int cycles;
624 int cycles;
625 int cycles;
626 int cycles;
627 int cycles;
628 int cycles;
629 int cycles;
630 int cycles;
631 int cycles;
632 int cycles;
633 int cycles;
634 int cycles;
635 int cycles;
636 int cycles;
637 int cycles;
638 int cycles;
639 int cycles;
640 int cycles;
641 int cycles;
642 int cycles;
643 int cycles;
644 int cycles;
645 int cycles;
646 int cycles;
647 int cycles;
648 int cycles;
649 int cycles;
650 int cycles;
651 int cycles;
652 int cycles;
```

```
549 // Popop the ShutterCorrection Panel;
550 DisplayPanel (panelID);
551 // Separate the Open and Close times...
552 //
553 //
554 //
555 //
556 //
557 //
558 //
559 //
560 //
561 //
562 //
563 //
564 //
565 //
566 //
567 //
568 //
569 //
570 //
571 //
572 //
573 //
574 //
575 //
576 //
577 //
578 //
579 //
580 //
581 //
582 //
583 //
584 //
585 //
586 //
587 //
588 //
589 //
590 //
591 //
592 //
593 //
594 //
595 //
596 //
597 //
598 //
599 //
600 //
601 //
602 //
603 //
```

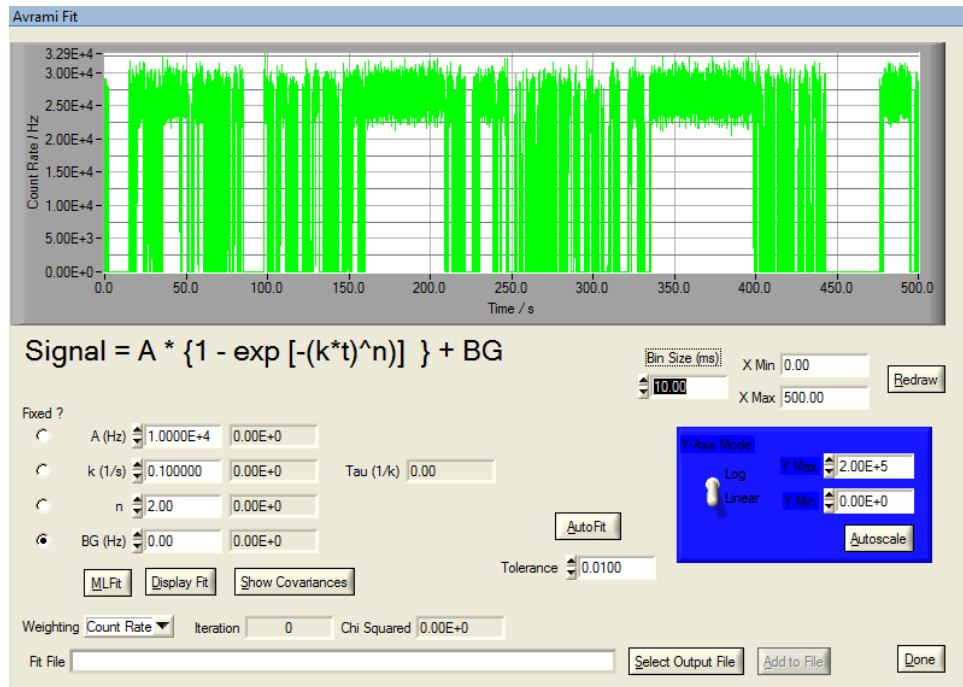
```
654 VAL_LEFT_AXIS, VAL_BOTTOM, 0.0, 0.0027);
655 //
656 //
657 //
658 //
659 //
660 //
661 //
662 //
663 //
664 //
665 //
666 //
667 //
668 //
669 //
670 //
671 //
672 //
673 //
674 //
675 //
676 //
677 //
678 //
679 //
680 //
681 //
682 //
683 //
684 //
685 //
686 //
687 //
688 //
689 //
690 //
691 //
692 //
693 //
694 //
695 //
696 //
697 //
698 //
699 //
700 //
701 //
702 //
703 //
704 //
705 //
706 //
707 //
708 //
709 //
710 //
711 //
712 //
713 //
714 //
715 //
716 //
717 //
718 //
719 //
720 //
721 //
722 //
723 //
724 //
725 //
726 //
727 //
728 //
729 //
730 //
731 //
732 //
733 //
734 //
735 //
736 //
737 //
738 //
739 //
740 //
741 //
742 //
743 //
744 //
745 //
746 //
747 //
748 //
```







## A.9 Avrami Fit









```

441 for (k=1, k < ubinary, k++)
442     dsig[k] = sqrt( efitime[k]);
443     break;
444 }
445 }
446 }
447 }
448 }
449 }
450 }
451 }
452 }
453 }
454 }
455 }
456 }
457 }
458 }
459 }
460 }
461 }
462 }
463 }
464 }
465 }
466 }
467 }
468 }
469 }
470 }
471 }
472 }
473 }
474 }
475 }
476 }
477 }
478 }
479 }
480 }
481 }
482 }
483 }
484 }
485 }
486 }
487 }
488 }
489 }
490 }
491 }
492 }
493 }
494 }
495 }

```

```

496 SecCtrlVal (panel4, PARAM_4_NUMERIC_031, sqrt( covar(1)(1)));
497 SecCtrlVal (panel4, PARAM_4_NUMERIC_032, sqrt( covar(1)(1)));
498 }
499 }
500 }
501 }
502 }
503 }
504 }
505 }
506 }
507 }
508 }
509 }
510 }
511 }
512 }
513 }
514 }
515 }
516 }
517 }
518 }
519 }
520 }
521 }
522 }
523 }
524 }
525 }
526 }
527 }
528 }
529 }
530 }
531 }
532 }
533 }
534 }
535 }
536 }
537 }
538 }
539 }
540 }
541 }
542 }
543 }
544 }
545 }
546 }
547 }
548 }
549 }
550 }

```

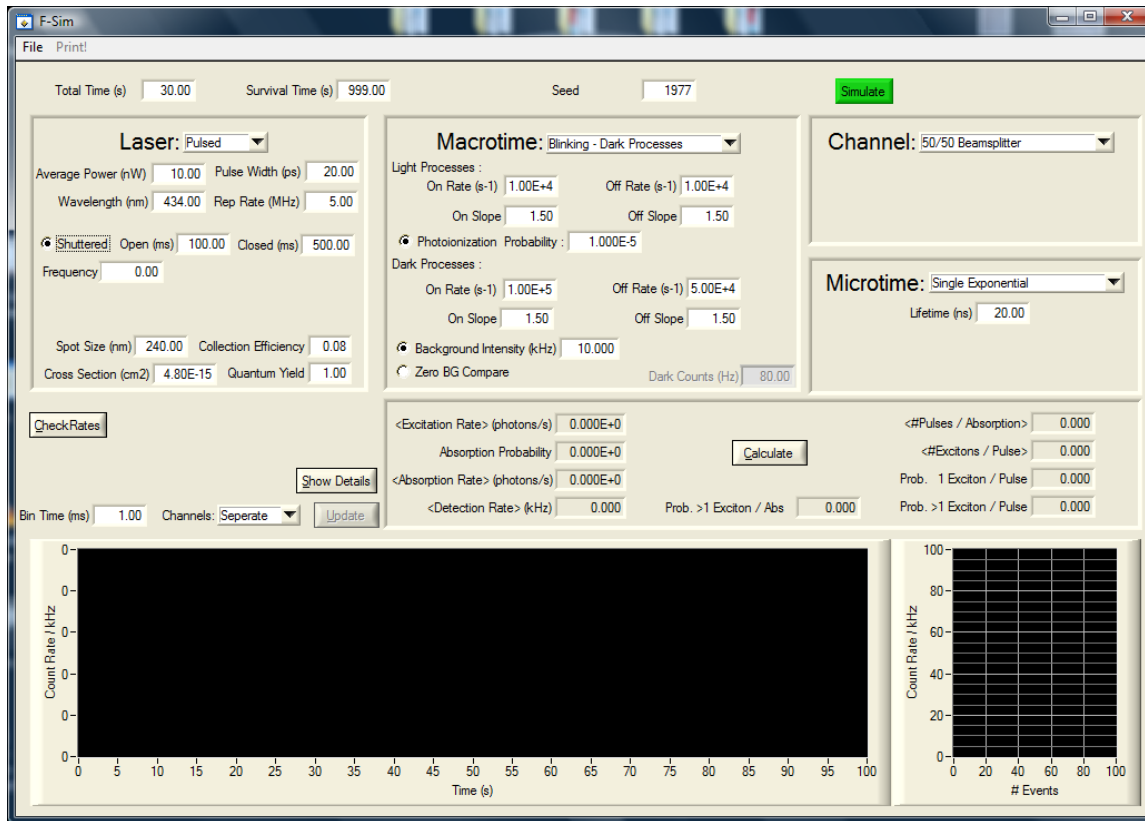
```

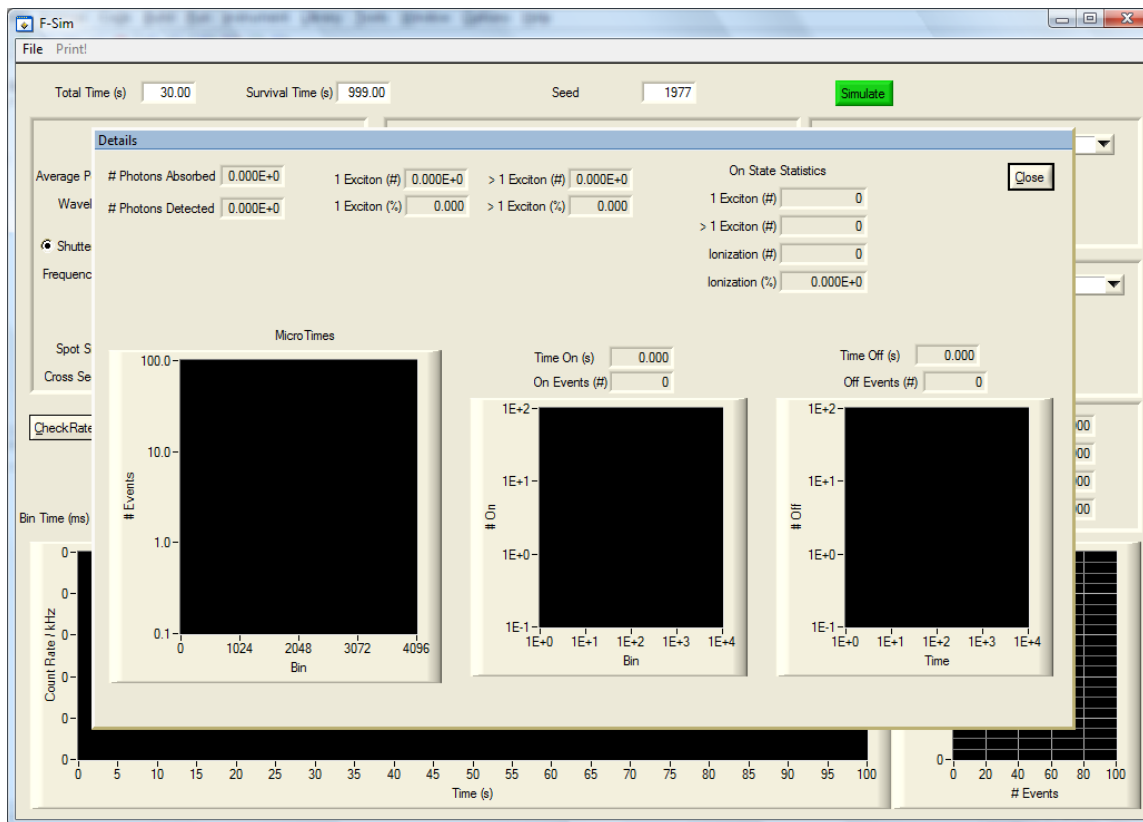
551 }
552 }
553 }
554 }
555 }
556 }
557 }
558 }
559 }
560 }
561 }
562 }
563 }
564 }
565 }
566 }
567 }
568 }
569 }
570 }
571 }
572 }
573 }
574 }
575 }
576 }

```

## Appendix B: Simulation Code

### B.1 User Interface









```
438 dbase = malloc(sizeof(struct dbase));
439 for (i=0; i<dbase->nt; i++)
440     dbase[i] = GetBase(dbase, dAlpha);
441
442
443
444
445     free(dbase);
446     break;
447 }
448 return 0;
449
450 }
```



### B.3 Simulation Details

<pre> 1 #include "Vec.h" 2 #include "Unit.h" 3 #include "cvrLite.h" 4 #include "Vec3.h" 5 #include "Vec4.h" 6 #include "gChals.h" 7 #include "Functions.h" 8 9 #define FORCE 1.2 10 double GetArea(double dx, double dAlpha); 11 void hpxot(int n, double a[]); 12 13 14 15 16 int CYCLOTRON_SIMULATOR(int panel, int control, int event, 17     void *chanceData, int eventData, int eventData2) 18 { 19     int i; 20     double chanceData, eventData; 21     int iMaxData, iMaxData2; 22     int iMaxData; 23     int iMaxData; 24     int iMaxData; 25     int iMaxData; 26     int iMaxData; 27     int iMaxData; 28     int iMaxData; 29     int iMaxData; 30     int iMaxData; 31     int iMaxData; 32     int iMaxData; 33     int iMaxData; 34     int iMaxData; 35     int iMaxData; 36     int iMaxData; 37     int iMaxData; 38     int iMaxData; 39     int iMaxData; 40     int iMaxData; 41     int iMaxData; 42     int iMaxData; 43     int iMaxData; 44     double dArea, dArea2, dArea3, dArea4; 45     double dArea, dArea2, dArea3, dArea4; 46     double dArea, dArea2, dArea3, dArea4; 47     double dArea, dArea2, dArea3, dArea4; 48     int iMaxData, iMaxData2; 49     int iMaxData, iMaxData2; 50     double dArea, dArea2, dArea3, dArea4; 51     double dArea, dArea2, dArea3, dArea4; 52     double dArea, dArea2, dArea3, dArea4; 53     double dArea, dArea2, dArea3, dArea4; 54     double dArea, dArea2, dArea3, dArea4; 55     double dArea, dArea2, dArea3, dArea4; </pre>	<pre> 56 double dArea, dArea2, dArea3, dArea4; 57 double dArea, dArea2, dArea3, dArea4; 58 double dArea, dArea2, dArea3, dArea4; 59 double dArea, dArea2, dArea3, dArea4; 60 double dArea, dArea2, dArea3, dArea4; 61 int iMaxData; 62 double dArea, dArea2, dArea3, dArea4; 63 double dArea, dArea2, dArea3, dArea4; 64 double dArea, dArea2, dArea3, dArea4; 65 double dArea, dArea2, dArea3, dArea4; 66 double dArea, dArea2, dArea3, dArea4; 67 int iMaxData, iMaxData2, iMaxData3, iMaxData4; 68 double dArea, dArea2, dArea3, dArea4; 69 double dArea, dArea2, dArea3, dArea4; 70 double dArea, dArea2, dArea3, dArea4; 71 int iMaxData, iMaxData2, iMaxData3, iMaxData4; 72 int iMaxData; 73 int iMaxData; 74 int iMaxData; 75 int iMaxData; 76 int iMaxData; 77 int iMaxData; 78 int iMaxData; 79 int iMaxData; 80 double dArea, dArea2, dArea3, dArea4; 81 double dArea, dArea2, dArea3, dArea4; 82 int iMaxData, iMaxData2, iMaxData3, iMaxData4; 83 int iMaxData, iMaxData2, iMaxData3, iMaxData4; 84 int iMaxData, iMaxData2, iMaxData3, iMaxData4; 85 double dArea, dArea2, dArea3, dArea4; 86 double dArea, dArea2, dArea3, dArea4; 87 double dArea, dArea2, dArea3, dArea4; 88 int iMaxData, iMaxData2, iMaxData3, iMaxData4; 89 int iMaxData, iMaxData2, iMaxData3, iMaxData4; 90 double dArea, dArea2, dArea3, dArea4; 91 double dArea, dArea2, dArea3, dArea4; 92 int iMaxData; 93 int iMaxData; 94 int iMaxData; 95 int iMaxData; 96 double dArea; 97 double dArea; 98 int iMaxData; 99 double dArea, dArea2, dArea3, dArea4; 100 double dArea, dArea2, dArea3, dArea4; 101 double dArea, dArea2, dArea3, dArea4; 102 double dArea, dArea2, dArea3, dArea4; 103 double dArea, dArea2, dArea3, dArea4; 104 double dArea, dArea2, dArea3, dArea4; 105 int iMaxData, iMaxData2, iMaxData3, iMaxData4; 106 int iMaxData, iMaxData2, iMaxData3, iMaxData4; 107 double dArea, dArea2, dArea3, dArea4; 108 int iMaxData, iMaxData2, iMaxData3, iMaxData4; 109 double dArea, dArea2, dArea3, dArea4; 110 double dArea, dArea2, dArea3, dArea4; </pre>
<pre> 111 switch (event) 112 { 113     case EVENT_COMMENT: 114         GetCIVIL(panelIn, PANEL_MAIN_NUMERIC_freq, dArea); 115         UpdateData(0, 0, 0, NULL, 0, 0); 116         PanelUpdateData(0); 117         PanelUpdateData(0); 118         PanelUpdateData(0); 119         PanelUpdateData(0); 120         PanelUpdateData(0); 121         PanelUpdateData(0); 122         PanelUpdateData(0); 123         PanelUpdateData(0); 124         PanelUpdateData(0); 125         PanelUpdateData(0); 126         PanelUpdateData(0); 127         PanelUpdateData(0); 128         PanelUpdateData(0); 129         PanelUpdateData(0); 130         PanelUpdateData(0); 131         PanelUpdateData(0); 132         PanelUpdateData(0); 133         PanelUpdateData(0); 134         PanelUpdateData(0); 135         PanelUpdateData(0); 136         PanelUpdateData(0); 137         PanelUpdateData(0); 138         PanelUpdateData(0); 139         PanelUpdateData(0); 140         PanelUpdateData(0); 141         PanelUpdateData(0); 142         PanelUpdateData(0); 143         PanelUpdateData(0); 144         PanelUpdateData(0); 145         PanelUpdateData(0); 146         PanelUpdateData(0); 147         PanelUpdateData(0); 148         PanelUpdateData(0); 149         PanelUpdateData(0); 150         PanelUpdateData(0); 151         PanelUpdateData(0); 152         PanelUpdateData(0); 153         PanelUpdateData(0); 154         PanelUpdateData(0); 155         PanelUpdateData(0); 156         PanelUpdateData(0); 157         PanelUpdateData(0); 158         PanelUpdateData(0); 159         PanelUpdateData(0); 160         PanelUpdateData(0); 161         PanelUpdateData(0); 162         PanelUpdateData(0); 163         PanelUpdateData(0); 164         PanelUpdateData(0); 165         PanelUpdateData(0); </pre>	<pre> 166 // Macro Time Settings 167 GetCIVIL(panelIn, PANEL_MAIN_NUMERIC_SurvivalTime, dSurvivalTime); 168 // Macro Time Settings 169 GetCIVIL(panelIn, PANEL_MAIN_NUMERIC_SurvivalTime, dSurvivalTime); 170 // Macro Time Settings 171 GetCIVIL(panelIn, PANEL_MAIN_NUMERIC_SurvivalTime, dSurvivalTime); 172 // Macro Time Settings 173 GetCIVIL(panelIn, PANEL_MAIN_NUMERIC_SurvivalTime, dSurvivalTime); 174 // Macro Time Settings 175 GetCIVIL(panelIn, PANEL_MAIN_NUMERIC_SurvivalTime, dSurvivalTime); 176 // Macro Time Settings 177 GetCIVIL(panelIn, PANEL_MAIN_NUMERIC_SurvivalTime, dSurvivalTime); 178 // Macro Time Settings 179 GetCIVIL(panelIn, PANEL_MAIN_NUMERIC_SurvivalTime, dSurvivalTime); 180 // Macro Time Settings 181 GetCIVIL(panelIn, PANEL_MAIN_NUMERIC_SurvivalTime, dSurvivalTime); 182 // Macro Time Settings 183 GetCIVIL(panelIn, PANEL_MAIN_NUMERIC_SurvivalTime, dSurvivalTime); 184 // Macro Time Settings 185 GetCIVIL(panelIn, PANEL_MAIN_NUMERIC_SurvivalTime, dSurvivalTime); 186 // Macro Time Settings 187 GetCIVIL(panelIn, PANEL_MAIN_NUMERIC_SurvivalTime, dSurvivalTime); 188 // Macro Time Settings 189 GetCIVIL(panelIn, PANEL_MAIN_NUMERIC_SurvivalTime, dSurvivalTime); 190 // Macro Time Settings 191 GetCIVIL(panelIn, PANEL_MAIN_NUMERIC_SurvivalTime, dSurvivalTime); 192 // Macro Time Settings 193 GetCIVIL(panelIn, PANEL_MAIN_NUMERIC_SurvivalTime, dSurvivalTime); 194 // Macro Time Settings 195 GetCIVIL(panelIn, PANEL_MAIN_NUMERIC_SurvivalTime, dSurvivalTime); 196 // Macro Time Settings 197 GetCIVIL(panelIn, PANEL_MAIN_NUMERIC_SurvivalTime, dSurvivalTime); 198 // Macro Time Settings 199 GetCIVIL(panelIn, PANEL_MAIN_NUMERIC_SurvivalTime, dSurvivalTime); 200 // Macro Time Settings 201 GetCIVIL(panelIn, PANEL_MAIN_NUMERIC_SurvivalTime, dSurvivalTime); 202 // Macro Time Settings 203 GetCIVIL(panelIn, PANEL_MAIN_NUMERIC_SurvivalTime, dSurvivalTime); 204 // Macro Time Settings 205 GetCIVIL(panelIn, PANEL_MAIN_NUMERIC_SurvivalTime, dSurvivalTime); 206 // Macro Time Settings 207 GetCIVIL(panelIn, PANEL_MAIN_NUMERIC_SurvivalTime, dSurvivalTime); 208 // Macro Time Settings 209 GetCIVIL(panelIn, PANEL_MAIN_NUMERIC_SurvivalTime, dSurvivalTime); 210 // Macro Time Settings 211 GetCIVIL(panelIn, PANEL_MAIN_NUMERIC_SurvivalTime, dSurvivalTime); 212 // Macro Time Settings 213 GetCIVIL(panelIn, PANEL_MAIN_NUMERIC_SurvivalTime, dSurvivalTime); 214 // Macro Time Settings 215 GetCIVIL(panelIn, PANEL_MAIN_NUMERIC_SurvivalTime, dSurvivalTime); 216 // Macro Time Settings 217 GetCIVIL(panelIn, PANEL_MAIN_NUMERIC_SurvivalTime, dSurvivalTime); 218 // Macro Time Settings 219 GetCIVIL(panelIn, PANEL_MAIN_NUMERIC_SurvivalTime, dSurvivalTime); 220 // Macro Time Settings 221 GetCIVIL(panelIn, PANEL_MAIN_NUMERIC_SurvivalTime, dSurvivalTime); 222 // Macro Time Settings 223 GetCIVIL(panelIn, PANEL_MAIN_NUMERIC_SurvivalTime, dSurvivalTime); </pre>

```

221 // Nonlinear Settings
222 GetCritical (pamMain, PAMEL_MAIN_NUMERICAL_Ratio_Dark, eDroptOff_Dark);
223 GetCritical (pamMain, PAMEL_MAIN_NUMERICAL_RatioOff_Dark, eDroptOff_Dark);
224 GetCritical (pamMain, PAMEL_MAIN_NUMERICAL_RatioOff_Dark, eDroptOff_Dark);
225 GetCritical (pamMain, PAMEL_MAIN_NUMERICAL_RatioOff_Dark, eDroptOff_Dark);
226 alphaOff_Dark = eDroptOff_Dark - 1.;
227 break;
228 //
229 //
230 // Nonlinear Settings
231 GetCritical (pamMain, PAMEL_MAIN_NUMERICAL_Ratio_Dark, eDroptOff_Dark);
232 GetCritical (pamMain, PAMEL_MAIN_NUMERICAL_RatioOff_Dark, eDroptOff_Dark);
233 switch (iChannel)
234 {
235 case 0: // No Photoionization
236     alphaOff = 0.0;
237     break;
238 case 1: // Dichroic Constant Biasion
239     //
240     //
241     //
242     //
243     //
244     //
245     //
246     //
247     //
248     //
249     //
250     //
251     //
252     //
253     //
254     //
255     //
256     //
257     //
258     //
259     //
260     //
261     //
262     //
263     //
264     //
265     //
266     //
267     //
268     //
269     //
270     //
271     //
272     //
273     //
274     //
275     //
276     //
277     //
278     //
279     //
280     //
281     //
282     //
283     //
284     //
285     //
286     //
287     //
288     //
289     //
290     //
291     //
292     //
293     //
294     //
295     //
296     //
297     //
298     //
299     //
300     //
301     //
302     //
303     //
304     //
305     //
306     //
307     //
308     //
309     //
310     //
311     //
312     //
313     //
314     //
315     //
316     //
317     //
318     //
319     //
320     //
321     //
322     //
323     //
324     //
325     //
326     //
327     //
328     //
329     //
330     //
331     //
332     //
333     //
334     //
335     //
336     //
337     //
338     //
339     //
340     //
341     //
342     //
343     //
344     //
345     //
346     //
347     //
348     //
349     //
350     //
351     //
352     //
353     //
354     //
355     //
356     //
357     //
358     //
359     //
360     //
361     //
362     //
363     //
364     //
365     //
366     //
367     //
368     //
369     //
370     //
371     //
372     //
373     //
374     //
375     //
376     //
377     //
378     //
379     //
380     //
381     //
382     //
383     //
384     //
385     //
386     //
387     //
388     //
389     //
390     //
391     //
392     //
393     //
394     //
395     //
396     //
397     //
398     //
399     //
400     //
401     //
402     //
403     //
404     //
405     //
406     //
407     //
408     //
409     //
410     //
411     //
412     //
413     //
414     //
415     //
416     //
417     //
418     //
419     //
420     //
421     //
422     //
423     //
424     //
425     //
426     //
427     //
428     //
429     //
430     //
431     //
432     //
433     //
434     //
435     //
436     //
437     //
438     //
439     //
440     //
441     //
442     //
443     //
444     //
445     //
446     //
447     //
448     //
449     //
450     //
451     //
452     //
453     //
454     //
455     //
456     //
457     //
458     //
459     //
460     //
461     //
462     //
463     //
464     //
465     //
466     //
467     //
468     //
469     //
470     //
471     //
472     //
473     //
474     //
475     //
476     //
477     //
478     //
479     //
480     //
481     //
482     //
483     //
484     //
485     //
486     //
487     //
488     //
489     //
490     //
491     //
492     //
493     //
494     //
495     //
496     //
497     //
498     //
499     //
500     //
501     //
502     //
503     //
504     //
505     //
506     //
507     //
508     //
509     //
510     //
511     //
512     //
513     //
514     //
515     //
516     //
517     //
518     //
519     //
520     //
521     //
522     //
523     //
524     //
525     //
526     //
527     //
528     //
529     //
530     //
531     //
532     //
533     //
534     //
535     //
536     //
537     //
538     //
539     //
540     //
541     //
542     //
543     //
544     //
545     //
546     //
547     //
548     //
549     //
550     //
551     //
552     //
553     //
554     //
555     //
556     //
557     //
558     //
559     //
560     //
561     //
562     //
563     //
564     //
565     //
566     //
567     //
568     //
569     //
570     //
571     //
572     //
573     //
574     //
575     //
576     //
577     //
578     //
579     //
580     //
581     //
582     //
583     //
584     //
585     //
586     //
587     //
588     //
589     //
590     //
591     //
592     //
593     //
594     //
595     //
596     //
597     //
598     //
599     //
600     //
601     //
602     //
603     //
604     //
605     //
606     //
607     //
608     //
609     //
610     //
611     //
612     //
613     //
614     //
615     //
616     //
617     //
618     //
619     //
620     //
621     //
622     //
623     //
624     //
625     //
626     //
627     //
628     //
629     //
630     //
631     //
632     //
633     //
634     //
635     //
636     //
637     //
638     //
639     //
640     //
641     //
642     //
643     //
644     //
645     //
646     //
647     //
648     //
649     //
650     //
651     //
652     //
653     //
654     //
655     //
656     //
657     //
658     //
659     //
660     //
661     //
662     //
663     //
664     //
665     //
666     //
667     //
668     //
669     //
670     //
671     //
672     //
673     //
674     //
675     //
676     //
677     //
678     //
679     //
680     //
681     //
682     //
683     //
684     //
685     //
686     //
687     //
688     //
689     //
690     //
691     //
692     //
693     //
694     //
695     //
696     //
697     //
698     //
699     //
700     //
701     //
702     //
703     //
704     //
705     //
706     //
707     //
708     //
709     //
710     //
711     //
712     //
713     //
714     //
715     //
716     //
717     //
718     //
719     //
720     //
721     //
722     //
723     //
724     //
725     //
726     //
727     //
728     //
729     //
730     //
731     //
732     //
733     //
734     //
735     //
736     //
737     //
738     //
739     //
740     //
741     //
742     //
743     //
744     //
745     //
746     //
747     //
748     //
749     //
750     //
751     //
752     //
753     //
754     //
755     //
756     //
757     //
758     //
759     //
760     //
761     //
762     //
763     //
764     //
765     //
766     //
767     //
768     //
769     //
770     //
771     //
772     //
773     //
774     //
775     //
776     //
777     //
778     //
779     //
780     //
781     //
782     //
783     //
784     //
785     //
786     //
787     //
788     //
789     //
790     //
791     //
792     //
793     //
794     //
795     //
796     //
797     //
798     //
799     //
800     //
801     //
802     //
803     //
804     //
805     //
806     //
807     //
808     //
809     //
810     //
811     //
812     //
813     //
814     //
815     //
816     //
817     //
818     //
819     //
820     //
821     //
822     //
823     //
824     //
825     //
826     //
827     //
828     //
829     //
830     //
831     //
832     //
833     //
834     //
835     //
836     //
837     //
838     //
839     //
840     //
841     //
842     //
843     //
844     //
845     //
846     //
847     //
848     //
849     //
850     //
851     //
852     //
853     //
854     //
855     //
856     //
857     //
858     //
859     //
860     //
861     //
862     //
863     //
864     //
865     //
866     //
867     //
868     //
869     //
870     //
871     //
872     //
873     //
874     //
875     //
876     //
877     //
878     //
879     //
880     //
881     //
882     //
883     //
884     //
885     //
886     //
887     //
888     //
889     //
890     //
891     //
892     //
893     //
894     //
895     //
896     //
897     //
898     //
899     //
900     //
901     //
902     //
903     //
904     //
905     //
906     //
907     //
908     //
909     //
910     //
911     //
912     //
913     //
914     //
915     //
916     //
917     //
918     //
919     //
920     //
921     //
922     //
923     //
924     //
925     //
926     //
927     //
928     //
929     //
930     //
931     //
932     //
933     //
934     //
935     //
936     //
937     //
938     //
939     //
940     //
941     //
942     //
943     //
944     //
945     //
946     //
947     //
948     //
949     //
950     //
951     //
952     //
953     //
954     //
955     //
956     //
957     //
958     //
959     //
960     //
961     //
962     //
963     //
964     //
965     //
966     //
967     //
968     //
969     //
970     //
971     //
972     //
973     //
974     //
975     //
976     //
977     //
978     //
979     //
980     //
981     //
982     //
983     //
984     //
985     //
986     //
987     //
988     //
989     //
990     //
991     //
992     //
993     //
994     //
995     //
996     //
997     //
998     //
999     //
1000    //

```





## B.4 Extra Functions

<pre> 1 #include &lt;math.h&gt; 2 #include &lt;stdlib.h&gt; 3 #include "UT_PSM.h" 4 #include "Functions.h" 5 #include "PseudoRNG.h" 6 7 int main(int argc, char* argv[]) { 8     // Initial conditions and parameters 9     double lambda = 1.0; // Photon production rate 10    double hbar = 1.0; // Planck constant 11    double m0 = 0.511; // Electron mass in MeV 12    double m1 = 0.511; // Electron mass in MeV 13    double m2 = 0.511; // Electron mass in MeV 14    double m3 = 0.511; // Electron mass in MeV 15    double m4 = 0.511; // Electron mass in MeV 16    double m5 = 0.511; // Electron mass in MeV 17    double m6 = 0.511; // Electron mass in MeV 18    double m7 = 0.511; // Electron mass in MeV 19    double m8 = 0.511; // Electron mass in MeV 20    double m9 = 0.511; // Electron mass in MeV 21    double m10 = 0.511; // Electron mass in MeV 22    // Simulation parameters 23    double total_time = 1000; // Total simulation time 24    double dt = 0.01; // Time step 25    double n_photons = 0; // Number of photons 26    double n_electrons = 0; // Number of electrons 27    double n_positrons = 0; // Number of positrons 28    double n_gamma = 0; // Number of gamma rays 29    double n_beta = 0; // Number of beta particles 30    double n_alpha = 0; // Number of alpha particles 31    // Arrays for tracking particles 32    double* x_pos = (double*) malloc(sizeof(double) * 1000); 33    double* y_pos = (double*) malloc(sizeof(double) * 1000); 34    double* z_pos = (double*) malloc(sizeof(double) * 1000); 35    double* vx_pos = (double*) malloc(sizeof(double) * 1000); 36    double* vy_pos = (double*) malloc(sizeof(double) * 1000); 37    double* vz_pos = (double*) malloc(sizeof(double) * 1000); 38    // Simulation loop 39    for (int i = 0; i &lt; total_time; i++) { 40        // Time step 41        double t = i * dt; 42        // Photon production 43        if (rand() &lt; lambda * dt) { 44            double energy = 1.0; // Photon energy 45            double direction = rand() - 0.5; // Photon direction 46            // Add photon to simulation 47            n_photons++; 48            // Photon decay 49            if (rand() &lt; m0 * dt) { 50                // Electron-positron pair production 51                double energy_e = 0.511; 52                double energy_p = 0.511; 53                // Add electron and positron to simulation 54                n_electrons++; 55                n_positrons++; 56            } 57            // Photon absorption 58            if (rand() &lt; m1 * dt) { 59                // Beta decay 60                double energy_beta = 0.511; 61                // Add beta particle to simulation 62                n_beta++; 63            } 64            // Photon scattering 65            if (rand() &lt; m2 * dt) { 66                // Compton scattering 67                // Add gamma ray to simulation 68                n_gamma++; 69            } 70            // Photon annihilation 71            if (rand() &lt; m3 * dt) { 72                // Annihilation 73                // Add alpha particle to simulation 74                n_alpha++; 75            } 76            // Photon production 77            if (rand() &lt; m4 * dt) { 78                // Photon production 79                // Add photon to simulation 80                n_photons++; 81            } 82            // Photon decay 83            if (rand() &lt; m5 * dt) { 84                // Photon decay 85                // Add photon to simulation 86                n_photons++; 87            } 88            // Photon absorption 89            if (rand() &lt; m6 * dt) { 90                // Photon absorption 91                // Add photon to simulation 92                n_photons++; 93            } 94            // Photon scattering 95            if (rand() &lt; m7 * dt) { 96                // Photon scattering 97                // Add photon to simulation 98                n_photons++; 99            } 100            // Photon annihilation 101            if (rand() &lt; m8 * dt) { 102                // Photon annihilation 103                // Add photon to simulation 104                n_photons++; 105            } 106            // Photon production 107            if (rand() &lt; m9 * dt) { 108                // Photon production 109                // Add photon to simulation 110                n_photons++; 111            } 112            // Photon decay 113            if (rand() &lt; m10 * dt) { 114                // Photon decay 115                // Add photon to simulation 116                n_photons++; 117            } 118        } 119        // End of time step 120        // Print results 121        printf("Time: %d, Photons: %d, Electrons: %d, Positrons: %d, Gamma: %d, Beta: %d, Alpha: %d\n", i, n_photons, n_electrons, n_positrons, n_gamma, n_beta, n_alpha); 122    } 123    // Free memory 124    free(x_pos); 125    free(y_pos); 126    free(z_pos); 127    free(vx_pos); 128    free(vy_pos); 129    free(vz_pos); 130    return 0; 131 } </pre>	<pre> 132 // Simulation parameters 133 double lambda = 1.0; // Photon production rate 134 double hbar = 1.0; // Planck constant 135 double m0 = 0.511; // Electron mass in MeV 136 double m1 = 0.511; // Electron mass in MeV 137 double m2 = 0.511; // Electron mass in MeV 138 double m3 = 0.511; // Electron mass in MeV 139 double m4 = 0.511; // Electron mass in MeV 140 double m5 = 0.511; // Electron mass in MeV 141 double m6 = 0.511; // Electron mass in MeV 142 double m7 = 0.511; // Electron mass in MeV 143 double m8 = 0.511; // Electron mass in MeV 144 double m9 = 0.511; // Electron mass in MeV 145 double m10 = 0.511; // Electron mass in MeV 146 // Simulation parameters 147 double total_time = 1000; // Total simulation time 148 double dt = 0.01; // Time step 149 double n_photons = 0; // Number of photons 150 double n_electrons = 0; // Number of electrons 151 double n_positrons = 0; // Number of positrons 152 double n_gamma = 0; // Number of gamma rays 153 double n_beta = 0; // Number of beta particles 154 double n_alpha = 0; // Number of alpha particles 155 // Arrays for tracking particles 156 double* x_pos = (double*) malloc(sizeof(double) * 1000); 157 double* y_pos = (double*) malloc(sizeof(double) * 1000); 158 double* z_pos = (double*) malloc(sizeof(double) * 1000); 159 double* vx_pos = (double*) malloc(sizeof(double) * 1000); 160 double* vy_pos = (double*) malloc(sizeof(double) * 1000); 161 double* vz_pos = (double*) malloc(sizeof(double) * 1000); 162 // Simulation loop 163 for (int i = 0; i &lt; total_time; i++) { 164     // Time step 165     double t = i * dt; 166     // Photon production 167     if (rand() &lt; lambda * dt) { 168         double energy = 1.0; // Photon energy 169         double direction = rand() - 0.5; // Photon direction 170         // Add photon to simulation 171         n_photons++; 172         // Photon decay 173         if (rand() &lt; m0 * dt) { 174             // Electron-positron pair production 175             double energy_e = 0.511; 176             double energy_p = 0.511; 177             // Add electron and positron to simulation 178             n_electrons++; 179             n_positrons++; 180         } 181         // Photon absorption 182         if (rand() &lt; m1 * dt) { 183             // Beta decay 184             double energy_beta = 0.511; 185             // Add beta particle to simulation 186             n_beta++; 187         } 188         // Photon scattering 189         if (rand() &lt; m2 * dt) { 190             // Compton scattering 191             // Add gamma ray to simulation 192             n_gamma++; 193         } 194         // Photon annihilation 195         if (rand() &lt; m3 * dt) { 196             // Annihilation 197             // Add alpha particle to simulation 198             n_alpha++; 199         } 200         // Photon production 201         if (rand() &lt; m4 * dt) { 202             // Photon production 203             // Add photon to simulation 204             n_photons++; 205         } 206         // Photon decay 207         if (rand() &lt; m5 * dt) { 208             // Photon decay 209             // Add photon to simulation 210             n_photons++; 211         } 212         // Photon absorption 213         if (rand() &lt; m6 * dt) { 214             // Photon absorption 215             // Add photon to simulation 216             n_photons++; 217         } 218         // Photon scattering 219         if (rand() &lt; m7 * dt) { 220             // Photon scattering 221             // Add photon to simulation 222             n_photons++; 223         } 224         // Photon annihilation 225         if (rand() &lt; m8 * dt) { 226             // Photon annihilation 227             // Add photon to simulation 228             n_photons++; 229         } 230         // Photon production 231         if (rand() &lt; m9 * dt) { 232             // Photon production 233             // Add photon to simulation 234             n_photons++; 235         } 236         // Photon decay 237         if (rand() &lt; m10 * dt) { 238             // Photon decay 239             // Add photon to simulation 240             n_photons++; 241         } 242     } 243     // End of time step 244     // Print results 245     printf("Time: %d, Photons: %d, Electrons: %d, Positrons: %d, Gamma: %d, Beta: %d, Alpha: %d\n", i, n_photons, n_electrons, n_positrons, n_gamma, n_beta, n_alpha); 246 } 247 // Free memory 248 free(x_pos); 249 free(y_pos); 250 free(z_pos); 251 free(vx_pos); 252 free(vy_pos); 253 free(vz_pos); 254 return 0; </pre>
---	---

```
221 a10wp = writefifo[1] / pow(2,12); // 8 Overflow of 12bit Microtime clock
222 if (a10wp == a10werr)
223     a10wp = 0;
224
225 //
226 if (a10wp == a10werr + 1)
227     // Simple Overflow
228     a10wp = 1 << 30;
229
230 else
231     // Lots of overflows....
232     // Write Microtime Overflow Record
233     writeMicroTimeOverflowRecord(a10wp, a10werr);
234     a10wp = 1 << 30;
235     a10wp = a10wp - a10werr;
236     a10werr = a10werr + a10wp + a10werr;
237     a10werr[a10werr] = a10werr;
238
239
240 a10wp = 0;
241
242
243 a10wco = writefifo[1] - a10wp + pow(2,12);
244 a10wco = (a10wco[1] << 12);
245 a10wco = a10wco << 16;
246 a10wco = (4095 - a10wco[1]) << 16;
247
248 a10wco = a10wco + a10wp + a10wco + a10wco;
249 a10wco = a10wco + a10wco;
250 a10wco = a10wco;
251 a10wco = a10wco;
252 a10wco = a10wco;
253 a10wco = a10wco;
254 a10wco = a10wco;
255 a10wco = a10wco;
256 a10wco = a10wco;
257
258 //
259
260 a10wco = writefifo[1] - a10wp + pow(2,12);
261 a10wco = (a10wco[1] << 12);
262 a10wco = a10wco << 16;
263 a10wco = (4095 - a10wco[1]) << 16;
264 a10wco = a10wco + a10wp + a10wco + a10wco;
265 a10wco = a10wco + a10wco;
266 a10wco = a10wco;
267 a10wco = a10wco;
268 a10wco = a10wco;
269 a10wco = a10wco;
270 a10wco = a10wco;
271 a10wco = a10wco;
272 a10wco = a10wco;
273 while (a10wco < (a10wco[1] / pow(2,12)))
274     //read a record
```

```
276 a10wco = writefifo[1] / pow(2,12);
277 a10wco = (a10wco[1] << 12);
278 a10wco = a10wco << 16;
279 a10wco = (4095 - a10wco[1]) << 16;
280 a10wco = a10wco + a10wp + a10wco + a10wco;
281 a10wco = a10wco + a10wco;
282 a10wco = a10wco;
283 a10wco = a10wco;
284 a10wco = a10wco;
285 a10wco = a10wco;
286 a10wco = a10wco;
287 a10wco = a10wco;
288 a10wco = a10wco;
289 a10wco = a10wco;
290 a10wco = a10wco;
291 a10wco = a10wco;
292 a10wco = a10wco;
293 a10wco = a10wco;
294 a10wco = a10wco;
295 a10wco = a10wco;
296 a10wco = a10wco;
297 a10wco = a10wco;
298 a10wco = a10wco;
299 a10wco = a10wco;
300 a10wco = a10wco;
```

```

1 #include "pch.h"
2 #include "Game_C.h"
3 #include "GameLife.h"
4 #include "GameLife.h"
5 #include "GameLife.h"
6 #include "Global.h"
7
8
9 int CYCLOMANK UpdateLaser (int panel, int control, int event,
10 void *callbackData, int eventData, int eventData2)
11 {
12 int i;
13 switch (event)
14 {
15 case EVENT_COMMIT:
16 GetCrivAl (panelMain, PANEL_MAIN_RING_LASER, &i);
17 switch (i)
18 {
19 case 0 : // Pulsed Laser
20 GetCrivAl (panelMain, PANEL_MAIN_NUMERIC_RINGS, ATTR_VISIBLE, 1);
21 GetCrivAl (panelMain, PANEL_MAIN_NUMERIC_PULSED_RING, ATTR_VISIBLE, 1);
22 break;
23 case 1 : // CW Laser
24 GetCrivAl (panelMain, PANEL_MAIN_NUMERIC_RING, ATTR_VISIBLE, 1);
25 GetCrivAl (panelMain, PANEL_MAIN_NUMERIC_PULSED_RING, ATTR_VISIBLE, 0);
26 break;
27 }
28 return 0;
29 }
30 int CYCLOMANK UpdateShutter (int panel, int control, int event,
31 void *callbackData, int eventData, int eventData2)
32 {
33 int i;
34 switch (event)
35 {
36 case EVENT_COMMIT:
37 GetCrivAl (panelMain, PANEL_MAIN_RADIOBUTTON_Shutter, &i);
38 switch (i)
39 {
40 case 0 : // Single Exponential
41 GetCrivAl (panelMain, PANEL_MAIN_NUMERIC_MPLOPP, ATTR_VISIBLE, 0);
42 GetCrivAl (panelMain, PANEL_MAIN_NUMERIC_MPLOPP, ATTR_VISIBLE, 0);
43 break;
44 case 1 : // Single Exponential w/ Top Gaussian
45 GetCrivAl (panelMain, PANEL_MAIN_NUMERIC_MPLOPP, ATTR_VISIBLE, 0);
46 GetCrivAl (panelMain, PANEL_MAIN_NUMERIC_MPLOPP, ATTR_VISIBLE, 1);
47 break;
48 case 2 : // Single Exponential w/ Same Top Fall
49 GetCrivAl (panelMain, PANEL_MAIN_NUMERIC_MPLOPP, ATTR_VISIBLE, 1);
50 GetCrivAl (panelMain, PANEL_MAIN_NUMERIC_MPLOPP, ATTR_VISIBLE, 0);
51 break;
52 }
53 return 0;
54 }
55 }
56 }
57
58 case 1 : // Spectral
59 GetCrivAl (panelMain, PANEL_MAIN_NUMERIC_TYKING, ATTR_VISIBLE, 1);
60 break;
61 }
62 }
63 }
64 }
65 }
66 }
67 }
68 }
69 }
70 }
71 }
72 }
73 }
74 }
75 }
76 }
77 }
78 }
79 }
80 }
81 }
82 }
83 }
84 }
85 }
86 }
87 }
88 }
89 }
90 }
91 }
92 }
93 }
94 }
95 }
96 }
97 }
98 }
99 }
100 }
101 }
102 }
103 }
104 }
105 }
106 }
107 }
108 }
109 }
110 }
111 }
112 }
113 }
114 }
115 }
116 }
117 }
118 }
119 }
120 }
121 }
122 }
123 }
124 }
125 }
126 }
127 }
128 }
129 }
130 }
131 }
132 }
133 }
134 }
135 }
136 }
137 }
138 }
139 }
140 }
141 }
142 }
143 }
144 }
145 }
146 }
147 }
148 }
149 }
150 }
151 }
152 }
153 }
154 }
155 }
156 }
157 }
158 }
159 }
160 }
161 }
162 }
163 }
164 }
165 }
166 }
167 }
168 }
169 }
170 }
171 }
172 }
173 }
174 }
175 }
176 }
177 }
178 }
179 }
180 }
181 }
182 }
183 }
184 }
185 }
186 }
187 }
188 }
189 }
190 }
191 }
192 }
193 }
194 }
195 }
196 }
197 }
198 }
199 }
200 }
201 }
202 }
203 }
204 }
205 }
206 }
207 }
208 }
209 }
210 }
211 }
212 }
213 }
214 }
215 }
216 }
217 }
218 }
219 }
220 }
221 }
222 }
223 }
224 }
225 }
226 }
227 }
228 }
229 }
230 }
231 }
232 }
233 }
234 }
235 }
236 }
237 }
238 }
239 }
240 }
241 }
242 }
243 }
244 }
245 }
246 }
247 }
248 }
249 }
250 }
251 }
252 }
253 }
254 }
255 }
256 }
257 }
258 }
259 }
260 }
261 }
262 }
263 }
264 }
265 }
266 }
267 }
268 }
269 }
270 }
271 }
272 }
273 }
274 }
275 }
276 }
277 }
278 }
279 }
280 }
281 }
282 }
283 }
284 }
285 }
286 }
287 }
288 }
289 }
290 }
291 }
292 }
293 }
294 }
295 }
296 }
297 }
298 }
299 }
300 }
301 }
302 }
303 }
304 }
305 }
306 }
307 }
308 }
309 }
310 }
311 }
312 }
313 }
314 }
315 }
316 }
317 }
318 }
319 }
320 }
321 }
322 }
323 }
324 }
325 }
326 }
327 }
328 }
329 }
330 }
331 }
332 }
333 }
334 }
335 }
336 }
337 }
338 }
339 }
340 }
341 }
342 }
343 }
344 }
345 }
346 }
347 }
348 }
349 }
350 }
351 }
352 }
353 }
354 }
355 }
356 }
357 }
358 }
359 }
360 }
361 }
362 }
363 }
364 }
365 }
366 }
367 }
368 }
369 }
370 }
371 }
372 }
373 }
374 }
375 }
376 }
377 }
378 }
379 }
380 }
381 }
382 }
383 }
384 }
385 }
386 }
387 }
388 }
389 }
390 }
391 }
392 }
393 }
394 }
395 }
396 }
397 }
398 }
399 }
400 }
401 }
402 }
403 }
404 }
405 }
406 }
407 }
408 }
409 }
410 }
411 }
412 }
413 }
414 }
415 }
416 }
417 }
418 }
419 }
420 }
421 }
422 }
423 }
424 }
425 }
426 }
427 }
428 }
429 }
430 }
431 }
432 }
433 }
434 }
435 }
436 }
437 }
438 }
439 }
440 }
441 }
442 }
443 }
444 }
445 }
446 }
447 }
448 }
449 }
450 }
451 }
452 }
453 }
454 }
455 }
456 }
457 }
458 }
459 }
460 }
461 }
462 }
463 }
464 }
465 }
466 }
467 }
468 }
469 }
470 }
471 }
472 }
473 }
474 }
475 }
476 }
477 }
478 }
479 }
480 }
481 }
482 }
483 }
484 }
485 }
486 }
487 }
488 }
489 }
490 }
491 }
492 }
493 }
494 }
495 }
496 }
497 }
498 }
499 }
500 }
501 }
502 }
503 }
504 }
505 }
506 }
507 }
508 }
509 }
510 }
511 }
512 }
513 }
514 }
515 }
516 }
517 }
518 }
519 }
520 }
521 }
522 }
523 }
524 }
525 }
526 }
527 }
528 }
529 }
530 }
531 }
532 }
533 }
534 }
535 }
536 }
537 }
538 }
539 }
540 }
541 }
542 }
543 }
544 }
545 }
546 }
547 }
548 }
549 }
550 }
551 }
552 }
553 }
554 }
555 }
556 }
557 }
558 }
559 }
560 }
561 }
562 }
563 }
564 }
565 }
566 }
567 }
568 }
569 }
570 }
571 }
572 }
573 }
574 }
575 }
576 }
577 }
578 }
579 }
580 }
581 }
582 }
583 }
584 }
585 }
586 }
587 }
588 }
589 }
590 }
591 }
592 }
593 }
594 }
595 }
596 }
597 }
598 }
599 }
600 }
601 }
602 }
603 }
604 }
605 }
606 }
607 }
608 }
609 }
610 }
611 }
612 }
613 }
614 }
615 }
616 }
617 }
618 }
619 }
620 }
621 }
622 }
623 }
624 }
625 }
626 }
627 }
628 }
629 }
630 }
631 }
632 }
633 }
634 }
635 }
636 }
637 }
638 }
639 }
640 }
641 }
642 }
643 }
644 }
645 }
646 }
647 }
648 }
649 }
650 }
651 }
652 }
653 }
654 }
655 }
656 }
657 }
658 }
659 }
660 }
661 }
662 }
663 }
664 }
665 }
666 }
667 }
668 }
669 }
670 }
671 }
672 }
673 }
674 }
675 }
676 }
677 }
678 }
679 }
680 }
681 }
682 }
683 }
684 }
685 }
686 }
687 }
688 }
689 }
690 }
691 }
692 }
693 }
694 }
695 }
696 }
697 }
698 }
699 }
700 }
701 }
702 }
703 }
704 }
705 }
706 }
707 }
708 }
709 }
710 }
711 }
712 }
713 }
714 }
715 }
716 }
717 }
718 }
719 }
720 }
721 }
722 }
723 }
724 }
725 }
726 }
727 }
728 }
729 }
730 }
731 }
732 }
733 }
734 }
735 }
736 }
737 }
738 }
739 }
740 }
741 }
742 }
743 }
744 }
745 }
746 }
747 }
748 }
749 }
750 }
751 }
752 }
753 }
754 }
755 }
756 }
757 }
758 }
759 }
760 }
761 }
762 }
763 }
764 }
765 }
766 }
767 }
768 }
769 }
770 }
771 }
772 }
773 }
774 }
775 }
776 }
777 }
778 }
779 }
780 }
781 }
782 }
783 }
784 }
785 }
786 }
787 }
788 }
789 }
790 }
791 }
792 }
793 }
794 }
795 }
796 }
797 }
798 }
799 }
800 }
801 }
802 }
803 }
804 }
805 }
806 }
807 }
808 }
809 }
810 }
811 }
812 }
813 }
814 }
815 }
816 }
817 }
818 }
819 }
820 }
821 }
822 }
823 }
824 }
825 }
826 }
827 }
828 }
829 }
830 }
831 }
832 }
833 }
834 }
835 }
836 }
837 }
838 }
839 }
840 }
841 }
842 }
843 }
844 }
845 }
846 }
847 }
848 }
849 }
850 }
851 }
852 }
853 }
854 }
855 }
856 }
857 }
858 }
859 }
860 }
861 }
862 }
863 }
864 }
865 }
866 }
867 }
868 }
869 }
870 }
871 }
872 }
873 }
874 }
875 }
876 }
877 }
878 }
879 }
880 }
881 }
882 }
883 }
884 }
885 }
886 }
887 }
888 }
889 }
890 }
891 }
892 }
893 }
894 }
895 }
896 }
897 }
898 }
899 }
900 }
901 }
902 }
903 }
904 }
905 }
906 }
907 }
908 }
909 }
910 }
911 }
912 }
913 }
914 }
915 }
916 }
917 }
918 }
919 }
920 }
921 }
922 }
923 }
924 }
925 }
926 }
927 }
928 }
929 }
930 }
931 }
932 }
933 }
934 }
935 }
936 }
937 }
938 }
939 }
940 }
941 }
942 }
943 }
944 }
945 }
946 }
947 }
948 }
949 }
950 }
951 }
952 }
953 }
954 }
955 }
956 }
957 }
958 }
959 }
960 }
961 }
962 }
963 }
964 }
965 }
966 }
967 }
968 }
969 }
970 }
971 }
972 }
973 }
974 }
975 }
976 }
977 }
978 }
979 }
980 }
981 }
982 }
983 }
984 }
985 }
986 }
987 }
988 }
989 }
990 }
991 }
992 }
993 }
994 }
995 }
996 }
997 }
998 }
999 }
1000 }

```

```

221 SecCtrlAttribute (panelMain, PANEL_MAIN_NUMERIC_Offset, ATTR_VISIBLE, 1);
222 SecCtrlAttribute (panelMain, PANEL_MAIN_NUMERIC_Offset, ATTR_VISIBLE, 1);
223 SecCtrlAttribute (panelMain, PANEL_MAIN_NUMERIC_Offset, ATTR_VISIBLE, 1);
224 //
225 SecCtrlAttribute (panelMain, PANEL_MAIN_RADIOBUTTON_Iconize, ATTR_VISIBLE, 1);
226 SecCtrlAttribute (panelMain, PANEL_MAIN_VIEWED_Dark, ATTR_VISIBLE, 1);
227 SecCtrlAttribute (panelMain, PANEL_MAIN_NUMERIC_RateOf_Change, ATTR_VISIBLE, 1);
228 SecCtrlAttribute (panelMain, PANEL_MAIN_NUMERIC_Offset_Dark, ATTR_VISIBLE, 1);
229 SecCtrlAttribute (panelMain, PANEL_MAIN_NUMERIC_Offset_Dark, ATTR_VISIBLE, 1);
230 SecCtrlAttribute (panelMain, PANEL_MAIN_NUMERIC_Offset_Dark, ATTR_VISIBLE, 1);
231 SecCtrlAttribute (panelMain, PANEL_MAIN_NUMERIC_Offset_Dark, ATTR_VISIBLE, 1);
232
233
234
235
236
237
238
239
240
241 int CVCOLORBACK UpdateBackground (int panel, int control, int event,
242 void *callBackData, int eventData1, int eventData2)
243 {
244 int i;
245 int iMethod;
246 switch (event)
247 {
248 case EVENT_COMMIT:
249 SecCtrl (panelMain, PANEL_MAIN_RADIOBUTTON_Icon, iMethod);
250 SecCtrlAttribute (panelMain, PANEL_MAIN_NUMERIC_RateOf_Change, iMethod);
251 SecCtrlAttribute (panelMain, PANEL_MAIN_NUMERIC_Offset, ATTR_VISIBLE, iMethod);
252 SecCtrlAttribute (panelMain, PANEL_MAIN_RADIOBUTTON_Iconize, ATTR_VISIBLE, iMethod);
253
254 }
255 break;
256
257 }
258 return 0;
259
260 int CVCOLORBACK UpdateColor (int panel, int control, int event,
261 void *callBackData, int eventData1, int eventData2)
262 {
263 switch (event)
264 {
265 case EVENT_COMMIT:
266
267 }
268 break;
269
270 }
271 return 0;
272
273 int CVCOLORBACK UpdateText (int panel, int control, int event,
274 void *callBackData, int eventData1, int eventData2)
275 {
276
277 }
278
279
280
281
282
283
284
285
286
287
288
289
290
291
292
293
294
295
296
297
298
299
300
301
302
303
304
305
306
307
308
309
310
311
312
313
314
315
316
317
318
319
320
321
322
323
324
325
326
327
328
329
330
331
332
333
334
335
336
337
338
339
340
341
342
343
344
345
346
347
348
349
350
351
352
353
354
355
356
357
358
359
360
361
362
363
364
365
366
367
368
369
370
371
372
373
374
375
376
377
378
379
380
381
382
383
384
385
386
387
388
389
390
391
392
393
394
395
396
397
398
399
400
401
402
403
404
405
406
407
408
409
410
411
412
413
414
415
416
417
418
419
420
421
422
423
424
425
426
427
428
429
430
431
432
433
434
435
436
437
438
439
440
441
442
443
444
445
446
447
448
449
450
451
452
453
454
455
456
457
458
459
460
461
462
463
464
465
466
467
468
469
470
471
472
473
474
475
476
477
478
479
480
481
482
483
484
485
486
487
488
489
490
491
492
493
494
495
496
497
498
499
500
501
502
503
504
505
506
507
508
509
510
511
512
513
514
515
516
517
518
519
520
521
522
523
524
525
526
527
528
529
530
531
532
533
534
535
536
537
538
539
540
541
542
543
544
545
546
547
548
549
550
551
552
553
554
555
556
557
558
559
560
561
562
563
564
565
566
567
568
569
570
571
572
573
574
575
576
577
578
579
580
581
582
583
584
585
586
587
588
589
590
591
592
593
594
595
596
597
598
599
600
601
602
603
604
605
606
607
608
609
610
611
612
613
614
615
616
617
618
619
620
621
622
623
624
625
626
627
628
629
630
631
632
633
634
635
636
637
638
639
640
641
642
643
644
645
646
647
648
649
650
651
652
653
654
655
656
657
658
659
660
661
662
663
664
665
666
667
668
669
670
671
672
673
674
675
676
677
678
679
680
681
682
683
684
685
686
687
688
689
690
691
692
693
694
695
696
697
698
699
700
701
702
703
704
705
706
707
708
709
710
711
712
713
714
715
716
717
718
719
720
721
722
723
724
725
726
727
728
729
730
731
732
733
734
735
736
737
738
739
740
741
742
743
744
745
746
747
748
749
750
751
752
753
754
755
756
757
758
759
760
761
762
763
764
765
766
767
768
769
770
771
772
773
774
775
776
777
778
779
780
781
782
783
784
785
786
787
788
789
790
791
792
793
794
795
796
797
798
799
800
801
802
803
804
805
806
807
808
809
810
811
812
813
814
815
816
817
818
819
820
821
822
823
824
825
826
827
828
829
830
831
832
833
834
835
836
837
838
839
840
841
842
843
844
845
846
847
848
849
850
851
852
853
854
855
856
857
858
859
860
861
862
863
864
865
866
867
868
869
870
871
872
873
874
875
876
877
878
879
880
881
882
883
884
885
886
887
888
889
890
891
892
893
894
895
896
897
898
899
900
901
902
903
904
905
906
907
908
909
910
911
912
913
914
915
916
917
918
919
920
921
922
923
924
925
926
927
928
929
930
931
932
933
934
935
936
937
938
939
940
941
942
943
944
945
946
947
948
949
950
951
952
953
954
955
956
957
958
959
960
961
962
963
964
965
966
967
968
969
970
971
972
973
974
975
976
977
978
979
980
981
982
983
984
985
986
987
988
989
990
991
992
993
994
995
996
997
998
999
1000

```